

nature

HUMAN DATA

Computational social science offers fresh perspectives on people and society



Coronavirus

Open or closed – the scientific debate over schools and COVID

Urban planning

Diverse supply lines help protect cities from food shortages

Protective effect

Promising early results for malaria vaccine that uses live parasites

Nature.2021.07.10

[Sat, 10 Jul 2021]

- [This Week](#)
- [News in Focus](#)
- [Opinion](#)
- [Work](#)
- [Research](#)
- [Amendments & Corrections](#)

| [Next section](#) | [Main menu](#) |

Donation

| [Next section](#) | [Main menu](#) |

This Week

- **[The powers and perils of using digital data to understand human behaviour](#)** [01 July 2021]
Editorial • Computational social science is a powerful research tool. But it needs its different disciplines to find a common language.
- **[Research managers are essential to a healthy research culture](#)** [07 July 2021]
Editorial • But for maximal benefit, more of these academic administrators need to get involved in the scholarly aspect of research.
- **[Beware performative reproducibility](#)** [06 July 2021]
World View • Well-meant changes to improve science could become empty gestures unless underlying values change.
- **[A piece of Triassic poo yields a beautifully preserved beetle](#)**
[30 June 2021]
Research Highlight • The dung of a dinosaur-like animal that lived more than 200 million years ago springs a surprise: a new insect species.
- **[Scraping icebergs trigger sea-floor landslides — and the risk is growing](#)** [01 July 2021]
Research Highlight • Climate change will allow more chunks of ice to break away from melting glaciers, with potentially grave effects.
- **[When was cosmic dawn? Some of the most distant galaxies known hold a clue](#)** [29 June 2021]
Research Highlight • Light from the early days of the Universe helps to pin-point when the stars switched on after the Big Bang.
- **[The ‘time neurons’ that help the brain keep track](#)** [30 June 2021]
Research Highlight • Cells in the hippocampus play a part in time-stamping unfolding events.
- **[Tracking a photon without leaving a trace](#)** [30 June 2021]
Research Highlight • Conventional detectors often obliterate photons, but the particles can escape a vacuum-based device unscathed.

- **Supersonic strikes leave just a dent in this super-light material** [30 June 2021]
Research Highlight • Honeycomb-like structure thwarts a projectile travelling as fast as a speeding bullet.
- **A hunter-gather's tooth yields the oldest known strain of plague** [29 June 2021]
Research Highlight • Genomic analysis suggests that the Black Death began as a less virulent and less transmissible disease.

| [Next section](#) | [Main menu](#) | [Previous section](#) |

- EDITORIAL
- 01 July 2021

The powers and perils of using digital data to understand human behaviour

Computational social science is a powerful research tool. But it needs its different disciplines to find a common language.





•

[Download PDF](#)



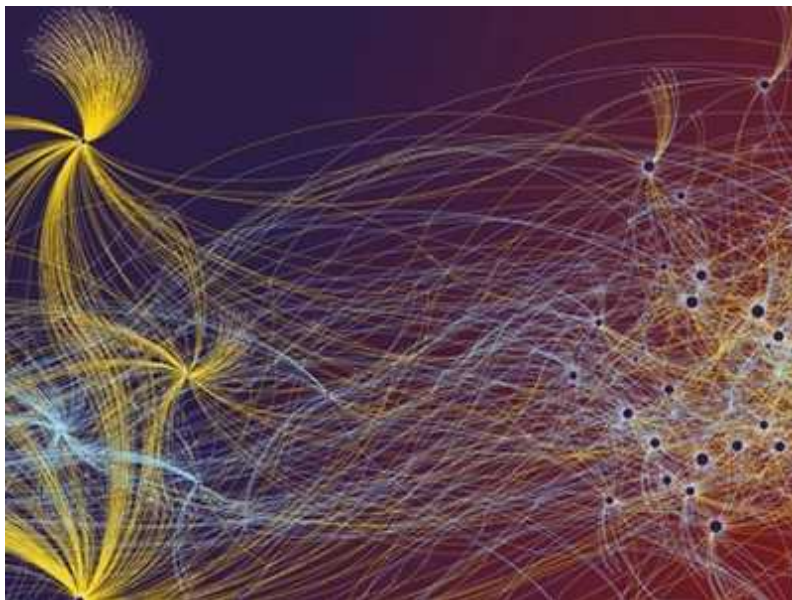
Computational social scientists have been using data from mobile phones to study the coronavirus pandemic. Credit: Paul Seheult/Eye Ubiquitous/Universal Images Group/Getty

What are the causes of vaccine hesitancy? How can people be encouraged to exercise more? What can governments do to improve the well-being of citizens?

Social scientists researching these questions observe how people behave, record data on those behaviours and then augment this knowledge by interviewing and/or polling those whom they are studying. Carrying out research in this way is a time-consuming and manual process. Moreover, it is difficult to obtain large amounts of data simultaneously.

But now, researchers have access to an unprecedented amount of social data, generated every second by continuous interactions on digital devices or platforms. These include data that trace people's movements, purchases and online social interactions — which are all proving extraordinarily powerful for research. As a result, work weaving large data analysis with social

questions, known as computational social science, has witnessed [huge growth in recent years](#).



[Nature special: Computational social science](#)

During the course of the coronavirus pandemic alone, researchers have been able to access millions of mobile-phone records to study how people's movement changed during the pandemic and the impact of those changes on how SARS-CoV-2 spread. They have been able to access anonymized credit-card purchase histories to study how people are spending money during the pandemic — information which is then used to understand how COVID-19 is affecting various sectors of the economy.

Using computers to analyse large data sets dates back to the earliest mainframe computers — and has been central to the work of actuaries and national statistics offices, both of which have long been important resources for studies of society and people. But the wealth of real-time and individual-level information is now unparalleled in its power to track trends, make predictions and inform decisions. And its availability puts it in reach of practically every social-science discipline: researchers in fields from psychology to economics and political science can now rely on data to enhance investigations of key societal questions.

Power and responsibility

At the same time, researchers need to remember that gathering and sharing such personal data — practices that are currently largely unregulated — pose many challenges to society. These include risks from increased surveillance, and the danger that people could be reidentified from otherwise anonymized data.



[Everyone should decide how their digital data are used — not just tech companies](#)

There are also concerns that people whose data are being used have not fully consented to this — and wider worries about the economic monopoly of tech corporations that own the majority of the data. These digital traces tend to be left disproportionately by relatively wealthy people in developed countries, biasing attempts to draw global conclusions. Acknowledging and working with these issues is key to ethical computational social science that promotes real societal progress.

The need to blend expertise in the social sciences with the skills required to collect, clean and analyse large data sets means that computational social science requires teams of researchers who can field a remarkably diverse set

of expertise and skills. But with collaborations across disciplines come other challenges.

This week, *Nature* is publishing a [special collection of articles](#) with the objective of bridging the research disciplines and perspectives on doing science that underpin computational social science. We're highlighting ways in which communities of social, natural and computational scientists can learn to better work together, to complement each other and overcome shared challenges.

Stronger bridges

To begin with, the varied disciplines need to overcome language barriers in which the same terms have different meanings. For example, in many of the social sciences (such as psychology and sociology), ‘prediction’ often refers to a correlation; in the physical sciences (such as physics, computer science and engineering), it usually means a forecast. True transdisciplinary research requires scientists first to learn each other’s languages, and then to develop a shared understanding of terms.

But the divide can run deeper than language, into how to curate, analyse and interpret data to explain a phenomenon. Jake Hofman at Microsoft Research in New York City and colleagues argue that computational social science could [most effectively answer research questions by combining complementary approaches](#). For example, researchers building a numerical forecast on, say, the causes of traffic jams would assemble data on traffic flows, with insights from drivers on their reasons for taking particular routes.



The battle for ethical AI at the world's biggest machine-learning conference

The results of any study are determined by not only the analytical strategies used, but also the quality of the data — and this becomes particularly delicate when dealing with social data. The vast amounts of available data that make computational social science possible — such as tweets or location data from phones — are usually not gathered for research purposes and so can easily be misinterpreted.

That is why, as David Lazer at Northeastern University in Boston, Massachusetts, and colleagues write, researchers who work with large data sets [must resist drawing conclusions from just the trends or patterns seen in the numbers](#) — and should account for factors that could affect a result. To extract real meaning from data, researchers need to ensure that they carefully define the objects of their measurement according to theory, validate them and interpret them appropriately.

The [widespread influence of algorithms is another source of potential error](#), as Claudia Wagner at the Leibniz Institute for the Social Sciences in Mannheim, Germany, and colleagues explain. They note that the algorithms that pervade our societies influence individual and group behaviour in many ways — meaning that any observations describe not just human behaviour, but also the effects of algorithms on how people behave. They argue that the theories that inform social science need to be updated to acknowledge these

influences; without these theories and a clear understanding of the impact of algorithms on the available data, researchers will not be able to draw meaningful conclusions.

Yet another complicating factor for computational social science is that large data sets are often the private property of commercial enterprises. Academic scientists need to liaise with corporations to obtain access, and this might introduce even more bias. This is partly because, for companies, data are valuable — and therefore sharing data is a risk to their bottom line. That is among the reasons [why firms tend to restrict what they share](#), as Jathan Sadowski at Monash University in Melbourne, Australia, and colleagues highlight. But in light of the potential of these data to provide societal benefits, companies — together with academic researchers and public bodies — need to collectively engage with these questions and set standards for quality, access and data ownership.

Ways forward

There are ways to obtain data that are can be useful and reliable, as Mirta Galesic at the Santa Fe Institute in New Mexico and colleagues describe in an [article on ‘human social sensing’](#). This is the study of how individuals gather information on others in their social networks. For instance, researchers could predict a swing in political opinions by interviewing people and asking them what their friends are talking about. Gathering data about people from other people can help to avoid some of the biases seen in self-reported data, and has the added benefit of generating anonymous data: the researchers never need to know any personal or sensitive details about the people whom they are receiving information about.



[COVID-19 recovery: science isn't enough to save us](#)

Another area ripe for growth lies in the intersection of infectious-disease modelling and behavioural science. As Caroline Buckee of the Harvard T. H. Chan School of Public Health in Boston and colleagues argue, an accurate model of contagion and infection [requires researchers to understand the cultures and behaviours of people](#) who have been — or might be — infected. It is hard to predict a disease's path without considering these and other social aspects of transmission. Structured and widespread collaborations cutting across disciplines are key to achieving this.

The pandemic has shown how lives can be saved when large-scale data sets are harnessed for science. This potential is only starting to be realized as researchers with backgrounds in computer science or applied mathematics join with social scientists. These relationships must deepen and encompass researchers in more fields — such as ethics, responsible research and science and technology studies — to ensure that we avoid known pitfalls and that we use these data in a way that maximizes gained knowledge and minimizes potential harm.

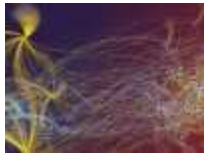
Transdisciplinary co-working is rarely easy, but it is essential for both better decisions and robust outcomes. *Nature* is committed to fostering this conversation, helping scientists to learn each other's languages so that

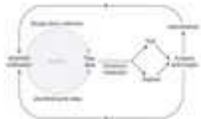
researchers can together make more progress on some of societies' most pressing problems.

Nature **595**, 149-150 (2021)

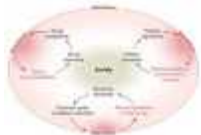
doi: <https://doi.org/10.1038/d41586-021-01736-y>

Related Articles

-  [Nature special: Computational social science](#)
-  [The battle for ethical AI at the world's biggest machine-learning conference](#)
-  [Everyone should decide how their digital data are used — not just tech companies](#)
-  [COVID-19 recovery: science isn't enough to save us](#)
-  [The physics of data](#)



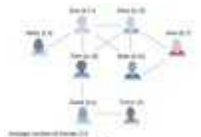
- Meaningful measures of human society in the twenty-first century



- Measuring algorithmically infused societies



- Thinking clearly about social aspects of infectious disease transmission



- Human social sensing is an untapped resource for computational social science
- Integrating explanation and prediction in computational social science

Subjects

- Computer science
- Society
- Databases
- Ethics
- Policy
- SARS-CoV-2

nature careers

[Jobs](#) >

- [**Canada Research Chair Tier 2 in Indigenous Natural Sciences**](#)

The University of British Columbia (UBC)
Vancouver, Canada

- [**Chemical/Environmental Engineer – Gas Chromatography and Mass Spectrometry**](#)

Jülich Research Centre (FZJ)
Jülich, Germany

- [**Chemical Technical Assistant \(m/f/d\)**](#)

Alfred Wegener Institute - Helmholtz Centre for Polar and Marine Research (AWI)

Bremerhaven, Germany

- [**Abteilungsassistent*in \(d/m/w\), Abteilung „IT“**](#)

Helmholtz Centre for Heavy Ion Research GmbH (GSI)
Darmstadt, Germany

[Download PDF](#)

Related Articles



- [**Nature special: Computational social science**](#)



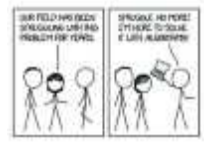
- The battle for ethical AI at the world's biggest machine-learning conference



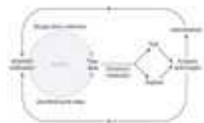
- Everyone should decide how their digital data are used — not just tech companies



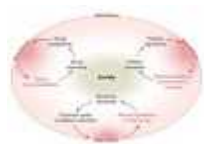
- COVID-19 recovery: science isn't enough to save us



- The physics of data



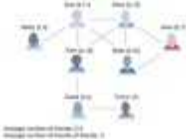
- Meaningful measures of human society in the twenty-first century



- Measuring algorithmically infused societies



- Thinking clearly about social aspects of infectious disease transmission



- [Human social sensing is an untapped resource for computational social science](#)
- [Integrating explanation and prediction in computational social science](#)

Subjects

- [Computer science](#)
- [Society](#)
- [Databases](#)
- [Ethics](#)
- [Policy](#)
- [SARS-CoV-2](#)

This article was downloaded by **calibre** from <https://www.nature.com/articles/d41586-021-01736-y>.

| [Section menu](#) | [Main menu](#) |

- EDITORIAL
- 07 July 2021

Research managers are essential to a healthy research culture

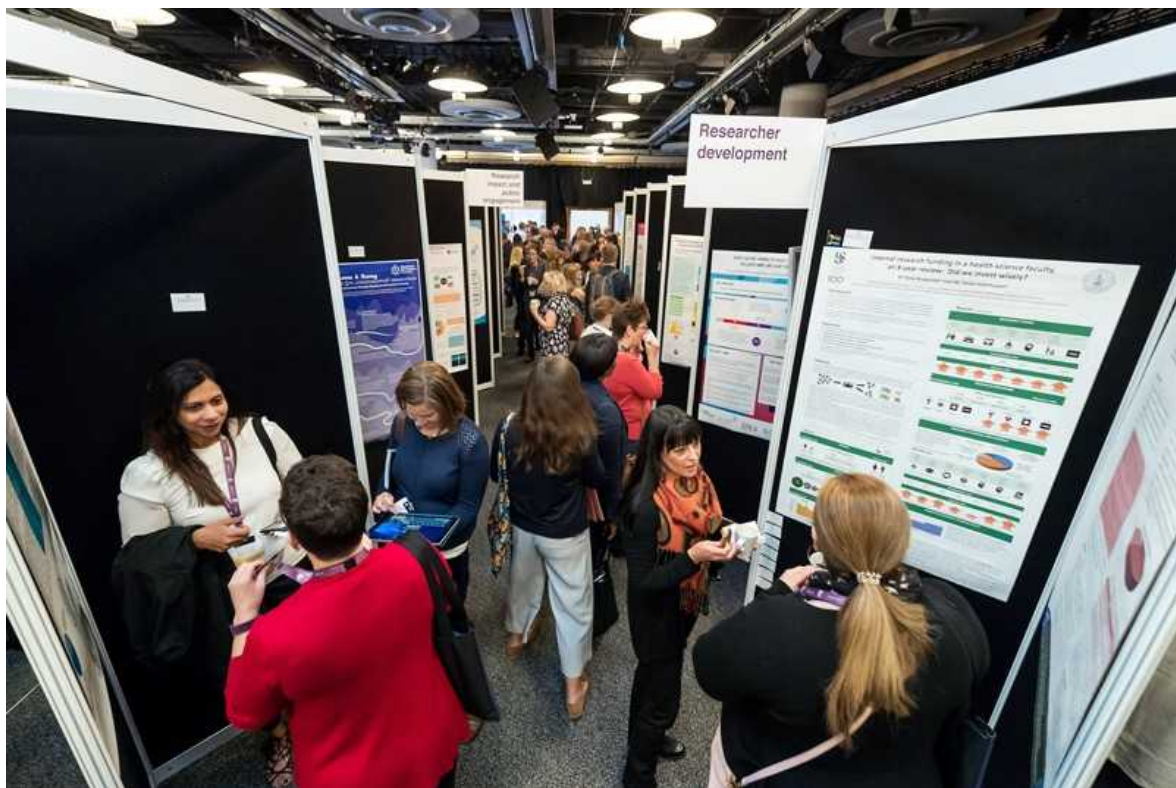
But for maximal benefit, more of these academic administrators need to get involved in the scholarly aspect of research.





•

[Download PDF](#)



A poster session at an international conference for research managers in Edinburgh in 2018. More academic administrators are getting involved with the scholarly side of their subject.Credit: Malcolm Cochrane Photography

In the space of three decades, academic research management has become an attractive career prospect for researchers around the world. Once focused principally on helping academics to manage funding, research managers and administrators (RMAs) are now part of a globally recognized profession that spans the research spectrum. There are some 20,000 RMAs working in universities; most are in high-income countries, but expansion is under way in lower-income nations, particularly in Africa.

The role has evolved as research has become more complex, and this, in turn, is attracting more candidates with research-level qualifications and experience. Today's managers and administrators need knowledge and experience of open science, equality and diversity, ethics and public engagement — as well as of more conventional areas such as accounting, project management and research policy.

RMA courses and qualifications are now offered by universities and by some of the 20 national and regional professional associations belonging to the International Network of Research Management Societies (INORMS).



'We're problem solvers': research administrators offer guidance to working scientists

But, as we [report in this issue](#), tensions between RMAs and the researchers they work with are not uncommon. There are still those who regard the academic as 'king' and the RMA as little more than research support. Meanwhile, at some institutions, university leaders expect RMAs to monitor academics' performance metrics — such as targets for publishing and research income — which can be [stressful for both researchers and managers](#).

As a result, RMAs and their professional organizations are becoming advocates for responsible research. And they are embracing the academic study of research management and administration. This is helping to establish good practice, as well as professional standards that can be used to hold universities and publishers to account.

For example, members of INORMS are taking a lead in addressing how university league tables might be improved to [make them fairer and more transparent](#). And the UK research managers association, ARMA, has been

involved in an independent review on the use of metrics in research evaluation, a project called the Metric Tide. This year also saw the launch by management professionals of the *Journal of Research Management and Administration*.

These are welcome developments. RMAs are crucial to the research enterprise. Moreover, their involvement in active scholarship is essential to achieving the aims set out above. Researchers and managers must work collegially and respectfully to make the research environment happier and more productive.

Nature **595**, 150 (2021)

doi: <https://doi.org/10.1038/d41586-021-01823-0>

Related Articles

-  [**‘We’re problem solvers’: research administrators offer guidance to working scientists**](#)
-  [**Row erupts over university’s use of research metrics in job-cut decisions**](#)
-  [**University rankings need a rethink**](#)
-  [**Calls for culture change as “them versus us” mindset drives rift between academic and non-academic**](#)

staff

Subjects

- [Careers](#)
- [Research management](#)
- [Lab life](#)

nature careers

Jobs >

- [Canada Research Chair Tier 2 in Indigenous Natural Sciences](#)

The University of British Columbia (UBC)

Vancouver, Canada

- [Chemical/Environmental Engineer – Gas Chromatography and Mass Spectrometry](#)

Jülich Research Centre (FZJ)

Jülich, Germany

- [Chemical Technical Assistant \(m/f/d\)](#)

Alfred Wegener Institute - Helmholtz Centre for Polar and Marine Research (AWI)

Bremerhaven, Germany

- [Abteilungsassistent*in \(d/m/w\), Abteilung „IT“](#)

Helmholtz Centre for Heavy Ion Research GmbH (GSI)

Darmstadt, Germany

[Download PDF](#)

Related Articles



- [**‘We’re problem solvers’: research administrators offer guidance to working scientists**](#)



- [**Row erupts over university’s use of research metrics in job-cut decisions**](#)



- [**University rankings need a rethink**](#)



- [**Calls for culture change as “them versus us” mindset drives rift between academic and non-academic staff**](#)

Subjects

- [**Careers**](#)
- [**Research management**](#)
- [**Lab life**](#)

| [Section menu](#) | [Main menu](#) |

- WORLD VIEW
- 06 July 2021

Beware performative reproducibility



Well-meant changes to improve science could become empty gestures unless underlying values change.

- [Stuart Buck](#) 0

1. [Stuart Buck](#)

1. Stuart Buck was vice-president of research at Arnold Ventures in Houston, Texas, from 2012 to 2021. He is now a consultant on rigorous research practices.

[View author publications](#)

You can also search for this author in [PubMed](#) [Google Scholar](#)





•

[Download PDF](#)

Almost a decade ago, at Arnold Ventures — a US\$2-billion philanthropic organization in Houston, Texas — we realized that using evidence to direct our giving required having more confidence in the evidence itself. As vice-president of research, I found myself deep in efforts to improve science, dispersing more than \$60 million in grants to make sure researchers can build on others' results. I was part of the discussions that led to widely adopted guidelines promoting transparency and openness, the clinical-trial repository Vivli and the launch of the Center for Open Science, a non-profit organization in Charlottesville, Virginia.

I've seen much positive change since then. But sometimes I worry that we might end up with the worst of all worlds: the pretence of reproducibility without the reality.

In 2012, very few people had even heard of preregistration, the anti-bias practice of specifying, in writing, intended analyses and hypotheses at the start of an experiment. Doing so was a requirement for our grantees.

These days, it seems all scientists know what preregistration is. Most agree that it can help to reduce publication bias and *P*-hacking — when data are tweaked to produce significant *P* values. Major professional societies now endorse the practice: the American Economic Association's registry lists more than 4,700 studies, and the American Psychological Association has created a set of 'Preregistration Standards for Quantitative Research in Psychology'. Indeed, there are some 75,000 registered research projects on the Center for Open Science's Open Science Framework repository.



[Our obsession with eminence warps research](#)

A similar story can be told about data-sharing through Zenodo from CERN, Europe's particle-physics laboratory near Geneva, Switzerland; Figshare from London-based analytics firm Digital Science; many National Institutes of Health repositories; and more. Although still far from routine in many disciplines, the rate at which scholarly articles share their underlying data is

growing: one study put it at increasing from around 0% in 2000 to almost 20% in 2018 ([S. Serghiou et al. PLoS Biol. 19, e3001107; 2021](#)).

But robust, sustainable change depends on whether underlying cultural values have altered, not just surface signals. If they haven't, then open-science practices can become just another hoop to jump through, a form of virtue signalling or a smokescreen.

I've seen it happen. At a conference a few months before the pandemic, a scholar told me how, in his department, everyone wrote lengthy pre-analysis plans that would, in theory, constrain *P*-hacking. In practice, he admitted, researchers could give cherry picking free rein, counting on the fact that no one has the time or patience to read a 100-page pre-analysis plan and compare it with the later publication.

More-systematic evidence comes from the COMParé Project led by Ben Goldacre at the University of Oxford, UK, an effort my department funded. That team reviewed publications from 67 clinical trials in top medical journals, and compared them against original descriptions. Only 9 matched. Of the others, 354 preregistered outcomes went unreported; another 357 outcomes were “silently added” ([B. Goldacre et al. Trials 20, 118; 2019](#)).



[A controlled trial for reproducibility](#)

Meanwhile, many preregistrations are too vague. In one study, reviewers were asked to count the number of hypotheses in 106 preregistrations. They agreed only 14% of the time ([M. Bakker et al. PLoS Biol. 18, e3000937; 2020](#)).

What about data sharing? The FAIR principles stipulate that shared data should be ‘findable, accessible, interoperable and reusable’. A 2020 analysis across 15 psychology journals concluded that the majority of data sets “were neither complete nor re-usable” ([J. N. Towse et al. Behav. Res. <https://doi.org/gkzk>; 2020](#)).

I worry that, by adopting the trappings of reproducibility, poor-quality work can look as if it has engaged in best practices. The problem is that sloppy work is driven by a scientific culture that overemphasizes exciting findings. When funders and journals reward showy claims at the expense of rigorous methods and reproducible results, reforms to change practice could become self-defeating. Helpful new practices, rules and policies are transformed into meaningless formalities on the way to continuing to grab headlines at any cost.

That said, I do see values shifting. In the first few years that Arnold Ventures began supporting these efforts, some researchers reacted with open hostility, using phrases such as “replication police”. Now such criticism is rare (at least in public). And in some communities, researchers now prioritize work that others can build on. For example, organizations such as the Society for Improving Psychological Science embody a groundswell of energy and idealism from mostly younger researchers.

Still, what really matters is whether scientists feel empowered and rewarded for doing robust work, publishing null results and following the data. Idealism from early-career scientists must be matched by strong signals from senior leaders and institutions that it is possible to be hired and get tenure while engaging in best practices. A hopeful sign is that some university job advertisements now ask about an applicant’s commitment to open-science practices.

That sort of cultural change is where the real challenge lies.

Nature **595**, 151 (2021)

doi: <https://doi.org/10.1038/d41586-021-01824-z>

Competing Interests

The author declares no competing interests.

Related Articles



- [Raising research quality will require collective action](#)



- [A controlled trial for reproducibility](#)



- [Five ways China must cultivate research integrity](#)



- [Our obsession with eminence warps research](#)

Subjects

- [Research management](#)
- [Institutions](#)

Jobs >

- [Canada Research Chair Tier 2 in Indigenous Natural Sciences](#)

The University of British Columbia (UBC)

Vancouver, Canada

- [Chemical/Environmental Engineer – Gas Chromatography and Mass Spectrometry](#)

Jülich Research Centre (FZJ)

Jülich, Germany

- [Chemical Technical Assistant \(m/f/d\)](#)

Alfred Wegener Institute - Helmholtz Centre for Polar and Marine Research (AWI)

Bremerhaven, Germany

- [Abteilungsassistent*in \(d/m/w\), Abteilung „IT“](#)

Helmholtz Centre for Heavy Ion Research GmbH (GSI)

Darmstadt, Germany

[Download PDF](#)

Related Articles



- Raising research quality will require collective action



- A controlled trial for reproducibility



- Five ways China must cultivate research integrity



- Our obsession with eminence warps research

Subjects

- Research management
- Institutions

This article was downloaded by **calibre** from <https://www.nature.com/articles/d41586-021-01824-z>



Scat surprise: scientists discovered the beetle species *Triamyxa coprolithica* in the petrified droppings of a dinosaur-like animal. Credit: M. Qvarnström *et al./Curr. Biol.* ([CC BY 4.0](#))

Palaeontology

30 June 2021

A piece of Triassic poo yields a beautifully preserved beetle

The dung of a dinosaur-like animal that lived more than 200 million years ago springs a surprise: a new insect species.





•

Treasures sometimes hide in the most unappealing places. Palaeontologists have discovered a 230-million-year-old beetle species in a piece of fossilized poo that was probably produced by a dinosaur relative.

Martin Qvarnström at Uppsala University in Sweden and his colleagues used powerful X-rays to scan a small fragment of fossilized animal dung unearthed in southern Poland. The faeces are thought to belong to *Silesaurus opolensis*, a beaked dinosaur ancestor that lived in the region during the Triassic era, which spanned the period from about 250 million to 200 million years ago.

The researchers found that the excrement contains almost complete fossils of a previously unknown insect species. The creature, which the team named *Triamyxa coprolithica*, measures about 1.5 millimetres in length and is the only known member of an extinct family of beetles whose modern relatives live on algae. Like its contemporary cousins, the ancient beetle might also have lived in wet environments.

Insect fragments have previously been found in fossilized faeces from vertebrates, but this is the first time that researchers have found intact insects. Studying preserved pieces of dung could help scientists to learn more about insect evolution and food webs of the past, the authors say.

[Curr. Biol. \(2021\)](#)

- [Palaeontology](#)
-

This article was downloaded by **calibre** from <https://www.nature.com/articles/d41586-021-01756-8>

| [Section menu](#) | [Main menu](#) |



Data collected by the Canadian Coast Guard Ship *Hudson* helped to determine that an iceberg (pictured) triggered an underwater landslide in early September 2018. Credit: A. Normandeau *et al.*/*Nature Geosci.*

Ocean sciences

01 July 2021

Scraping icebergs trigger sea-floor landslides — and the risk is growing

Climate change will allow more chunks of ice to break away from melting glaciers, with potentially grave effects.





•

When icebergs gouge the sea floor, they can trigger submarine landslides that pose a threat to underwater infrastructure such as the cables underpinning the global Internet.

Submarine landslides are often orders of magnitude larger than their counterparts on land. Some have been linked to earthquakes, but determining their cause remains difficult.

Alexandre Normandeau at the Geological Survey of Canada in Dartmouth and his colleagues used sonar to document changes in the sea floor at Canada's Baffin Island. They determined that a submarine landslide occurred between 4 and 9 September 2018 — at the precise location where

satellite imagery captured an iceberg running aground, capsizing and breaking in two in the same month. No major earthquakes took place nearby during this period.

The team analysed sediment collected near the landslide's location in August 2018 and determined that the iceberg's impact could have been large enough to cause the collapse of the otherwise stable sea floor.

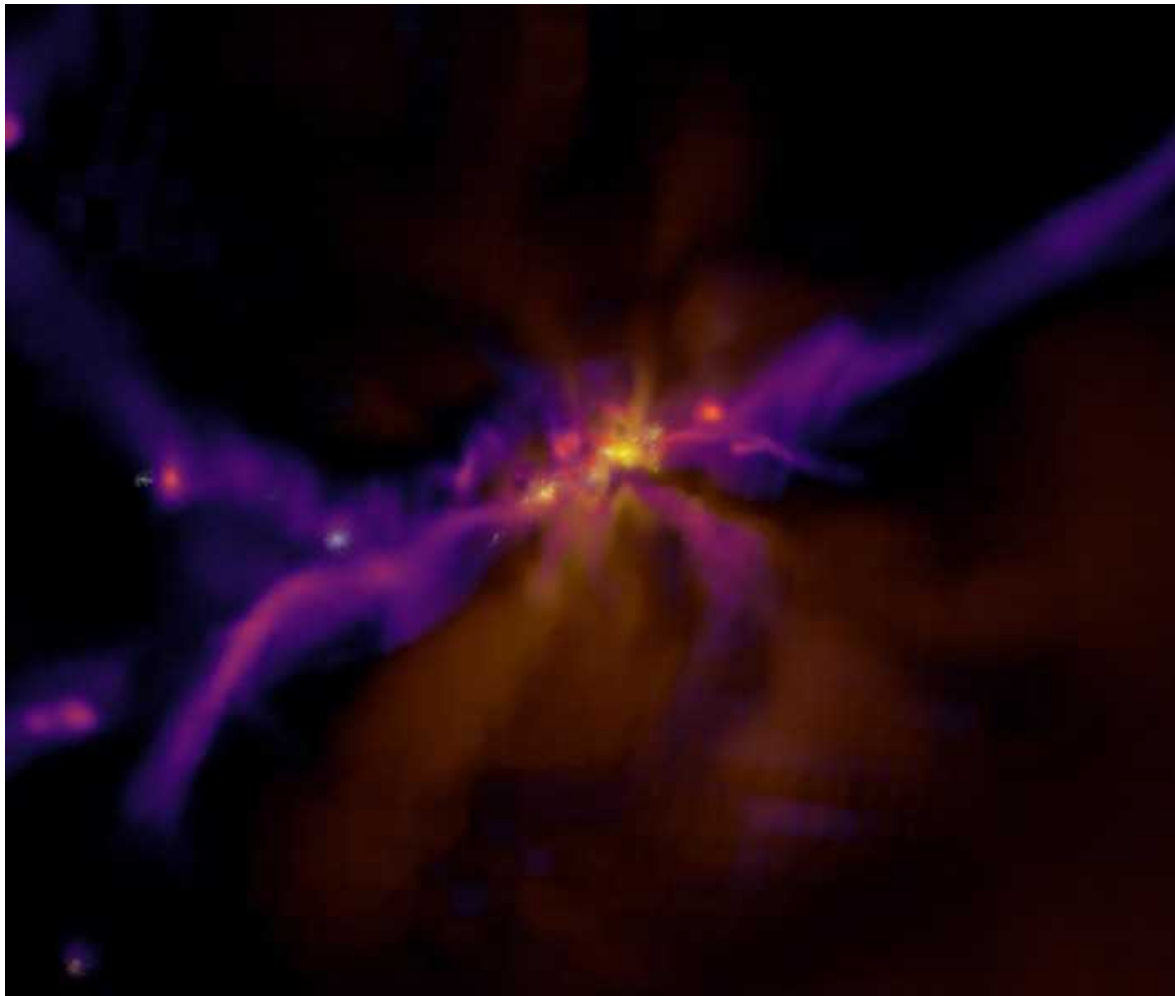
The results suggest that icebergs in Antarctica, Greenland and the Arctic could present a more significant threat than previously believed as the planet warms and more icebergs break free from melting glaciers.

[Nature Geosci. \(2021\)](#)

- [Ocean sciences](#)

This article was downloaded by **calibre** from <https://www.nature.com/articles/d41586-021-01768-4>

| [Section menu](#) | [Main menu](#) |



A snapshot of galaxies and stars evolving a few hundred million years after the Big Bang (image extracted from a simulation). Gas filaments are depicted in purple, starlight in white, and highly energetic radiation from the most massive stars in yellow. Credit: Harley Katz, Beecroft Fellow/Univ. Oxford

Astronomy and astrophysics

29 June 2021

When was cosmic dawn? Some of the most distant galaxies known hold a clue

Light from the early days of the Universe helps to pin-point when the stars switched on after the Big Bang.





•

If you know someone's age, it's easy to work out when they were born. Now astronomers have performed that same calculation for some of the Universe's most ancient galaxies. That has allowed them to estimate the timing of cosmic dawn — the period when the very first stars appeared.

Nicolas Laporte at the University of Cambridge, UK, and his colleagues examined six galaxies that had previously been identified as potentially ancient. To estimate the galaxies' age, the team studied the starlight coming from them, looking for a hydrogen signature that becomes more pronounced as the stars in a galaxy age. The group also determined that light from some of the galaxies had travelled for more than 13 billion years before it reached

Earth, which means we are seeing them as they were less than 550 million years after the Big Bang.

Taken together, the two measurements suggest that the first stars in these galaxies lit up when the Universe was between 250 million and 350 million years old.

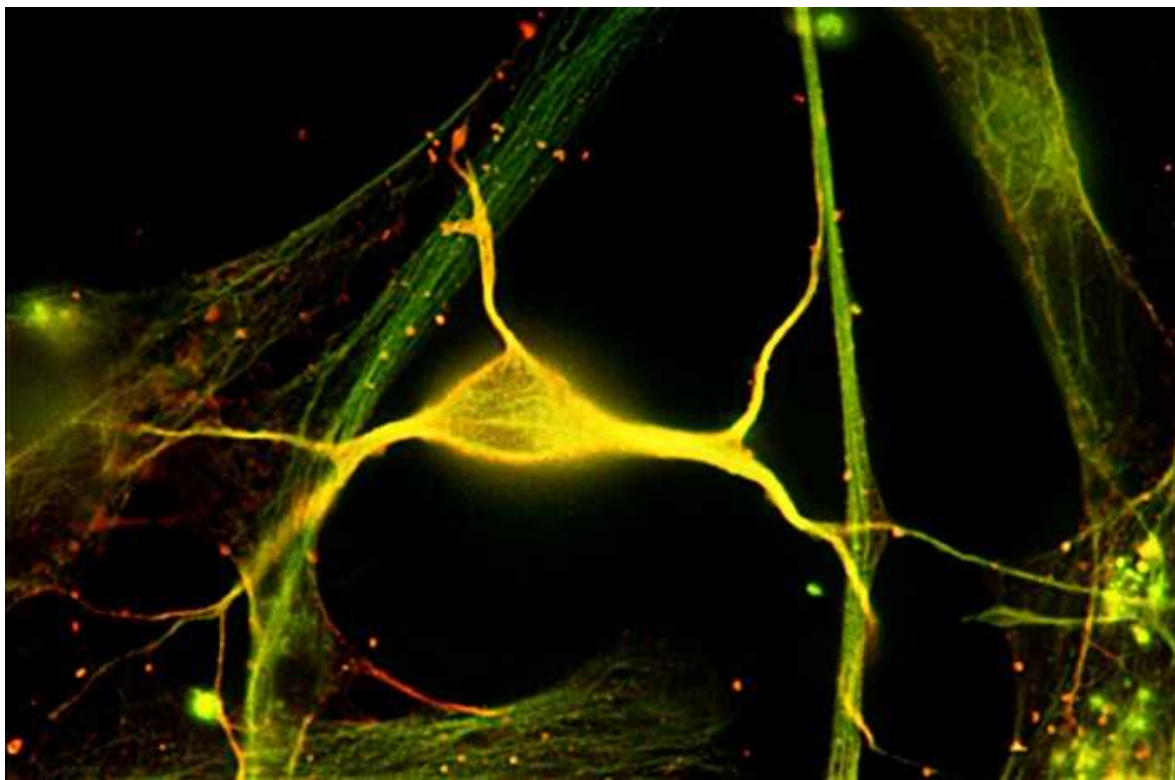
The authors expect NASA's James Webb Space Telescope, which is due to launch late this year, to be able to see galaxies such as these in their earliest stages of formation.

[Mon. Not. R. Astron. Soc. \(2021\)](#)

- [Astronomy and astrophysics](#)

This article was downloaded by **calibre** from <https://www.nature.com/articles/d41586-021-01766-6>

| [Section menu](#) | [Main menu](#) |



A cell in the brain region called the hippocampus, which contains neurons that can encode information about elapsed time. Credit: Robert McNeil, Baylor College of Medicine/SPL

Neuroscience

30 June 2021

The ‘time neurons’ that help the brain keep track

Cells in the hippocampus play a part in time-stamping unfolding events.





•

To recall a past experience, we need to piece together when specific events happened and in what order. Now, scientists have confirmed that humans have “time neurons” that encode this information.

Rodents have long been known to have time-keeping cells in the hippocampus, a seahorse-shaped brain structure that has an essential role in memory. To look for similar cells in humans, Leila Reddy at the French national research agency CNRS in Toulouse and her colleagues recorded electrical activity in the hippocampal neurons of volunteers while the volunteers memorized a series of images and were quizzed, periodically, on which image came next in the sequence.

The researchers pinpointed a subset of neurons that fired one after the other during the approximately 6.5-second intervals between quizzes. These neurons showed similar patterns of activity during gaps when participants stared at a blank screen, suggesting that they were encoding time, rather than other information about the task.

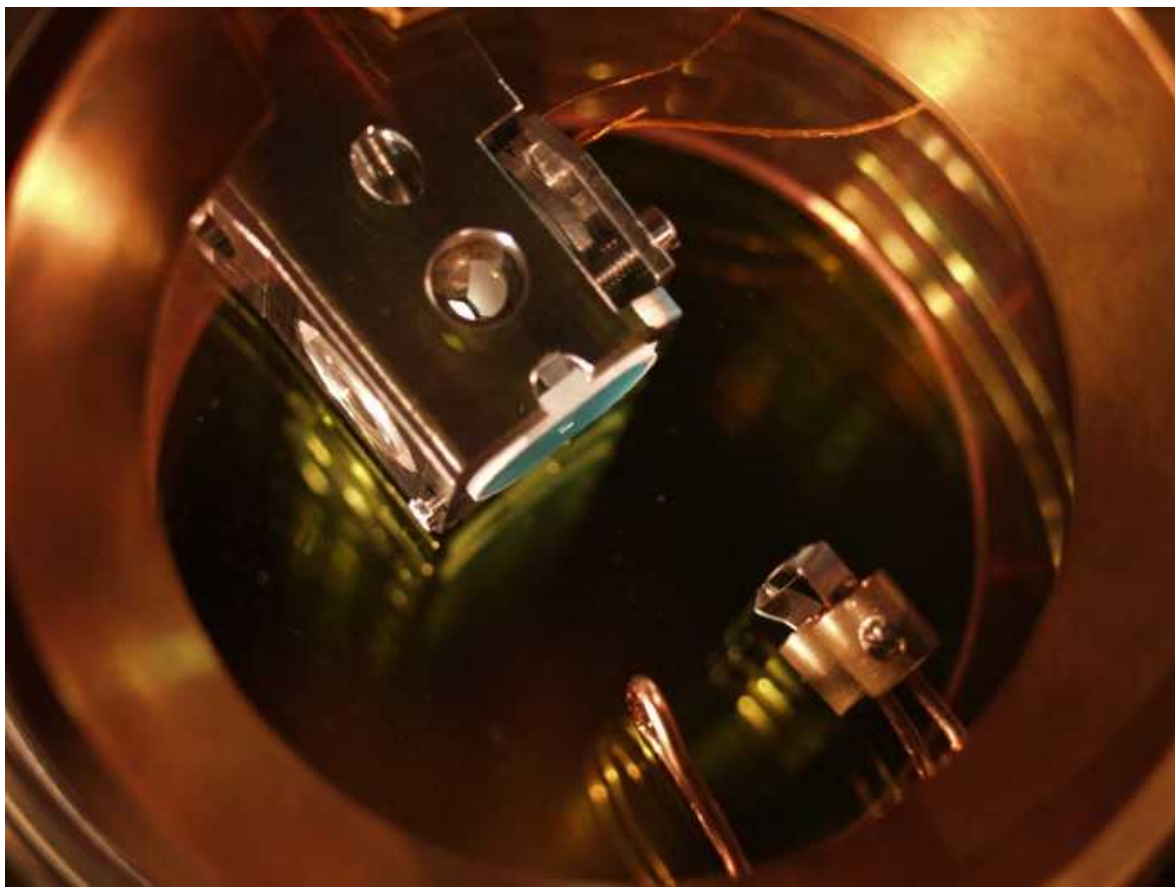
The team was also able to decode the firing patterns of groups of time neurons to retrieve the identity of the specific time periods they encoded — affirming the neurons' role as timekeepers in the brain.

[J. Neurosci. \(2021\)](#)

- [Neuroscience](#)
-

This article was downloaded by **calibre** from <https://www.nature.com/articles/d41586-021-01769-3>

| [Section menu](#) | [Main menu](#) |



A detector that measures photons without altering them includes two mirrors (white cones in round aperture) inside a vacuum chamber (silver enclosure).
Credit: Max Planck Institute for Quantum Optics

Optics and photonics

30 June 2021

Tracking a photon without leaving a trace

Conventional detectors often obliterate photons, but the particles can escape a vacuum-based device unscathed.





•

In quantum-physics experiments, measuring a particle such as a photon typically means changing its quantum state — or even destroying it. But now physicists have tracked photons travelling down an optical fibre while preserving both the particles and their quantum state.

Conventional detectors reveal the presence of photons by absorbing them; this destroys them. Stephan Welte at the Max Planck Institute for Quantum Optics in Garching, Germany, and his collaborators designed a detector using a vacuum chamber, which contains an atom trapped between two mirrors. The researchers placed two such detectors along the path of an optical fibre.

Photons travelling inside the fibre entered each detector, bounced back and forth between the mirrors roughly 20,000 times, then exited and resumed their trip down the fibre. In the process, the photons changed the atom's quantum state, revealing their passage. But they did not lose any energy to the atom, and their quantum state was unchanged.

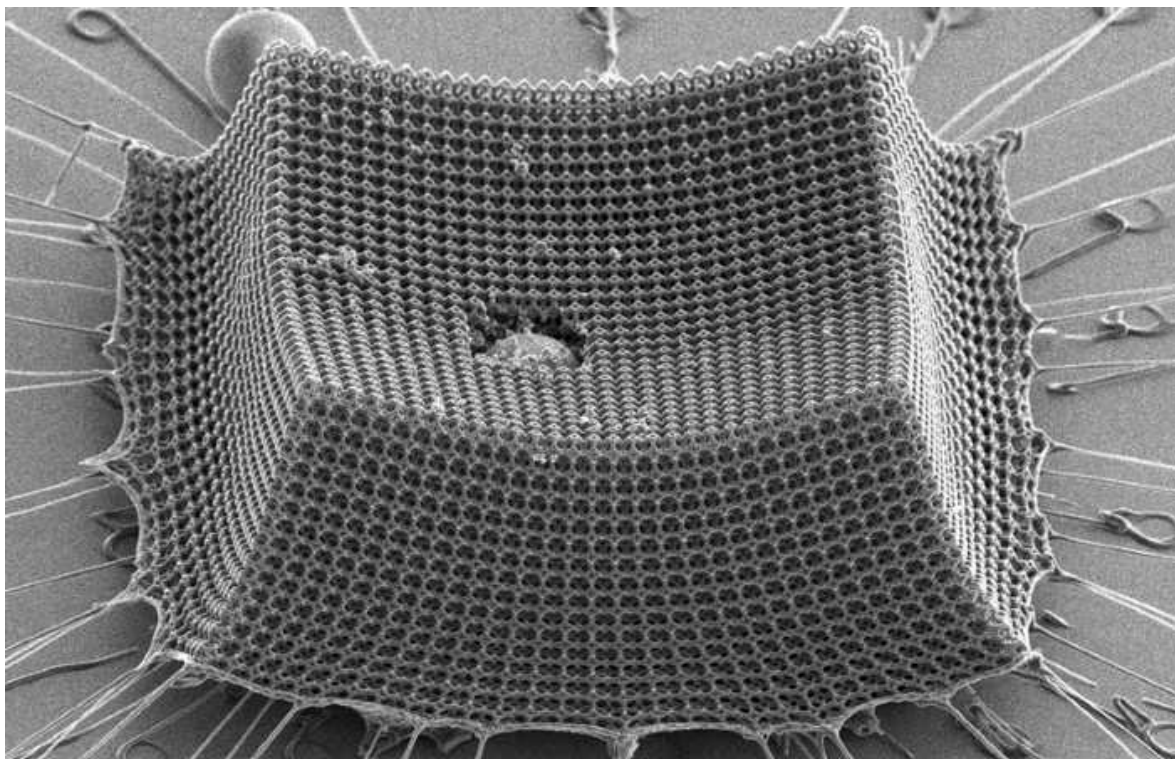
The authors' technique could be applied in quantum communications, to ensure that information carried by photons arrives at its destination untouched. It's as if "you track a parcel but you learn nothing about the contents", Welte says.

[Phys. Rev. Lett. \(2021\)](#)

- [Optics and photonics](#)

This article was downloaded by **calibre** from <https://www.nature.com/articles/d41586-021-01755-9>

| [Section menu](#) | [Main menu](#) |



A carbon latticework (above) can cushion speeding projectiles or send them bouncing off its surface. Credit: Carlos Portela *et al.*

Materials science

30 June 2021

Supersonic strikes leave just a dent in this super-light material

Honeycomb-like structure thwarts a projectile travelling as fast as a speeding bullet.





•

A carbon sheet that is no thicker than a human hair can withstand the impact of minuscule ‘bullets’ that hurtle towards it at twice the speed of sound.

Researchers are keen to find materials that can take hits from objects such as rogue shrapnel and space debris. Carlos Portela at the Massachusetts Institute of Technology in Cambridge, Julia Greer at the California Institute of Technology in Pasadena and their colleagues designed a lattice, not unlike a 3D honeycomb, whose individual cells have 14 sides. They used 3D printing to precisely construct the lattice from a flexible polymer and heated it until only pure carbon remained.

The researchers fired spheres resembling sand particles, only a few micrometres in diameter, at the material. At lower speeds, the spheres simply bounced off the lattice. But at higher speeds, they gouged out neat ‘craters’ and crushed the lattice underneath while remaining lodged in the pits, rather than piercing the material.

By adjusting a model that describes cratering by meteors, the researchers could predict crater formation in their materials. They hope their model can inform other lightweight, blast-proof designs.

[Nature Mater. \(2021\)](#)

- [Materials science](#)

This article was downloaded by **calibre** from <https://www.nature.com/articles/d41586-021-01754-w>

| [Section menu](#) | [Main menu](#) |



The skull of a young man buried millennia ago in what is now Latvia. Genetic material extracted from the man's remains has revealed DNA from an ancient form of plague. Credit: Dominik Göldner, BGAEU

Genomics

29 June 2021

A hunter-gather's tooth yields the oldest known strain of plague

Genomic analysis suggests that the Black Death began as a less virulent and less transmissible disease.





•

The first strain of the plague bacterium *Yersinia pestis* might have jumped from beavers to people, and might have caused a milder illness than later deadly versions.

Ben Krause-Kyora at Kiel University in Germany and his colleagues extracted DNA from the tooth of a male hunter-gatherer who was buried more than 5,000 years ago in what is now Latvia. Sequencing revealed genomic material from a strain of *Y. pestis* — the oldest known.

The man was carefully buried, and was the only one of four people interred at the site whose remains held traces of plague DNA. This shows that the disease was probably not a severe, contagious illness that killed within days,

the authors conclude. They argue that beavers (*Castor fiber*), which carry a related bacterium and whose remains are abundant at archaeological sites in the region, are the most likely animal host.

Past research has suggested that plague outbreaks caused by ancient *Y. pestis* strains might have caused deadly epidemics in Europe 5,000 years ago. But the latest work offers evidence to the contrary, the authors say.

[Cell Rep. \(2021\)](#)

- [Genomics](#)

This article was downloaded by **calibre** from <https://www.nature.com/articles/d41586-021-01767-5>

| [Section menu](#) | [Main menu](#) |

News in Focus

- **[CRISPR-therapy promise, malaria vaccine and pandemic parenting](#)** [07 July 2021]
News Round-Up • The latest science news, in brief.
- **[Black scientist network celebrates successes — but calls for more support](#)** [28 June 2021]
News • A year after the first ‘Black in X’ campaigns debuted, organizers reflect on their fight against racism in academia, and the challenges ahead.
- **[Killing at Chinese university highlights tensions over tenure system](#)** [25 June 2021]
News • The tragic incident has exposed frustrations among academics who are under great pressure to publish papers, but face uncertain futures.
- **[Deadly Myanmar mine disaster caused by poor planning, say data sleuths](#)** [29 June 2021]
News • First scientific study of Myanmar’s worst mining accident reveals that human error contributed to the 2020 disaster that killed at least 172 people.
- **[Is one vaccine dose enough if you’ve had COVID? What the science says](#)** [25 June 2021]
News • Research shows that a previous coronavirus infection plus one dose of vaccine provides powerful protection — but concerns linger.
- **[Controversial Alzheimer’s drug approval could affect other diseases](#)** [29 June 2021]
News • Aducanumab’s fast-tracking has researchers both worried and hopeful about the future of drugs for neurodegenerative diseases such as Huntington’s and Parkinson’s.
- **[COVID and schools: the evidence for reopening safely](#)** [07 July 2021]
News Feature • After a school term filled with anxiety and vitriol, researchers assess the spread of coronavirus and the prospects for a return to normal.

- NEWS ROUND-UP
- 07 July 2021

CRISPR-therapy promise, malaria vaccine and pandemic parenting

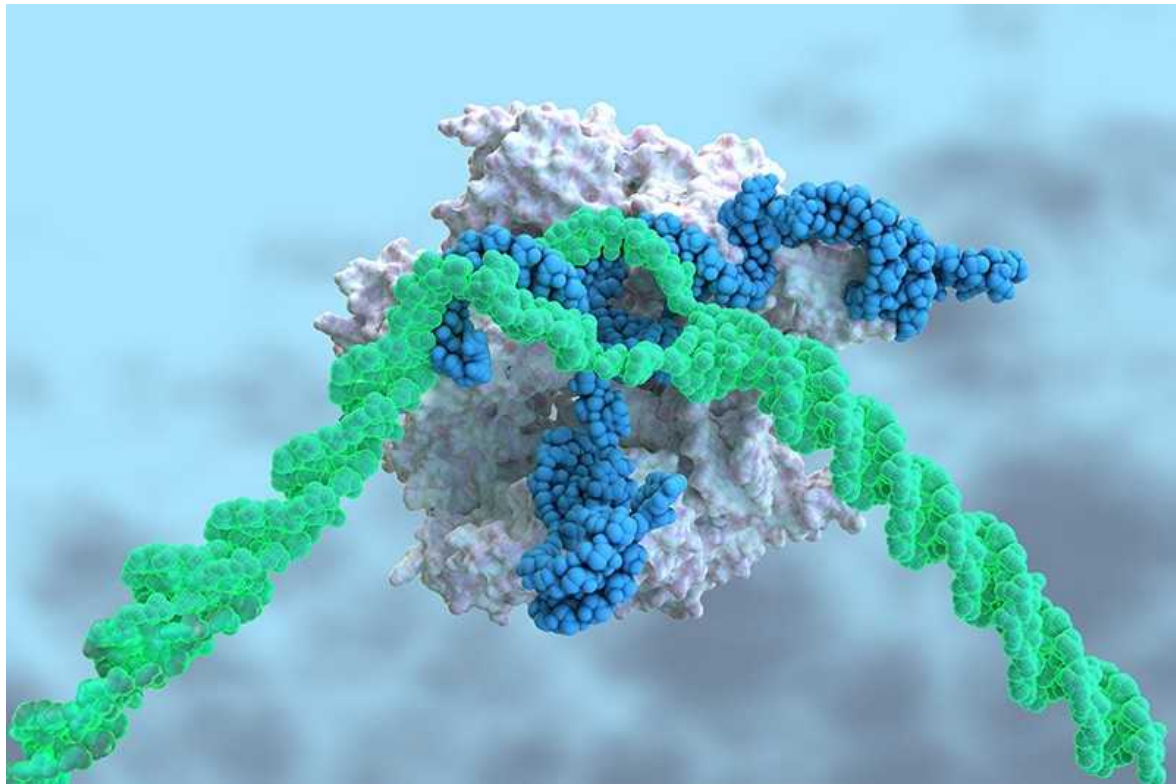
The latest science news, in brief.





•

[Download PDF](#)



The CRISPR–Cas9 complex (white and blue) can cut DNA (green), disabling genes that cause disease. Credit: Ella Maru Studio/Science Photo Library

CRISPR trial shows promise against deadly disease

Preliminary results from a [landmark clinical trial](#) suggest that CRISPR–Cas9 gene editing can be deployed directly into the body to treat disease.

The study is the first to show that the technique can be safe and effective if the CRISPR–Cas9 components (illustration pictured) — in this case targeting a protein that is made mainly in the liver — are infused into the bloodstream. In the trial, six people with a rare and fatal condition called transthyretin amyloidosis received a single treatment with the gene-editing therapy. All experienced a drop in the level of a misshapen protein associated with the disease. Those who received the higher of two doses tested saw levels of the protein, called TTR, decline by an average of 87% ([J. D. Gillmore et al. N. Engl. J. Med. https://doi.org/gkxvcs; 2021](https://doi.org/gkxvcs)).

Previous CRISPR–Cas9 clinical trials have suggested that the technique can be used in cells that have been removed from the body. But to be able to edit genes directly in the body would open the door to treating a wider range of diseases.

“It’s an important moment for the field,” says Daniel Anderson, a biomedical engineer at the Massachusetts Institute of Technology in Cambridge. “It’s a whole new era of medicine.”



Anopheles stephensi mosquitoes, a primary vector for malaria. Credit: Solvin Zankl/Nature Picture Library

Early success for live-parasite malaria vaccine

An experimental malaria vaccine that contains live parasites [protected nearly all recipients from infection](#) in a small clinical trial.

Participants in the study, which was published on 30 June ([A. Mwakingwe-Omari et al. Nature 595, 289–302; 2021](#)), were given a shot containing live

Plasmodium falciparum, along with drugs to kill any parasites that reached the liver or blood, where they can cause malaria symptoms. Participants were then intentionally infected with malaria three months later to test the vaccine's efficacy.

The vaccination protected 87.5% of participants who were infected with the strain of parasite that was used in the inoculation, and 77.8% of those who were infected with a different strain. This is a significant improvement on earlier efforts to use live parasites in a malaria vaccine; these did not perform as well against different strains.

The study also yielded important information about how immunity against malaria can be achieved, says Pedro Alonso, director of the World Health Organization's Global Malaria Programme in Geneva, Switzerland. "It contributes considerably to the science of vaccines," he says.

Pandemic made parents consider quitting academia

The stress of balancing work and home life during the COVID-19 pandemic has left many medical scientists with children questioning their future careers, according to a survey at a US university.

Last September, researchers at the University of Texas Southwestern Medical Center in Dallas sent a [survey about work-life balance](#) to the more than 3,000 members of academic staff in the university's faculty of medicine. Around one-third responded.

The survey asked about two periods of time: one before the pandemic, from March 2019 to March 2020, and one more recent, from March to September 2020.

The proportion of respondents considering leaving the university rose by 9 percentage points to 23% between the pre- and post-pandemic time periods, with women and working parents particularly affected.

The study ([S. A. Matulevicius et al. JAMA Netw. Open 4, e2113539; 2021](#)) concluded that an increase in reported work–life stress since the start of the pandemic “may disproportionately decrease the long-term retention and promotion of junior and midcareer women faculty”.

PANDEMIC PRESSURES

A survey of medical scientists at a US university asked whether they had considered leaving because of problems with work–life balance.

■ Before COVID-19 ■ Since COVID-19

All faculty members (966 respondents)



Women (551)



Men (373)



Respondents with children (548)



Respondents without children (418)



©nature

Source: Matulevicius, S. A., Kho, K. A., Reisch, J. & Yin, H. *JAMA Netw. Open* 4, e2113539 (2021).

Nature 595, 155 (2021)

doi: <https://doi.org/10.1038/d41586-021-01825-y>

Subjects

- [Gene therapy](#)
- [Lab life](#)
- [Malaria](#)
- [Diseases](#)

nature careers

Jobs >

- [Canada Research Chair Tier 2 in Indigenous Natural Sciences](#)

The University of British Columbia (UBC)

Vancouver, Canada

- [Chemical/Environmental Engineer – Gas Chromatography and Mass Spectrometry](#)

Jülich Research Centre (FZJ)

Jülich, Germany

- [Chemical Technical Assistant \(m/f/d\)](#)

Alfred Wegener Institute - Helmholtz Centre for Polar and Marine Research (AWI)

Bremerhaven, Germany

- [Abteilungsassistent*in \(d/m/w\), Abteilung „IT“](#)

Helmholtz Centre for Heavy Ion Research GmbH (GSI)

Darmstadt, Germany

[Download PDF](#)

Subjects

- [Gene therapy](#)
- [Lab life](#)
- [Malaria](#)
- [Diseases](#)

This article was downloaded by **calibre** from <https://www.nature.com/articles/d41586-021-01825-y>.

| [Section menu](#) | [Main menu](#) |

- NEWS
- 28 June 2021
- Correction [29 June 2021](#)

Black scientist network celebrates successes — but calls for more support

A year after the first ‘Black in X’ campaigns debuted, organizers reflect on their fight against racism in academia, and the challenges ahead.

- [Ariana Remmel](#)
 1. Ariana Remmel
[View author publications](#)

You can also search for this author in [PubMed](#) [Google Scholar](#)





•

[Download PDF](#)



The ‘Black In X’ movement, which emerged during the past year, fights systemic racism in academia. Credit: Steffi Loos/Getty

In the wake of global protests against anti-Black racism last year, a movement emerged to celebrate Black scientists and fight systemic oppression in academia. Researchers in fields across science, technology, engineering and mathematics (STEM) worldwide, but especially in the United States, rallied around social-media hashtags and attended online community events. A year later, they are celebrating all that they have accomplished with the movement now known collectively as Black in X — but also highlight the challenges they still face in fighting racism in science, including the need for more institutional support and funding.

“2020 did a number on all of us,” says Carlotta Berry, who co-founded both Black In Engineering and Black In Robotics. “I want us to come together and look at each other and say, ‘Look what we did! ’”



Grieving and frustrated: Black scientists call out racism in the wake of police killings

Berry and other movement leaders will do that during this week's [virtual Black in X conference](#), organized by a network of more than 80 groups, including Black In Geoscience and Black In Neuro. Its organizers hope the event, set to begin on 29 June, will increase representation of Black scientists and provide opportunities for participants to network. They also want to draw renewed focus to the need for anti-racist policies at research institutions.

“The reason why we’re here [organizing these events] is not because the system that we work in supports us,” says Tyrone Grandison, an information-technology specialist and founder of the non-profit Data-Driven Institute in Seattle, Washington, who is a leader of both Black In Computing and Black In Engineering. “The system is systematically racist, and people have been ignoring it for way too long.”

‘We’ve always been here’

The first hashtag connected with the Black In X movement was #BlackBirdersWeek, which emerged last May to celebrate Black nature enthusiasts and highlight the challenges they face, after a white woman called the police on birdwatcher Christian Cooper in a racial-profiling incident in New York City’s Central Park. But in the wake of the murder of

George Floyd in Minneapolis, Minnesota, the same month, more hashtags launched, including #BlackInTheIvory on Twitter, which Black academics [used to share their lived experiences of discrimination](#) in academia. Over time, many of the campaigns moved beyond social media, transforming into organizations that plan events such as networking and professional-development workshops.



[How #BlackInTheIvory put a spotlight on racism in academia](#)

It wasn't a new idea, organizers tell *Nature*. "We've always been here," says Quincy Brown, a computer scientist in Washington DC and head of programmes at AnitaB.org, a non-profit organization that supports women in technology fields. Black scientists have been fighting for recognition for decades, and she points out that the Black In X movement's social media advocacy stands on the shoulders of campaigns including #BLACKandSTEM, founded in 2014, and #VanguardSTEM, founded in 2015, which are still active today. But the deluge of events in mid-2020 galvanized efforts like never before.

One thing that stands out to leaders a year later is how popular the Black In X organizations have become. When launching them, "we were almost a little blindsided by the amount of people who wanted to connect with us", says Berry, a computer and electrical engineer at Rose-Hulman Institute of Technology in Terre Haute, Indiana. Berry says that soon after she and her colleagues launched #BlackInEngineering in June 2020, Black researchers interested in organizing their own Black In X events began coming to her and other campaign leaders asking for advice and guidance.

As leaders came together to share knowledge — and as the media began discussing the movement as a whole — Berry and others realized that there was an opportunity to form a larger network to collectively confront anti-Black racism in their workplaces.

Similar to earlier groups, today's Black In X organizations help Black scientists to feel connected with others, even if they are the only Black person in their university's science department, says Grandison. Virtual events also provide opportunities for participants to geek out over their research with other scientists, organizers say. "We're creating space for us to show off and highlight what we do in our technical discipline," says Brown, who is a leader of Black In Computing and Black In Robotics. "A lot of times, people want to look at us with a DEI [diversity, equity and inclusion] lens, and not as scientists, not as engineers, not as experts in our field."

The next level

Black In X leaders tell *Nature* that they are proud of how their collective efforts have helped to amplify the voices of Black scientists, but there is still much work to be done to dismantle oppression in science — work that requires direct action by institutions. "The onus is not on us to fix racism in the academy," says Samantha Theresa Mensah, a materials chemist at the University of California, Los Angeles, and co-founder of #BlackInChem.

On 10 June last year, thousands of researchers worldwide [shut down their laboratories](#) to plan actions they and their institutions could take against systemic racism, under the banners #ShutDownSTEM and #Strike4BlackLives. Universities, professional societies, academic publishers and journals, [including *Nature*](#), issued statements condemning racism in their organizations and promising to take concrete steps to implement anti-racist policies.



[Universities scrub names of racist leaders — students say it's a first step](#)

A year later, although many organizers feel that they have support from their colleagues, “it hasn’t gone beyond statements” at the institutional level, says Grandison. ([In an Editorial](#) in May, *Nature* reported on initial steps it had taken in the year after its #ShutDownSTEM commitment and acknowledged there is far more to be done.)

Shirley Malcom, director of STEM Equity Achievement (SEA) Change at the American Association for the Advancement of Science in Washington DC, agrees with Black In X leaders that institutions are dragging their feet. Malcom works to transform institutional support for historically marginalized scientists, especially at colleges and universities. After four decades promoting DEI in STEM, “I’ve remained impatient,” she says, “but I’m also mindful of the fact that change takes time.” Even knowing that the pace of change is frustratingly slow, Malcom is heartened by the progress these movements have already made: “We have to celebrate every win, every milestone.”

To keep making progress, Black In X leaders told *Nature*, they need financial support. “The more impact we can make, the more we can normalize, amplify and promote Black STEM. And to do that, we need more eyes on us and more resources,” says Berry, who is working to establish non-profit status for Black In Engineering.



[Major physics society won't meet in cities with racist policing record](#)

Funding would also help leaders to compensate organizers who volunteer their time to keep the movement going. “This culture of volunteerism takes people away from their studies, or from their area of disciplinary expertise,” says Brown.

Organizers also emphasize that non-Black allies, especially those in positions of power, need to step up to lighten the burden for the Black scientists who are the target of systemic racism. Many member organizations of the Black In X Network list actions on their websites that allies can take. “Racism is a white-people problem that affects Black people,” says Grandison. “For us to even have the slimmest chance of actually fixing the current system, it has to be done with the people that [control] the levers, which are not Black people at this point.”

Leaders and participants will discuss these issues and more at the conference this week, which will include virtual networking spaces, a poster session and keynote addresses. The event took root after Zemen Berhe, a photochemist at the University of Massachusetts Dartmouth and a founder of Black In Swimming, tweeted that the various Black In X movements should have a “homecoming” at which they celebrate their identity. Berhe hopes that the conference, and the success of the movement, will inspire a new generation of Black scientists simply by demonstrating that “we are here, and we are here to stay”.

Nature **595**, 157-158 (2021)

doi: <https://doi.org/10.1038/d41586-021-01734-0>

Updates & Corrections

- **Correction 29 June 2021:** An earlier version of this story stated that Quincy Brown's title was senior director of innovation research at AnitaB.org. Her current title is head of programmes.

Related Articles



- [**Grieving and frustrated: Black scientists call out racism in the wake of police killings**](#)



- [**How #BlackInTheIvory put a spotlight on racism in academia**](#)



- [**Thousands of scientists worldwide to go on strike for Black lives**](#)



- [**Major physics society won't meet in cities with racist policing record**](#)



- [**Universities scrub names of racist leaders — students say it's a first step**](#)

Subjects

- [Institutions](#)
- [Scientific community](#)
- [Lab life](#)
- [Society](#)

nature careers

[Jobs](#) >

- [Canada Research Chair Tier 2 in Indigenous Natural Sciences](#)

The University of British Columbia (UBC)

Vancouver, Canada

- [Chemical/Environmental Engineer – Gas Chromatography and Mass Spectrometry](#)

Jülich Research Centre (FZJ)

Jülich, Germany

- [Chemical Technical Assistant \(m/f/d\)](#)

Alfred Wegener Institute - Helmholtz Centre for Polar and Marine Research (AWI)

Bremerhaven, Germany

- [Abteilungsassistent*in \(d/m/w\), Abteilung „IT“](#)

Helmholtz Centre for Heavy Ion Research GmbH (GSI)

Darmstadt, Germany

[Download PDF](#)

Related Articles

-  [Grieving and frustrated: Black scientists call out racism in the wake of police killings](#)
-  [How #BlackInTheIvory put a spotlight on racism in academia](#)
-  [Thousands of scientists worldwide to go on strike for Black lives](#)
-  [Major physics society won't meet in cities with racist policing record](#)
-  [Universities scrub names of racist leaders — students say it's a first step](#)

Subjects

- [Institutions](#)
- [Scientific community](#)
- [Lab life](#)
- [Society](#)

This article was downloaded by **calibre** from <https://www.nature.com/articles/d41586-021-01734-0>

| [Section menu](#) | [Main menu](#) |

- NEWS
- 25 June 2021

Killing at Chinese university highlights tensions over tenure system

The tragic incident has exposed frustrations among academics who are under great pressure to publish papers, but face uncertain futures.

- [Smriti Mallapaty](#)

1. Smriti Mallapaty
[View author publications](#)

You can also search for this author in [PubMed](#) [Google Scholar](#)





•

[Download PDF](#)



Mourners pay their respects to Wang Yongzhen on 17 June.Credit: Fudan University

The killing of a maths faculty member on a Shanghai campus has sent shock waves through China's research community. The motive behind the fatal stabbing remains unknown — but the suspect is a researcher at Fudan University, and the tragedy has stirred up debate over what many researchers argue are flaws in China's tenure-track system.

According to Fudan University, Wang Yongzhen, 49, the secretary of the Communist Party of China at the School of Mathematical Sciences and a former deputy dean, was killed on its Shanghai campus in the afternoon of 7 June. The police identified the suspect as a 39-year-old man named Jiang, who they announced on Monday had been charged with "suspicion of intentional homicide".

Fudan University later issued [statements](#) "expressing deep condolences for the tragic murder of Comrade Wang Yongzhen". Wang was hired by Fudan

University as an associate researcher in 2007, and held several senior administrative roles there.

In a 17 June [statement](#), the university fully named the suspect as Jiang Wenhua, a researcher in the school's department of probability, statistics and actuarial sciences, who has published several papers on statistics. Jiang is on a tenure-track employment scheme, which some of China's leading universities have modelled on that of US universities.

Examining tenure system

A video that has circulated online, from an unverified source, reportedly shows Jiang at the scene of the crime, kneeling on the ground while being questioned by police. The filmed suspect informs the police that he had been treated badly.

Fudan University did not respond to requests for comment on possible issues with China's tenure track system. But researchers say that, irrespective of what motivated the stabbing, the incident highlights the stressful tenure process and that the system needs to be examined.



[Academia: The changing face of tenure](#)

Fudan University says Jiang was hired in September 2016 on a three-year contract, with the chance of a second three-year contract following a review — and the prospect of gaining permanent employment, or ‘tenure’, at the end of the six years.

This ‘three-plus-three’ scheme is common at Chinese universities, say researchers. Similar systems are in place at US institutions, where tenure is typically granted after about six years, and include annual evaluations with three-year contracts.

However, Fudan University says Jiang’s initial three-year contract was not renewed because he had not met contractual obligations — details of which have not been made public. The university says it agreed to give Jiang two extensions, each for one year: the first in July 2019 and the second in November 2020. However, before the incident on 7 June, the university says it had made no decision to end Jiang’s contract. But this hasn’t stopped speculation online that the motive for the crime was related to the potential loss of his employment.



Based in Shanghai, Fudan University is more than a century old. Credit: Alamy

Precarious employment

Researchers say Jiang's precarious employment situation is not uncommon at Chinese universities. In one widely cited example from Wuhan University, only 3% of tenure-track candidates there passed their first 3-year assessment. By comparison, 50–60% of tenure-track candidates at many US institutions typically succeed, although rates vary and the proportion of tenured US faculty members is declining overall.

The problem is not with the tenure-track system per se, but with its discretionary implementation at particular institutions, argues Rao Yi, a neuroscientist and president of Capital Medical University in Beijing. The three-year review is intended to support junior faculty members on their path to tenure, and the majority of candidates should pass this assessment, he says.

Even candidates who meet all their requirements for tenure are often not successful because positions are limited, says Shu Fei, a bibliometrics scientist at Hangzhou Dianzi University in China and the University of Montreal, Canada, where he is based. Universities often over-recruit and push young researchers to publish lots of papers, which helps to drive up their rankings, says Shu. "Chinese universities try to abuse the tenure-track system to their advantage," he says. "Many Chinese young scholars are very angry."

Failed candidates typically have to accept administrative roles or must find employment elsewhere. Furthermore, many "are not fully informed of the tenure process and the low tenure rate", so the loss of their employment can come as a shock, he says.



The busy lives of academics have hidden costs — and universities must take better care of their faculty members

Researchers also say that decisions to renew contracts or grant tenure are often based on personal connections rather than on academic merit, which has generated “a strong sentiment of unfair treatment”, says Joy Zhang, a sociologist at the University of Kent in Canterbury, UK, who says she has heard similar complaints during her many years of research in China.

One recent blog post by an anonymous Chinese academic about problems with the tenure-track system at domestic universities says the suspect’s actions, although indefensible, should teach universities a lesson that “young people must not be bullied”.

“Universities should make more efforts to build a stronger mentorship system, especially for young and newly recruited faculty members,” says Futaoh Huang, a researcher in higher education at Hiroshima University in Japan.

Inconsistent criteria

Although China has adopted the criteria of the US tenure-track system in theory, “in practice, there are often large disparities among how these criteria

are applied,” says Zhang.

Rao argues that, in places where the system has been applied as intended, it has proved “far better than any of the other alternatives previously used”, in which researchers were either guaranteed lifetime employment on arrival or had to undergo annual reviews. He gives the examples of Tsinghua University and Peking University, both in Beijing (Rao previously served as dean at the latter).

The tenure system was designed to give tenured academics financial security and academic freedom to pursue research of their choosing. Chinese universities began adopting the system several decades ago.

In theory, the system should be fair because all positions are recruited through open competition, not by internal appointment, adds Rao. But “the tenure system has effectively functioned in only a few Chinese universities so far,” he says.

A full police investigation of the incident at Fudan University is underway.

Nature **595**, 158-159 (2021)

doi: <https://doi.org/10.1038/d41586-021-01716-2>

Related Articles

-  [**Academia: the changing face of tenure**](#)
-  [**India debates a nationwide tenure system**](#)

-  The busy lives of academics have hidden costs — and universities must take better care of their faculty members

Subjects

- [Institutions](#)
- [Careers](#)
- [Policy](#)

nature careers

[Jobs](#) >

- [Canada Research Chair Tier 2 in Indigenous Natural Sciences](#)

The University of British Columbia (UBC)

Vancouver, Canada

- [Chemical/Environmental Engineer – Gas Chromatography and Mass Spectrometry](#)

Jülich Research Centre (FZJ)

Jülich, Germany

- [Chemical Technical Assistant \(m/f/d\)](#)

Alfred Wegener Institute - Helmholtz Centre for Polar and Marine Research (AWI)

Bremerhaven, Germany

- [Abteilungsassistent*in \(d/m/w\), Abteilung „IT“](#)

Helmholtz Centre for Heavy Ion Research GmbH (GSI)
Darmstadt, Germany

[Download PDF](#)

Related Articles

-  [Academia: the changing face of tenure](#)
-  [India debates a nationwide tenure system](#)
-  [The busy lives of academics have hidden costs — and universities must take better care of their faculty members](#)

Subjects

- [Institutions](#)
- [Careers](#)
- [Policy](#)

This article was downloaded by **calibre** from <https://www.nature.com/articles/d41586-021-01716-2>

- NEWS
- 29 June 2021

Deadly Myanmar mine disaster caused by poor planning, say data sleuths

First scientific study of Myanmar's worst mining accident reveals that human error contributed to the 2020 disaster that killed at least 172 people.

- [Andrew Silver](#)

1. Andrew Silver

[View author publications](#)

You can also search for this author in [PubMed](#) [Google Scholar](#)





•

[Download PDF](#)



Hundreds of people were buried by a landslide when the wall of the Wai Khar open mine collapsed on 2 July 2020. Credit: Zaw Moe Htet/AFP via Getty

A detailed analysis of satellite and remote-sensing data has uncovered poor conditions at the Wai Khar jade mine in northern Myanmar, where a landslide last July killed more than 170 people.

The international team of authors behind [the study¹](#) — the first to rigorously document a mining accident in Myanmar — says the results suggest that mismanagement and poor design contributed to the tragedy, not simply monsoon rains, as was initially assumed.

As well as shedding light on the causes of the disaster, which have not yet been fully resolved, the authors hope the findings will aid documentation of mine collapses and improve site planning — both in Myanmar and in other countries that see frequent mining accidents.

Mining of jade, largely for jewellery and carvings destined for China, has exploded in Myanmar in recent years. About 400,000 miners scavenge jade

from the slopes of open-pit mines, often with little safety equipment. They feed an industry that supplies 90% of the world's jade and earned an estimated US\$8 billion in 2011 — 20% of the southeast Asian state's export revenue.

Hundreds of deaths

The jade industry in Myanmar is poorly regulated and mine collapses are common, causing many hundreds of deaths since 2004, according to the study authors. But a lack of transparency from the Myanmar authorities — together with political and ethnic conflict in northern Kachin state, where jade mining is centred — means field surveys of mine sites are “nearly impossible”, the authors argue.



Quake-prone Myanmar leads the way in seismic monitoring

In what is thought to have been Myanmar's worst mining disaster, in June last year rain began to saturate the ground at the northern section of the Wai Khar open-pit jade mine in the region of Hpakant. Eventually, on 2 July, a huge volume of quarry slope materials “collapsed into a flooded open pit, burying and killing at least 172 jade miners”, write the authors.

Although mining companies in Hpakant had been ordered by the authorities to suspend operations from 1 July for three months for the monsoon season, impoverished freelance scavengers were still hunting for unpicked jade

exposed by rain. Heavy rainfall was initially assumed to be the trigger for the collapse.

Myanmar's National Human Rights Commission blamed the landslide on the lack of due diligence and risk assessment from mining companies — at least 12 of which owned licences covering specific parts of the Wai Khar mine at the time of the accident. But non-governmental organizations say that a lack of regulatory oversight from the government in the mining industry is also a major problem endangering the lives of miners in Myanmar.



Myanmar's poorly regulated mines provide up to 90% of the world's jade. Credit: Mladen Antonov/AFP via Getty

A spokesperson for Myanmar Gems Enterprise — the Myanmar government-owned regulator and issuer of mining licences — told *Nature* that mining operations at the Wai Khar open-pit mine ended on 29 June, before the accident, and that a government investigation concluded rainfall had infiltrated the ground through fractures in the rock, leading to the

landslide. They added that the research findings will be valuable for assisting in future governance of the mining sector.

The mining companies either could not be reached for comment on the study, or did not respond to *Nature*'s queries on the causes of the disaster.

Given the lack of access to mine sites in Myanmar, a team of researchers from Taiwan, Singapore, Brazil and Thailand used data from remote sensing and satellites to investigate the collapse. These are often used to monitor mine sites in nations that have strict mining regulations. “There are a lot of things we can do from space,” says study co-author Wang Yu, a geologist at National Taiwan University in Taipei.

Aggressive mining cycles

To look for deformation in the landscape around the Wai Khar mine over time, Wang and his team combined online video footage of the accident from the ground with aerial and satellite data, as well as historical data from a NASA space-shuttle mission in 2000.

The authors found two factors that they think triggered the wall collapse, in addition to rainfall. Firstly, the walls of the mine were dangerously steep given the weak nature of the rock surrounding the pit. Google Earth images captured at intervals between 2013 and 2020 indicated periodic landslides had occurred in the pit, even where special steps had been dug out of the wall to prevent collapse, Wang says.

“The mining site is under aggressive mining cycles that are exacerbated by frequent, uncontrolled landslides,” he and his co-authors write. This process allows jade to be extracted more quickly, but creates dangerous conditions.

“The argument that the slope was too steep is very likely to be correct,” says Dave Petley, a geographer who studies landslides at the University of Sheffield, UK. He says he can’t be sure the landslide was associated with mining practices, but that operations should be designed to prevent deformation. “The authors show that the mine walls were actively deforming before failure,” he adds.

Poor mine design

Secondly, the study authors say that piles of mine waste acted like a sponge for rainfall or groundwater, and probably gradually leaked water that eroded the walls of the pit, aiding its collapse. The waste piles, detected in digital elevation data from NASA's space shuttle in 2000 and Japan's Advanced Land Observing Satellite from 2006–11, shouldn't have been so close to the mine, they say.



How do natural hazards cascade to cause disasters?

In an e-mail to *Nature*, the authors said that “there are issues of mismanagement and bad design in the pit”, but stop short of blaming anyone for the collapse. “Our analysis is only from the scientific viewpoint. It should be considered as an autopsy report, not a criminal complaint,” they said. “A thorough investigation will be needed in order to determine the correct share of responsibility among different parties.”

Kyi Htun, an independent mining geology consultant in Myanmar's capital, Yangon, says that after reading the study, he thinks that poor site management — such as not monitoring how the slope changed over time and not disposing of waste properly — probably played a part in the

accident. “No one has done mine design properly” at the Wai Khar mine, he says.

Assisting other nations

San Htoi, a spokesperson for advocacy group Kachin Women’s Association Thailand, who visited the mine after the landslide, also says the findings are consistent with her observations: “The slope is too steep. It’s so dangerous.”

The authors of the study say they hope that the team’s work will encourage other scientists to perform similar analyses in nations where mining is poorly regulated. Between 2004 and 2016, mine accidents led to deaths in 32 countries, according to [one report²](#).

As for the latest study, “It is a very comprehensive analysis of the mining accident,” says Birendra Bajracharya, coordinator of SERVIR-Hindu Kush Himalaya in Kathmandu, an international initiative that uses geospatial technologies to inform responses to environmental challenges. “The methodology will be useful to other researchers,” he adds.

Study co-author Yunung Nina Lin, a geologist at Academia Sinica in Taipei, says she hopes “the families of those who died can have a chance to learn about what had been happening on the mining site over the years”, and that “those in power can take the messages from this research and transform them into real actions”.

Nature **595**, 160-161 (2021)

doi: <https://doi.org/10.1038/d41586-021-01740-2>

References

1. 1.

Lin, Y. N. *et al. ISPRS J. Photogramm. Remote Sens.* **177**, 291–305 (2021).

[Article](#) [Google Scholar](#)

2. 2.

Froude, M. J. & Petley, D. N. *Nat. Hazards Earth Syst. Sci.* **18**, 2161–2181 (2018).

[Article](#) [Google Scholar](#)

[Download references](#)

Related Articles



- [How do natural hazards cascade to cause disasters?](#)



- [Quake-prone Myanmar leads the way in seismic monitoring](#)

Subjects

- [Government](#)
- [Industry](#)
- [Geology](#)

nature careers

[Jobs](#) >

- [Canada Research Chair Tier 2 in Indigenous Natural Sciences](#)

The University of British Columbia (UBC)

Vancouver, Canada

- [Chemical/Environmental Engineer – Gas Chromatography and Mass Spectrometry](#)

Jülich Research Centre (FZJ)

Jülich, Germany

- [Chemical Technical Assistant \(m/f/d\)](#)

Alfred Wegener Institute - Helmholtz Centre for Polar and Marine Research (AWI)

Bremerhaven, Germany

- [Abteilungsassistent*in \(d/m/w\), Abteilung „IT“](#)

Helmholtz Centre for Heavy Ion Research GmbH (GSI)

Darmstadt, Germany

[Download PDF](#)

Related Articles



- [How do natural hazards cascade to cause disasters?](#)



- **Quake-prone Myanmar leads the way in seismic monitoring**

Subjects

- Government
- Industry
- Geology

This article was downloaded by **calibre** from <https://www.nature.com/articles/d41586-021-01740-2>

| [Section menu](#) | [Main menu](#) |

- NEWS
- 25 June 2021

Is one vaccine dose enough if you've had COVID? What the science says

Research shows that a previous coronavirus infection plus one dose of vaccine provides powerful protection — but concerns linger.

- [Elie Dolgin](#) 0

1. Elie Dolgin

1. Elie Dolgin is a science journalist in Somerville, Massachusetts.

[View author publications](#)

You can also search for this author in [PubMed](#) [Google Scholar](#)





•

[Download PDF](#)



A worker prepares a dose of COVID-19 vaccine. Governments are advising that only one dose of vaccine be given to those with a history of coronavirus infection. Credit: Chaiwat Subprasom/SOPA Images/LightRocket/Getty

Many people who've been infected with the coronavirus might be able to safely skip the second jab of any two-dose vaccine regimen, a growing number of studies suggest. These results could help to stretch scarce vaccine supplies and are already influencing vaccination policies in some countries. But questions remain about whether the findings hold for all individuals and all vaccines — and therefore how policymakers should respond to the findings.

Studies show that people with previous exposure to SARS-CoV-2 tend to mount powerful immune responses to single shots, and gain little added benefit from another injection^{[1,2,3](#)}. What's more, for people with immunity gained through infection, one dose typically boosts antibody numbers to

levels that are equal to, or often greater than, those found in individuals who have not been infected and have received double doses⁴.

France, Germany and Italy, among other countries, now advise only one dose of vaccine for people with a healthy immune system and a confirmed previous diagnosis. Many scientists who have studied immune responses to vaccination say such policies are a sensible way to make the most of limited supplies in countries that are racing to inoculate their populations.

“To follow the current two-dose vaccination schedule in previously infected individuals, when there are millions of people waiting for their first dose, simply does not make sense,” says Jordi Ochando, an immunologist at the Icahn School of Medicine at Mount Sinai in New York City, who has advised the Spanish government on vaccination guidelines.



Mix-and-match COVID vaccines trigger potent immune response

But scientists still don't know whether one-jab programmes for the previously infected could leave some individuals with suboptimal protection. Nor is it clear that such programmes would be effective for all types of vaccine.

“If you have been infected before, then probably one dose is sufficient,” says Giuliana Magri, an immunologist at the Hospital del Mar Research Institute in Barcelona, Spain. But putting that knowledge into practice? “It’s complicated,” she concedes.

Just one jab

There's ample laboratory-based evidence that people who've been infected by SARS-CoV-2 benefit from vaccination, prompting the World Health Organization and other public-health agencies to recommend that such individuals still get vaccinated. There's less clarity, however, on whether they need to roll up their sleeves twice.

A paper published in *Nature* on 14 June provides some of the most recent evidence that one shot could be all that's necessary for people who've had COVID-19⁵. A team of researchers at the Rockefeller University in New York City and elsewhere studied 26 people who had contracted the virus early in the course of the pandemic. All of them subsequently received at least one dose of either the Pfizer–BioNTech or the Moderna vaccine, both of which are based on messenger RNA.

The researchers analysed participants' levels of 'neutralizing' antibodies, potent immune molecules that can block the virus from entering cells. At the moment, the quantity and vigour of a person's neutralizing antibodies are the best markers for assessing whether that person is protected from infection and illness — although scientists are [still working to confirm](#) that antibody levels can serve as a realistic stand-in for immune protection.

The team also assessed participants' levels of memory B cells, which remember pathogens and can quickly crank out targeted antibodies if they encounter an infectious agent that they've seen before. Within a month or two of vaccination, study participants' levels of memory B cells had risen, on average, nearly 10-fold and their 'titres', or levels, of neutralizing antibodies had shot up around 50-fold. Those gains were apparent in previously infected participants whether they'd received one shot or two.



China's COVID vaccines are going global — but questions remain

In fact, just one dose of vaccine generated titres equal to — or higher than — those produced by two doses of vaccine in people without previous infections. “It’s really amazing,” says virologist Theodora Hatzioannou, who co-led the study. “I wish everyone’s titres were like this.”

Memory booster

The findings from Hatzioannou and her colleagues also hint at the biological underpinnings of one jab’s effectiveness in exposed people. In the 12 months after participants were infected, their memory B cells had not been static. Instead, those cells spent the entire year evolving, which left them able to craft antibodies even more potent and versatile than those that they produced immediately after infection.

Other studies corroborate that thinking, with some showing that one shot can spur the growth of antibodies and infection-fighting T cells alike^{6,7}. “We’re all seeing pretty much the same thing,” says John Wherry, an immunologist at the University of Pennsylvania Perelman School of Medicine in Philadelphia. For people who have recovered from COVID-19, “the second shot doesn’t seem to do a whole lot”.

And although most research on the topic so far has focused on mRNA vaccines, preliminary evidence from studies done in the United Kingdom

and India suggests that single-dose strategies could succeed if they rely on using [the shot from Oxford-AstraZeneca](#), which uses an engineered adenovirus to stimulate an immune response against SARS-CoV-2^{8,9}.

A study published last month, for example, showed that one dose of the AstraZeneca jab produced a much more powerful immune response in health-care workers who'd been infected than in colleagues who'd escaped infection. The results "support a single-dose vaccination strategy for previously infected individuals to increase coverage and protect a larger number of populations", the authors write⁹.



[How can countries stretch COVID vaccine supplies? Scientists are divided over dosing strategies](#)

A one-jab policy for those who've been infected might even help to overcome vaccine apathy, says Stacy Wood of North Carolina State University in Raleigh, a marketing expert who has studied vaccine messaging. She argues that rather than sowing confusion, outreach that accounts for individual characteristics can help convince people who feel that their own circumstances, including infection history, make them unique. Cutting down the number of shots — and all the attendant side effects, anxiety, and time involved — can also be an attractive proposition to [some who are on the fence about getting immunized](#).

“The more tailored approach is probably better at this point,” Wood says.

Stretching vaccine doses

The accumulating evidence has been enough to convince many scientists that second doses of precious vaccine should not be allotted to people who’ve been infected.

Providing only one dose to those who’ve had COVID-19 “would free up many urgently needed vaccine doses. With the additional available vaccines, there would be no need to delay the second vaccine dose for naïve individuals”, argues a letter published in May in *EBioMedicine* and signed by eight COVID-19 scientists¹⁰. And increasingly, countries and regions that are short of vaccine are following the scientists’ lead, at least for younger adults who do not have compromised immune systems.

But not all governments are on board with this approach. In the United States, for instance, where vaccine is relatively plentiful, officials still recommend two doses for all. Determining prior infection history “is not recommended for the purposes of vaccine decision-making”, says Kate Grusich, a spokesperson for the US Centers for Disease Control and Prevention in Atlanta, Georgia.



'Unprecedented achievement': who received the first billion COVID vaccinations?

Scientists also point out that some people who become infected with SARS-CoV-2 mount a relatively weak immune response. Such a response is especially common in people who don't develop COVID-19 symptoms. "There's a huge range of antibody generation and durability in those individuals," notes Wherry. "Making decisions based on previous PCR-confirmed infections might miss some people."

That's where diagnostic antibody testing could help.

Screening for antibodies to the hepatitis B virus is already routine in some settings to guide vaccination strategies against that infectious agent — and the same could be done with antibodies to the SARS-CoV-2 spike protein, a marker of both natural and vaccine-induced immunity, says Viviana Simon, an infectious disease specialist at Mount Sinai and a signatory to the *EBioMedicine* letter.

"When in doubt, I'm all for a second dose," she says. "But I personally hope that we can move eventually to more personalized schedules and recommendations."

Nature **595**, 161-162 (2021)

doi: <https://doi.org/10.1038/d41586-021-01609-4>

References

1. 1.

Stamatatos, L. *et al. Science* **372**, 1413–1418 (2021).

[Article](#) [Google Scholar](#)

2. 2.

Goel, R. R. *et al. Sci. Immunol.* **6**, eabi6950 (2021).

[PubMed](#) [Article](#) [Google Scholar](#)

3. 3.

Ebinger, J. E. *et al.* *Nature Med.* **27**, 981–984 (2021).

[Article](#) [Google Scholar](#)

4. 4.

Krammer, F. *et al.* *N. Engl. J. Med.* **384**, 1372–1374 (2021).

[PubMed](#) [Article](#) [Google Scholar](#)

5. 5.

Wang, Z. *et al.* *Nature* <https://doi.org/10.1038/s41586-021-03696-9> (2021).

[Article](#) [Google Scholar](#)

6. 6.

Camara, C., *et al.* Preprint at bioRxiv
<https://doi.org/10.1101/2021.03.22.436441> (2021).

7. 7.

Mazzoni, A. *et al.* *J. Clin. Invest.* <https://doi.org/10.1172/JCI149150> (2021).

[PubMed](#) [Google Scholar](#)

8. 8.

Nadesalingam, A. *et al.* Preprint at medRxiv
<https://doi.org/10.1101/2021.06.03.21257901> (2021).

9. 9.

Sasikala, M. et al. *Int. J. Infect. Dis.* **108**, 183–186 (2021).

[PubMed](#) [Article](#) [Google Scholar](#)

10. 10.

Frieman, M. et al. *eBioMedicine* **68**, 103401 (2021).

[PubMed](#) [Article](#) [Google Scholar](#)

[Download references](#)

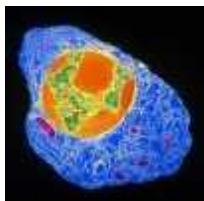
Related Articles



- [Does vaccinating adults stop kids from spreading COVID too?](#)



- [Six months of COVID vaccines: what 1.7 billion doses have taught scientists](#)



- [Had COVID? You'll probably make antibodies for a lifetime](#)



- [COVID reinfections are unusual — but could still help the virus to spread](#)

Subjects

- [SARS-CoV-2](#)
- [Immunology](#)
- [Virology](#)
- [Infection](#)
- [Public health](#)

nature careers

[Jobs](#) >

- [Canada Research Chair Tier 2 in Indigenous Natural Sciences](#)

The University of British Columbia (UBC)

Vancouver, Canada

- [Chemical/Environmental Engineer – Gas Chromatography and Mass Spectrometry](#)

Jülich Research Centre (FZJ)

Jülich, Germany

- [Chemical Technical Assistant \(m/f/d\)](#)

Alfred Wegener Institute - Helmholtz Centre for Polar and Marine Research (AWI)

Bremerhaven, Germany

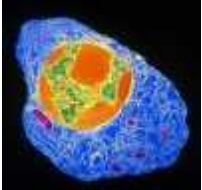
- [Abteilungsassistent*in \(d/m/w\), Abteilung „IT“](#)

Helmholtz Centre for Heavy Ion Research GmbH (GSI)

Darmstadt, Germany

[Download PDF](#)

Related Articles

-  [Does vaccinating adults stop kids from spreading COVID too?](#)
-  [Six months of COVID vaccines: what 1.7 billion doses have taught scientists](#)
-  [Had COVID? You'll probably make antibodies for a lifetime](#)
-  [COVID reinfections are unusual — but could still help the virus to spread](#)

Subjects

- [SARS-CoV-2](#)
- [Immunology](#)
- [Virology](#)
- [Infection](#)
- [Public health](#)

This article was downloaded by **calibre** from <https://www.nature.com/articles/d41586-021-01609-4>

- NEWS
- 29 June 2021

Controversial Alzheimer's drug approval could affect other diseases

Aducanumab's fast-tracking has researchers both worried and hopeful about the future of drugs for neurodegenerative diseases such as Huntington's and Parkinson's.

- [Asher Mullard](#)
 1. Asher Mullard
[View author publications](#)

You can also search for this author in [PubMed](#) [Google Scholar](#)





•

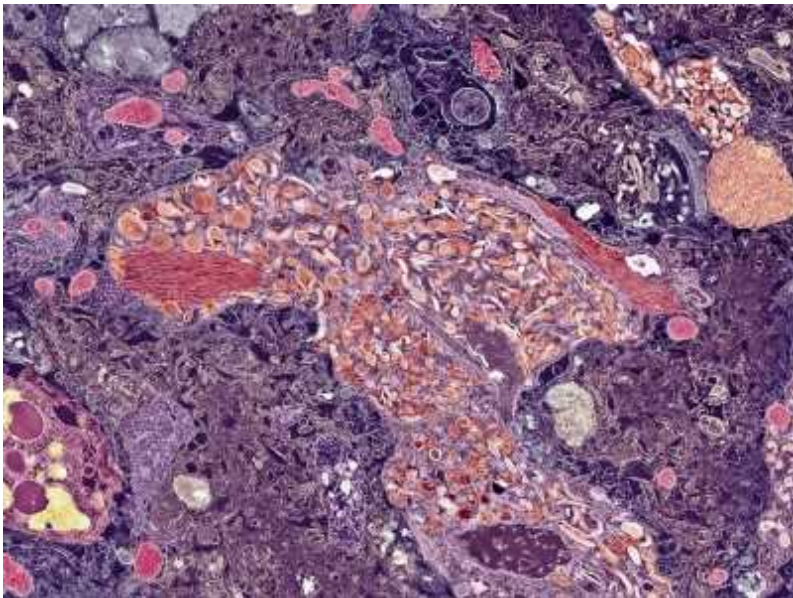
[Download PDF](#)



People with Parkinson's disease often undergo various types of therapy to improve their motor function. Credit: Amelie-Benoist/BSIP/Science Photo Library

The recent [controversial approval](#) of the Alzheimer's drug aducanumab by the US Food and Drug Administration (FDA) has raised the possibility that the agency could now be more willing to fast-track treatments for a swathe of neurodegenerative diseases — illnesses that have so far thwarted drug developers. But an independent advisory panel fiercely questioned the new drug's effectiveness, and researchers are divided on whether the potentially smoother approval path that aducanumab has paved will really deliver useful therapies for people with conditions such as amyotrophic lateral sclerosis (ALS), Huntington's disease and Parkinson's disease.

Drug developers including Amgen, in Thousand Oaks, California, and Pfizer, based in New York City, have shut down their neuroscience programmes in recent years because of the difficulties of finding successful treatments for brain diseases. So Eric Siemers, a drug-development consultant in Zionsville, Indiana, thinks aducanumab's approval could bring renewed investment and innovation.



Landmark Alzheimer's drug approval confounds research community

On the basis of conversations he has had with investors and clients, he says the tide is already turning. “There’s a lot more interest now in research in neurodegenerative diseases,” says Siemers, who is also chief medical officer of the Alzheimer’s disease company Acumen Pharmaceuticals in Charlottesville, Virginia. Acumen filed paperwork for an initial public offering just days after the approval of aducanumab.

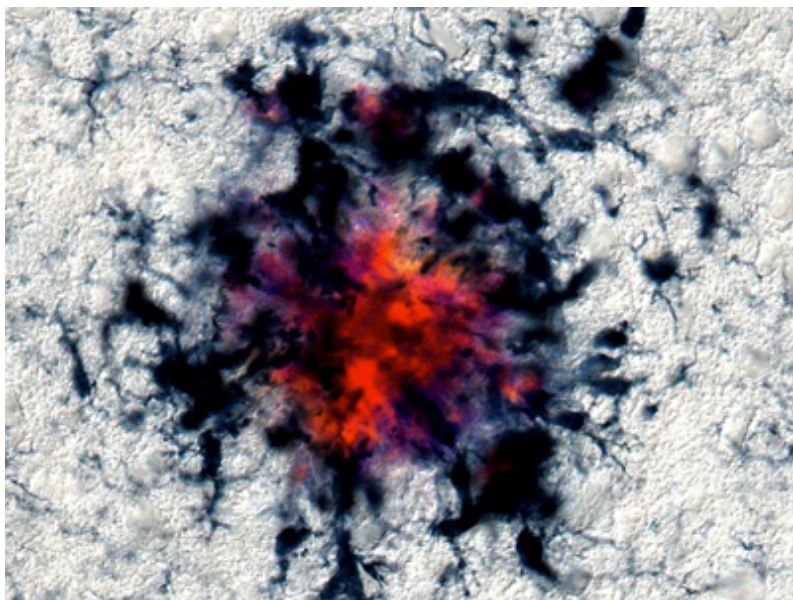
Some advocacy groups are also encouraged, on behalf of desperate patients with few or no therapeutic options. “If the FDA can find a way to be flexible for Alzheimer’s, maybe they can find a way to be flexible for ALS,” says Neil Thakur, chief mission officer at the ALS Association.

But many researchers fear that this regulatory precedent puts false hope above solid clinical science, and harms patients in the process. “Folks who are considering this approach should take a deep breath and a cold shower,” says Fyodor Urnov, scientific director of the Innovative Genomics Institute at the University of California, Berkeley, and a former drug hunter at Sangamo Therapeutics in Brisbane, California.

“I don’t want a future where we have multiple prescribable medicines. I want a future where we have multiple prescribable medicines that work.”

Reading between the lines

Aducanumab — developed by the biotechnology firm Biogen in Cambridge, Massachusetts — followed an unusual route to approval. In March 2019, Biogen halted two phase III trials of the drug candidate after an interim analysis showed that it was unlikely to improve cognition for people with mild Alzheimer's. But when Biogen re-evaluated the data and found that a subset of people in one of the trials might have benefited, it reversed course; the firm submitted aducanumab for approval in 2020.



Is ‘friendly fire’ in the brain provoking Alzheimer’s disease?

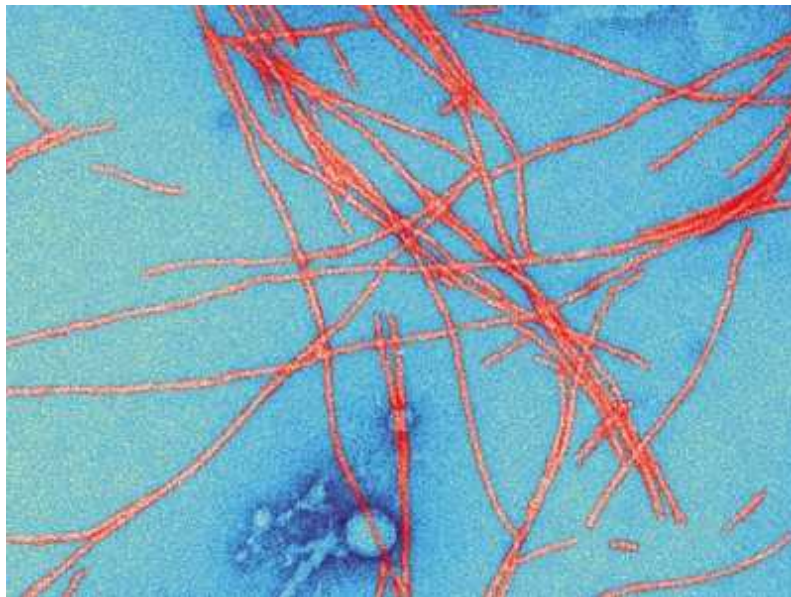
The FDA’s eventual decision to ignore the advice of its advisory committee and approve the drug, it says, was based on aducanumab’s ability to lower levels of amyloid plaques in the brain — protein clumps that some scientists think cause Alzheimer’s.

Instead of granting the drug a standard approval, which is typically reserved for agents that have demonstrated benefit for people in large phase III trials, the FDA opted to use its ‘accelerated approval’ pathway. This is for treatments that are “reasonably likely”, but not certain, to help patients.

The agency has embraced this pathway in cancer, using results from small phase II trials to green-light drugs for narrow sets of patients with late-stage

disease. With aducanumab, the agency has shown that it is willing to push the paradigm to a broader set of people. One reason that decision has attracted criticism is that decreased levels of amyloid plaques are an unvalidated and contentious marker of a drug's activity.

In large trials of other Alzheimer's drug candidates, amyloid lowering has not led to cognitive benefits, and this has made it a sticking point for researchers.



The red-hot debate about transmissible Alzheimer's

Biogen can now sell its US\$56,000-per-year drug to 6 million people with Alzheimer's at all disease stages in the United States. As a condition of the accelerated approval, the firm has until 2030 to report the results of a 'post marketing' trial to prove the drug's cognitive benefit.

Internal memos [released last week by the FDA](#) shed some light on the decision. Clinical reviewers argued that aducanumab is likely to provide a cognitive benefit, whereas statistical reviewers said the data did not support approval.

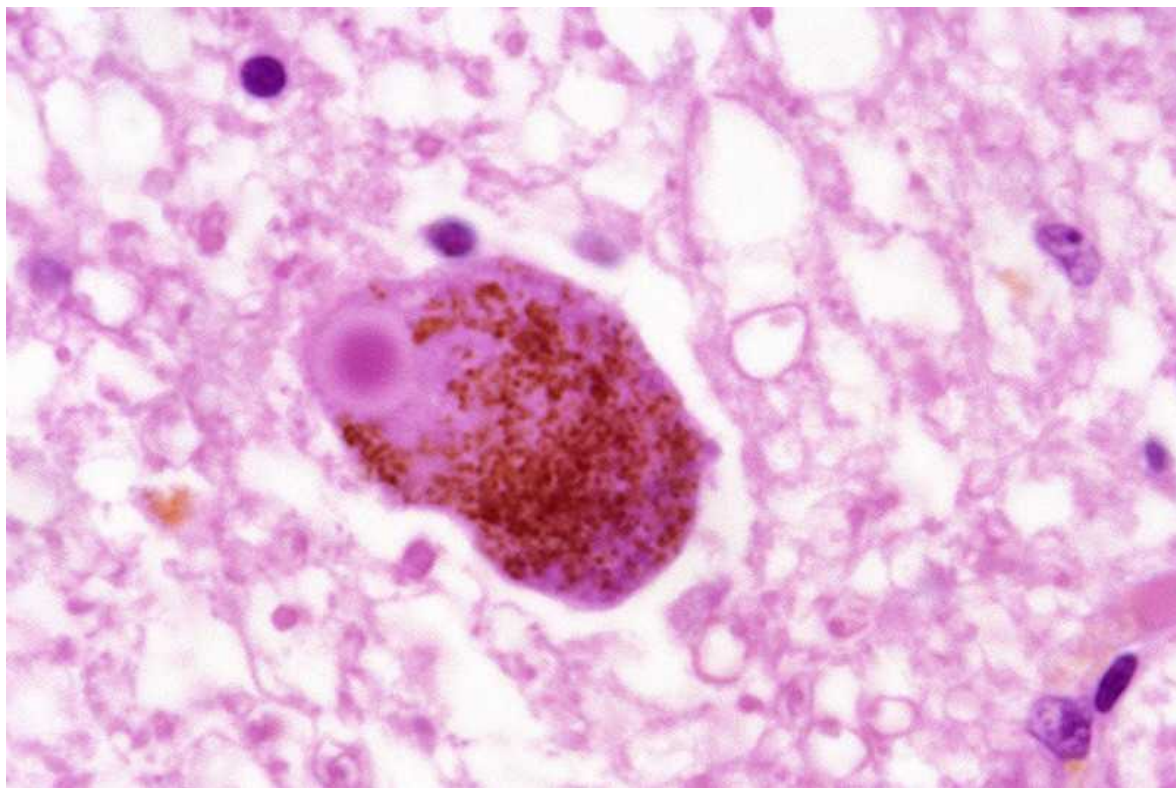
Asked by *Nature* to elaborate on the implications for Parkinson's disease, Huntington's disease and ALS, an FDA spokesperson replied that "the FDA stands ready to work with research communities and drug developers to

study more therapies for Alzheimer's disease and other neurodegenerative disorders".

Patrizia Cavazzoni, a high-ranking FDA official, has given a nod to aducanumab's broader impact. "The accelerated approval pathway has been an incredibly useful tool in oncology," she said in a press meeting. "We believe it serves as a model that we hope can be replicated with neurodegenerative diseases."

Silver linings?

One neurodegenerative condition whose treatment could benefit from aducanumab's approval is Parkinson's disease, which affects an estimated one million people in the United States. Although approved drugs help to alleviate the symptoms of this disease, none of these slows its progression. For Joseph Jankovic, a neurologist at Baylor College of Medicine in Houston, Texas, a more flexible approach to drug development could speed up progress.



The protein α -synuclein builds up in deposits like this one in the brains of people with Parkinson's disease. Credit: J. J. Hauw, ISM/Science Photo Library

The approval of aducanumab "is one of the worst decisions the FDA has ever made," says Jankovic, who is unconvinced that the drug's benefits outweigh its risks. But accelerated approval does have value for drugs that offer better hints of efficacy, he argues. "I'm always looking at a glass half full. I hope that this will soften the FDA when they review drugs for other diseases."

He has his eye on drug candidates that mop up α -synuclein, a protein that builds up in the brains of people with Parkinson's.

A recent phase II trial of an α -synuclein-targeted antibody called prasinezumab failed to make an overall dent in the symptoms of Parkinson's disease, Jankovic explains, but it delayed the worsening of people's tremors, stiffness and slowness of movement. Drug-development partners Roche, based in Basel, Switzerland, and Prothena, in Dublin, have since launched a larger phase II trial to look at the motor-function benefits of the drug candidate.

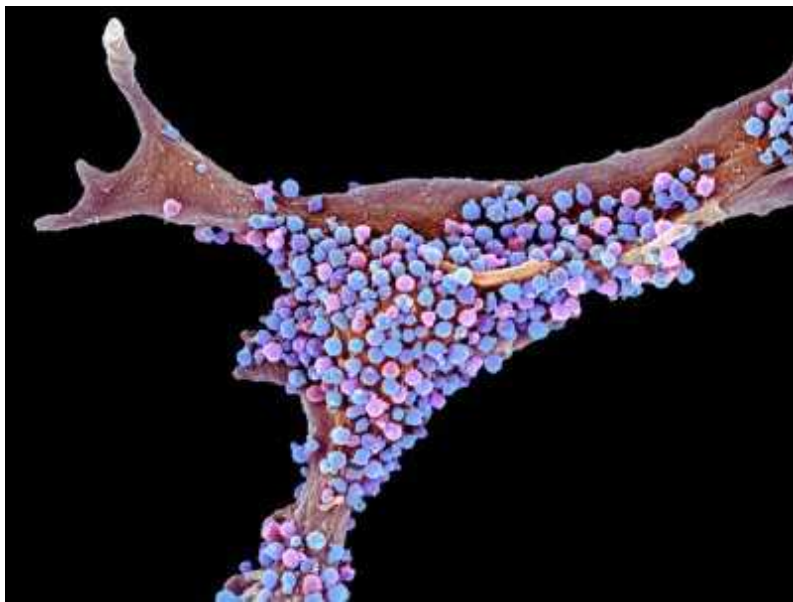
Results are expected in 2023, at which point this programme could test the FDA's resolve in relation to neurodegenerative diseases. "In my view, if the phase II study is positive, the FDA should seriously look at the approval of this drug," says Jankovic, an investigator in trials of the antibody and a consultant to Prothena.

Regulatory goalposts

Huntington's disease — an inherited neurodegenerative disease that causes involuntary jerking movements and dementia in 30,000 people in the United States — is another one to watch. People with this condition carry a mutant, toxic form of a protein called huntingtin (HTT), so researchers have developed drug candidates to lower its levels.

The most advanced of these had been tominersen, developed by Roche and Ionis Pharmaceuticals, which lowers mutant HTT in the cerebrospinal fluid

by 44%. Tominersen entered a phase III trial in 2018. Roche stopped that trial early, in March of this year, after patients worsened on treatment.



[Are infections seeding some cases of Alzheimer's disease?](#)

HTT-lowering drugs are not yet out of the running, however. Candidates that target other forms of HTT might still slow the disease. And if Roche's ongoing analysis of the tominersen data identifies any positive trends, the firm will have to decide how to proceed — and whether aducanumab provides a model that it can replicate.

But for Urnov, the failure of tominersen is a prime example of why the FDA should not approve drugs using regulatory goalposts such as amyloid plaques or HTT.

“This is going to harm the prospects for safe, effective, approved medicines for neurodegeneration,” says Urnov. “This is not how our field should be working. This is just not what any of us signed up to do.”

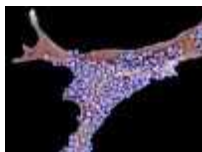
Nature **595**, 162-163 (2021)

doi: <https://doi.org/10.1038/d41586-021-01763-9>

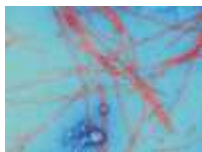
Related Articles



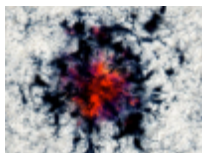
- [Landmark Alzheimer's drug approval confounds research community](#)



- [Are infections seeding some cases of Alzheimer's disease?](#)



- [The red-hot debate about transmissible Alzheimer's](#)



- [Is 'friendly fire' in the brain provoking Alzheimer's disease?](#)

Subjects

- [Neurodegeneration](#)
- [Alzheimer's disease](#)
- [Drug discovery](#)
- [Policy](#)

nature careers

[Jobs](#) >

- [Canada Research Chair Tier 2 in Indigenous Natural Sciences](#)

The University of British Columbia (UBC)

Vancouver, Canada

- [Chemical/Environmental Engineer – Gas Chromatography and Mass Spectrometry](#)

Jülich Research Centre (FZJ)

Jülich, Germany

- [Chemical Technical Assistant \(m/f/d\)](#)

Alfred Wegener Institute - Helmholtz Centre for Polar and Marine Research (AWI)

Bremerhaven, Germany

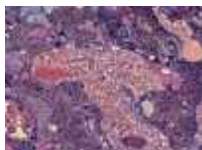
- [Abteilungsassistent*in \(d/m/w\), Abteilung „IT“](#)

Helmholtz Centre for Heavy Ion Research GmbH (GSI)

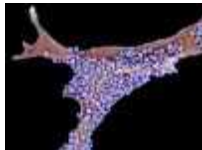
Darmstadt, Germany

[Download PDF](#)

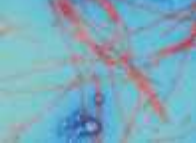
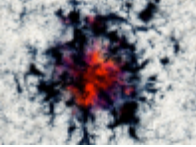
Related Articles



- [Landmark Alzheimer's drug approval confounds research community](#)



- [Are infections seeding some cases of Alzheimer's disease?](#)

-  **The red-hot debate about transmissible Alzheimer's**
-  **Is ‘friendly fire’ in the brain provoking Alzheimer’s disease?**

Subjects

- [Neurodegeneration](#)
- [Alzheimer's disease](#)
- [Drug discovery](#)
- [Policy](#)

This article was downloaded by **calibre** from <https://www.nature.com/articles/d41586-021-01763-9>

| [Section menu](#) | [Main menu](#) |

- NEWS FEATURE
- 07 July 2021

COVID and schools: the evidence for reopening safely

After a school term filled with anxiety and vitriol, researchers assess the spread of coronavirus and the prospects for a return to normal.

- [Cassandra Willyard](#) ⁰

1. Cassandra Willyard

1. Cassandra Willyard is a science journalist based in Madison, Wisconsin.

[View author publications](#)

You can also search for this author in [PubMed](#) [Google Scholar](#)





•



Open-air learning forms part of the Felix Rodriguez de la Fuente school's programme in Cartagena, Spain, during the COVID-19 pandemic. Credit: Alfonso Duran/Getty

[Download PDF](#)

On a bright, crisp morning in March, Salah Goyut said goodbye to his stuffed tiger, Stripes, and his cat, Meowington, and started walking the two short blocks to Herbert Schenk Elementary School in Madison, Wisconsin.

He had started kindergarten there months ago, but he had only seen his teacher on a computer screen.

This would be his first day inside the school. He looked tiny in his NASA mask and raccoon hat, which he had pulled down over the hood of his coat. He felt shy and a little nervous about the transition from ‘zoomie’ to ‘roomie’.

Outside the school, carefully chalked messages lined the pavement: “We can’t wait to see you!” and “Welcome Ks”. Signs directed parents to “Drop your shark off here” and “Hug and kiss goodbye here”. Salah hesitated briefly, then made his way to the open double doors.

Back in March, the decision to reopen Schenk and other shuttered schools across the United States sparked heated debate. The US Centers for Disease Control and Prevention (CDC) had announced that schools could reopen safely without driving up community spread or putting teachers and students at risk, as long as steps were taken to mitigate transmission of the virus. But that did little to calm the anxiety among parents, school staff and even scientists. It sometimes spilled into public arguments.

Monica Gandhi, an infectious-disease researcher at the University of California, San Francisco, often tweets about COVID-19 and schools, but she took a break in March. The discourse became too emotional, especially when people lobbed horrible accusations at her. “There is one thing that always ends an argument,” she says. That’s “the statement that you would want children dead”.

Now, as the academic year wraps up in many countries, school administrators are taking stock of their experiences and looking to public-health officials to help them plan for the coming school year. In the United Kingdom, children returned to school in March and April. In France, a third COVID-19 wave shuttered schools briefly around that time, but pupils were back in class by May. In the United States, more than half of all school districts had resumed full-time instruction by early June, and nearly all offered at least some in-person learning.



Does vaccinating adults stop kids from spreading COVID too?

But across the world, 770 million children still weren't going to school full time by the end of June 2021. And more than 150 million kids in 19 countries had no access to in-person schooling. They were either learning virtually or had no schooling at all. Even when schools open back up, many kids won't return. The United Nations cultural organization UNESCO estimated last year that around 24 million schoolchildren will drop out as a result of the pandemic. Because they provide so many essential services in addition to learning, schools should be the last to close and the first to open, says Robert Jenkins, chief of education for the UN children's charity UNICEF in New York City. "There are many countries in which parents can go out and have a nice steak dinner, but their seven-year-old is not going to school," he says. "That's a problem."

A growing body of evidence suggests that schools can be opened safely. But that hasn't quelled debate over whether they should be open and, if so, what steps should be taken to limit the spread of the virus. By September, when schools in many parts of the world will open again, fresh concerns and debates will be in play. Many teenagers and preteens will have been vaccinated in the United States and other wealthy countries. But in some low- and middle-income countries, vaccine access will still be limited. Younger children will probably still be in the queue in most parts of the world. And the virus continues to mutate and evolve. "The big unknown is a new variant," says Christina Pagel, a mathematician at University College London.

Debate club

In March 2020, when many schools shut their doors, little was known about SARS-CoV-2. “We closed schools early, not only to help flatten the curve, but also because for most respiratory illnesses, children are the most at risk,” says John Bailey, a visiting fellow at the right-leaning American Enterprise Institute think tank in Washington DC who recently reviewed the literature on schools and COVID-19.

Scientists soon discovered that kids are the least likely to develop serious illness, but it wasn’t yet clear whether children were as susceptible to infection as adults, and whether kids who did get infected could pass the virus on to others. Some researchers worried that sending children back to school might fuel the pandemic. But the debate soon shifted from a scientific one to a political one.

“SCHOOLS MUST OPEN IN THE FALL!!!” tweeted then-President Donald Trump in July 2020. “That became a partisan moment,” Bailey says. “So many of us we were wired to not believe anything the president was saying.” Tracy Høeg, an epidemiologist at the University of California, Davis, agrees. “It suddenly became sacrilegious for anyone in science to say it was OK for schools to be open,” she says.



What the science says about lifting mask mandates

Some of the political divisiveness was inevitable, says Ellen Peters, a decision researcher and director of the Center for Science Communication Research at the University of Oregon in Eugene. People who are conservative have different world views from people who are more liberal. But “Trump so vastly exacerbated that”, she says.

Other countries weren’t immune to the squabbling. When Danish primary schools reopened in April 2020, some parents worried that their kids were being used as guinea pigs. In France, where schools have mostly remained open, teens protested last November, saying that COVID-19 protections inside classrooms were inadequate. In some districts, teachers failed to show up as the coronavirus swept through communities. And parents were reluctant to report cases because they would have to isolate at home with their children and might lose their jobs. In Berlin, authorities scrapped plans to partially reopen schools in January, in the middle of a national lockdown, after backlash from parents, teachers and government officials.

One sticking point was the issue of prioritizing vaccines. When schools began to open up in March and April, the vast majority of teachers hadn’t yet been vaccinated. That made weighing up the risks and benefits particularly tricky. “The biggest risks are for the adults in the school system,” says Jennifer Nuzzo, an epidemiologist at the Johns Hopkins Center for Health Security in Baltimore, Maryland. “And the benefits of being in the classroom are for the kids.”

Equity also became a flashpoint in the debate. Researchers argued that remote learning would widen disparities between white students and students of colour in many countries. “The fear is that achievement gaps will become achievement chasms for those kids,” says Robin Lake, director of the Center on Reinventing Public Education, a non-partisan research and policy analysis organization in Seattle, Washington. And kids of colour aren’t the only groups that have been forgotten, Lake says. “We also know that students with disabilities have been left behind, and kids with other complex needs.”

In the United States, however, surveys showed that families of colour didn't necessarily want in-person schooling. When schools did open, these families were among those least willing to send their kids back. That's not surprising, says Durryle Brooks, a social scientist at Johns Hopkins University and policy chair for the Baltimore City Board of School Commissioners.

"Systems have continually failed Black and brown people in this country," he adds. Why would that trust suddenly appear now? And sending pupils back to in-person school wouldn't fix the achievement gap. "In Baltimore City, Black students have been underperforming" for a long time, even before the pandemic, Brooks says.

Study hall

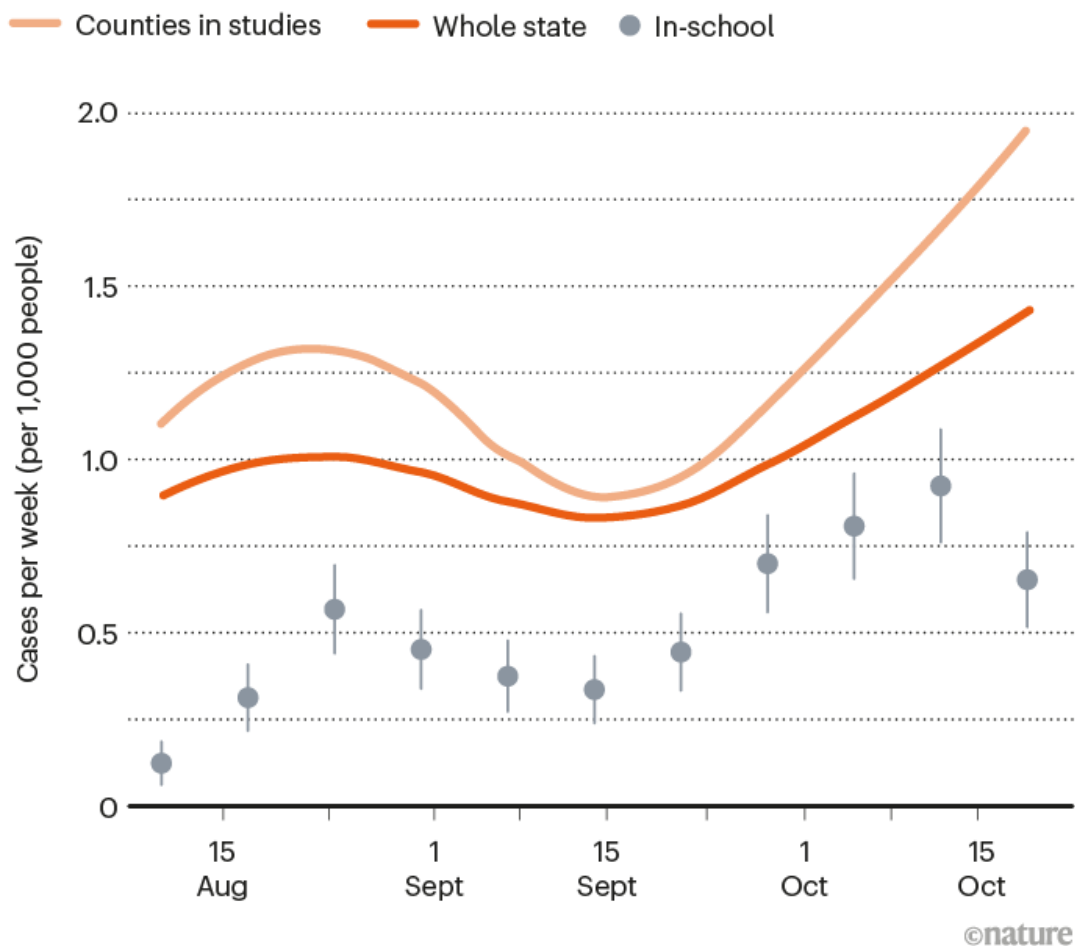
Now, more than a year after the pandemic began, researchers know a lot more about COVID-19. And they know more about how the disease does (and doesn't) spread. Although some kids and teachers have caught SARS-CoV-2, schools don't seem to be environments where transmission is rampant. "The rates in the schools have not been higher than in the community," Høeg says.

Tracking cases in schools is relatively straightforward. But what public-health officials really want to know is whether students and staff are spreading the virus on school grounds, or just bringing in cases they acquired elsewhere. That's trickier to tease out.

One of the largest studies¹ on COVID-19 in schools in the United States looked at more than 90,000 pupils and teachers in North Carolina over 9 weeks last autumn. Given the rate of transmission in the community, "we would have expected to see about 900 cases" in the schools, says Daniel Benjamin, a paediatrician at Duke Clinical Research Institute in Durham, North Carolina, and co-lead author on the study. But when the researchers conducted contact tracing to identify school-related transmissions, they identified only 32 cases (see 'Meagre spread').

MEAGRE SPREAD

Data from 11 school districts in North Carolina show that rates of COVID-19 transmission in 2020 were lower for students attending schools in person than they were for all residents in those districts and for the entire state.



Source: Ref. 1

That study, published in January, “should have been a watershed event for people who were really going to just be data driven with their policy”, says Jeanne Noble, an emergency physician who directs the COVID-19 response at the University of California, San Francisco’s medical centre. Yet many schools remained closed. Since then, “it’s just been a slew of other similar studies”, Noble says.

Another study² looked at 17 schools in rural Wisconsin. The research team observed 191 COVID-19 cases in staff and students during 13 weeks in the autumn of 2020, a time of high transmission for that area. Only seven of those cases seemed to originate in the schools. A second study, not yet published, looked at Nebraska. “They were open the whole year with over 20,000 students and staff, and there were only 2 transmission events during that entire study period,” Høeg says.

Critics argue that without surveillance testing, kids who don’t have symptoms won’t be identified or counted, so the true number could be much higher. But even if the real case numbers were double or even triple the numbers in these studies, the transmission rate would have been much lower than in the community, Benjamin says. “It’s safer for them to be in school than to be outside of school.”

Studies that have included testing tend to show similarly low transmission rates. Researchers in Norway³ identified 13 confirmed cases in children aged 5–13 in schools, and tested nearly 300 of their close contacts to assess the secondary attack rate — the percentage of contacts who become infected from a single case. Just 0.9% of the child contacts and 1.7% of the adult contacts contracted the virus.



[Why indoor spaces are still prime COVID hotspots](#)

In Salt Lake City⁴, researchers went one step further. They offered COVID-19 tests to more than 1,000 students and staff who had come into contact with any of 51 pupils who had tested positive. Of the roughly 700 people who took the tests, just 12 tested positive. The scientists then used contact tracing and genetic sequencing to identify transmissions that occurred at school. Only 5 of the 12 were school-related — an attack rate of just 0.7%. This suggests that students who contract the virus don't tend to spread it at school. A similar study⁵ in New York City found that the attack rate was even lower, just 0.5%.

When mitigation measures aren't in place, however, attack rates can be much higher. In Israel⁶, schools reopened in mid-May 2020. Within two weeks, a large outbreak occurred in one secondary school. Administrators tested more than 1,200 close contacts of the two people who initially tested positive. They identified 153 infected students and 25 infected staff members — attack rates of 13.2% and 16.6%, respectively. By mid-June, the Ministry of Health had identified nearly 90 more cases among the close contacts of those who were initially infected, including family members, friends and team mates. The outbreak was probably exacerbated by a heatwave. To make conditions less stifling, the government had rolled back its mask-wearing rules, and schools had closed windows and started using air conditioning, which recycled air inside the classroom. There were too many students to ensure social distancing.

The bulk of the literature on transmission in schools, however, suggests that kids aren't driving viral spread. Investigations in Germany, France, Ireland, Australia, Singapore and the United States show no, or very low, secondary attack rates within school settings.

"It has been perpetuated in the American media that COVID is dangerous and kids are superspreaders and schools are super-spreader places," Høeg says. "And none of that has been validated in the scientific literature."

That's not to say there are no risks. Some children have died of the disease. A study⁷ looking at COVID-19-related deaths in children in 7 countries found that 231 kids died of the disease between March 2020 and February 2021. In the United States, the number as of June was 471. Some who died succumbed to a rare, but terrifying inflammatory syndrome. And emerging

evidence hints that at least some kids who become infected have symptoms that persist. Deepti Gurdasani, an epidemiologist at the Queen Mary University of London, says some of her colleagues seem too blasé about the impact of COVID-19 on children. “It has really puzzled me why we’re so comfortable exposing children to a virus that we haven’t studied that much,” she says.



Preschoolers at Stark Elementary School in Stamford, Connecticut, practise social distancing.Credit: John Moore/Getty

But keeping kids out of school comes with its own set of risks. Many parents have seen the social isolation take its toll and witnessed their children struggling to stay engaged with lessons delivered by screen. Emerging studies suggest that kids in remote-learning situations are falling behind academically, especially children who were already struggling. Schools provide more than education. They serve as a safety net for many kids, offering free meals and a safe place to spend the day. Educators and school counsellors are often the first to spot signs of domestic or sexual abuse and intervene. What’s more, the closure of schools has been a disaster for many

working parents. Those with young children were left trying to juggle virtual school, normal parenting duties and their own jobs.

Emergency physician Leana Wen, currently at George Washington University's Milken Institute School of Public Health in Washington DC, argues that many have been focused on the wrong question. "Stop asking whether schools are safe. Instead, acknowledge that in-person instruction is essential; then apply the principles we learned from other essential services to keep schools open," she wrote in a *Washington Post* opinion piece.

Justin Lessler, an epidemiologist at Johns Hopkins University, agrees. "We've already decided school is important," he says. And "we should do important things, even when they're hard".

Advanced calculus

In countries where vaccination programmes have moved forwards rapidly, it looks like schools will open in the next academic year with fewer restrictions and mitigation measures than they have had over the past few months.

The greatest source of uncertainty, however, is the emergence of new variants. The [variant of concern B.1.617.2, or Delta](#), which was first identified in India, seems to be about 40–60% more transmissible than the Alpha variant, B.1.1.7, which was first noticed in the United Kingdom, and has supplanted Alpha to become the dominant variant.

In the United Kingdom, cases have begun to skyrocket. In a study⁸ posted on a preprint server, researchers randomly swabbed individuals across the nation for COVID-19. Between 20 May and 7 June, the rate of positive cases grew exponentially, with a doubling time of 11 days. By 7 June, about 90% of the cases were attributed to the Delta variant. The prevalence was highest in children aged 5–12 and in young adults. That worries Gurdasani.

Measures such as [mask wearing and improved ventilation](#) should help to curb the spread of the virus in schools, even for the more transmissible variants. But the science around which mitigation measures matter most is

not yet settled. Initially, the CDC advised schools to keep students 6 feet (1.83 metres) apart; in March, it halved that, on the basis of new studies. In the United Kingdom, the guidance is to distance when and where it's feasible. "Doing this where you can, even some of the time will help," the documents note. In the Wisconsin schools, says Høeg, "we actually had students at less than three feet in the classroom this spring", she says. Yet they identified only two cases of in-school spread even with surveillance testing of people with no symptoms. "The distance of two, versus three, versus six feet doesn't seem to be what's making the difference," she says.



[COVID-19 rarely spreads through surfaces. So why are we still deep cleaning?](#)

And although the evidence supporting mask use indoors has been accumulating, it is still a controversial topic. When schools reopened in England in March, only secondary-school students were required to wear masks. But the UK Department of Education stopped recommending face coverings for pupils and staff on 17 May "based on the current state of the pandemic and the positive progress being made". Some schools in which cases have surged have reintroduced mask policies. In US schools, mask use varies from state to state and district to district. The CDC [changed its guidance on masks in May](#), and now says that vaccinated people do not need to wear them. In the wake of that announcement, mask mandates have been

dropped across the country. A handful of states even passed laws that prohibit local school districts from requiring them indoors.

Gandhi, Høeg and two other specialists wrote an [op-ed in the Washington Post](#) arguing that kids should “return to their normal lives in the upcoming school year, without masks and regardless of their vaccination status”.

But others take a more cautious view. Katelyn Jetelina, an epidemiologist at the University of Texas Health Science Center at Houston, [found the op-ed unconvincing](#). “It doesn’t give the full story,” she says. Jetelina points out that transmission is still really high among unvaccinated people in the United States, and most kids aren’t yet vaccinated. “We need to keep that at the forefront of our minds,” she says.

Still, case numbers in the United States are at the lowest they’ve been since late March 2020. The number of deaths has plummeted, and more than 80% of teachers have been vaccinated. In May, New York City, the country’s largest school district, announced that schools will be opening full time in the autumn. “We have every reason for optimism,” Gandhi says.

Høeg agrees: “At some point we have to say that COVID has reached a level of risk where we would be better served by going back to a more normal life.”

Whether that time is now is up for debate. The United Kingdom might prove to be a cautionary tale about the risks of lifting restrictions and mitigation measures too soon in the face of fresh variants such as Delta.

Lake hopes the pandemic will provide a much-needed reset for public schools. “Public education has really been designed to do things the same way and to minimize risk, not to innovate and solve unsolved problems,” Lake says. The pandemic highlighted the huge disadvantages of that model. “The system just collapsed because everybody was looking at everybody else waiting for direction,” she says.

UNICEF’s Jenkins also wants to avoid a return to the status quo. Even before the pandemic, there were plenty of schools that were failing kids. Jenkins wants teachers and administrators to think creatively about how to

bring the technology that students relied on for virtual learning into the classrooms, how to teach important skills such as problem solving, and how to address not just learning, but mental health, nutrition, social-emotional development and more. “We have a once-in-a-generation opportunity to welcome kids back to vibrant new interactive ways of learning,” Jenkins says. “It would be a great shame if we didn’t seize that opportunity.”

Nature **595**, 164-167 (2021)

doi: <https://doi.org/10.1038/d41586-021-01826-x>

References

1. 1.

Zimmerman, K. O. *et al.* *Pediatrics* **147**, e2020048090 (2021).

[PubMed](#) [Article](#) [Google Scholar](#)

2. 2.

Falk, A. *et al.* *MMWR Morb. Mortal. Wkly Rep.* **70**, 136–140 (2021).

[PubMed](#) [Article](#) [Google Scholar](#)

3. 3.

Brandal, L. T. *et al.* *Euro Surveill.* **26**, 2002011 (2021).

[Article](#) [Google Scholar](#)

4. 4.

Hershaw, R. B. *et al.* *MMWR Morb. Mortal. Wkly Rep.* **70**, 442–448 (2021).

[PubMed](#) [Article](#) [Google Scholar](#)

5. 5.

Varma, J. K. *et al.* *Pediatrics* **147**, e2021050605 (2021).

[PubMed](#) [Article](#) [Google Scholar](#)

6. 6.

Stein-Zamir, C. *et al.* *Euro Surveill.* **25**, 2001352 (2021).

[Article](#) [Google Scholar](#)

7. 7.

Bhopal, S. S., Bagaria, J., Olabi, B. & Bhopal, R. *Lancet Child Adolesc. Health* **5**, e12–e13 (2021).

[PubMed](#) [Article](#) [Google Scholar](#)

8. 8.

Riley, S. *et al.* Preprint at medRxiv
<https://doi.org/10.1101/2021.06.17.21259103> (2021).

[Download references](#)

Related Articles



- [**What the science says about lifting mask mandates**](#)



- [**Six months of COVID vaccines: what 1.7 billion doses have taught scientists**](#)

-  [Why indoor spaces are still prime COVID hotspots](#)
-  [COVID-19 rarely spreads through surfaces. So why are we still deep cleaning?](#)

Subjects

- [SARS-CoV-2](#)
- [Epidemiology](#)
- [Diseases](#)

nature careers

Jobs >

- [Canada Research Chair Tier 2 in Indigenous Natural Sciences](#)

The University of British Columbia (UBC)

Vancouver, Canada

- [Chemical/Environmental Engineer – Gas Chromatography and Mass Spectrometry](#)

Jülich Research Centre (FZJ)

Jülich, Germany

- [Chemical Technical Assistant \(m/f/d\)](#)

Alfred Wegener Institute - Helmholtz Centre for Polar and Marine Research (AWI)

Bremerhaven, Germany

- [Abteilungsassistent*in \(d/m/w\), Abteilung „IT“](#)

Helmholtz Centre for Heavy Ion Research GmbH (GSI)

Darmstadt, Germany

[Download PDF](#)

Related Articles



- [What the science says about lifting mask mandates](#)



- [Six months of COVID vaccines: what 1.7 billion doses have taught scientists](#)



- [Why indoor spaces are still prime COVID hotspots](#)



- [COVID-19 rarely spreads through surfaces. So why are we still deep cleaning?](#)

Subjects

- [SARS-CoV-2](#)
 - [Epidemiology](#)
 - [Diseases](#)
-

This article was downloaded by **calibre** from <https://www.nature.com/articles/d41586-021-01826-x>

| [Section menu](#) | [Main menu](#) |

Opinion

- [**Ei-ichi Negishi \(1935–2021\)**](#) [01 July 2021]
Obituary • Organic chemist whose cross-coupling reaction builds many drugs.
- [**Everyone should decide how their digital data are used — not just tech companies**](#) [01 July 2021]
Comment • Smartphones, sensors and consumer habits reveal much about society. Too few people have a say in how these data are created and used.
- [**UK biodiversity: close gap between reality and rhetoric**](#) [06 July 2021]
Correspondence •
- [**China's homeless elephants need linked reserves**](#) [06 July 2021]
Correspondence •
- [**COVID-19: living guidelines help fix cracks in evidence pipeline**](#) [06 July 2021]
Correspondence •
- [**Protect pollinators — reform pesticide regulations**](#) [06 July 2021]
Correspondence •

- OBITUARY
- 01 July 2021
- Correction [09 July 2021](#)

Ei-ichi Negishi (1935–2021)

Organic chemist whose cross-coupling reaction builds many drugs.

- [Kit Chapman](#) ⁹

1. [Kit Chapman](#)

1. Kit Chapman is a journalist and historian specializing in chemistry. He was due to interview Negishi in 2017 but the Nobel laureate decided he'd rather go for a walk.

[View author publications](#)

You can also search for this author in [PubMed](#) [Google Scholar](#)





•

[Download PDF](#)

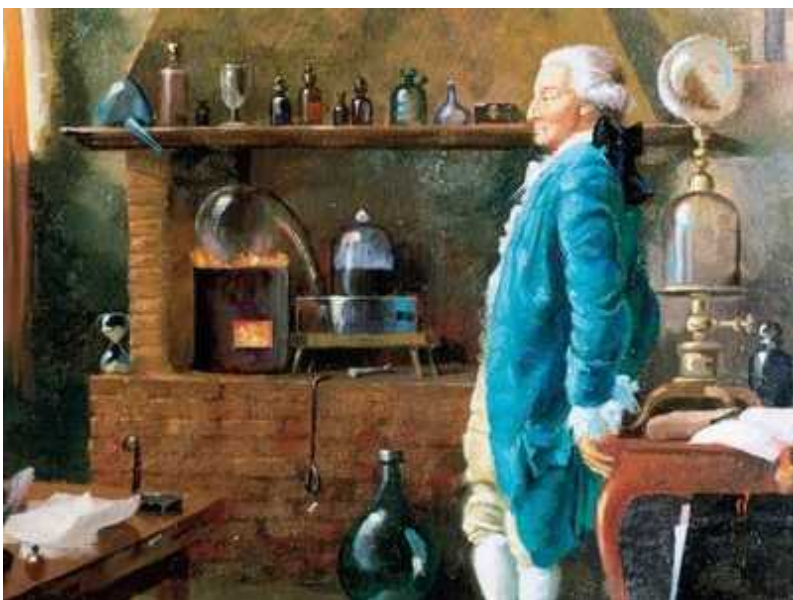


Credit: Brian Kersey/UPI/Alamy

Knitting carbon atoms together is fundamental to creating complex molecules for pharmaceuticals or industrial chemistry. In 2010, the architects of three of the most important reactions that make this possible, all using the rare metal palladium as a catalyst, were awarded the Nobel prize in chemistry. One was Japanese chemist Ei-ichi Negishi, whose cross-coupling is estimated to be used in at least one-quarter of all reactions in the pharmaceutical industry today. He has died, aged 85.

Carbon atoms are stable and difficult to react. Historically, organic chemists focused on making carbon more reactive, but this leads to unwanted by-products and is not effective for larger structures, such as drugs or plastics. Instead, in the 1970s, Negishi developed a reaction in which two intermediate molecules both bond to a metal catalyst, ultimately breaking away and forming a carbon–carbon bond with each other. The catalyst is then reused as the reaction repeats.

Negishi was born in 1935 in Hsinking (now Changchun), the capital of the Japanese puppet state of Manchukuo in northeast China. His father was a railway worker, and as a child he lived in Japanese-occupied Harbin, as well as Incheon and Seoul in South Korea, before moving to Japan at the end of the Second World War. There, he excelled as a student. He was admitted to the elite Shonan High School a year early, and at 17 gained admission to the University of Tokyo.

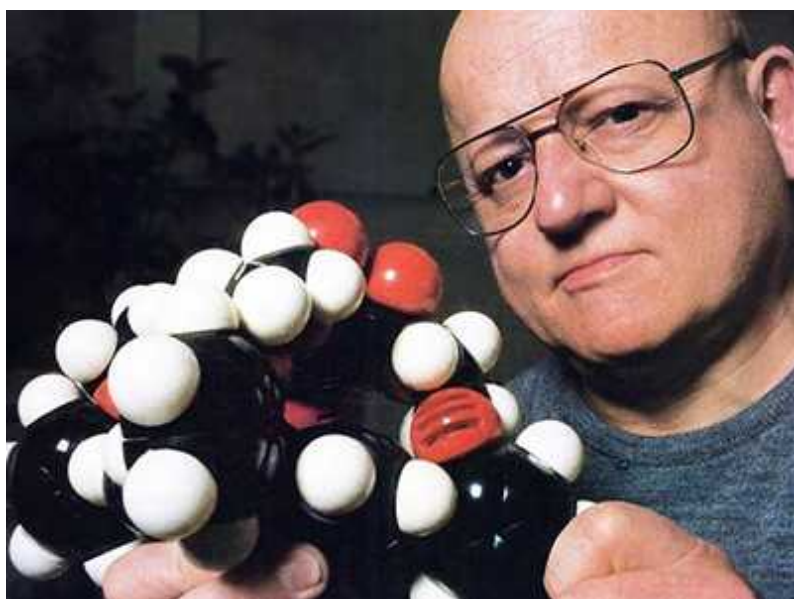


The chemistry chronicles

After graduation in 1958, he joined Teijin, a synthetic polymer company, but soon realized that his knowledge of organic chemistry wasn't a match for that of his colleagues. Unable to afford further education in Japan, with the company's support he did a Fulbright scholarship at the University of Pennsylvania in Philadelphia, where he was awarded his PhD in 1963. He returned to work at Teijin, but with his heart now set on a career in academia. Unable to find a position in Japan, he returned to the United States in 1966 as a postdoc at Purdue University in West Lafayette, Indiana, under Herbert Brown. He narrowly missed fellow Japanese organic chemist Akira Suzuki, who had left Brown's group the year before, and with whom he was destined (along with Richard Heck of the University of Delaware in Newark) to share the Nobel prize.

Negishi thrived, despite the contrast between his calm, conflict-averse personality and that of the eccentric and argumentative Brown. He later described his mentor as a “true master of exploring chemistry”. After six years, he moved to Syracuse University, New York, where he focused on the problem of joining carbon molecules together efficiently. Since the mid-twentieth century, transition metals such as copper had been used as catalysts for these reactions, and by the late 1960s palladium had started to be used too. The problem was finding suitable carbon molecules that could be catalysed.

Between 1976 and 1978, Negishi and his collaborators published a series of papers detailing a new approach. This used an organic zinc compound and a palladium or nickel catalyst to bond with an organic halide (containing a halogen such as chlorine or iodine). As the two molecules bond with the palladium, the halogen and zinc are stripped away, allowing the two organic molecules to form a new carbon–carbon bond.



[Jack Baldwin \(1938–2020\)](#)

Negishi could now make a great variety of molecules in an easy way that was cost- and energy-efficient. The reaction also limited waste through reusing the palladium and by being more targeted than earlier coupling techniques, reducing the amount of side products. Negishi coupling remains one of the most widely used techniques for forming large organic

compounds, with a long list of applications in the synthesis of natural products. Its uses range from the development of new antibiotics to the creation of antifungal agents for agriculture, and even to the building of light-emitting diodes in computer monitors.

In 1979, Negishi returned to Purdue, just in time to see Brown receive the Nobel prize in chemistry. He remained for the next 40 years. Here, Negishi was known for his approachable nature. His door always open, the laureate would press his students relentlessly to excel. He had a competitive streak — in the laboratory and at karaoke, for which he could sing more than 1,000 tunes. In addition to the Nobel prize, he received Japan's Order of Culture in 2010. He retired from academic life only in 2019, aged 84.

Palladium-catalysed cross-coupling reactions revolutionized organic synthesis and reshaped an entire branch of science. However, recognizing the importance of his work, Negishi refused to patent his idea in the hope that it could be used widely. Throughout his career, Negishi emphasized the importance of work–life balance, believing there were four key ingredients to happiness: good health; happy surroundings, including family; pursuit of a worthy career; and at least one long-lasting hobby. Negishi's was reading anything he could find, from the Bible (although he was not Christian) to ‘how to’ guides and poetry.

Nature **595**, 168 (2021)

doi: <https://doi.org/10.1038/d41586-021-01828-9>

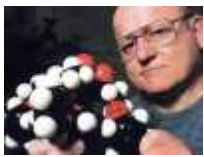
Updates & Corrections

- **Correction 09 July 2021:** An earlier version of this Obituary incorrectly located Purdue University in Illinois.

Related Articles



- [Ronald Breslow \(1931–2017\)](#)

-  [Gilbert Stork \(1921–2017\)](#)
-  [Jack Baldwin \(1938–2020\)](#)
-  [The chemistry chronicles](#)

Subjects

- [History](#)
- [Chemistry](#)
- [Drug discovery](#)

nature careers

Jobs >

- [Canada Research Chair Tier 2 in Indigenous Natural Sciences](#)

The University of British Columbia (UBC)

Vancouver, Canada

- [Chemical/Environmental Engineer – Gas Chromatography and Mass Spectrometry](#)

Jülich Research Centre (FZJ)

Jülich, Germany

- [Chemical Technical Assistant \(m/f/d\)](#)

Alfred Wegener Institute - Helmholtz Centre for Polar and Marine Research (AWI)

Bremerhaven, Germany

- [Abteilungsassistent*in \(d/m/w\), Abteilung „IT“](#)

Helmholtz Centre for Heavy Ion Research GmbH (GSI)

Darmstadt, Germany

[Download PDF](#)

Related Articles



- [Ronald Breslow \(1931–2017\)](#)



- [Gilbert Stork \(1921–2017\)](#)



- [Jack Baldwin \(1938–2020\)](#)



- [The chemistry chronicles](#)

Subjects

- [History](#)
 - [Chemistry](#)
 - [Drug discovery](#)
-

This article was downloaded by **calibre** from <https://www.nature.com/articles/d41586-021-01828-9>

| [Section menu](#) | [Main menu](#) |

- COMMENT
- 01 July 2021

Everyone should decide how their digital data are used — not just tech companies

Smartphones, sensors and consumer habits reveal much about society. Too few people have a say in how these data are created and used.

- [Jathan Sadowski](#) ⁰,
- [Salomé Viljoen](#) ¹ &
- [Meredith Whittaker](#) ²

1. [Jathan Sadowski](#)

1. Jathan Sadowski is a research fellow in the Emerging Technologies Research Lab in the Faculty of Information Technology and in the Centre of Excellence for Automated Decision-Making and Society in the Faculty of Arts, both at Monash University, Melbourne, Australia.

[View author publications](#)

You can also search for this author in [PubMed](#) [Google Scholar](#)

2. Salomé Viljoen

1. Salomé Viljoen is an academic fellow at Columbia Law School in New York City, USA.

[View author publications](#)

You can also search for this author in [PubMed](#) [Google Scholar](#)

3. Meredith Whittaker

1. Meredith Whittaker is the Minderoo Research Professor at New York University and co-founder and faculty director of the AI Now Institute in New York, USA.

[View author publications](#)

You can also search for this author in [PubMed](#) [Google Scholar](#)





•

[Download PDF](#)



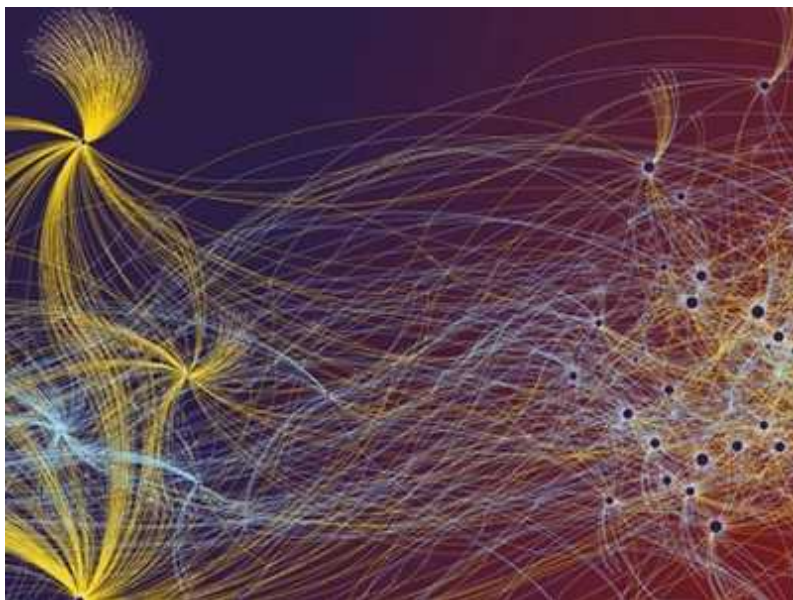
Taiwan's innovative civic data culture shaped its rapid and effective pandemic response. Credit: Ceng Shou Yi/NurPhoto via Getty

A few decades ago, if a researcher wanted to ask how bad weather affected commuting patterns — the transport modes people use, the routes they take, the times they travel — they might have surveyed hundreds of people and counted cars, buses and bikes at major junctions.

Today, it is possible to access data on the movements of millions of people, taken from location trackers in phones or vehicles, sometimes in real time. These data can be combined with analyses of COVID-19 vaccinations to investigate the effects of commuters returning to the office. And weather data can be incorporated to determine whether more people are now more likely to work from home when heavy rain hits than they were a few years ago.

In theory. Reality often falls far short of this rosy vision.

Most of the data available to — or sought by — computational social scientists today are generated to answer questions that have nothing to do with their research. The data instead bear the mark of their original purpose, be that targeted advertisements or personalized insurance premiums. These data can be cautiously repurposed to answer other questions — wearable fitness trackers could inform studies of obesity, for example — but crucial gaps usually remain. As a result, scientists often use workarounds to glean meaning from what they can get¹.



Nature special: Computational social science

For instance, analysts trying to answer questions about transportation patterns for a city government in Greater Sydney, Australia, had to make use of the low-quality spatial and temporal data created when mobile phones ping cell towers². What's more, they had to purchase these data at high cost from a telecommunications provider.

In our view, the current model, in which the digital traces of our lives are monopolized by corporations, threatens the ability of society to produce the rigorous, independent research needed to tackle pressing issues. It also restricts what information can be accessed and the questions that can be asked. This limits progress in understanding complex phenomena, from how vaccine coverage alters behaviour to how algorithms influence the spread of misinformation.

Instead, we call for the creation, management and curation of behavioural data in public data trusts.

Access denied

This political economy of data puts social scientists in a difficult position. Access comes with conditions: companies have an active interest in the questions researchers ask (or don't) as well as the data they can access and how it is analysed. And it is rarely possible for scientists to determine what information was not included when the gatekeepers do grant access, or how the data were generated in the first place.

At best, this can have a chilling effect on scholarship. Some studies won't be done if they could threaten the data provider's reputation or bottom line. At worst, researchers can feel pressure to align their studies and results with the values and priorities of technology companies. Unflattering findings could see data access revoked, imperilling the continuity of a researcher's work, and potentially also their standing in their institution and with their peers.

In March, for example, a report on the Responsible AI team at Facebook showed that researchers were restricted in the types of problems they could study and the solutions they could propose. Rather than being able to root out the disinformation and hate speech that contributes to engagement, their work had to focus on technical changes to bias in systems (see go.nature.com/2t5kudw).



Wanted: rules for pandemic data access that everyone can trust

A reliance on the largesse of private companies also challenges tenets of scientific rigour and responsibility. Contractual restrictions can prevent researchers from reproducing and validating others' results. In 2019, health researchers reported that 'significant racial bias' in the training data for a proprietary commercial algorithm meant that US\$1,800 less per year was spent on the treatment of Black patients compared with white patients with the same level of health³. The bias — which is disputed by the company — was revealed only when researchers did an independent audit of the records of a large university hospital.

The status quo poses serious problems. Increasingly, approaches that amass demographic data, study behaviours and predict risk factors are equated with big tech's unscrupulous practices — diminishing the reputation and credibility of the techniques in the long-term. And the dominance of a few walled gardens of data is shaping computational social science. PhDs and tenure are often granted on the basis of the funding, data, publications and prestige secured through industry partnerships.

Data pipeline

What we face is not simply limited access to proprietary data, but fundamental questions regarding the entire pipeline of how those data arise and where they go.

What companies deem valuable can distort the kinds of data available for analysis. Tech giants place great importance on behavioural information about people as a new asset class⁴. This influences research agendas, in part because the data are available in large amounts. Computational social scientists often use social-media data, for instance, as an imperfect proxy for many other factors such as mobility or health, even when they are far from ideal for answering their questions⁵.

Moreover, insights can be tainted by data that were, often unknowingly, constructed using inappropriate assumptions and harmful biases. For instance, AI researchers have uncovered how large data sets such as ImageNet, used to train and assess machine-learning systems for more than a decade, are encoded with sexist and racist stereotypes, which then carry forward into software^{6,7}.

Democratic governance

There's little recourse to address these fundamental issues without transformative change to the private monopolization of data. Systems need to be established that are more suitable for the analysis of social phenomena, and in ways that are ethical, equitable and scientifically sound. Just as patented knowledge enters the public domain when intellectual-property rights expire, so, too, should behavioural data gathered by companies come under democratic control after some time.

A model with better control would involve collective stewardship of the data pipeline, in public trusts that are subjected to scientific oversight and democratic accountability. Existing work paves the way for such instruments. For example, a report by Element AI and Nesta outlines how trusts are an attractive policy tool for pooling the rights of data subjects and setting terms of use (see go.nature.com/3decirk; S.V. was a participant in the workshop on which the report is based).



Data sovereignty champion Francesca Bria helped to found Barcelona's Smart City initiative to give residents control over their data. Credit: Matthias Balk/dpa/Alamy

Barcelona in Spain has piloted a promising approach. In 2017, it created a 'city data commons', giving residents control over how data about them and their communities were produced, as well as the power to participate in governance decisions. Its Open Data portal currently contains 503 data sets about the municipality, including real-time information on the use of the city's bicycle-sharing system.

Such democratic control helps to protect the people these data purport to be about. Public governance confers extra rights and rules — including anti-discrimination, due process and greater accountability. In most cases, these protections extend much further than do private obligations, although there is variation between countries and regions.

Collective stewardship can emphasize the socially valuable aspect of information — not what is known about a person, but what that reveals about how people are alike and connected⁸. Instead of focusing only on the rights of individuals, a public trust can and should also represent the interests and values of groups affected by downstream uses of data products. For instance, when photos were scraped from cloud-storage websites and used by the company ClearView AI in New York to train powerful facial recognition software, the people photographed weren't aware this was happening. What of the businesses and police departments who bought the package?

Of course, the owning of data by public institutions comes with its own challenges. Governments sometimes use data to inflict serious harms, such as by targeting marginalized populations, and they can escape accountability through authoritarian measures. This is why public trusts must be designed for democratic governance from the outset. They must be representative of and responsive to the communities that the data are created about.

Strict siloes must be put in place so that the public data pipeline is not accessible to or influenced by other government organizations, such as the police or military. Singapore, for example, has used GPS data from mobile phones for contact-tracing during the COVID-19 pandemic. But citizens' trust was eroded when it was revealed that police used these same data during murder investigations.

Three steps

We recommend three steps that policymakers and scientific institutions should take towards the safeguarding of behavioural data as a public good.

Build public infrastructure. Measurement, computational and storage systems should be funded and maintained to support the construction of large data sets that are appropriate for quantitative and qualitative research. Resources should go to communities and organizations that are already engaging in these practices, including Indigenous peoples working to govern, classify and control their knowledge using principles of 'data sovereignty'. The infrastructure must be buttressed with robust participation

mechanisms, so that those whom the data are ‘about’ are able to set the collection agenda as well as challenge and remedy inaccurate or harmful use.

Take control. Policies are needed that transfer data created and controlled by private entities to public institutions. They must also cover details of the underlying measurement methodologies, collection processes and storage environment.



Time for the Human Screenome Project

There is already a legal precedent for granting private companies restricted rights to non-tangible assets that eventually revert to the public domain. For instance, the Hatch–Waxman Act governs intellectual property in generic drug production⁹. We propose a policy in which companies have a limited monopoly over the data they create and own. After a set period of time — say 3 years — these data either become a public resource or are eliminated.

Such a policy can also apply to any models that the data have been used to train or inform, because they could pose an undue risk to people if retained. There is precedent for this, too: in May, the US Federal Trade Commission required the destruction of facial-recognition algorithms trained on photos that were obtained deceptively. Provisions could also be tied to existing data-privacy regulations by giving companies favourable terms and

incentives if they turn over data sets and metadata to universities, archives or other public institutions to manage.

Expand governance. Dedicated institutions should be created with the capacities to steward data in the public interest. There is no need to start from scratch. In the United States, the Library of Congress, National Science Foundation and National Institutes of Health could all serve as institutional models — and all have representatives on public data trusts.

Such institutions would be staffed by database managers who are trained in the ethical standards of library science, which balance knowledge curation for the public good against the risks that arise from sharing information. Experts in measurement and quantitative and qualitative methods could develop new efforts to generate data, working closely with researchers and communities to determine what socially minded questions to ask.

Computational social scientists, following the model of sworn statistical officers in the US Census Bureau, would evaluate the sensitivity of the source. Data from low-sensitivity sources could be published — as aggregated, anonymized information. And access to high-sensitivity data would be strictly safeguarded — including individual, identifiable information. A public data trust could also invite community groups and advocacy organizations to help shape protocols for consent and dispute; agendas for data construction and research goals; and requirements for accessing and using data.

Demand change

We are not alone in this fight. We need only look at the sweeping investigations into antitrust actions against platforms such as Google, Facebook, Amazon and Alibaba in the United States, European Union, Australia and China. The COVID-19 pandemic has also provided momentum. This March, the science academies of the G7 group called for a mechanism to oblige public and private organizations to share relevant data during health emergencies (see go.nature.com/2sjqj2v).

To get the ball rolling, scientists whose work relies on large proprietary data sets should speak out — on social media and at conferences such as NeurIPS — about the perils of corporate data gatekeeping and share their lived experiences with these difficult ethical choices. They should pressure universities to call for changes in current data-ownership regimes and ally with community groups already campaigning for redress from harm enabled by surveillance.

Representatives from academic associations and government bodies such as census offices and national libraries should form an interdisciplinary working group to develop policy for the creation of public data trusts. Computational social scientists must play their part as public stewards of an important collective resource for knowing ourselves and our societies.

Nature **595**, 169–171 (2021)

doi: <https://doi.org/10.1038/d41586-021-01812-3>

References

1. 1.

Lazer, D. *et al.* *Nature* **595**, 189–196 (2021).

[Article](#) [Google Scholar](#)

2. 2.

Dowling, R., McGuirk, P., Maalsen, S. & Sadowski, J. *Urban Stud.* <https://doi.org/10.1177/0042098020986292> (2021).

[Article](#) [Google Scholar](#)

3. 3.

Obermeyer, Z., Powers, B., Vogeli, C. & Mullainathan, S. *Science* **366**, 447–453 (2019).

[PubMed](#) [Article](#) [Google Scholar](#)

4. 4.

Sadowski, J. *Big Data Soc.* <https://doi.org/10.1177/2053951718820549> (2019).

[Article](#) [Google Scholar](#)

5. 5.

Sloan, L. & Quan-Haase, A. (eds) *The Sage Handbook of Social Media Research Methods* (Sage Publications, 2017).

[Google Scholar](#)

6. 6.

Hutchinson, B. *et al.* in *Proceedings of the 2021 ACM Conference on Fairness, Accountability, and Transparency* 560–575 (Association for Computing Machinery, 2021).

[Google Scholar](#)

7. 7.

Raji, I. D. *et al.* in *Proceedings of the AAAI/ACM Conference on AI, Ethics, and Society* 145–151 (Association for Computing Machinery, 2020).

[Google Scholar](#)

8. 8.

Viljoen, S. Preprint at SSRN <https://doi.org/10.2139/ssrn.3727562> (2021).

9. 9.

Lewis, R. A. *J. Contemp. Health Law Policy* **8**, 361–378 (1992).

[PubMed](#) [Google Scholar](#)

[Download references](#)

Competing Interests

The authors declare no competing interests.

Related Articles



- [Nature special: Computational social science](#)



- [Cities — try to predict superspreading hotspots for COVID-19](#)



- [Time for the Human Screenome Project](#)



- [Wanted: rules for pandemic data access that everyone can trust](#)

Subjects

- [Human behaviour](#)
- [Information technology](#)
- [Intellectual-property rights](#)
- [Society](#)

- [Databases](#)

nature careers

[Jobs](#) >

- [Canada Research Chair Tier 2 in Indigenous Natural Sciences](#)

The University of British Columbia (UBC)

Vancouver, Canada

- [Chemical/Environmental Engineer – Gas Chromatography and Mass Spectrometry](#)

Jülich Research Centre (FZJ)

Jülich, Germany

- [Chemical Technical Assistant \(m/f/d\)](#)

Alfred Wegener Institute - Helmholtz Centre for Polar and Marine Research (AWI)

Bremerhaven, Germany

- [Abteilungsassistent*in \(d/m/w\), Abteilung „IT“](#)

Helmholtz Centre for Heavy Ion Research GmbH (GSI)

Darmstadt, Germany

[Download PDF](#)

Related Articles

-  [Nature special: Computational social science](#)
-  [Cities — try to predict superspreading hotspots for COVID-19](#)
-  [Time for the Human Screenome Project](#)
-  [Wanted: rules for pandemic data access that everyone can trust](#)

Subjects

- [Human behaviour](#)
- [Information technology](#)
- [Intellectual-property rights](#)
- [Society](#)
- [Databases](#)

This article was downloaded by **calibre** from <https://www.nature.com/articles/d41586-021-01812-3>

- CORRESPONDENCE
- 06 July 2021

UK biodiversity: close gap between reality and rhetoric

- [Sophus O. S. E. zu Ermgassen](#)⁰,
- [Joseph W. Bull](#)¹ &
- [Ben Groom](#)²

1. [Sophus O. S. E. zu Ermgassen](#)

1. Durrell Institute of Conservation and Ecology, Canterbury, UK.

[View author publications](#)

You can also search for this author in [PubMed](#) [Google Scholar](#)

2. Joseph W. Bull

1. Durrell Institute of Conservation and Ecology, Canterbury, UK.

[View author publications](#)

You can also search for this author in [PubMed](#) [Google Scholar](#)

3. Ben Groom

1. University of Exeter Business School, Exeter, UK.

[View author publications](#)

You can also search for this author in [PubMed](#) [Google Scholar](#)





•

[Download PDF](#)

In a bid to position the United Kingdom as a global environmental leader before this year's United Nations biodiversity conference (COP15) and climate-change conference (COP26), the UK government has announced biodiversity initiatives to halt species declines by 2030 and to protect 30% of its land area (see, for example, go.nature.com/3x4yk1k). These plans are at odds with its current spending on conservation.

The government's conservation funding fell by 42% in real terms between 2008 and 2018 to just 0.02% of gross domestic product (GDP; see

go.nature.com/2udg3od). It missed 14 of its 20 international biodiversity commitments (Aichi targets) in 2020 (see go.nature.com/3dor8ra). This year it commissioned the Dasgupta Review, which calls for economic changes to stop biodiversity loss (see go.nature.com/3jozldl).

However, even taking into account the May announcement of a 47% increase in Natural England's funding (see go.nature.com/2t96qjn), the country still spends less than other nations with comparable GDP (see [A. Seidl et al. *Nature Ecol. Evol.* **5**, 530–539; 2021](https://doi.org/10.1038/natureecologyevolution.530) and go.nature.com/2udg3od). The United Kingdom needs to reconsider its public expenditure priorities if it is to close the gap between rhetoric and reality.

Nature **595**, 172 (2021)

doi: <https://doi.org/10.1038/d41586-021-01819-w>

Competing Interests

The authors declare no competing interests.

Related Articles

- [See more letters to the editor](#)

Subjects

- [Biodiversity](#)
- [Government](#)
- [Funding](#)

nature careers

[Jobs](#) >

- [Canada Research Chair Tier 2 in Indigenous Natural Sciences](#)

The University of British Columbia (UBC)

Vancouver, Canada

- [Chemical/Environmental Engineer – Gas Chromatography and Mass Spectrometry](#)

Jülich Research Centre (FZJ)

Jülich, Germany

- [Chemical Technical Assistant \(m/f/d\)](#)

Alfred Wegener Institute - Helmholtz Centre for Polar and Marine Research (AWI)

Bremerhaven, Germany

- [Abteilungsassistent*in \(d/m/w\), Abteilung „IT“](#)

Helmholtz Centre for Heavy Ion Research GmbH (GSI)

Darmstadt, Germany

[Download PDF](#)

Related Articles

- [See more letters to the editor](#)

Subjects

- [Biodiversity](#)
- [Government](#)
- [Funding](#)

This article was downloaded by **calibre** from <https://www.nature.com/articles/d41586-021-01819-w>

| [Section menu](#) | [Main menu](#) |

- CORRESPONDENCE
- 06 July 2021

China's homeless elephants need linked reserves

- [Nian Yang](#)⁰,
- [Wenwen Li](#)¹,
- [Peng Liu](#)² &
- [Li Zhang](#)³

1. Nian Yang

1. Beijing Normal University, Beijing, China.

[View author publications](#)

You can also search for this author in [PubMed](#) [Google Scholar](#)

2. Wenwen Li

1. First Institute of Oceanography, Ministry of Natural Resources, Qingdao, China.

[View author publications](#)

You can also search for this author in [PubMed](#) [Google Scholar](#)

3. Peng Liu

1. The University of Hong Kong, Hong Kong, China

[View author publications](#)

You can also search for this author in [PubMed](#) [Google Scholar](#)

4. [Li Zhang](#)

1. Beijing Normal University, Beijing, China.

[View author publications](#)

You can also search for this author in [PubMed](#) [Google Scholar](#)

•



•

[Download PDF](#)

Fifteen Asian elephants caught the world's attention as they trekked northwards for about 500 kilometres from Xishuangbanna prefecture in China's southwestern province of Yunnan (see go.nature.com/3wofhfc). Their epic journey is widely considered to be a quest for better resources — almost 40% of the animals' habitat in Xishuangbanna has been lost to commercial development over the past 20 years. We call for an integrated system of national park reserves for China's elephants. This should be protected and take into account their foraging habits, migration patterns and other phased activities.

Conservation efforts have nearly doubled China's Asian elephant population to about 300 individuals over 40 years ([L. Zhang et al. PLoS ONE 10, e0124834; 2015](#)). However, the destruction of habitat by extensive planting of cash crops such as rubber and tea has put them in conflict with humans. The government paid out about 22 million yuan (US\$3.25 million) in compensation last year alone (unpublished data).

Reconnecting, restoring and expanding existing habitats would cut the cost of such conflicts and boost profits from ecosystem services (see, for example, [P. Liu et al. Ecosyst. Serv. 38, 100949; 2019](#)).

Nature **595**, 172 (2021)

doi: <https://doi.org/10.1038/d41586-021-01820-3>

Competing Interests

The authors declare no competing interests.

Related Articles

- [See more letters to the editor](#)

Subjects

- [Animal behaviour](#)
- [Human behaviour](#)
- [Conservation biology](#)

nature careers

[Jobs](#) >

- [Canada Research Chair Tier 2 in Indigenous Natural Sciences](#)

The University of British Columbia (UBC)

Vancouver, Canada

- [Chemical/Environmental Engineer – Gas Chromatography and Mass Spectrometry](#)

Jülich Research Centre (FZJ)

Jülich, Germany

- [Chemical Technical Assistant \(m/f/d\)](#)

Alfred Wegener Institute - Helmholtz Centre for Polar and Marine Research (AWI)

Bremerhaven, Germany

- [Abteilungsassistent*in \(d/m/w\), Abteilung „IT“](#)

Helmholtz Centre for Heavy Ion Research GmbH (GSI)

Darmstadt, Germany

[Download PDF](#)

Related Articles

- [See more letters to the editor](#)

Subjects

- [Animal behaviour](#)
 - [Human behaviour](#)
 - [Conservation biology](#)
-

This article was downloaded by **calibre** from <https://www.nature.com/articles/d41586-021-01820-3>

| [Section menu](#) | [Main menu](#) |

- CORRESPONDENCE
- 06 July 2021

COVID-19: living guidelines help fix cracks in evidence pipeline

- [Per Olav Vandvik](#)⁰,
- [Lisa Askie](#)¹,
- [Fiona Glen](#)²,
- [Britta Tendal](#)³ &
- [Thomas Agoritsas](#)⁴

1. [Per Olav Vandvik](#)

1. MAGIC Evidence Ecosystem Foundation, Oslo, Norway.

[View author publications](#)

You can also search for this author in [PubMed](#) [Google Scholar](#)

2. Lisa Askie

1. World Health Organization, Geneva, Switzerland.

[View author publications](#)

You can also search for this author in [PubMed](#) [Google Scholar](#)

3. Fiona Glen

1. National Institute for Health and Care Excellence, Manchester, UK.

[View author publications](#)

You can also search for this author in [PubMed](#) [Google Scholar](#)

4. Britta Tendal

1. Australian COVID-19 Clinical Evidence Taskforce, Melbourne, Australia.

[View author publications](#)

You can also search for this author in [PubMed](#) [Google Scholar](#)

5. Thomas Agoritsas

1. University of Geneva, Switzerland.

[View author publications](#)

You can also search for this author in [PubMed](#) [Google Scholar](#)





•

[Download PDF](#)

Continually updated as new research findings come out, ‘living guidelines’ provide invaluable support for clinicians having to make timely and informed decisions in treating people with COVID-19 (see [Nature 593, 168; 2021](#) and [Nature 593, 182–185; 2021](#)).

Pioneered in Australia, these living guidelines process new clinical-trial evidence into widely accessible, practice-changing recommendations within just a few weeks, without compromising standards for trustworthiness ([B. Tendal et al. J. Clin. Epidemiol. 131, 11–21; 2021](#)). Living systematic

reviews of network meta-analyses feed into every update. These include structured evidence summaries, and they are published in user-friendly formats.

Producing living guidelines for COVID-19 has required global collaboration and innovations in methods, processes and technology. They need to be widely used: living evidence and guidance have broad applications in health care beyond the current pandemic. Efficient implementation and evaluation of impact on delivered care will greatly enhance the evidence ecosystem ([P. O. Vandvik and L. Brandt *J. Clin. Epidemiol.* 123, 166–170; 2020](#)).

Nature **595**, 172 (2021)

doi: <https://doi.org/10.1038/d41586-021-01821-2>

Related Articles

- [See more letters to the editor](#)

Subjects

- [Medical research](#)
- [Health care](#)

nature careers

[Jobs](#) >

- [Canada Research Chair Tier 2 in Indigenous Natural Sciences](#)

The University of British Columbia (UBC)

Vancouver, Canada

- [Chemical/Environmental Engineer – Gas Chromatography and Mass Spectrometry](#)

Jülich Research Centre (FZJ)

Jülich, Germany

- [Chemical Technical Assistant \(m/f/d\)](#)

Alfred Wegener Institute - Helmholtz Centre for Polar and Marine Research (AWI)

Bremerhaven, Germany

- [Abteilungsassistent*in \(d/m/w\), Abteilung „IT“](#)

Helmholtz Centre for Heavy Ion Research GmbH (GSI)

Darmstadt, Germany

[Download PDF](#)

Related Articles

- [See more letters to the editor](#)

Subjects

- [Medical research](#)
- [Health care](#)

This article was downloaded by **calibre** from <https://www.nature.com/articles/d41586-021-01821-2>

- CORRESPONDENCE
- 06 July 2021

Protect pollinators — reform pesticide regulations

- [Adrian Fisher](#) [ORCID: http://orcid.org/0000-0001-5300-1910](http://orcid.org/0000-0001-5300-1910) 0
 1. Arizona State University, Tempe, Arizona, USA. On behalf of 14 co-signatories.

[View author publications](#)

You can also search for this author in [PubMed](#) [Google Scholar](#)





•

[Download PDF](#)

Many approved pesticides still damage pollinator health at doses used in agriculture (see, for example, [A. R. Main *et al.* Agric. Ecosyst. Environ. 287, 106693; 2020](#)). We argue that this is due to a systemic failure in pesticide regulations (see, for instance, [S. López-Cubillo *et al.* Nature 573, 196; 2019](#)) that has been exacerbated by weak enforcement. Stricter laws are needed that are evidence-based, override vested interests and recognize pollinators as essential contributors to food security.

Policymakers must learn from failures in neonicotinoid regulation (see, for example, [F. Sgolastra et al. *Biol. Conserv.* **241**, 108356; 2020](#)). Before approval, pesticide risk assessment should incorporate protocols that address sub-lethal effects on pollinators. These include alterations in their behaviour and fitness under ecologically realistic conditions; mandatory testing on diverse species of native pollinators and of colonies for eusocial pollinators; and toxicity evaluation when combined with other chemicals such as proprietary additives, co-occurring pesticides and environmental residues.

Long-term monitoring after approval by appropriate governmental organizations will be necessary to pick up unforeseen environmental interactions promptly.

Nature **595**, 172 (2021)

doi: <https://doi.org/10.1038/d41586-021-01818-x>

A full list of co-signatories to this letter appears in Supplementary Information.

Supplementary Information

1. [List of co-signatories](#)

Competing Interests

The authors declare no competing interests.

Related Articles

- [See more letters to the editor](#)

Subjects

- [Law](#)

- [Ecology](#)
- [Agriculture](#)

nature careers

[Jobs](#) >

- [Canada Research Chair Tier 2 in Indigenous Natural Sciences](#)

The University of British Columbia (UBC)

Vancouver, Canada

- [Chemical/Environmental Engineer – Gas Chromatography and Mass Spectrometry](#)

Jülich Research Centre (FZJ)

Jülich, Germany

- [Chemical Technical Assistant \(m/f/d\)](#)

Alfred Wegener Institute - Helmholtz Centre for Polar and Marine Research (AWI)

Bremerhaven, Germany

- [Abteilungsassistent*in \(d/m/w\), Abteilung „IT“](#)

Helmholtz Centre for Heavy Ion Research GmbH (GSI)

Darmstadt, Germany

[Download PDF](#)

Related Articles

- [See more letters to the editor](#)

Subjects

- [Law](#)
- [Ecology](#)
- [Agriculture](#)

This article was downloaded by **calibre** from <https://www.nature.com/articles/d41586-021-01818-x>

| [Section menu](#) | [Main menu](#) |

Work

- **‘We’re problem solvers’: research administrators offer guidance to working scientists** [05 July 2021]

Career Feature • Helping with grant applications, ensuring compliance and coordinating with funders is all part of the job.

- **Shifting shores: delving into the past with mud cores** [05 July 2021]

Where I Work • Geologist Nicole Khan examines coastal sediment samples to find out how sea levels have changed over the past 1,000 years.

- CAREER FEATURE
- 05 July 2021

‘We’re problem solvers’: research administrators offer guidance to working scientists

Helping with grant applications, ensuring compliance and coordinating with funders is all part of the job.

- [Sara Reardon](#) 0

1. Sara Reardon

1. Sara Reardon is a freelance writer in Bozeman, Montana.

[View author publications](#)

You can also search for this author in [PubMed](#) [Google Scholar](#)





•

[Find a new job](#)

[Download PDF](#)



Research administrators provide essential support in organizing grants and collaborations. Credit: Getty

The 2011 earthquake in Japan changed neuroscientist Tadashi Sugihara's career path forever. Sugihara had been working as a senior research scientist at the RIKEN Brain Science Institute in Wako, but the damage to his laboratory and other setbacks from the quake prompted him to reconsider his dream of becoming a principal investigator.

His lab had been partnering with Japanese automotive manufacturer Toyota to integrate brain science into car-safety systems, and Sugihara had learnt that he was good at the intensive budgeting and report writing that such a collaboration entailed. "I realized some of the researchers really did not like these kinds of negotiations with a big company," he says. "I was gradually understanding another side of my skills that made me very useful."

So when the Japanese Ministry of Education launched an initiative in 2011 to fund the appointments of academic administrators, Sugihara applied for a

job as research administrator at Kyoto University. Although he was initially worried about abandoning his dream, he was able to move past those concerns. “I didn’t feel bad at all,” he says. “The transition was very smooth.”

Now a research-grant-application manager, Sugihara helps scientists at the Okinawa Institute of Science and Technology to apply for funds and manages the budgets of existing awards. Relationships between research and administrative operations can be thorny, but he is pleased with his role. “This kind of job makes us very happy because we feel we are welcome,” he says. When researchers receive a grant, they are pleased to be able to call on him and his colleagues for help with editing papers and other support.

Long seen as a supporting role, research administration has increasingly come to be recognized in academia as a profession in its own right. At least three institutions in the United States offer master’s degrees in the field, and numerous professional societies worldwide help administrators with career development and networking. The Research Administrators Certification Council, a non-profit organization in Westminster, Colorado, offers education and testing for a professional certificate that is required for many US government jobs in the field, and the Awards for Training and Higher Education organization performs a similar service in the United Kingdom. The United States has a National Research Administrator Day (25 September) to recognize those in the field.

Universities, non-profit organizations and other institutions hire research administrators for positions that include helping scientists to apply for grants, ensuring scientists comply with institutional policies and federal laws, and coordinating research with international collaborators. Many academic administrators work closely with scientists to manage their grants, whereas others liaise more often with their counterparts in government agencies.



Tadashi Sugihara (left), with a colleague at the Okinawa Institute of Science and Technology.Credit: Tadashi Sugihara

The number and roles of research administrators at a single employer vary widely depending on the type of organization and location, says Simon Kerridge, director of research policy and support at the University of Kent, UK. Large institutions such as his own might have hundreds of administrative staff members, although small, primarily undergraduate institutions could have just one.

In smaller nations, some scientists might split their time between their own bench research and administration. Institutional culture could determine how administrators are viewed, Kerridge says. “In some cultures, the academic is king and the [administrator] is support and must do what they’re told,” he says. “But if the profession has been around a little bit longer, then you develop that expertise, and the academic staff will trust you to know the things that they don’t know.” It can be difficult for busy scientists to keep up with constantly shifting regulations and protocols, particularly around

grants, and administrators ensure that faculty researchers do not fall foul of any rule changes.

The backgrounds of research administrators are as diverse as their roles. Sugihara's path from research into administration is common, although others come from business-management positions or studied public administration at university. According to an unpublished 2019 survey of 4,325 research-management and administration professionals from more than 70 countries, 28% hold a PhD and 24% hold a master's degree.

The survey found that about one-third of research administrators think it's important that people in their position have a scientific background, whereas another third say it isn't. People who enter the field from science or technology positions have some advantages when dealing with scientists at their institutions, says Rosemary Madnick, executive director of the Office of Grants & Contracts Administration at the University of Alaska Fairbanks. "You understand the faculty more from the aspect of 'I was there before, I used to write proposals, I know what you're going through,'" she says. But nearly all the survey respondents agreed that the most important attributes of a successful research administrator are soft skills, such as the ability to resolve conflicts among researchers and to multitask.



Rosemary Madnick notes that administrators can stay involved in research without having to worry about earning tenure.Credit: NCURA

Some research administrators don't have an academic background. Debra Schaller-Demers has a bachelor's degree in fine arts and worked for ten years as a conflict manager in New York City public schools, helping parents to find non-violent solutions to problems. In 2002, at the age of 46, she applied on a whim to be a compliance officer at Weill Cornell Medical College in New York City — and got the job. She thinks that the institution recognized the value of her communication and negotiation experience. She recalls a research-administrator mentor telling her that although scientists might have more-advanced degrees than hers, she had the skill set they needed to continue to do their work. “‘You have a part to play,’” she remembers the mentor telling her, “‘and deserve a seat at this table’.”

Schaller-Demers now runs the research outreach and compliance office at Memorial Sloan Kettering Cancer Center in New York City, where she trains scientists in research ethics and oversees committees on animal care,

biosafety and export control. “We do things a scientist cannot,” she says. “We grease the wheels so they don’t run afoul of regulations. With research administrators doing all that work, scientists can be left to do the good work they do in the world.”



Debra Schaller-Demers was previously a conflict manager in New York City public schools. She now runs the research outreach and compliance office at Memorial Sloan Kettering Cancer Center in New York City. Credit: SRAI

Administrators at universities and research institutes frequently work with their counterparts at funding agencies, who help to clarify agency policy, ensure that grants adhere to budgets and provide a line of communication for funded researchers. “Folks think of us as this bureaucracy there, a hurdle to get through,” says Erik Edgerton, chief grants management officer at the National Institute of Arthritis and Musculoskeletal and Skin Diseases (NIAMS), part of the US National Institutes of Health in Bethesda, Maryland. “What we’re really doing on our side is being problem solvers.” NIAMS handles some 1,700 extramural grants, and administrators there

often have to find creative ways to make grant budgets work across multiple years of funding, or to manage complex international collaborations among researchers at different institutions. “I think of this as a really good career path for someone who likes puzzles,” Edgerton says.

The job comes with other challenges as well. Among them is staying ahead of constantly shifting government regulations in areas such as digital privacy, open access to data and publications, and international exports of research materials and information. Conversations about money or regulations can also test administrators’ people skills. “Scientists in general don’t want to be told ‘no,’” Schaller-Demers says. “Without a certain baseline skill set, it can go downhill quickly.”

Cultural differences between a university’s research operations and administrative offices can strain relationships. Some administrators struggle with the entrenched idea that scientists who leave academic research for an administrative career have somehow failed. “It’s an unhelpful attitude and old-fashioned, and I hope it’s changing,” says Hilary Noone, a faculty research and projects officer at Newcastle University, UK.

[Collection: Research leadership](#)

Still, Noone describes a ‘them versus us’ culture between academic researchers and support staff members, including research administrators. In a March survey, she found that many of the 281 administrators and lab technicians felt undervalued and that their opinions were seen as less important than those of academics. Direct bullying, harassment or discrimination was reported by 44% of respondents. “A lot of this is not intended,” Noone says. “It’s unconscious and has taken a long time to form.”

In truth, Noone says, academics and administrators face many of the same challenges, and recognizing each other’s strengths and expertise could go a long way towards building camaraderie. “If we join up, we open the potential for collaboration and more porosity between different sectors.” Sharing experiences about bullying and harassment can help foster change, for instance.

Educating faculty members about why certain regulations and procedures exist would also help to improve relations, she adds. “We’re not breathing barriers and paperwork,” Noone says. “Academics are annoyed about paperwork and processes, but we also share frustration in that, and we don’t like it either. Sometimes you can bond over frustration — that can be fun.”

Madnick and others encourage junior scientists who are considering careers outside research to assess whether administration would play to their strengths. If a junior scientist feels as though they are at a professional crossroads, it might help to remember why they are working in a lab in the first place. “It’s because you enjoy the science,” she says, and administrators are able to stay involved in research without having to worry about earning tenure or winning their next grant. They might also have more flexible working conditions than those of research scientists. Plus, Madnick adds, “they’ve got such a huge impact on what happens, and they get to see the benefit of research from the beginning all the way to when it hits the public”.

Sugihara agrees. “There are many opportunities and possibilities,” he says. “Even if [junior scientists] have to change their career from research to something else, that’s good. They will get a chance to dance on another stage of their life.”

Nature **595**, 321-322 (2021)

doi: <https://doi.org/10.1038/d41586-021-01829-8>

Related Articles



- [Calls for culture change as “them versus us” mindset drives rift between academic and non-academic staff](#)



- [Why academic administration was the right choice for me](#)
- [Collection: Research leadership](#)

Subjects

- [Careers](#)
- [Research management](#)
- [Lab life](#)

nature careers

[Jobs](#) >

- [Canada Research Chair Tier 2 in Indigenous Natural Sciences](#)

The University of British Columbia (UBC)

Vancouver, Canada

- [Chemical/Environmental Engineer – Gas Chromatography and Mass Spectrometry](#)

Jülich Research Centre (FZJ)

Jülich, Germany

- [Chemical Technical Assistant \(m/f/d\)](#)

Alfred Wegener Institute - Helmholtz Centre for Polar and Marine Research (AWI)

Bremerhaven, Germany

- [Abteilungsassistent*in \(d/m/w\), Abteilung „IT“](#)

Helmholtz Centre for Heavy Ion Research GmbH (GSI)

Darmstadt, Germany

[Download PDF](#)

Related Articles



- [Calls for culture change as “them versus us” mindset drives rift between academic and non-academic staff](#)



- [Why academic administration was the right choice for me](#)
- [Collection: Research leadership](#)

Subjects

- [Careers](#)
- [Research management](#)
- [Lab life](#)

| [Section menu](#) | [Main menu](#) |

- WHERE I WORK
- 05 July 2021

Shifting shores: delving into the past with mud cores

Geologist Nicole Khan examines coastal sediment samples to find out how sea levels have changed over the past 1,000 years.

- [Amber Dance](#) ⁰

1. Amber Dance

1. Amber Dance is a freelance writer in Los Angeles, California.

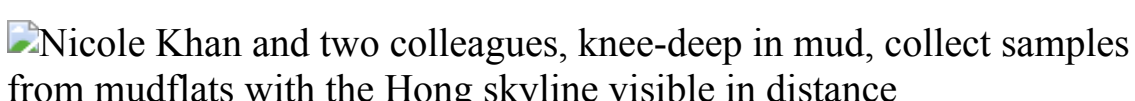
[View author publications](#)

You can also search for this author in [PubMed](#) [Google Scholar](#)





•



Nicole Khan is a geologist at the University of Hong Kong. Credit: Suzanne Lee/Panos Pictures

[Download PDF](#)

We often hear that sea levels will rise by a metre or two because of climate change. But that's a global estimate: if you're a city planner on, say, the China coast or in Miami, you want to know how sea level is going to change in your area. My work as a geologist helps us to predict future

coastal changes by determining how much sea levels have risen and fallen in the past 1,000 years.

My team and I study soil samples collected from shorelines around the world. When we're not hampered by pandemic-related restrictions, we might spend two weeks knee-deep in mud, in a jungle gym of coastal mangroves. But the pandemic has limited us to our backyard, so to speak: in this picture, we're on a coastal mudflat in Hong Kong. Across the bay is the city of Shenzhen on mainland China. Both Shenzhen and Hong Kong are part of the Pearl River delta, where low-lying lands are at risk from rising seas.

I'm with my two graduate students, Howard Yu and Kayla Murai. We examine long, narrow samples of soil from deep in the ground that were collected with the kind of sediment corer we're holding here. Because Earth formed in layers, the deeper we go, the further into the past we can explore. If we can identify features of these cores indicating that they were part of coastal environments such as mudflats and mangrove swamps during a particular era, we can map out where the shores used to be and how they changed over time.

For a coastal marker, Howard is using fossils of foraminifera, single-celled creatures with spiral shells, most of which live on, or inside, sea-floor sediment. We'll work out what kinds of foraminifera show up in modern-day mudflats, then look for them in archived sediment cores. That will allow us to fill a gap in our understanding of what the China coastline was like between 500 and 1,000 years ago.

I love this work because it's like being a detective: you collect something from the field, look at the evidence and unravel the story of what happened in the past.

Nature **595**, 324 (2021)

doi: <https://doi.org/10.1038/d41586-021-01830-1>

Related Articles

-  [Transfixed by the glow of Arctic ice under starlight](#)
-  [Politics and the pandemic disrupt migration patterns in research](#)
-  [Geoscience: Ups and downs](#)

Subjects

- [Careers](#)
- [Climate change](#)
- [Geology](#)

nature careers

[Jobs >](#)

- [Canada Research Chair Tier 2 in Indigenous Natural Sciences](#)

The University of British Columbia (UBC)

Vancouver, Canada

- [Chemical/Environmental Engineer – Gas Chromatography and Mass Spectrometry](#)

Jülich Research Centre (FZJ)

Jülich, Germany

- [**Chemical Technical Assistant \(m/f/d\)**](#)

Alfred Wegener Institute - Helmholtz Centre for Polar and Marine Research (AWI)

Bremerhaven, Germany

- [**Abteilungsassistent*in \(d/m/w\), Abteilung „IT“**](#)

Helmholtz Centre for Heavy Ion Research GmbH (GSI)

Darmstadt, Germany

[Download PDF](#)

Related Articles



- [**Transfixed by the glow of Arctic ice under starlight**](#)



- [**Politics and the pandemic disrupt migration patterns in research**](#)



- [**Geoscience: Ups and downs**](#)

Subjects

- [Careers](#)
 - [Climate change](#)
 - [Geology](#)
-

This article was downloaded by **calibre** from <https://www.nature.com/articles/d41586-021-01830-1>

| [Section menu](#) | [Main menu](#) |

Research

- **[Malaria vaccine gets a parasite boost in the liver](#)** [30 June 2021]
News & Views • Effective malaria vaccines are urgently needed. Now, clinical evidence indicates that a vaccination approach that uses live parasites growing in the liver can generate high levels of immune protection from infection.
- **[How to buffer against an urban food shortage](#)** [07 July 2021]
News & Views • There is widespread concern that the risk of food shocks — sudden disruptions to food supply — is increasing. It emerges that a city's vulnerability to food shocks can be reduced by diversifying its supply chains.
- **[Engineered single-domain antibodies tackle COVID variants](#)** [30 June 2021]
News & Views • Camels and llamas make antibodies that bind to targets using small, 'nobody' protein domains. Mice have now been engineered to make nanobodies that might be more effective than conventional antibodies in treating COVID-19.
- **[Fluid-rich extinct volcanoes cause small earthquakes beneath New Zealand](#)** [07 July 2021]
News & Views • Imaging of a region where an oceanic tectonic plate descends below another plate reveals evidence that fluid-rich extinct volcanoes can help to lubricate the interface between plates — reducing the potential for large earthquakes.
- **[Integrating explanation and prediction in computational social science](#)** [30 June 2021]
Perspective • The combination of computational and social sciences requires the integration of explanatory and predictive approaches into 'integrative modelling', according to Hofman and colleagues.
- **[Meaningful measures of human society in the twenty-first century](#)** [30 June 2021]
Perspective • Approaches for the management, use and analysis of large-scale behavioural datasets that were not originally intended or created for research are described.
- **[Measuring algorithmically infused societies](#)** [30 June 2021]
Perspective • This Perspective discusses the challenges for social science practices imposed by the ubiquity of algorithms and large-scale measurement and what should—and should not—be measured in societies pervaded by algorithms.

- **Thinking clearly about social aspects of infectious disease transmission** [30 June 2021]

Perspective • The use of new datastreams and local knowledge to shed light on social aspects of disease transmission will allow more accurate modelling and prediction of epidemics.

- **Human social sensing is an untapped resource for computational social science** [30 June 2021]

Perspective • The ability of people to understand the thoughts and actions of others—known as social sensing—can be combined with computational social science to advance research into human sociality.

- **r-Process elements from magnetorotational hypernovae** [07 July 2021]

Article • Observations of an extremely metal-poor star suggest that rapidly rotating massive stars with large magnetic fields were a source of r-process elements in the early Universe.

- **Quantum phases of matter on a 256-atom programmable quantum simulator** [07 July 2021]

Article • A programmable quantum simulator with 256 qubits is created using neutral atoms in two-dimensional optical tweezer arrays, demonstrating a quantum phase transition and revealing new quantum phases of matter.

- **Quantum simulation of 2D antiferromagnets with hundreds of Rydberg atoms** [07 July 2021]

Article • Programmable quantum simulation of two-dimensional antiferromagnets is achieved with up to 196 neutral atoms, and the capability of the platform is demonstrated on square and triangular arrays.

- **Optical manipulation of electronic dimensionality in a quantum material** [07 July 2021]

Article • Two-dimensional electronic states are observed at the induced domain walls of a three-dimensional charge density wave material by manipulating the periodic lattice distortion via femtosecond infrared pulses.

- **Bifunctional nanoprecipitates strengthen and ductilize a medium-entropy alloy** [07 July 2021]

Article • Increased strength and ductility in a medium-entropy alloy of Fe, Ni, Al and Ti is demonstrated using nanoprecipitates that simultaneously hinder phase transformation and block dislocation motion.

- **Supply chain diversity buffers cities against food shocks** [07 July 2021]

Article • An intensity–duration–frequency model linking food shock risk to supply chain diversity in the USA finds that boosting a city's food supply chain diversity increases the resistance of a city to food shocks of mild to moderate severity.

- **Fluid-rich subducting topography generates anomalous forearc porosity** [07 July 2021]

Article • Electromagnetic data collected at the northern Hikurangi Margin, New Zealand show that a seamount on the incoming plate allows more water to subduct, compared with normal, unfaulted oceanic lithosphere.
- **GluD1 is a signal transduction device disguised as an ionotropic receptor** [16 June 2021]

Article • The ionotropic glutamate delta receptors GluD1 and GluD2 form distinct neurexin–cerebellin complexes that differentially regulate postsynaptic glutamate receptor activities.
- **Obesity accelerates hair thinning by stem cell-centric converging mechanisms** [23 June 2021]

Article • Obesity in mice, caused by a high-fat diet, induces hair loss as a result of changes in the differentiation of hair follicle stem cells.
- **Caloric restriction disrupts the microbiota and colonization resistance** [23 June 2021]

Article • Severe caloric restriction in humans leads to reversible changes in the gut microbiota that promote weight loss and the expansion of an enteric pathogen in mice.
- **Nanobodies from camelid mice and llamas neutralize SARS-CoV-2 variants** [07 June 2021]

Article • Multivalent nanobodies against SARS-CoV-2 from mice engineered to produce camelid nanobodies recognize conserved epitopes that are inaccessible to human antibodies and show promise as a strategy for dealing with viral escape mutations.
- **Diverse functional autoantibodies in patients with COVID-19** [19 May 2021]

Article • Rapid extracellular antigen profiling of a cohort of 194 individuals infected with SARS-CoV-2 uncovers diverse autoantibody responses that affect COVID-19 disease severity, progression and clinical and immunological characteristics.
- **Two chemoattenuated PfSPZ malaria vaccines induce sterile hepatic immunity** [30 June 2021]

Article • Two malaria vaccines comprising Plasmodium falciparum sporozoites and treatment with either pyrimethamine or chloroquine induced durable protective responses against both the African vaccine strain and a heterologous South American strain of P. falciparum.
- **Base editing of haematopoietic stem cells rescues sickle cell disease in mice** [02 June 2021]

Article • A custom adenine base editor can edit the variant of the β-globin gene that causes sickle cell disease into a non-pathogenic variant in human and mouse cells, and transplantation of the edited cells rescues sickle cell disease in mice.

- **NORAD-induced Pumilio phase separation is required for genome stability** [09 June 2021]

Article • The noncoding RNA NORAD maintains genome stability in mammalian cells by sequestering Pumilio proteins in phase-separated compartments.

- **Epigenetic silencing by SETDB1 suppresses tumour intrinsic immunogenicity** [05 May 2021]

Article • A CRISPR–Cas9 screen of chromatin regulators in mouse tumour models treated with immune checkpoint blockade identifies SETDB1 as an epigenetic checkpoint protein that suppresses tumour-intrinsic immunogenicity.

- **Structural basis of omega-3 fatty acid transport across the blood–brain barrier** [16 June 2021]

Article • Cryo-electron microscopy and molecular dynamics simulations reveal how MFSD2A transports essential omega-3 fatty acids across the blood–brain and blood–retina barriers as lysolipids.

- **Shark mortality cannot be assessed by fishery overlap alone** [07 July 2021]

Matters Arising •

- **Reply to: Shark mortality cannot be assessed by fishery overlap alone** [07 July 2021]

Matters Arising •

- **Caution over the use of ecological big data for conservation**

[07 July 2021]

Matters Arising •

- **Reply to: Caution over the use of ecological big data for conservation** [07 July 2021]

Matters Arising •

- **Treatment of missing data determined conclusions regarding moralizing gods** [07 July 2021]

Matters Arising •

- NEWS AND VIEWS
- 30 June 2021

Malaria vaccine gets a parasite boost in the liver

Effective malaria vaccines are urgently needed. Now, clinical evidence indicates that a vaccination approach that uses live parasites growing in the liver can generate high levels of immune protection from infection.

- [Nana K. Minkah](#) ⁰ &
- [Stefan H. I. Kappe](#) ¹

1. [Nana K. Minkah](#)

1. Nana K. Minkah is at the Center for Global Infectious Disease Research, Seattle Children’s Research Institute, Seattle, Washington 98109, USA.

[View author publications](#)

You can also search for this author in [PubMed](#) [Google Scholar](#)

2. [Stefan H. I. Kappe](#)

1. Stefan H. I. Kappe is at the Center for Global Infectious Disease Research, Seattle Children’s Research Institute, Seattle, Washington 98109, USA, and in the Department of Pediatrics, University of Washington, Seattle.

[View author publications](#)

You can also search for this author in [PubMed](#) [Google Scholar](#)

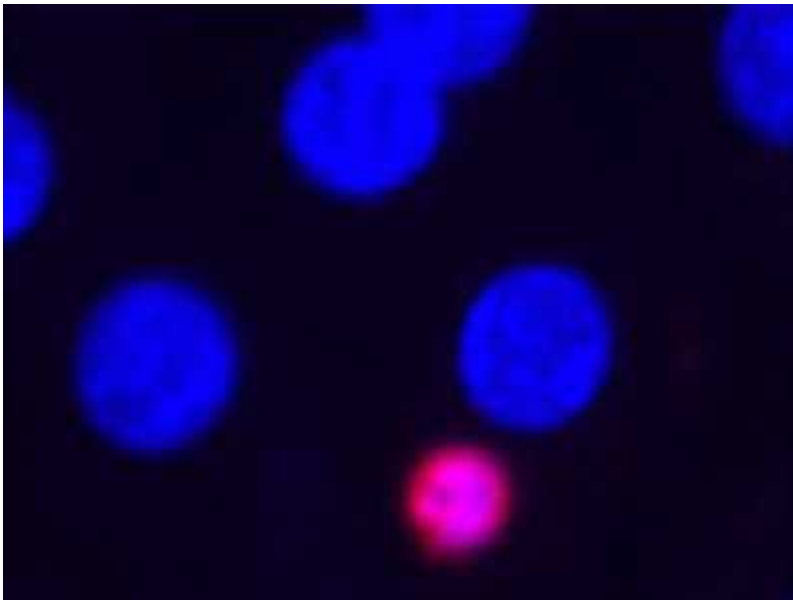




•

[Download PDF](#)

Malaria has long remained among the worst infectious-disease threats to human health. There were 229 million clinical cases of malaria and more than 400,000 deaths from this disease reported during 2019, according to the World Health Organization¹. Although more than 140 years have passed since *Plasmodium* parasites were identified as the causative agents of malaria, a vaccine that offers a high level of protection against *Plasmodium* infection has not yet reached the market. Creation of such a vaccine has been hindered by the genomic complexity of *Plasmodium*, which has approximately 5,300 genes², and by the parasite's elaborate life cycle.



[Read the paper: Two chemoattenuated PfSPZ malaria vaccines induce sterile hepatic immunity](#)

[Writing in *Nature*](#), Mwakingwe-Omari *et al.*³ report a vaccination strategy using live, whole *Plasmodium falciparum* parasites that provides unmatched, high levels of protection against infection. This work represents a major advance in the quest for an effective malaria vaccine.

Human infection by *P. falciparum* begins when the mosquito-transmitted parasite (in a form known as a sporozoite) moves from the bloodstream to the liver and infects the organ's main cells, called hepatocytes (Fig. 1), in which the parasite grows and replicates. This liver stage of its life cycle is not associated with any disease symptoms. Within a week, tens of thousands of parasites are generated in a form that can infect red blood cells. These enter the blood, multiply in red blood cells, and can cause disease and death.

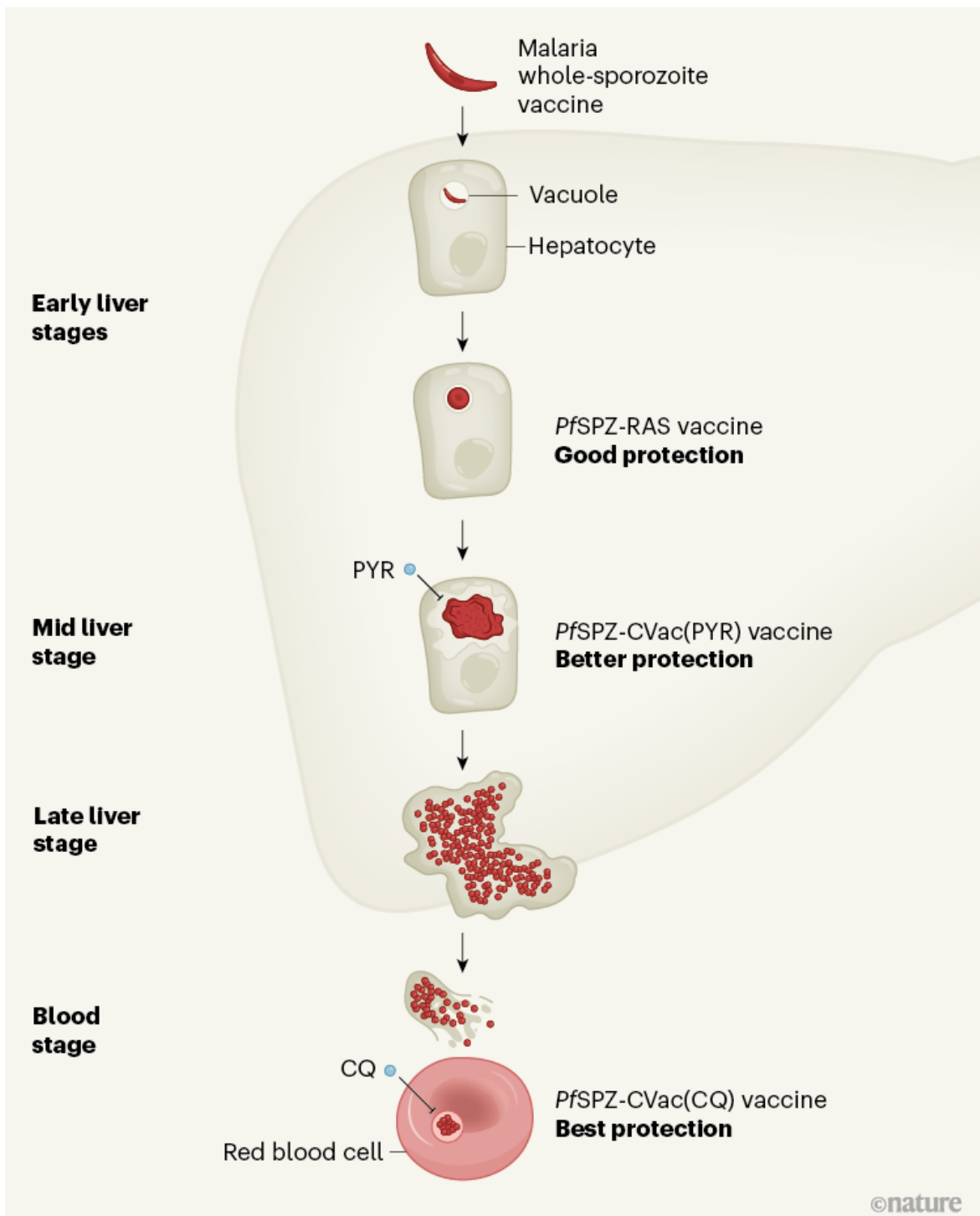


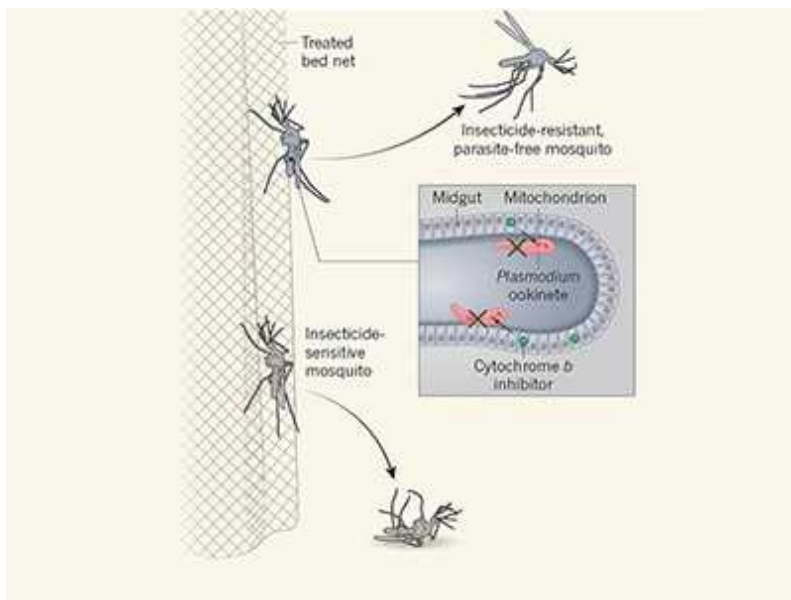
Figure 1 | Vaccine strategies. Attention is turning towards malaria-vaccination approaches that use whole *Plasmodium falciparum* (*Pf*) parasites, which are the disease-causing agent. After the parasite enters the bloodstream in a form called a sporozoite, it reaches the liver, where it resides inside a vacuole in cells called hepatocytes. The parasite develops in

the liver and then returns to the bloodstream to infect red blood cells and cause illness. Previous work^{8,9} indicates that vaccination using a weakened form of the parasite (*PfSPZ*-RAS), which cannot develop in the liver, offers some protection against malaria. Mwakingwe-Omari *et al.*³ report a clinical trial of vaccines containing whole, live parasites given with drug treatments to kill the parasite at a particular developmental stage. The *PfSPZ*-CVac(PYR) vaccine, which harnesses the drug pyrimethamine (PYR), offered improved protection against malaria compared with that reported^{8,9} for *PfSPZ*-RAS vaccines. The best vaccine results were for the *PfSPZ*-CVac(CQ) vaccine, which requires the drug chloroquine (CQ).

Sporozoites and liver-stage parasites, which together are called pre-erythrocytic (PE) parasites, have been the target of vaccine development since observations more than 50 years ago sparked interest in them as a promising target. Those observations showed that immunization with high doses of sporozoites weakened by radiation treatment can confer protection from subsequent parasite infection (termed sterile immunity) in animal models and in humans challenged with the malaria parasite in a controlled human malaria infection (CHMI) trial setting^{4,5}. However, subsequent vaccine efforts focused instead on the development of a malaria vaccine that targets a single parasite protein (called CSP) that is expressed in PE stages. These efforts culminated in a licenced vaccine that confers moderate, short-lived protection against malaria⁶. An updated version of a CSP-based vaccine achieved improved levels of protection in a phase II clinical trial⁷.

Given the limitations of a vaccine approach using a single parasite protein, vaccines using whole, live PE parasites that infect the liver but do not cause malaria have been revived as a promising alternative strategy⁸. Immunization with replication-deficient *P. falciparum* radiation-attenuated sporozoites (*PfSPZ*-RAS), which infect the liver but cannot develop into a liver-stage parasite, remains the most-studied whole-parasite vaccine so far. At high doses, this type of vaccine induces robust protection against CHMI. When tested in Africa, it provided protection against natural transmission of malaria, albeit with reduced efficacy compared with that observed in CHMI⁹.

In a whole-parasite vaccine approach called chemoprophylaxis vaccination, fully infectious sporozoites are administered together with a drug, such as chloroquine, that kills the blood-stage form of the parasite. The chloroquine-assisted form of this vaccine was shown to confer sterile immunity in CHMI studies, even when scientists used 18-fold fewer parasites than the quantity used in trials of *PfSPZ*-RAS vaccines. However, the possibility that the introduced parasites might transition to a lethal blood-stage infection, as well as evidence that blood-stage infection might itself compromise protective liver-stage immunity, has raised concerns about this approach^{[10](#)}.



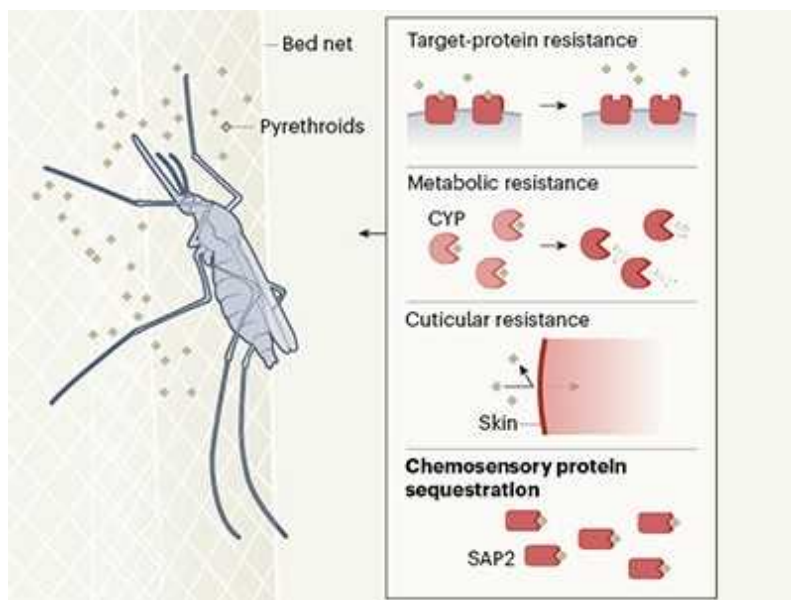
Battling disease by giving mosquitoes an antimalarial drug

To address these issues, Mwakingwe-Omari and colleagues report a whole-parasite vaccine, in which immunization with infectious sporozoites is followed by the administration of the drug pyrimethamine a few days later. This timing of the drug administration kills liver-stage parasites halfway through their development in the liver (Fig. 1). A low-dose vaccination using this approach was minimally protective against CHMI when tested with the same (homologous) parasitic strain (NF54, which is of African origin) as that used for vaccination. However, a fourfold increase in the dose of parasites resulted in sterile immunity in nearly 90% of vaccinated individuals. This level of protection is comparable to that achieved against the homologous parasite strain using the vaccination approach with chloroquine^{[10,11](#)}. A high level of protection from the homologous strain as a

consequence of vaccination using chloroquine was also confirmed by Mwakingwe-Omari and colleagues.

A considerable obstacle to the development of a successful malaria vaccine is the substantial global diversity in *P. falciparum* strains. This partially explains the lower protection conferred by high-dose *PfSPZ*-RAS in Africa compared with the results from the CHMI trial that tested protection against the homologous strain^{12,13}. To test how whole-parasite vaccination with pyrimethamine treatment might perform outside a laboratory setting, Mwakingwe-Omari and colleagues carried out CHMI using a different strain (the 7G8 strain, which is found in Brazil) from the NF54 strain used for vaccination. Impressively, the authors' vaccination strategy maintained nearly 80% sterile immunity in the 7G8 CHMI, even though the 7G8 strain is very different from the hundreds of African *P. falciparum* strains characterized so far¹⁴, including NF54.

The immune responses underlying whole-parasite-mediated vaccination protection in humans are poorly understood. Animal models indicate that immune cells called CD8 T cells, which eliminate parasite-infected hepatocytes, have a key role¹⁵. Immune protection in Mwakingwe-Omari and colleagues' study correlated with higher frequencies of circulating subsets of $\gamma\delta$ T cells, a type of immune cell shown to promote superior responses by CD8 T cells in animal models¹⁶.



Malaria-carrying mosquitoes get a leg up on insecticides

Rodent models of malaria¹⁷ have indicated that, to mount an effective defence response to the parasite, it is important to have encounters between components of the parasite (protein fragments called antigens) that are undergoing liver-stage development and components of the immune system. Now, Mwakingwe-Omari *et al.* establish for the first time in humans that antigens from the liver-stage parasite are crucial for the induction of durable, strain-transcending immunity against *P. falciparum* infection. Furthermore, the authors' observation that pyrimethamine was not quite as protective as chloroquine hints at the potential to further enhance the immune response by using a type of vaccination in which the parasites undergo full liver-stage development but cannot progress to the blood stage of infection.

However, several issues remain that limit this type of vaccine approach for the half of humanity that is at risk of malaria. The foremost concern is that these live-parasite vaccines, administered in three doses, require stringent compliance in taking the accompanying drug, to prevent malaria caused by vaccination. This is feasible in controlled clinical trials but would be difficult to implement if vaccinating billions of people. Thus, although there is strong evidence for liver-stage-directed immunity in humans as a result of live-parasite vaccination and drug treatment, a way to intrinsically weaken the parasite in the vaccine is desirable. This would remove the need for the accompanying parasite-killing drugs and would avoid the associated safety issues. Genetically attenuated parasite vaccines, in which the parasite is weakened by an engineered deletion of genes that are essential for its liver-stage development¹⁸, might represent a future strategy.

Another matter to consider is that any whole-parasite vaccine strategy currently requires sporozoite production in live mosquitoes, and therefore faces formidable challenges in scaling up production. This might be overcome by investments in technologies that allow large-scale manufacturing of whole-sporozoite vaccines.

Ultimately, this study by Mwakingwe-Omari *et al.* has reinforced the importance of PE antigens in the induction of protective immunity after whole-parasite vaccination. Future efforts to identify which PE antigens are recognized by CD8 T cells should also re-energize the individual-antigen

vaccine approach. Both of these immunization avenues, as well as investigations into the immune responses to vaccination, should be priorities for the malaria-vaccine field, and should certainly receive renewed impetus from the work of Mwakingwe-Omari and colleagues.

Nature **595**, 173–174 (2021)

doi: <https://doi.org/10.1038/d41586-021-01720-6>

References

1. 1.

World Health Organization. *World Malaria Report 2020* <https://www.who.int/publications/i/item/9789240015791> (WHO, 2020).

[Google Scholar](#)

2. 2.

Gardner, M. J. *et al.* *Nature* **419**, 498–511 (2002).

[PubMed](#) [Article](#) [Google Scholar](#)

3. 3.

Mwakingwe-Omari, A. *et al.* *Nature* **595**, 289–294 (2021).

[Article](#) [Google Scholar](#)

4. 4.

Clyde, D. F., McCarthy, V. C., Miller, R. M. & Hornick, R. B. *Am. J. Med. Sci.* **266**, 398–403 (1973).

[PubMed](#) [Article](#) [Google Scholar](#)

5. 5.

Nussenzweig, R. S., Vanderberg, J., Most, H. & Orton, C. *Nature* **216**, 160–162 (1967).

[PubMed](#) [Article](#) [Google Scholar](#)

6. 6.

RTS,S Clinical Trials Partnership. *Lancet* **386**, 31–45 (2015).

[PubMed](#) [Article](#) [Google Scholar](#)

7. 7.

Datoo, M. S. *et al.* *Lancet* **397**, 1809–1818 (2021).

[PubMed](#) [Article](#) [Google Scholar](#)

8. 8.

Richie, T. L. *et al.* *Vaccine* **33**, 7452–7461 (2015).

[PubMed](#) [Article](#) [Google Scholar](#)

9. 9.

Goswami, D., Minkah, N. K. & Kappe, S. H. I. *J. Immunol.* **202**, 20–28 (2019).

[PubMed](#) [Article](#) [Google Scholar](#)

10. 10.

Murphy, S. C. *et al.* *PLoS Pathog.* **17**, e1009594 (2021).

[PubMed](#) [Article](#) [Google Scholar](#)

11. 11.

Sulyok, Z. *et al.* *Nature Commun.* **12**, 2518 (2021).

[PubMed](#) [Article](#) [Google Scholar](#)

12. 12.

Sissoko, M. S. *et al.* *Lancet Infect. Dis.* **17**, 498–509 (2017).

[PubMed](#) [Article](#) [Google Scholar](#)

13. 13.

Ishizuka, A. S. *et al.* *Nature Med.* **22**, 614–623 (2016).

[PubMed](#) [Article](#) [Google Scholar](#)

14. 14.

Moser, K. A. *et al.* *Genome Med.* **12**, 6 (2020).

[PubMed](#) [Article](#) [Google Scholar](#)

15. 15.

Lefebvre, M. N. & Harty, J. T. *Trends Parasitol.* **36**, 147–157 (2020).

[PubMed](#) [Article](#) [Google Scholar](#)

16. 16.

Howard, J. *et al.* *Front. Immunol.* **9**, 2760 (2018).

[PubMed](#) [Article](#) [Google Scholar](#)

17. 17.

Butler, N. S. *et al.* *Cell Host Microbe* **9**, 451–462 (2011).

[PubMed](#) [Article](#) [Google Scholar](#)

18. 18.

Goswami, D. *et al.* *JCI Insight* **5**, e135589 (2020).

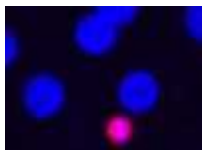
[Article](#) [Google Scholar](#)

[Download references](#)

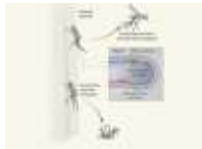
Competing Interests

S.H.I.K. is pursuing a genetically attenuated whole-parasite approach to a malaria vaccine.

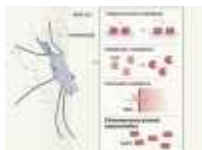
Related Articles



- [Read the paper: Two chemoattenuated PfSPZ malaria vaccines induce sterile hepatic immunity](#)



- [Battling disease by giving mosquitoes an antimalarial drug](#)



- [Malaria-carrying mosquitoes get a leg up on insecticides](#)
- [See all News & Views](#)

Subjects

- [Malaria](#)
- [Medical research](#)

- [Immunology](#)

nature careers

[Jobs](#) >

- [Canada Research Chair Tier 2 in Indigenous Natural Sciences](#)

The University of British Columbia (UBC)

Vancouver, Canada

- [Chemical/Environmental Engineer – Gas Chromatography and Mass Spectrometry](#)

Jülich Research Centre (FZJ)

Jülich, Germany

- [Chemical Technical Assistant \(m/f/d\)](#)

Alfred Wegener Institute - Helmholtz Centre for Polar and Marine Research (AWI)

Bremerhaven, Germany

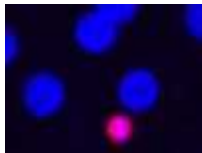
- [Abteilungsassistent*in \(d/m/w\), Abteilung „IT“](#)

Helmholtz Centre for Heavy Ion Research GmbH (GSI)

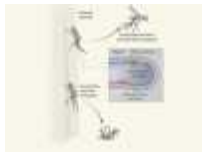
Darmstadt, Germany

[Download PDF](#)

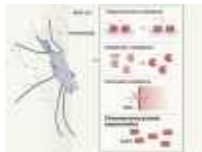
Related Articles



- [Read the paper: Two chemoattenuated PfSPZ malaria vaccines induce sterile hepatic immunity](#)



- [Battling disease by giving mosquitoes an antimalarial drug](#)



- [Malaria-carrying mosquitoes get a leg up on insecticides](#)
- [See all News & Views](#)

Subjects

- [Malaria](#)
- [Medical research](#)
- [Immunology](#)

This article was downloaded by **calibre** from <https://www.nature.com/articles/d41586-021-01720-6>

- NEWS AND VIEWS
- 07 July 2021

How to buffer against an urban food shortage

There is widespread concern that the risk of food shocks — sudden disruptions to food supply — is increasing. It emerges that a city's vulnerability to food shocks can be reduced by diversifying its supply chains.

- [Zia Mehrabi](#) 0

1. [Zia Mehrabi](#)

1. Zia Mehrabi is at the Sustainability Innovation Lab at Colorado and at the Environmental Studies Program, University of Colorado Boulder, Boulder, Colorado 80303, USA.

[View author publications](#)

You can also search for this author in [PubMed](#) [Google Scholar](#)





•

[Download PDF](#)

More than half of the world's population lives in urban areas, a proportion that is set to increase¹ to 68% by 2050. These urban residents depend on supply chains to produce, procure, prepare and deliver food, and they are exposed to potential supply-chain disruptions and food shortages from changes in human activity and natural processes. There is growing recognition that food-system resilience needs to be improved, but how best to buffer against urban food shortages remains an open question for both research and policy. [Writing in Nature](#), Gomez *et al.*² assess how the flow of agricultural products to a city depends on the diversity of the city's trading

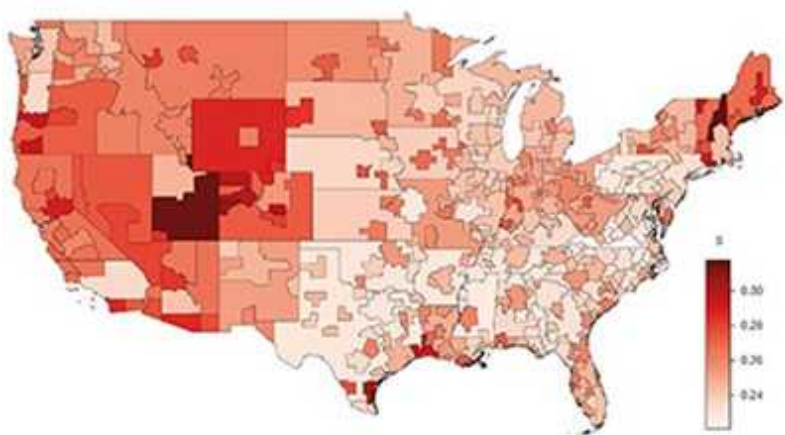
partners. The authors apply ideas from engineering — such as those used when ensuring infrastructure is protected from flooding — to inform the design of food systems that can buffer cities against food shortfalls.

For decades, scientists and industry have been warning governments and consumers about the risks of food shortages. Such shortages have a range of possible causes, including droughts and heatwaves, pest and disease outbreaks, financial downturns and trade policies³. More recently, the COVID-19 pandemic has led academics, and society more generally, to revisit the question of how fragile urban food supplies really are (Fig. 1).



Figure 1 | Empty supermarket shelves during the COVID-19 pandemic. Many city dwellers around the world experienced such scenes, which were largely driven by panic buying and changing consumer behaviour. Gomez *et al.*² demonstrate that the resilience of food supply chains can be increased by boosting their diversity. Credit: Oli Scarff/AFP/Getty

There have been many proposed solutions to deal with the dangers of food shortages, from climate-resilient agricultural management practices to promoting local food systems and self-sufficiency⁴. One solution that is gaining attention is to increase the number and variety of agricultural products, farms and companies procuring and delivering food. Diverse food supply chains might buffer cities against food shortages — in the same way that, in finance, a varied portfolio of stocks limits investment risk and, in ecology, a diverse mixture of species maintains ecosystem functions.



[Read the paper: Supply chain diversity buffers cities against food shocks](#)

Gomez *et al.* used data on the origin and destination of different agricultural commodities for 284 cities and 45 non-city geographical areas in the United States. They identified domestic food systems for each city — that is, all of the geographical areas that supply crops, meat, live animals or animal feed to that city. The authors then determined how many cities faced different thresholds of abrupt food-supply disruptions, known as food shocks, using the percentage difference between the minimum and mean of supply amounts for each food sector over four years for each city. More specifically, they counted the number of cities in which the minimum was more than a particular percentage (ranging from 3% to 15%) smaller than the mean in any one of those four years.

Next, Gomez and colleagues combined those data with simple indicators of geographical similarity — such as the physical distance and difference in climate between each city and the geographical areas in that city's supply network. With this information in hand, the authors tested the idea that groups of cities with more-diverse supply chains are better able to buffer against food shocks than are groups whose supply chains are less diverse. Indeed, they found that cities importing food from suppliers that are more dissimilar from themselves are less likely to face shocks than are cities whose supply-chain partners are less diverse. Such supply-chain benefits would not be reaped from having solely local food systems.

Gomez *et al.* then considered design concepts from engineering, where infrastructure systems should be planned to withstand shocks — such as extreme flooding — of a given frequency and magnitude. The authors undertook some bold extrapolations, in which they estimated the size of food shocks that would be faced by different US cities given their current supply-chain diversity. They found that a rare shock, such as one occurring once in 100 years, would cause a food-supply loss of about 22–32% across different cities.



Transforming the global food system

The other implicit finding from Gomez and colleagues' model is that even moderate supply-chain diversity is effective at reducing the probability of

extremely large shocks. The authors also applied their analysis to shocks happening in multiple food sectors simultaneously. They obtained similar results to those for single-sector shocks — with supply-chain diversity also providing a buffering effect for these even rarer occurrences.

Gomez and colleagues' work has major implications for the way in which resilient food systems should be built, but it also has a few caveats. First, the authors used only four years of data for each city, posing problems for characterizing the distribution of shocks at each city. This limited time series makes it difficult to define the baseline variation in food supply — that is, what is considered normal — for consumers and retailers alike. It also makes it hard to see to what extent diversified supply chains buffer against food shortages under normal conditions compared with years marked by extreme events, and whether the net benefits are large enough to trigger a change in food-procurement policies.

Second, the food-flow data used by Gomez *et al.* do not represent actual flows for each year, but instead are simply annual production quantities proportionally distributed according to observed flows⁵ in 2012. Therefore, the authors' analysis does not capture, or allow for, rerouting or other social responses at the onset of extreme events. Such social responses within and after shock years would result in changing food flows across the supply network.



Rural areas drive increases in global obesity

Third, Gomez and colleagues did not validate the predictive worth of their model beyond the four years considered, or outside the United States. This lack of verification is perhaps most limiting for applying the findings in practice — partly because the stability of food supply is itself dynamic, and will change with increasing volumes and types of food consumed, as well as with production technology. Although the observed phenomenon and general patterns might hold in other years and geographical regions, no data or analyses exist to validate whether the authors' design suggestions will protect against future shocks to the degree claimed.

Designing urban food systems to specification is not as easy as engineering a bridge or dam that won't fail in 100 years. The major global concern with respect to urban food shortages and food security is for populations of middle- to low-income countries, particularly those that are dependent on imports⁶. Theoretically, supply-chain diversity will also have a buffering effect for these populations when the number of urban dwellers starts to drastically increase in the coming years, especially in Africa. However, such nations are probably not accurately described by the model presented. Moreover, they have different policy options and capacities for producing diverse supply chains compared with those possible in the United States. Nevertheless, Gomez and colleagues' work provides a timely and refreshing reminder that building diverse supply chains offers a crucial mechanism for protecting urban dwellers from food shortages.

Nature **595**, 175-176 (2021)

doi: <https://doi.org/10.1038/d41586-021-01758-6>

References

1. 1.

United Nations Department of Economic and Social Affairs. *World Urbanization Prospects: The 2018 Revision* (United Nations, 2019).

[Google Scholar](#)

2. 2.

Gomez, M., Mejia, A., Ruddell, B. L. & Rushforth, R. R. *Nature* **595**, 250–254 (2021).

[Article](#) [Google Scholar](#)

3. 3.

Lloyd's. *Emerging Risk Report – 2015* (Lloyd's, 2015).

[Google Scholar](#)

4. 4.

UK–US Taskforce on Extreme Weather and Global Food System Resilience. *Extreme Weather and Resilience of the Global Food System* (UK Global Food Security Programme, 2015).

[Google Scholar](#)

5. 5.

Hwang, H-L. *et al. Building the FAF4 Regional Database: Data Sources and Estimation Methodologies* (US Department of Transportation, 2016).

[Google Scholar](#)

6. 6.

Food Security Information Network (FSIN). *Global Report on Food Crises 2020* (FSIN, 2020).

[Google Scholar](#)

[Download references](#)

Competing Interests

The author declares no competing interests.

Related Articles



- [**Read the paper: Supply chain diversity buffers cities against food shocks**](#)



- [**Rural areas drive increases in global obesity**](#)
-  [**Transforming the global food system**](#)
- [**See all News & Views**](#)

Subjects

- [Ecology](#)
- [Environmental sciences](#)

nature careers

Jobs >

- [**Canada Research Chair Tier 2 in Indigenous Natural Sciences**](#)

The University of British Columbia (UBC)

Vancouver, Canada

- [Chemical/Environmental Engineer – Gas Chromatography and Mass Spectrometry](#)

Jülich Research Centre (FZJ)

Jülich, Germany

- [Chemical Technical Assistant \(m/f/d\)](#)

Alfred Wegener Institute - Helmholtz Centre for Polar and Marine Research (AWI)

Bremerhaven, Germany

- [Abteilungsassistent*in \(d/m/w\), Abteilung „IT“](#)

Helmholtz Centre for Heavy Ion Research GmbH (GSI)

Darmstadt, Germany

[Download PDF](#)

Related Articles



- [Read the paper: Supply chain diversity buffers cities against food shocks](#)



- [Rural areas drive increases in global obesity](#)



- [Transforming the global food system](#)
- [See all News & Views](#)

Subjects

- [Ecology](#)
- [Environmental sciences](#)

This article was downloaded by **calibre** from <https://www.nature.com/articles/d41586-021-01758-6>

| [Section menu](#) | [Main menu](#) |

- NEWS AND VIEWS
- 30 June 2021

Engineered single-domain antibodies tackle COVID variants

Camels and llamas make antibodies that bind to targets using small, ‘nanobody’ protein domains. Mice have now been engineered to make nanobodies that might be more effective than conventional antibodies in treating COVID-19.

- [James E. Voss](#) 0

1. [James E. Voss](#)

1. James E. Voss is in the Department of Immunology and Microbiology, The Scripps Research Institute, La Jolla, California 92037, USA.

[View author publications](#)

You can also search for this author in [PubMed](#) [Google Scholar](#)





•

[Download PDF](#)

How might the emergence of SARS-CoV-2 variants affect efforts to control the COVID-19 pandemic? The threat posed by such variants is focusing attention on vaccination and therapeutic options to grapple with the evolving coronavirus. [Writing in Nature](#), Xu *et al.*¹ describe the development of a genetically engineered mouse that can generate antibodies similar to those produced by camelids (an animal grouping that includes camels and llamas). These antibodies recognize targets using a single, small protein domain called a nanobody, also known as a VHH domain. Vaccination of these mice using proteins based on the SARS-CoV-2 spike protein resulted in the

generation of antiviral nanobodies. These nanobodies could be produced in formats that were highly effective against COVID-19 variants that are impervious to many conventional antibodies being developed as therapies.

Conventional antibodies such as those produced by humans and mice recognize antigens (protein fragments of disease-causing agents) by means of two variable domains (VH and VL), which are components of separate heavy- and light-chain proteins (Fig. 1). By contrast, camelids and cartilaginous fishes (such as sharks) can make heavy-chain-only antibodies that recognize antigens using single, variable VHH domains, or nanobodies. One advantage of nanobodies is their small size, which enables them to penetrate tissues and recognize epitopes (the region of an antigen to which an antibody binds) that are normally inaccessible to conventional antibodies.

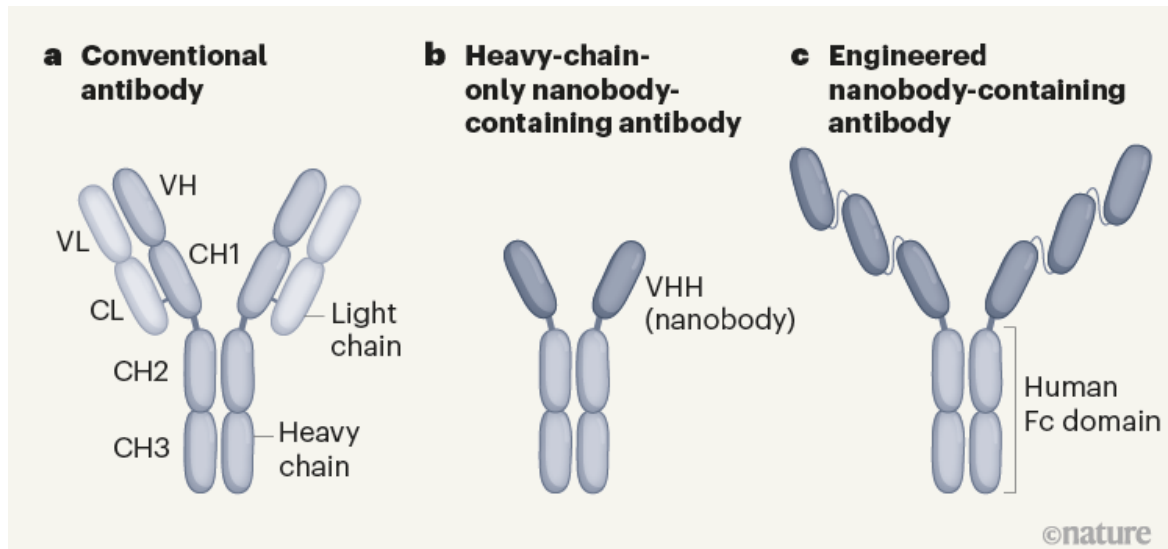
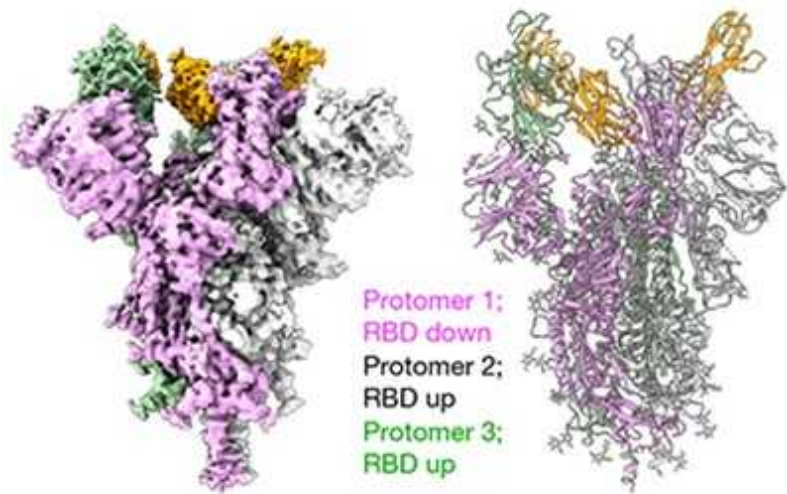


Figure 1 | Different types of antibody can target SARS-CoV-2. **a**, Human and mouse antibodies bind to their targets using two variable domains (VH and VL) on separate light- and heavy-chain proteins. These light and heavy chains pair through a connection between the light-chain CL domain and the heavy-chain CH1 domain. The paired domains are part of the constant regions of the heavy and light chains. The heavy-chain constant region consists of two other domains (CH2 and CH3, which form what is called the Fc domain) that help antibodies to travel around the body and interact with other components of the immune system. **b**, Camelid animals, such as camels and llamas, can produce heavy-chain-only antibodies because some of their genes encode heavy-chain proteins that lack CH1 domains. These

antibodies recognize their targets using only a single variable domain (VHH) region, which is also known as a nanobody. Xu *et al.*¹ have developed mice that make a similar type of antibody. c, The authors genetically engineered mice to produce antibodies consisting of heavy chains containing three tandem copies of camelid nanobodies and a human Fc domain. They report that these antibodies could prevent SARS-CoV-2 from infecting human cells when tested *in vitro*, and that such ‘neutralizing’ antibodies were effective against SARS-CoV-2 variants of concern that emerged during the second and third waves of the pandemic.

Nanobodies are generally extremely stable and soluble, and their modular nature means they can be readily expressed alone or in a variety of formats: for example, fused to the human antibody Fc domain that boosts defence responses². These features make nanobody-based therapeutics a promising alternative to conventional monoclonal antibodies (antibodies with heavy and light chains that have a particular amino-acid sequence and antigen specificity). However, although 2021 saw regulatory approval of the 100th monoclonal-antibody treatment³, only one nanobody-based therapy has been approved for clinical use by the US Food and Drug Administration (FDA)⁴.

Currently, the only human monoclonal antibodies in advanced development as COVID-19 therapies (see go.nature.com/3xt9ku2) are a type called neutralizing antibodies (which block viral entry). Most of these were obtained from the antibody-producing cells of people who were infected during the first wave of the pandemic. Such antibodies target the receptor-binding domain (RBD) of the spike protein; the virus uses this domain to bind to the receptor that enables it to infect cells⁵. Human monoclonal antibodies are strongly preferred for clinical development because they are highly specific, are easily manufactured and work in concert with, and are well tolerated by, the human immune system⁶. However, there are strong arguments in favour of developing alternative, nanobody-based therapeutics in response to evolving human respiratory viruses such as SARS-CoV-2.

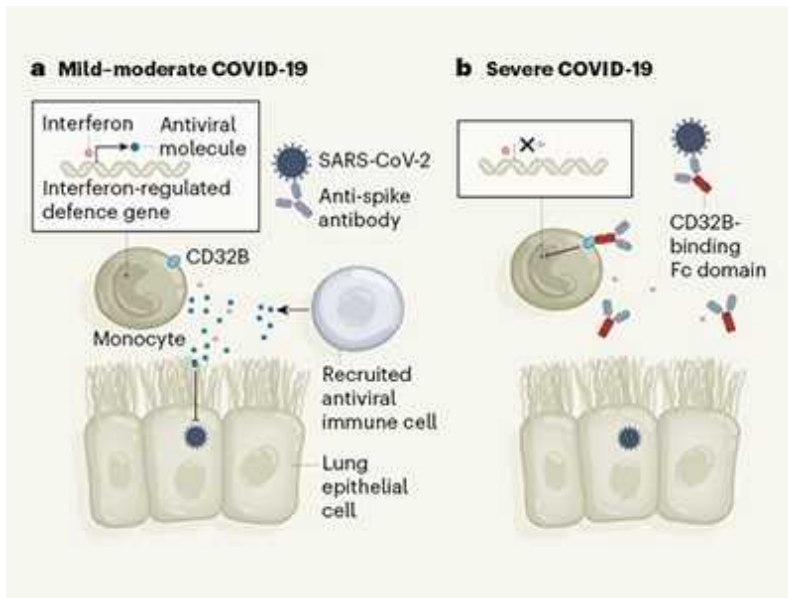


[Read the paper: Nanobodies from camelid mice and llamas neutralize SARS-CoV-2 variants](#)

Since the virus began infecting people more than a year ago, the collective human neutralizing-antibody response generated against SARS-CoV-2 has applied a strong selection pressure on the spike-protein RBD. In fact, only two or three amino-acid-residue changes in versions of the virus that became dominant during the second and third waves of the pandemic were enough to render those versions substantially more resistant to neutralization by antibodies generated during the first wave — as assessed by tests on blood samples, known as convalescent serum, from individuals who have had COVID-19⁷.

It therefore follows that monoclonal-antibody therapies mined from antibody responses generated during the first wave of the pandemic might quickly become obsolete. RBD epitopes of the spike protein that are recognized by neutralizing nanobodies, and that are not under selection pressure as a consequence of epitope recognition by human antibodies, might provide COVID-19 antivirals that do not quickly become ineffective as viral variants emerge. Broadly neutralizing nanobodies — nanobodies that recognize evolutionarily conserved epitopes of the spike protein — might even be useful against other coronaviruses with the capacity to drive a future pandemic.

The small and soluble nature of nanobodies means that they should be inexpensive to produce and easy to administer directly by inhalation to target key initial sites of viral replication in the respiratory tract. A study⁸ in hamsters, assessing the intranasal aerosol delivery of neutralizing nanobodies targeting SARS-CoV-2, reports that nanobodies were effectively deposited throughout the animals' respiratory tract, and that this treatment notably reduced the level of virus. As long as nanobody therapies are administered only once over a short period of time to people with an acute infection, then strong immune responses should not be directed towards the nanobody itself, rendering it ineffective. The issue of such immune responses is generally a concern in relation to monoclonal-antibody therapies being developed to treat diseases that require repeated antibody administration over longer periods of time.

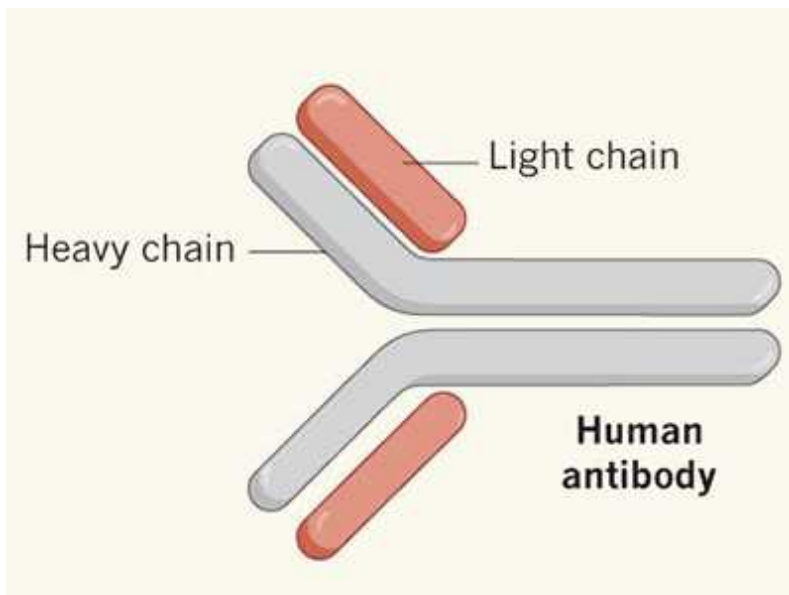


Some antibodies can dampen antiviral defences in people with severe COVID

Although there has been some hesitancy in moving nanobodies to the clinic, many studies have found that potently neutralizing nanobodies can be elicited in camelids using SARS-CoV-2 vaccines based on the spike protein^{9–13}. Xu and colleagues now offer a way forward through their generation of heavy-chain-only antibody-producing ‘nanomice’. The approach offers a system that should make nanobody discovery easier, faster and less expensive than was previously possible. Laboratory facilities to care

for mice are inexpensive and ubiquitous, the mouse immune system is well understood, and high-quality tools such as those needed for cell sorting are readily available. Furthermore, immunizations in mice can occur on a much faster timescale than is possible for larger animal models — an important consideration when a rapid response to a newly emerging pandemic is required.

To generate these nanomice, Xu *et al.* replaced a large region of genomic DNA, containing all of the mouse heavy-chain variable (*V*) genes, with a region of DNA comprising 30 heavy-chain *V* genes derived from alpaca, dromedary and Bactrian camels. Each gene was fused to a DNA sequence that enabled the gene to form the usual connection (through a process termed recombination) to mouse heavy-chain *D* and *J* genes to make complete *VHH* genes. The *V* genes were also fused to promoter DNA sequences so that the *VHH* genes could be expressed in mouse antibody-producing B cells. Each developing B cell could indeed recombine a single camelid *V*, mouse *D* and mouse *J* gene to generate B-cell populations expressing different *VHH*-gene sequences as heavy-chain-only antibodies. The authors demonstrated that these cells could respond normally to immunization, undergoing a process (termed affinity maturation) that boosts the potency and specificity of antibodies for the antigen that they respond to.



[All for one and one for all to fight flu](#)

Xu and colleagues then immunized three nanomice and one llama with the SARS-CoV-2 spike protein and RBD. They identified neutralizing nanobodies in both animal models. These nanobodies could be formatted to be expressed as three tandem nanobody copies fused to a human antibody Fc domain (Fig. 1). This domain is a key feature of conventional antibodies: it enables an antibody to transit around the body, improves the antibody's lifespan and boosts interactions with other components of the immune system. This format using tandem nanobodies should help to boost antigen binding by the antibodies. The authors' evidence indicates that these engineered antibodies could potently neutralize all of the tested SARS-CoV-2 variants of concern (viruses with RBD mutations and which were associated with the second and third waves of the pandemic). Moreover, the proteins from nanomice recognized evolutionarily conserved epitopes on the RBD that do not overlap with regions commonly recognized by human antibodies.

The COVID-19 pandemic presents a unique opportunity for nanobodies to shine in the clinic, and the nanomouse platform is poised to help bring higher-quality therapeutic-nanobody options to the table, pushing the odds of success even higher. Just as the development of mice with antibodies containing human variable domains (such as Regeneron's VelocImmune mouse) has helped to deliver the 100th FDA-approved monoclonal antibody, perhaps the nanomouse will give nanobody-based therapeutics a push in the same direction.

Nature **595**, 176-178 (2021)

doi: <https://doi.org/10.1038/d41586-021-01721-5>

References

1. 1.

Xu, J. *et al. Nature* **595**, 278–282 (2021).

[Article](#) [Google Scholar](#)

2. 2.

Sasisekharan, R. *N. Engl. J. Med.* **384**, 1568–1571 (2021).

[PubMed](#) [Article](#) [Google Scholar](#)

3. 3.

Nature Rev. Drug Discov. <https://doi.org/10.1038/d41573-021-00079-7> (2021).

[Article](#) [Google Scholar](#)

4. 4.

Nature Rev. Drug Discov. **18**, 485–487 (2019).

[PubMed](#) [Article](#) [Google Scholar](#)

5. 5.

Liu, L. D., Lian, C., Yeap, L.-S. & Meng, F.-L. *J. Mol. Cell Biol.* **12**, 980–986 (2020).

[Article](#) [Google Scholar](#)

6. 6.

Harding, F. A., Stickler, M. M., Razo, J. & DuBridge, R. *mAbs* **2**, 256–265 (2010).

[PubMed](#) [Article](#) [Google Scholar](#)

7. 7.

Dejnirattisai, W. *et al.* *Cell* **184**, 2939–2954 (2021).

[PubMed](#) [Article](#) [Google Scholar](#)

8. 8.

Nambulli, S. *et al.* *Sci. Adv.* **7**, eabh0319 (2021).

[PubMed](#) [Article](#) [Google Scholar](#)

9. 9.

Hanke, L. *et al.* *Nature Commun.* **11**, 4420 (2020).

[PubMed](#) [Article](#) [Google Scholar](#)

10. 10.

Koenig, P.-A. *et al.* *Science* **371**, eabe6230 (2021).

[PubMed](#) [Article](#) [Google Scholar](#)

11. 11.

Schoof, M. *et al.* *Science* **370**, 1473–1479 (2020).

[PubMed](#) [Google Scholar](#)

12. 12.

Esparza, T. J., Martin, N. P., Anderson, G. P., Goldman, E. R. & Brody, D. L. *Sci. Rep.* **10**, 22370 (2020).

[PubMed](#) [Article](#) [Google Scholar](#)

13. 13.

Xiang, Y. *et al.* *Science* **370**, 1479–1484 (2020).

[PubMed](#) [Google Scholar](#)

[Download references](#)

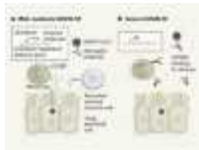
Competing Interests

The author declares no competing interests.

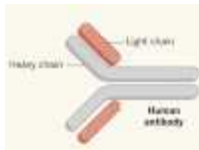
Related Articles



- [Read the paper: Nanobodies from camelid mice and llamas neutralize SARS-CoV-2 variants](#)



- [Some antibodies can dampen antiviral defences in people with severe COVID](#)



- [All for one and one for all to fight flu](#)
- [See all News & Views](#)

Subjects

- [SARS-CoV-2](#)
- [Immunology](#)
- [Medical research](#)

nature careers

[Jobs](#) >

- [Canada Research Chair Tier 2 in Indigenous Natural Sciences](#)

The University of British Columbia (UBC)

Vancouver, Canada

- [Chemical/Environmental Engineer – Gas Chromatography and Mass Spectrometry](#)

Jülich Research Centre (FZJ)

Jülich, Germany

- [Chemical Technical Assistant \(m/f/d\)](#)

Alfred Wegener Institute - Helmholtz Centre for Polar and Marine Research (AWI)

Bremerhaven, Germany

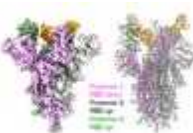
- [Abteilungsassistent*in \(d/m/w\), Abteilung „IT“](#)

Helmholtz Centre for Heavy Ion Research GmbH (GSI)

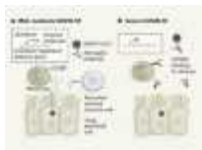
Darmstadt, Germany

[Download PDF](#)

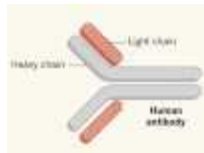
Related Articles



- [Read the paper: Nanobodies from camelid mice and llamas neutralize SARS-CoV-2 variants](#)



- [Some antibodies can dampen antiviral defences in people with severe COVID](#)



- [**All for one and one for all to fight flu**](#)
- [**See all News & Views**](#)

Subjects

- [SARS-CoV-2](#)
- [Immunology](#)
- [Medical research](#)

This article was downloaded by **calibre** from <https://www.nature.com/articles/d41586-021-01721-5>

| [Section menu](#) | [Main menu](#) |

- NEWS AND VIEWS
- 07 July 2021

Fluid-rich extinct volcanoes cause small earthquakes beneath New Zealand

Imaging of a region where an oceanic tectonic plate descends below another plate reveals evidence that fluid-rich extinct volcanoes can help to lubricate the interface between plates — reducing the potential for large earthquakes.

- [Catherine A. Rychert](#) ⁰ &
- [Nicholas Harmon](#) ¹

1. [Catherine A. Rychert](#)

1. Catherine A. Rychert is in Ocean and Earth Science, National Oceanography Centre, University of Southampton, Southampton SO14 3ZH, UK.

[View author publications](#)

You can also search for this author in [PubMed](#) [Google Scholar](#)

2. Nicholas Harmon

1. Nicholas Harmon is in Ocean and Earth Science, National Oceanography Centre, University of Southampton, Southampton SO14 3ZH, UK.

[View author publications](#)

You can also search for this author in [PubMed](#) [Google Scholar](#)

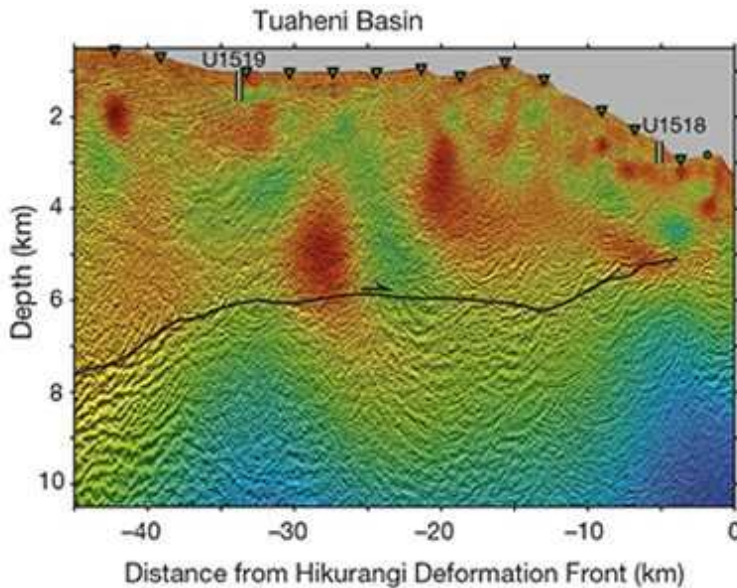




•

[Download PDF](#)

At subduction zones, the force of gravity drags dense tectonic plates beneath other, more buoyant plates. As the plates slide past one another, stress builds and is eventually released in the largest and most destructive types of earthquake on Earth. Various factors are thought to have a role in determining the location, type and magnitude of these earthquakes. Working out when and where each of these factors is at play is central to understanding earthquake processes and mitigating the associated hazards. The characteristics of the down-going plate are thought to be a crucial contributor.



[Read the paper: Fluid-rich subducting topography generates anomalous forearc porosity](#)

However, finding direct links between the features of a down-going plate and the associated earthquake characteristics has proved challenging.

Chesley *et al.*¹ report in *Nature* their use of a technique called electromagnetic imaging to investigate extinct underwater volcanoes, known as seamounts, on the Pacific plate as it descends beneath New Zealand. The authors show that the seamounts bring fluid into Earth's interior that is later released into the overlying plate, effectively lubricating the system and potentially lowering the likelihood of large earthquakes. This use of electromagnetic imaging has produced one of the first high-resolution images of a feature on the down-going slab that directly links the release of fluids to the type and size of earthquakes.

A range of factors dictate the probable location and magnitude of earthquakes². One such factor is the frictional properties of the interface between the plates. Fluids that are carried into Earth by the down-going plate can reduce the force of friction if they increase the fluid pressure in the fault zone. This, in turn, could decrease the likelihood of large earthquakes³. Alternatively, if the sea floor of the down-going plate is rough, because of features such as seamounts, this might produce areas of higher friction at a fault interface, increasing the likelihood of large earthquakes⁴.

To investigate this issue, Chesley *et al.* carried out electromagnetic imaging of the subduction zone in New Zealand. The technology uses either artificial or naturally occurring electric and magnetic fields to determine the degree to which geological features in Earth's interior are electrically conductive or resistive. The method is particularly sensitive to the presence of interconnected fluids.

The authors produced high-resolution images of a seamount on a section of the Pacific plate that is about to be subducted. They observed that the interior of the seamount is highly conductive, but is overlain by a thin, electrically resistive layer of material (Fig. 1). The authors propose that the conductive interior is fluid-rich, and that the resistive layer is fluid-poor, with low porosity. The resistive layer therefore acts as a cap, limiting the release of fluids from the deeper conductive region until the plate reaches greater depths.

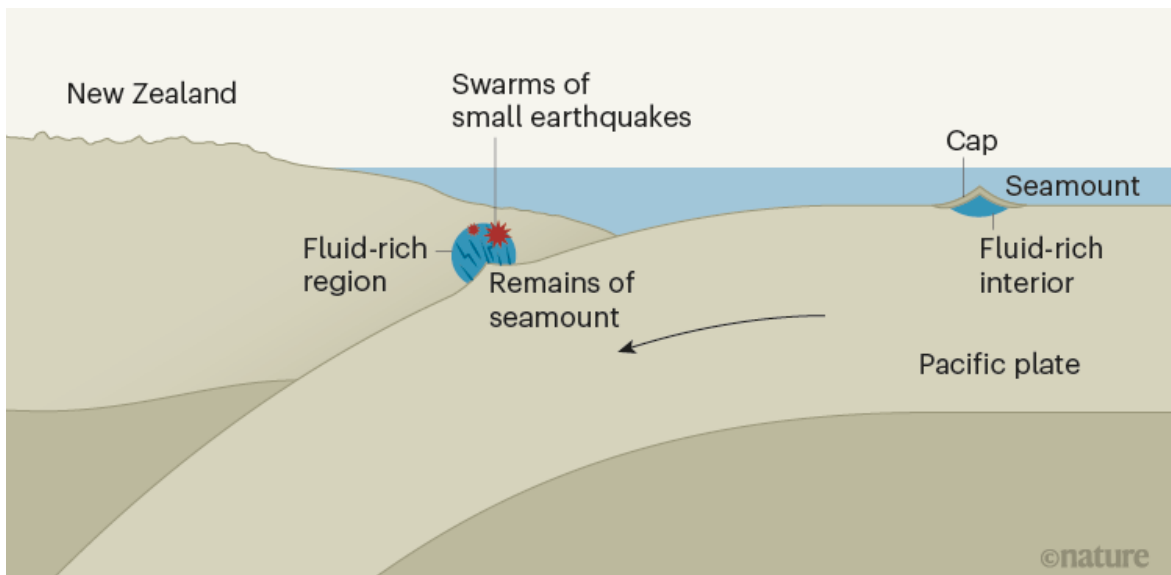


Figure 1 | Evidence that a seamount has altered seismic behaviour beneath New Zealand. The oceanic tectonic plate known as the Pacific plate descends (subducts) beneath the tectonic plate that supports New Zealand. Chesley *et al.*¹ report electromagnetic imaging of a seamount — an extinct underwater volcano — on part of the Pacific plate that is about to subduct, and find that it has a fluid-rich interior capped by a thin, low-porosity layer of material. The authors also observed the remains of a seamount at the interface between the Pacific plate and the overlying plate.

The region of the overlying plate above the remains is damaged and fluid-rich, and corresponds to an area in which many small earthquakes have been reported. The authors suggest that the subducted seamount damaged the overlying plate and that its cap broke, releasing fluid to the upper plate. The fluids reduced friction between the plates, thereby decreasing the likelihood of large earthquakes, which often occur at subduction zones.

Chesley *et al.* also imaged an anomalously resistive feature deeper in the subduction zone, on top of the down-going plate. This corresponds to another seamount that had previously been imaged using seismic waves^{5,6}. The anomaly resides beneath a conductive, fluid-rich region of the over-riding plate and is associated with a swarm of overlying small earthquakes (Fig. 1). The authors conclude that the previously observed seamount was the origin of the fluid in the conductive region now observed over the anomaly, and infer that the small earthquakes occur as the fluid moves through the system. So, although the rough topography of seamounts might be expected to increase friction at faults, seamounts can also decrease friction — and the potential for large ‘mega-thrust’ earthquakes — if they damage the upper plate and release fluids.

Some questions remain. How much fluid is left in the subducted seamount, and how much, if any, is carried deeper into the subduction zone? Deeply transported fluids are also important in subduction-zone settings, because they decrease the melting temperature of the mantle, resulting in hazardous volcanism at the surface⁷.



Determining whether the worst earthquake has passed

More work is required to determine the global role of seamounts in influencing subduction dynamics and earthquake hazard. In some locations, seamounts have been associated with aseismic slip⁸ (movement on faults that does not cause big earthquakes), whereas in other locations they have been linked to large earthquakes⁴. One explanation for these divergent effects is that seamounts have different hydration levels and are variably fractured around the world; those that are strong, dry and less fractured produce large earthquakes. If this is correct, then what processes cause seamounts to become hydrated or weak? And what is the relative contribution of factors such as sea-floor characteristics, the age of the plate beneath the volcano and the time elapsed since the seamount was an active volcano?

Another unanswered question is, how much fluid do seamounts contribute to subduction zones, compared with other sources of fluid in down-going plates? For instance, processes that occur near sea-floor features called mid-ocean ridges can add fluids to oceanic plates by altering the mineral composition of the rocks⁹, or through the formation of faults and associated damaged zones^{10,11}, or both. Moreover, further hydration might occur when a plate is bent and broken as it enters the subduction zone¹², or, as Chesley *et al.* suggest, when a local hotspot generates a volcano that eventually

becomes a seamount¹³. The contributions of these diverse mechanisms could vary with location and time. Further imaging of oceanic plates that formed at different times and rates, and with different degrees and times of emergence of volcanic activity, is now required — in particular, by combining electromagnetic and seismic imaging techniques, which have complementary sensitivities to the properties of Earth’s interior.

Nature **595**, 178–179 (2021)

doi: <https://doi.org/10.1038/d41586-021-01703-7>

References

1. 1.

Chesley, C., Naif, S., Key, K. & Bassett, D. *Nature* **595**, 255–260 (2021).

[Article](#) [Google Scholar](#)

2. 2.

Peng, Z. & Gomberg, J. *Nature Geosci.* **3**, 599–607 (2010).

[Article](#) [Google Scholar](#)

3. 3.

King Hubbert, M. & Rubey, W. W. *Geol. Soc. Am. Bull.* **70**, 115–205 (1959).

[Article](#) [Google Scholar](#)

4. 4.

Cloos, M. *Geology* **20**, 601–604 (1992).

[Article](#) [Google Scholar](#)

5. 5.

Arai, R. *et al.* *J. Geophys. Res. Solid Earth* **125**, e2020JB020433 (2020).

[Article](#) [Google Scholar](#)

6. 6.

Bell, R. *et al.* *Geophys. J. Int.* **180**, 34–48 (2010).

[Article](#) [Google Scholar](#)

7. 7.

Stern, R. L. *Rev. Geophys.* **40**, 3 (2002).

[Article](#) [Google Scholar](#)

8. 8.

Bonnet, G., Agard, P., Angiboust, S., Fournier, M. & Omrani, J. *Geology* **47**, 407–410 (2019).

[Article](#) [Google Scholar](#)

9. 9.

Bach, W. & Früh-Green, G. L. *Elements* **6**, 173–178 (2010).

[Article](#) [Google Scholar](#)

10. 10.

Cooper, G. F. *et al.* *Nature* **582**, 525–529 (2020).

[PubMed](#) [Article](#) [Google Scholar](#)

11. 11.

Davy, R. G., Collier, J. S., Henstock, T. J. & the VoiLA Consortium. *J. Geophys. Res. Solid Earth* **125**, e2019JB019100 (2020).

[Article](#) [Google Scholar](#)

12. 12.

Ranero, C. R., Morgan, J. P., McIntosh, K. & Reichert, C. *Nature* **425**, 367–373 (2003).

[PubMed](#) [Article](#) [Google Scholar](#)

13. 13.

Park, J. & Rye, D. M. *Geochem. Geophys. Geosyst.* **20**, 4779–4809 (2019).

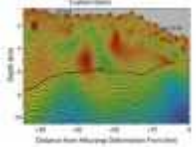
[Article](#) [Google Scholar](#)

[Download references](#)

Competing Interests

The authors declare no competing interests.

Related Articles

-  [Read the paper: Fluid-rich subducting topography generates anomalous forearc porosity](#)
-  [Determining whether the worst earthquake has passed](#)



- [Small and large earthquakes can have similar starts](#)
- [See all News & Views](#)

Subjects

- [Solid Earth sciences](#)
- [Geology](#)
- [Geophysics](#)
- [Seismology](#)

nature careers

[Jobs](#) >

- [Canada Research Chair Tier 2 in Indigenous Natural Sciences](#)

The University of British Columbia (UBC)

Vancouver, Canada

- [Chemical/Environmental Engineer – Gas Chromatography and Mass Spectrometry](#)

Jülich Research Centre (FZJ)

Jülich, Germany

- [Chemical Technical Assistant \(m/f/d\)](#)

Alfred Wegener Institute - Helmholtz Centre for Polar and Marine Research (AWI)

Bremerhaven, Germany

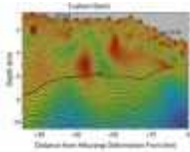
- [Abteilungsassistent*in \(d/m/w\), Abteilung „IT“](#)

Helmholtz Centre for Heavy Ion Research GmbH (GSI)

Darmstadt, Germany

[Download PDF](#)

Related Articles



- [Read the paper: Fluid-rich subducting topography generates anomalous forearc porosity](#)



- [Determining whether the worst earthquake has passed](#)



- [Small and large earthquakes can have similar starts](#)

- [See all News & Views](#)

Subjects

- [Solid Earth sciences](#)
- [Geology](#)
- [Geophysics](#)

- Seismology

This article was downloaded by **calibre** from <https://www.nature.com/articles/d41586-021-01703-7>

| [Section menu](#) | [Main menu](#) |

- Perspective
- [Published: 30 June 2021](#)

Integrating explanation and prediction in computational social science

- [Jake M. Hofman](#) [ORCID: orcid.org/0000-0002-9364-9604¹](#) na1,
- [Duncan J. Watts](#) [ORCID: orcid.org/0009-0002-6355-1102^{2,3,4}](#) na1,
- [Susan Athey](#) [ORCID: orcid.org/0000-0001-6934-562X⁵](#),
- [Filiz Garip⁶](#),
- [Thomas L. Griffiths^{7,8}](#),
- [Jon Kleinberg^{9,10}](#),
- [Helen Margetts^{11,12}](#),
- [Sendhil Mullainathan¹³](#),
- [Matthew J. Salganik⁶](#),
- [Simine Vazire¹⁴](#),
- [Alessandro Vespignani](#) [ORCID: orcid.org/0000-0003-3419-4205¹⁵](#) &
- [Tal Yarkoni](#) [ORCID: orcid.org/0000-0002-6558-5113¹⁶](#)

[Nature](#) volume **595**, pages 181–188 (2021) [Cite this article](#)

- 461 Accesses
- 74 Altmetric
- [Metrics details](#)

Subjects

- [Interdisciplinary studies](#)

- [Scientific community](#)

Abstract

Computational social science is more than just large repositories of digital data and the computational methods needed to construct and analyse them. It also represents a convergence of different fields with different ways of thinking about and doing science. The goal of this Perspective is to provide some clarity around how these approaches differ from one another and to propose how they might be productively integrated. Towards this end we make two contributions. The first is a schema for thinking about research activities along two dimensions—the extent to which work is explanatory, focusing on identifying and estimating causal effects, and the degree of consideration given to testing predictions of outcomes—and how these two priorities can complement, rather than compete with, one another. Our second contribution is to advocate that computational social scientists devote more attention to combining prediction and explanation, which we call integrative modelling, and to outline some practical suggestions for realizing this goal.

Access options

Subscribe to Journal

Get full journal access for 1 year

\$199.00

only \$3.90 per issue

[Subscribe](#)

All prices are NET prices.

VAT will be added later in the checkout.

Tax calculation will be finalised during checkout.

Rent or Buy article

Get time limited or full article access on ReadCube.

from \$8.99

[Rent or Buy](#)

All prices are NET prices.

Additional access options:

- [Log in](#)
- [Access through your institution](#)
- [Learn about institutional subscriptions](#)

References

1. 1.

Watts, D. J. A twenty-first century science. *Nature* **445**, 489 (2007).

[CAS](#) [PubMed](#) [ADS](#) [Google Scholar](#)

2. 2.

Lazer, D. et al. Computational social science. *Science* **323**, 721–723 (2009).

[CAS](#) [PubMed](#) [PubMed Central](#) [Google Scholar](#)

3. 3.

Salganik, M. J. *Bit by Bit: Social Research in the Digital Age* (Princeton Univ. Press, 2018).

4. 4.

Lazer, D. M. J. et al. Computational social science: obstacles and opportunities. *Science* **369**, 1060–1062 (2020).

[CAS](#) [PubMed](#) [ADS](#) [Google Scholar](#)

5. 5.

Lazer, D. et al. Meaningful measures of human society in the twenty-first century. *Nature* <https://doi.org/10.1038/s41586-021-03660-7> (2021).

6. 6.

Wing, J. M. Computational thinking. *Commun. ACM* **49**, 33–35 (2006).

[Google Scholar](#)

7. 7.

Hedström, P. & Ylikoski, P. Causal mechanisms in the social sciences. *Annu. Rev. Sociol.* **36**, 49–67 (2010).

[Google Scholar](#)

8. 8.

Breiman, L. Statistical modeling: the two cultures (with comments and a rejoinder by the author). *Stat. Sci.* **16**, 199–231 (2001). **We view our paper as an extension of Breiman's dichotomy (the 'algorithmic' and 'data modelling' cultures), arguing that these approaches should be integrated.**

[MATH](#) [Google Scholar](#)

9. 9.

Mullainathan, S. & Spiess, J. Machine learning: an applied econometric approach. *J. Econ. Perspect.* **31**, 87–106 (2017). **This paper explores the relationships between predictive models and causal inference.**

[Google Scholar](#)

10. 10.

Molina, M. & Garip, F. Machine learning for sociology. *Annu. Rev. Sociol.* **45**, 27–45 (2019).

11. 11.

Shmueli, G. To explain or to predict? *Stat. Sci.* **25**, 289–310 (2010).
We build on Schmueli's distinction between prediction and explanation and propose a framework for integrating the two approaches.

[MathSciNet](#) [MATH](#) [Google Scholar](#)

12. 12.

Agrawal, M., Peterson, J. C. & Griffiths, T. L. Scaling up psychology via Scientific Regret Minimization. *Proc. Natl Acad. Sci. USA* **117**, 8825–8835 (2020). **This paper exemplifies what we call integrative modelling.**

[CAS](#) [PubMed](#) [PubMed Central](#) [Google Scholar](#)

13. 13.

Munafò, M. R. et al. A manifesto for reproducible science. *Nat. Hum. Behav.* **1**, 0021 (2017).

[PubMed](#) [PubMed Central](#) [Google Scholar](#)

14. 14.

Yarkoni, T. The generalizability crisis. *Behav. Brain Sci.* <https://doi.org/10.1017/S0140525X20001685> (2020).

15. 15.

Ward, M. D., Greenhill, B. D. & Bakke, K. M. The perils of policy by p-value: predicting civil conflicts. *J. Peace Res.* **47**, 363–375 (2010).

[Google Scholar](#)

16. 16.

Yarkoni, T. & Westfall, J. Choosing prediction over explanation in psychology: lessons from machine learning. *Perspect. Psychol. Sci.* **12**, 1100–1122 (2017).

[PubMed](#) [PubMed Central](#) [Google Scholar](#)

17. 17.

Watts, D. J. Should social science be more solution-oriented? *Nat. Hum. Behav.* **1**, 0015 (2017).

[Google Scholar](#)

18. 18.

Berkman, E. T. & Wilson, S. M. So useful as a good theory? The practicality crisis in (social) psychological theory. *Perspect. Psychol. Sci.* <https://doi.org/10.1177/1745691620969650> (2021).

19. 19.

Athey, S. Beyond prediction: Using big data for policy problems. *Science* **355**, 483–485 (2017).

[CAS](#) [PubMed](#) [ADS](#) [Google Scholar](#)

20. 20.

Lipton, Z. C. The mythos of model interpretability. *Queue* **16**, 31–57 (2018).

[Google Scholar](#)

21. 21.

Kleinberg, J., Ludwig, J., Mullainathan, S. & Sunstein, C. R. Discrimination in the age of algorithms. *J. Legal Anal.* **10**, 113–174 (2018).

[Google Scholar](#)

22. 22.

Coveney, P. V., Dougherty, E. R. & Highfield, R. R. Big data need big theory too. *Philos. Trans. R. Soc. A* **374**, 20160153 (2016).

[ADS](#) [Google Scholar](#)

23. 23.

Gigerenzer, G. Mindless statistics. *J. Socio-Econ.* **33**, 587–606 (2004).

[Google Scholar](#)

24. 24.

Cohen, J. The earth is round ($p < .05$). *Am. Psychol.* **49**, 997–1003 (1994).

[Google Scholar](#)

25. 25.

Bertrand, M. & Mullainathan, S. Are Emily and Greg more employable than Lakisha and Jamal? A field experiment on labor market discrimination. *Am. Econ. Rev.* **94**, 991–1013 (2004).

[Google Scholar](#)

26. 26.

Ioannidis, J. P. A. Why most published research findings are false. *PLoS Med.* **2**, e124 (2005).

[PubMed](#) [PubMed Central](#) [Google Scholar](#)

27. 27.

Simmons, J. P., Nelson, L. D. & Simonsohn, U. False-positive psychology: undisclosed flexibility in data collection and analysis allows presenting anything as significant. *Psychol. Sci.* **22**, 1359–1366 (2011).

[PubMed](#) [Google Scholar](#)

28. 28.

Open Science Collaboration. Estimating the reproducibility of psychological science. *Science* **349**, aac4716 (2015).

[Google Scholar](#)

29. 29.

Meehl, P. E. Why summaries of research on psychological theories are often uninterpretable. *Psychol. Rep.* **66**, 195–244 (1990).

[Google Scholar](#)

30. 30.

Gelman, A. Causality and statistical learning. *Am. J. Sociol.* **117**, 955–966 (2011).

[Google Scholar](#)

31. 31.

Dienes, Z. *Understanding Psychology as a Science: An Introduction to Scientific and Statistical Inference* (Macmillan, 2008).

32. 32.

Schrodt, P. A. Seven deadly sins of contemporary quantitative political analysis. *J. Peace Res.* **51**, 287–300 (2014).

[Google Scholar](#)

33. 33.

Lazer, D., Kennedy, R., King, G. & Vespignani, A. The parable of Google flu: traps in big data analysis. *Science* **343**, 1203–1205 (2014).

[CAS](#) [PubMed](#) [ADS](#) [Google Scholar](#)

34. 34.

Obermeyer, Z., Powers, B., Vogeli, C. & Mullainathan, S. Dissecting racial bias in an algorithm used to manage the health of populations. *Science* **366**, 447–453 (2019).

[CAS](#) [PubMed](#) [ADS](#) [Google Scholar](#)

35. 35.

Goel, S., Hofman, J. M., Lahaie, S., Pennock, D. M. & Watts, D. J. Predicting consumer behavior with web search. *Proc. Natl Acad. Sci. USA* **107**, 17486–17490 (2010).

[CAS](#) [PubMed](#) [PubMed Central](#) [ADS](#) [Google Scholar](#)

36. 36.

Hofman, J. M., Sharma, A. & Watts, D. J. Prediction and explanation in social systems. *Science* **355**, 486–488 (2017).

[CAS](#) [PubMed](#) [ADS](#) [Google Scholar](#)

37. 37.

Case, A. & Deaton, A. Rising morbidity and mortality in midlife among white non-Hispanic Americans in the 21st century. *Proc. Natl Acad. Sci. USA* **112**, 15078–15083 (2015).

[CAS](#) [PubMed](#) [PubMed Central](#) [ADS](#) [Google Scholar](#)

38. 38.

Oliver, M. L., Shapiro, T. M. & Shapiro, T. *Black Wealth, White Wealth: A New Perspective on Racial Inequality* (Taylor & Francis, 2006).

39. 39.

Chetty, R., Hendren, N., Kline, P. & Saez, E. Where is the land of opportunity? The geography of intergenerational mobility in the United States. *Q. J. Econ.* **129**, 1553–1623 (2014).

[Google Scholar](#)

40. 40.

Wagner, C. et al. Measuring algorithmically infused societies. *Nature* <https://doi.org/10.1038/s41586-021-03666-1> (2021).

41. 41.

Ba, B. A., Knox, D., Mummolo, J. & Rivera, R. The role of officer race and gender in police–civilian interactions in Chicago. *Science* **371**, 696–702 (2021).

[CAS](#) [PubMed](#) [ADS](#) [Google Scholar](#)

42. 42.

Provost, F. & Fawcett, T. *Data Science for Business: What You Need to Know about Data Mining and Data-Analytic Thinking* (O'Reilly Media, 2013).

43. 43.

Makridakis, S., Wheelwright, S. C. & Hyndman, R. J. *Forecasting Methods and Applications* (Wiley, 1998).

44. 44.

Tetlock, P. E. *Expert Political Judgment: How Good Is It? How Can We Know?* (Princeton Univ. Press, 2005).

45. 45.

Kleinberg, J., Ludwig, J., Mullainathan, S. & Obermeyer, Z. Prediction policy problems. *Am. Econ. Rev.* **105**, 491–495 (2015).

[PubMed](#) [PubMed Central](#) [Google Scholar](#)

46. 46.

Dowding, K. & Miller, C. On prediction in political science. *Eur. J. Polit. Res.* **58**, 1001–1018 (2019).

[Google Scholar](#)

47. 47.

Galesic, M. et al. Human social sensing is an untapped resource for computational social science. *Nature* <https://doi.org/10.1038/s41586-021-03649-2> (2021).

[Article](#) [PubMed](#) [Google Scholar](#)

48. 48.

Cheng, J., Adamic, L., Dow, P. A., Kleinberg, J. M. & Leskovec, J. Can cascades be predicted? In *WWW '14: Proc. 23rd International Conference on World Wide Web* 925–936 (2014).

49. 49.

Pearl, J. The seven tools of causal inference, with reflections on machine learning. *Commun. ACM* **62**, 54–60 (2019). **This paper outlines the need for causal thinking in building predictive models.**

[Google Scholar](#)

50. 50.

Salganik, M. J. et al. Measuring the predictability of life outcomes with a scientific mass collaboration. *Proc. Natl Acad. Sci. USA* **117**, 8398–8403 (2020).

[CAS](#) [PubMed](#) [PubMed Central](#) [Google Scholar](#)

51. 51.

Fudenberg, D., Kleinberg, J., Liang, A. & Mullainathan, S. Measuring the completeness of theories. *SSRN* <https://doi.org/10.2139/ssrn.3018785> (2019).

52. 52.

Martin, T., Hofman, J. M., Sharma, A., Anderson, A. & Watts, D. J. Exploring limits to prediction in complex social systems. In *WWW '16: Proc 25th International Conference on World Wide Web* 683–694 (2016).

53. 53.

Watts, D. J. Common sense and sociological explanations. *Am. J. Sociol.* **120**, 313–351 (2014). **This paper argues that sociologists should pay more attention to prediction versus interpretability when evaluating their explanations.**

[Google Scholar](#)

54. 54.

Zhou, F., Xu, X., Trajcevski, G. & Zhang, K. A survey of information cascade analysis: models, predictions, and recent advances. *ACM Comput. Surv.* **54**, 1–36 (2021).

[Google Scholar](#)

55. 55.

Goel, S., Watts, D. J. & Goldstein, D. G. The structure of online diffusion networks. In *EC'12: Proc. 13th ACM Conference on Electronic Commerce* (2012).

56. 56.

Wu, S., Hofman, J. M., Mason, W. A. & Watts, D. J. Who says what to whom on Twitter. In *WWW'11: Proc. 20th International Conference on World Wide Web* 705–714 (2011).

57. 57.

Goel, S., Anderson, A., Hofman, J. & Watts, D. J. The structural virality of online diffusion. *Manage. Sci.* **62**, 180–196 (2015).

[Google Scholar](#)

58. 58.

Berger, J. & Milkman, K. L. What makes online content viral? *J. Mark. Res.* **49**, 192–205 (2012).

[Google Scholar](#)

59. 59.

Bakshy, E., Hofman, J. M., Mason, W. A. & Watts, D. J. Everyone's an influencer: quantifying influence on Twitter. In *WSDM'11: Proc. Fourth ACM International Conference on Web Search and Data Mining* 65–74 (2011).

60. 60.

Tan, C., Lee, L. & Pang, B. The effect of wording on message propagation: topic- and author-controlled natural experiments on Twitter. In *Proc. 52nd Annual Meeting of the Association for Computational Linguistics* 175–185 (2014).

61. 61.

Liu, T., Ungar, L. & Kording, K. Quantifying causality in data science with quasi-experiments. *Nat. Comput. Sci.* **1**, 24–32 (2021).

[Google Scholar](#)

62. 62.

Hochberg, I. et al. Encouraging physical activity in patients with diabetes through automatic personalized feedback via reinforcement learning improves glycemic control. *Diabetes Care* **39**, e59–e60 (2016).

[PubMed](#) [Google Scholar](#)

63. 63.

Athey, S. & Imbens, G. Recursive partitioning for heterogeneous causal effects. *Proc. Natl Acad. Sci. USA* **113**, 7353–7360 (2016).

[MathSciNet](#) [CAS](#) [PubMed](#) [PubMed Central](#) [MATH](#) [Google Scholar](#)

64. 64.

Charles, D., Chickering, M. & Simard, P. Counterfactual reasoning and learning systems: the example of computational advertising. *J. Mach. Learn. Res.* **14**, 3207–3260 (2013).

[MathSciNet](#) [MATH](#) [Google Scholar](#)

65. 65.

Low, H. & Meghir, C. The use of structural models in econometrics. *J. Econ. Perspect.* **31**, 33–58 (2017).

[Google Scholar](#)

66. 66.

Athey, S., Levin, J. & Seira, E. Comparing open and sealed bid auctions: evidence from timber auctions*. *Q. J. Econ.* **126**, 207–257 (2011).

[Google Scholar](#)

67. 67.

Awad, E. et al. The Moral Machine experiment. *Nature* **563**, 59–64 (2018).

[CAS](#) [PubMed](#) [ADS](#) [Google Scholar](#)

68. 68.

Aczel, B. et al. A consensus-based transparency checklist. *Nat. Hum. Behav.* **4**, 4–6 (2020).

[PubMed](#) [Google Scholar](#)

69. 69.

Kidwell, M. C. et al. Badges to acknowledge open practices: a simple, low-cost, effective method for increasing transparency. *PLoS Biol.* **14**, e1002456 (2016).

[PubMed](#) [PubMed Central](#) [Google Scholar](#)

70. 70.

Nosek, B. A. et al. Promoting an open research culture. *Science* **348**, 1422–1425 (2015).

[CAS](#) [PubMed](#) [PubMed Central](#) [ADS](#) [Google Scholar](#)

71. 71.

Nosek, B. A., Ebersole, C. R., DeHaven, A. C. & Mellor, D. T. The preregistration revolution. *Proc. Natl Acad. Sci. USA* **115**, 2600–2606 (2018).

[CAS](#) [PubMed](#) [PubMed Central](#) [Google Scholar](#)

72. 72.

Donoho, D. 50 years of data science. *J. Comput. Graph. Stat.* **26**, 745–766 (2017).

[MathSciNet](#) [Google Scholar](#)

73. 73.

Gelman, A. & Loken, E. The statistical crisis in science. *Am. Sci.* **102**, 460 (2014).

[Google Scholar](#)

74. 74.

Rao, R. B., Fung, G. & Rosales, R. On the dangers of cross-validation. An experimental evaluation. In *Proc. 2008 SIAM International Conference on Data Mining* 588–596 (Society for Industrial and Applied Mathematics, 2008).

75. 75.

Dwork, C. et al. The reusable holdout: preserving validity in adaptive data analysis. *Science* **349**, 636–638 (2015).

[MathSciNet](#) [CAS](#) [PubMed](#) [MATH](#) [ADS](#) [Google Scholar](#)

76. 76.

Chambers, C. D. Registered reports: a new publishing initiative at *Cortex*. *Cortex* **49**, 609–610 (2013).

[PubMed](#) [Google Scholar](#)

77. 77.

Nosek, B. A. & Lakens, D. Registered reports: a method to increase the credibility of published reports. *Soc. Psychol.* **45**, 137–141 (2014).

[Google Scholar](#)

78. 78.

Bennett, J. & Lanning, S. The Netflix Prize. In *Proc. KDD Cup and Workshop 2007* (2007).

79. 79.

Dorie, V., Hill, J., Shalit, U., Scott, M. & Cervone, D. Automated versus do-it-yourself methods for causal inference: lessons learned from a data analysis competition. *SSO Schweiz. Monatsschr. Zahnheilkd.* **34**, 43–68 (2019).

[MathSciNet](#) [MATH](#) [Google Scholar](#)

80. 80.

Lin, A., Merchant, A., Sarkar, S. K. & D'Amour, A. Universal causal evaluation engine: an API for empirically evaluating causal inference models. in *Proc. Machine Learning Research* (eds Le, T. D. et al.) Vol. 104, 50–58 (PMLR, 2019).

81. 81.

Craver, C. F. *Explaining the Brain: Mechanisms and the Mosaic Unity of Neuroscience* (Clarendon, 2007).

82. 82.

Salganik, M. J., Lundberg, I., Kindel, A. T. & McLanahan, S. Introduction to the special collection on the Fragile Families Challenge. *Socius* <https://doi.org/10.1177/2378023119871580> (2019).

83. 83.

Strathern, M. ‘Improving ratings’: audit in the British university system. *Eur. Rev.* **5**, 305–321 (1997).

[Google Scholar](#)

84. 84.

Peterson, J. C., Bourgin, D. D., Agrawal, M., Reichman, D. & Griffiths, T. L. Using large-scale experiments and machine learning to discover new theories of human decision-making. *Science* **372**, 1209–1214 (2021).

[Download references](#)

Author information

Author notes

1. These authors contributed equally: Jake M. Hofman, Duncan J. Watts

Affiliations

1. Microsoft Research, New York, NY, USA

Jake M. Hofman

2. Department of Computer and Information Science, University of Pennsylvania, Philadelphia, PA, USA

Duncan J. Watts

3. The Annenberg School of Communication, University of Pennsylvania, Philadelphia, PA, USA

Duncan J. Watts

4. Operations, Information, and Decisions Department, University of Pennsylvania, Philadelphia, PA, USA

Duncan J. Watts

5. Graduate School of Business, Stanford University, Stanford, CA, USA

Susan Athey

6. Department of Sociology, Princeton University, Princeton, NJ, USA

Filiz Garip & Matthew J. Salganik

7. Department of Psychology, Princeton University, Princeton, NJ, USA

Thomas L. Griffiths

8. Department of Computer Science, Princeton University, Princeton, NJ, USA

Thomas L. Griffiths

9. Department of Computer Science, Cornell University, Ithaca, NY, USA

Jon Kleinberg

10. Department of Information Science, Cornell University, Ithaca, NY, USA

Jon Kleinberg

11. Oxford Internet Institute, University of Oxford, Oxford, UK

Helen Margetts

12. Public Policy Programme, The Alan Turing Institute, London, UK

Helen Margetts

13. Booth School of Business, University of Chicago, Chicago, IL, USA

Sendhil Mullainathan

14. Melbourne School of Psychological Sciences, University of Melbourne, Melbourne, Victoria, Australia

Simine Vazire

15. Laboratory for the Modeling of Biological and Socio-technical Systems, Northeastern University, Boston, MA, USA

Alessandro Vespignani

16. Department of Psychology, University of Texas at Austin, Austin, TX, USA

Tal Yarkoni

Authors

1. Jake M. Hofman

[View author publications](#)

You can also search for this author in [PubMed](#) [Google Scholar](#)

2. Duncan J. Watts

[View author publications](#)

You can also search for this author in [PubMed](#) [Google Scholar](#)

3. Susan Athey

[View author publications](#)

You can also search for this author in [PubMed](#) [Google Scholar](#)

4. Filiz Garip

[View author publications](#)

You can also search for this author in [PubMed](#) [Google Scholar](#)

5. Thomas L. Griffiths

[View author publications](#)

You can also search for this author in [PubMed](#) [Google Scholar](#)

6. Jon Kleinberg

[View author publications](#)

You can also search for this author in [PubMed](#) [Google Scholar](#)

7. Helen Margetts

[View author publications](#)

You can also search for this author in [PubMed](#) [Google Scholar](#)

8. Sendhil Mullainathan

[View author publications](#)

You can also search for this author in [PubMed](#) [Google Scholar](#)

9. Matthew J. Salganik

[View author publications](#)

You can also search for this author in [PubMed](#) [Google Scholar](#)

10. Simine Vazire

[View author publications](#)

You can also search for this author in [PubMed](#) [Google Scholar](#)

11. Alessandro Vespignani
[View author publications](#)

You can also search for this author in [PubMed](#) [Google Scholar](#)

12. Tal Yarkoni
[View author publications](#)

You can also search for this author in [PubMed](#) [Google Scholar](#)

Contributions

J.M.H. and D.J.W. conceptualized and helped to write and prepare the manuscript. They contributed equally to these efforts. All authors were involved in and discussed the structure of the manuscript at various stages of its development.

Corresponding authors

Correspondence to [Jake M. Hofman](#) or [Duncan J. Watts](#).

Ethics declarations

Competing interests

The authors declare no competing interests.

Additional information

Peer review information *Nature* thanks Noortje Marres, Melanie Mitchell and Scott Page for their contribution to the peer review of this work.

Publisher's note Springer Nature remains neutral with regard to jurisdictional claims in published maps and institutional affiliations.

Rights and permissions

[Reprints and Permissions](#)

About this article



Check for
updates

Cite this article

Hofman, J.M., Watts, D.J., Athey, S. *et al.* Integrating explanation and prediction in computational social science. *Nature* **595**, 181–188 (2021). <https://doi.org/10.1038/s41586-021-03659-0>

[Download citation](#)

- Received: 23 February 2021
- Accepted: 20 May 2021
- Published: 30 June 2021
- Issue Date: 08 July 2021
- DOI: <https://doi.org/10.1038/s41586-021-03659-0>

Comments

By submitting a comment you agree to abide by our [Terms](#) and [Community Guidelines](#). If you find something abusive or that does not comply with our terms or guidelines please flag it as inappropriate.

[Access through your institution](#)

[Change institution](#)

[Buy or subscribe](#)

Associated Content

Special

[Computational social science](#)

Advertisement

This article was downloaded by **calibre** from <https://www.nature.com/articles/s41586-021-03659-0>

| [Section menu](#) | [Main menu](#) |

Meaningful measures of human society in the twenty-first century

[Download PDF](#)

- Perspective
- [Published: 30 June 2021](#)

Meaningful measures of human society in the twenty-first century

- [David Lazer](#) ^{1,2},
- [Eszter Hargittai](#) [ORCID: orcid.org/0000-0003-4199-4868](#)³,
- [Deen Freelon](#) [ORCID: orcid.org/0000-0001-5055-0316](#)⁴,
- [Sandra Gonzalez-Bailon](#) [ORCID: orcid.org/0000-0002-8372-798X](#)⁵,
- [Kevin Munger](#)⁶,
- [Katherine Ognyanova](#) [ORCID: orcid.org/0000-0003-3038-7077](#)⁷ &
- [Jason Radford](#) [ORCID: orcid.org/0000-0003-3045-5527](#)¹

[Nature](#) volume 595, pages 189–196 (2021) [Cite this article](#)

- 2497 Accesses
- 1 Citations
- 177 Altmetric
- [Metrics details](#)

Subjects

- [Scientific community](#)

Abstract

Science rarely proceeds beyond what scientists can observe and measure, and sometimes what can be observed proceeds far ahead of scientific understanding. The twenty-first century offers such a moment in the study of human societies. A vastly larger share of behaviours is observed today than would have been imaginable at the close of the twentieth century. Our interpersonal communication, our movements and

many of our everyday actions, are all potentially accessible for scientific research; sometimes through purposive instrumentation for scientific objectives (for example, satellite imagery), but far more often these objectives are, literally, an afterthought (for example, Twitter data streams). Here we evaluate the potential of this massive instrumentation—the creation of techniques for the structured representation and quantification—of human behaviour through the lens of scientific measurement and its principles. In particular, we focus on the question of how we extract scientific meaning from data that often were not created for such purposes. These data present conceptual, computational and ethical challenges that require a rejuvenation of our scientific theories to keep up with the rapidly changing social realities and our capacities to capture them. We require, in other words, new approaches to manage, use and analyse data.

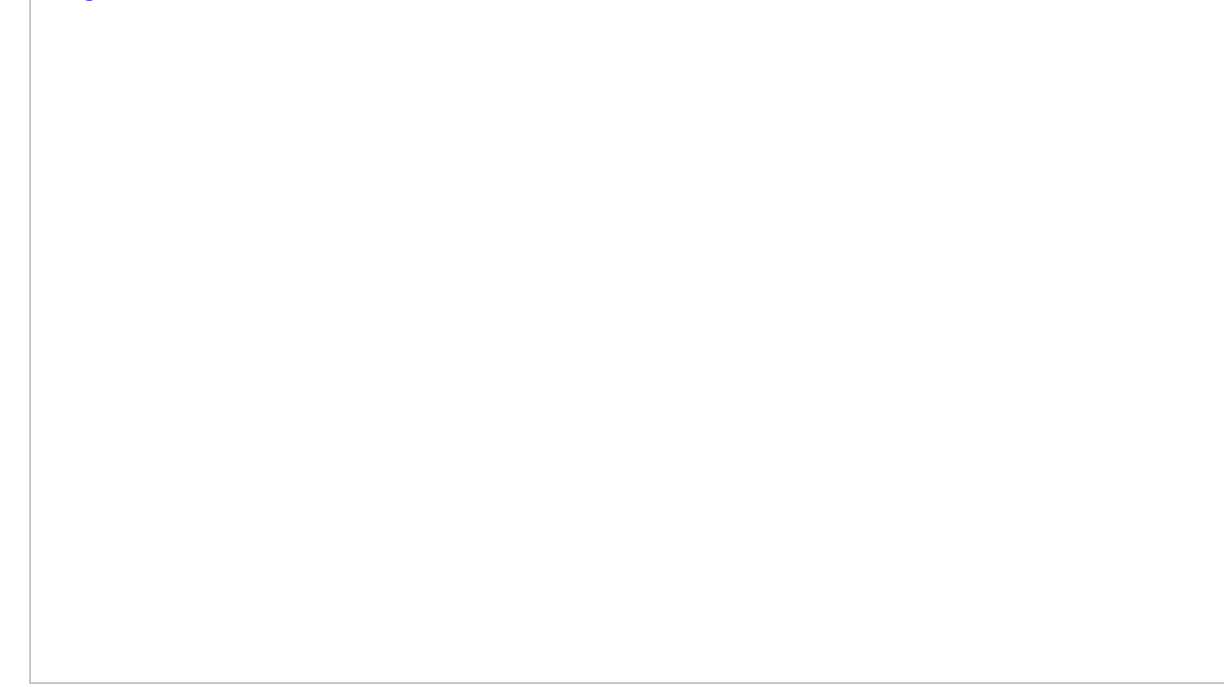
[Download PDF](#)

Sensor technologies have multiplied across many realms of human activity, from tracking devices in cars to online browsing. Satellites scan and digitize the planet at regular intervals. The development of techniques for processing unstructured data such as text, images, audio and video by computer scientists animates the conversion of—for example—books¹, radio broadcasts² and television shows³ into data. In the twenty-first century, human behaviour—from mobility to information consumption to various types of interpersonal communication—is increasingly recorded somewhere and potentially computationally tractable. Past communication technologies, from mail to print to fax, typically left far fewer durable and accessible artefacts; those that did have become computationally accessible only in the past decade or so, as the relevant physical artefacts were digitized. The digitization of books is an example, which enables the computational analysis of a massive corpus of human expression that stretches back centuries⁴.

The emergence of these new data streams has often been compared to the development of the telescope. As Robert Merton famously wrote, “Perhaps sociology is not yet ready for its Einstein because it has not yet found its Kepler....”⁵ Merton’s provocation was that sociology did not yet have the empirical foundations on which to build great theory. Duncan Watts, in response, writes 62 years later, “... by rendering the unmeasurable measurable, the technological revolution in mobile, Web, and Internet communications has the potential to revolutionize our understanding of ourselves and how we interact. Merton was right: social science still has not found its Kepler. But three hundred years after Alexander Pope argued that the proper study of mankind should lie not in the heavens but in ourselves, we have finally found our telescope.”⁶.

We believe in the potential of digital data sources to transform the social sciences. However, the metaphor of the data streams from the instrumented society as a ‘telescope’ is misleading in important ways. First, the study of societies is different from the study of the stars, because the patterns that characterize human behaviour will generally differ across time and place. Second, the measures built from these streams are potentially suspect in ways that must be actively interrogated, because these sources were not built with scientific goals in mind. We now turn to the first point; the remainder of the paper is devoted to the second.

Fig. 1: Measurement in social science.



Measurement is the bridge connecting scientific motivations and data with insight and applications.

[Full size image](#)

The unstable logics of society and measurement

Empirical social science is largely focused on finding generalizable but not universal patterns in human behaviour. The part of the social sciences that has the intent of finding such universal patterns in human behaviour (for example, evolutionary psychology) is tiny relative to the whole field. The issue of the instability of the rules that govern human society is exacerbated by the very sociotechnical systems that are gathering the data about people, which are actively (and in some cases intentionally)

changing the social world that social science would study. Through what social scientists call reflexivity and self-fulfilling prophecies, humans actively change the world that they are observing by acting on the knowledge gained (in part by measurement instruments).⁷⁸

Reflexivity refers to the loop that links social reality with the theories and the metrics that we devise to explain it. The ‘bandwagon’ and ‘underdog’ effects, for instance, have long been identified in the analysis of electoral politics to explain the impact that polls and forecasts have on voting behaviour. If candidates are projected as likely winners, more people may decide to vote for them (bandwagon effect) or, conversely, more people could mobilize to increase support for the candidate expected to lose (underdog effect).⁷ These effects reflect the impact that measurements have on attitudes and behaviour^{8,9}, and how our measures can distort the phenomena that they were designed to monitor. These distortions, in turn, can be amplified by algorithmic decision-making in public health, law enforcement, sentencing, education and hiring.^{10,11}.

Reflexivity also takes the form of the observer effect, which happens when people modify their behaviour if they know they are being watched^{12,13}. Digital technologies have created a new version of the reflexivity problem, amplifying the performative aspect that is intrinsic in social indicators. When Google launched the Flu Trends project in 2008, the goal was to use search queries to estimate the prevalence of flu symptoms in the population. In 2013, however, Flu Trends substantially overestimated peak flu levels. One of the reasons was the flawed assumption that search behaviour was driven by external events, such as having flu symptoms. In fact, Google’s algorithms were driving those patterns as well: by trying to anticipate the intent of the users through recommended search terms, Google was distorting the information users would have otherwise revealed¹⁴. The reaction to the observed phenomenon, in other words, changed the phenomenon itself.

Obfuscation tactics represent another version of the observer effect: we can now disrupt measurements by deliberately adding ambiguous or misleading information to interfere with data collection. Examples of obfuscation include editing profile photographs to prevent facial recognition; using virtual private networking (VPN) to hide one’s location when browsing the web; or using group identity (for example, many people under one user account) to obscure specifics about the actions of one user.¹⁵ The reflexivity loop here is created by the awareness that behavioural traces feed into metrics and surveillance, so the meaning of that behaviour is intentionally altered. This is similar to when respondents lie to survey researchers, but on a much larger scale. And because the skills needed to know that surveillance is happening and how to implement obfuscation to address this are not randomly distributed across the

population, the individuals whose data will be altered in such ways will not be random either.

The unobtrusive nature of many digital measures suggests that, overall, observer effects may be less of an issue with these new data sources compared to the past when—for example—the gender, age and race of the person conducting an interview could vastly change the answers that respondents provided¹⁶. However, the loop that connects social reality with the metrics that we devise to analyse it has been strengthened—reflexivity is now embedded in the instruments used to monitor and predict human behaviour. It is as if the Hubble telescope were organizing the placement and behaviour of the stars at the same time as it is observing them. Social media, for example, not only capture human behaviour, but also have the potential to alter important patterns of human society, such as the speed of information flows, the scope of media production and the actors responsible for defining public opinion.

As a result of the fluidity of the principles organizing human society, the meaning of a given measure will also evolve. Part of why the social sciences must accommodate these new types of data is that emerging sociotechnical systems are reducing the relevance of some old scientific instruments used to measure human behaviour.

Existing measures of key concepts such as gross domestic product and geographical mobility are shaped by the strengths and weaknesses of twentieth century data. If we only evaluate new measures against the old, we simply replicate their shortcomings, mistaking the gold standard of the twentieth century for objective truth. For example, consider the standard question (originally from 1978) from the American National Election Studies¹⁷ about radio consumption regarding an election: “Would you say you listened to a good many, several, or just one or two speeches or discussions on the radio about ‘the campaign’?”

This construction of ‘media consumption’ as consisting of a countable number of discrete units is an artefact of the technology of the broadcast era. This question bears little relation to how people access digital media today. It would be futile to attempt to capture behaviour regarding social media by asking questions such as ‘How many tweets did you see today?’ or ‘What Twitter accounts showed up in your feed?’. Many of the ways to measure behaviour developed in the early days of quantitative social science were: (1) necessary given constraints on measurement at the time; and (2) grounded in a social reality that was markedly different.

Figure 1 summarizes how measurement fits into the general scientific process. We discuss below the central challenges of turning data from these sociotechnical systems into scientific measurements. We include in this discussion two motivating examples of data streams that have been the basis of much social science research: location data from mobile phones and social media posts on Twitter. The key questions we turn to

now are what and whom we measure with massively instrumented human behaviour, focusing on the key principles of measurement summarized in Box 1.

Box 1 Central principles of measurement

Measurement should follow definitions of what matters

Efforts to measure observed phenomena are premised on the identification of relevant questions. What matters is driven by research questions, which may be motivated by normative goals, theoretical debates or empirical puzzles.

Measures must be actively constructed out of data

Instrumentation designed for research purposes often generates scientific data. But data collected for purposes other than scientific research are also frequently repurposed by scholars. Data do not have meaning in themselves—to become measures of some theoretical construct, they must be transformed by methods that make them systematically relatable to one another, and to scientific theory.

Scientific measurement follows from the above principles in a constantly evolving loop

Scientific motivation directs researchers to design a data-collection protocol, use third-party data or develop some fusion of the two. In their raw format, data offer the observations that are processed into the measures that will enable testing pre-conceived hypotheses (in a deductive way) or derive new hypotheses from exploratory analyses (in an inductive, data-driven way). These deductive and inductive analyses aim to offer insights that can then feed back into scientific motivations, inform policy interventions, or—more generally—drive the basic and applied arms of research.

What trace data measure

The goal of measurement using behavioural trace data is to extract meaning from the raw data generated from instrumentation. All scientific data instrumentation confronts this issue, but the leap from raw data to meaningful measures is often particularly large when we use data recycled from systems designed for other purposes¹⁸. For example, mobility data from mobile phones reporting specific latitudes and longitudes are largely uninteresting without further processing, which enables us to measure proximity, mobility and other socially relevant concepts.

The key challenge is whether our measurement accurately captures the construct that we want to examine. Does it closely match other measures of the same thing? What is

the potential slippage between construct and concept (for example, if measuring physical activity from mobile phones, how consequential are the missed stationary activities, such as a treadmill?). When we examine supposedly unrelated constructs, do our measures reflect the expected lack of association? By and large, twenty-first century observational data are not designed for research and need to be linked to known concepts before we can use the data to answer scientific research questions.

The meaning of measures is derived, in part, from theory. Theoretically driven designs that apply existing knowledge to interpret digital signals can overcome many of the problems of using instrumented behavioural data. Conversely, undertheorized ad hoc operationalizations can make research findings difficult to interpret and inconsistent across studies. As noted previously¹⁹, formal theory is useful not only in generating hypotheses, but also in selecting an appropriate way of measuring constructs with big data.

Consider, for example, the use of mobility data to study the spread of COVID-19. Multiple studies used real-time travel data to track the movement of people from Wuhan to other provinces in China^{20,21}. The researchers found that population movements from Wuhan were strongly predictive of the introduction of the coronavirus to a region. Local controls then predicted the subsequent spread of the virus. In these studies there is a well-theorized process based on the assumption that the spread of the virus is driven by the proximity of individuals. The chosen theoretical framework, in turn, informs how generalizable those findings could be to other cases. That is, we might expect similar patterns in the USA²², but not in Australia, given the rigorous testing and isolation procedures that were imposed on visitors in the latter country. The results of any given empirical study are necessarily local, in both time and space; theory is needed for the appropriate movement of any measurement to a new geographical or temporal context^{23,24}.

As we conduct more research using high-volume, complex data sources and formats, methods that offer insights into the validity of new measures become especially valuable. One promising approach is to examine classic validated self-reported scales in conjunction with new ways of measuring related concepts. For instance, self-reported news attention and exposure can be used in conjunction with eye-tracking to capture visual attention to online content²⁵. A similar triangulation of approaches to measurement can also be useful in confirming the validity and robustness of new behavioural constructs²⁶. Researchers have used mobile phone data to design proximity-based measures capturing the amount of time that people spend close to each other²⁷. These metrics can serve a variety of useful purposes. They can be used as a proxy for relationship strength, or give us a way to track possible pathways of virus contagion. There is, however, the potential for error—two people whose devices appear near each other as measured by their Bluetooth beacons may, for instance, be

separated by a wall or may simply be charging their phones from the same outlet. In cases such as this, triangulation can come from the inclusion of self-reported data, such as sending a message to someone's phone to ask them who else is nearby at the time.

For internet-based research, both basic population characteristics and underlying mechanisms that structure user behaviour on digital platforms remain relatively poorly understood. Many basic concepts remain difficult to measure even in online platforms that offer easy data access to researchers. Despite the thousands of papers based on Twitter data in recent years, social media scholars still find that identifying the demographic characteristics of individual users remains a big challenge. Additionally, researchers still cannot reliably distinguish humans from non-humans (for example, bots, collective accounts or organizations), although there have been important strides made in that direction^{28,29}. As a result, the large majority of Twitter research is making inferences about accounts or tweets; very little of Twitter research can reasonably claim to be making statements about the behaviours of humans. For research questions that focus on human behaviour on Twitter, methods that link user accounts to administrative data or to survey responses offer promise in identifying humans and their demographic attributes on Twitter³⁰.

Even when it is clear that humans are the source of a given behaviour, there may be a challenge in attribution of specific behaviours to specific humans. In its early days, audience research for broadcast television, for instance, encountered challenges with multi-member households³¹. The data in those cases would suggest the existence of someone with a taste for children's cartoons and cable news, when, in fact, there were two different individuals involved. Technological sensors can thus be actively misleading when behaviour is divided across humans (two people using the same Netflix account) or across sensors (the same person viewing Twitter on a smartphone and a desktop). Further exacerbating the issue is that the sensor–human mismatch could rapidly evolve over time. Thus, for example, a finding based on desktop browsing data that news consumption has systematically changed could simply be an artefact of the progressive shift from desktop browsers to mobile apps³². The lack of stability of human use of these different systems (and sensors) may make such a comparison over time essentially impossible.

The use of models based on other data can facilitate the measurement of focal behaviour. For example, who uses which device can be modelled from other data, and the outputs of this model will be less sensitive than discrete assumptions about the identity of a device user. The cable news viewer may be the grandparent and the Xbox user the grandchild. However, the data that are included in these models must always come from the past, and the relationship between measures is itself unstable. This is the fundamental problem of induction, and while it cannot be surmounted without a

metaphysical revolution, we propose that constantly updated measurements and models represent our best amelioration of the problem. That is, we should plan for the slippage of our measurements and conduct an ongoing assessment of how particular measures capture the current social reality. For example, measures of inflation need to assess how the set of goods that people consume changes over time. This is a useful recalibration, although it also illustrates the limits of this approach, because the emergence of completely new items (no one was buying smartphones in 2000) makes consumption across time inherently incomparable.

The proliferation of communication technologies, driven by the internet, also yields a fragmentation of behaviours into different data silos. Consider a research question that explores whether non-proximate synchronous voice-mediated communication is important to reducing feelings of social isolation. The past half century has seen a steady fracturing of this behaviour into different systems—from government-mandated monopolies (for example, Ma Bell in the USA) to oligopolies to a countless number of internet providers. Furthermore, there are plausibly systematic biases in the data captured in any one of these systems—whom you talk to on your mobile phone might be systematically different from whom you talk to via Zoom, Skype or WhatsApp³³. Even the tortured linguistic construction used above reflects the sociotechnical complexity: not too long ago ‘non-proximate synchronous voice-mediated communication’ would have been described simply as a ‘phone call’. One important consequence of this technological fragmentation is that measurements relying on a single digital device or service should be interpreted with considerable caution. The answers that we find could plausibly differ from those we could get by measuring the behaviour in a similar but different technology. Ironically, because of that complexity, an accurate picture of whom someone generally talks to may be better captured through a simple survey question than through records from a single platform.

Conversely, behaviours observed in different silos that seem similar might actually be capturing very different phenomena. Just as various name generators that are used in surveys to generate lists of contacts result in the identification of different social ties³⁴, a friend on Facebook does not denote the same relationship as a Twitter follower or a LinkedIn contact. Moreover, none of these relations denote a ‘friend’ as used either colloquially or scientifically, although there are very likely some strong statistical connections among these concepts. These systems, furthermore, change over time and their affordances—what they allow users to do—also evolve. This in turn means that the causal processes that underlie our online social actions, relationships and structures are constantly changing. As such, we must now be aware of system-varying properties of measures such as temporal and inter-system validity. The challenge then becomes developing measures that provide some degree of generalizability over time or across systems for a given research question.

Another deep problem is the algorithmic confounding of measurement³⁵. Confounding here refers to our inability to distinguish signals that represent typical human behaviour from ones that result from the rules that govern a digital platform. Without knowing how a system is designed, we could easily attribute social motives to behaviour driven by algorithmic decisions. If Twitter's feed suddenly starts to prioritize sports, a user may find out who won an Olympics competition without any changes in their underlying interest in sports. Such changes are often difficult to detect, both because they are sometimes introduced without notice and because they may roll out unevenly, affecting certain user populations before others. This mechanism also functions in more subtle ways, such as how natural human proclivities are enhanced by algorithmic prompts. For instance, if Twitter systematically suggests that you follow back people who already follow you, that can boost our natural tendency to reciprocate social ties³⁶. More generally, internet companies aim to manipulate human behaviour so as to increase engagement on their platforms (for example, Facebook, Twitter and Instagram) or money spent on their products (such as Amazon and Ebay). Those machine-learning-based manipulations are pervasive, and any efforts to develop measures from platform data need to evaluate the extent to which algorithms will distort both the measures and any downstream analyses. Because of their importance, those algorithms are worthy of closer study^{11,37}.

Although an in-depth discussion of causal inference is outside the scope of this paper, we should note that a number of measurement issues identified here present a particular problem for research that aims to establish cause and effect. Lack of stability in measurement over time, for instance, may induce researchers to attribute the changes in a focal outcome to an unrelated external event. The discussion above regarding Google Flu Trends is also relevant here. In that case, there was an implicit assumption that the flu was causally related to flu-related searches on Google. However, if Google around 2013 was proposing flu-related searches during flu season because it had, deep in its complex algorithmic machinery, inferred it was flu season, the measure of exactly the same behaviour in 2013 would mean something very different than it did in 2008.

The malleability of human expression and language also poses general challenges around inferences of attitudes and opinions from language and image data³⁸. Expressions of sentiment on Twitter are notoriously difficult for computers to decode, as they typically stumble over sarcasm, irony and hyperbole³⁹. How problematic that is depends on the structure of the noise and, again, on what matters—that is, the research question.

Whom trace data measure

Human behaviour is a multi-level concept that often requires measurements at the individual level to make inferences about the distribution of behaviours, attitudes and attributes at the collective level. The research question should make clear what population is of interest to a particular study. That population could include people everywhere of all types, or it could be specific to a certain geographical region (a city or country), a particular community (a hobby group or company) or a myriad of other subpopulations (youths, immigrants, or politicians). Especially when entire populations are concerned, it is not feasible, logically or financially, to collect data about everybody. In such cases, researchers should ideally collect data about a random sample of the population, which means that each member of the population has an equal probability of being in the sample. This ideal was never quite achievable, and is even less relevant in a world in which response rates to survey requests are below 10%, with uneven rates of accessibility of people across modalities of recruitment⁴⁰.

With system-level data, one may be tempted to think that everybody is represented since the actions of all of the users are in the dataset. However, the sampling in this case happens at the level of who is a user of the system from which the data are collected as well as who is most active on said system⁴¹. It is, at best, a ‘convenience census’ of the platform under investigation rather than the whole population⁴². If the scientific objective is to make a statement about the people on the platform, that census might be compelling. However, any leap to generalize beyond that platform must be viewed more critically. This is a particular problem for research on Twitter, the most commonly cited source of emerging data, as it is used by only about 20% of the US population and is even less popular in most other countries^{43,44,45}. Importantly, users of social media platforms do not mirror the general population of internet users either demographically⁴¹ or regarding other attributes such as their interests^{41,44,46}. In light of recent progress in promoting the representativeness of research populations in other domains^{42,47}, it is imperative to think carefully about these issues in the realm of social media⁴⁷. We also note that methods that recalibrate data to make reasonable population-level inferences can be particularly powerful when applied to large-scale data⁴⁸.

The issue of generalizability is amplified when only a subset of the platform population is studied. The key question is whether and how the nature of the sample affects the inferences being drawn. Thus, for example, a study of Twitter users who include their names and locations in their profiles⁴⁹ raises the question: do these findings generalize to Twitter users who do not divulge such details? Similarly, another study⁵⁰ examines the consumption patterns of political information, based on the small minority of Facebook users who provided partisan labels in their profiles—but do the resulting findings generalize to individuals who do not divulge their political affiliations? The relatively large sample size in these studies—by social science standards—does not alleviate the concern that the sample is not representative

of the population using the platform⁵¹. This issue is exacerbated by the sometimes large changes in who uses a platform over time (Facebook was once the exclusive domain of Harvard undergraduates), in which case these demographic shifts by themselves affect what happens on the platform.

Other critical problems in generalizability include the fact that different platforms elicit systematically different behaviours. For example, the same person will often behave differently on Facebook and on Twitter⁵². More generally, some human behaviour is highly dependent on the setting—if we could only observe the same people at work, at home or in a religious setting, we might make radically different conclusions about humanity. Generalizability is a function not only of the population, but also of the particular observational contexts. Depending on the research question, this may or may not be a problem. A clearly defined question and population will help to establish how well the measurement lines up with the research intent.

Finally, we note the key measurement question of what are the systematic biases with respect to sampling. Generally, our data collection systems are biased away from minority and, especially, marginal populations; furthermore, our theoretical questions regarding populations typically focus on the middle of the distribution.

Representativeness is an issue of transcendent importance in understanding humanity, now and in the past. Consider studies that analyse the text of Google Books (the largest digitized collection of human knowledge), which want to draw conclusions on how linguistic shifts in the texts over the centuries correspond with shifts in, say, national sentiment⁴. This corpus suffers both as a representation of language use, because its composition systematically changed over time (for example, with a much higher representation of scientific texts in the twentieth century)¹ and because even a well-curated set of books will reflect the reality of unrepresentative elites. Not even the largest library ever compiled can cast light on those who—although unrepresented in published texts—still had the ability to act and change the course of history.

These representativeness issues were a major concern in the social science methods of the twentieth century. Reaching respondents through postal mail systematically excludes homeless populations, telephone surveys exclude those without a phone, and surveys conducted in person are subject to people’s comfort with and trust in that type of interaction with a stranger.

Observational behavioural streams are potentially subject to similar biases. First, often the instrumentation that collects the data are a consumer good owned by an individual (for example, a mobile phone or a computer), for which costs present a barrier. Second, the instrumentation is often driven by corporate business models aimed at people with money to spend. Third, people more concerned or knowledgeable about

privacy matters may be less represented in systems that track behaviours as they opt out of using such services.

However, these data streams have some critical compensating features. Sensor technologies may fill in important data gaps, giving visibility to those who would otherwise be erased from the map. Satellite imagery, for instance, has been used to build indicators of wealth and poverty in the Global South when surveys of household income and consumption do not exist⁵³. The banal pervasiveness of modern technology means representation will in many cases be superior to traditional data-collection mechanisms—it is cheaper to own a mobile phone than a home. There are parallels here to the administrative data that W. E. B. Du Bois used to study African-American individuals in the late nineteenth and early twentieth century⁵⁴. The data of an administrative state that enforced racial hierarchy were surely not neutral, yet still had critical value in providing visibility of those most precariously positioned in society.

Furthermore, large sample sizes allow us to look at the behaviour of subsets of the data, for example, minorities (generally construed) and events that are statistically uncommon but consequential (for example, hate speech or misinformation)^{49,55,56}. In these cases, sample size and our ability to zoom into smaller populations and infrequent data points matters more than the representativeness of the sample⁵⁷. As Pareto observed long ago, many human behaviours are concentrated in tiny slices of the population⁵⁸; however, twentieth century methods were generally poorly suited to studying that social reality. Perhaps the social theories of the twenty-first century will be able to use micro-level behavioural data to understand how structures of interdependence yield certain macro-level patterns⁵⁹.

Access and ethics in measurement

Emerging data streams from sociotechnical systems present two additional challenges, compared with—for example—the data from the Hubble telescope. First, the Hubble telescope is controlled by the scientific establishment, whose goal, presumably, is to answer scientific questions. The institutional goal of a platform, such as Twitter, is clearly not to answer scientific inquiries. The first question is therefore, what can be measured? Second, humans as research participants pose ethical issues that far-away galaxies clearly do not. The question that follows then is what should be measured? We deal with these two questions in turn.

What can be measured varies markedly depending on the system that is generating the data. It is possible to design a small-scale data collection system that relies on consenting participants;⁶⁰ however, access to data from millions of people generally requires partnership with a platform. There is a wide spectrum of availability for

internet-based communication data with access rules that differ greatly across data holders and time. At the least restrictive end, platforms such as Reddit and Wikipedia allow access to nearly everything the end user can view in machine-readable formats. By contrast, companies such as Facebook and Twitter offer far more restrictive access regimes that are limited by time, data volume and the fact that not all publicly visible data are programmatically accessible. Notably, none of the current major platforms offers individual-level data on what people pay attention to, a remarkably large gap in current internet-based measurements⁶¹. Furthermore, none of the platforms provide access to information on the extensive randomized control trials (in the form of AB testing) that they do, which could—in principle—enable inferences of the influences of their algorithms on individuals⁶². Generally, any private authority that controls data of interest to researchers can, in the absence of regulation to the contrary, dictate the terms of data access as it chooses. The fact that the actions of platforms such as Twitter and Facebook are a compelling focus for scientific questions of public interest (consider: does a platform amplify the spread of misinformation? What steps does a platform take in response to hate speech?) makes this control deeply problematic⁶³. A duty of scholarship in these spaces is to inform public discourse on these important questions. A corollary to the question of what can be measured must be: is it possible to speak truth to power if the power in question controls access to the data used to construct that ‘truth’? And, if not, is it (ever) possible to trust any measures that are allowed to be extracted from a given system?

Emerging data sources also pose new ethical challenges. We focus on those that intersect with measurement, and, in particular, on what can and should be measured. More extensive discussions of trace data ethics, as well as alternative models for data access, are available elsewhere^{18,64,65,66}; here we briefly present five particularly pressing concerns. First, although informed consent is a mainstay of research on human participants, anonymous data acquired by third parties are often not considered ‘human participant data’ and are therefore exempt from review by institutional review boards. What are the ethical obligations of the researcher to consider the circumstances under which the data were collected? In a recent example, over 70 gigabytes of data from the far-right social network Parler were publicly released in early January 2021, including GPS-derived location data⁶⁷. Whether researchers can ethically analyse this dataset is a topic of ongoing debate, particularly in light of the use of the website as a planning space for the US Capitol insurrection of 6 January 2021. Far more generally, people are probably unaware of how different systems track them, whether it is through mobility data from phones⁶⁸, or browsing data. What then are the ethics of using tracking data from third parties when the targets of that tracking are, at most, nominally aware of that fact?

Second, the level of detail in behavioural datasets means that anonymization that is robust to re-identification efforts is often practically difficult or impossible⁶⁹. It is

important to note that de-identified anonymous data can be both the type that cannot be re-identified and the type that can. There have emerged approaches around ‘differential privacy’ that allow the addition of noise to a dataset that guarantees a degree of anonymity in the data, making it robust to re-identification efforts^{70,71}. There is a trade-off, however, because the privacy-enhancing addition of noise diminishes the utility of the data. This was the approach taken in the Social Science One project that provided analytical access to Facebook data⁷² (Box 2). One of the struggles confronting the teams granted access was whether the resulting data retained value for answering their questions. (Note: some of the authors are involved in Social Science One and the Facebook 2020 Election Research Project.)

Third, what expectations of privacy are reasonable for publicly visible behaviours, such as tweets? What obligations are incumbent on the researcher to cloak those behaviours? For example, when should researchers avoid mentioning (in publications or presentations) information such as user screen names and complete social media messages, because of the possibility of negative attention or harassment? Some have argued that automatic anonymization of public data may not be the right approach either, rather, content creators should be consulted about their preferences⁷³.

Fourth, the reliance on the principle of individual autonomy is intrinsically limited, for two reasons. In a world of networked information and insight there will generally be informational spillover from what one person discloses to other individuals. The function of networked media, by definition, is to facilitate interpersonal visibility⁷⁴. An individual who shares their email data, for example, is necessarily providing information from other individuals. The Cambridge Analytica scandal demonstrates the perils of this kind of networked disclosure of information, in which individuals used a Facebook app, which in turn provided access to the behavioural data of the friends of those individuals. However, the risk of informational spillover is a more general principle that is not new with digital trace data: there are almost always potential spillovers from individual disclosure. Genetic data, for instance, potentially shed light on close relatives of an individual;⁷⁵ and almost all data about an individual provide information about others. A response from one individual regarding their political preferences provides insights into the preferences of other household members. Knowledge about the drug use of one individual provides insights into the potential drug use of the friends of that individual.

There is also intra-individual informational inference, where information provided (perhaps with consent) enables inferences that the individual may not have anticipated⁷⁶. The practical ethical upshot cannot be that all research for which there is the possibility of informational spillover or inference from disclosure is forbidden; however, it does mean that often there will need to be important limits to data sharing and data visibility. It also highlights the importance of data security.

Building on our discussion regarding ‘whom do we measure’, care must be taken when attempting to generalize the results of trace-data-based research to populations beyond the platform(s) examined, as well as to the offline lives of the participants⁴¹. It is essential to find ways to include participants who are digitally underrepresented, especially when such research is used to inform decisions about wide-ranging social or corporate policies.

Conversely, when digital forms of measurement can offer a better representation of marginal groups compared to a traditional twentieth century approach, our ethical obligation should be to use them, as the example of satellite data above highlights. The choice confronting society is not whether digital technologies will be used to measure human behaviour, but when, how and whether anyone outside of corporate or state surveillance will have access to those data. Ideally, large-scale digital data sources would feed into measures that inform nuanced policies and targeted interventions, going beyond one-size-fits-all initiatives, which tend to work less well for minority groups.

Finally, it is a duty of the field to critique decision-making practices that result from problematic measurement procedures. A previously published study, which demonstrated the racial biases of an algorithm used by many hospitals that was driven by errors of measurement, is an excellent example of both the dangers that result from flawed measurement in automated decision-making and the potential for good science to help to rectify those issues¹¹.

Box 2 Data access and ethical issues

Implications of platform control of data access

- Research tools may be rendered obsolete without notice by changes to data access by platforms.
- Private data holders may require external researchers to collaborate closely with them as a condition of data access. Furthermore, products of such collaborations can be subject to review by private data holders before publication. Research under such direct control of platforms cannot be a source of critical insights regarding a given platform.
- Researchers whose work falls outside the scope of interest of the data holders or who are uncomfortable collaborating directly with data holders may be relegated to methods that violate the terms of service of the platforms.
- Examples of incipient models to facilitate access to platform data while maintaining independence of researchers include:

Social Science One: this effort involved external approval and funding of research on aggregate Facebook data that had had differential privacy applied to them^{[72](#)}.

The Facebook 2020 Election Research Project: this project involved the collaboration of external researchers with Facebook, in which the data analysis was performed by Facebook researchers, using pre-registered analysis plans and measures defined by outside experts, who also oversaw the execution of the analyses and had full control over the interpretation of results^{[77](#)}.

Ethical questions

- What are the ethical obligations of researchers to consider the circumstances under which data were collected (for example, through leaks or hacking)?
- How can the research community resolve trade-offs introduced by data anonymization techniques that reduce data utility (for example, by adding noise)?
- What expectations of privacy are reasonable for publicly visible behaviours, such as social media posts?
- How can we manage informational spillovers, in which data collected from consenting individuals reveal insights about others without the knowledge or consent of those people?
- How can we ensure that marginalized populations are adequately and accurately represented in research?

Outlook

Box [3](#) summarizes the essential arguments of this paper. The massive instrumentation of global society has enormous potential to transform our understanding of the social world. However, the revolution in instrumenting human behaviour requires a revolution in the measurement of human behaviour. Any new measurement regime needs to match the possibilities of both old and new theories of society, deal with the essential instability of human measurement within these heavily instrumented sociotechnical systems, and develop a new model of ethical research of human participants that balances individual rights and collective benefits.

Box 3 Key questions of measurement

What counts?

There are many concepts that we can measure. We must be clear about the ideas, values, priorities and principles that are guiding our selection of research questions and how we frame a topic as worthy of study.

What is the temporal, spatial, structural and cultural integrity of the measure?

Ostensibly similar constructs can be measured in very different ways and the same measure can change over time as the system measuring it changes, or be inconsistent across geographic, demographic, and cultural groups.

Who is counted?

Who opts into the use of various systems such as social media platforms is not random, and nor is what parts of those systems they use and how actively.

Accordingly, the trace data of users of such systems that form the basis of many studies may not generalize to the broader population, or even to other, seemingly similar, platforms.

What is accessible to counting?

Science is limited by who is allowed access to what data. The data are limited by the functions, purposes, and protocols of the organizations and technologies that produce them. These limits will never be fully resolved and thus should be a central concern for the field.

What is ethical to count?

Digital data touch many more people than ever before and information can be gleaned about the people not only in a study but around those in the study. This issue of informational spillover is intrinsic in a networked world for all research, which undermines the foundational principle of individual autonomy in current ethical frameworks for research, and greatly increases the duties of researchers to maintain data security. The standards and practices for consent, privacy and confidentiality must take these realities into account.

References

1. 1.

Pechenick, E. A., Danforth, C. M. & Dodds, P. S. Characterizing the Google Books Corpus: strong limits to inferences of socio-cultural and linguistic evolution. *PLoS ONE* **10**, e0137041 (2015).

[PubMed](#) [PubMed Central](#) [Google Scholar](#)

2. 2.

Dietrich, B. J., Hayes, M. & O'Brien, D. Z. Pitch perfect: vocal pitch and the emotional intensity of congressional speech. *Am. Polit. Sci. Rev.* **113**, 941–962 (2019).

[Google Scholar](#)

3. 3.

Dietrich, B. J. Using motion detection to measure social polarization in the U.S. House of Representatives. *Polit. Anal.* **29**, 250–259 (2021).

[Google Scholar](#)

4. 4.

Michel, J.-B. et al. Quantitative analysis of culture using millions of digitized books. *Science* **331**, 176–182 (2011). **In this study, 4% of all books that have been published were digitized and used to examine changes in phonology, word use and the adoption of new technologies over long periods of time.**

[CAS](#) [PubMed](#) [ADS](#) [Google Scholar](#)

5. 5.

Merton, R. K. in *Social Theory and Social Structure* 39–72 (Free Press, 1968).

6. 6.

Watts, D. J. *Everything Is Obvious: Once You Know the Answer* (Crown Business, 2011).

7. 7.

Simon, H. A. Bandwagon and underdog effects and the possibility of election predictions. *Public Opin. Q.* **18**, 245–253 (1954).

[Google Scholar](#)

8. 8.

Mutz, D. C. *Impersonal Influence in American Politics* (Cambridge Univ. Press, 1998).

9. 9.

Westwood, S. J., Messing, S. & Lelkes, Y. Projecting confidence: how the probabilistic horse race confuses and demobilizes the public. *J. Polit.* **82**, 1530–1544 (2020).

[Google Scholar](#)

10. 10.

O’Neil, C. *Weapons of Math Destruction: How Big Data Increases Inequality and Threatens Democracy* (Crown, 2016).

11. 11.

Obermeyer, Z., Powers, B., Vogeli, C. & Mullainathan, S. Dissecting racial bias in an algorithm used to manage the health of populations. *Science* **366**, 447–453 (2019).

[CAS](#) [PubMed](#) [ADS](#) [Google Scholar](#)

12. 12.

Landsberger, H. A. *Hawthorne Revisited* (The New York State School of Industrial and Labor Relations, 1958).

13. 13.

Mayo, E. *The Human Problems of an Industrial Civilization* (Routledge, 2004).

14. 14.

Lazer, D., Kennedy, R., King, G. & Vespignani, A. The parable of Google Flu: traps in big data analysis. *Science* **343**, 1203–1205 (2014). **This paper shows that the increasing over-prediction of flu prevalence of Google Flu Trends was largely the result of changes to Google’s search algorithm, which altered the terms that people used to find flu-related information.**

[CAS](#) [PubMed](#) [ADS](#) [Google Scholar](#)

15. 15.

Brunton, F. & Nissenbaum, H. *Obfuscation: A User's Guide for Privacy and Protest* (MIT Press, 2015).

16. 16.

Davis, D. W. The direction of race of interviewer effects among African-Americans: donning the Black mask. *Am. J. Pol. Sci.* **41**, 309–322 (1997).

[Google Scholar](#)

17. 17.

American National Election Studies. *1978 Time Series Study*
https://electionstudies.org/wp-content/uploads/2018/03/anes_timeseries_1978_qnaire_post.pdf (1978).

18. 18.

Salganik, M. J. *Bit by Bit: Social Research in the Digital Age* (Princeton Univ. Press, 2017).

19. 19.

Patty, J. W. & Penn, E. M. Analyzing big data: social choice and measurement. *PS Polit. Sci. Polit.* **48**, 95–101 (2015).

[Google Scholar](#)

20. 20.

Kraemer, M. U. G. et al. The effect of human mobility and control measures on the COVID-19 epidemic in China. *Science* **368**, 493–497 (2020).

[CAS](#) [PubMed](#) [PubMed Central](#) [ADS](#) [Google Scholar](#)

21. 21.

Jia, J. S. et al. Population flow drives spatio-temporal distribution of COVID-19 in China. *Nature* **582**, 389–394 (2020).

[CAS](#) [PubMed](#) [ADS](#) [Google Scholar](#)

22. 22.

Badr, H. S. et al. Association between mobility patterns and COVID-19 transmission in the USA: a mathematical modelling study. *Lancet Infect. Dis.* **20**, 1247–1254 (2020).

[CAS](#) [PubMed](#) [PubMed Central](#) [Google Scholar](#)

23. 23.

Munger, K. The limited value of non-replicable field experiments in contexts with low temporal validity. *Soc. Media Soc.* **5**, 1–4 (2019).

[Google Scholar](#)

24. 24.

Deaton, A. & Cartwright, N. Understanding and misunderstanding randomized controlled trials. *Soc. Sci. Med.* **210**, 2–21 (2018).

[PubMed](#) [Google Scholar](#)

25. 25.

Vraga, E. K., Bode, L., Smithson, A.-B. & Troller-Renfree, S. Accidentally attentive: comparing visual, close-ended, and open-ended measures of attention on social media. *Comput. Human Behav.* **99**, 235–244 (2019).

[Google Scholar](#)

26. 26.

Guess, A., Munger, K., Nagler, J. & Tucker, J. How accurate are survey responses on social media and politics? *Polit. Commun.* **36**, 241–258 (2019).

[Google Scholar](#)

27. 27.

Aleta, A. et al. Modelling the impact of testing, contact tracing and household quarantine on second waves of COVID-19. *Nat. Hum. Behav.* **4**, 964–971 (2020).

[PubMed](#) [Google Scholar](#)

28. 28.

Echeverría, J. et al. LOBO: evaluation of generalization deficiencies in Twitter bot classifiers. In *Proc. 34th Annual Computer Security Applications Conference* 137–146 (ACM, 2018).

29. 29.

Ferrara, E., Varol, O., Davis, C., Menczer, F. & Flammini, A. The rise of social bots. *Commun. ACM* **59**, 96–104 (2016).

[Google Scholar](#)

30. 30.

Hughes, A. G. et al. Using administrative records and survey data to construct samples of Tweeters and Tweets. *Public Opin. Q.* <https://doi.org/10.1093/poq/nfab020> (2021).

31. 31.

Napoli, P. M. *Audience Evolution: New Technologies and the Transformation of Media Audiences* (Columbia Univ. Press, 2011).

32. 32.

Yang, T., Majó-Vázquez, S., Nielsen, R. K. & González-Bailón, S. Exposure to news grows less fragmented with an increase in mobile access. *Proc. Natl Acad. Sci. USA* **117**, 28678–28683 (2020). **This study tracked the news consumption of users across mobile and desktop devices and found that most individuals do not self-sort their news consumption by partisanship but, instead, consume news from a diversity of sources including partisan and nonpartisan ones.**

[CAS](#) [PubMed](#) [PubMed Central](#) [Google Scholar](#)

33. 33.

Haythornthwaite, C. Exploring multiplexity: social network structures in a computer-supported distance learning class. *Inf. Soc.* **17**, 211–226 (2001).

[Google Scholar](#)

34. 34.

Campbell, K. E. & Lee, B. A. Name generators in surveys of personal networks. *Soc. Netw.* **13**, 203–221 (1991).

[Google Scholar](#)

35. 35.

Wagner, C. Measuring algorithmically infused societies. *Nature* <https://doi.org/10.1038/s41586-021-03666-1> (2021).

36. 36.

Healy, K. The performativity of networks. *Eur. J. Sociol.* **56**, 175–205 (2015).

[Google Scholar](#)

37. 37.

Rahwan, I. et al. Machine behaviour. *Nature* **568**, 477–486 (2019).

[CAS](#) [PubMed](#) [ADS](#) [Google Scholar](#)

38. 38.

Neuendorf, K. A. *The Content Analysis Guidebook* (Sage, 2017).

39. 39.

Davidov, D., Tsur, O. & Rappoport, A. Semi-supervised recognition of sarcasm in Twitter and Amazon. In *Proc. 14th Conference on Computational Natural Language Learning* 107–116 (Association for Computational Linguistics, 2010).

40. 40.

Groves, R. M. Nonresponse rates and nonresponse bias in household surveys. *Public Opin. Q.* **70**, 646–675 (2006).

[Google Scholar](#)

41. 41.

Hargittai, E. Potential biases in big data: omitted voices on social media. *Soc. Sci. Comput. Rev.* **38**, 10–24 (2020). **Using survey data, this study finds that younger, wealthier and more technically skilled people tend to use social**

media and that there were substantial gender and education differences in which platforms people used.

[Google Scholar](#)

42. 42.

Lazer, D. & Radford, J. Data ex machina: introduction to big data. *Annu. Rev. Sociol.* **43**, 19–39 (2017).

[Google Scholar](#)

43. 43.

Correa, T. & Valenzuela, S. A trend study in the stratification of social media use among urban youth: Chile 2009–2019. *J. Quant. Descr. Digit. Media* **1**, <https://doi.org/10.51685/jqd.2021.009> (2021).

44. 44.

Mellan, J. & Prosser, C. Twitter and Facebook are not representative of the general population: political attitudes and demographics of British social media users. *Res. Polit.* **4**, 1–9 (2017).

[Google Scholar](#)

45. 45.

Beisch, N. & Schäfer, C. Internetnutzung mit großer Dynamik: Medien, Kommunikation, Social Media. *AS&S* <https://www.ard-werbung.de/media-perspektiven/fachzeitschrift/2020/detailseite-2020/internetnutzung-mit-grosserer-dynamik-medien-kommunikation-social-media/> (2020).

46. 46.

Hargittai, E. & Litt, E. The Tweet smell of celebrity success: explaining variation in Twitter adoption among a diverse group of young adults. *New Media Soc.* **13**, 824–842 (2011).

[Google Scholar](#)

47. 47.

Henrich, J., Heine, S. J. & Norenzayan, A. Most people are not WEIRD. *Nature* **466**, 29 (2010).

[CAS](#) [PubMed](#) [ADS](#) [Google Scholar](#)

48. 48.

Wang, W., Rothschild, D., Goel, S. & Gelman, A. Forecasting elections with non-representative polls. *Int. J. Forecast.* **31**, 980–991 (2015).

[Google Scholar](#)

49. 49.

Grinberg, N., Joseph, K., Friedland, L., Swire-Thompson, B. & Lazer, D. Fake news on Twitter during the 2016 U.S. presidential election. *Science* **363**, 374–378 (2019).

[CAS](#) [PubMed](#) [ADS](#) [Google Scholar](#)

50. 50.

Bakshy, E., Messing, S. & Adamic, L. A. Exposure to ideologically diverse news and opinion on Facebook. *Science* **348**, 1130–1132 (2015).

[MathSciNet](#) [CAS](#) [PubMed](#) [MATH](#) [ADS](#) [Google Scholar](#)

51. 51.

Meng, X.-L. Statistical paradises and paradoxes in big data (I): law of large populations, big data paradox, and the 2016 US presidential election. *Ann. Appl. Stat.* **12**, 685–726 (2018).

[MathSciNet](#) [MATH](#) [Google Scholar](#)

52. 52.

Hargittai, E., Füchslin, T. & Schäfer, M. S. How do young adults engage with science and research on social media? Some preliminary findings and an agenda for future research. *Soc. Media Soc.* **4**, 1–10 (2018).

[Google Scholar](#)

53. 53.

Blumenstock, J. Don't forget people in the use of big data for development. *Nature* **561**, 170–172 (2018).

[CAS](#) [PubMed](#) [ADS](#) [Google Scholar](#)

54. 54.

Battle-Baptiste, W. & Rusert, B. (eds) *W. E. B. Du Bois's Data Portraits: Visualizing Black America* (Princeton Architectural Press, 2018).

55. 55.

Siegel, A. A. et al. Trumping hate on Twitter? Online hate speech in the 2016 US election campaign and its aftermath. *Quart. J. Polit. Sci.* **16**, 71–104 (2021).

[Google Scholar](#)

56. 56.

Allen, J., Howland, B., Mobius, M., Rothschild, D. & Watts, D. J. Evaluating the fake news problem at the scale of the information ecosystem. *Sci. Adv.* **6**, eaay3539 (2020).

[PubMed](#) [PubMed Central](#) [ADS](#) [Google Scholar](#)

57. 57.

Foucault Welles, B. On minorities and outliers: the case for making big data small. *Big Data Soc.* **1**, 1–2 (2014).

[Google Scholar](#)

58. 58.

Newman, M. E. J. Power laws, Pareto distributions and Zipf's law. *Contemp. Phys.* **46**, 323–351 (2005).

[ADS](#) [Google Scholar](#)

59. 59.

González-Bailón, S. *Decoding the Social World: Data Science and the Unintended Consequences of Communication* (MIT Press, 2017).

60. 60.

Stopczynski, A. et al. Measuring large-scale social networks with high resolution. *PLoS ONE* **9**, e95978 (2014).

[PubMed](#) [PubMed Central](#) [ADS](#) [Google Scholar](#)

61. 61.

Lazer, D. Studying human attention on the Internet. *Proc. Natl Acad. Sci. USA* **117**, 21–22 (2020).

[CAS](#) [PubMed](#) [Google Scholar](#)

62. 62.

Aral, S. & Eckles, D. Protecting elections from social media manipulation. *Science* **365**, 858–861 (2019).

[CAS](#) [PubMed](#) [ADS](#) [Google Scholar](#)

63. 63.

Puschmann, C. & Burgess, J. The politics of Twitter data. *IIIG Discussion Paper Series No. 2013-01* <http://www.ssrn.com/abstract=2206225> (2013).

64. 64.

Chen, W. & Quan-Haase, A. Big data ethics and politics: toward new understandings. *Soc. Sci. Comput. Rev.* **38**, 3–9 (2020).

[Google Scholar](#)

65. 65.

Breuer, J., Bishop, L. & Kinder-Kurlanda, K. The practical and ethical challenges in acquiring and sharing digital trace data: negotiating public–private partnerships. *New Media Soc.* **22**, 2058–2080 (2020).

[Google Scholar](#)

66. 66.

Zook, M. et al. Ten simple rules for responsible big data research. *PLOS Comput. Biol.* **13**, e1005399 (2017).

[PubMed](#) [PubMed Central](#) [Google Scholar](#)

67. 67.

Greenberg, A. An absurdly basic bug let anyone grab all of parler's data. *Wired* (12 January 2021).

68. 68.

Valentino-DeVries, J., Singer, N., Keller, M. H. & Krolik, A. your apps know where you were last night, and they're not keeping it secret. *The New York Times* <https://www.nytimes.com/interactive/2018/12/10/business/location-data-privacy-apps.html> (10 December 2021).

69. 69.

Sweeney, L. Simple demographics often identify people uniquely. *Privacy Working Paper 3* <https://dataprivacylab.org/projects/identifiability/paper1.pdf> (Carnegie Mellon University, 2000). **Using census data, this paper shows that 87% of the US population could be uniquely identified by date of birth, postal code and gender; demonstrating the ease with which study respondents can be re-identified from ostensibly anonymous data.**

70. 70.

Wood, A. et al. Differential privacy: a primer for a non-technical audience. *Vanderbilt J. Entertain. Technol. Law* **21**, 209–276 (2019).

[Google Scholar](#)

71. 71.

Dwork, C. & Roth, A. The algorithmic foundations of differential privacy. *Found. Trends Theor. Comput. Sci.* **9**, 211–407 (2013).

[MathSciNet](#) [MATH](#) [Google Scholar](#)

72. 72.

King, G. & Persily, N. A new model for industry–academic partnerships. *PS Polit. Sci. Polit.* **53**, 703–709 (2020).

[Google Scholar](#)

73. 73.

Bruckman, A., Luther, K. & Fiesler, C. in *Digital Research Confidential: The Secrets of Studying Behavior Online* (eds Hargittai, E. & Sandvig, C.) 243–258 (MIT Press, 2015).

74. 74.

Marwick, A. E. & boyd, d. Networked privacy: how teenagers negotiate context in social media. *New Media Soc.* **16**, 1051–1067 (2014).

[Google Scholar](#)

75. 75.

Bieber, F. R., Brenner, C. H. & Lazer, D. Finding criminals through DNA of their relatives. *Science* **312**, 1315–1316 (2006).

[CAS](#) [PubMed](#) [Google Scholar](#)

76. 76.

Zheleva, E. & Getoor, L. To join or not to join: the illusion of privacy in social networks with mixed public and private user profiles. In *Proc. 18th International Conference on World Wide Web* 531–540 (2009).

77. 77.

Miller, G. As U.S. election nears, researchers are following the trail of fake news. *Science* (26 October 2020).

78. 78.

Merton, R. K. The self-fulfilling prophecy. *Antioch Rev.* **8**, 193–210 (1948).

[Download references](#)

Acknowledgements

D.L. acknowledges support from the William & Flora Hewlett Foundation. E.H. acknowledges support from the Alfred P. Sloan Foundation.

Author information

Affiliations

1. Network Science Institute, Northeastern University, Boston, MA, USA

David Lazer & Jason Radford

2. Institute for Quantitative Social Science, Harvard University, Cambridge, MA, USA

David Lazer

3. Department of Communication and Media Research, University of Zurich, Zurich, Switzerland

Eszter Hargittai

4. Hussman School of Journalism and Media, University of North Carolina at Chapel Hill, Chapel Hill, NC, USA

Deen Freelon

5. Annenberg School for Communication, University of Pennsylvania, Philadelphia, PA, USA

Sandra Gonzalez-Bailon

6. Department of Political Science, Pennsylvania State University, State College, PA, USA

Kevin Munger

7. School of Communication and Information, Rutgers University, New Brunswick, NJ, USA

Katherine Ognyanova

Authors

1. David Lazer

[View author publications](#)

You can also search for this author in [PubMed](#) [Google Scholar](#)

2. Eszter Hargittai

[View author publications](#)

You can also search for this author in [PubMed](#) [Google Scholar](#)

3. Deen Freelon

[View author publications](#)

You can also search for this author in [PubMed](#) [Google Scholar](#)

4. Sandra Gonzalez-Bailon

[View author publications](#)

You can also search for this author in [PubMed](#) [Google Scholar](#)

5. Kevin Munger

[View author publications](#)

You can also search for this author in [PubMed](#) [Google Scholar](#)

6. Katherine Ognyanova

[View author publications](#)

You can also search for this author in [PubMed](#) [Google Scholar](#)

7. Jason Radford

[View author publications](#)

You can also search for this author in [PubMed](#) [Google Scholar](#)

Contributions

All authors contributed to the concepts, writing and/or revisions of the manuscript.

Corresponding author

Correspondence to [David Lazer](#).

Ethics declarations

Competing interests

The authors declare no competing interests.

Additional information

Peer review information *Nature* thanks Paramveer Dhillon and the other, anonymous, reviewer(s) for their contribution to the peer review of this work.

Publisher's note Springer Nature remains neutral with regard to jurisdictional claims in published maps and institutional affiliations.

Rights and permissions

[Reprints and Permissions](#)

About this article



Check for
updates

Cite this article

Lazer, D., Hargittai, E., Freelon, D. *et al.* Meaningful measures of human society in the twenty-first century. *Nature* **595**, 189–196 (2021). <https://doi.org/10.1038/s41586-021-03660-7>

[Download citation](#)

- Received: 03 March 2021
- Accepted: 20 May 2021
- Published: 30 June 2021
- Issue Date: 08 July 2021
- DOI: <https://doi.org/10.1038/s41586-021-03660-7>

Further reading

- [Measuring algorithmically infused societies](#)

- Claudia Wagner
- , Markus Strohmaier
- , Alexandra Olteanu

- , Emre KÄ±cÄ±man
- , Noshir Contractor
- & Tina Eliassi-Rad

Nature (2021)

Comments

By submitting a comment you agree to abide by our [Terms](#) and [Community Guidelines](#). If you find something abusive or that does not comply with our terms or guidelines please flag it as inappropriate.

[Download PDF](#)

Associated Content

Special

[**Computational social science**](#)

Advertisement

This article was downloaded by **calibre** from <https://www.nature.com/articles/s41586-021-03660-7>

| [Section menu](#) | [Main menu](#) |

- Perspective
- [Published: 30 June 2021](#)

Measuring algorithmically infused societies

- [Claudia Wagner](#) ORCID: [orcid.org/0000-0002-0640-8221^{1,2,3}](https://orcid.org/0000-0002-0640-8221),
- [Markus Strohmaier](#) ORCID: [orcid.org/0000-0002-5485-5720^{1,2,3}](https://orcid.org/0000-0002-5485-5720),
- [Alexandra Olteanu^{4,5}](#),
- [Emre Kıcıman⁶](#),
- [Noshir Contractor⁷](#) &
- [Tina Eliassi-Rad^{7,8}](#)

[Nature](#) volume 595, pages 197–204 (2021) [Cite this article](#)

- 536 Accesses
- 2 Citations
- 92 Altmetric
- [Metrics details](#)

Subjects

- [Social sciences](#)
- [Society](#)

Abstract

It has been the historic responsibility of the social sciences to investigate human societies. Fulfilling this responsibility requires social theories,

measurement models and social data. Most existing theories and measurement models in the social sciences were not developed with the deep societal reach of algorithms in mind. The emergence of ‘algorithmically infused societies’—societies whose very fabric is co-shaped by algorithmic and human behaviour—raises three key challenges: the insufficient quality of measurements, the complex consequences of (mis)measurements, and the limits of existing social theories. Here we argue that tackling these challenges requires new social theories that account for the impact of algorithmic systems on social realities. To develop such theories, we need new methodologies for integrating data and measurements into theory construction. Given the scale at which measurements can be applied, we believe measurement models should be trustworthy, auditable and just. To achieve this, the development of measurements should be transparent and participatory, and include mechanisms to ensure measurement quality and identify possible harms. We argue that computational social scientists should rethink what aspects of algorithmically infused societies should be measured, how they should be measured, and the consequences of doing so.

Access options

Subscribe to Journal

Get full journal access for 1 year

\$199.00

only \$3.90 per issue

[Subscribe](#)

All prices are NET prices.

VAT will be added later in the checkout.

Tax calculation will be finalised during checkout.

Rent or Buy article

Get time limited or full article access on ReadCube.

from \$8.99

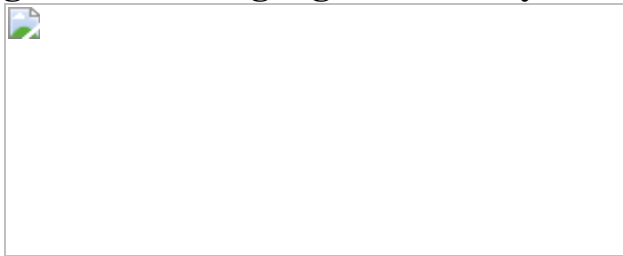
[Rent or Buy](#)

All prices are NET prices.

Additional access options:

- [Log in](#)
- [Access through your institution](#)
- [Learn about institutional subscriptions](#)

Fig. 1: Measuring algorithmically infused societies.



References

1. 1.

boyd, d. The future of privacy: how privacy norms can inform regulation. In *32nd Intl Conf. Data Protection and Privacy Commissioners* (2010);
<https://www.danah.org/papers/talks/2010/PrivacyGenerations.html>.

2. 2.

Gill, K. S. The internet of things! Then what? *AI Soc.* **28**, 367–371 (2013).

[Google Scholar](#)

3. 3.

O'Reilly, T. Open data and algorithmic regulation. In *Beyond Transparency: Open Data and the Future of Civic Innovation* (eds Goldstein, B. & Dyson, L.) 289–300 (Code for America Press, 2013).

4. 4.

Castells, M. *The Information Age: Economy, Society and Culture. Vol. 1: The Rise of the Network Society* (Wiley–Blackwell, 1996).

5. 5.

Fleder, D. & Hosanagar, K. Blockbuster culture's next rise or fall: the impact of recommender systems on sales diversity. *Manage. Sci.* **55**, 697–712 (2009).

[Google Scholar](#)

6. 6.

Tufekci, Z. Engineering the public: big data, surveillance and computational politics. *First Monday* **19**, <https://doi.org/10.5210/fm.v19i7.4901> (2014).

7. 7.

Bakshy, E., Messing, S. & Adamic, L. A. Exposure to ideologically diverse news and opinion on Facebook. *Science* **348**, 1130–1132 (2015).

[MathSciNet](#) [CAS](#) [PubMed](#) [MATH](#) [ADS](#) [Google Scholar](#)

8. 8.

Ferrara, E., Varol, O., Davis, C., Menczer, F. & Flammini, A. The rise of social bots. *Commun. ACM* **59**, 96–104 (2016).

[Google Scholar](#)

9. 9.

Le Chen, A. M. & Wilson, C. An empirical analysis of algorithmic pricing on Amazon Marketplace. In *Proc. 25th Intl Conf. World Wide Web (WWW'16)* (eds Bourdeau, J. et al.) 1339–1349 (International World Wide Web Conferences Steering Committee, 2016); <https://doi.org/10.1145/2872427.2883089>.

10. 10.

Salganik, M. J., Sheridan Dodds, P. & Watts, D. J. Experimental study of inequality and unpredictability in an artificial cultural market. *Science* **311**, 854–856 (2006).

[CAS](#) [PubMed](#) [ADS](#) [Google Scholar](#)

11. 11.

Baym, N. K. *Playing to the Crowd: Musicians, Audiences, and the Intimate Work of Connection* (NYU Press, 2018).

12. 12.

Burgess, J. & Green, J. *YouTube: Online Video and Participatory Culture* (Wiley, 2018).

13. 13.

Hitsch, G. J., Hortaçsu, A. & Ariely, D. Matching and sorting in online dating. *Am. Econ. Rev.* **100**, 130–163 (2010).

[Google Scholar](#)

14. 14.

Zignani, M. et al. Link and triadic closure delay: temporal metrics for social network dynamics. In *Proc. 8th Intl AAAI Conf. Web and Social Media* (eds Adar, E. & Resnick, P.) 564–573 (2014).

15. 15.

Malik, M. & Pfeffer, J. Identifying platform effects in social media data. In *Proc. 10th Intl AAAI Conf. Web and Social Media* (eds Krishna, G. & Strohmaier, M.) 241–249 (2016).

16. 16.

Su, J., Sharma, A. & Goel, S. The effect of recommendations on network structure. In *Proc. 25th Intl Conf. World Wide Web (WWW' 16)* (eds Bourdeau, J. et al.) 1157–1167 (International World Wide Web Conferences Steering Committee, 2016);
<https://doi.org/10.1145/2872427.2883040>.

17. 17.

Loscalzo, J. & Barabasi, A.-L. Systems biology and the future of medicine. *Wiley Interdiscip. Rev. Syst. Biol. Med.* **3**, 619–627 (2011).

[PubMed](#) [PubMed Central](#) [Google Scholar](#)

18. 18.

Frizzell, J. D., et al. Prediction of 30-day all-cause readmissions in patients hospitalized for heart failure: comparison of machine learning and other statistical approaches. *JAMA Cardiol.* **2**, 204–209 (2017).

[PubMed](#) [Google Scholar](#)

19. 19.

Obermeyer, Z., Powers, B., Vogeli, C. & Mullainathan, S. Dissecting racial bias in an algorithm used to manage the health of populations. *Science* **366**, 447–453 (2019).

[CAS](#) [PubMed](#) [ADS](#) [Google Scholar](#)

20. 20.

Huang, C.-L., Chen, M.-C. & Wang, C.-J. Credit scoring with a data mining approach based on support vector machines. *Expert Syst. Appl.* **33**, 847–856 (2007).

[Google Scholar](#)

21. 21.

Perry, W. L., McInnis, B., Price, C. C., Smith, S. C. & Hollywood, J. S. *Predictive Policing: The Role of Crime Forecasting in Law Enforcement Operations* (RAND Corporation, 2013).

22. 22.

Dressel, J. & Farid, H. The accuracy, fairness, and limits of predicting recidivism. *Sci. Adv.* **4**, eaao5580 (2018).

[PubMed](#) [PubMed Central](#) [ADS](#) [Google Scholar](#)

23. 23.

Raghavan, M., Barocas, S., Kleinberg, J. & Levy, K. Mitigating bias in algorithmic hiring: evaluating claims and practices. In *Proc. 2020 Conf. Fairness, Accountability, and Transparency* (eds Hildebrandt, M. & Castillo, C.) 469–481 (ACM, 2020);
<https://doi.org/10.1145/3351095.3372828>.

24. 24.

Hannák, A. et al. Bias in online freelance marketplaces: evidence from TaskRabbit and Fiverr. In *Proc. 2017 ACM Conf. Computer Supported Cooperative Work and Social Computing (CSCW' 17)* (eds Lee, C. P. & Poltrock, S.) 1914–1933 (ACM, 2017);
<https://doi.org/10.1145/2998181.2998327>. **This study reports on sociodemographic inequalities in online marketplaces.**

25. 25.

Gray, M. L. & Suri, S. *Ghost Work: How to Stop Silicon Valley From Building a New Global Underclass* (Eamon Dolan Books, 2019).

26. 26.

Beer, D. The social power of algorithms. *Inf. Commun. Soc.* **20**, 1–13 (2017).

[Google Scholar](#)

27. 27.

Kleinberg, J., Ludwig, J., Mullainathan, S. & Sunstein, C. R. Algorithms as discrimination detectors. *Proc. Natl Acad. Sci. USA* **117**, 30096–30100 (2020).

[MathSciNet](#) [CAS](#) [PubMed](#) [PubMed Central](#) [Google Scholar](#)

28. 28.

Buolamwini, J. & Gebru, T. Gender shades: intersectional accuracy disparities in commercial gender classification. In *Proc. 1st Conf. Fairness, Accountability and Transparency* (eds Friedler, S. A. & Wilson, C.) 77–91 (2018).

29. 29.

Moy, L. How police technology aggravates racial inequity: a taxonomy of problems and a path forward. *Univ. Illinois Law Rev.* **2021**, 139–193 (2021).

[Google Scholar](#)

30. 30.

Hutchinson, B. & Mitchell, M. 50 years of test (un)fairness: lessons for machine learning. In *Proc. Conf. Fairness, Accountability, and Transparency* (eds Morgenstern, J. & boyd, d.) 49–58 (2019).

31. 31.

Barocas, S. & Selbst, A. D. Big data's disparate impact. *Calif. Law Rev.* **104**, 671–732 (2016).

[Google Scholar](#)

32. 32.

Milli, S., Miller, J., Dragan, A. D. & Hardt M. The social cost of strategic classification. In *Proc. Conf. Fairness, Accountability, and Transparency* 230–239 (2019).

33. 33.

Bender, E. M., Gebru, T., McMillan-Major, A. & Shmitchell. S. On the dangers of stochastic parrots: can language models be too big? In *Proc. Conf. Fairness, Accountability, and Transparency* (eds Elish, M. C. et al.) 610–623 (2021).

34. 34.

Schnabel, T., Swaminathan, A., Singh, A., Chandak, N. & Joachims, T. Recommendations as treatments: debiasing learning and evaluation. In *Intl Conf. Machine Learning* (eds Balcan, M. F. & Weinberger, K. Q.) 1670–1679 (2016).

35. 35.

Sztompka, P. in *Polish Essays in the Methodology of the Social Sciences* (ed. Wiatr, J. J.) 173–194 (Springer, 1979).

36. 36.

Jaccard, J. & Jacoby, J. *Theory Construction and Model Building Skills: A Practical Guide for Social Scientists* (Guilford, 2010).

37. 37.

Lord, F. M. & Novick, M. R. *Statistical Theories of Mental Test Scores* (Addison-Wesley, 1968).

38. 38.

Allen, M. J. & Yen, W. M. *Introduction to Measurement Theory* (Waveland, 2002).

39. 39.

Joye, D., Wolf, C., Smith, T. W. & Fu, Y. in *The SAGE Handbook of Survey Methodology* (eds Wolf, C. et al.) 3–15 (Sage, 2016).

40. 40.

Strathern, M. ‘Improving ratings’: audit in the British university system. *Eur. Rev.* **5**, 305–321 (1997).

[Google Scholar](#)

41. 41.

Campbell, D. T. Assessing the impact of planned social change. *Eval. Program Plann.* **2**, 67–90 (1979).

[Google Scholar](#)

42. 42.

Festinger, L. *A Theory of Cognitive Dissonance* (Stanford Univ. Press, 1957).

43. 43.

Heider, F. Attitudes and cognitive organization. *J. Psychol.* **21**, 107–112 (1946).

[CAS](#) [PubMed](#) [Google Scholar](#)

44. 44.

Cartwright, D. & Harary, F. Structural balance: a generalization of Heider's theory. *Psychol. Rev.* **63**, 277–293 (1956).

[CAS](#) [PubMed](#) [Google Scholar](#)

45. 45.

McPherson, M., Smith-Lovin, L. & Cook, J. M. Birds of a feather: homophily in social networks. *Annu. Rev. Sociol.* **27**, 415–444 (2001).

[Google Scholar](#)

46. 46.

Seitlinger, P., Kowald, D., Trattner, C. & Ley, T. Recommending tags with a model of human categorization. In *Proc. 22nd ACM Intl Conf. on Information & Knowledge Management* (eds He, Q. & Iyengar, A.) 2381–2386 (ACM, 2013).

47. 47.

Bowker, G. C. & Star, S. L. *Sorting Things Out: Classification and its Consequences* (MIT Press, 2000).

48. 48.

Healy, K. The performativity of networks. *Euro. J. Sociol.* **56**, 175–205 (2015). **This article argues that theories have the potential to reformat and reorganize the phenomena that models purport to describe.**

[Google Scholar](#)

49. 49.

Zuboff, S. *The Age of Surveillance Capitalism: The Fight for a Human Future at the New Frontier of Power* (Profile Books, 2018).

50. 50.

Pasquale, F. *The Black Box Society: The Secret Algorithms that Control Money and Information* (Harvard Univ. Press, 2015).

51. 51.

Nissenbaum, H. *How Computer Systems Embody Values* (IEEE Computer Society Press, 2001).

52. 52.

Seaver, N. Knowing algorithms. In *DigitalSTS* (eds Vertesi, J. & Ribes, D.) 412–422 (Princeton Univ. Press, 2013).

53. 53.

boyd, d. & Crawford, K. Critical questions for big data: provocations for a cultural, technological, and scholarly phenomenon. *Inf. Commun. Soc.* **15**, 662–679 (2012).

[Google Scholar](#)

54. 54.

Graham, S. & Wood, D. Digitizing surveillance: categorization, space, inequality. *Crit. Soc. Policy* **23**, 227–248 (2003).

[Google Scholar](#)

55. 55.

Benjamin, R. Catching our breath: critical race STS and the carceral imagination. *Engaging Sci. Technol. Soc.* **2**, 145–156 (2016).

[Google Scholar](#)

56. 56.

Lazer, D. et al. Computational social science. *Science* **323**, 721–723 (2009). **This landmark article discussed the early potential of computational approaches for the social sciences.**

[CAS](#) [PubMed](#) [PubMed Central](#) [Google Scholar](#)

57. 57.

Lazer, D. M. J. et al. Computational social science: obstacles and opportunities. *Science* **369**, 1060–1062 (2020).

[CAS](#) [PubMed](#) [ADS](#) [Google Scholar](#)

58. 58.

Vosoughi, S., Roy, D. & Aral, S. The spread of true and false news online. *Science* **359**, 1146–1151 (2018).

[CAS](#) [PubMed](#) [ADS](#) [Google Scholar](#)

59. 59.

Del Vicario, M. et al. The spreading of misinformation online. *Proc. Natl Acad. Sci. USA* **113**, 554–559 (2016).

[PubMed](#) [PubMed Central](#) [ADS](#) [Google Scholar](#)

60. 60.

Bail, C. A. et al. Exposure to opposing views on social media can increase political polarization. *Proc. Natl Acad. Sci. USA* **115**, 9216–9221 (2018).

[CAS](#) [PubMed](#) [PubMed Central](#) [Google Scholar](#)

61. 61.

Blalock, H. M. *Conceptualization and Measurement in the Social Sciences* (Sage, 1982).

62. 62.

RatSWD Quality Standards Working Group. *Quality Standards for the Development, Application, and Evaluation of Measurement Instruments in Social Science Survey Research* RatSWD Working Papers 245 (German Data Forum (RatSWD), 2015). **This paper proposes quality standards and guidelines for the development, application and evaluation of measurement instruments in social science survey research.**

63. 63.

Jacobs, A. Z. & Wallach, H. Measurement and fairness. In *FAccT 21: Proc. 2021 ACM Conf. Fairness, Accountability, and Transparency* (eds Elish, M. C. et al.) 375–385 (ACM, 2019);
<https://doi.org/10.1145/3442188.3445901>. **This paper describes how validity issues can lead to fairness issues.**

64. 64.

Adcock, R. & Collier, D. Measurement validity: a shared standard for qualitative and quantitative research. *Am. Polit. Sci. Rev.* **95**, 529–546 (2001).

[Google Scholar](#)

65. 65.

Hofman, J. M., Sharma, A. & Watts, D. J. Prediction and explanation in social systems. *Science* **355**, 486–488 (2017).

[CAS](#) [PubMed](#) [ADS](#) [Google Scholar](#)

66. 66.

Peters, J., Janzing, D. & Schoelkopf, B. *Elements of Causal Inference: Foundations and Learning Algorithms* (MIT Press, 2017).

67. 67.

Jungherr, A. in *Digital Discussions: How Big Data Informs Political Communication* (eds Stroud, N. J. & McGregor, S.) 9–35 (Routledge, 2018).

68. 68.

Donoho, D. 50 years of data science. *J. Comput. Graph. Stat.* **26**, 745–766 (2017).

[MathSciNet](#) [Google Scholar](#)

69. 69.

Blodgett, S. L., Lopez, G., Olteanu, A., Sim, R. & Wallach, H. Stereotyping Norwegian salmon: an inventory of pitfalls in fairness benchmark datasets. In *Proc. 59th Annual Meeting of the Association for Computational Linguistics* (ed. Zong, C.) (2021).

70. 70.

Ethayarajh, K. & Jurafsky, D. Utility is in the eye of the user: a critique of NLP leaderboard design. In *Proc. 2020 Conf. Empirical Methods in Natural Language Processing (EMNLP)* (eds Webber, B. et al.) 4846–4853 (2020).

71. 71.

Jungherr, A., Schoen, H., Posegga, O. & Jürgens, P. Digital trace data in the study of public opinion: an indicator of attention toward politics rather than political support. *Soc. Sci. Comput. Rev.* **35**, 336–356 (2017).

[Google Scholar](#)

72. 72.

Samory, M., Sen, I., Kohne, J., Flöck, F. & Wagner, C. Call me sexist, but...: Revisiting sexism detection using psychological scales and

adversarial samples. In *Intl AAAI Conf. Web and Social Media* 573–584 (2021).

73. 73.

Gebru, T. et al. Datasheets for datasets. Preprint at <https://arxiv.org/abs/1803.09010> (2018).

74. 74.

Olteanu, A., Castillo, C., Diaz, F. & Kıcıman, E. Social data: biases, methodological pitfalls, and ethical boundaries. *Front. Big Data* **2**, 13 (2019).

[PubMed](#) [PubMed Central](#) [Google Scholar](#)

75. 75.

Sen, I., Floeck, F., Weller, K., Weiss, B. & Wagner, C. A total error framework for digital traces of human behavior on online platforms. *Public Opin. Q.* (in the press). **This paper gives a systematic overview of errors that may be introduced when analysing digital traces of human behavior.**

76. 76.

Lazer, D. Issues of construct validity and reliability in massive, passive data collections. *The City Papers: An Essay Collection from The Decent City Initiative* <http://citiespapers.ssrc.org/issues-of-construct-validity-and-reliability-in-massive-passive-data-collections/> (2015).

77. 77.

Perdomo, J., Zrnic, T., Mendler-Dünner, C. & Hardt, M. Performative prediction. In *Proc. 37th Intl Conf. Machine Learning* (eds Daumé III, H. & Singh, A.) 7599–7609 (PMLR, 2020).

78. 78.

Hannak, A. et al. Measuring personalization of web search. In *Proc. 22nd Intl Conf. World Wide Web (WWW' 13)* (eds Schwabe, D. et al.) 527–538 (ACM, 2013).

79. 79.

Ali, M. et al. Discrimination through optimization: how Facebook’s ad delivery can lead to biased outcomes. *Proc. ACM Hum.–Comp. Interact.* **3**, 199 (2019).

80. 80.

Thomas, P. & Brunskill, E. Data-efficient off-policy policy evaluation for reinforcement learning. In *Intl Conf. Machine Learning* (eds Balcan, M. F. & Weinberger, K. Q.) 2139–2148 (PMLR, 2016).

81. 81.

Sinha, A., Gleich, D. F. & Ramani, K. Deconvolving feedback loops in recommender systems. In *Advances in Neural Information Processing Systems 29* (eds Lee, D. et al.) 3243–3251 (2016).

82. 82.

Tomašev, N. et al. AI for social good: unlocking the opportunity for positive impact. *Nat. Commun.* **11**, 2468 (2020).

[PubMed](#) [PubMed Central](#) [ADS](#) [Google Scholar](#)

83. 83.

Mau, S. *Das metrische Wir: Über die Quantifizierung des Sozialen* (Suhrkamp, 2017). **This book explores the implications of measurements on social systems.**

84. 84.

D’Ignazio, C. & Klein, L. F. *Data Feminism* (MIT Press, 2020).

85. 85.

Muller, J. Z. *The Tyranny of Metrics* (Princeton Univ. Press, 2018).

86. 86.

Lee, M. K., Jain, A., Cha, H. J., Ojha, S. & Kusbit, D. Procedural justice in algorithmic fairness: leveraging transparency and outcome control for fair algorithmic mediation. *Proc. ACM Hum.–Comp. Interact.* **3**, 182 (2019).

[Google Scholar](#)

87. 87.

Weller, A. Challenges for transparency. Preprint at <https://arxiv.org/abs/1708.01870> (2017).

88. 88.

Shokri, R., Strobel, M. & Zick, Y. Exploiting transparency measures for membership inference: a cautionary tale. In *The AAAI Workshop on Privacy-Preserving Artificial Intelligence (PPAI)* (eds Fioretto, F. et al.) 17 (AAAI, 2020).

89. 89.

Shokri, R., Strobel, M. & Zick, Y. On the privacy risks of model explanations. Preprint at <https://arxiv.org/abs/1907.00164> (2019).

90. 90.

Lahoti, P. et al. Fairness without demographics through adversarially reweighted learning. In *Advances in Neural Information Processing Systems 33* (eds Larochelle, H. et al.) 728–740 (2020).

91. 91.

Dwork, C., Hardt, M., Pitassi, T., Reingold, O. & Zemel, R. Fairness through awareness. In *Proc. 3rd Innovations in Theoretical Computer Science Conf.* (eds Goldwasser, S.) 214–226 (ACM, 2012).

92. 92.

Hardt, M., Price, E. & Srebro, N. Equality of opportunity in supervised learning. In *Proc. 30th Intl Conf. on Neural Information Processing Systems* (eds Lee, D. et al.) 3323–3331 (Curran, 2016).

93. 93.

Werner, D. *Nothing About Us Without Us: Developing Innovative Technologies for, by and with Disabled Persons* (Healthwrights, 1998).

94. 94.

Charlton, J. I. *Nothing About Us Without Us: Disability Oppression and Empowerment* (Univ. California Press, 1998).

95. 95.

Costanza-Chock, S. Design justice, A.I., and escape from the matrix of domination. *J. Design Sci.* <https://doi.org/10.21428/96c8d426> (2018).

96. 96.

Scott, J. C. *Seeing Like a State* (Yale Univ. Press, 2008).

97. 97.

Lazer, D. et al. Meaningful measures of human society in the twenty-first century. *Nature* <https://doi.org/10.1038/s41586-021-03660-7> (2021).

98. 98.

Goel, S., Anderson, A., Hofman, J. & Watts, D. J. The structural virality of online diffusion. *Manage. Sci.* **62**, 180–196 (2016).

[Google Scholar](#)

99. 99.

Aral, S. & Nicolaides, C. Exercise contagion in a global social network. *Nat. Commun.* **8**, 14753 (2017).

[CAS](#) [PubMed](#) [PubMed Central](#) [ADS](#) [Google Scholar](#)

100. 100.

Eagle, N., Macy, M. & Claxton, R. Network diversity and economic development. *Science* **328**, 1029–1031 (2010).

[MathSciNet](#) [CAS](#) [PubMed](#) [MATH](#) [ADS](#) [Google Scholar](#)

101. 101.

Contractor, N. in *The Oxford Handbook of Networked Communication* (eds Welles, B. F. and González-Bailón, S.) (Oxford Univ. Press, 2018).

102. 102.

Contractor, N., Monge, P. R. & Leonardi, P. M. Multidimensional networks and the dynamics of sociomateriality: bringing technology inside the network. *Int. J. Commun.* **5**, 682–720 (2011).

[Google Scholar](#)

103. 103.

Rahwan, I. et al. Machine behaviour. *Nature* **568**, 477–486 (2019).
This paper argues that studies of machine behaviour are necessary to control AI-enabled systems and to avoid harm.

[CAS](#) [PubMed](#) [ADS](#) [Google Scholar](#)

104. 104.

Salganik, M. J. *Bit By Bit: Social Research in the Digital Age* (Princeton Univ. Press, 2017). **This book gives an overview of methods deployed in computational social science.**

105. 105.

Baeza-Yates, R. Big data or right data? In *Proc. 7th Alberto Mendelzon Intl Workshop on Foundations of Data Management* (eds Bravo, L. & Lenzerini, M.) 14 (CEUR-WS, 2013).

106. 106.

Schwarz, G. & Stensaker, I. Time to take off the theoretical straightjacket and (re-)introduce phenomenon-driven research. *J. Appl. Behav. Sci.* **50**, 478–501 (2014).

[Google Scholar](#)

107. 107.

Mathieu, J. E. The problem with [in] management theory. *J. Organ. Behav.* **37**, 1132–1141 (2016).

[Google Scholar](#)

108. 108.

Watts, D. Should social science be more solution-oriented? *Nat. Hum. Behav.* **1**, 15 (2017).

[Google Scholar](#)

109. 109.

Stier, S., Breuer, J., Siegers, P. & Thorson, K. Integrating survey data and digital trace data: key issues in developing an emerging field. *Soc. Sci. Comput. Rev.* **38**, 503–516 (2020).

[Google Scholar](#)

110. 110.

Mellon, J. Internet search data and issue salience: the properties of google trends as a measure of issue salience. *J. Elections Public Opin. Parties* **24**, 45–72 (2014).

[Google Scholar](#)

111. 111.

Stier, S., Bleier, A., Lietz, H. & Strohmaier, M. Election campaigning on social media: politicians, audiences, and the mediation of political communication on Facebook and Twitter. *Polit. Commun.* **35**, 50–74 (2018).

[Google Scholar](#)

112. 112.

Bernard, H. R., Killworth, P. D. & Sailer, L. Informant accuracy in social-network data: V. An experimental attempt to predict actual communication from recall data. *Soc. Sci. Res.* **11**, 30–66 (1982).

[Google Scholar](#)

113. 113.

Prince, S. A. et al. A comparison of direct versus self-report measures for assessing physical activity in adults: a systematic review. *Int. J. Behav. Nutr. Phys. Act.* **5**, 56 (2008).

[PubMed](#) [PubMed Central](#) [Google Scholar](#)

114. 114.

Scharkow, M. The accuracy of self-reported internet use—a validation study using client log data. *Commun. Methods Meas.* **10**, 13–27 (2016).

[Google Scholar](#)

115. 115.

Boase, J. & Ling, R. Measuring mobile phone use: self-report versus log data. *J. Comput. Mediat. Commun.* **18**, 508–519 (2013).

[Google Scholar](#)

116. 116.

Revilla, M., Ochoa, C. & Loewe, G. Using passive data from a meter to complement survey data in order to study online behavior. *Soc. Sci. Comput. Rev.* **35**, 521–536 (2017).

[Google Scholar](#)

117. 117.

Elmer, T., Chaitanya, K., Purwar, P. & Stadtfeld, C. The validity of RFID badges measuring face-to-face interactions. *Behav. Res. Methods* **51**, 2120–2138 (2019).

[PubMed](#) [PubMed Central](#) [Google Scholar](#)

118. 118.

Sapiezynski, P., Stopczynski, A., Lassen, D. D. & Lehmann, S. Interaction data from the Copenhagen Networks Study. *Sci. Data* **6**, 315 (2019).

[PubMed](#) [PubMed Central](#) [Google Scholar](#)

119. 119.

Groves, R. M. & Lyberg, L. Total survey error: past, present, and future. *Public Opin. Q.* **74**, 849–879 (2010).

[Google Scholar](#)

120. 120.

Coravos, A., Chen, I., Gordhandas, A. & Stern, A. D. We should treat algorithms like prescription drugs. *Quartz*,
<https://qz.com/1540594/treating-algorithms-like-prescription-drugs-could-reduce-ai-bias/> (February 2019).

121. 121.

Arnold, M. et al. FactSheets: increasing trust in AI services through supplier's declarations of conformity. Preprint at
<https://arxiv.org/abs/1808.07261> (2019).

122. 122.

Bender, E. & Friedman, B. Data statements for natural language processing: toward mitigating system bias and enabling better science. *Trans. Assoc. Comput. Linguist.* **6**, 587–604 (2018).

[Google Scholar](#)

123. 123.

Mitchell, M. et al. Model cards for model reporting. In *Proc. Conf. Fairness, Accountability, and Transparency* (eds Morgenstern, J. & boyd, d.) 220–229 (ACM, 2019). **This paper argues for higher standards in documenting machine learning models.**

124. 124.

Kuh, A., Petsche, T. & Rivest, R. Learning time-varying concepts. In *Advances in Neural Information Processing Systems 3* (eds Lippmann, R. P. et al.) 183–189 (Morgan-Kaufmann, 1991).

125. 125.

Bartlett, P. L., Ben-David, S. & Kulkarni, S. R. Learning changing concepts by exploiting the structure of change. *Mach. Learn.* **41**, 153–174 (2000).

[MATH](#) [Google Scholar](#)

126. 126.

Gama, J., Žliobaitundefined, I., Bifet, A., Pechenizkiy, M. & Bouchachia, A. A survey on concept drift adaptation. *ACM Comput. Surv.* **46**, 44 (2014).

[MATH](#) [Google Scholar](#)

127. 127.

Abbasi, M., Friedler, S. A., Scheidegger, C. & Venkatasubramanian, S. Fairness in representation: quantifying stereotyping as a representational harm. In *Proc. 2019 SIAM Intl Conf. Data Mining* (eds Berger-Wolf, T. & Chawla, N.) 801–809 (SIAM, 2019).

128. 128.

Abebe, R. et al. Roles for computing in social change. In *Proc. 2020 Conf. Fairness, Accountability, and Transparency* (eds Castillo, C. & Hildebrandt, M.) 252–260 (ACM, 2020).

129. 129.

Hampton, L. M. Black feminist musings on algorithmic oppression. In *Proc. 2021 Conf. Fairness, Accountability, and Transparency* (eds Elish, M. C. et al.) 1 (ACM, 2021).

130. 130.

De-Arteaga, M., Fogliato, R. & Chouldechova, A. A case for humans-in-the-loop: decisions in the presence of erroneous algorithmic scores. In *Proc. 2020 CHI Conf. Human Factors in Computing Systems* (eds Bernhaupt, R. et al.) 1–12 (ACM, 2020).

131. 131.

Boyarskaya, M., Olteanu, A. & Crawford, K. Overcoming failures of imagination in AI infused system development and deployment. Preprint at <https://arxiv.org/abs/2011.13416> (2020).

132. 132.

Nanayakkara, P., Diakopoulos, N. & Hullman, J. Anticipatory ethics and the role of uncertainty. Preprint at <https://arxiv.org/abs/2011.13170> (2020).

133. 133.

Friedman, B. Value-sensitive design. *Interaction* **3**, 16–23 (1996).

[Google Scholar](#)

134. 134.

Olteanu, A., Diaz, F. & Kazai, G. When are search completion suggestions problematic? *Proc. ACM Hum.–Comp. Interact.* **4**, 1–25 (2020).

[Google Scholar](#)

135. 135.

Jiang, J. A., Wade, K., Fiesler, C. & Brubaker, J. R. Supporting serendipity: opportunities and challenges for human–AI collaboration in qualitative analysis. *Proc. ACM Hum.–Comp. Interact.* **5**, 1–23 (2021).

[Google Scholar](#)

136. 136.

Churchill, E., van Allen, P. & Kuniavsky, M. Designing AI: introduction. *Interaction* **25**, 34–37 (2018).

[Google Scholar](#)

137. 137.

Selbst, A. D. boyd, d., Friedler, S., Venkatasubramanian, S. & Vertesi, J. Fairness and abstraction in sociotechnical systems. In *Proc. Conf. Fairness, Accountability, and Transparency* (eds Morgenstern, J. & boyd, d.) 59–68 (ACM, 2019).

138. 138.

Barcas, S., Biega, A. J., Fish, B., Niklas, J. & Stark, L. When not to design, build, or deploy. In *Proc. 2020 Conf. Fairness, Accountability, and Transparency* (eds Castillo, C. & Hildebrandt, M.) 695–695 (ACM, 2020).

139. 139.

Monge, P. & Contractor, N. *Theories of Communication Networks* (Oxford Univ. Press, 2003).

140. 140.

Glaser, B. & Strauss, A. *The Discovery of Grounded Theory: Strategies for Qualitative Research* (Aldine de Gruyter, 1967).

141. 141.

Bryant, A. Re-grounding grounded theory. *J. Inf. Technol. Theory Appl.* **4**, 25–42 (2002).

[Google Scholar](#)

142. 142.

Charmaz, K. *Constructing Grounded Theory: A Practical Guide Through Qualitative Analysis* (Sage, 2006).

143. 143.

Timmermans, S. & Tavory, I. Theory construction in qualitative research: from grounded theory to abductive analysis. *Sociol. Theory* **30**, 167–186 (2012).

[Google Scholar](#)

144. 144.

Nelson, L. Computational grounded theory: a methodological framework. *Sociol. Methods Res.* **49**, 3–42 (2020). **This paper proposes a methodological framework to combine expert human knowledge and hermeneutic skills with the processing power and pattern recognition of computers.**

[MathSciNet](#) [Google Scholar](#)

145. 145.

McFarland, D., Lewis, K. & Goldberg, A. Sociology in the era of big data: the ascent of forensic social science. *Am. Sociol.* **47**, 12–35 (2015).

[Google Scholar](#)

146. 146.

Radford, J. & Joseph, K. Theory in, theory out: the uses of social theory in machine learning for social science. *Front. Big Data* **3**, 18 (2020).

[PubMed](#) [PubMed Central](#) [Google Scholar](#)

147. 147.

Macy, M. & Willer, R. From factors to actors: computational sociology and agent-based modeling. *Annu. Rev. Sociol.* **28**, 143–166 (2002).

[Google Scholar](#)

148. 148.

Smith, E. R. & Conrey, F. R. Agent-based modeling: a new approach for theory building in social psychology. *Pers. Soc. Psychol. Rev.* **11**, 87–104 (2007).

[PubMed](#) [Google Scholar](#)

149. 149.

Keuschnigg, M., Lovsjö, N. & Hedström, P. Analytical sociology and computational social science. *J. Comp. Soc. Sci.* **1**, 3–14 (2018).

[Google Scholar](#)

150. 150.

Hedström, P. & Bearman, P. in *The Oxford Handbook of Analytical Sociology* (eds Hedström, P. & Bearman, P.) (Oxford Univ. Press, 2011).

151. 151.

Lemmerich, F. et al. Mining subgroups with exceptional transition behavior. In *Proc. 22nd ACM SIGKDD Intl Conf. Knowledge Discovery and Data Mining* (eds Krishnapuram, B. & Shah, M.) 965–974 (ACM, 2016).

152. 152.

Singer, P. et al. Why we read Wikipedia. In *Proc. 26th Intl Conf. World Wide Web* (eds Barrett, R. & Cummings, R.) 1591–1600 (ACM, 2017).

153. 153.

Aguera y Arcas, B., Mitchell, M. & Todorov, A. Physiognomy's new clothes. *Medium*, <https://medium.com/@blaisea/physiognomys-new-clothesf2d4b59fdd6a> (6 May 2017).

[Download references](#)

Acknowledgements

We thank the reviewers for their contributions to this work.

Author information

Affiliations

1. GESIS – Leibniz Institute for the Social Sciences, Cologne, Germany

Claudia Wagner & Markus Strohmaier

2. RWTH Aachen University, Aachen, Germany

Claudia Wagner & Markus Strohmaier

3. Complexity Science Hub Vienna, Vienna, Austria

Claudia Wagner & Markus Strohmaier

4. Microsoft Research Montreal, Montreal, Quebec, Canada

Alexandra Olteanu

5. Microsoft Research New York, New York, NY, USA

Alexandra Olteanu

6. Microsoft Research Redmond, Redmond, WA, USA

Emre Kıcıman

7. Northwestern University, Evanston, IL, USA

Noshir Contractor & Tina Eliassi-Rad

8. Northeastern University, Boston, MA, USA

Tina Eliassi-Rad

Authors

1. Claudia Wagner

[View author publications](#)

You can also search for this author in [PubMed](#) [Google Scholar](#)

2. Markus Strohmaier

[View author publications](#)

You can also search for this author in [PubMed](#) [Google Scholar](#)

3. Alexandra Olteanu

[View author publications](#)

You can also search for this author in [PubMed](#) [Google Scholar](#)

4. Emre Kıcıman

[View author publications](#)

You can also search for this author in [PubMed](#) [Google Scholar](#)

5. Noshir Contractor

[View author publications](#)

You can also search for this author in [PubMed](#) [Google Scholar](#)

6. Tina Eliassi-Rad

[View author publications](#)

You can also search for this author in [PubMed](#) [Google Scholar](#)

Contributions

All authors have contributed to the formation, discussion, and writing of this article.

Corresponding author

Correspondence to [Claudia Wagner](#).

Ethics declarations

Competing interests

The authors declare no competing interests.

Additional information

Peer review information *Nature* thanks Ceren Budak, Johan Ugander and the other, anonymous, reviewer(s) for their contribution to the peer review of this work.

Rights and permissions

[Reprints and Permissions](#)

About this article



Check for
updates

Cite this article

Wagner, C., Strohmaier, M., Olteanu, A. *et al.* Measuring algorithmically infused societies. *Nature* **595**, 197–204 (2021).

<https://doi.org/10.1038/s41586-021-03666-1>

Download citation

- Received: 05 March 2021
- Accepted: 21 May 2021
- Published: 30 June 2021
- Issue Date: 08 July 2021
- DOI: <https://doi.org/10.1038/s41586-021-03666-1>

Further reading

- [Integrating explanation and prediction in computational social science](#)
 - Jake M. Hofman
 - , Duncan J. Watts
 - , Susan Athey
 - , Filiz Garip
 - , Thomas L. Griffiths
 - , Jon Kleinberg
 - , Helen Margetts
 - , Sendhil Mullainathan
 - , Matthew J. Salganik
 - , Simine Vazire
 - , Alessandro Vespignani
 - & Tal Yarkoni

Nature (2021)

- [Human social sensing is an untapped resource for computational social science](#)
 - Mirta Galesic
 - , WÃ¶ndi Bruine de Bruin

- , Jonas Dalege
- , Scott L. Feld
- , Frauke Kreuter
- , Henrik Olsson
- , Drazen Prelec
- , Daniel L. Stein
- & Tamara van der Does

Nature (2021)

Comments

By submitting a comment you agree to abide by our [Terms](#) and [Community Guidelines](#). If you find something abusive or that does not comply with our terms or guidelines please flag it as inappropriate.

[Access through your institution](#)

[Change institution](#)

[Buy or subscribe](#)

Associated Content

Special

[Computational social science](#)

Advertisement

This article was downloaded by **calibre** from <https://www.nature.com/articles/s41586-021-03666-1>

Thinking clearly about social aspects of infectious disease transmission

[Download PDF](#)

- Perspective
- [Published: 30 June 2021](#)

Thinking clearly about social aspects of infectious disease transmission

- [Caroline Buckee](#) [ORCID: orcid.org/0000-0002-8386-5899¹](#),
- [Abdisalan Noor²](#) &
- [Lisa Sattenspiel](#) [ORCID: orcid.org/0000-0003-4534-3392³](#)

Nature volume 595, pages 205–213 (2021) [Cite this article](#)

- 808 Accesses
- 81 Altmetric
- [Metrics details](#)

Subjects

- [Computational models](#)
- [Diseases](#)

Abstract

Social and cultural forces shape almost every aspect of infectious disease transmission in human populations, as well as our ability to measure, understand, and respond to epidemics. For directly transmitted infections, pathogen transmission relies on human-to-human contact, with kinship, household, and societal structures shaping contact patterns that in turn determine epidemic dynamics. Social, economic, and cultural forces also shape patterns of exposure, health-seeking behaviour, infection outcomes, the likelihood of diagnosis and reporting of cases, and the uptake of interventions. Although these social aspects of epidemiology are hard to quantify and have limited the generalizability of modelling frameworks in a policy context, new sources of data on relevant aspects of human behaviour are increasingly available. Researchers have

begun to embrace data from mobile devices and other technologies as useful proxies for behavioural drivers of disease transmission, but there is much work to be done to measure and validate these approaches, particularly for policy-making. Here we discuss how integrating local knowledge in the design of model frameworks and the interpretation of new data streams offers the possibility of policy-relevant models for public health decision-making as well as the development of robust, generalizable theories about human behaviour in relation to infectious diseases.

[Download PDF](#)

Main

The ongoing COVID-19 pandemic highlights the continuing importance of global infectious disease threats, and the need to develop rigorous scientific theories to understand, quantify, and forecast the risks that pathogens pose to humanity. One of the most important lessons of the pandemic so far is that the central forces shaping local and global variation in disease burden and dynamics have been social, not biological. Although substantial biological questions remain unanswered, the multiple waves of infection that have been driven by shifting control policies and the heterogeneous public response to them^{1,2}, as well as the disproportionate impact of the disease on poor and marginalized communities around the world^{3,4,5,6}, are the defining features of the pandemic's trajectory on local and global scales.

Epidemiological models that describe the spread of infectious diseases through populations have been developed during the pandemic to understand and predict pathogen transmission and to guide public health policies^{7,8}. As a tool for synthesizing current knowledge, identifying key drivers of transmission, and planning public health policy, such models have a long history in research and public health^{9,10}, and are increasingly used to make decisions about health policy and global funding¹¹. Although uncertainties about biological aspects of pathogen transmission may be problematic for modelling, it is the social context—which is important not only in terms of model structure and parameterization but also with respect to the availability and interpretation of epidemiological data—that often presents the biggest challenges for capturing the essential features of disease dynamics^{8,12,13}.

Human societies are structured by cultural forces that define social relations, particularly between kin, and the spread of infection reflects these social structures—starting with the household or family unit, and extending to the structure of workplaces and public spaces, and the physical layouts of villages, towns, cities, and countries. The purpose of a model, whether purely theoretical or fit to data to inform decision-making in a specific context, will determine how detailed these social aspects of transmission need to be, with the adage that a model should be ‘as simple as

possible but no simpler’ likewise taking on different meanings depending on the model’s intended function. Intrinsic to this decision is a question of scale¹³: capturing population-level dynamics may not require individual-level detail about social interactions, but a model intended to understand local drivers of transmission may.

Data about social relationships that are relevant for modelling pathogen transmission are traditionally collected by censuses and other surveys^{14,15,16}, but the expansion of access to the internet has started to open up possibilities for a more expansive, real-time, and global approach to the collection of survey data^{17,18,19} and the development of relevant social science theories about human behaviour. Furthermore, new data streams from mobile devices—for example, via social media—are offering vast, relatively unexplored datasets about human mobility on a global scale^{20,21}. Despite the recent marked increase in the availability of these new datasets—a trend that has accelerated during the COVID-19 pandemic^{22,23,24}—challenges remain in using them to parameterize transmission models. In particular, the extent to which data from mobile phones provide an accurate proxy for contact rates that spread disease remains unclear^{25,26}. In fact, it is still difficult to parameterize social aspects of transmission in mechanistic models even in the context of sophisticated approaches to modelling and the addition of powerful new data. Nevertheless, as social scientists embrace and grapple with new data streams, infectious disease modellers have the opportunity to use them in the context of transmission models as “a way of thinking clearly”⁹ about the social drivers of epidemics.

Here we describe key social parameters that modellers must consider to effectively capture the dynamics of pathogen transmission on different scales. We draw a distinction between models in which appropriately disaggregated data about baseline human social dynamics—grounded in local knowledge—can provide mechanistic insights into disease transmission, and the challenges introduced when the quality, resolution, or paucity of epidemiological and behavioural data may constrain predictive power even if the social aspects of a model are well-specified. We also discuss the importance of understanding and predicting deviations from baseline behaviour that result from infection and public health policies, an issue that may need to be addressed using a fundamentally different kind of model structure. Models are increasingly informing target product profiles, global strategies, and investments in global public health programs for many infectious diseases. Social and behavioural aspects of transmission are often ignored in the name of generalizability and parsimony, with authors adopting the language of physics to justify these simplifications while also claiming to provide public health value to specific populations. Too often the integration of these models in decision-making processes at the national level remains weak. We believe that one of the most important challenges for our field is the development of flexible frameworks that integrate social contexts

that are relevant for disease, a challenge that requires closer collaboration between social scientists and infectious disease epidemiologists.

Parameterizing local contact rates

All mechanistic frameworks of infectious disease transmission make assumptions about how frequently people are exposed to disease, for example owing to close physical contact between susceptible and infectious people (the contact rate), and about the probability of infection when exposure occurs. In the well-studied susceptible–infectious–recovered (SIR) model—first developed by Kermack and McKendrick nearly a century ago²⁷—mixing within a single homogeneous population, and therefore infection risk, was assumed to be random. The conceptual separation of the transmission coefficient into social and biological components was not the norm until the 1980s, as it became increasingly apparent that the population dynamics of HIV were driven disproportionately by transmission within particular demographic groups, which reflected highly non-random patterns of sexual contact^{28,29,30,31,32,33,34}. This separation provides conceptual differentiation of the social and cultural forces that drive uneven infection risk within a population from the biology of transmission itself^{30,35,36}, and is an essential feature to include to incorporate the effect of heterogeneous social interactions on transmission (Box 1).

In reality, assumptions of random mixing are always violated, even at the local and within-household scales, and the extent to which models must account for departures from them will depend on the mode of transmission of the pathogen and the purpose of the model. Kin structures are at the heart of all communities (Fig. 1). Comprehensive diary studies have revealed strong, age-structured mixing patterns related to household structures of nuclear families and peer groups shaped by schooling and patterns of employment^{14,16}, but these contact rates can change over time¹⁷ and vary substantially around the world³⁷. Recent technological developments have facilitated bluetooth-based and GPS studies of contact patterns^{37,38,39}, providing rich, granular data with increasingly large sample sizes, and a foundation for developing general principles of human interaction that could be used in epidemic models. Passively collected, aggregated mobile phone data have also become increasingly available on a near real-time basis and at scale²¹. During the COVID-19 pandemic, many modellers have begun to examine whether local mobility metrics and foot-traffic data are useful proxies for contact rates within populations^{40,41,42,43,44,45,46}. This can be effective when changes in mobility that occur on a scale that is measurable using mobile phone data are strongly correlated with contact rates. For example, at the beginning of the COVID-19 pandemic, Badr et al.⁴⁶ used aggregated mobility metrics from mobile phones to show that marked reductions in mobility occurred throughout the USA in mid-March of 2020, regardless of local social distancing policies, and that

this was strongly associated with a drop in COVID-19 growth rates across the country. In this case, aggregated mobility data provided a meaningful proxy for the contact rates that drove changes in transmission on a county level. In general, however, if contact rates are decoupled from mobility patterns measured in this way—which the authors suggest occurred after April 2020 in the USA²⁵—an understanding of local transmission patterns still requires local data collection and/or contextual knowledge.

Fig. 1: The nature of the kin structures in a community strongly influences who mixes with whom.

 figure1

Kin structures can affect patterns of interaction at all geographic scales. For example, at the local level, in some cultures extended families live and interact within the same house or complex. Kin relationships also strongly affect normal patterns of visiting behaviour, as much movement in all human cultures involves visiting kin. In places without running water, it is common for laundry to be done in streams or rivers, and this is often an important social activity, especially for women and children. In some cultures, women and men have different roles, including differential participation in labour migration and agricultural work, and women may be confined to family compounds during the day. At the regional level, families regularly congregate for larger-scale social events such as weddings and holidays, with longer-distance travel connecting communities. When disease does occur, it is often measured by routine surveillance systems that only identify cases when treatment is sought, and when they are correctly diagnosed and reported.

[Full size image](#)

Careful examination of the interactions between people inside and outside their households that lead to heterogeneous infection risk can produce epidemiological models that yield powerful and generalizable insights, despite their specificity. For example, for the *Aedes* mosquito-borne virus that causes dengue fever, household

variation in disease incidence has often been assumed to almost exclusively reflect the spatial distribution of mosquito vectors. However, by closely monitoring people's movements in relation to dengue clusters in Iquitos, Peru, Stoddard et al.^{47,48} showed that patterns of inter-household mobility associated with visiting friends and family were also a major driver of dengue transmission and needed to be considered in addition to spatial variation in mosquito densities. Similarly, by combining detailed survey data and precise location information about an outbreak of another *Aedes* mosquito-borne disease, Chikungunya, in Bangladesh, Salje et al.⁴⁹ reconstructed transmission chains to show that this disease was highly localized to socially connected households within particular communities, and that the 1.5 times higher risk of infection among women coincided with the 1.5 times higher likelihood that they stayed in the home during the day. The power of these studies reflects the combination of social science data and rich epidemiological information, coupled with sophisticated analytics. It is not that models without these details would be wrong per se, but rather that the addition of social science data provides important mechanistic insights into how transmission works on this local scale; behaviours and patterns of household visiting will define the course of any particular outbreak and must be understood when generating context-specific policy.

These concerns in turn emphasize the continuing importance of on-the-ground data collection from surveys, the value of gender-disaggregated data—which the WHO only made standard practice for global health statistics in 2019⁵⁰—and the role of local knowledge in model and study design. Local knowledge is also key for interpreting epidemiological data used to fit and validate models (Box 2). Despite this, local social phenomena are often left out of disease models¹², sometimes because they are developed in a different context, for use at a different scale, or for academic purposes by researchers who are unaware of local realities, or because the social science data are time-consuming to collect or unavailable. The rich new data sources discussed above raise the question of how much detail should be included in order to understand the mechanisms that drive disease or to capture population-level dynamics at different scales. In all models, a trade-off exists between parsimony and realism that hinges on the scale and purpose of the model: while it is certainly true that “it makes no sense to convey a beguiling sense of ‘reality’ with irrelevant detail, when other equally important factors can only be guessed at,”⁹ it is also the case that a failure to capture the critical deviations from assumptions of random mixing may lead to weak predictions, misspecified estimates of transmission⁵¹, and poor policy decisions. Therefore, matching the model and data structures to the scale of the research or policy question becomes the most important challenge for capturing the social drivers of epidemiological dynamics within a population.

Box 1 SEIR models and heterogeneous mixing

Susceptible-exposed-infectious-recovered (SEIR) models provide a mechanistic description of the transmission of a pathogen as it spreads between people in a population. In the simplest of these frameworks, the reproduction number (R_0) of a disease (the average number of secondary cases arising from a single infected individual in an entirely susceptible population) can be defined as $R_0 = bk/r$, where b is the probability of infection given contact, k is the contact rate between people in the population, and r is the rate of recovery. As the contact rate is directly proportional to the reproduction number (R_0) of a disease, the size, speed, spatial heterogeneity, and effect of an epidemic, as well as the interventions needed to prevent and contain it, are all fundamentally linked to the social and cultural processes that generate patterns of exposure. Assumptions must be made about how the contact rate scales with population size, and will depend on the transmission route of the pathogen. Beyond single population models, epidemic models designed to study the spread of infectious diseases in subdivided or geographically separate populations (also often called metapopulations) also have a long history. Early models of this type considered an arbitrary number of mixing populations^{[35](#),^{[54](#)},^{[96](#)},^{[97](#)},^{[98](#)},^{[99](#)},^{[100](#)},^{[101](#)},^{[102](#)}}, and several of these efforts were stimulated by the need to develop models that could be used to help control the transmission of gonorrhoea in the USA^{[103](#)},^{[104](#)}. These models established the importance of core groups of highly sexually active individuals for the spread of sexually transmitted diseases. Similar early frameworks were developed to describe the importance of non-random biting of mosquito vectors for malaria transmission^{[105](#)},^{[106](#)}, and many early models focused on the fundamental question of ‘who mixes with whom’^{[28](#)},^{[29](#)},^{[107](#)}. Since then, a substantial body of theoretical work has been developed that examines how heterogeneous local mixing patterns, sometimes formalized as explicit contact network structures, can influence epidemics within a population^{[108](#)},^{[109](#)},^{[110](#)}, often using stylized abstractions of human interactions^{[111](#)},^{[112](#)},^{[113](#)}. The ubiquitous finding of these studies is that heterogeneous contact patterns can be important for both the spread and control of disease.

Box 2 Model fitting and validation

Perhaps one of the least measured or understood uncertainties associated with models of pathogen transmission is in the epidemiological data that are used to parameterize, fit, and validate them. In particular, understanding the social and institutional environments in which case data are generated and reported is essential for any meaningful evaluation of whether a model is fit for purpose. For many pathogens, the data available to fit an epidemiological model are derived from surveillance systems based on the reporting of cases from clinics or hospitals around the country to a central government agency (Fig. 1). Any infection that is not diagnosed within this system will of course not be captured by routine surveillance, and missing cases can occur if infections are asymptomatic, if healthcare is not sought by the infected individual, if cases are misdiagnosed or there is a lack of diagnostic capacity, or if there are reporting delays or failures. These issues are exacerbated among marginalized populations who may not wish to engage in the health system, and in poorly resourced or designed health systems where reporting may be slow, incomplete, and lacking essential metadata. In the context of the COVID-19 pandemic, asymptomatic infections have made it challenging to assess the total number of cases in a community, but additional factors—patchy access to diagnostic tests throughout the epidemic, variable testing criteria in different contexts, culturally specific treatment-seeking behaviours, and misaligned reporting incentives at different levels of government—have all contributed to wildly unreliable case counts. This has led to challenges in fitting models and estimating the reproduction number^{114,115} during the pandemic. ‘Nowcasting’ approaches have been developed to adjust for reporting delays¹¹⁶, and these have been successfully adapted for COVID-19 in some settings¹¹⁷. In addition, the use of alternative epidemiological data that may be more reliable, or are reported in a different way—for example, using excess mortality¹¹⁸ or even environmental proxies of transmission such as viral concentration in wastewater¹¹⁹—can provide a proxy for cases. Serological studies that measure antibodies in the wake of an infection can also be used to inform models about transmission dynamics^{120,121}. However, few models consider the institutional and social aspects of epidemiological data as more than a ‘reporting rate’ that can be estimated or assumed and is usually opaque with respect to mechanism. Exactly how social aspects of surveillance should be included in modelling frameworks in different settings remains unclear, but is an important consideration for future work.

Regional mobility and between-population transmission

Travel outside the community also plays a key role in spreading diseases (Fig. 1), and spatial models of infectious diseases often incorporate travel as a migration rate

between populations. Traditionally, simple, theoretically derived gravity and radiation models—both based on the reasonable idea that large populations attract travellers, but not requiring specific data about mobility—have often been used as fixed parameters to describe mobility dynamics in these metapopulation models^{52,53,54}. The increasing availability of mobile-phone-derived data on regional mobility is permitting the validation of these frameworks in real-world settings. The results of such studies suggest that gravity models systematically underestimate the volume of long-distance travel in our highly connected world, and may do poorly in rural areas^{55,56,57}. They also highlight the importance of seasonal patterns of connectivity or asymmetric population shifts, such as holiday travel or displacement due to conflict or natural disasters. A recent comparison of aggregated mobile phone data from three countries showed that seasonal patterns of travel are a general feature of modern societies⁵⁸. For example, in Kenya, this seasonal flux in population density, coinciding with school term times, was shown to be a stronger predictor of the regional patterns of the childhood infection rubella than rainfall and other explanations, explaining Kenya's unusual three-peak pattern of rubella incidence⁵⁹. Using mobile phone data to measure travel patterns in Bangladesh, Mahmud et al.⁶⁰ observed large travel surges occurring out of the capital city of Dhaka to all parts of Bangladesh during the Eid festivals. In 2017, this holiday coincided with a large Chikungunya outbreak in the city, which spread throughout Bangladesh after the holiday, just as outbreaks of respiratory viruses in the global north at the end of December are often associated with holiday travel^{61,62}.

Mobile phone data therefore provide valuable insights about these relative travel routes of millions of people between different places for the first time, as well as asymmetric movement patterns and large shifts in population density. There are limits to the insights mobile phone data streams can afford, however, primarily related to a gap in social insight; they are spatially coarse relative to contact patterns that spread disease, as previously discussed; they have implicit biases (for example, they do not include children and other people without phones); and they usually do not tell us anything about who is travelling and why. It will be important to measure and quantify bias and representativeness in these datasets^{26,63,64} as they are used more routinely, as well as to engage in meaningful efforts to standardize approaches to both analysis and privacy for this relatively new public health application²⁶.

Analogous to the problems with random mixing assumptions in single-population models, the contact rate between populations often reflects travel by particular subsets of the population; in other words, the probability of travelling is not randomly distributed, but the mobility rates in most models assume that it is, and usually mobile phone data are not disaggregated demographically, in order to preserve the privacy of subscribers. When mobility data are available that are disaggregated, by gender for example, striking differences in mobility may emerge. A study of an urban setting in Latin America⁴¹ illustrates this heterogeneity well—women are both more localized in

their movements and visit fewer locations than men, which may be important for infection dynamics in a given setting, depending on the pathogen. Surveys have shown that women with children also travel less to urban centres across sub-Saharan Africa compared to other demographics⁵⁶. In a rural setting in Bangladesh, a survey of patients with malaria showed similar trends, with men travelling much greater distances than women⁶⁵. Given that global gender roles often follow this pattern, it is likely that these findings are general and relevant for building robust disease models, especially when combined with gender-disaggregated health data. Contextual understanding coupled with disaggregated data, often generated using traditional social science approaches, is therefore not something we can do away with in the era of big data. Rather, these new data streams are uncovering dynamics that will be much more powerful when complemented by social science data and analysis.

Some of these gender differences in regional mobility are related to occupational activities, which is another important factor that drives contact rates between populations. Labour migration has long been studied by social scientists, but is challenging to incorporate into epidemic models. The importance of labour migration in particular demographic groups, for example linked to forest and plantation work, agriculture and livestock, or gold mining^{66,67}, has been known to drive regional patterns of malaria transmission for decades⁶⁸. In the Sahel region of Africa, where the malaria burden is intense and highly seasonal, pastoral livestock farming is a key economic activity, and pastoralist communities are highly mobile as they search for pasture and water for their livestock, often in areas that expose them to malaria, and they exhibit seasonal migration within and between countries (Fig. 2). Rapid environmental changes and competition for land have adversely affected pastoralist production systems, which has resulted in conflicts, volatility in mobility patterns, and various other adaptive behaviours that are hard to generalize, but are fundamental to malaria transmission and control in the region.

Fig. 2: Transhumant pastoralists cross through these climatic zones during the course of the year.

 **figure2**

Transhumance is a type of nomadism in which the seasonal movement of people is driven by the need for livestock pasture. In the rainy season, pastoralists in the Sahel region spread into rich, but short-lived, pastures, while they move further south with the onset of the dry season. After spending the height of the dry season in the more humid south, they move back north before the beginning of the agricultural activities of the rainy season⁹⁴. These seasonal movements involve both cross-border (red arrows) and national (blue arrows) travel patterns that shape the lifestyles of these populations. The influence of seasonal movements of particular subsets of a population on these different national and international scales is challenging to measure and capture within transmission models of disease. Adapted with permission from ref. ⁹⁵.

[Full size image](#)

Mathematical frameworks of malaria, which were among the first epidemiological models to be developed for any infectious disease⁶⁹, struggle to accommodate this kind of mobility. In fact, projections for future scenarios of malaria transmission under various interventions in sub-Saharan Africa that are based in part on mechanistic frameworks may not include any mobility parameters⁷⁰. In the absence of understanding of these social contexts, models may assume that the prevalence of infection reflects local transmission characteristics, rather than imported infections. However, surveillance data from around the world suggest that imported infections actually represent the majority of cases in some settings. In a study in Nairobi, for example, two-thirds of patients with malaria tested in a facility in an informal settlement had a history of travel and nearly 80% of those who had travelled had

visited counties with high malaria transmission⁷¹. In settings with frequent importation, therefore, policy targets and funding should focus on managing infections in travellers, not local mosquito control, and models of malaria transmission that fail to account for mobility will fail to capture the key socioeconomic mechanisms that drive the disease. Although these human aspects of malaria transmission continue to be emphasized as major impediments to elimination⁷², both generalizable and specific mobility frameworks are lacking and are often ignored in malaria transmission models that are used to guide elimination scenario planning, leading to the mistaken general assumption that low incidence regions are straightforward elimination targets⁷³.

New data streams—not only from mobile phones but also from surveys and malaria parasite genetic data, which yield insights into the relatedness of different parasite populations—are allowing more sophisticated modelling approaches to identifying the ‘sources’ and ‘sinks’ of malaria infections, however. Chang et al.⁷⁴ combined mobile phone data with parasite genetic data and surveys to model the spread of malaria in rural Bangladesh, for example. Modelling the expected flow of parasites using these different inputs as mobility parameters showed that there was broad agreement between models; parasites moved east to west as people travelled between the forests and more populous regions, with the survey confirming the importance of labour migration to the forest. In many ways, the relatively sophisticated modelling approach confirmed what the National Malaria Control Program already knew—that people get malaria in the forest—but it provided useful evidence for this local knowledge, as well as estimates about the volumes of importation and specific routes and hotspots on which to focus interventions. Efforts to combine and validate new data streams, as well as more theoretical models such as gravity and radiation models⁵⁷, with surveys and other social science tools will be an important next step in the development of general mobility frameworks that describe labour migration around the world.

Epidemics are not like the weather

So far we have focused on behaviours that can be included as model parameters, such as contact rates between groups and baseline travel behaviour. In these cases, more, better quality, or different data about contact rates can improve model accuracy. However, human behaviour can also change in response to their awareness of, and information about, a disease. This can create feedback between the real (prevalence-based) or perceived (belief-based) risk of an infection, assessed by individuals in a population based on available information, and the behaviours that in turn drive its transmission, such as contact rate or the use of preventive interventions⁷⁵. Here, human behaviour must be built into epidemiological models, with social parameters mechanistically linked to changes in the disease itself or beliefs about the disease⁷⁶.

For endemic diseases for which prevention requires active participation by affected communities, such as treatment seeking and the use of preventive measures, understanding human behaviour in the context of risk perception and avoidance is essential for the development of dynamic frameworks to predict the impact of public health policies. Treatment seeking and adherence to drug regimens in the context of tuberculosis^{77,78}, the use of condoms in the prevention of HIV transmission^{79,80}, and sleeping under insecticide treated nets to prevent malaria⁸¹ all represent examples of complex human behaviours—particularly adherence to treatment and other interventions—that are challenging to integrate into model frameworks. In fact, these three major infectious disease threats are arguably among the most challenging for which to create robust theoretical frameworks in the context of interventions, for this reason⁸².

Epidemics, and the public alarm they can generate, create particularly strong feedback between behaviour and disease dynamics. For example, Epstein et al.⁸³ modelled two interacting contagion processes that describe the spread of infectious disease and the spread of fear about the epidemic, which leads individuals to effectively remove themselves from the population. These social–epidemiological feedback loops lead to more complex disease dynamics than expected under a model with fixed behaviours; fear of the disease drives behavioural changes in contact rate as people take steps to isolate themselves, leading to flattened epidemic peaks and multiple waves of infection as the perceived and/or real risk of disease fluctuates. This is exactly what we have observed during the COVID-19 pandemic, with the social response to specific interventions such as social distancing driving the variable course of SARS-CoV-2 incidence around the world². The publicly available data from online information sharing on platforms such as Twitter, where information and misinformation spread in parallel with the epidemic itself, will provide a rich source of information for investigating how different societies have reacted to the pandemic⁸⁴. These social media data come with the same caveats discussed above in the context of mobile phone data, and the representativeness of new data streams in different contexts should be reported by data providers, and adequately measured—through social science studies, among others—and accounted for in modelling research and application.

In this context, the COVID-19 pandemic has created an incredible natural experiment on a global scale, with similar policies being enacted around the world in diverse social contexts. Similarities and differences in the trajectories of local epidemics of the same virus reflect the variable populations involved. Some social dynamics related to the contact rate parameters that we have discussed above do appear to be generalizable over time and in different contexts, and have been repeated around the world during the COVID-19 pandemic. In early 2020, Kissler et al.⁸⁵ measured SARS-CoV-2 prevalence in women who gave birth at different New York City hospitals and found

that there were marked differences across the city, ranging from about 10% in Manhattan to as high as 50% in the Bronx. Analysis of mobility data from Facebook users over the same time period showed that these local variations in incidence were strongly associated with continuing commuting behaviour in neighbourhoods with lower socioeconomic status, consistent with the inability of essential workers to lock down. In fact, this inability of lower-income people to reduce mobility as much as those in wealthier neighbourhoods has been associated with differential disease burden and mortality in cities around the world^{5,86}.

Another characteristic response to policies during the pandemic has been an emptying out of urban centres. Throughout history, people have always fled urban centres when an epidemic hits, whether due to an outbreak of cholera in historical London, or due to a perceived but non-existent outbreak of bubonic plague that caused mass panic and the displacement of hundreds of thousands of people from Surat, India in 1995⁷⁶. These shifts in population density and increases in long-distance travel have important and general implications for understanding infectious diseases and designing public health policies. In response to COVID-19 lockdown policies, mobile phone data from around the world have uncovered similar behavioural responses to lockdown policies and travel restrictions, with similar dynamics occurring in urban centres in the USA, France, Spain, India, and Bangladesh⁸⁷. It is likely that the social and demographic factors that drive this urban–rural migration vary greatly in these different settings, with the exodus from Manhattan perhaps representing wealthy people going to country homes and the movement patterns of people in Bangladesh corresponding to the movement of workers in response to the closing and re-opening of garment factories. These differences emphasize the power of coupling large-scale datasets with local context, and highlight the importance of further setting-specific research to untangle the general versus local drivers of these behaviours.

There is currently strong interest in the development of national epidemic modelling and forecasting centres in the USA and elsewhere, with parallels being drawn to the evolution of weather forecasting services. The cases described above bring into question the extent to which disease forecasting efforts can be compared to weather forecasts; however, are shifting behaviours based on local and global information about epidemics (and related policies) ever going to be predictable in the way that physical laws are? If a weatherman forecasts rain and everyone stays at home, it still rains. Not so with infectious diseases. We argue that short-term forecasting efforts that use ensemble or consensus approaches^{88,89,90} are promising, and for models with the goal of making predictions rather than understanding mechanisms, simple approaches are often adequate, if not more tractable and therefore desirable. This is highlighted by disease forecasting efforts for COVID-19⁸⁸, Ebola⁸⁹, and influenza⁹¹, in which simple models can produce predictions as powerful as those of more complex models over a short timescale. However, a deeper understanding of social and behavioural aspects of

risk perception and decision-making is likely to be needed to make medium-term predictions and mechanistic statements about possible future trajectories of epidemics, or to develop models designed to inform interventions in different settings.

Key to these latter models will be more research to understand how people's behaviours will change in response to particular policies; in this case, experimental or quasi-experimental evidence may be required to improve the predictive power of models that include social–epidemiological feedback mechanisms⁹². We argue, therefore, that rather than creating one large model to forecast disease outbreaks, like a weather forecast, developing distributed research capacity that can respond to specific outbreaks in particular contexts by designing models flexibly and with feedback from local health systems is perhaps a wiser investment.

Thinking clearly about modelling epidemics

If mathematical models are “no more and no less than a way of thinking clearly,”⁹ then it is essential for modellers to think clearly about how modelling decisions about social aspects of transmission reflect the model’s function. In particular, what social phenomena contribute to mechanistic aspects of transmission that are important for population-level dynamics, are these measurable, and, if not, how do they constrain the model’s utility in different contexts? What principles should guide decisions about the scale of a model (for example, individual versus population) given the questions that are being addressed, and what kinds of data are needed to parameterize and validate the resulting model?

There are important distinctions between epidemiological models developed with scientific goals of understanding disease ecology, and epidemiological models developed to inform public health policies, for example. Models with primarily academic or theoretical goals tend to err on the side of abstraction, whereas policy-relevant models may have a more ‘realistic’ depiction of contact rates. Indeed, there is sometimes an implicit assumption in the infectious disease modelling field that integrating setting-specific social interactions in a disease model will inevitably detract from its generalizability, limiting its relevance beyond a particular case study. We argue against this dogma and propose that for models intended to understand mechanisms driving outbreaks—particularly on local scales—“data is the plural of anecdote.”⁹³ It is often by understanding specific social contexts and integrating insights from multiple applications to different contexts that general principles can be drawn. This philosophy requires a distributed generation of knowledge that is unwieldy to integrate into a unified theory, but ultimately can lead to general principles about what can, and what cannot, be ignored about local social contexts for models with different purposes.

In the public health context, substantial investment in modelling capacity is needed at the local and regional levels—not just in the context of dynamical modelling, but also for general statistical and quantitative capacity—to translate the sophisticated and data-rich approaches now available to us into better decision-making. This would ensure that models are being used appropriately in the context of policy. For example, many of the decisions we have discussed, such as whether a simple or a complex model is needed or whether new or different data streams would be helpful, require local literacy in quantitative methods that may be lacking. Partnerships between academic centres or research institutes and public health agencies and governments, as well as better training infrastructure, is therefore needed on an ongoing basis and in the context of endemic pathogens, so that modelling tools can be developed rapidly when a crisis such as COVID-19 occurs.

References

1. 1.

Liu, Y., Morgenstern, C., Kelly, J., Lowe, R. & Jit, M. The impact of non-pharmaceutical interventions on SARS-CoV-2 transmission across 130 countries and territories. *BMC Med.* **19**, 40 (2021).

[PubMed](#) [PubMed Central](#) [Google Scholar](#)

2. 2.

Li, Y. et al. The temporal association of introducing and lifting non-pharmaceutical interventions with the time-varying reproduction number (R) of SARS-CoV-2: a modelling study across 131 countries. *Lancet Infect. Dis.* **21**, 193–202 (2021).

[PubMed](#) [Google Scholar](#)

3. 3.

Malani, A. et al. Seroprevalence of SARS-CoV-2 in slums versus non-slums in Mumbai, India. *Lancet Glob. Health* **9**, e110–e111 (2021). **In this study, seroprevalence estimates in different parts of Mumbai, India, showed marked differences in SARS-CoV-2 exposure by July 2020, with between 55% and 64% of people in slum regions testing positive for antibodies against SARS-CoV-2, compared with 12–19% of people in non-slum regions.**

[PubMed](#) [Google Scholar](#)

4. 4.

Mackey, K. et al. Racial and ethnic disparities in COVID-19-related infections, hospitalizations, and deaths : a systematic review. *Ann. Intern. Med.* **174**, 362–373 (2021).

[PubMed](#) [Google Scholar](#)

5. 5.

Mena, G. E. et al. Socioeconomic status determines COVID-19 incidence and related mortality in Santiago, Chile. *Science* **372**, eabg5298 (2021). **This paper showed that in Santiago, Chile, the socioeconomic status of neighbourhoods is strongly associated with COVID-19-associated morbidity and mortality, and linked to mobility patterns and access to healthcare, for example, testing rates.**

[CAS](#) [PubMed](#) [PubMed Central](#) [Google Scholar](#)

6. 6.

Karmakar, M., Lantz, P. M. & Tipirneni, R. Association of social and demographic factors with COVID-19 incidence and death rates in the US. *JAMA Netw. Open* **4**, e2036462 (2021).

[PubMed](#) [PubMed Central](#) [Google Scholar](#)

7. 7.

Donnelly, C. & Ghani, A. Real-time epidemiology: understanding the spread of SARS. *Significance* **1**, 176–179 (2004).

[MathSciNet](#) [PubMed](#) [Google Scholar](#)

8. 8.

Grassly, N. C. & Fraser, C. Mathematical models of infectious disease transmission. *Nat. Rev. Microbiol.* **6**, 477–487 (2008).

[CAS](#) [PubMed](#) [PubMed Central](#) [Google Scholar](#)

9. 9.

May, R. M. Uses and abuses of mathematics in biology. *Science* **303**, 790–793 (2004).

[CAS](#) [PubMed](#) [ADS](#) [Google Scholar](#)

10. 10.

Anderson, R. M. & May, R. M. Population biology of infectious diseases: part I. *Nature* **280**, 361–367 (1979).

[CAS](#) [PubMed](#) [ADS](#) [Google Scholar](#)

11. 11.

Heesterbeek, H. et al. Modeling infectious disease dynamics in the complex landscape of global health. *Science* **347**, aaa4339 (2015).

[PubMed](#) [PubMed Central](#) [Google Scholar](#)

12. 12.

Ferguson, N. Capturing human behaviour. *Nature* **446**, 733 (2007).

[CAS](#) [PubMed](#) [ADS](#) [Google Scholar](#)

13. 13.

Funk, S. et al. Nine challenges in incorporating the dynamics of behaviour in infectious diseases models. *Epidemics* **10**, 21–25 (2015).

[PubMed](#) [Google Scholar](#)

14. 14.

Mossong, J. et al. Social contacts and mixing patterns relevant to the spread of infectious diseases. *PLoS Med.* **5**, e74 (2008). **In this large diary-based study across countries in Europe, strong age-structured contact patterns were described with variation between different countries; these contact matrices—and others collected in similar ways—are frequently used to parameterize mathematical models of infectious disease transmission.**

[PubMed](#) [PubMed Central](#) [Google Scholar](#)

15. 15.

Kretzschmar, M. & Mikolajczyk, R. T. Contact profiles in eight European countries and implications for modelling the spread of airborne infectious diseases. *PLoS One* **4**, e5931 (2009).

[PubMed](#) [PubMed Central](#) [ADS](#) [Google Scholar](#)

16. 16.

Prem, K., Cook, A. R. & Jit, M. Projecting social contact matrices in 152 countries using contact surveys and demographic data. *PLOS Comput. Biol.* **13**, e1005697 (2017).

[PubMed](#) [PubMed Central](#) [ADS](#) [Google Scholar](#)

17. 17.

Feehan, D. M. & Mahmud, A. S. Quantifying population contact patterns in the United States during the COVID-19 pandemic. *Nat. Commun.* **12**, 893 (2021).

[CAS](#) [PubMed](#) [PubMed Central](#) [ADS](#) [Google Scholar](#)

18. 18.

Feehan, D. M. & Cobb, C. Using an online sample to estimate the size of an offline population. *Demography* **56**, 2377–2392 (2019).

[PubMed](#) [Google Scholar](#)

19. 19.

Lazer, D. et al. Computational social science. *Science* **323**, 721–723 (2009).

[CAS](#) [PubMed](#) [PubMed Central](#) [Google Scholar](#)

20. 20.

Wesolowski, A., Buckee, C. O., Engø-Monsen, K. & Metcalf, C. J. E. Connecting mobility to infectious diseases: the promise and limits of mobile phone data. *J. Infect. Dis.* **214** (Suppl. 4), S414–S420 (2016).

[PubMed](#) [PubMed Central](#) [Google Scholar](#)

21. 21.

Buckee, C. O. et al. Aggregated mobility data could help fight COVID-19. *Science* **368**, 145–146 (2020).

[PubMed](#) [ADS](#) [Google Scholar](#)

22. 22.

SafeGraph Inc. *SafeGraph Data for Academics* (accessed 27 May 2021); <https://www.safegraph.com/academics>

23. 23.

Google. *COVID-19 Community Mobility Reports* (accessed 27 May 2021); <https://www.google.com/covid19/mobility/>

24. 24.

COVID-19 Mobility Data Network. *Facebook Data for Good Mobility Dashboard* (accessed 27 May 2021); <https://visualization.covid19mobility.org/?region=WORLD>

25. 25.

Badr, H. S. & Gardner, L. M. Limitations of using mobile phone data to model COVID-19 transmission in the USA. *Lancet Infect. Dis.* **21**, e113 (2021).

[CAS](#) [PubMed](#) [Google Scholar](#)

26. 26.

Kishore, N. et al. Measuring mobility to monitor travel and physical distancing interventions: a common framework for mobile phone data analysis. *Lancet Digit. Health* **2**, E622–E628 (2020).

[PubMed](#) [PubMed Central](#) [Google Scholar](#)

27. 27.

Kermack, W. O. & McKendrick, A. G. Contributions to the mathematical theory of epidemics—I. *Bull. Math. Biol.* **53**, 33–55 (1991).

[CAS](#) [PubMed](#) [Google Scholar](#)

28. 28.

May, R. M. & Anderson, R. M. Transmission dynamics of HIV infection. *Nature* **326**, 137–142 (1987).

[CAS](#) [PubMed](#) [ADS](#) [Google Scholar](#)

29. 29.

Diekmann, O., Dietz, K. & Heesterbeek, J. A. P. The basic reproduction ratio for sexually transmitted diseases: I. Theoretical considerations. *Math. Biosci.* **107**, 325–339 (1991).

[CAS](#) [PubMed](#) [MATH](#) [Google Scholar](#)

30. 30.

Jacquez, J. A., Simon, C. P., Koopman, J., Sattenspiel, L. & Perry, T. Modeling and analyzing HIV transmission: the effect of contact patterns. *Math. Biosci.* **92**, 119–199 (1988).

[MathSciNet](#) [MATH](#) [Google Scholar](#)

31. 31.

Anderson, R. M., Gupta, S. & Ng, W. The significance of sexual partner contact networks for the transmission dynamics of HIV. *J. Acquir. Immune Defic. Syndr.* **3**, 417–429 (1990).

[CAS](#) [PubMed](#) [Google Scholar](#)

32. 32.

Gupta, S., Anderson, R. M. & May, R. M. Networks of sexual contacts: implications for the pattern of spread of HIV. *AIDS* **3**, 807–818 (1989).

[CAS](#) [PubMed](#) [Google Scholar](#)

33. 33.

Anderson, R. M., Blythe, S. P., Gupta, S. & Konings, E. The transmission dynamics of the human immunodeficiency virus type 1 in the male homosexual community in the United Kingdom: the influence of changes in sexual behaviour. *Phil. Trans. R. Soc. Lond. B* **325**, 45–98 (1989).

[CAS](#) [ADS](#) [Google Scholar](#)

34. 34.

Diekmann, O., Heesterbeek, J. A. P. & Metz, J. A. J. On the definition and the computation of the basic reproduction ratio R_0 in models for infectious diseases in heterogeneous populations. *J. Math. Biol.* **28**, 365–382 (1990).

[MathSciNet](#) [CAS](#) [PubMed](#) [MATH](#) [Google Scholar](#)

35. 35.

Nold, A. Heterogeneity in disease-transmission modeling. *Math. Biosci.* **52**, 227–240 (1980).

[MathSciNet](#) [MATH](#) [Google Scholar](#)

36. 36.

Sattenspiel, L. Population structure and the spread of disease. *Hum. Biol.* **59**, 411–438 (1987).

[CAS](#) [PubMed](#) [Google Scholar](#)

37. 37.

Kiti, M. C. et al. Quantifying social contacts in a household setting of rural Kenya using wearable proximity sensors. *EPJ Data Sci.* **5**, 21 (2016).

[PubMed](#) [PubMed Central](#) [Google Scholar](#)

38. 38.

Cattuto, C. et al. Dynamics of person-to-person interactions from distributed RFID sensor networks. *PLoS One* **5**, e11596 (2010).

[PubMed](#) [PubMed Central](#) [ADS](#) [Google Scholar](#)

39. 39.

Salathé, M. et al. Digital epidemiology. *PLOS Comput. Biol.* **8**, e1002616 (2012).

[PubMed](#) [PubMed Central](#) [Google Scholar](#)

40. 40.

Zhou, Y. et al. Effects of human mobility restrictions on the spread of COVID-19 in Shenzhen, China: a modelling study using mobile phone data. *Lancet Digit. Health* **2**, e417–e424 (2020).

[PubMed](#) [PubMed Central](#) [Google Scholar](#)

41. 41.

Grantz, K. H. et al. The use of mobile phone data to inform analysis of COVID-19 pandemic epidemiology. *Nat. Commun.* **11**, 4961 (2020).

[PubMed](#) [PubMed Central](#) [ADS](#) [Google Scholar](#)

42. 42.

Khataee, H., Scheuring, I., Czirok, A. & Neufeld, Z. Effects of social distancing on the spreading of COVID-19 inferred from mobile phone data. *Sci. Rep.* **11**, 1661 (2021).

[CAS](#) [PubMed](#) [PubMed Central](#) [ADS](#) [Google Scholar](#)

43. 43.

Gao, S. et al. Association of mobile phone location data indications of travel and stay-at-home mandates with COVID-19 infection rates in the US. *JAMA Netw. Open* **3**, e2020485 (2020).

[PubMed](#) [PubMed Central](#) [Google Scholar](#)

44. 44.

Xiong, C., Hu, S., Yang, M., Luo, W. & Zhang, L. Mobile device data reveal the dynamics in a positive relationship between human mobility and COVID-19 infections. *Proc. Natl Acad. Sci. USA* **117**, 27087–27089 (2020).

[CAS](#) [PubMed](#) [PubMed Central](#) [ADS](#) [Google Scholar](#)

45. 45.

Cot, C., Cacciapaglia, G. & Sannino, F. Mining Google and Apple mobility data: temporal anatomy for COVID-19 social distancing. *Sci. Rep.* **11**, 4150 (2021).

[CAS](#) [PubMed](#) [PubMed Central](#) [ADS](#) [Google Scholar](#)

46. 46.

Badr, H. S. et al. Association between mobility patterns and COVID-19 transmission in the USA: a mathematical modelling study. *Lancet Infect. Dis.* **20**, 1247–1254 (2020). **In this study, the authors demonstrate a strong association between mobility patterns measured using aggregated mobile phone data across the USA and the transmission of SARS-CoV-2 at the early stages of the pandemic.**

[CAS](#) [PubMed](#) [PubMed Central](#) [Google Scholar](#)

47. 47.

Stoddard, S. T. et al. House-to-house human movement drives dengue virus transmission. *Proc. Natl Acad. Sci. USA* **110**, 994–999 (2013).

[CAS](#) [PubMed](#) [ADS](#) [Google Scholar](#)

48. 48.

Reiner, R. C., Jr, Stoddard, S. T. & Scott, T. W. Socially structured human movement shapes dengue transmission despite the diffusive effect of mosquito dispersal. *Epidemics* **6**, 30–36 (2014).

[PubMed](#) [PubMed Central](#) [Google Scholar](#)

49. 49.

Salje, H. et al. How social structures, space, and behaviors shape the spread of infectious diseases using chikungunya as a case study. *Proc. Natl Acad. Sci. USA* **113**, 13420–13425 (2016).

[CAS](#) [PubMed](#) [PubMed Central](#) [Google Scholar](#)

50. 50.

World Health Organization. *Closing Data Gaps in Gender* (accessed 2 May 2021); <https://www.who.int/activities/closing-data-gaps-in-gender>

51. 51.

Hébert-Dufresne, L., Althouse, B. M., Scarpino, S. V. & Allard, A. Beyond R_0 : heterogeneity in secondary infections and probabilistic epidemic forecasting. *J. R. Soc. Interface* **17**, 20200393 (2020).

52. 52.

Riley, S. Large-scale spatial-transmission models of infectious disease. *Science* **316**, 1298–1301 (2007).

[CAS](#) [PubMed](#) [ADS](#) [Google Scholar](#)

53. 53.

Simini, F., González, M. C., Maritan, A. & Barabási, A. L. A universal model for mobility and migration patterns. *Nature* **484**, 96–100 (2012).

[CAS](#) [PubMed](#) [ADS](#) [Google Scholar](#)

54. 54.

Xia, Y., Bjørnstad, O. N. & Grenfell, B. T. Measles metapopulation dynamics: a gravity model for epidemiological coupling and dynamics. *Am. Nat.* **164**, 267–281 (2004). **The authors developed a gravity model formulation that described the mobility between populations in England and Wales, and effectively captured the dynamics of measles in the pre-vaccination era.**

[PubMed](#) [Google Scholar](#)

55. 55.

Wesolowski, A., O'Meara, W. P., Eagle, N., Tatem, A. J. & Buckee, C. O. Evaluating spatial interaction models for regional mobility in sub-Saharan Africa. *PLOS Comput. Biol.* **11**, e1004267 (2015).

[PubMed](#) [PubMed Central](#) [ADS](#) [Google Scholar](#)

56. 56.

Marshall, J. M. et al. Key traveller groups of relevance to spatial malaria transmission: a survey of movement patterns in four sub-Saharan African countries. *Malar. J.* **15**, 200 (2016).

[PubMed](#) [PubMed Central](#) [Google Scholar](#)

57. 57.

Marshall, J. M. et al. Mathematical models of human mobility of relevance to malaria transmission in Africa. *Sci. Rep.* **8**, 7713 (2018).

[PubMed](#) [PubMed Central](#) [ADS](#) [Google Scholar](#)

58. 58.

Wesolowski, A. et al. Multinational patterns of seasonal asymmetry in human movement influence infectious disease dynamics. *Nat. Commun.* **8**, 2069 (2017). **In this study, the authors compare seasonal travel patterns using aggregated mobile phone data from Namibia, Pakistan, and Kenya, showing strong seasonal, asymmetric movements on a population level in each country.**

[PubMed](#) [PubMed Central](#) [ADS](#) [Google Scholar](#)

59. 59.

Wesolowski, A. et al. Quantifying seasonal population fluxes driving rubella transmission dynamics using mobile phone data. *Proc. Natl Acad. Sci. USA* **112**, 11114–11119 (2015).

[CAS](#) [PubMed](#) [PubMed Central](#) [ADS](#) [Google Scholar](#)

60. 60.

Mahmud, A. S. et al. Megacities as drivers of national outbreaks: The 2017 chikungunya outbreak in Dhaka, Bangladesh. *PLoS Negl. Trop. Dis.* **15**, e0009106 (2021).

[PubMed](#) [PubMed Central](#) [Google Scholar](#)

61. 61.

Ewing, A., Lee, E. C., Viboud, C. & Bansal, S. Contact, travel, and transmission: The impact of winter holidays on influenza dynamics in the United States. *J. Infect. Dis.* **215**, 732–739 (2017).

[PubMed](#) [Google Scholar](#)

62. 62.

Viboud, C. et al. Synchrony, waves, and spatial hierarchies in the spread of influenza. *Science* **312**, 447–451 (2006).

[CAS](#) [PubMed](#) [ADS](#) [Google Scholar](#)

63. 63.

Wesolowski, A., Eagle, N., Noor, A. M., Snow, R. W. & Buckee, C. O. The impact of biases in mobile phone ownership on estimates of human mobility. *J. R. Soc. Interface* **10**, 20120986 (2013).

[PubMed](#) [PubMed Central](#) [Google Scholar](#)

64. 64.

Wesolowski, A., Eagle, N., Noor, A. M., Snow, R. W. & Buckee, C. O. Heterogeneous mobile phone ownership and usage patterns in Kenya. *PLoS One* **7**, e35319 (2012).

[CAS](#) [PubMed](#) [PubMed Central](#) [ADS](#) [Google Scholar](#)

65. 65.

Sinha, I. et al. Mapping the travel patterns of people with malaria in Bangladesh. *BMC Med.* **18**, 45 (2020).

[PubMed](#) [PubMed Central](#) [Google Scholar](#)

66. 66.

Douine, M. et al. Malaria in gold miners in the Guianas and the Amazon: current knowledge and challenges. *Curr. Trop. Med. Rep.* **7**, 37–47 (2020).

[Google Scholar](#)

67. 67.

Yan, S. D. et al. Digging for care-seeking behaviour among gold miners in the Guyana hinterland: a qualitative doer non-doer analysis of social and behavioural motivations for malaria testing and treatment. *Malar. J.* **19**, 235 (2020).

[PubMed](#) [PubMed Central](#) [Google Scholar](#)

68. 68.

Prothero, R. M. Disease and mobility: a neglected factor in epidemiology. *Int. J. Epidemiol.* **6**, 259–267 (1977).

[CAS](#) [PubMed](#) [Google Scholar](#)

69. 69.

Smith, D. L. et al. Ross, Macdonald, and a theory for the dynamics and control of mosquito-transmitted pathogens. *PLoS Pathog.* **8**, e1002588 (2012).

[CAS](#) [PubMed](#) [PubMed Central](#) [Google Scholar](#)

70. 70.

Feachem, R. G. A. et al. Malaria eradication within a generation: ambitious, achievable, and necessary. *Lancet* **394**, 1056–1112 (2019).

[PubMed](#) [Google Scholar](#)

71. 71.

Njuguna, H. N. et al. Malaria parasitemia among febrile patients seeking clinical care at an outpatient health facility in an urban informal settlement area in Nairobi, Kenya. *Am. J. Trop. Med. Hyg.* **94**, 122–127 (2016).

[CAS](#) [PubMed](#) [PubMed Central](#) [Google Scholar](#)

72. 72.

Heggenhougen, H. K., Hackethal, V. & Vivek, P. *The Behavioural and Social Aspects of Malaria and its Control. An Introduction and Annotated Bibliography* (TDR, WHO, 2003).

73. 73.

World Health Organization. *A Framework for Malaria Elimination* (WHO, 2018).

74. 74.

Chang, H. H. et al. Mapping imported malaria in Bangladesh using parasite genetic and human mobility data. *eLife* **8**, e43481 (2019). **In this study, genomic data of the malaria parasite are combined with travel histories and mobile phone data to quantify the routes and volumes of imported cases of malaria in southeast Bangladesh.**

[PubMed](#) [PubMed Central](#) [Google Scholar](#)

75. 75.

Funk, S., Salathé, M. & Jansen, V. A. A. Modelling the influence of human behaviour on the spread of infectious diseases: a review. *J. R. Soc. Interface* **7**, 1247–1256 (2010).

[PubMed](#) [PubMed Central](#) [Google Scholar](#)

76. 76.

Edmunds, W. J., Eames, K. & Keogh-Brown, M. in *Modeling the Interplay Between Human Behavior and the Spread of Infectious Diseases* 311–321 (Springer, 2013).

77. 77.

Dowdy, D. W., Dye, C. & Cohen, T. Data needs for evidence-based decisions: a tuberculosis modeler's 'wish list'. *Int. J. Tuberc. Lung Dis.* **17**, 866–877 (2013).

[CAS](#) [PubMed](#) [Google Scholar](#)

78. 78.

Houben, R. M. G. J. et al. TIME Impact — a new user-friendly tuberculosis (TB) model to inform TB policy decisions. *BMC Med.* **14**, 56 (2016).

[CAS](#) [PubMed](#) [PubMed Central](#) [Google Scholar](#)

79. 79.

Abuelezam, N. N. et al. Can the heterosexual HIV epidemic be eliminated in South Africa using combination prevention? A modeling analysis. *Am. J. Epidemiol.* **184**, 239–248 (2016).

[PubMed](#) [PubMed Central](#) [Google Scholar](#)

80. 80.

Kremer, M. Integrating behavioral choice into epidemiological models of AIDS. *Q. J. Econ.* **111**, 549–573 (1996).

81. 81.

Chitnis, N., Schapira, A., Smith, T. & Steketee, R. Comparing the effectiveness of malaria vector-control interventions through a mathematical model. *Am. J. Trop. Med. Hyg.* **83**, 230–240 (2010).

[PubMed](#) [PubMed Central](#) [Google Scholar](#)

82. 82.

Childs, L. M. et al. Modelling challenges in context: lessons from malaria, HIV, and tuberculosis. *Epidemics* **10**, 102–107 (2015).

[PubMed](#) [PubMed Central](#) [Google Scholar](#)

83. 83.

Epstein, J. M., Parker, J., Cummings, D. & Hammond, R. A. Coupled contagion dynamics of fear and disease: mathematical and computational explorations. *PLoS One* **3**, e3955 (2008).

[PubMed](#) [PubMed Central](#) [ADS](#) [Google Scholar](#)

84. 84.

Gallotti, R., Valle, F., Castaldo, N., Sacco, P. & De Domenico, M. Assessing the risks of ‘infodemics’ in response to COVID-19 epidemics. *Nat. Hum. Behav.* **4**, 1285–1293 (2020).

[PubMed](#) [Google Scholar](#)

85. 85.

Kissler, S. M. et al. Reductions in commuting mobility correlate with geographic differences in SARS-CoV-2 prevalence in New York City. *Nat. Commun.* **11**, 4674 (2020).

[CAS](#) [PubMed](#) [PubMed Central](#) [ADS](#) [Google Scholar](#)

86. 86.

Scannell Bryan, M. et al. Coronavirus disease 2019 (COVID-19) mortality and neighborhood characteristics in Chicago. *Ann. Epidemiol.* **56**, 47–54.e5 (2021).

[PubMed](#) [Google Scholar](#)

87. 87.

Kishore, N. et al. Lockdowns result in changes in human mobility which may impact the epidemiologic dynamics of SARS-CoV-2. *Sci. Rep.* **11**, 6995 (2021).

[PubMed](#) [PubMed Central](#) [ADS](#) [Google Scholar](#)

88. 88.

Cramer, E. Y. et al. Evaluation of individual and ensemble probabilistic forecasts of COVID-19 mortality in the US. Preprint at <https://doi.org/10.1101/2021.02.03.21250974> (2021). **The authors compared multiple different forecasts of COVID-19 in the USA to evaluate their accuracy, and found that in general, predictions were only accurate on relatively short timescales, and that simple models were often just as accurate as more complex frameworks.**

89. 89.

Viboud, C. et al. The RAPIDD ebola forecasting challenge: synthesis and lessons learnt. *Epidemics* **22**, 13–21 (2018).

[PubMed](#) [Google Scholar](#)

90. 90.

Borcherding, R. K. et al. Modeling of future COVID-19 cases, hospitalizations, and deaths, by vaccination rates and nonpharmaceutical intervention scenarios — United States, April–September 2021. *MMWR Morb. Mortal. Wkly. Rep.* **70**, 719–724 (2021).

[CAS](#) [PubMed](#) [PubMed Central](#) [Google Scholar](#)

91. 91.

Lutz, C. S. et al. Applying infectious disease forecasting to public health: a path forward using influenza forecasting examples. *BMC Public Health* **19**, 1659 (2019).

[PubMed](#) [PubMed Central](#) [Google Scholar](#)

92. 92.

Haushofer, J. & Metcalf, C. J. Which interventions work best in a pandemic? *Science* **368**, 1063–1065 (2020).

[CAS](#) [PubMed](#) [ADS](#) [Google Scholar](#)

93. 93.

LISTSERV 14.4 (accessed 2 May 2021);
<https://web.archive.org/web/20080523225000/http://listserv.linguistlist.org/cgi-bin/wa?A2=ind0407a&L=ads-l&P=8874>

94. 94.

Migration, U. N. *Regional Policies and Response to Manage Pastoral Movements within the ECOWAS Region* (IOM, 2019).

95. 95.

OECD/SWAC. *An Atlas of the Sahara-Sahel: Geography, Economics and Security* (OECD Publishing, 2014).

96. 96.

Post, W. M., DeAngelis, D. L. & Travis, C. C. Endemic disease in environments with spatially heterogeneous host populations. *Math. Biosci.* **63**, 289–302 (1983).

[MathSciNet](#) [MATH](#) [Google Scholar](#)

97. 97.

Watson, R. K. On an epidemic in a stratified population. *J. Appl. Probab.* **9**, 659–666 (1972).

[MathSciNet](#) [MATH](#) [Google Scholar](#)

98. 98.

Rushton, S. & Mautner, A. J. The deterministic model of a simple epidemic for more than one community. *Biometrika* **42**, 126 (1955).

[MathSciNet](#) [MATH](#) [Google Scholar](#)

99. 99.

Etienne, R. S. *Mathematical Models & Methods Meet Metapopulation Management* Thesis, Wageningen University (2002).

100. 100.

Hanski, I. & Simberloff, D. in *Metapopulation Biology* (eds Hanski, I. & Gilpin, M. E.) 5–26 (Academic, 1997).

101. 101.

Hethcote, H. W. An immunization model for a heterogeneous population. *Theor. Popul. Biol.* **14**, 338–349 (1978).

[MathSciNet](#) [CAS](#) [PubMed](#) [MATH](#) [Google Scholar](#)

102. 102.

Anderson, R. M. & May, R. M. Spatial, temporal, and genetic heterogeneity in host populations and the design of immunization programmes. *IMA J. Math. Appl. Med. Biol.* **1**, 233–266 (1984).

[MathSciNet](#) [CAS](#) [PubMed](#) [MATH](#) [Google Scholar](#)

103. 103.

Pinsky, P. & Shonkwiler, R. A gonorrhea model treating sensitive and resistant strains in a multigroup population. *Math. Biosci.* **98**, 103–126 (1990).

[MathSciNet](#) [CAS](#) [PubMed](#) [MATH](#) [Google Scholar](#)

104. 104.

Yorke, J. A., Hethcote, H. W. & Nold, A. Dynamics and control of the transmission of gonorrhea. *Sex. Transm. Dis.* **5**, 51–56 (1978).

[CAS](#) [PubMed](#) [Google Scholar](#)

105. 105.

Hasibeder, G. & Dye, C. Population dynamics of mosquito-borne disease: persistence in a completely heterogeneous environment. *Theor. Popul. Biol.* **33**, 31–53 (1988).

[MathSciNet](#) [CAS](#) [PubMed](#) [MATH](#) [Google Scholar](#)

106. 106.

Dye, C. & Hasibeder, G. Population dynamics of mosquito-borne disease: effects of flies which bite some people more frequently than others. *Trans. R. Soc. Trop. Med. Hyg.* **80**, 69–77 (1986).

[CAS](#) [PubMed](#) [Google Scholar](#)

107. 107.

Hethcote, H. W., Van Ark, J. W. & Karon, J. M. A simulation model of AIDS in San Francisco: II. Simulations, therapy, and sensitivity analysis. *Math. Biosci.* **106**, 223–247 (1991).

[CAS](#) [PubMed](#) [Google Scholar](#)

108. 108.

Lloyd-Smith, J. O., Schreiber, S. J., Kopp, P. E. & Getz, W. M. Superspreading and the effect of individual variation on disease emergence. *Nature* **438**, 355–359 (2005).

109. 109.

Bansal, S., Grenfell, B. T. & Meyers, L. A. When individual behaviour matters: homogeneous and network models in epidemiology. *J. R. Soc. Interface* **4**, 879–891 (2007).

110. 110.

Newman, M. E. J. Spread of epidemic disease on networks. *Phys. Rev. E* **66**, 016128 (2002).

111. 111.

Keeling, M. The implications of network structure for epidemic dynamics. *Theor. Popul. Biol.* **67**, 1–8 (2005).

[PubMed](#) [MATH](#) [Google Scholar](#)

112. 112.

Keeling, M. J. & Eames, K. T. D. Networks and epidemic models. *J. R. Soc. Interface* **2**, 295–307 (2005).

[PubMed](#) [PubMed Central](#) [Google Scholar](#)

113. 113.

Meyers, L. A., Pourbohloul, B., Newman, M. E. J., Skowronski, D. M. & Brunham, R. C. Network theory and SARS: predicting outbreak diversity. *J. Theor. Biol.* **232**, 71–81 (2005).

[MathSciNet](#) [PubMed](#) [MATH](#) [ADS](#) [Google Scholar](#)

114. 114.

Pitzer, V. E. et al. The impact of changes in diagnostic testing practices on estimates of COVID-19 transmission in the United States. *Am. J. Epidemiol.* kwab089 (2021).

115. 115.

Gostic, K. M. et al. Practical considerations for measuring the effective reproductive number R_t . *PLOS Comput. Biol.* **16**, e1008409 (2020).

[CAS](#) [PubMed](#) [PubMed Central](#) [Google Scholar](#)

116. 116.

McGough, S. F., Johansson, M. A., Lipsitch, M. & Menzies, N. A. Nowcasting by Bayesian Smoothing: A flexible, generalizable model for real-time epidemic tracking. *PLOS Comput. Biol.* **16**, e1007735 (2020).

[CAS](#) [PubMed](#) [PubMed Central](#) [ADS](#) [Google Scholar](#)

117. 117.

Greene, S. K. et al. Nowcasting for real-time COVID-19 tracking in New York City: an evaluation using reportable disease data from early in the pandemic. *JMIR Public Health Surveill.* **7**, e25538 (2021).

[PubMed](#) [PubMed Central](#) [Google Scholar](#)

118. 118.

Woolf, S. H. et al. Excess deaths from COVID-19 and other causes, March–July 2020. *J. Am. Med. Assoc.* **324**, 1562–1564 (2020).

[CAS](#) [Google Scholar](#)

119. 119.

Peccia, J. et al. Measurement of SARS-CoV-2 RNA in wastewater tracks community infection dynamics. *Nat. Biotechnol.* **38**, 1164–1167 (2020).

[CAS](#) [PubMed](#) [Google Scholar](#)

120. 120.

Clapham, H. et al. Seroepidemiologic study designs for determining SARS-CoV-2 transmission and immunity. *Emerg. Infect. Dis.* **26**, 1978–1986 (2020).

[CAS](#) [PubMed](#) [PubMed Central](#) [Google Scholar](#)

121. 121.

Metcalf, C. J. E., Viboud, C., Spiro, D. J. & Grenfell, B. T. Using serology with models to clarify the trajectory of the SARS-CoV-2 emerging outbreak. *Trends Immunol.* **41**, 849–851 (2020).

[CAS](#) [PubMed](#) [PubMed Central](#) [Google Scholar](#)

[Download references](#)

Author information

Affiliations

1. Center for Communicable Disease Dynamics, Department of Epidemiology, Harvard T. H. Chan School of Public Health, Boston, MA, USA

Caroline Buckee

2. World Health Organization, Geneva, Switzerland

Abdisalan Noor

3. Department of Anthropology, University of Missouri, Columbia, MO, USA

Lisa Sattenspiel

Authors

1. Caroline Buckee

[View author publications](#)

You can also search for this author in [PubMed](#) [Google Scholar](#)

2. Abdisalan Noor

[View author publications](#)

You can also search for this author in [PubMed](#) [Google Scholar](#)

3. Lisa Sattenspiel

[View author publications](#)

You can also search for this author in [PubMed](#) [Google Scholar](#)

Contributions

C.O.B., A.N. and L.S. all contributed to the planning and writing of this manuscript.

Corresponding author

Correspondence to [Caroline Buckee](#).

Ethics declarations

Competing interests

The authors declare no competing interests.

Additional information

Peer review information *Nature* thanks the anonymous reviewers for their contribution to the peer review of this work.

Publisher's note Springer Nature remains neutral with regard to jurisdictional claims in published maps and institutional affiliations.

Rights and permissions

[Reprints and Permissions](#)

About this article



Check for
updates

Cite this article

Buckee, C., Noor, A. & Sattenspiel, L. Thinking clearly about social aspects of infectious disease transmission. *Nature* **595**, 205–213 (2021).
<https://doi.org/10.1038/s41586-021-03694-x>

[Download citation](#)

- Received: 02 May 2021
- Accepted: 04 June 2021
- Published: 30 June 2021
- Issue Date: 08 July 2021
- DOI: <https://doi.org/10.1038/s41586-021-03694-x>

Comments

By submitting a comment you agree to abide by our [Terms](#) and [Community Guidelines](#). If you find something abusive or that does not comply with our terms or guidelines please flag it as inappropriate.

[Download PDF](#)

Associated Content

Special

[Computational social science](#)

Advertisement

This article was downloaded by **calibre** from <https://www.nature.com/articles/s41586-021-03694-x>

- Perspective
- [Published: 30 June 2021](#)

Human social sensing is an untapped resource for computational social science

- [Mirta Galesic](#) [ORCID: orcid.org/0000-0002-1712-9455^{1,2,3,4}](#),
- [Wändi Bruine de Bruin⁵](#),
- [Jonas Dalege¹](#),
- [Scott L. Feld⁶](#),
- [Frauke Kreuter](#) [ORCID: orcid.org/0000-0002-7339-2645^{7,8}](#),
- [Henrik Olsson¹](#),
- [Drazen Prelec^{9,10,11}](#),
- [Daniel L. Stein¹²](#) &
- [Tamara van der Does](#) [ORCID: orcid.org/0000-0003-0275-6429¹](#)

[Nature](#) volume 595, pages 214–222 (2021) [Cite this article](#)

- 391 Accesses
- 1 Citations
- 160 Altmetric
- [Metrics details](#)

Subjects

- [Human behaviour](#)
- [Interdisciplinary studies](#)

- [Sociology](#)

Abstract

The ability to ‘sense’ the social environment and thereby to understand the thoughts and actions of others allows humans to fit into their social worlds, communicate and cooperate, and learn from others’ experiences. Here we argue that, through the lens of computational social science, this ability can be used to advance research into human sociality. When strategically selected to represent a specific population of interest, human social sensors can help to describe and predict societal trends. In addition, their reports of how they experience their social worlds can help to build models of social dynamics that are constrained by the empirical reality of human social systems.

Access options

Subscribe to Journal

Get full journal access for 1 year

\$199.00

only \$3.90 per issue

[Subscribe](#)

All prices are NET prices.

VAT will be added later in the checkout.

Tax calculation will be finalised during checkout.

Rent or Buy article

Get time limited or full article access on ReadCube.

from \$8.99

[Rent or Buy](#)

All prices are NET prices.

Additional access options:

- [Log in](#)
- [Access through your institution](#)
- [Learn about institutional subscriptions](#)

Fig. 1: Human social sensing as a resource for computational social science.

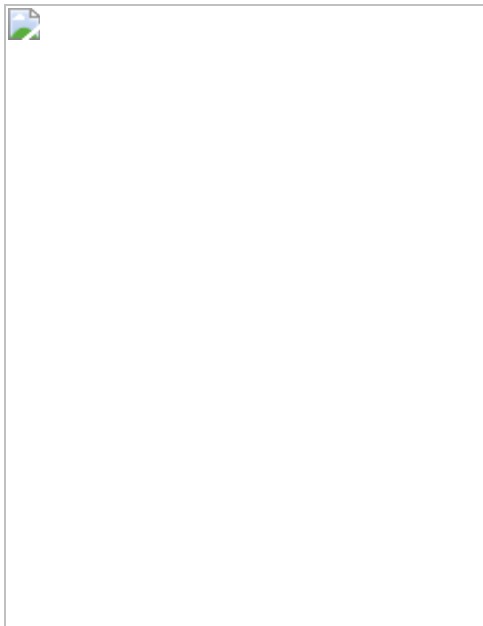
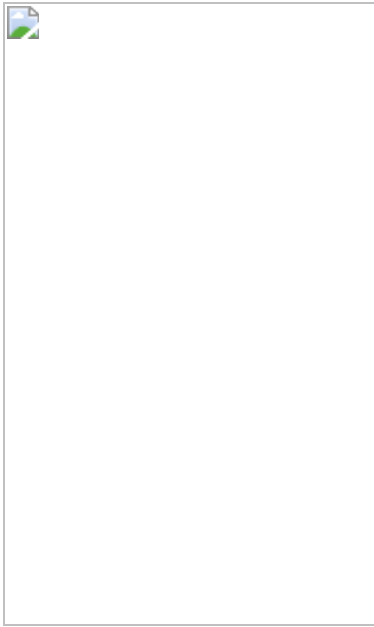


Fig. 2: Friendship paradox.



References

1. 1.

Tomasello, M. *Becoming Human: A Theory of Ontogeny* (Belknap, 2019).

2. 2.

Galesic, M. et al. Asking about social circles improves election predictions. *Nat. Hum. Behav.* **2**, 187–193 (2018). **Shows that human social sensing outperformed traditional polling questions in forecasting for the 2016 US and 2017 French elections.**

[Google Scholar](#)

3. 3.

Olsson, H., Bruine de Bruin, W., Galesic, M. & Prelec, D. Election polling is not dead: a Bayesian bootstrap method yields accurate forecasts. Preprint at <https://doi.org/10.31219/osf.io/nqcg5> (2021). **Developed an information integration method that provided**

accurate forecasts of the 2018 and 2020 US elections by combining own intentions with human social sensor reports.

4. 4.

Bruine de Bruin, W. et al. Asking about social circles improves election predictions even with many political parties. Preprint at <https://doi.org/10.31219/osf.io/8g5ce> (2021). **Shows that human social sensing outperformed traditional polling questions in forecasting for the 2017 Dutch and 2018 Swedish elections.**

5. 5.

Bruine de Bruin, W., Parker, A. M., Galesic, M. & Vardavas, R. Reports of social circles' and own vaccination behavior: a national longitudinal survey. *Health Psychol.* **38**, 975–983 (2019). **Shows that perceived social circle vaccination coverage helps to predict own future vaccination behaviour.**

[PubMed](#) [Google Scholar](#)

6. 6.

Christakis, N. A. & Fowler, J. H. Social network sensors for early detection of contagious outbreaks. *PLoS One* **5**, e12948 (2010). **Shows that asking people about their friends helps to predict outbreaks of contagious diseases.**

[PubMed](#) [PubMed Central](#) [ADS](#) [Google Scholar](#)

7. 7.

Graefe, A. Accuracy of vote expectation surveys in forecasting elections. *Public Opin. Q.* **78**, 204–232 (2014). **Shows that the people's expectations about the election winner help to forecast US elections from 1932 to 2012.**

[Google Scholar](#)

8. 8.

Berg, J. E., Nelson, F. D. & Rietz, T. A. Prediction market accuracy in the long run. *Int. J. Forecast.* **24**, 285–300 (2008). **Shows that prediction markets outperformed polls in forecasting US elections from 1988 to 2004.**

[Google Scholar](#)

9. 9.

Rothschild, D. M. & Wolfers, J. Forecasting elections: Voter intentions versus expectations. *SSRN Electron. J.* <https://doi.org/10.2139/ssrn.1884644> (2011). **Shows that accuracy of human social sensing is likely to stem from people's knowledge about their immediate social environments.**

10. 10.

Garcia-Herranz, M., Moro, E., Cebrian, M., Christakis, N. A. & Fowler, J. H. Using friends as sensors to detect global-scale contagious outbreaks. *PLoS One* **9**, e92413 (2014). **Shows that monitoring the friends of randomly selected Twitter users helps to predict the use of novel hashtags a week earlier than monitoring random users.**

[PubMed](#) [PubMed Central](#) [ADS](#) [Google Scholar](#)

11. 11.

Galesic, M., Olsson, H., Dalege, J., van der Does, T. & Stein, D. L. Integrating social and cognitive aspects of belief dynamics: towards a unifying framework. *J. R. Soc. Interface* **18**, rsif.2020.0857 (2021). **Introduces a unifying framework for modelling both social and cognitive aspects of belief dynamics.**

[Google Scholar](#)

12. 12.

van der Does, T., Stein, D. L., Fedoroff, N. & Galesic, M. Moral and social foundations of beliefs about scientific issues: predicting and understanding belief change. Preprint at <https://doi.org/10.31219/osf.io/zs7dq> (2021). **Develops a statistical-physics-inspired model to show that belief change is more likely when educational interventions decrease belief dissonance and at the same time highlight this dissonance.**

13. 13.

Dalege, J. & van der Does, T. Changing beliefs about scientific issues: the role of moral and social belief networks. Preprint at <https://arxiv.org/abs/2102.10751> (2021). **Shows that dissonance in one's reports on moral and social beliefs predicts belief change.**

14. 14.

Happé, F., Cook, J. L. & Bird, G. The structure of social cognition: in(ter)dependence of sociocognitive processes. *Annu. Rev. Psychol.* **68**, 243–267 (2017).

[PubMed](#) [Google Scholar](#)

15. 15.

Krueger, J. I. & Funder, D. C. Towards a balanced social psychology: causes, consequences, and cures for the problem-seeking approach to social behavior and cognition. *Behav. Brain Sci.* **27**, 313–327, discussion 328–376 (2004).

[PubMed](#) [Google Scholar](#)

16. 16.

Ross, L., Greene, D. & House, P. The “false consensus effect”: an egocentric bias in social perception and attribution processes. *J. Exp. Soc. Psychol.* **13**, 279–301 (1977).

[Google Scholar](#)

17. 17.

Chambers, J. R. & Windschitl, P. D. Biases in social comparative judgments: the role of nonmotivated factors in above-average and comparative-optimism effects. *Psychol. Bull.* **130**, 813–838 (2004).

[PubMed](#) [Google Scholar](#)

18. 18.

Moreno, J. L. *Sociometry, Experimental Method and the Science of Society* (Beacon House, 1951).

19. 19.

Goodman, L. A. Snowball sampling. *Ann. Math. Stat.* **32**, 148–170 (1961).

[MathSciNet](#) [MATH](#) [Google Scholar](#)

20. 20.

Heckathorn, D. D. Respondent-driven sampling: a new approach to the study of hidden populations. *Soc. Probl.* **44**, 174–199 (1997).

[Google Scholar](#)

21. 21.

Killworth, P. D., Johnsen, E. C., McCarty, C., Shelley, G. A. & Bernard, H. R. A social network approach to estimating seroprevalence in the United States. *Soc. Networks* **20**, 23–50 (1998).

[Google Scholar](#)

22. 22.

Centola, D. *How Behavior Spreads: The Science of Complex Contagions* (Princeton Univ. Press, 2018).

23. 23.

Christakis, N. A. & Fowler, J. H. *Connected: The Amazing Power of Social Networks and How They Shape Our Lives* (Harper Collins, 2010).

24. 24.

Moldoveanu, M. C. & Baum, J. A. C. *Epinets: The Epistemic Structure and Dynamics of Social Networks* (Stanford Univ. Press, 2014).

25. 25.

Keusch, F. & Kreuter, F. in *Handbook of Computational Social Science, Volume 1 Theory, Case Studies and Ethics* (eds Engel, U., Quan-Haase, A., Xun Lui, S. & Lyberg, L. E.) (Routledge, 2021). **Describes different sources of digital trace data and issues related to their use in the computational social sciences, including inferential challenges, measures of reproducibility and replicability, and transparency.**

26. 26.

Kreuter, F., Haas, G.-C., Keusch, F., Bähr, S. & Trappmann, M. Collecting survey and smartphone sensor data with an app: opportunities and challenges around privacy and informed consent. *Soc. Sci. Comput. Rev.* **38**, 533–549 (2020).

[Google Scholar](#)

27. 27.

Lazer, D. & Radford, J. Data ex machina: introduction to big data. *Annu. Rev. Sociol.* **43**, 19–39 (2017).

[Google Scholar](#)

28. 28.

Varian, H. R. Big data: new tricks for econometrics. *J. Econ. Perspect.* **28**, 3–28 (2014).

[Google Scholar](#)

29. 29.

Feld, S. L. & McGail, A. Egonets as systematically biased windows on society. *Netw. Sci.* **8**, 399–417 (2020). **Discusses how the friendship paradox biases the information that people receive from their social environments.**

[Google Scholar](#)

30. 30.

Lee, E. et al. Homophily and minority-group size explain perception biases in social networks. *Nat. Hum. Behav.* **3**, 1078–1087 (2019).

[PubMed](#) [PubMed Central](#) [Google Scholar](#)

31. 31.

Lerman, K., Yan, X. & Wu, X.-Z. The “majority illusion” in social networks. *PLoS One* **11**, e0147617 (2016).

[PubMed](#) [PubMed Central](#) [Google Scholar](#)

32. 32.

Chakraborti, A., Toke, I. M., Patriarca, M. & Abergel, F. Econophysics review: II. Agent-based models. *Quant. Finance* **11**, 1013–1041 (2011).

[MathSciNet](#) [Google Scholar](#)

33. 33.

Edelmann, A., Wolff, T., Montagne, D. & Bail, C. A. Computational social science and sociology. *Annu. Rev. Sociol.* **46**, 61–81 (2020).

[Google Scholar](#)

34. 34.

Epstein, J. M. *Agent_Zero: Toward Neurocognitive Foundations for Generative Social Science* (Princeton Univ. Press, 2014).

35. 35.

Miller, J. H. & Page, S. E. *Complex Adaptive Systems: An Introduction to Computational Models of Social Life* (Princeton Univ. Press, 2007).

36. 36.

Pentland, A. *Social Physics: How Social Networks Can Make Us Smarter* (Penguin, 2014). **Describes applications of statistical physics and other analogies for modelling complex social systems.**

37. 37.

Proskurnikov, A. V. & Tempo, R. A tutorial on modeling and analysis of dynamic social networks. Part I. *Annu. Rev. Contr.* **43**, 65–79 (2017).

[Google Scholar](#)

38. 38.

Jung, J., Bramson, A., Crano, W., Page, S. E. & Miller, J. H. Cultural drift, indirect minority influence, network structure and their impacts on cultural change and diversity. *Am. Psychol.* (in the press).

39. 39.

Geanakoplos, J. et al. Getting at systemic risk via an agent-based model of the housing market. *Am. Econ. Rev.* **102**, 53–58 (2012).

[Google Scholar](#)

40. 40.

Hammond, R., Ornstein, J. T., Purcell, R., Haslam, M. D., & Kasman, M. Modeling robustness of COVID-19 containment policies. Preprint at <https://doi.org/10.31219/osf.io/h5ua7> (2021).

41. 41.

Nowak, A., Szamrej, J. & Latané, B. From private attitude to public opinion: a dynamic theory of social impact. *Psychol. Rev.* **97**, 362–376 (1990).

[Google Scholar](#)

42. 42.

Vallacher, R. R., Read, S. J. & Nowak, A. *Computational Social Psychology* (Routledge, 2017).

43. 43.

Enns, P. K., Lagodny, J. & Schuldt, J. P. Understanding the 2016 US presidential polls: the importance of hidden Trump supporters. *Stat. Politics Policy* **8**, 41–63 (2017).

[Google Scholar](#)

44. 44.

Krumpal, I. Determinants of social desirability bias in sensitive surveys: a literature review. *Qual. Quant.* **47**, 2025–2047 (2013).

[Google Scholar](#)

45. 45.

Wang, D., Szymanski, B. K., Abdelzaher, T., Ji, H. & Kaplan, L. The age of social sensing. *Computer* **52**, 36–45 (2019).

[Google Scholar](#)

46. 46.

Tucker, J. et al. Social media, political polarization, and political disinformation: a review of the scientific literature. *SSRN* <https://doi.org/10.2139/ssrn.3144139> (2018).

47. 47.

Smaldino, P. E., Flamson, T. J. & McElreath, R. The evolution of covert signaling. *Sci. Rep.* **8**, 4905 (2018).

[PubMed](#) [PubMed Central](#) [ADS](#) [Google Scholar](#)

48. 48.

Alipourfard, N., Nettasinghe, B., Abeliuk, A., Krishnamurthy, V. & Lerman, K. Friendship paradox biases perceptions in directed networks. *Nat. Commun.* **11**, 707 (2020).

[CAS](#) [PubMed](#) [PubMed Central](#) [ADS](#) [Google Scholar](#)

49. 49.

Sudman, S. & Bradburn, N. M. *Asking Questions: A Practical Guide to Questionnaire Design* (Jossey-Bass, 1982).

50. 50.

Chin, A. & Bruine de Bruin, W. Understanding the formation of consumers' stock market expectations. *J. Consum. Aff.* **51**, 200–210 (2017).

[Google Scholar](#)

51. 51.

Bruine de Bruin, W., Parker, A. M. & Fischhoff, B. Can adolescents predict significant life events? *J. Adolesc. Health* **41**, 208–210 (2007).

[PubMed](#) [Google Scholar](#)

52. 52.

Bruine de Bruin, W., Downs, J. S., Murray, P. & Fischhoff, B. Can female adolescents tell whether they will test positive for Chlamydia infection? *Med. Decis. Making* **30**, 189–193 (2010).

[PubMed](#) [Google Scholar](#)

53. 53.

Hurd, M. D. & McGarry, K. The predictive validity of subjective probabilities of survival. *Econ. J. (Lond.)* **112**, 966–985 (2002).

[Google Scholar](#)

54. 54.

Lewis-Beck, M. S. & Tien, C. Voters as forecasters: a micromodel of election prediction. *Int. J. Forecast.* **15**, 175–184 (1999).

[Google Scholar](#)

55. 55.

Murr, A. E. The wisdom of crowds: what do citizens forecast for the 2015 British General Election? *Elect. Stud.* **41**, 283–288 (2016).

[Google Scholar](#)

56. 56.

Spann, M. & Skiera, B. Internet-based virtual stock markets for business forecasting. *Manage. Sci.* **49**, 1310–1326 (2003).

[Google Scholar](#)

57. 57.

Polgreen, P. M., Nelson, F. D., Neumann, G. R. & Weinstein, R. A. Use of prediction markets to forecast infectious disease activity. *Clin. Infect. Dis.* **44**, 272–279 (2007).

[PubMed](#) [Google Scholar](#)

58. 58.

Spann, M. & Skiera, B. Sports forecasting: a comparison of the forecast accuracy of prediction markets. *J. Forecast.* **28**, 55–72 (2009).

[MathSciNet](#) [Google Scholar](#)

59. 59.

Jussim, L. *Social Perception and Social Reality: Why Accuracy Dominates Bias and Self-Fulfilling Prophecy* (Oxford Univ. Press, 2012).

60. 60.

Brunswik, E. *The Conceptual Framework of Psychology* (Univ. Chicago Press, 1952).

61. 61.

Fiedler, K. Beware of samples! A cognitive-ecological sampling approach to judgment biases. *Psychol. Rev.* **107**, 659–676 (2000).

[CAS](#) [PubMed](#) [Google Scholar](#)

62. 62.

Fiedler, K. & Juslin, P. *Information Sampling and Adaptive Cognition* (Cambridge Univ. Press, 2006).

63. 63.

Gigerenzer, G., Hertwig, R. & Pachur, T. *Heuristics: The Foundations of Adaptive Behavior* (Oxford Univ. Press, 2011).

64. 64.

Pachur, T., Hertwig, R. & Rieskamp, J. Intuitive judgments of social statistics: how exhaustive does sampling need to be? *J. Exp. Soc. Psychol.* **49**, 1059–1077 (2013).

[Google Scholar](#)

65. 65.

Simon, H. A. *Models of Man; Social and Rational* (Wiley, 1957).

66. 66.

Hertwig, R. & Hoffrage, U. *Simple Heuristics in a Social World* (Oxford Univ. Press, 2013).

67. 67.

Schulze, C., Hertwig, R. & Pachur, T. Who you know is what you know: modeling boundedly rational social sampling. *J. Exp. Psychol. Gen.* **150**, 221–241 (2021).

[PubMed](#) [Google Scholar](#)

68. 68.

McPherson, M., Smith-Lovin, L. & Cook, J. M. Birds of a feather: homophily in social networks. *Annu. Rev. Sociol.* **27**, 415–444 (2001).

[Google Scholar](#)

69. 69.

Galesic, M., Olsson, H. & Rieskamp, J. A sampling model of social judgment. *Psychol. Rev.* **125**, 363–390 (2018). **Develops a computational model of social judgment based on people's perceptions of their immediate social environment.**

[PubMed](#) [Google Scholar](#)

70. 70.

Frable, D. E. S. Being and feeling unique: statistical deviance and psychological marginality. *J. Pers.* **61**, 85–110 (1993).

[CAS](#) [PubMed](#) [Google Scholar](#)

71. 71.

Kruger, J. Lake Wobegon be gone! The “below-average effect” and the egocentric nature of comparative ability judgments. *J. Pers. Soc. Psychol.* **77**, 221–232 (1999).

[CAS](#) [PubMed](#) [ADS](#) [Google Scholar](#)

72. 72.

Kruger, J. & Dunning, D. Unskilled and unaware of it: how difficulties in recognizing one's own incompetence lead to inflated self-assessments. *J. Pers. Soc. Psychol.* **77**, 1121–1134 (1999).

[CAS](#) [PubMed](#) [Google Scholar](#)

73. 73.

Sudman, S. & Kalton, G. New developments in the sampling of special populations. *Annu. Rev. Sociol.* **12**, 401–429 (1986).

[Google Scholar](#)

74. 74.

Feld, S. L. Why your friends have more friends than you do. *Am. J. Sociol.* **96**, 1464–1477 (1991). **Introduces the friendship paradox, the phenomenon in which the mean number of friends of friends is always greater than the mean number of friends of individuals.**

[Google Scholar](#)

75. 75.

Cohen, R., Havlin, S. & Ben-Avraham, D. Efficient immunization strategies for computer networks and populations. *Phys. Rev. Lett.* **91**, 247901 (2003).

[PubMed](#) [ADS](#) [Google Scholar](#)

76. 76.

Kumar, V., Krackhardt, D. & Feld, S. Interventions with inversty in unknown networks can help regulate contagion. Preprint at <https://arxiv.org/abs/2105.08758> (2021). **Based on the logic underlying the friendship paradox, this paper develops strategies to use reports from random individuals to identify better connected individuals in networks where the overall structures are unknown or evolving.**

77. 77.

Kim, D. A. et al. Social network targeting to maximise population behaviour change: a cluster randomised controlled trial. *Lancet* **386**, 145–153 (2015).

[PubMed](#) [PubMed Central](#) [Google Scholar](#)

78. 78.

Aggarwal, C. C. & Abdelzaher, T. in *Managing and Mining Sensor Data* 237–297 (Springer, 2013).

79. 79.

Szell, M., Lambiotte, R. & Thurner, S. Multirelational organization of large-scale social networks in an online world. *Proc. Natl Acad. Sci. USA* **107**, 13636–13641 (2010).

[CAS](#) [PubMed](#) [PubMed Central](#) [ADS](#) [Google Scholar](#)

80. 80.

Centola, D. & Macy, M. Complex contagions and the weakness of long ties. *Am. J. Sociol.* **113**, 702–734 (2007).

[Google Scholar](#)

81. 81.

Guilbeault, D., Baronchelli, A. & Centola, D. Experimental evidence for scale-induced category convergence across populations. *Nat. Commun.* **12**, 327 (2021).

[CAS](#) [PubMed](#) [PubMed Central](#) [ADS](#) [Google Scholar](#)

82. 82.

Bruch, E. & Mare, R. D. Neighborhood choice and neighborhood change. *Am. J. Sociol.* **112**, 667–709 (2006).

[Google Scholar](#)

83. 83.

Bruch, E., Feinberg, F. & Lee, K. Y. Extracting multistage screening rules from online dating activity data. *Proc. Natl Acad. Sci. USA* **113**, 10530–10535 (2016).

[CAS](#) [PubMed](#) [PubMed Central](#) [Google Scholar](#)

84. 84.

Yang, V. C., Abrams, D. M., Kernell, G. & Motter, A. E. Why are U.S. parties so polarized? A “satisficing” dynamical model. *SIAM Rev.* **62**, 646–657 (2020).

[MathSciNet](#) [MATH](#) [Google Scholar](#)

85. 85.

Dalege, J. et al. Toward a formalized account of attitudes: The Causal Attitude Network (CAN) model. *Psychol. Rev.* **123**, 2–22 (2016).

Introduces a measurement model of attitudes relying on network principles.

[PubMed](#) [Google Scholar](#)

86. 86.

Jackson, M. O. *Social and Economic Networks* (Princeton Univ. Press, 2010).

87. 87.

Jędrzejewski, A. & Sznajd-Weron, K. Statistical physics of opinion formation: is it a SPOOF? *C. R. Phys.* **20**, 244–261 (2019).

[ADS](#) [Google Scholar](#)

88. 88.

Redner, S. Reality-inspired voter models: a mini-review. *C. R. Phys.* **20**, 275–292 (2019).

[CAS](#) [ADS](#) [Google Scholar](#)

89. 89.

Simon, H. A. Invariants of human behavior. *Annu. Rev. Psychol.* **41**, 1–20 (1990).

[CAS](#) [PubMed](#) [Google Scholar](#)

90. 90.

Durkheim, E. *The Division of Labour in Society* (trans. Simpson, G.) (Free Press, 1893).

91. 91.

Thomas, W. I. & Swaine Thomas, D. *The Child in America: Behaviour Problems and Programs* (Knopf, 1928).

92. 92.

DiMaggio, P. Culture and cognition. *Annu. Rev. Sociol.* **23**, 263–287 (1997).

[Google Scholar](#)

93. 93.

Johnson, C., Dowd, T. J. & Ridgeway, C. L. Legitimacy as a social process. *Annu. Rev. Sociol.* **32**, 53–78 (2006).

[Google Scholar](#)

94. 94.

Newman, M. E. J. Network structure from rich but noisy data. *Nat. Phys.* **14**, 542–545 (2018).

[CAS](#) [Google Scholar](#)

95. 95.

Smith, E. R. & Zárate, M. A. Exemplar-based model of social judgment. *Psychol. Rev.* **99**, 3–21 (1992).

[Google Scholar](#)

96. 96.

Denrell, J. Why most people disapprove of me: experience sampling in impression formation. *Psychol. Rev.* **112**, 951–978 (2005).

[PubMed](#) [Google Scholar](#)

97. 97.

Gonzalez, C., Ben-Asher, N., Martin, J. M. & Dutt, V. A cognitive model of dynamic cooperation with varied interdependency information. *Cogn. Sci.* **39**, 457–495 (2015).

[PubMed](#) [Google Scholar](#)

98. 98.

Cialdini, R. B. & Goldstein, N. J. Social influence: compliance and conformity. *Annu. Rev. Psychol.* **55**, 591–621 (2004).

[PubMed](#) [Google Scholar](#)

99. 99.

Efferson, C., Lalive, R., Richerson, P. J., McElreath, R. & Lubell, M. Conformists and mavericks: the empirics of frequency-dependent cultural transmission. *Evol. Hum. Behav.* **29**, 56–64 (2008).

[Google Scholar](#)

100. 100.

McElreath, R., Wallin, A. & Fasolo, B. in *Simple Heuristics in a Social World* (eds Hertwig, R. & Hoffrage, U.) 381–408 (Oxford Univ. Press, 2013).

101. 101.

Tump, A. N., Pleskac, T. J. & Kurvers, R. H. J. M. Wise or mad crowds? The cognitive mechanisms underlying information cascades. *Sci. Adv.* **6**, eabb0266 (2020).

[PubMed](#) [PubMed Central](#) [ADS](#) [Google Scholar](#)

102. 102.

Moussaïd, M., Kämmer, J. E., Analytis, P. P. & Neth, H. Social influence and the collective dynamics of opinion formation. *PLoS One* **8**, e78433 (2013).

[PubMed](#) [PubMed Central](#) [ADS](#) [Google Scholar](#)

103. 103.

Analytis, P. P., Barkoczi, D. & Herzog, S. M. Social learning strategies for matters of taste. *Nat. Hum. Behav.* **2**, 415–424 (2018).

[PubMed](#) [Google Scholar](#)

104. 104.

Molleman, L. et al. Strategies for integrating disparate social information. *Proc. R. Soc. Lond. B* **287**, 20202413 (2020).

[Google Scholar](#)

105. 105.

Boyd, R. & Richerson, P. J. *Culture and the Evolutionary Process* (Univ. Chicago Press, 1985).

106. 106.

Degroot, M. H. Reaching a consensus. *J. Am. Stat. Assoc.* **69**, 118–121 (1974).

[MATH](#) [Google Scholar](#)

107. 107.

Condorcet, M. *Essai sur l'Application de l'Analyse à la Probabilité des Décisions Rendues à la Pluralité des Voix* [Essay on the Application of Analysis to the Probability of Majority Decisions] (Imprimerie Royale, 1785).

108. 108.

Krapivsky, P. L. & Redner, S. Dynamics of majority rule in two-state interacting spin systems. *Phys. Rev. Lett.* **90**, 238701 (2003).

[CAS](#) [PubMed](#) [ADS](#) [Google Scholar](#)

109. 109.

Hoppitt, W. & Laland, K. N. *Social Learning: An Introduction to Mechanisms, Methods, and Models* (Princeton Univ. Press, 2013).

110. 110.

Galesic, M. & Stein, D. L. Statistical physics models of belief dynamics: theory and empirical tests. *Phys. A Stat. Mech. Appl.* **519**, 275–294 (2019).

[Google Scholar](#)

111. 111.

Marr, D. *Vision* (Freeman, 1982).

112. 112.

Anderson, J. R. *The Adaptive Character of Thought* (Lawrence Erlbaum, 1990).

113. 113.

Chater, N., Tenenbaum, J. B. & Yuille, A. Probabilistic models of cognition: conceptual foundations. *Trends Cogn. Sci.* **10**, 287–291 (2006).

[PubMed](#) [Google Scholar](#)

114. 114.

Baker, C., Saxe, R., Tenenbaum, J. & Baker, C. L. Bayesian theory of mind: modeling joint belief-desire attribution. In *Proc. Annual Meeting of the Cognitive Science Society* 2469–2474 (2011).

115. 115.

Krafft, P. M., Shmueli, E., Griffiths, T. L., Tenenbaum, J. B. & Pentland, A. S. Bayesian collective learning emerges from heuristic social learning. *Cognition* **212**, 104469 (2021).

[CAS](#) [PubMed](#) [Google Scholar](#)

116. 116.

Baltag, A., Christoff, Z., Rendsvig, R. K. & Smets, S. Dynamic epistemic logics of diffusion and prediction in social networks. *Stud. Log.* **107**, 489–531 (2019).

[MathSciNet](#) [MATH](#) [Google Scholar](#)

117. 117.

Schweighofer, S., Schweitzer, F. & Garcia, D. A weighted balance model of opinion hyperpolarization. *JASSS* **23**, 5 (2020). **Proposes a model of belief change based on balanced networks accounting for the importance of related issues and other individuals.**

[Google Scholar](#)

118. 118.

Schweitzer, F., Krivachy, T. & Garcia, D. An agent-based model of opinion polarization driven by emotions. *Complexity* **2020**, 1–11 (2020).

[Google Scholar](#)

119. 119.

Castellano, C., Fortunato, S. & Loreto, V. Statistical physics of social dynamics. *Rev. Mod. Phys.* **81**, 591–646 (2009). **Reviews many models of social dynamics inspired by analogies from statistical physics.**

[ADS](#) [Google Scholar](#)

120. 120.

Perc, M. et al. Statistical physics of human cooperation. *Phys. Rep.* **687**, 1–51 (2017).

[MathSciNet](#) [MATH](#) [ADS](#) [Google Scholar](#)

121. 121.

Dalege, J., Borsboom, D., van Harreveld, F. & van der Maas, H. L. J. The attitudinal entropy (AE) framework as a general theory of individual attitudes. *Psychol. Inq.* **29**, 175–193 (2018). **Develops a general theory on individual attitudes using a statistical physics framework.**

[Google Scholar](#)

122. 122.

Minh Pham, T., Kondor, I., Hanel, R. & Thurner, S. The effect of social balance on social fragmentation. *J. R. Soc. Interface* **17**, 20200752 (2020).

[PubMed](#) [PubMed Central](#) [Google Scholar](#)

123. 123.

Rodriguez, N., Bollen, J. & Ahn, Y.-Y. Collective dynamics of belief evolution under cognitive coherence and social conformity. *PLoS One* **11**, e0165910 (2016). **Proposes a belief change model that combines social and cognitive factors as interacting networks driven towards stable triads.**

[PubMed](#) [PubMed Central](#) [Google Scholar](#)

124. 124.

Salganik, M. J. *Bit by Bit: Social Research in the Digital Age* (Princeton Univ. Press, 2018).

125. 125.

Pikler, A. G. Utility theories in field physics and mathematical economics (I). *Br. J. Philos. Sci.* **5**, 47–58 (1954).

[Google Scholar](#)

126. 126.

Festinger, L. *A Theory of Cognitive Dissonance* (Stanford Univ. Press, 1957).

127. 127.

Lewenstein, M., Nowak, A. & Latané, B. Statistical mechanics of social impact. *Phys. Rev. A* **45**, 763–776 (1992).

[MathSciNet](#) [CAS](#) [PubMed](#) [ADS](#) [Google Scholar](#)

128. 128.

Morone, F. & Makse, H. A. Influence maximization in complex networks through optimal percolation. *Nature* **524**, 65–68 (2015).

[CAS](#) [PubMed](#) [ADS](#) [Google Scholar](#)

129. 129.

Haven, E. & Khrennikov, A. *Quantum Social Science* (Cambridge Univ. Press, 2013).

130. 130.

Bettencourt, L. M. A., Cintrón-Arias, A., Kaiser, D. I. & Castillo-Chávez, C. The power of a good idea: quantitative modeling of the spread of ideas from epidemiological models. *Phys. A Stat. Mech. Appl.* **364**, 513–536 (2006).

[Google Scholar](#)

131. 131.

Daley, D. J. & Kendall, D. G. Epidemics and rumours. *Nature* **204**, 1118 (1964).

[CAS](#) [PubMed](#) [ADS](#) [Google Scholar](#)

132. 132.

Henrich, J. & McElreath, R. The evolution of cultural evolution. *Evol. Anthropol.* **12**, 123–135 (2003).

[Google Scholar](#)

133. 133.

Holyoak, K. J. & Thagard, P. *Mental Leaps: Analogy in Creative Thought* (MIT Press, 1995).

134. 134.

Gigerenzer, G. From tools to theories: a heuristic of discovery in cognitive psychology. *Psychol. Rev.* **98**, 254–267 (1991).

[Google Scholar](#)

135. 135.

Dasgupta, A., Kumar, R. & Sivakumar, D. Social sampling. In *Proc. 18th ACM SIGKDD International Conference on Knowledge Discovery and Data Mining* 235 (ACM Press, 2012).

136. 136.

Nettasinghe, B. & Krishnamurthy, V. ‘What do your friends think?’: efficient polling methods for networks using friendship paradox. *IEEE Trans. Knowl. Data Eng.* **33**, 1291–1305 (2019).

[Google Scholar](#)

137. 137.

Kim, D., Gile, K. J., Guarino, H. & Mateu-Gelabert, P. Inferring bivariate association from respondent-driven sampling data. *J. R. Stat. Soc. Ser. C* **70**, 415–433 (2021).

[MathSciNet](#) [Google Scholar](#)

138. 138.

Gile, K. J. & Handcock, M. S. Respondent-driven sampling: an assessment of current methodology. *Sociol. Methodol.* **40**, 285–327 (2010).

[PubMed](#) [PubMed Central](#) [Google Scholar](#)

139. 139.

Kim, B. J. & Handcock, M. S. Population size estimation using multiple respondent-driven sampling surveys. *J. Surv. Stat. Methodol.* **9**, 94–120 (2021).

[PubMed](#) [Google Scholar](#)

140. 140.

Berchenko, Y., Rosenblatt, J. D. & Frost, S. D. W. Modeling and analyzing respondent-driven sampling as a counting process. *Biometrics* **73**, 1189–1198 (2017).

[MathSciNet](#) [PubMed](#) [MATH](#) [Google Scholar](#)

141. 141.

Crawford, F. W., Wu, J. & Heimer, R. Hidden population size estimation from respondent-driven sampling: a network approach. *J. Am. Stat. Assoc.* **113**, 755–766 (2018).

[MathSciNet](#) [CAS](#) [PubMed](#) [PubMed Central](#) [MATH](#) [Google Scholar](#)

142. 142.

Klingwort, J., Buelens, B. & Schnell, R. Capture–recapture techniques for transport survey estimate adjustment using permanently installed highway-sensors. *Soc. Sci. Comput. Rev.* <https://doi.org/10.1177/0894439319874684> (2019).

143. 143.

Tourangeau, R., Rips, L. T. & Rasinski, K. *The Psychology of Survey Response* (Cambridge Univ. Press, 2000).

144. 144.

Batchelder, W. H. & Romney, A. K. Test theory without an answer key. *Psychometrika* **53**, 71–92 (1988).

[MathSciNet](#) [MATH](#) [Google Scholar](#)

145. 145.

Romney, A. K., Weller, S. C. & Batchelder, W. H. Culture as consensus: a theory of culture and informant accuracy. *Am. Anthropol.* **88**, 313–338 (1986).

[Google Scholar](#)

146. 146.

Prelec, D. A Bayesian truth serum for subjective data. *Science* **306**, 462–466 (2004). **Develops a Bayesian algorithm that incentivizes honest answers in a survey even if honesty is not independently verifiable.**

[CAS](#) [PubMed](#) [ADS](#) [Google Scholar](#)

147. 147.

Miller, N., Resnick, P. & Zeckhauser, R. Eliciting informative feedback: the peer-prediction method. *Manage. Sci.* **51**, 1359–1373 (2005).

[Google Scholar](#)

148. 148.

Baillon, A. Bayesian markets to elicit private information. *Proc. Natl Acad. Sci. USA* **114**, 7958–7962 (2017).

[MathSciNet](#) [CAS](#) [PubMed](#) [PubMed Central](#) [MATH](#) [Google Scholar](#)

149. 149.

Cvitanić, J., Prelec, D., Riley, B. & Tereick, B. Honesty via choice-matching. *Am. Econ. Rev. Insights* **1**, 179–192 (2019).

[Google Scholar](#)

150. 150.

John, L. K., Loewenstein, G. & Prelec, D. Measuring the prevalence of questionable research practices with incentives for truth telling. *Psychol. Sci.* **23**, 524–532 (2012).

[PubMed](#) [Google Scholar](#)

151. 151.

Prelec, D., Seung, H. S. & McCoy, J. A solution to the single-question crowd wisdom problem. *Nature* **541**, 532–535 (2017). **Addressing Galton's original crowd wisdom problem** (*Nature* 1907), this study provides a Bayesian criterion that identifies correct answers to a multiple choice questions even if the majority of polled individuals are wrong.

[CAS](#) [PubMed](#) [ADS](#) [Google Scholar](#)

152. 152.

Foster, I., Ghani, R., Jarmin, R. S., Kreuter, F. & Lane, J. *Big Data and Social Science: A Practical Guide to Methods and Tools* (CRC Press, 2017). **Provides practical guidance on combining methods and tools from computer science, statistics, and social science.**

153. 153.

Lane, J. *Democratizing Our Data: A Manifesto* (MIT Press, 2020).

154. 154.

Haas, G. C., Trappmann, M., Keusch, F., Bähr, S. & Kreuter, F. Using geofences to collect survey data: lessons learned from the IAB-SMART study. *Surv. Methods Insights Field* <https://doi.org/10.13094/SMIF-2020-00023> (2020).

155. 155.

Christen, P., Ranbaduge, T. & Schnell, R. *Linking Sensitive Data: Methods and Techniques for Practical Privacy-Preserving Information*

Sharing (Springer, 2020).

156. 156.

Couper, M. P. Is the sky falling? New technology, changing media, and the future of surveys. *Surv. Res. Methods* **7**, 145–156 (2013).

[Google Scholar](#)

157. 157.

Hill, C. et al. *Big Data Meets Survey Science: A Collection of Innovative Methods* (Wiley, 2020).

158. 158.

Schnell, R. *Survey-Interviews: Methoden standardisierter Befragungen* (Springer, 2019).

159. 159.

Olsson, H., Barman-Adhikari, A., Galesic, M., Hsu, H.-T. & Rice, E. Cognitive strategies for peer judgments. Preprint at <https://doi.org/10.31219/osf.io/s3hxj> (2021).

160. 160.

van der Maas, H. L. J., Dalege, J. & Waldorp, L. The polarization within and across individuals: the hierarchical Ising opinion model. *J. Complex Netw.* **8**, cnaa010 (2020).

[MathSciNet](#) [Google Scholar](#)

161. 161.

Fails, J. A. & Olsen, D. R. Interactive machine learning. in *Proc. 8th International Conference on Intelligent User Interfaces* 39 (ACM Press, 2003).

162. 162.

Jiang, L., Liu, S. & Chen, C. Recent research advances on interactive machine learning. *J. Vis.* **22**, 401–417 (2019).

[Google Scholar](#)

163. 163.

Ware, M., Frank, E., Holmes, G., Hall, M. & Witten, I. H. Interactive machine learning: letting users build classifiers. *Int. J. Hum. Comput. Stud.* **55**, 281–292 (2001).

[MATH](#) [Google Scholar](#)

164. 164.

Fortuna, P. & Nunes, S. A survey on automatic detection of hate speech in text. *ACM Comput. Surv.* **51**, 1–30 (2018).

[Google Scholar](#)

165. 165.

Garland, J., Ghazi-Zahedi, K., Young, J.-G., Hébert-Dufresne, L. & Galesic, M. Impact and dynamics of hate and counter speech online. Preprint at <https://arxiv.org/abs/2009.08392> (2020).

166. 166.

Leader Maynard, J. & Benesch, S. Dangerous speech and dangerous ideology: an integrated model for monitoring and prevention. *Genocide Stud. Prev.* **9**, 70–95 (2016).

[Google Scholar](#)

167. 167.

Abeliuk, A., Benjamin, D. M., Morstatter, F. & Galstyan, A. Quantifying machine influence over human forecasters. *Sci. Rep.* **10**, 15940 (2020).

[CAS](#) [PubMed](#) [PubMed Central](#) [ADS](#) [Google Scholar](#)

168. 168.

Huber, D. J. et al. MATRICS: A system for human-machine hybrid forecasting of geopolitical events. In *2019 IEEE Intl Conf. Big Data* 2028–2032 (IEEE, 2019).

169. 169.

Morstatter, F. et al. SAGE: a hybrid geopolitical event forecasting system. In *Intl Joint Conf. Artificial Intelligence* 6557–6559 (2019).

170. 170.

Evans, J. Social computing unhinged. *J. Soc. Comput.* **1**, 1–13 (2020).

[Google Scholar](#)

171. 171.

Wagner, C. et al. Measuring algorithmically infused societies. *Nature* <https://doi.org/10.1038/s41586-021-03666-1> (2021).

172. 172.

Hidalgo, C. A., Orghiain, D., Canals, J. A., De Almeida, F. & Martín, N. *How Humans Judge Machines* (MIT Press, 2021).

173. 173.

Rahwan, I. et al. Machine behaviour. *Nature* **568**, 477–486 (2019).

[CAS](#) [PubMed](#) [ADS](#) [Google Scholar](#)

174. 174.

Lazer, D. et al. Meaningful measures of human society in the twenty-first century. *Nature* <https://doi.org/10.1038/s41586-021-03660-7> (2021).

175. 175.

Hofman, J. M. et al. Integrating explanation and prediction in computational social science. *Nature* <https://doi.org/10.1038/s41586-021-03659-0> (2021).

176. 176.

Trouille, L., Lintott, C. J. & Fortson, L. F. Citizen science frontiers: Efficiency, engagement, and serendipitous discovery with human-machine systems. *Proc. Natl Acad. Sci. USA* **116**, 1902–1909 (2019).

[CAS](#) [PubMed](#) [PubMed Central](#) [Google Scholar](#)

177. 177.

Outbreaks near me; <https://outbreaksnearme.org/us/en-US/>

178. 178.

Schurz, M. et al. Toward a hierarchical model of social cognition: a neuroimaging meta-analysis and integrative review of empathy and theory of mind. *Psychol. Bull.* **147**, 293–327 (2021).

[PubMed](#) [Google Scholar](#)

179. 179.

Adolphs, R. Cognitive neuroscience of human social behaviour. *Nat. Rev. Neurosci.* **4**, 165–178 (2003).

[CAS](#) [PubMed](#) [Google Scholar](#)

180. 180.

Feng, C. et al. Common brain networks underlying human social interactions: evidence from large-scale neuroimaging meta-analysis. *Neurosci. Biobehav. Rev.* **126**, 289–303 (2021).

[PubMed](#) [Google Scholar](#)

181. 181.

Estes, W. K. *Classification and Cognition* (Oxford Univ. Press, 1994).

182. 182.

Rieskamp, J. & Hoffrage, U. Inferences under time pressure: how opportunity costs affect strategy selection. *Acta Psychol.* **127**, 258–276 (2008).

[Google Scholar](#)

183. 183.

Ambady, N. & Rosenthal, R. Thin slices of expressive behavior as predictors of interpersonal consequences: a meta-analysis. *Psychol. Bull.* **111**, 256–274 (1992).

[Google Scholar](#)

184. 184.

Jern, A. & Kemp, C. A decision network account of reasoning about other people's choices. *Cognition* **142**, 12–38 (2015).

[PubMed](#) [PubMed Central](#) [Google Scholar](#)

185. 185.

Zacks, R. T. & Hasher, L. in *Etc. Frequency Processing and Cognition* Vol. 6, 21–36 (Oxford Univ. Press, 2002).

186. 186.

Conrad, F. G., Brown, N. R. & Cashman, E. R. Strategies for estimating behavioural frequency in survey interviews. *Memory* **6**, 339–366 (1998).

[CAS](#) [PubMed](#) [Google Scholar](#)

187. 187.

Lynn, C. W. & Bassett, D. S. How humans learn and represent networks. *Proc. Natl Acad. Sci. USA* **117**, 29407–29415 (2020).

[MathSciNet](#) [CAS](#) [PubMed](#) [PubMed Central](#) [Google Scholar](#)

188. 188.

Gagné, F. M. & Lydon, J. E. Bias and accuracy in close relationships: an integrative review. *Pers. Soc. Psychol. Rev.* **8**, 322–338 (2004).

[PubMed](#) [Google Scholar](#)

189. 189.

Goel, S., Mason, W. & Watts, D. J. Real and perceived attitude agreement in social networks. *J. Pers. Soc. Psychol.* **99**, 611–621 (2010).

[PubMed](#) [Google Scholar](#)

190. 190.

Dawes, R. M. Statistical criteria for establishing a truly false consensus effect. *J. Exp. Soc. Psychol.* **25**, 1–17 (1989).

[Google Scholar](#)

191. 191.

Nisbett, R. E. & Kunda, Z. Perception of social distributions. *J. Pers. Soc. Psychol.* **48**, 297–311 (1985).

[CAS](#) [PubMed](#) [Google Scholar](#)

192. 192.

Galesic, M., Olsson, H. & Rieskamp, J. Social sampling explains apparent biases in judgments of social environments. *Psychol. Sci.* **23**, 1515–1523 (2012).

[PubMed](#) [Google Scholar](#)

193. 193.

Killworth, P. D. & Bernard, H. Informant accuracy in social network data. *Hum. Organ.* **35**, 269–286 (1976).

[Google Scholar](#)

194. 194.

Bernard, H. R. & Killworth, P. D. Informant accuracy in social network data II. *Hum. Commun. Res.* **4**, 3–18 (1977).

[Google Scholar](#)

195. 195.

Freeman, L. C., Romney, A. K. & Freeman, S. C. Cognitive structure and informant accuracy. *Am. Anthropol.* **89**, 310–325 (1987).

[Google Scholar](#)

196. 196.

Chang, L. & Krosnick, J. A. Measuring the frequency of regular behaviors: comparing the “typical week” to the “past week”. *Sociol. Methodol.* **33**, 55–80 (2003).

[CAS](#) [Google Scholar](#)

197. 197.

Feld, S. L. & Carter, W. C. Detecting measurement bias in respondent reports of personal networks. *Soc. Networks* **24**, 365–383 (2002).

[ADS](#) [Google Scholar](#)

198. 198.

Banerjee, A. V., Chandrasekhar, A. G., Duflo, E. & Jackson, M. O. Using gossips to spread information: theory and evidence from two randomized controlled trials. *MIT Department of Economics Working Paper No. 14–15* <http://www.ssrn.com/abstract=2425379> (2014).

[Download references](#)

Acknowledgements

We thank F. Gerdon, J. Foster, R. Kurvers, M. Schierholz, P. Schenk, T. Wallsten, and C. Wagner for comments on an earlier version of the manuscript, as well as our many collaborators for their contributions to this work. M.G., H.O., T.v.d.D., J.D., W.B.d.B., and D.P. were supported in part by grants from the National Science Foundation (M.G.: DRMS-1757211; H.O., M.G., and J.D.: BCS-1918490; M.G., H.O., and T.v.d.D.: DRMS-1949432; H.O., M.G., W.B.d.B., and D.P.: MMS-2019982), M.G., T.v.d.D., and D.L.S. were supported in part by a grant from the National Institute of Food and Agriculture (NIFA 2018-67023-27677), and J.D. was supported in part by an EU Horizon 2020 Marie Curie Global Fellowship (no. 889682).

Author information

Affiliations

1. Santa Fe Institute, Santa Fe, NM, USA

Mirta Galesic, Jonas Dalege, Henrik Olsson & Tamara van der Does

2. Complexity Science Hub Vienna, Vienna, Austria

Mirta Galesic

3. Vermont Complex Systems Center, University of Vermont, Burlington,
VT, USA

Mirta Galesic

4. Harding Center for Risk Literacy, University of Potsdam, Potsdam,
Germany

Mirta Galesic

5. Sol Price School of Public Policy, University of South California, Los
Angeles, CA, USA

Wändi Bruine de Bruin

6. Department of Sociology, Purdue University, West Lafayette, IN, USA

Scott L. Feld

7. Joint Program in Survey Methodology, University of Maryland,
Maryland, MD, USA

Frauke Kreuter

8. Ludwig Maximilians Universität München, München, Germany

Frauke Kreuter

9. Sloan School of Management, MIT, Cambridge, MA, USA

Drazen Prelec

10. Department of Economics, MIT, Cambridge, MA, USA

Drazen Prelec

11. Department of Brain and Cognitive Sciences, MIT, Cambridge, MA, USA

Drazen Prelec

12. Department of Physics and Courant Institute of Mathematical Sciences, New York University, New York, NY, USA

Daniel L. Stein

Authors

1. Mirta Galesic

[View author publications](#)

You can also search for this author in [PubMed](#) [Google Scholar](#)

2. Wändi Bruine de Bruin

[View author publications](#)

You can also search for this author in [PubMed](#) [Google Scholar](#)

3. Jonas Dalege

[View author publications](#)

You can also search for this author in [PubMed](#) [Google Scholar](#)

4. Scott L. Feld

[View author publications](#)

You can also search for this author in [PubMed](#) [Google Scholar](#)

5. Frauke Kreuter

[View author publications](#)

You can also search for this author in [PubMed](#) [Google Scholar](#)

6. Henrik Olsson

[View author publications](#)

You can also search for this author in [PubMed](#) [Google Scholar](#)

7. Drazen Prelec

[View author publications](#)

You can also search for this author in [PubMed](#) [Google Scholar](#)

8. Daniel L. Stein

[View author publications](#)

You can also search for this author in [PubMed](#) [Google Scholar](#)

9. Tamara van der Does

[View author publications](#)

You can also search for this author in [PubMed](#) [Google Scholar](#)

Contributions

All authors contributed equally to the writing of this Perspective.

Corresponding author

Correspondence to [Mirta Galesic](#).

Ethics declarations

Competing interests

The authors declare no competing interests.

Additional information

Peer review information *Nature* thanks Jacob Foster, Ralf Kurvers and the other, anonymous, reviewer(s) for their contribution to the peer review of this work.

Publisher's note Springer Nature remains neutral with regard to jurisdictional claims in published maps and institutional affiliations.

Rights and permissions

[Reprints and Permissions](#)

About this article



Check for
updates

Cite this article

Galesic, M., Bruine de Bruin, W., Dalege, J. *et al.* Human social sensing is an untapped resource for computational social science. *Nature* **595**, 214–222 (2021). <https://doi.org/10.1038/s41586-021-03649-2>

[Download citation](#)

- Received: 23 February 2021
- Accepted: 17 May 2021
- Published: 30 June 2021
- Issue Date: 08 July 2021
- DOI: <https://doi.org/10.1038/s41586-021-03649-2>

Further reading

- **Integrating explanation and prediction in computational social science**

- Jake M. Hofman
- , Duncan J. Watts
- , Susan Athey
- , Filiz Garip
- , Thomas L. Griffiths
- , Jon Kleinberg
- , Helen Margetts
- , Sendhil Mullainathan
- , Matthew J. Salganik
- , Simine Vazire
- , Alessandro Vespignani
- & Tal Yarkoni

Nature (2021)

Comments

By submitting a comment you agree to abide by our [Terms](#) and [Community Guidelines](#). If you find something abusive or that does not comply with our terms or guidelines please flag it as inappropriate.

[Access through your institution](#)

[Change institution](#)

[Buy or subscribe](#)

Associated Content

Special

[**Computational social science**](#)

Advertisement

This article was downloaded by **calibre** from <https://www.nature.com/articles/s41586-021-03649-2>

| [Section menu](#) | [Main menu](#) |

- Article
- [Published: 07 July 2021](#)

r-Process elements from magnetorotational hypernovae

- [D. Yong](#) [ORCID: orcid.org/0000-0002-6502-1406](#)^{1,2},
- [C. Kobayashi](#)^{2,3},
- [G. S. Da Costa](#) [ORCID: orcid.org/0000-0001-7019-649X](#)^{1,2},
- [M. S. Bessell](#)¹,
- [A. Chiti](#) [ORCID: orcid.org/0000-0002-7155-679X](#)⁴,
- [A. Frebel](#) [ORCID: orcid.org/0000-0002-2139-7145](#)⁴,
- [K. Lind](#)⁵,
- [A. D. Mackey](#) [ORCID: orcid.org/0000-0002-6529-8093](#)^{1,2},
- [T. Nordlander](#) [ORCID: orcid.org/0000-0001-5344-8069](#)^{1,2},
- [M. Asplund](#)⁶,
- [A. R. Casey](#) [ORCID: orcid.org/0000-0003-0174-0564](#)^{2,7},
- [A. F. Marino](#)⁸,
- [S. J. Murphy](#) [ORCID: orcid.org/0000-0003-4932-7699](#)^{1,9} &
- [B. P. Schmidt](#) [ORCID: orcid.org/0000-0002-8538-9195](#)¹

[Nature](#) volume **595**, pages 223–226 (2021) [Cite this article](#)

- 501 Altmetric
- [Metrics details](#)

Subjects

- [Early universe](#)
- [Stars](#)
- [Stellar evolution](#)

Abstract

Neutron-star mergers were recently confirmed as sites of rapid-neutron-capture (r-process) nucleosynthesis^{1,2,3}. However, in Galactic chemical evolution models, neutron-star mergers alone cannot reproduce the observed element abundance patterns of extremely metal-poor stars, which indicates the existence of other sites of r-process nucleosynthesis^{4,5,6}. These sites may be investigated by studying the element abundance patterns of chemically primitive stars in the halo of the Milky Way, because these objects retain the nucleosynthetic signatures of the earliest generation of stars^{7,8,9,10,11,12,13}. Here we report the element abundance pattern of the extremely metal-poor star SMSS J200322.54–114203.3. We observe a large enhancement in r-process elements, with very low overall metallicity. The element abundance pattern is well matched by the yields of a single 25-solar-mass magnetorotational hypernova. Such a hypernova could produce not only the r-process elements, but also light elements during stellar evolution, and iron-peak elements during explosive nuclear burning. Hypernovae are often associated with long-duration γ -ray bursts in the nearby Universe⁸. This connection indicates that similar explosions of fast-spinning strongly magnetized stars occurred during the earliest epochs of star formation in our Galaxy.

Access options

Subscribe to Journal

Get full journal access for 1 year

\$199.00

only \$3.90 per issue

[Subscribe](#)

All prices are NET prices.
VAT will be added later in the checkout.

Tax calculation will be finalised during checkout.

Rent or Buy article

Get time limited or full article access on ReadCube.

from \$8.99

[Rent or Buy](#)

All prices are NET prices.

Additional access options:

- [Log in](#)
- [Access through your institution](#)
- [Learn about institutional subscriptions](#)

Fig. 1: r-Process element abundance pattern of SMSS 2003–1142.

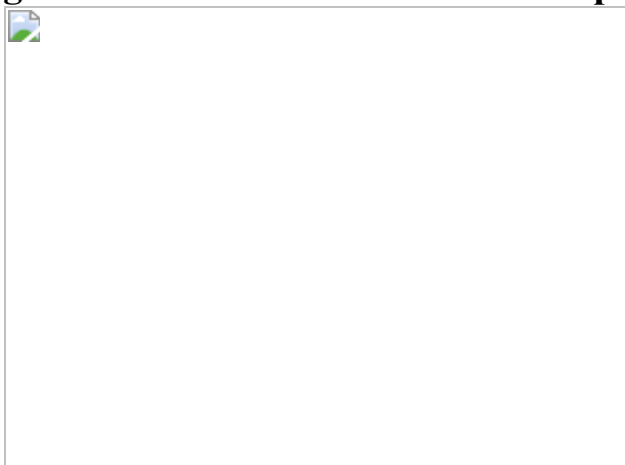
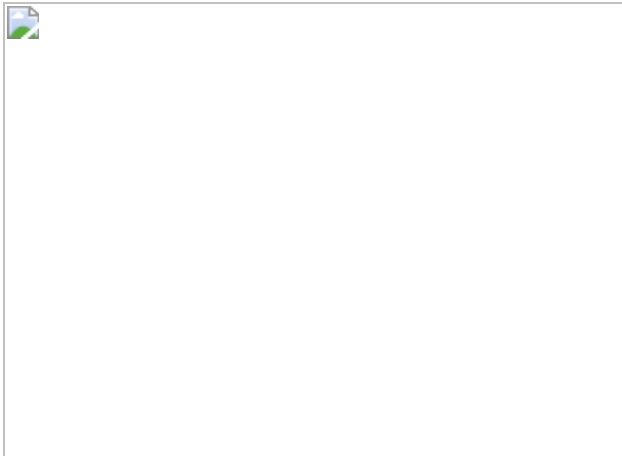


Fig. 2: Comparison of models and data.



Data availability

The data used in this study are available in the ESO archive (https://archive.eso.org/eso/eso_archive_main.html) under program ID 2103.D-5062(A).

Code availability

The stellar line analysis program MOOG is available at <https://www.as.utexas.edu/~chris/moog.html>. The stellar model atmospheres are available at <http://kurucz.harvard.edu/grids.html>.

References

1. 1.

Ji, A. P., Frebel, A., Chiti, A. & Simon, J. D. r-Process enrichment from a single event in an ancient dwarf galaxy. *Nature* **531**, 610–613 (2016).

[CAS](#) [PubMed](#) [PubMed Central](#) [ADS](#) [Google Scholar](#)

2. 2.

Pian, E. et al. Spectroscopic identification of r-process nucleosynthesis in a double neutron-star merger. *Nature* **551**, 67–70 (2017).

[CAS](#) [PubMed](#) [PubMed Central](#) [ADS](#) [Google Scholar](#)

3. 3.

Kasen, D., Metzger, B., Barnes, J., Quataert, E. & Ramirez-Ruiz, E. Origin of the heavy elements in binary neutron-star mergers from a gravitational-wave event. *Nature* **551**, 80–84 (2017).

[PubMed](#) [PubMed Central](#) [ADS](#) [Google Scholar](#)

4. 4.

Winteler, C. et al. Magnetorotationally driven supernovae as the origin of early galaxy r-process elements? *Astrophys. J.* **750**, L22 (2012).

[ADS](#) [Google Scholar](#)

5. 5.

Haynes, C. J. & Kobayashi, C. Galactic simulations of r-process elemental abundances. *Mon. Not. R. Astron. Soc.* **483**, 5123–5134 (2019).

[CAS](#) [ADS](#) [Google Scholar](#)

6. 6.

Siegel, D. M., Barnes, J. & Metzger, B. D. Collapsars as a major source of r-process elements. *Nature* **569**, 241–244 (2019).

[CAS](#) [PubMed](#) [PubMed Central](#) [ADS](#) [Google Scholar](#)

7. 7.

Umeda, H. & Nomoto, K. First-generation black-hole-forming supernovae and the metal abundance pattern of a very iron-poor star.

Nature **422**, 871–873 (2003).

[CAS](#) [PubMed](#) [PubMed Central](#) [ADS](#) [Google Scholar](#)

8. 8.

Nomoto, K., Kobayashi, C. & Tominaga, N. Nucleosynthesis in stars and the chemical enrichment of galaxies. *Annu. Rev. Astron. Astrophys.* **51**, 457–509 (2013).

[CAS](#) [ADS](#) [Google Scholar](#)

9. 9.

Frebel, A. & Norris, J. E. Near-field cosmology with extremely metal-poor stars. *Annu. Rev. Astron. Astrophys.* **53**, 631–688 (2015).

[CAS](#) [ADS](#) [Google Scholar](#)

10. 10.

Bessell, M. S. et al. Nucleosynthesis in a primordial supernova: carbon and oxygen abundances in SMSS J031300.36–670839.3. *Astrophys. J.* **806**, L16 (2015).

[ADS](#) [Google Scholar](#)

11. 11.

Nordlander, T. et al. 3D NLTE analysis of the most iron-deficient star, SMSS0313–6708. *Astron. Astrophys.* **597**, A6 (2017).

[Google Scholar](#)

12. 12.

Ishigaki, M. N. et al. The initial mass function of the first stars inferred from extremely metal-poor stars. *Astrophys. J.* **857**, 46 (2018).

[ADS](#) [Google Scholar](#)

13. 13.

Ezzeddine, R. et al. Evidence for an aspherical population III supernova explosion inferred from the hyper-metal-poor star HE 1327–2326. *Astrophys. J.* **876**, 97 (2019).

[CAS](#) [ADS](#) [Google Scholar](#)

14. 14.

Wolf, C. et al. SkyMapper southern survey: first data release (DR1). *Publ. Astron. Soc. Aust.* **35**, e010 (2018).

[ADS](#) [Google Scholar](#)

15. 15.

Da Costa, G. S. et al. The SkyMapper DR1.1 search for extremely metal-poor stars. *Mon. Not. R. Astron. Soc.* **489**, 5900–5918 (2019).

[ADS](#) [Google Scholar](#)

16. 16.

Maeder, A. & Meynet, G. Rotating massive stars: from first stars to gamma ray bursts. *Rev. Mod. Phys.* **84**, 25–63 (2012).

[CAS](#) [ADS](#) [Google Scholar](#)

17. 17.

Sneden, C. S., Cowan, J. J. & Gallino, R. Neutron-capture elements in the early galaxy. *Annu. Rev. Astron. Astrophys.* **46**, 241–288 (2008).

[CAS](#) [ADS](#) [Google Scholar](#)

18. 18.

Kobayashi, C., Karakas, A. I. & Lugardo, M. The origin of elements from carbon to uranium. *Astrophys. J.* **900**, 179 (2020).

[CAS](#) [ADS](#) [Google Scholar](#)

19. 19.

Symbalisty, E. M. D. Magnetorotational iron core collapse. *Astrophys. J.* **285**, 729–746 (1984).

[CAS](#) [ADS](#) [Google Scholar](#)

20. 20.

Nishimura, N., Takiwaki, T. & Thielemann, F.-K. The r-process nucleosynthesis in the various jet-like explosions of magnetorotational core-collapse supernovae. *Astrophys. J.* **810**, 109 (2015).

[ADS](#) [Google Scholar](#)

21. 21.

Kobayashi, C. et al. Galactic chemical evolution: carbon through zinc. *Astrophys. J.* **653**, 1145–1171 (2006).

[CAS](#) [ADS](#) [Google Scholar](#)

22. 22.

Lattimer, J. M. & Schramm, D. N. Black-hole-neutron-star collisions. *Astrophys. J.* **192**, L145–L147 (1974).

[ADS](#) [Google Scholar](#)

23. 23.

Abbott, B. P. et al. GW170817: observation of gravitational waves from a binary neutron star inspiral. *Phys. Rev. Lett.* **119**, 161101 (2017).

[CAS](#) [PubMed](#) [PubMed Central](#) [ADS](#) [Google Scholar](#)

24. 24.

Wanajo, S. et al. Production of all the r-process nuclides in the dynamical ejecta of neutron star mergers. *Astrophys. J.* **789**, L39 (2014).

[ADS](#) [Google Scholar](#)

25. 25.

Janka, H.-T. Explosion mechanisms of core-collapse supernovae. *Annu. Rev. Nucl. Part. Sci.* **62**, 407–451 (2012).

[CAS](#) [ADS](#) [Google Scholar](#)

26. 26.

Bruenn, S. W. et al. The development of explosions in axisymmetric ab initio core-collapse supernova simulations of 12–25 M_⊙ stars. *Astrophys. J.* **818**, 123 (2016).

[ADS](#) [Google Scholar](#)

27. 27.

MacFadyen, A. I. & Woosley, S. E. Collapsars: gamma-ray bursts and explosions in “failed supernovae”. *Astrophys. J.* **524**, 262–289 (1999).

[CAS](#) [ADS](#) [Google Scholar](#)

28. 28.

Metzger, B. D., Giannios, D., Thompson, T. A., Bucciantini, N. & Quataert, E. The protomagnetar model for gamma-ray bursts. *Mon. Not. R. Astron. Soc.* **413**, 2031–2056 (2011).

[ADS](#) [Google Scholar](#)

29. 29.

Dopita, M. et al. The Wide Field Spectrograph (WiFeS): performance and data reduction. *Astrophys. Space Sci.* **327**, 245–257 (2010).

[ADS](#) [Google Scholar](#)

30. 30.

Gustafsson, B. et al. A grid of MARCS model atmospheres for late-type stars. I. Methods and general properties. *Astron. Astrophys.* **486**, 951–970 (2008).

[CAS](#) [ADS](#) [Google Scholar](#)

31. 31.

Bernstein, R., Shectman, S. A., Gunnels, S. M., Mochnacki, S. & Athey, A. E. MIKE: a double echelle spectrograph for the Magellan telescopes at Las Campanas Observatory. *Proc. SPIE* **4841**, 1694–1704 (2003).

[ADS](#) [Google Scholar](#)

32. 32.

Kelson, D. D. Optimal techniques in two-dimensional spectroscopy: background subtraction for the 21st century. *Publ. Astron. Soc. Pacif.* **115**, 688–699 (2003).

[ADS](#) [Google Scholar](#)

33. 33.

Dekker, H., D’Odorico, S., Kaufer, A., Delabre, B. & Kotzlowski, H. Design, construction, and performance of UVES, the echelle spectrograph for the UT2 Kueyen Telescope at the ESO Paranal. *Proc. SPIE* **4008**, 534–545 (2000).

[ADS](#) [Google Scholar](#)

34. 34.

Norris, J. et al. The most metal-poor stars. I. Discovery, data, and atmospheric parameters. *Astrophys. J.* **762**, 25 (2013).

[ADS](#) [Google Scholar](#)

35. 35.

Yong, D. et al. The most metal-poor stars. II. Chemical abundances of 190 metal-poor stars including 10 new stars with $[\text{Fe}/\text{H}] \leq -3.5$. *Astrophys. J.* **762**, 26 (2013).

[ADS](#) [Google Scholar](#)

36. 36.

Gaia Collaboration. Gaia early data release 3: summary of the contents and survey properties. *Astron. Astrophys.* **469**, A1 (2021).

[Google Scholar](#)

37. 37.

Yong, D. et al. A chemical signature from fast-rotating low-metallicity massive stars: ROA 276 in ω Centauri. *Astrophys. J.* **837**, 176 (2017).

[ADS](#) [Google Scholar](#)

38. 38.

Sneden, C. The nitrogen abundance of the very metal-poor star HD 122563. *Astrophys. J.* **184**, 839–849 (1973).

[CAS](#) [ADS](#) [Google Scholar](#)

39. 39.

Sobeck, J. et al. The abundances of neutron-capture species in the very metal-poor globular cluster M15: a uniform analysis of red giant branch and red horizontal branch stars. *Astron. J.* **141**, 175 (2011).

[ADS](#) [Google Scholar](#)

40. 40.

Castelli, F. & Kurucz, R. L. New grids of ATLAS9 model atmospheres. In *Proc. IAU Symp. No. 210 Modelling of Stellar Atmospheres* (eds Piskunov, N. et al.) poster A20 (2003).

41. 41.

Placco, V. et al. Carbon-enhanced metal-poor star frequencies in the Galaxy: corrections for the effect of evolutionary status on carbon abundances. *Astrophys. J.* **797**, 21 (2014).

[CAS](#) [ADS](#) [Google Scholar](#)

42. 42.

Mackereth, J. T. & Bovy, J. Fast estimation of orbital parameters in Milky Way-like potentials. *Publ. Astron. Soc. Pacif.* **130**, 114501 (2018).

[ADS](#) [Google Scholar](#)

43. 43.

Cordoni, G. et al. Exploring the Galaxy's halo and very metal-weak thick disk with SkyMapper and Gaia DR2. *Mon. Not. R. Astron. Soc.* **503**, 2539–2561 (2021).

[ADS](#) [Google Scholar](#)

44. 44.

Mösta, P. et al. Magnetorotational core-collapse supernovae in three dimensions. *Astrophys. J.* **785**, L29 (2014).

[ADS](#) [Google Scholar](#)

45. 45.

Kuroda, T., Arcones, A., Takiwaki, T. & Kotake, K. Magnetorotational explosion of a massive star supported by neutrino heating in general relativistic three-dimensional simulations. *Astrophys. J.* **896**, 102 (2020).

[CAS](#) [ADS](#) [Google Scholar](#)

46. 46.

Obergaulinger, M. & Aloy, M.-A. Magnetorotational core collapse of possible GRB progenitors. III. Three-dimensional models. *Mon. Not. R. Astron. Soc.* **503**, 4942–4963 (2021).

[ADS](#) [Google Scholar](#)

47. 47.

Takiwaki, T., Kotake, K. & Sato, K. Special relativistic simulations of magnetically dominated jets in collapsing massive stars. *Astrophys. J.* **691**, 1360 (2009).

[ADS](#) [Google Scholar](#)

48. 48.

Kobayashi, C., Ishigaki, M. N., Tominaga, N. & Nomoto, K. The origin of low $[\alpha/\text{Fe}]$ ratios in extremely metal-poor stars. *Astrophys. J.* **785**, L5 (2014).

[ADS](#) [Google Scholar](#)

49. 49.

Reichert, M., Obergaulinger, M., Eichler, M., Aloy, M. A. & Arcones, A. Nucleosynthesis in magneto-rotational supernovae. *Mon. Not. R. Astron. Soc.* **501**, 5733–5745 (2021).

[ADS](#) [Google Scholar](#)

50. 50.

Placco, V. et al. The r-process alliance: the peculiar chemical abundance pattern of RAVE J183013.5–455510. *Astrophys. J.* **897**, 78 (2020).

[CAS](#) [ADS](#) [Google Scholar](#)

51. 51.

Choplin, A., Tominaga, N. & Meyer, B. S. A strong neutron burst in jet-like supernovae of spinstars. *Astron. Astrophys.* **639**, A126 (2020).

[CAS](#) [ADS](#) [Google Scholar](#)

52. 52.

Skinner, D. & Wise, J. H. Cradles of the first stars: self-shielding, halo masses, and multiplicity. *Mon. Not. R. Astron. Soc.* **492**, 4386–4397 (2020).

[CAS](#) [ADS](#) [Google Scholar](#)

53. 53.

Mennekens, N. & Vanbeveren, D. Massive double compact object mergers: gravitational wave sources and r-process element production sites. *Astron. Astrophys.* **564**, A134 (2014).

[ADS](#) [Google Scholar](#)

54. 54.

Belczynski, K. et al. The origin of the first neutron star–neutron star merger. *Astron. Astrophys.* **615**, A91 (2018).

[Google Scholar](#)

55. 55.

Vigna-Gómez, A. et al. On the formation history of Galactic double neutron stars. *Mon. Not. R. Astron. Soc.* **481**, 4009–4029 (2018).

[ADS](#) [Google Scholar](#)

56. 56.

van de Voort, F. et al. Neutron star mergers and rare core-collapse supernovae as sources of r-process enrichment in simulated galaxies. *Mon. Not. R. Astron. Soc.* **494**, 4867–4883 (2020).

[ADS](#) [Google Scholar](#)

57. 57.

Goriely, S., Bauswein, A. & Janka, H.-T. r-process nucleosynthesis in dynamically ejected matter of neutron star mergers. *Astrophys. J.* **738**, L32 (2011).

[ADS](#) [Google Scholar](#)

[Download references](#)

Acknowledgements

This paper includes data gathered with the 6.5-m Magellan Telescopes located at Las Campanas Observatory, Chile, and is based on observations collected at the European Southern Observatory under ESO programme DDT 2103.D-5062(A). This research was supported by the Australian Research Council Centre of Excellence for All Sky Astrophysics in 3 Dimensions (ASTRO 3D), through project number CE170100013. C.K.

acknowledges funding from the UK Science and Technology Facility Council (STFC) through grant ST/M000958/1 and ST/ R000905/1, and the Stromlo Distinguished Visitor Program at ANU. K.L. acknowledges funds from the European Research Council (ERC) under the European Union's Horizon 2020 research and innovation programme (grant agreement number 852977). A.F.M. acknowledges support from the European Union's Horizon 2020 research and innovation programme under Marie Skłodowska-Curie grant agreement number 797100. A.R.C. acknowledges Australian Research Council grant DE190100656.

Author information

Affiliations

1. Research School of Astronomy and Astrophysics, Australian National University, Canberra, Australian Capital Territory, Australia
D. Yong, G. S. Da Costa, M. S. Bessell, A. D. Mackey, T. Nordlander, S. J. Murphy & B. P. Schmidt
2. ARC Centre of Excellence for All Sky Astrophysics in 3 Dimensions (ASTRO 3D), Canberra, Australian Capital Territory, Australia
D. Yong, C. Kobayashi, G. S. Da Costa, A. D. Mackey, T. Nordlander & A. R. Casey
3. Centre for Astrophysics Research, Department of Physics, Astronomy and Mathematics, University of Hertfordshire, Hatfield, UK
C. Kobayashi
4. Department of Physics and Kavli Institute for Astrophysics and Space Research, Massachusetts Institute of Technology, Cambridge, MA, USA
A. Chiti & A. Frebel

5. Department of Astronomy, Stockholm University, AlbaNova
University Center, Stockholm, Sweden

K. Lind

6. Max Planck Institute for Astrophysics, Garching, Germany

M. Asplund

7. School of Physics and Astronomy, Monash University, Melbourne,
Victoria, Australia

A. R. Casey

8. Istituto Nazionale di Astrofisica - Osservatorio Astronomico di
Arcetri, Florence, Italy

A. F. Marino

9. School of Science, The University of New South Wales, Canberra,
Australian Capital Territory, Australia

S. J. Murphy

Authors

1. D. Yong

[View author publications](#)

You can also search for this author in [PubMed](#) [Google Scholar](#)

2. C. Kobayashi

[View author publications](#)

You can also search for this author in [PubMed](#) [Google Scholar](#)

3. G. S. Da Costa

[View author publications](#)

You can also search for this author in [PubMed](#) [Google Scholar](#)

4. M. S. Bessell

[View author publications](#)

You can also search for this author in [PubMed](#) [Google Scholar](#)

5. A. Chiti

[View author publications](#)

You can also search for this author in [PubMed](#) [Google Scholar](#)

6. A. Frebel

[View author publications](#)

You can also search for this author in [PubMed](#) [Google Scholar](#)

7. K. Lind

[View author publications](#)

You can also search for this author in [PubMed](#) [Google Scholar](#)

8. A. D. Mackey

[View author publications](#)

You can also search for this author in [PubMed](#) [Google Scholar](#)

9. T. Nordlander

[View author publications](#)

You can also search for this author in [PubMed](#) [Google Scholar](#)

10. M. Asplund

[View author publications](#)

You can also search for this author in [PubMed](#) [Google Scholar](#)

11. A. R. Casey

[View author publications](#)

You can also search for this author in [PubMed](#) [Google Scholar](#)

12. A. F. Marino

[View author publications](#)

You can also search for this author in [PubMed](#) [Google Scholar](#)

13. S. J. Murphy

[View author publications](#)

You can also search for this author in [PubMed](#) [Google Scholar](#)

14. B. P. Schmidt

[View author publications](#)

You can also search for this author in [PubMed](#) [Google Scholar](#)

Contributions

G.S.D.C., M.S.B., M.A., A.D.M., A.F.M., S.J.M. and T.N. were involved in the target selection and low-resolution spectroscopic observation campaigns. D.Y., G.S.D.C., A.C., A.F. and T.N. were involved in the high-resolution spectroscopic observations. K.L. and T.N. computed the non-LTE corrections. The manuscript was written by D.Y., C.K. and G.S.D.C., with contributions from all authors.

Corresponding author

Correspondence to [D. Yong](#).

Ethics declarations

Competing interests

The authors declare no competing interests.

Additional information

Peer review information *Nature* thanks Timothy Beers and Kim Venn for their contribution to the peer review of this work. Peer reviewer reports are available.

Publisher's note Springer Nature remains neutral with regard to jurisdictional claims in published maps and institutional affiliations.

Extended data figures and tables

Extended Data Fig. 1 Spectrum of SMSS 2003–1142.

a, b, Spectrum synthesis fit to the 4,810-Å Zn i line (**a**) and the 4,129-Å Eu ii line (**b**). The observed spectra are shown as small circles, the best-fitting synthetic spectrum is shown as the solid black line and the yellow region indicates ± 0.2 dex from the best fit.

Extended Data Fig. 2 Abundance ratios in halo stars.

a–f, Element to Fe ratios, [X/Fe], as a function of metallicity, [Fe/H], based on literature data²⁰ (small crosses), for C (**a**), N (**b**), Zn (**c**), Ba (**d**), Eu (**e**) and Th (**f**). The lines are the Galactic chemical evolution model predictions for the solar neighbourhood²⁰. SMSS 2003–1142 is shown as the large five-pointed star. The locations of well-studied r-process-rich stars (CS 22892–052, HD 122563, CS 29497–004, CS 31082–001 and RAVE J183013.5–455510) are highlighted by large symbols. Arrow indicate upper limits.

Supplementary information

Peer Review File

Rights and permissions

[Reprints and Permissions](#)

About this article



Check for
updates

Cite this article

Yong, D., Kobayashi, C., Da Costa, G.S. *et al.* r-Process elements from magnetorotational hypernovae. *Nature* **595**, 223–226 (2021).

<https://doi.org/10.1038/s41586-021-03611-2>

[Download citation](#)

- Received: 05 November 2020
- Accepted: 04 May 2021
- Published: 07 July 2021
- Issue Date: 08 July 2021
- DOI: <https://doi.org/10.1038/s41586-021-03611-2>

Comments

By submitting a comment you agree to abide by our [Terms](#) and [Community Guidelines](#). If you find something abusive or that does not comply with our terms or guidelines please flag it as inappropriate.

[Access through your institution](#)

[Change institution](#)

[Buy or subscribe](#)

Advertisement

This article was downloaded by **calibre** from <https://www.nature.com/articles/s41586-021-03611-2>

| [Section menu](#) | [Main menu](#) |

- Article
- [Published: 07 July 2021](#)

Quantum phases of matter on a 256-atom programmable quantum simulator

- [Sepehr Ebadi](#)¹,
- [Tout T. Wang](#)¹,
- [Harry Levine](#)¹,
- [Alexander Keesling](#)^{1,2},
- [Giulia Semeghini](#)¹,
- [Ahmed Omran](#)^{1,2},
- [Dolev Bluvstein](#)¹,
- [Rhine Samajdar](#) [ORCID: orcid.org/0000-0001-5171-7798](#)¹,
- [Hannes Pichler](#)^{3,4},
- [Wen Wei Ho](#) [ORCID: orcid.org/0000-0001-7702-2900](#)^{1,5},
- [Soonwon Choi](#) [ORCID: orcid.org/0000-0002-1247-062X](#)⁶,
- [Subir Sachdev](#) [ORCID: orcid.org/0000-0002-2432-7070](#)¹,
- [Markus Greiner](#)¹,
- [Vladan Vuletić](#) [ORCID: orcid.org/0000-0002-9786-0538](#)⁷ &
- [Mikhail D. Lukin](#) [ORCID: orcid.org/0000-0002-8658-1007](#)¹

[Nature](#) volume **595**, pages 227–232 (2021) [Cite this article](#)

- 1 Citations
- 112 Altmetric
- [Metrics details](#)

Subjects

- [Phase transitions and critical phenomena](#)
- [Quantum simulation](#)
- [Ultracold gases](#)

Abstract

Motivated by far-reaching applications ranging from quantum simulations of complex processes in physics and chemistry to quantum information processing¹, a broad effort is currently underway to build large-scale programmable quantum systems. Such systems provide insights into strongly correlated quantum matter^{2,3,4,5,6}, while at the same time enabling new methods for computation^{7,8,9,10} and metrology¹¹. Here we demonstrate a programmable quantum simulator based on deterministically prepared two-dimensional arrays of neutral atoms, featuring strong interactions controlled by coherent atomic excitation into Rydberg states¹². Using this approach, we realize a quantum spin model with tunable interactions for system sizes ranging from 64 to 256 qubits. We benchmark the system by characterizing high-fidelity antiferromagnetically ordered states and demonstrating quantum critical dynamics consistent with an Ising quantum phase transition in (2 + 1) dimensions¹³. We then create and study several new quantum phases that arise from the interplay between interactions and coherent laser excitation¹⁴, experimentally map the phase diagram and investigate the role of quantum fluctuations. Offering a new lens into the study of complex quantum matter, these observations pave the way for investigations of exotic quantum phases, non-equilibrium entanglement dynamics and hardware-efficient realization of quantum algorithms.

Access options

Subscribe to Journal

Get full journal access for 1 year

\$199.00

only \$3.90 per issue

[Subscribe](#)

All prices are NET prices.

VAT will be added later in the checkout.

Tax calculation will be finalised during checkout.

Rent or Buy article

Get time limited or full article access on ReadCube.

from \$8.99

[Rent or Buy](#)

All prices are NET prices.

Additional access options:

- [Log in](#)
- [Access through your institution](#)
- [Learn about institutional subscriptions](#)

Fig. 1: Programmable two-dimensional arrays of strongly interacting Rydberg atoms.

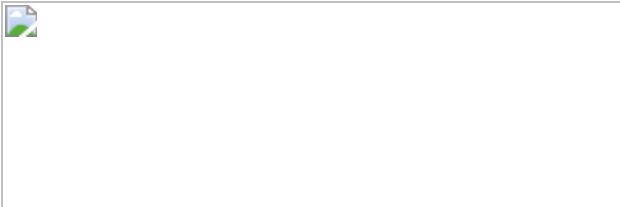


Fig. 2: Benchmarking of quantum simulator using chequerboard ordering.

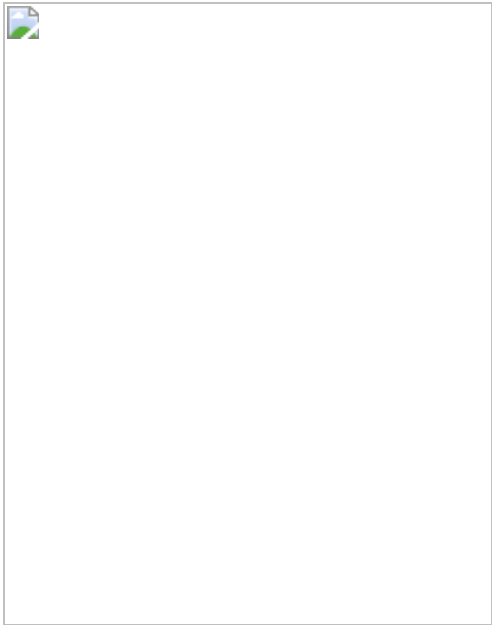


Fig. 3: Observation of the $(2 + 1)$ D Ising quantum phase transition on a 16×16 array.

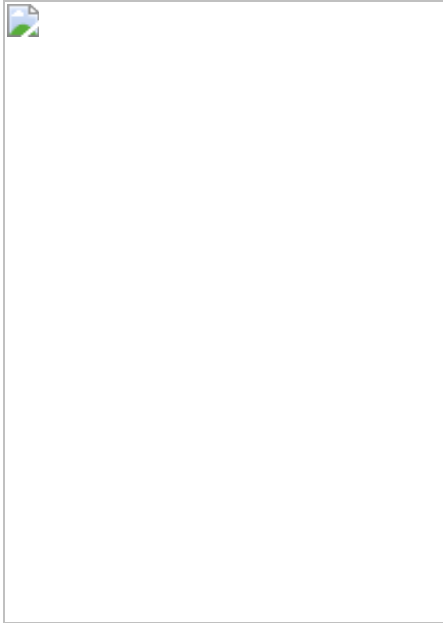


Fig. 4: Phase diagram of the two-dimensional square lattice.

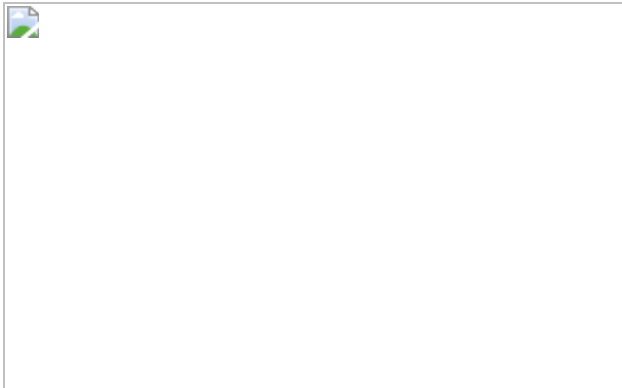


Fig. 5: Probing correlations and coherence in the striated phase via quench dynamics.



Data availability

The data that support the findings of this study are available from the corresponding author on reasonable request.

References

1. 1.

Preskill, J. Quantum computing in the NISQ era and beyond. *Quantum* **2**, 79 (2018).

[Google Scholar](#)

2. 2.

Zhang, J. et al. Observation of a many-body dynamical phase transition with a 53-qubit quantum simulator. *Nature* **551**, 601–604 (2017).

[ADS](#) [CAS](#) [PubMed](#) [PubMed Central](#) [Google Scholar](#)

3. 3.

Gross, C. & Bloch, I. Quantum simulations with ultracold atoms in optical lattices. *Science* **357**, 995–1001 (2017).

[ADS](#) [CAS](#) [Google Scholar](#)

4. 4.

Choi, J.-y. et al. Exploring the many-body localization transition in two dimensions. *Science* **352**, 1547–1552 (2016).

[ADS](#) [MathSciNet](#) [CAS](#) [PubMed](#) [PubMed Central](#) [MATH](#) [Google Scholar](#)

5. 5.

Mazurenko, A. et al. A cold-atom Fermi–Hubbard antiferromagnet. *Nature* **545**, 462–466 (2017).

[ADS](#) [CAS](#) [PubMed](#) [PubMed Central](#) [Google Scholar](#)

6. 6.

Bernien, H. et al. Probing many-body dynamics on a 51-atom quantum simulator. *Nature* **551**, 579–584 (2017).

[ADS](#) [CAS](#) [Google Scholar](#)

7. 7.

Neill, C. et al. Accurately computing electronic properties of a quantum ring. Preprint at <https://arxiv.org/abs/2012.00921v2> (2021).

8. 8.

Wang, C. S. et al. Efficient multiphoton sampling of molecular vibronic spectra on a superconducting bosonic processor. *Phys. Rev. X* **10**, 021060 (2020).

[ADS](#) [CAS](#) [Google Scholar](#)

9. 9.

Arute, F. et al. Quantum supremacy using a programmable superconducting processor. *Nature* **574**, 505–510 (2019).

[ADS](#) [CAS](#) [PubMed](#) [PubMed Central](#) [Google Scholar](#)

10. 10.

Zhong, H.-S. et al. Quantum computational advantage using photons. *Science* **370**, 1460–1463 (2020).

[ADS](#) [CAS](#) [PubMed](#) [PubMed Central](#) [Google Scholar](#)

11. 11.

Giovannetti, V., Lloyd, S. & Maccone, L. Advances in quantum metrology. *Nat. Photon.* **5**, 222–229 (2011).

[ADS](#) [CAS](#) [Google Scholar](#)

12. 12.

Browaeys, A. & Lahaye, T. Many-body physics with individually controlled Rydberg atoms. *Nat. Phys.* **16**, 132–142 (2020).

[CAS](#) [Google Scholar](#)

13. 13.

Sachdev, S. *Quantum Phase Transitions* 2nd edn (Cambridge Univ. Press, 2011).

14. 14.

Samajdar, R., Ho, W. W., Pichler, H., Lukin, M. D. & Sachdev, S. Complex density wave orders and quantum phase transitions in a model of square-lattice Rydberg atom arrays. *Phys. Rev. Lett.* **124**, 103601 (2020).

[ADS](#) [CAS](#) [PubMed](#) [PubMed Central](#) [Google Scholar](#)

15. 15.

Pagano, G. et al. Quantum approximate optimization of the long-range Ising model with a trapped-ion quantum simulator. *Proc. Natl Acad. Sci. USA* **117**, 25396–25401 (2020).

[ADS](#) [CAS](#) [PubMed](#) [PubMed Central](#) [Google Scholar](#)

16. 16.

Friis, N. et al. Observation of entangled states of a fully controlled 20-qubit system. *Phys. Rev. X* **8**, 021012 (2018).

[CAS](#) [Google Scholar](#)

17. 17.

Harris, R. et al. Phase transitions in a programmable quantum spin glass simulator. *Science* **361**, 162–165 (2018).

[ADS](#) [MathSciNet](#) [CAS](#) [PubMed](#) [PubMed Central](#) [Google Scholar](#)

18. 18.

Labuhn, H. et al. Tunable two-dimensional arrays of single Rydberg atoms for realizing quantum Ising models. *Nature* **534**, 667–670 (2016).

[ADS](#) [CAS](#) [PubMed](#) [PubMed Central](#) [Google Scholar](#)

19. 19.

Morgado, M. & Whitlock, S. Quantum simulation and computing with Rydberg qubits. *AVS Quantum Sci.* **3**, 023501 (2021).

[ADS](#) [Google Scholar](#)

20. 20.

Lienhard, V. et al. Observing the space- and time-dependent growth of correlations in dynamically tuned synthetic Ising models with antiferromagnetic interactions. *Phys. Rev. X* **8**, 021070 (2018).

[CAS](#) [Google Scholar](#)

21. 21.

Guardado-Sanchez, E. et al. Probing the quench dynamics of antiferromagnetic correlations in a 2D quantum Ising spin system. *Phys. Rev. X* **8**, 021069 (2018).

[CAS](#) [Google Scholar](#)

22. 22.

Kim, H., Park, Y., Kim, K., Sim, H.-S. & Ahn, J. Detailed balance of thermalization dynamics in Rydberg-atom quantum simulators. *Phys. Rev. Lett.* **120**, 180502 (2018).

[ADS](#) [CAS](#) [PubMed](#) [PubMed Central](#) [Google Scholar](#)

23. 23.

de Léséleuc, S. et al. Observation of a symmetry-protected topological phase of interacting bosons with Rydberg atoms. *Science* **365**, 775–780 (2019).

[ADS](#) [MathSciNet](#) [PubMed](#) [PubMed Central](#) [MATH](#) [Google Scholar](#)

24. 24.

Keesling, A. et al. Quantum Kibble–Zurek mechanism and critical dynamics on a programmable Rydberg simulator. *Nature* **568**, 207–211 (2019).

[ADS](#) [CAS](#) [PubMed](#) [PubMed Central](#) [Google Scholar](#)

25. 25.

Madjarov, I. S. et al. High-fidelity entanglement and detection of alkaline-earth Rydberg atoms. *Nat. Phys.* **16**, 857–861 (2020).

[CAS](#) [Google Scholar](#)

26. 26.

Omran, A. et al. Generation and manipulation of Schrödinger cat states in Rydberg atom arrays. *Science* **365**, 570–574 (2019).

[ADS](#) [MathSciNet](#) [CAS](#) [PubMed](#) [PubMed Central](#) [Google Scholar](#)

27. 27.

Graham, T. M. et al. Rydberg mediated entanglement in a two-dimensional neutral atom qubit array. *Phys. Rev. Lett.* **123**, 230501 (2019).

[ADS](#) [CAS](#) [PubMed](#) [PubMed Central](#) [Google Scholar](#)

28. 28.

Levine, H. et al. Parallel implementation of high-fidelity multiqubit gates with neutral atoms. *Phys. Rev. Lett.* **123**, 170503 (2019).

[ADS](#) [CAS](#) [PubMed](#) [PubMed Central](#) [Google Scholar](#)

29. 29.

Madjarov, I. S. et al. An atomic-array optical clock with single-atom readout. *Phys. Rev. X* **9**, 041052 (2019).

[CAS](#) [Google Scholar](#)

30. 30.

Young, A. W. et al. Half-minute-scale atomic coherence and high relative stability in a tweezer clock. *Nature* **588**, 408–413 (2020).

[ADS](#) [CAS](#) [PubMed](#) [PubMed Central](#) [Google Scholar](#)

31. 31.

Schymik, K.-N. et al. Enhanced atom-by-atom assembly of arbitrary tweezers arrays. *Phys. Rev. A* **102**, 063107 (2020).

[ADS](#) [CAS](#) [Google Scholar](#)

32. 32.

Kumar, A., Wu, T.-Y., Giraldo, F. & Weiss, D. S. Sorting ultracold atoms in a three-dimensional optical lattice in a realization of Maxwell’s demon. *Nature* **561**, 83–87 (2018).

[ADS](#) [CAS](#) [PubMed](#) [PubMed Central](#) [Google Scholar](#)

33. 33.

Ohl de Mello, D. et al. Defect-free assembly of 2D clusters of more than 100 single-atom quantum systems. *Phys. Rev. Lett.* **122**, 203601 (2019).

[ADS](#) [CAS](#) [PubMed](#) [PubMed Central](#) [Google Scholar](#)

34. 34.

Barredo, D., Lienhard, V., de Léséleuc, S., Lahaye, T. & Browaeys, A. Synthetic three-dimensional atomic structures assembled atom by atom. *Nature* **561**, 79–82 (2018).

[ADS](#) [CAS](#) [Google Scholar](#)

35. 35.

Barredo, D., de Léséleuc, S., Lienhard, V., Lahaye, T. & Browaeys, A. An atom-by-atom assembler of defect-free arbitrary 2D atomic arrays. *Science* **354**, 1021–1023 (2016).

[ADS](#) [CAS](#) [PubMed](#) [PubMed Central](#) [Google Scholar](#)

36. 36.

Jaksch, D. et al. Fast quantum gates for neutral atoms. *Phys. Rev. Lett.* **85**, 2208 (2000).

[ADS](#) [CAS](#) [Google Scholar](#)

37. 37.

Lukin, M. D. et al. Dipole blockade and quantum information processing in mesoscopic atomic ensembles. *Phys. Rev. Lett.* **87**, 037901 (2001).

[ADS](#) [CAS](#) [PubMed](#) [PubMed Central](#) [Google Scholar](#)

38. 38.

Gardas, B., Dziarmaga, J., Zurek, W. H. & Zwolak, M. Defects in quantum computers. *Sci. Rep.* **8**, 4539 (2018).

[ADS](#) [PubMed](#) [PubMed Central](#) [Google Scholar](#)

39. 39.

Zurek, W. H., Dorner, U. & Zoller, P. Dynamics of a quantum phase transition. *Phys. Rev. Lett.* **95**, 105701 (2005).

[ADS](#) [PubMed](#) [PubMed Central](#) [Google Scholar](#)

40. 40.

Felser, T., Notarnicola, S. & Montangero, S. Efficient tensor network ansatz for high-dimensional quantum many-body problems. *Phys. Rev. Lett.* **126**, 170603 (2021).

[ADS](#) [MathSciNet](#) [CAS](#) [PubMed](#) [PubMed Central](#) [Google Scholar](#)

41. 41.

Huang, H.-Y., Kueng, R. & Preskill, J. Predicting many properties of a quantum system from very few measurements. *Nat. Phys.* **16**, 1050–1057 (2020).

[CAS](#) [Google Scholar](#)

42. 42.

Verresen, R., Lukin, M. D. & Vishwanath, A. Prediction of toric code topological order from Rydberg blockade. Preprint at <https://arxiv.org/abs/2011.12310> (2020).

43. 43.

Samajdar, R., Ho, W. W., Pichler, H., Lukin, M. D. & Sachdev, S. Quantum phases of Rydberg atoms on a kagome lattice. *Proc. Natl Acad. Sci. USA* **118**, e2015785118 (2021).

[CAS](#) [PubMed](#) [PubMed Central](#) [Google Scholar](#)

44. 44.

Semeghini, G. et al. Probing topological spin liquids on a programmable quantum simulator. Preprint at <https://arxiv.org/abs/2104.04119> (2021).

45. 45.

Saskin, S., Wilson, J. T., Grinkemeyer, B. & Thompson, J. D. Narrow-line cooling and imaging of ytterbium atoms in an optical tweezer array. *Phys. Rev. Lett.* **122**, 143002 (2019).

[ADS](#) [CAS](#) [PubMed](#) [PubMed Central](#) [Google Scholar](#)

46. 46.

Anderegg, L. et al. An optical tweezer array of ultracold molecules. *Science* **365**, 1156–1158 (2019).

[ADS](#) [CAS](#) [PubMed](#) [PubMed Central](#) [Google Scholar](#)

47. 47.

Liu, L. R. et al. Building one molecule from a reservoir of two atoms. *Science* **360**, 900–903 (2018).

[ADS](#) [CAS](#) [PubMed](#) [PubMed Central](#) [Google Scholar](#)

48. 48.

Turner, C. J., Michailidis, A. A., Abanin, D. A., Serbyn, M. & Papić, Z. Weak ergodicity breaking from quantum many-body scars. *Nat. Phys.* **14**, 745–749 (2018).

[CAS](#) [Google Scholar](#)

49. 49.

Surace, F. M. et al. Lattice gauge theories and string dynamics in Rydberg atom quantum simulators. *Phys. Rev. X* **10**, 021041 (2020).

[CAS](#) [Google Scholar](#)

50. 50.

Bluvstein, D. et al. Controlling quantum many-body dynamics in driven Rydberg atom arrays. *Science* **371**, 1355–1359 (2021).

[ADS](#) [CAS](#) [PubMed](#) [PubMed Central](#) [Google Scholar](#)

51. 51.

Diehl, H. W. The theory of boundary critical phenomena. *Int. J. Mod. Phys. B* **11**, 3503–3523 (1997).

[ADS](#) [Google Scholar](#)

52. 52.

Bañuls, M. C. et al. Simulating lattice gauge theories within quantum technologies. *Eur. Phys. J. D* **74**, 165 (2020).

[ADS](#) [Google Scholar](#)

53. 53.

Notarnicola, S., Collura, M. & Montangero, S. Real-time-dynamics quantum simulation of (1 + 1)-dimensional lattice QED with Rydberg atoms. *Phys. Rev. Research* **2**, 013288 (2020).

[ADS](#) [CAS](#) [Google Scholar](#)

54. 54.

Weimer, H., Müller, M., Lesanovsky, I., Zoller, P. & Büchler, H. P. A Rydberg quantum simulator. *Nat. Phys.* **6**, 382–388 (2010).

[CAS](#) [Google Scholar](#)

55. 55.

Auger, J. M., Bergamini, S. & Browne, D. E. Blueprint for fault-tolerant quantum computation with Rydberg atoms. *Phys. Rev. A* **96**, 052320 (2017).

[Google Scholar](#)

56. 56.

Farhi, E., Goldstone, J. & Gutmann, S. A quantum approximate optimization algorithm. Preprint at <https://arxiv.org/abs/1411.4028> (2014).

57. 57.

Zhou, L., Wang, S.-T., Choi, S., Pichler, H. & Lukin, M. D. Quantum approximate optimization algorithm: performance, mechanism, and implementation on near-term devices. *Phys. Rev. X* **10**, 021067 (2020).

[CAS](#) [Google Scholar](#)

58. 58.

Wild, D. S., Sels, D., Pichler, H. & Lukin, M. D. Quantum sampling algorithms for near-term devices. Preprint at <https://arxiv.org/abs/2005.14059> (2020).

59. 59.

Scholl, P. et al. Programmable quantum simulation of 2D antiferromagnets with hundreds of Rydberg atoms. *Nature* <https://doi.org/10.1038/s41586-021-03585-1> (2021).

60. 60.

Kim, D. et al. Large-scale uniform optical focus array generation with a phase spatial light modulator. *Opt. Lett.* **44**, 3178–3181 (2019).

[ADS](#) [PubMed](#) [PubMed Central](#) [Google Scholar](#)

61. 61.

Endres, M. et al. Atom-by-atom assembly of defect-free one-dimensional cold atom arrays. *Science* **354**, 1024–1027 (2016).

[ADS](#) [CAS](#) [PubMed](#) [PubMed Central](#) [Google Scholar](#)

62. 62.

Lee, W., Kim, H. & Ahn, J. Defect-free atomic array formation using the Hungarian matching algorithm. *Phys. Rev. A* **95**, 053424 (2017).

[ADS](#) [Google Scholar](#)

63. 63.

Sheng, C. et al. Efficient preparation of 2D defect-free atom arrays with near-fewest sorting-atom moves. *Phys. Rev. Research* **3**, 023008 (2021).

[ADS](#) [Google Scholar](#)

64. 64.

Levine, H. et al. High-fidelity control and entanglement of Rydberg-atom qubits. *Phys. Rev. Lett.* **121**, 123603 (2018).

[ADS](#) [CAS](#) [PubMed](#) [PubMed Central](#) [Google Scholar](#)

65. 65.

Bowman, D. et al. High-fidelity phase and amplitude control of phase-only computer generated holograms using conjugate gradient minimisation. *Opt. Express* **25**, 11692–11700 (2017).

[ADS](#) [CAS](#) [PubMed](#) [PubMed Central](#) [Google Scholar](#)

66. 66.

Zupancic, P. et al. Ultra-precise holographic beam shaping for microscopic quantum control. *Opt. Express* **24**, 13881–13893 (2016).

[ADS](#) [CAS](#) [PubMed](#) [PubMed Central](#) [Google Scholar](#)

67. 67.

Beterov, I. I., Ryabtsev, I. I., Tretyakov, D. B. & Entin, V. M. Quasiclassical calculations of blackbody-radiation-induced depopulation rates and effective lifetimes of Rydberg nS , nP , and nD alkali-metal atoms with $n \leq 80$. *Phys. Rev. A* **79**, 052504 (2009).

[ADS](#) [Google Scholar](#)

68. 68.

Bhattacharjee, S. M. & Seno, F. A measure of data collapse for scaling. *J. Phys. Math. Gen.* **34**, 6375 (2001).

[ADS](#) [CAS](#) [MATH](#) [Google Scholar](#)

69. 69.

Hasenbusch, M. Monte Carlo study of surface critical phenomena: The special point. *Phys. Rev. B* **84**, 134405 (2011).

[ADS](#) [Google Scholar](#)

70. 70.

White, S. R. Density matrix formulation for quantum renormalization groups. *Phys. Rev. Lett.* **69**, 2863 (1992).

[ADS](#) [CAS](#) [PubMed](#) [PubMed Central](#) [Google Scholar](#)

71. 71.

White, S. R. Density-matrix algorithms for quantum renormalization groups. *Phys. Rev. B* **48**, 10345 (1993).

[ADS](#) [CAS](#) [Google Scholar](#)

72. 72.

Stoudenmire, E. M. & White, S. R. Studying two-dimensional systems with the density matrix renormalization group. *Annu. Rev. Condens. Matter Phys.* **3**, 111–128 (2012).

[Google Scholar](#)

73. 73.

Fishman, M., White, S. R. & Stoudenmire, E. M. The ITensor software library for tensor network calculations. Preprint at <https://arxiv.org/abs/2007.14822> (2020).

[Download references](#)

Acknowledgements

We thank many members of the Harvard AMO community, particularly E. Urbach, S. Dakoulas and J. Doyle for enabling safe and productive operation of our laboratories during 2020. We thank H. Bernien, D. Englund, M. Endres, N. Gemelke, D. Kim, P. Stark and A. Zibrov for discussions and experimental help. We acknowledge financial support from the Center for Ultracold Atoms, the US National Science Foundation, the Vannevar Bush Faculty Fellowship, the US Department of Energy (DE-SC0021013 and DOE Quantum Systems Accelerator Center, contract no. 7568717), the Office of Naval Research, the Army Research Office MURI and the DARPA ONISQ programme. T.T.W. acknowledges support from Gordon College. H.L. acknowledges support from the National Defense Science and Engineering Graduate (NDSEG) fellowship. G.S. acknowledges support from a fellowship from the Max Planck/Harvard Research Center for Quantum Optics. D.B. acknowledges support from the NSF Graduate Research Fellowship Program (grant DGE1745303) and the Fannie and John Hertz Foundation. W.W.H. is supported by the Moore Foundation’s EPiQS Initiative grant no. GBMF4306, the NUS development

grant AY2019/2020, and the Stanford Institute of Theoretical Physics. S.C. acknowledges support from the Miller Institute for Basic Research in Science. R.S. and S.S. were supported by the US Department of Energy under grant DE-SC0019030. The DMRG calculations were performed using the ITensor Library^{[73](#)}. The computations in this paper were run on the FASRC Cannon cluster supported by the FAS Division of Science Research Computing Group at Harvard University.

Author information

Affiliations

1. Department of Physics, Harvard University, Cambridge, MA, USA

Sepehr Ebadi, Tout T. Wang, Harry Levine, Alexander Keesling, Giulia Semeghini, Ahmed Omran, Dolev Bluvstein, Rhine Samajdar, Wen Wei Ho, Subir Sachdev, Markus Greiner & Mikhail D. Lukin

2. QuEra Computing Inc., Boston, MA, USA

Alexander Keesling & Ahmed Omran

3. Institute for Theoretical Physics, University of Innsbruck, Innsbruck, Austria

Hannes Pichler

4. Institute for Quantum Optics and Quantum Information, Austrian Academy of Sciences, Innsbruck, Austria

Hannes Pichler

5. Department of Physics, Stanford University, Stanford, CA, USA

Wen Wei Ho

6. Department of Physics, University of California Berkeley, Berkeley, CA, USA

Soonwon Choi

7. Department of Physics and Research Laboratory of Electronics,
Massachusetts Institute of Technology, Cambridge, MA, USA

Vladan Vuletić

Authors

1. Sepehr Ebadi

[View author publications](#)

You can also search for this author in [PubMed](#) [Google Scholar](#)

2. Tout T. Wang

[View author publications](#)

You can also search for this author in [PubMed](#) [Google Scholar](#)

3. Harry Levine

[View author publications](#)

You can also search for this author in [PubMed](#) [Google Scholar](#)

4. Alexander Keesling

[View author publications](#)

You can also search for this author in [PubMed](#) [Google Scholar](#)

5. Giulia Semeghini

[View author publications](#)

You can also search for this author in [PubMed](#) [Google Scholar](#)

6. Ahmed Omran

[View author publications](#)

You can also search for this author in [PubMed](#) [Google Scholar](#)

7. Dolev Bluvstein

[View author publications](#)

You can also search for this author in [PubMed](#) [Google Scholar](#)

8. Rhine Samajdar

[View author publications](#)

You can also search for this author in [PubMed](#) [Google Scholar](#)

9. Hannes Pichler

[View author publications](#)

You can also search for this author in [PubMed](#) [Google Scholar](#)

10. Wen Wei Ho

[View author publications](#)

You can also search for this author in [PubMed](#) [Google Scholar](#)

11. Soonwon Choi

[View author publications](#)

You can also search for this author in [PubMed](#) [Google Scholar](#)

12. Subir Sachdev

[View author publications](#)

You can also search for this author in [PubMed](#) [Google Scholar](#)

13. Markus Greiner

[View author publications](#)

You can also search for this author in [PubMed](#) [Google Scholar](#)

14. Vladan Vuletić

[View author publications](#)

You can also search for this author in [PubMed](#) [Google Scholar](#)

15. Mikhail D. Lukin

[View author publications](#)

You can also search for this author in [PubMed](#) [Google Scholar](#)

Contributions

S.E., T.T.W., H.L., A.K., G.S, A.O. and D.B. contributed to building the experimental set-up, performed the measurements and analysed the data. Theoretical analysis was performed by R.S., H.P., W.W.H. and S.C. All work was supervised by S.S., M.G., V.V. and M.D.L. All authors discussed the results and contributed to the manuscript.

Corresponding author

Correspondence to [Mikhail D. Lukin](#).

Ethics declarations

Competing interests

M.G., V.V. and M.D.L. are co-founders and shareholders of QuEra Computing. A.K. and A.O. are shareholders of QuEra Computing. All other authors declare no competing interests.

Additional information

Peer review information *Nature* thanks the anonymous reviewer(s) for their contribution to the peer review of this work.

Publisher's note Springer Nature remains neutral with regard to jurisdictional claims in published maps and institutional affiliations.

Extended data figures and tables

Extended Data Fig. 1 Large arrays of optical tweezers.

The experimental platform produces optical tweezer arrays with up to ~1,000 tweezers and ~50% loading probability per tweezer after 100 ms of magneto-optical trap loading time. **a**, Camera image of an array of 34×30 tweezers (1,020 traps), including aberration correction. **b**, Sample image of random loading into this tweezer array, with 543 loaded atoms. Atoms are detected on an EMCCD camera with fluorescence imaging.

Extended Data Fig. 2 Correcting for aberrations in the SLM tweezer array.

The aberration correction procedure uses the orthogonality of Zernike polynomials and the fact that correcting aberrations increases tweezer light shifts on the atoms. To independently measure and correct each aberration type, Zernike polynomials are added with variable amplitude to the SLM phase hologram, with values optimized to maximize tweezer light shifts. **a**, Two common aberration types: horizontal coma (upper) and primary spherical (lower), for which ~50 milliwaves compensation on each reduces aberrations and results in higher-depth traps. **b**, Correcting for aberrations associated with the 13 lowest-order Zernike polynomials. The sum of all polynomials with their associated coefficients gives the total wavefront correction (RMS ~70 milliwaves) for our optical system, which is summed with the optical tweezer hologram on the SLM. **c**, Trap depths across a 26×13 trap array before and after correction for aberrations. Aberration correction results in tighter focusing (higher trap light shift) and improved homogeneity. Trap depths are measured by probing the light shift of each trap on the $\langle |5\{S\}_{1/2}, F=2\rangle \rightarrow |5\{P\}_{3/2}, F'\rangle$ transition. **d**, Aberration correction also results in higher and more homogeneous trap frequencies across the array. Trap frequencies are measured by modulating tweezer depths at variable frequencies, resulting in parametric heating and atom loss when the modulation frequency is twice the radial trap frequency. The measurement after correction for aberrations shows a narrower spectrum and higher trap frequencies (averaged over the whole array).

Extended Data Fig. 3 Rearrangement protocol.

a, Sample sequence of individual rearrangement steps. There are two pre-sorting moves (1, 2). Move 3 is the single ejection move. Moves 4–6 consist of parallel vertical sorting within each column, including both upward and downward moves. The upper panel illustrates the frequency spectrum of the waveform in the vertical and horizontal AODs during these moves, with the underlying grid corresponding to the calibrated frequencies that map to SLM array rows and columns. **b**, Spectrograms representing the horizontal and vertical AOD waveforms over the duration of a single vertical frequency scan during a realistic rearrangement procedure for a 26×13 array. The heat-maps show frequency spectra of the AOD waveforms over small time intervals during the scan.

Extended Data Fig. 4 Generating homogeneous Rydberg beams.

a, Measured Gaussian-beam illumination on the SLM for shaping the 420-nm Rydberg beam. A Gaussian fit to these data is used as an input for the hologram optimization algorithm. **b**, Measured wavefront error through our optical system (after correction), showing a reduction of aberrations to $\lambda/100$. **c**, Computer-generated hologram for creating the 420-nm top-hat beam. **d**, Measured light intensity of the 420-nm top-hat beam (top), and the cross-section along where atoms will be positioned (bottom). Vertical lines denote the 105- μm region where the beam should be flat. **e**, Using the measured top-hat intensity, a phase correction is calculated for adding to the initial hologram. **f**, Resulting top-hat beam after feedback shows considerably improved homogeneity. pk–pk, peak to peak.

Extended Data Fig. 5 Characterizing microwave-enhanced Rydberg detection fidelity.

The effect of strong microwave (MW) pulses on Rydberg atoms is measured by preparing atoms in $|\langle g \rangle\rangle$, exciting to $|\langle r \rangle\rangle$ with a Rydberg π -pulse, and then applying the microwave pulse before de-exciting residual Rydberg atoms with a final Rydberg π -pulse. (The entire sequence

occurs while tweezers are briefly turned off.) **a**, Broad resonances are observed with varying microwave frequency, corresponding to transitions from $\langle |r\rangle = \langle |70S\rangle$ to other Rydberg states. Note that the transitions to $\langle |69P\rangle$ and $\langle |70P\rangle$ are in the range of 10–12 GHz, and over this entire range there is strong transfer out of $\langle |r\rangle$. Other resonances might be due to multiphoton effects. **b**, With fixed 6.9-GHz microwave frequency and varying pulse time, there is a rapid transfer out of the Rydberg state on the timescale of several nanoseconds. Over short timescales, there may be coherent oscillations that return population back to $\langle |r\rangle$, so a 100-ns pulse is used for enhancement of loss signal of $\langle |r\rangle$ in the experiment.

Extended Data Fig. 6 Coarse-grained local staggered magnetization.

a, Examples of Rydberg populations n_i after a faster (top) and slower (bottom) linear sweep. **b**, Corresponding coarse-grained local staggered magnetizations m_i clearly show larger extents of antiferromagnetically ordered domains (dark blue or dark red) for the slower sweep (bottom) than for the faster sweep (top), as expected from the Kibble–Zurek mechanism. **c**, Isotropic correlation functions $\langle \{G\}_m^2 \rangle$ for the corresponding coarse-grained local staggered magnetizations after a faster (top) or a slower (bottom) sweep. **d**, As a function of radial distance, correlations $\langle \{G\}_m^2 \rangle$ decay exponentially with a length scale corresponding to the correlation length ξ . The two decay curves correspond to faster (orange) and slower (blue) sweeps.

Extended Data Fig. 7 Extracting the quantum critical point.

a, The mean Rydberg excitation density $\langle \langle n \rangle \rangle$ versus detuning Δ/Ω on a 16×16 array. The data are fitted within a window (dashed lines) to a cubic polynomial (red curve) as a means of smoothing the data. **b**, The peak in the numerical derivative of the fitted data (red curve) corresponds to the critical point $\Delta_c/\Omega = 1.12(4)$ (red shaded regions show uncertainty ranges, obtained from varying fit windows). In contrast, the point-by-point slope of the data (grey) is too noisy to be useful. **c**, Order parameter \langle

($\langle \mathcal{F} \rangle \sim (\pi, \pi)$) for the chequerboard phase versus Δ/Ω measured on a 16×16 array with the value of the critical point from **b** superimposed (red line), showing the clear growth of the order parameter after the critical point. **d**, DMRG simulations of $\langle n \rangle$ versus Δ/Ω on a 10×10 array. For comparison against the experimental fitting procedure, the data from numerics are also fitted to a cubic polynomial within the indicated window (dashed lines). **e**, The point-by-point slope of the numerical data (blue curve) has a peak at $\Delta_c/\Omega = 1.18$ (blue dashed line), in good agreement with the results (red dashed line) from both the numerical derivative of the cubic fit on the same data (red curve) and the result of the experiment. **f**, DMRG simulation of $\langle \mathcal{F} \rangle \sim (\pi, \pi)$ versus Δ/Ω , with the exact quantum critical point from numerics shown (red line).

Extended Data Fig. 8 Optimization of data collapse.

a, Distance D between rescaled correlation length $\langle \xi \rangle \sim (\varDelta)$ versus $\langle \varDelta \rangle \sim (\varDelta)$ curves depends on both the location of the quantum critical point Δ_c/Ω and on the correlation length critical exponent v . The independently determined Δ_c/Ω (blue line, with uncertainty range in grey) and the experimentally extracted value of v (dashed red line, with uncertainty range corresponding to the red shaded region) are marked on the plot. **b**, Our determination of v (red) from data collapse around the independently determined Δ_c/Ω (blue) is consistent across arrays of different sizes. **c–e**, Data collapse is clearly better at the experimentally determined value ($v = 0.62$) as compared with the mean-field ($v = 0.5$) or the $(1 + 1)D$ ($v = 1$) values. The horizontal extent of the data corresponds to the region of overlap of all rescaled datasets.

Rights and permissions

Reprints and Permissions

About this article



Check for
updates

Cite this article

Ebadi, S., Wang, T.T., Levine, H. *et al.* Quantum phases of matter on a 256-atom programmable quantum simulator. *Nature* **595**, 227–232 (2021).
<https://doi.org/10.1038/s41586-021-03582-4>

[Download citation](#)

- Received: 21 December 2020
- Accepted: 26 April 2021
- Published: 07 July 2021
- Issue Date: 08 July 2021
- DOI: <https://doi.org/10.1038/s41586-021-03582-4>

Further reading

- [Quantum simulation of 2D antiferromagnets with hundreds of Rydberg atoms](#)
 - Pascal Scholl
 - , Michael Schuler
 - , Hannah J. Williams
 - , Alexander A. Eberharter
 - , Daniel Barredo
 - , Kai-Niklas Schymik
 - , Vincent Lienhard
 - , Louis-Paul Henry
 - , Thomas C. Lang

- , Thierry Lahaye
- , Andreas M. LÄuchli
- & Antoine Browaeys

Nature (2021)

Comments

By submitting a comment you agree to abide by our [Terms](#) and [Community Guidelines](#). If you find something abusive or that does not comply with our terms or guidelines please flag it as inappropriate.

[Access through your institution](#)

[Change institution](#)

[Buy or subscribe](#)

Advertisement

This article was downloaded by **calibre** from <https://www.nature.com/articles/s41586-021-03582-4>

| [Section menu](#) | [Main menu](#) |

- Article
- [Published: 07 July 2021](#)

Quantum simulation of 2D antiferromagnets with hundreds of Rydberg atoms

- [Pascal Scholl](#) [ORCID: orcid.org/0000-0002-5675-4237](#)^{1 na1},
- [Michael Schuler](#) [ORCID: orcid.org/0000-0003-3557-8913](#)^{2 na1},
- [Hannah J. Williams](#) [ORCID: orcid.org/0000-0001-8356-8539](#)^{1 na1},
- [Alexander A. Eberharter](#)^{3 na1},
- [Daniel Barredo](#) [ORCID: orcid.org/0000-0001-5307-1927](#)^{1,4},
- [Kai-Niklas Schymik](#)¹,
- [Vincent Lienhard](#)¹,
- [Louis-Paul Henry](#)⁵,
- [Thomas C. Lang](#) [ORCID: orcid.org/0000-0001-9619-6762](#)³,
- [Thierry Lahaye](#) [ORCID: orcid.org/0000-0002-2260-9859](#)¹,
- [Andreas M. Läuchli](#) [ORCID: orcid.org/0000-0002-2272-2691](#)³ &
- [Antoine Browaeys](#) [ORCID: orcid.org/0000-0001-9941-8869](#)¹

[Nature](#) volume **595**, pages 233–238 (2021) [Cite this article](#)

- 22 Altmetric
- [Metrics details](#)

Subjects

- [Phase transitions and critical phenomena](#)
- [Quantum simulation](#)
- [Ultracold gases](#)

Abstract

Quantum simulation using synthetic systems is a promising route to solve outstanding quantum many-body problems in regimes where other approaches, including numerical ones, fail¹. Many platforms are being developed towards this goal, in particular based on trapped ions^{2,3,4}, superconducting circuits^{5,6,7}, neutral atoms^{8,9,10,11} or molecules^{12,13}. All of these platforms face two key challenges: scaling up the ensemble size while retaining high-quality control over the parameters, and validating the outputs for these large systems. Here we use programmable arrays of individual atoms trapped in optical tweezers, with interactions controlled by laser excitation to Rydberg states¹¹, to implement an iconic many-body problem—the antiferromagnetic two-dimensional transverse-field Ising model. We push this platform to a regime with up to 196 atoms manipulated with high fidelity and probe the antiferromagnetic order by dynamically tuning the parameters of the Hamiltonian. We illustrate the versatility of our platform by exploring various system sizes on two qualitatively different geometries—square and triangular arrays. We obtain good agreement with numerical calculations up to a computationally feasible size (approximately 100 particles). This work demonstrates that our platform can be readily used to address open questions in many-body physics.

Access options

Subscribe to Journal

Get full journal access for 1 year

\$199.00

only \$3.90 per issue

[Subscribe](#)

All prices are NET prices.
VAT will be added later in the checkout.

Tax calculation will be finalised during checkout.

Rent or Buy article

Get time limited or full article access on ReadCube.

from \$8.99

[Rent or Buy](#)

All prices are NET prices.

Additional access options:

- [Log in](#)
- [Access through your institution](#)
- [Learn about institutional subscriptions](#)

Fig. 1: Emergence of AF ordering from the Rydberg blockade in square and triangular arrays.

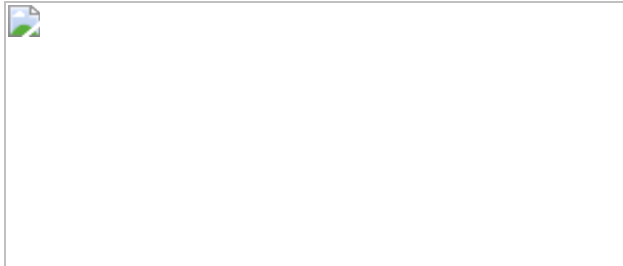


Fig. 2: The Ising model on a square lattice.



Fig. 3: Quantum real-time evolution versus classical equilibrium.

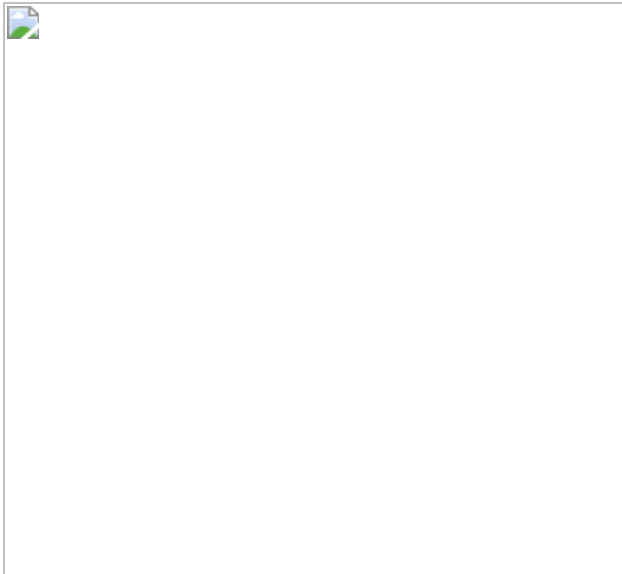
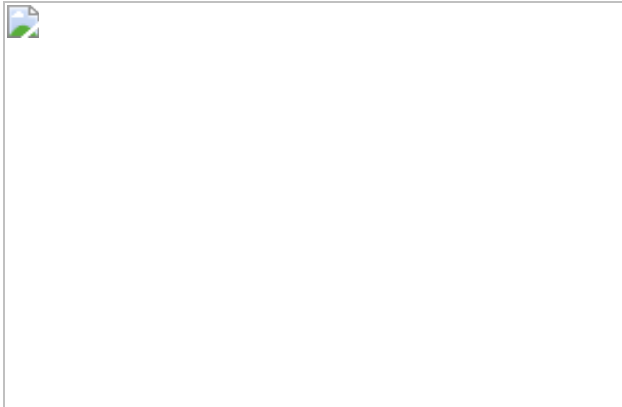


Fig. 4: AF ordering on a triangular array.



Data availability

The data presented in the figures and that support the other findings of this study are available from the corresponding author on reasonable request.

Code availability

The codes are available upon reasonable request from the corresponding author.

References

1. 1.

Georgescu, I. M., Ashhab, S. & Nori, F. Quantum simulation. *Rev. Mod. Phys.* **86**, 153–185 (2014).

[ADS](#) [Google Scholar](#)

2. 2.

Blatt, R. & Roos, C. F. Quantum simulations with trapped ions. *Nat. Phys.* **8**, 277–284 (2012).

[CAS](#) [Google Scholar](#)

3. 3.

Monroe, C. et al. Programmable quantum simulations of spin systems with trapped ions. *Rev. Mod. Phys.* **93**, 025001 (2021).

[ADS](#) [Google Scholar](#)

4. 4.

Gärttner, M. et al. Measuring out-of-time-order correlations and multiple quantum spectra in a trapped-ion quantum magnet. *Nat. Phys.* **13**, 781–786 (2017).

[Google Scholar](#)

5. 5.

Song, C. et al. 10-qubit entanglement and parallel logic operations with a superconducting circuit. *Phys. Rev. Lett.* **119**, 180511 (2017).

[ADS](#) [Google Scholar](#)

6. 6.

King, A. D. et al. Observation of topological phenomena in a programmable lattice of 1,800 qubits. *Nature* **560**, 456–460 (2018).

[ADS](#) [CAS](#) [Google Scholar](#)

7. 7.

Kjaergaard, M. et al. Superconducting qubits: current state of play. *Annu. Rev. Condens. Matter Phys.* **11**, 369–395 (2020).

[Google Scholar](#)

8. 8.

Bloch, I., Dalibard, J. & Zwerger, W. Many-body physics with ultracold gases. *Rev. Mod. Phys.* **80**, 885–964 (2008).

[ADS](#) [CAS](#) [Google Scholar](#)

9. 9.

Bloch, I., Dalibard, J. & Nascimbène, S. Quantum simulations with ultracold quantum gases. *Nat. Phys.* **8**, 267–276 (2012).

[CAS](#) [Google Scholar](#)

10. 10.

Gross, C. & Bloch, I. Quantum simulations with ultracold atoms in optical lattices. *Science* **357**, 995–1001 (2017).

[ADS](#) [CAS](#) [Google Scholar](#)

11. 11.

Browaeys, A. & Lahaye, T. Many-body physics with individually controlled Rydberg atoms. *Nat. Phys.* **16**, 132–142 (2020).

[CAS](#) [Google Scholar](#)

12. 12.

Yan, B. et al. Observation of dipolar spin-exchange interactions with lattice-confined polar molecules. *Nature* **501**, 521–525 (2013).

[ADS](#) [CAS](#) [Google Scholar](#)

13. 13.

Zhou, Y. L., Ortner, M. & Rabl, P. Long-range and frustrated spin–spin interactions in crystals of cold polar molecules. *Phys. Rev. A* **84**, 052332 (2011).

[ADS](#) [Google Scholar](#)

14. 14.

Bernien, H. et al. Probing many-body dynamics on a 51-atom quantum simulator. *Nature* **551**, 579–584 (2017).

[ADS](#) [CAS](#) [Google Scholar](#)

15. 15.

Keesling, A. et al. Quantum Kibble–Zurek mechanism and critical dynamics on a programmable Rydberg simulator. *Nature* **568**, 207–211 (2019).

[ADS](#) [CAS](#) [PubMed](#) [PubMed Central](#) [Google Scholar](#)

16. 16.

Lienhard, V. et al. Observing the space- and time-dependent growth of correlations in dynamically tuned synthetic Ising antiferromagnets. *Phys. Rev. X* **8**, 021070 (2018).

[CAS](#) [Google Scholar](#)

17. 17.

Levine, H. et al. Parallel implementation of high-fidelity multiqubit gates with neutral atoms. *Phys. Rev. Lett.* **123**, 170503 (2019).

[ADS](#) [CAS](#) [PubMed](#) [PubMed Central](#) [Google Scholar](#)

18. 18.

Omran, A. et al. Generation and manipulation of Schrödinger cat states in Rydberg atom arrays. *Science* **365**, 570–574 (2019).

[ADS](#) [MathSciNet](#) [CAS](#) [PubMed](#) [PubMed Central](#) [Google Scholar](#)

19. 19.

Madjarov, I. S. et al. High-fidelity entanglement and detection of alkaline-earth Rydberg atoms. *Nat. Phys.* **16**, 857–861 (2020); correction **17**, 144 (2021).

[CAS](#) [Google Scholar](#)

20. 20.

Schauß, P. et al. Crystallization in Ising quantum magnets. *Science* **347**, 1455–1458 (2015).

[ADS](#) [Google Scholar](#)

21. 21.

Guardado-Sánchez, E. et al. Probing the quench dynamics of antiferromagnetic correlations in a 2D quantum Ising spin system. *Phys. Rev. X* **8**, 021069 (2018).

[CAS](#) [Google Scholar](#)

22. 22.

Song, Y., Kim, M., Hwang, H., Lee, W. & Ahn, J. Quantum simulation of Cayley-tree Ising Hamiltonians with three-dimensional Rydberg

atoms. *Phys. Rev. Res.* **3**, 013286 (2021).

[CAS](#) [Google Scholar](#)

23. 23.

Wannier, G. H. Antiferromagnetism. The triangular Ising net. *Phys. Rev.* **79**, 357–364 (1950).

[ADS](#) [MathSciNet](#) [MATH](#) [Google Scholar](#)

24. 24.

Jaksch, D. et al. Fast quantum gates for neutral atoms. *Phys. Rev. Lett.* **85**, 2208–2211 (2000).

[ADS](#) [CAS](#) [Google Scholar](#)

25. 25.

Schymik, K.-N. et al. Enhanced atom-by-atom assembly of arbitrary tweezer arrays. *Phys. Rev. A* **102**, 063107 (2020).

[ADS](#) [CAS](#) [Google Scholar](#)

26. 26.

Levine, H. et al. High-fidelity control and entanglement of Rydberg-atom qubits. *Phys. Rev. Lett.* **121**, 123603 (2018).

[ADS](#) [CAS](#) [PubMed](#) [PubMed Central](#) [Google Scholar](#)

27. 27.

Janke, W. & Villanova, R. Three-dimensional 3-state Potts model revisited with new techniques. *Nucl. Phys. B* **489**, 679–696 (1997).

[ADS](#) [MathSciNet](#) [MATH](#) [Google Scholar](#)

28. 28.

Laumann, C. R., Moessner, R., Scardicchio, A. & Sondhi, S. L. Quantum adiabatic algorithm and scaling of gaps at first-order quantum phase transitions. *Phys. Rev. Lett.* **109**, 030502 (2012).

[ADS](#) [CAS](#) [Google Scholar](#)

29. 29.

Fey, S., Kapfer, S. C. & Schmidt, K. P. Quantum criticality of two-dimensional quantum magnets with long-range interactions. *Phys. Rev. Lett.* **122**, 017203 (2019).

[ADS](#) [CAS](#) [Google Scholar](#)

30. 30.

Samajdar, R., Ho, W. W., Pichler, H., Lukin, M. D. & Sachdev, S. Complex density wave orders and quantum phase transitions in a model of square-lattice Rydberg atom arrays. *Phys. Rev. Lett.* **124**, 103601 (2020).

[ADS](#) [CAS](#) [PubMed](#) [PubMed Central](#) [Google Scholar](#)

31. 31.

Ebadi, S. et al. Quantum phases of matter on a 256-atom programmable quantum simulator. *Nature* <https://doi.org/10.1038/s41586-021-03582-4> (2021).

32. 32.

Stoli, E. & Domb, C. Shape and size of two-dimensional percolation clusters with and without correlations. *J. Phys. A* **12**, 1843–1855 (1979).

[ADS](#) [Google Scholar](#)

33. 33.

Kim, H., Park, Y., Kim, K., Sim, H.-S. & Ahn, J. Detailed balance of thermalization dynamics in Rydberg-atom quantum simulators. *Phys. Rev. Lett.* **120**, 180502 (2018).

[ADS](#) [CAS](#) [PubMed](#) [PubMed Central](#) [Google Scholar](#)

34. 34.

Pichler, H., Wang, S.-T., Zhou, L., Choi, S. & Lukin, M. D. Quantum optimization for maximum independent set using Rydberg atom arrays. Preprint at <https://arxiv.org/abs/1808.10816> (2018).

35. 35.

Henriet, L. Robustness to spontaneous emission of a variational quantum algorithm. *Phys. Rev. A* **101**, 012335 (2020).

[ADS](#) [CAS](#) [Google Scholar](#)

36. 36.

Serret, M. F., Marchand, B. & Ayral, T. Solving optimization problems with Rydberg analog quantum computers: realistic requirements for quantum advantage using noisy simulation and classical benchmarks. *Phys. Rev. A* **102**, 052617 (2020).

[ADS](#) [CAS](#) [Google Scholar](#)

37. 37.

Villain, J., Bidaux, R., Carton, J.-P. & Conte, R. Order as an effect of disorder. *J. Phys. France* **41**, 1263–1272 (1980).

[MathSciNet](#) [CAS](#) [Google Scholar](#)

38. 38.

Moessner, R., Sondhi, S. L. & Chandra, P. Two-dimensional periodic frustrated Ising models in a transverse field. *Phys. Rev. Lett.* **84**, 4457–4460 (2000).

[ADS](#) [CAS](#) [Google Scholar](#)

39. 39.

Moessner, R. & Sondhi, S. L. Ising models of quantum frustration. *Phys. Rev. B* **63**, 224401 (2001).

[ADS](#) [Google Scholar](#)

40. 40.

Isakov, S. V. & Moessner, R. Interplay of quantum and thermal fluctuations in a frustrated magnet. *Phys. Rev. B* **68**, 104409 (2003).

[ADS](#) [Google Scholar](#)

41. 41.

Koziol, J., Fey, S., Kapfer, S. C. & Schmidt, K. P. Quantum criticality of the transverse-field Ising model with long-range interactions on triangular-lattice cylinders. *Phys. Rev. B* **100**, 144411 (2019).

[ADS](#) [CAS](#) [Google Scholar](#)

42. 42.

Madjarov, I. S. et al. An atomic-array optical clock with single-atom readout. *Phys. Rev. X* **9**, 041052 (2019).

[CAS](#) [Google Scholar](#)

43. 43.

Norgia, M. A. et al. Seconds-scale coherence on an optical clock transition in a tweezer array. *Science* **366**, 93–97 (2019).

[ADS](#) [CAS](#) [Google Scholar](#)

44. 44.

Saffman, M., Walker, T. G. & Mølmer, K. Quantum information with Rydberg atoms. *Rev. Mod. Phys.* **82**, 2313–2363 (2010).

[ADS](#) [CAS](#) [Google Scholar](#)

45. 45.

Henriet, L. et al. Quantum computing with neutral atoms. *Quantum* **4**, 327 (2020).

[Google Scholar](#)

46. 46.

Morgado, M. & Whitlock, S. Quantum simulation and computing with Rydberg qubits. *AVS Quantum Sci.* **3**, 023501 (2021).

[ADS](#) [Google Scholar](#)

47. 47.

Barredo, D., Lienhard, V., de Léséleuc, S., Lahaye, T. & Browaeys, A. Synthetic three-dimensional atomic structures assembled atom by atom. *Nature* **561**, 79–82 (2018).

[ADS](#) [CAS](#) [Google Scholar](#)

48. 48.

de Léséleuc, S., Barredo, D., Lienhard, V., Browaeys, A. & Lahaye, T. Analysis of imperfections in the coherent optical excitation of single atoms to Rydberg states. *Phys. Rev. A* **97**, 053803 (2018).

[ADS](#) [Google Scholar](#)

49. 49.

Schollwöck, U. The density-matrix renormalization group in the age of matrix product states. *Ann. Phys.* **326**, 96–192 (2011).

[ADS](#) [MathSciNet](#) [MATH](#) [Google Scholar](#)

50. 50.

Paeckel, S. et al. Time-evolution methods for matrix-product states. *Ann. Phys.* **50**, 167998 (2019).

[MathSciNet](#) [MATH](#) [Google Scholar](#)

51. 51.

Stoudenmire, E. M. & White, S. R. Studying two-dimensional systems with the density matrix renormalization group. *Annu. Rev. Condens. Matter Phys.* **3**, 111–128 (2012).

[Google Scholar](#)

52. 52.

Eisert, J., Cramer, M. & Plenio, M. B. Area laws for the entanglement entropy. *Rev. Mod. Phys.* **82**, 277–306 (2010).

[ADS](#) [MathSciNet](#) [MATH](#) [Google Scholar](#)

53. 53.

Haegeman, J. et al. Time-dependent variational principle for quantum lattices. *Phys. Rev. Lett.* **107**, 070601 (2011).

[ADS](#) [Google Scholar](#)

54. 54.

Haegeman, J., Lubich, C., Oseledets, I., Vandereycken, B. & Verstraete, F. Unifying time evolution and optimization with matrix product states. *Phys. Rev. B* **94**, 165116 (2016).

[ADS](#) [Google Scholar](#)

55. 55.

Hauschild, J. & Pollmann, F. Efficient numerical simulations with Tensor Networks: Tensor Network Python (TeNPy). *SciPost Phys. Lect. Notes* **5** <https://doi.org/10.21468/SciPostPhysLectNotes.5> (2018).

56. 56.

Stoudenmire, E. M. & White, S. R. Minimally entangled typical thermal state algorithms. *New J. Phys.* **12**, 055026 (2010).

[ADS](#) [MATH](#) [Google Scholar](#)

57. 57.

Marcuzzi, M. et al. Facilitation dynamics and localization phenomena in Rydberg lattice gases with position disorder. *Phys. Rev. Lett.* **118**, 063606 (2017).

[ADS](#) [Google Scholar](#)

58. 58.

Binder, K. Finite size scaling analysis of Ising model block distribution functions. *Z. Phys. B* **43**, 119–140 (1981).

[ADS](#) [Google Scholar](#)

59. 59.

Onsager, L. Crystal statistics. I. A two-dimensional model with an order-disorder transition. *Phys. Rev.* **65**, 117–149 (1944).

[ADS](#) [MathSciNet](#) [CAS](#) [MATH](#) [Google Scholar](#)

[Download references](#)

Acknowledgements

This project has received funding from the European Union’s Horizon 2020 research and innovation programme under grant agreement number 817482 (PASQuanS). M.S. acknowledges support by the Austrian Science Fund (FWF) through grant number P 31701 (ULMAC). D.B. acknowledges support from the Ramón y Cajal programme (RYC2018-025348-I). K.-N.S. acknowledges support by the Studienstiftung des Deutschen Volkes. A.A.E. and A.M.L. acknowledge support by the Austrian Science Fund (FWF) through grant number I 4548. The computational results presented have been achieved in part using the Vienna Scientific Cluster (VSC) and the LEO HPC infrastructure of the University of Innsbruck.

Author information

Author notes

1. These authors contributed equally: Pascal Scholl, Michael Schuler, Hannah J. Williams, Alexander A. Eberharter

Affiliations

1. Laboratoire Charles Fabry, Institut d’Optique Graduate School, Université Paris-Saclay, CNRS, Palaiseau, France

Pascal Scholl, Hannah J. Williams, Daniel Barredo, Kai-Niklas Schymik, Vincent Lienhard, Thierry Lahaye & Antoine Browaeys

2. Vienna Center for Quantum Science and Technology, Atominstitut, TU Wien, Vienna, Austria

Michael Schuler

3. Institut für Theoretische Physik, Universität Innsbruck, Innsbruck, Austria

Alexander A. Eberharter, Thomas C. Lang & Andreas M. Läuchli

4. Nanomaterials and Nanotechnology Research Center (CINN-CSIC), Universidad de Oviedo (UO), Principado de Asturias, El Entrego, Spain

Daniel Barredo

5. Zentrum für Optische Quantentechnologien, Institut für Laser-Physik, Universität Hamburg, Hamburg, Germany

Louis-Paul Henry

Authors

1. Pascal Scholl

[View author publications](#)

You can also search for this author in [PubMed](#) [Google Scholar](#)

2. Michael Schuler

[View author publications](#)

You can also search for this author in [PubMed](#) [Google Scholar](#)

3. Hannah J. Williams

[View author publications](#)

You can also search for this author in [PubMed](#) [Google Scholar](#)

4. Alexander A. Eberharter

[View author publications](#)

You can also search for this author in [PubMed](#) [Google Scholar](#)

5. Daniel Barredo

[View author publications](#)

You can also search for this author in [PubMed](#) [Google Scholar](#)

6. Kai-Niklas Schymik

[View author publications](#)

You can also search for this author in [PubMed](#) [Google Scholar](#)

7. Vincent Lienhard

[View author publications](#)

You can also search for this author in [PubMed](#) [Google Scholar](#)

8. Louis-Paul Henry

[View author publications](#)

You can also search for this author in [PubMed](#) [Google Scholar](#)

9. Thomas C. Lang

[View author publications](#)

You can also search for this author in [PubMed](#) [Google Scholar](#)

10. Thierry Lahaye

[View author publications](#)

You can also search for this author in [PubMed](#) [Google Scholar](#)

11. Andreas M. Läuchli

[View author publications](#)

You can also search for this author in [PubMed](#) [Google Scholar](#)

12. Antoine Browaeys

[View author publications](#)

You can also search for this author in [PubMed](#) [Google Scholar](#)

Contributions

P.S., M.S., H.J.W. and A.A.E. contributed equally to this work. P.S., H.J.W., D.B., K.-N.S. and V.L. carried out the experiments. M.S., A.A.E., L.-P.H. and T.C.L. performed the simulations. All authors contributed to the data analysis, progression of the project, and on both the experimental and theoretical side. All authors contributed to the writing of the manuscript.

Corresponding author

Correspondence to [Pascal Scholl](#).

Ethics declarations

Competing interests

A.B. and T.C.L. are co-founders and shareholders of Pasqal.

Additional information

Peer review information *Nature* thanks the anonymous reviewer(s) for their contribution to the peer review of this work.

Publisher's note Springer Nature remains neutral with regard to jurisdictional claims in published maps and institutional affiliations.

Extended data figures and tables

[Extended Data Fig. 1 MPS sampling and scaling with bond dimension \$\chi\$.](#)

a, b, Average Rydberg density (**a**) and nearest-neighbour correlation function (**b**) during the MPS state dynamics on the 10×10 square lattice. The black lines show the observables computed from standard tensor contraction and the blue dots show the corresponding sample average of

1,000 generated snapshots. **c–f**, Scaling with bond dimension. **c, d**, Rydberg density (**c**) and order parameter m_{stag} (**d**) during the MPS state dynamics, including experimental imperfections, for different χ on the 10×10 square lattice. The insets show the distribution due to the multiple U_{ij} disorder realizations, at final $t_{\text{off}} = 6 \mu\text{s}$ for $\chi = 256$. **e, f**, Scaling of n (**e**) and m_{stag} (**f**) with χ at the end of the state preparation protocol for different system sizes. The lightly coloured lines show the multiple disorder instances.

Extended Data Fig. 2 Testing the coherence of the Rydberg excitation on a single atom.

a, Rabi oscillations showing the probability of measuring the atom in $\langle \downarrow \rangle$ as a function of the excitation time. The line is a fit to the data by the function $Ae^{-\Gamma t}\cos(\Omega t) + B$, yielding $\Gamma = 0.04(1) \mu\text{s}^{-1}$, $\Omega = 2\pi \times 1.32(1) \text{ MHz}$, $A = 0.488(3)$ and $B = 0.507(3)$. **b**, High-resolution measurement of the first period of the oscillation. Error bars are statistical and often smaller than marker size.

Extended Data Fig. 3 Benchmarking multiple sweeps on the 4×4 array.

a–c, Time evolution of sweep shape (**a**), Rydberg density (**b**) and staggered magnetization (**c**) for three distinct sweeps (of durations $2.5 \mu\text{s}$ (left), $4 \mu\text{s}$ (middle) and $8 \mu\text{s}$ (right)) on the 4×4 array. In **b, c**, experimental data are shown in purple circles and the green (red) dashed lines show solutions to the Schrödinger equation (Lindblad master equation, equation (3)). The solid grey lines show solutions of the Schrödinger equation for several random instances of the interaction disorder (see text), the black line is the average over these instances.

Extended Data Fig. 4 Experimental imperfections.

a, b, Sweep shape for the average Rabi frequency Ω (**a**) and the average detuning δ (**b**) versus time. The dashed line shows the proposed protocol and the solid line shows the experimentally obtained parameters. **c, d**, Spatial dependence of Ω (**c**) and δ (**d**) at the maximal values during the

protocol. **e**, **f**, Distribution of the Rydberg interactions U_{ij} caused by the fluctuations in the atom positions. **e**, The long-range interactions up to a distance of about 50 μm . **f**, The distribution of the nearest-neighbour interactions. The dashed vertical line shows the average nearest-neighbour interaction U_{nnb} . The vertical grey line shows, as a reference, the programmed value for non-fluctuating atoms $U_{\text{programmed}}$. **g**, The left (right) column shows the average density (order parameter m_{stag}) during the sweep for different sizes of the square lattice. Different lines show successive additions of imperfections on the MPS simulations. Starting from the programmed pulse shape without imperfections (blue), we include the real pulse shape measured in the experiment (yellow), add the inhomogeneous fields (green), apply the detection deficiency (red) and, finally, include the interaction disorder from fluctuations in the atom positions. The grey lines show individual samples of atom positions and the black line shows the sample average. Experimental data are shown by circles.

Extended Data Fig. 5 Effect of vacancies on AF ordering.

a, Histogram of the number of defects for the 14×14 array. Out of the roughly 17,000 experimental realizations shown here, we kept only the approximately 500 defect-free shots for the results presented in the main text. **b**, m_{stag} for different filling fractions. We observe a substantial increase in m_{stag} for defect-free array experiments, compared with approximately 99%-filled-array experiments.

Extended Data Fig. 6 Long-term stability of the growth of AF ordering on the 8×8 array.

Staggered magnetization m_{stag} at different times t_{off} during the sweep shown in Extended Data Fig. 2a with several measurements using the same parameters, realized over 15 h. We observe a dispersion of the measurements due to long-term drift of the experimental setup. The dashed line is a phenomenological fit to the data. The standard error on the mean is smaller than symbol size.

Extended Data Fig. 7 Growth of AF ordering on a 10×10 array during the sweep.

Maps of the connected correlations $C_{k,l}$ and histograms of the staggered magnetization for different times t_{off} , defined in Fig. 2. The upper (lower) part of the plots show experimental (MPS) results.

Extended Data Fig. 8 Hypothetical temperature.

a, Assigning a hypothetical temperature. Classical energy density for the instantaneous state $\langle|\Psi(t)\rangle_{\text{off}}\rangle$ of the experiment during the last part of the state preparation protocol (left), and for the corresponding classical equilibrium system versus temperature T (right). Here $\delta = \delta_f$ for all datasets. We assign a hypothetical temperature T_{hyp} at each time t_{off} by matching the classical energy, as illustrated by the red line. In the right panel, T_c denotes the critical temperature in the thermodynamic limit $N \rightarrow \infty$. **b**, The Binder cumulant U_2 and its $(L, 2L)$ crossing points (black markers) for different linear system dimensions L , which allow the estimation of the critical temperature in the thermodynamic limit. The solid (dotted) grey lines indicate the finite size extrapolated T_c and its standard error. **c–f**, Evolution of the hypothetical temperature. **c**, Programmed state preparation protocol. **d–f**, Corresponding hypothetical temperatures $T_{\text{hyp}}(t_{\text{off}})$ during the sweep for different system sizes for the experiment (**d**) and MPS simulations without (**e**) and with (**f**) experimental imperfections. The dashed lines show the classical critical temperature T_c for an infinite system with disorder averaged $U/\hbar = 2\pi \times 1.86$ MHz for $\delta_f = 2\pi \times 2$ MHz.

Extended Data Fig. 9 Quantum real-time evolution versus classical equilibrium.

Distribution of the largest Néel cluster sizes s_{\max} during (left) and at the end (right) of the quantum time evolution (blue) compared with the classical equilibrium results (yellow) on a 10×10 square lattice. **a**, Experimental results. **b**, MPS simulation in the setup without including any experimental

imperfections. **c**, MPS simulation including the known experimental imperfections.

Extended Data Fig. 10 Triangular geometries.

a, b, m_{stag} histogram in the 2/3 plateau obtained from Monte Carlo results on a 108-site triangular cluster with $\hbar\delta/U = 4$ and temperature $T/U = 0.1$. **a**, The real space Rydberg density n_i shows that the outermost shell becomes fully populated at low temperature, as also illustrated in the inset, which shows the Rydberg density at the edge. **b**, The corresponding sublattice magnetization histogram does not reach its full potential width (outer hexagon), as the edge sites cannot participate in the formation of the 2/3-filling states. The dashed hexagon shows the maximum extent of the histogram when only the sites of the system without the edge are considered. **c, d**, Quantum real-time evolution versus classical equilibrium on the triangular lattice. We plot the distribution of the triangular order parameter m_{stag} at the end of the state preparation protocols entering the 1/3 (**c**) and 2/3 (**d**) regimes on a 108-site triangular cluster. Blue (yellow) bars show experimental (corresponding classical) results. The dashed line in **d** shows the maximal value of m_{stag} in the 2/3 regime induced by the cluster boundaries. **e**, Distribution of m_{stag} for a 10×10 square lattice at the end of the sweep entering the AF phase, as a comparison.

Rights and permissions

Reprints and Permissions

About this article



Check for
updates

Cite this article

Scholl, P., Schuler, M., Williams, H.J. *et al.* Quantum simulation of 2D antiferromagnets with hundreds of Rydberg atoms. *Nature* **595**, 233–238 (2021). <https://doi.org/10.1038/s41586-021-03585-1>

[Download citation](#)

- Received: 21 December 2020
- Accepted: 27 April 2021
- Published: 07 July 2021
- Issue Date: 08 July 2021
- DOI: <https://doi.org/10.1038/s41586-021-03585-1>

Comments

By submitting a comment you agree to abide by our [Terms](#) and [Community Guidelines](#). If you find something abusive or that does not comply with our terms or guidelines please flag it as inappropriate.

[Access through your institution](#)

[Change institution](#)

[Buy or subscribe](#)

Advertisement

This article was downloaded by **calibre** from <https://www.nature.com/articles/s41586-021-03585-1>

- Article
- [Published: 07 July 2021](#)

Optical manipulation of electronic dimensionality in a quantum material

- [Shaofeng Duan](#)¹_{na1},
- [Yun Cheng](#)²_{na1},
- [Wei Xia](#)³,
- [Yuanyuan Yang](#)¹,
- [Chengyang Xu](#)⁴,
- [Fengfeng Qi](#)²,
- [Chaozhi Huang](#)¹,
- [Tianwei Tang](#)¹,
- [Yanfeng Guo](#) ORCID: orcid.org/0000-0002-9386-4857³,
- [Weidong Luo](#) ORCID: orcid.org/0000-0003-3829-1547^{4,5},
- [Dong Qian](#)^{1,6},
- [Dao Xiang](#) ORCID: orcid.org/0000-0003-1590-7193^{2,6,7},
- [Jie Zhang](#)² &
- [Wentao Zhang](#) ORCID: orcid.org/0000-0001-8904-1252¹

[Nature](#) volume **595**, pages 239–244 (2021) [Cite this article](#)

- 15 Altmetric
- [Metrics details](#)

Subjects

- [Superconducting properties and materials](#)

- [Surfaces, interfaces and thin films](#)

Abstract

Exotic phenomena can be achieved in quantum materials by confining electronic states into two dimensions. For example, relativistic fermions are realized in a single layer of carbon atoms¹, the quantized Hall effect can result from two-dimensional (2D) systems^{2,3}, and the superconducting transition temperature can be considerably increased in a one-atomic-layer material^{4,5}. Ordinarily, a 2D electronic system can be obtained by exfoliating the layered materials, growing monolayer materials on substrates, or establishing interfaces between different materials. Here we use femtosecond infrared laser pulses to invert the periodic lattice distortion sectionally in a three-dimensional (3D) charge density wave material (1T-TiSe₂), creating macroscopic domain walls of transient 2D ordered electronic states with unusual properties. The corresponding ultrafast electronic and lattice dynamics are captured by time-resolved and angle-resolved photoemission spectroscopy⁶ and ultrafast electron diffraction at energies of the order of megaelectronvolts⁷. Moreover, in the photoinduced 2D domain wall near the surface we identify a phase with enhanced density of states and signatures of potential opening of an energy gap near the Fermi energy. Such optical modulation of atomic motion is an alternative path towards realizing 2D electronic states and will be a useful platform upon which novel phases in quantum materials may be discovered.

Access options

Subscribe to Journal

Get full journal access for 1 year

\$199.00

only \$3.90 per issue

[Subscribe](#)

All prices are NET prices.
VAT will be added later in the checkout.
Tax calculation will be finalised during checkout.

Rent or Buy article

Get time limited or full article access on ReadCube.

from \$8.99

[Rent or Buy](#)

All prices are NET prices.

Additional access options:

- [Log in](#)
- [Access through your institution](#)
- [Learn about institutional subscriptions](#)

Fig. 1: Time-resolved electronic structure and electron diffraction patterns in TiSe₂.

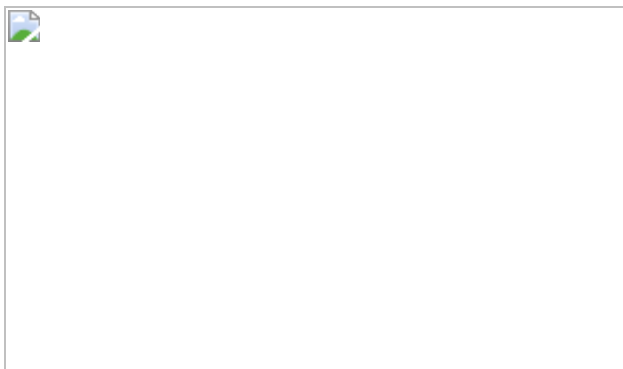


Fig. 2: Experimental and simulated electronic structure and PLD dynamics.

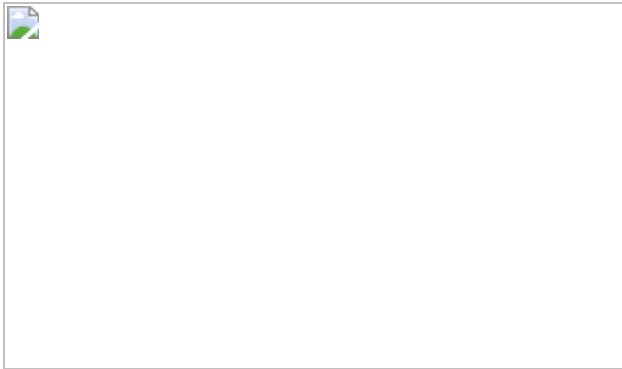


Fig. 3: Photoinduced domain wall.



Fig. 4: Energy gap in the pump-induced domain wall.



Data availability

The data that support the plots within this paper and other findings of this study are available from the corresponding author upon reasonable request. Correspondence and requests for materials regarding trARPES

experimental data and the simulation should be addressed to W.Z. and regarding UED experimental data should be addressed to D.X.

References

1. 1.

Castro Neto, A. H., Guinea, F., Peres, N. M. R., Novoselov, K. S. & Geim, A. K. The electronic properties of graphene. *Rev. Mod. Phys.* **81**, 109–162 (2009).

[ADS](#) [CAS](#) [Google Scholar](#)

2. 2.

von Klitzing, K., Dorda, G. & Pepper, M. New method for high-accuracy determination of the fine-structure constant based on quantized Hall resistance. *Phys. Rev. Lett.* **45**, 494–497 (1980).

[ADS](#) [Google Scholar](#)

3. 3.

Tsui, D. C., Stormer, H. L. & Gossard, A. C. Two-dimensional magnetotransport in the extreme quantum limit. *Phys. Rev. Lett.* **48**, 1559–1562 (1982).

[ADS](#) [CAS](#) [Google Scholar](#)

4. 4.

He, S. L. et al. Phase diagram and electronic indication of high-temperature superconductivity at 65 K in single-layer FeSe films. *Nat. Mater.* **12**, 605–610 (2013).

[ADS](#) [CAS](#) [PubMed](#) [PubMed Central](#) [Google Scholar](#)

5. 5.

Tan, S. Y. et al. Interface-induced superconductivity and strain-dependent spin density waves in FeSe/SrTiO₃ thin films. *Nat. Mater.* **12**, 634–640 (2013).

[ADS](#) [CAS](#) [PubMed](#) [PubMed Central](#) [Google Scholar](#)

6. 6.

Yang, Y. et al. A time- and angle-resolved photoemission spectroscopy with probe photon energy up to 6.7 eV. *Rev. Sci. Instrum.* **90**, 063905 (2019).

[ADS](#) [PubMed](#) [PubMed Central](#) [Google Scholar](#)

7. 7.

Qi, F. F. et al. Breaking 50 femtosecond resolution barrier in MeV ultrafast electron diffraction with a double bend achromat compressor. *Phys. Rev. Lett.* **124**, 134803 (2020).

[ADS](#) [CAS](#) [PubMed](#) [PubMed Central](#) [Google Scholar](#)

8. 8.

Fausti, D. et al. Light-induced superconductivity in a stripe-ordered cuprate. *Science* **331**, 189–191 (2011).

[ADS](#) [CAS](#) [PubMed](#) [PubMed Central](#) [Google Scholar](#)

9. 9.

Mitrano, M. et al. Possible light-induced superconductivity in K₃C₆₀ at high temperature. *Nature* **530**, 461–464 (2016).

[ADS](#) [CAS](#) [PubMed](#) [PubMed Central](#) [Google Scholar](#)

10. 10.

Ichikawa, H. et al. Transient photoinduced ‘hidden’ phase in a manganite. *Nat. Mater.* **10**, 101–105 (2011).

[ADS](#) [CAS](#) [PubMed](#) [PubMed Central](#) [Google Scholar](#)

11. 11.

Stojchevska, L. et al. Ultrafast switching to a stable hidden quantum state in an electronic crystal. *Science* **344**, 177–180 (2014).

[ADS](#) [CAS](#) [PubMed](#) [PubMed Central](#) [Google Scholar](#)

12. 12.

Rini, M. et al. Control of the electronic phase of a manganite by mode-selective vibrational excitation. *Nature* **449**, 72–74 (2007).

[ADS](#) [CAS](#) [PubMed](#) [PubMed Central](#) [Google Scholar](#)

13. 13.

Li, X. et al. Terahertz field-induced ferroelectricity in quantum paraelectric SrTiO₃. *Science* **364**, 1079–1082 (2019).

[ADS](#) [CAS](#) [PubMed](#) [PubMed Central](#) [Google Scholar](#)

14. 14.

Sie, E. J. et al. An ultrafast symmetry switch in a Weyl semimetal. *Nature* **565**, 61–66 (2019).

[ADS](#) [CAS](#) [PubMed](#) [PubMed Central](#) [Google Scholar](#)

15. 15.

Horstmann, J. G. et al. Coherent control of a surface structural phase transition. *Nature* **583**, 232–236 (2020).

[ADS](#) [CAS](#) [PubMed](#) [PubMed Central](#) [Google Scholar](#)

16. 16.

Morrison, V. R. et al. A photoinduced metal-like phase of monoclinic VO_2 revealed by ultrafast electron diffraction. *Science* **346**, 445–448 (2014).

[ADS](#) [CAS](#) [PubMed](#) [PubMed Central](#) [Google Scholar](#)

17. 17.

Nova, T. F., Disa, A. S., Fechner, M. & Cavalleri, A. Metastable ferroelectricity in optically strained SrTiO_3 . *Science* **364**, 1075–1079 (2019).

[ADS](#) [CAS](#) [PubMed](#) [PubMed Central](#) [Google Scholar](#)

18. 18.

Wang, Y. H., Steinberg, H., Jarillo-Herrero, P. & Gedik, N. Observation of Floquet–Bloch states on the surface of a topological insulator. *Science* **342**, 453–457 (2013).

[ADS](#) [CAS](#) [PubMed](#) [PubMed Central](#) [Google Scholar](#)

19. 19.

Lian, C., Zhang, S.-J., Hu, S.-Q., Guan, M.-X. & Meng, S. Ultrafast charge ordering by self-amplified exciton–phonon dynamics in TiSe_2 . *Nat. Commun.* **11**, 43 (2020).

[ADS](#) [CAS](#) [PubMed](#) [PubMed Central](#) [Google Scholar](#)

20. 20.

Trigo, M. et al. Ultrafast formation of domain walls of a charge density wave in SmTe_3 . *Phys. Rev. B* **103**, 054109 (2021).

[ADS](#) [CAS](#) [Google Scholar](#)

21. 21.

Yusupov, R. et al. Coherent dynamics of macroscopic electronic order through a symmetry-breaking transition. *Nat. Phys.* **6**, 681–684 (2010).

[CAS](#) [Google Scholar](#)

22. 22.

Huber, T. et al. Coherent structural dynamics of a prototypical charge-density-wave-to-metal transition. *Phys. Rev. Lett.* **113**, 026401 (2014).

[ADS](#) [CAS](#) [PubMed](#) [PubMed Central](#) [Google Scholar](#)

23. 23.

Di Salvo, F. J., Moncton, D. E. & Waszczak, J. V. Electronic properties and superlattice formation in the semimetal TiSe_2 . *Phys. Rev. B* **14**, 4321–4328 (1976).

[ADS](#) [Google Scholar](#)

24. 24.

Cercellier, H. et al. Evidence for an excitonic insulator phase in 1T- TiSe_2 . *Phys. Rev. Lett.* **99**, 146403 (2007).

[ADS](#) [CAS](#) [PubMed](#) [PubMed Central](#) [Google Scholar](#)

25. 25.

Möhr-Vorobeva, E. et al. Nonthermal melting of a charge density wave in TiSe_2 . *Phys. Rev. Lett.* **107**, 036403 (2011).

[ADS](#) [PubMed](#) [PubMed Central](#) [Google Scholar](#)

26. 26.

Kogar, A. et al. Signatures of exciton condensation in a transition metal dichalcogenide. *Science* **358**, 1314–1317 (2017).

[ADS](#) [CAS](#) [PubMed](#) [PubMed Central](#) [Google Scholar](#)

27. 27.

Hildebrand, B. et al. Local real-space view of the achiral 1T-TiSe₂ 2 × 2 × 2 charge density wave. *Phys. Rev. Lett.* **120**, 136404 (2018).

[ADS](#) [CAS](#) [PubMed](#) [PubMed Central](#) [Google Scholar](#)

28. 28.

Pillo, T. et al. Photoemission of bands above the Fermi level: the excitonic insulator phase transition in 1T-TiSe₂. *Phys. Rev. B* **61**, 16213–16222 (2000).

[ADS](#) [CAS](#) [Google Scholar](#)

29. 29.

Watson, M. D. et al. Orbital-and $k(z)$ -selective hybridization of Se 4p and Ti 3d states in the charge density wave phase of TiSe₂. *Phys. Rev. Lett.* **122**, 076404 (2019).

[ADS](#) [CAS](#) [PubMed](#) [PubMed Central](#) [Google Scholar](#)

30. 30.

Rohwer, T. et al. Collapse of long-range charge order tracked by time-resolved photoemission at high momenta. *Nature* **471**, 490–493 (2011).

[ADS](#) [CAS](#) [PubMed](#) [PubMed Central](#) [Google Scholar](#)

31. 31.

Porer, M. et al. Non-thermal separation of electronic and structural orders in a persisting charge density wave. *Nat. Mater.* **13**, 857–861 (2014).

[ADS](#) [CAS](#) [PubMed](#) [PubMed Central](#) [Google Scholar](#)

32. 32.

Hedayat, H. et al. Excitonic and lattice contributions to the charge density wave in 1T-TiSe₂ revealed by a phonon bottleneck. *Phys. Rev. Res.* **1**, 023029 (2019).

[CAS](#) [Google Scholar](#)

33. 33.

Holy, J. A., Woo, K. C., Klein, M. V. & Brown, F. C. Raman and infrared studies of superlattice formation in TiSe₂. *Phys. Rev. B* **16**, 3628–3637 (1977).

[ADS](#) [CAS](#) [Google Scholar](#)

34. 34.

Snow, C. S., Karpus, J. F., Cooper, S. L., Kidd, T. E. & Chiang, T. C. Quantum melting of the charge-density-wave state in 1T-TiSe₂. *Phys. Rev. Lett.* **91**, 136402 (2003).

[ADS](#) [CAS](#) [PubMed](#) [PubMed Central](#) [Google Scholar](#)

35. 35.

Schaefer, H., Kabanov, V. V. & Demsar, J. Collective modes in quasi-one-dimensional charge-density wave systems probed by femtosecond time-resolved optical studies. *Phys. Rev. B* **89**, 045106 (2014).

[ADS](#) [Google Scholar](#)

36. 36.

Joe, Y. I. et al. Emergence of charge density wave domain walls above the superconducting dome in 1T-TiSe₂. *Nat. Phys.* **10**, 421–425 (2014).

[CAS](#) [Google Scholar](#)

37. 37.

Yan, S. C. et al. Influence of domain walls in the incommensurate charge density wave state of Cu-intercalated 1T-TiSe₂. *Phys. Rev. Lett.* **118**, 106405 (2017).

[ADS](#) [PubMed](#) [PubMed Central](#) [Google Scholar](#)

38. 38.

Li, L. J. et al. Controlling many-body states by the electric-field effect in a two-dimensional material. *Nature* **529**, 185–189 (2016).

[ADS](#) [CAS](#) [PubMed](#) [PubMed Central](#) [Google Scholar](#)

39. 39.

Li, S. Y., Wu, G., Chen, X. H. & Taillefer, L. Single-gap *s*-wave superconductivity near the charge-density-wave quantum critical point in Cu_xTiSe₂. *Phys. Rev. Lett.* **99**, 107001 (2007).

[ADS](#) [CAS](#) [PubMed](#) [PubMed Central](#) [Google Scholar](#)

40. 40.

Hu, W. et al. Optically enhanced coherent transport in YBa₂Cu₃O_{6.5} by ultrafast redistribution of interlayer coupling. *Nat. Mater.* **13**, 705–711 (2014).

[ADS](#) [CAS](#) [PubMed](#) [PubMed Central](#) [Google Scholar](#)

41. 41.

Norman, M. R. et al. Destruction of the Fermi surface underdoped high- T_c superconductors. *Nature* **392**, 157–160 (1998).

[ADS](#) [CAS](#) [Google Scholar](#)

42. 42.

Bayliss, S. C. & Liang, W. Y. Reflectivity, joint density of states and band structure of group IVb transition-metal dichalcogenides. *J. Phys. C* **18**, 3327–3335 (1985).

[ADS](#) [CAS](#) [Google Scholar](#)

43. 43.

McMillan, W. L. Landau theory of charge-density waves in transition-metal dichalcogenides. *Phys. Rev. B* **12**, 1187–1196 (1975).

[ADS](#) [CAS](#) [Google Scholar](#)

44. 44.

Strocov, V. N. et al. Three-dimensional electron realm in VSe₂ by soft-X-ray photoelectron spectroscopy: origin of charge-density waves. *Phys. Rev. Lett.* **109**, 086401 (2012).

[ADS](#) [PubMed](#) [PubMed Central](#) [Google Scholar](#)

45. 45.

Xia, Y. et al. Observation of a large-gap topological-insulator class with a single Dirac cone on the surface. *Nat. Phys.* **5**, 398–402 (2009).

[CAS](#) [Google Scholar](#)

46. 46.

Shen, Z.-X. et al. Anomalously large gap anisotropy in the a - b plane of $\text{Bi}_2\text{Sr}_2\text{CaCu}_2\text{O}_{8+\delta}$. *Phys. Rev. Lett.* **70**, 1553–1556 (1993).

[ADS](#) [CAS](#) [PubMed](#) [PubMed Central](#) [Google Scholar](#)

47. 47.

Hashimoto, M., Vishik, I. M., He, R.-H., Devereaux, T. P. & Shen, Z.-X. Energy gaps in high-transition-temperature cuprate superconductors. *Nat. Phys.* **10**, 483–495 (2014).

[CAS](#) [Google Scholar](#)

48. 48.

Hohenberg, P. & Kohn, W. Inhomogeneous electron gas. *Phys. Rev.* **136**, B864–B871 (1964).

[ADS](#) [MathSciNet](#) [Google Scholar](#)

49. 49.

Kohn, W. & Sham, L. J. Self-consistent equations including exchange and correlation effects. *Phys. Rev.* **140**, A1133–A1138 (1965).

[ADS](#) [MathSciNet](#) [Google Scholar](#)

50. 50.

Kresse, G. & Furthmuller, J. Efficiency of ab-initio total energy calculations for metals and semiconductors using a plane-wave basis set. *Comput. Mater. Sci.* **6**, 15–50 (1996).

[CAS](#) [Google Scholar](#)

51. 51.

Kresse, G. & Furthmuller, J. Efficient iterative schemes for ab initio total-energy calculations using a plane-wave basis set. *Phys. Rev. B* **54**,

11169–11186 (1996).

[ADS](#) [CAS](#) [Google Scholar](#)

52. 52.

Blöchl, P. E. Projector augmented-wave method. *Phys. Rev. B* **50**, 17953–17979 (1994).

[ADS](#) [Google Scholar](#)

53. 53.

Perdew, J. P., Burke, K. & Ernzerhof, M. Generalized gradient approximation made simple. *Phys. Rev. Lett.* **78**, 1396 (1997).

[ADS](#) [CAS](#) [Google Scholar](#)

[Download references](#)

Acknowledgements

W.Z. acknowledges support from the Ministry of Science and Technology of China (2016YFA0300501) and the National Natural Science Foundation of China (11974243), and additional support from a Shanghai talent programme. Y.G. acknowledges support from the National Natural Science Foundation of China (grant no. 11874264). D.Q. acknowledges support from the Ministry of Science and Technology of China (grant no. 2016YFA0301003). D.Q. and W.L. acknowledge support from the National Natural Science Foundation of China (grant nos 12074248 and 11521404). D.X. and J.Z. acknowledge support from the National Natural Science Foundation of China (grant nos 11925505, 11504232 and 11721091) and from the office of Science and Technology, Shanghai Municipal Government (nos 16DZ2260200 and 18JC1410700). First-principles computations were performed at the Center for High Performance Computing of Shanghai Jiao Tong University.

Author information

Author notes

1. These authors contributed equally: Shaofeng Duan, Yun Cheng

Affiliations

1. Key Laboratory of Artificial Structures and Quantum Control (Ministry of Education), Shenyang National Laboratory for Materials Science, School of Physics and Astronomy, Shanghai Jiao Tong University, Shanghai, China

Shaofeng Duan, Yuanyuan Yang, Chaozhi Huang, Tianwei Tang, Dong Qian & Wentao Zhang

2. Key Laboratory for Laser Plasmas (Ministry of Education), School of Physics and Astronomy, Shanghai Jiao Tong University, Shanghai, China

Yun Cheng, Fengfeng Qi, Dao Xiang & Jie Zhang

3. School of Physical Science and Technology, ShanghaiTech University, Shanghai, China

Wei Xia & Yanfeng Guo

4. Key Laboratory of Artificial Structures and Quantum Control (Ministry of Education), School of Physics and Astronomy, Shanghai Jiao Tong University, Shanghai, China

Chengyang Xu & Weidong Luo

5. Institute of Natural Sciences, Shanghai Jiao Tong University, Shanghai, China

Weidong Luo

6. Tsung-Dao Lee Institute, Shanghai Jiao Tong University, Shanghai, China

Dong Qian & Dao Xiang

7. Zhangjiang Institute for Advanced Study, Shanghai Jiao Tong University, Shanghai, China

Dao Xiang

Authors

1. Shaofeng Duan

[View author publications](#)

You can also search for this author in [PubMed](#) [Google Scholar](#)

2. Yun Cheng

[View author publications](#)

You can also search for this author in [PubMed](#) [Google Scholar](#)

3. Wei Xia

[View author publications](#)

You can also search for this author in [PubMed](#) [Google Scholar](#)

4. Yuanyuan Yang

[View author publications](#)

You can also search for this author in [PubMed](#) [Google Scholar](#)

5. Chengyang Xu

[View author publications](#)

You can also search for this author in [PubMed](#) [Google Scholar](#)

6. Fengfeng Qi

[View author publications](#)

You can also search for this author in [PubMed](#) [Google Scholar](#)

7. Chaozhi Huang

[View author publications](#)

You can also search for this author in [PubMed](#) [Google Scholar](#)

8. Tianwei Tang

[View author publications](#)

You can also search for this author in [PubMed](#) [Google Scholar](#)

9. Yanfeng Guo

[View author publications](#)

You can also search for this author in [PubMed](#) [Google Scholar](#)

10. Weidong Luo

[View author publications](#)

You can also search for this author in [PubMed](#) [Google Scholar](#)

11. Dong Qian

[View author publications](#)

You can also search for this author in [PubMed](#) [Google Scholar](#)

12. Dao Xiang

[View author publications](#)

You can also search for this author in [PubMed](#) [Google Scholar](#)

13. Jie Zhang

[View author publications](#)

You can also search for this author in [PubMed](#) [Google Scholar](#)

14. Wentao Zhang

[View author publications](#)

You can also search for this author in [PubMed](#) [Google Scholar](#)

Contributions

W.Z. and D.X. proposed and designed the research. S.D., Y.Y., C.H., T.T. and W.Z. contributed to the development and maintenance of the trARPES system. S.D., Y.Y. and C.H. collected the trARPES data. Y.C. and F.Q. took the UED measurements. W.X. and Y.G. prepared the single-crystal sample. S.D., Y.C., D.X. and W.Z. performed the phenomenological simulation. C.X. and W.L. performed the DFT calculation. W.Z. wrote the paper with S.D., Y.C., W.L., D.Q., D.X. and J.Z. All authors discussed the results and commented on the manuscript.

Corresponding authors

Correspondence to [Dao Xiang](#) or [Wentao Zhang](#).

Ethics declarations

Competing interests

The authors declare no competing interests.

Additional information

Peer review information *Nature* thanks Claude Monney and the other, anonymous, reviewer(s) for their contribution to the peer review of this work. Peer reviewer reports are available.

Publisher's note Springer Nature remains neutral with regard to jurisdictional claims in published maps and institutional affiliations.

Extended data figures and tables

Extended Data Fig. 1 Simulated and experimental electron diffraction patterns in TiSe₂.

a, b, Simulated and experimental electron diffraction patterns based on the kinetical theory with the sample thickness of 60 nm. **c**, Experimental diffraction patterns at 12 ps with a tilted angle. Data were taken with the same pump fluence and equilibrium temperature as in Fig. 1d. The intensity units on the colour scale are arbitrary.

Extended Data Fig. 2 Ultrafast electronic dynamics.

a, Time-dependent photoemission spectroscopy intensity at different pump fluences. The intensity is the integration of non-equilibrium electrons between 0 and 0.03 eV above the Fermi energy. **b**, The decay rates of nonequilibrium electrons as a function of pump fluence. The three different regions separated by the two critical pump fluences are indicated by different colours in the background.

Extended Data Fig. 3 Additional measurements on two other samples (samples II and III).

a, Spectral intensity as a function of the pump fluence integrated from -0.1 eV (Se $4p_{x,y}$ band top) to the Fermi level for samples II and III at a delay time of 12 ps. **b**, Photoemission spectra difference between fluences I' and I ($I(I) - I(I')$) from 3 to 40 ps for sample II. The colour scale is in arbitrary units, and ‘-’ (green) indicates <0 and ‘+’ (red) indicates >0 . **c**, EDCs at the momentum of the dashed line shown in the inset of Fig. 4b for pump fluences at I' and I for samples II and III. EDCs are normalized to the same height. **d**, Spectral intensity as a function of the pump fluence integrated from -0.1 eV (Se $4p_{x,y}$ band top) to the Fermi level for sample II. **e**, Original EDCs without normalization between 3 and 40 ps for sample II. **f**, Normalized EDCs from e.

Extended Data Fig. 4 DFT calculations and experimental electronic structures of the bulk and 2D domain wall.

a, Charge density isosurface plot of the domain-wall bands at the Γ point. The Ti and Se atoms are shown in blue and green spheres, and the outer and inner surfaces of the density state isosurface on the domain wall are shown in purple and blue. **b**, Band structure of the periodic eight-layer supercell with domain wall. The p_x and p_y orbitals are projected to the three layers at the domain wall (shown in red circles); the symbol size denotes the relative weight of the orbitals. The reference bands are drawn in orange lines. **c**, Energy shifts of the domain-wall bands at different strengths of CDW displacements. The label ‘CDW’ means a single CDW phase, and ‘domain’ means the presence of sharp domain wall. **d**, Time-resolved photoemission spectra at 12 ps for pump fluences at I' and I , as indicated in the inset to **e**. **e**, EDCs at the momentum of -0.13 \AA^{-1} for pump fluence I' and I , as indicated by the solid line cuts (the same colour as the corresponding EDC) in **d**. Inset shows the same spectra at 12 ps for sample II as that shown in Extended Data Fig. [3a](#). EDCs are normalized to the same height.

Supplementary information

Supplementary Information

This Supplementary Information file contains sections (I) Numerical solution of the motion equation; and (II) Pump probe fluence resolution; including Supplementary figure 1 and 2.

Peer Review File

Rights and permissions

Reprints and Permissions

About this article



Check for
updates

Cite this article

Duan, S., Cheng, Y., Xia, W. *et al.* Optical manipulation of electronic dimensionality in a quantum material. *Nature* **595**, 239–244 (2021). <https://doi.org/10.1038/s41586-021-03643-8>

[Download citation](#)

- Received: 14 January 2021
- Accepted: 13 May 2021
- Published: 07 July 2021
- Issue Date: 08 July 2021
- DOI: <https://doi.org/10.1038/s41586-021-03643-8>

Comments

By submitting a comment you agree to abide by our [Terms](#) and [Community Guidelines](#). If you find something abusive or that does not comply with our terms or guidelines please flag it as inappropriate.

[Access through your institution](#)

[Change institution](#)

[Buy or subscribe](#)

Advertisement

This article was downloaded by **calibre** from <https://www.nature.com/articles/s41586-021-03643-8>

- Article
- [Published: 07 July 2021](#)

Bifunctional nanoprecipitates strengthen and ductilize a medium-entropy alloy

- [Ying Yang](#) [ORCID: orcid.org/0000-0001-6480-2254¹](#),
- [Tianyi Chen¹](#) [nAffs](#),
- [Lizhen Tan¹](#),
- [Jonathan D. Poplawsky](#) [ORCID: orcid.org/0000-0002-4272-7043²](#),
- [Ke An](#) [ORCID: orcid.org/0000-0002-6093-429X³](#),
- [Yanli Wang¹](#),
- [German D. Samolyuk¹](#),
- [Ken Littrell](#) [ORCID: orcid.org/0000-0003-2308-8618³](#),
- [Andrew R. Lupini](#) [ORCID: orcid.org/0000-0002-1874-7925²](#),
- [Albina Borisevich²](#) &
- [Easo P. George](#) [ORCID: orcid.org/0000-0001-9898-9694^{1,4}](#)

[Nature](#) volume 595, pages 245–249 (2021) [Cite this article](#)

- 75 Altmetric
- [Metrics details](#)

Subjects

- [Mechanical properties](#)
- [Metals and alloys](#)

Abstract

Single-phase high- and medium-entropy alloys with face-centred cubic (fcc) structure can exhibit high tensile ductility^{1,2} and excellent toughness^{2,3}, but their room-temperature strengths are low^{1,2,3}. Dislocation obstacles such as grain boundaries⁴, twin boundaries⁵, solute atoms⁶ and precipitates^{7,8,9} can increase strength. However, with few exceptions^{8,9,10,11}, such obstacles tend to decrease ductility. Interestingly, precipitates can also hinder phase transformations^{12,13}. Here, using a model, precipitate-strengthened, Fe–Ni–Al–Ti medium-entropy alloy, we demonstrate a strategy that combines these dual functions in a single alloy. The nanoprecipitates in our alloy, in addition to providing conventional strengthening of the matrix, also modulate its transformation from fcc-austenite to body-centred cubic (bcc) martensite, constraining it to remain as metastable fcc after quenching through the transformation temperature. During subsequent tensile testing, the matrix progressively transforms to bcc-martensite, enabling substantial increases in strength, work hardening and ductility. This use of nanoprecipitates exploits synergies between precipitation strengthening and transformation-induced plasticity, resulting in simultaneous enhancement of tensile strength and uniform elongation. Our findings demonstrate how synergistic deformation mechanisms can be deliberately activated, exactly when needed, by altering precipitate characteristics (such as size, spacing, and so on), along with the chemical driving force for phase transformation, to optimize strength and ductility.

Access options

Subscribe to Journal

Get full journal access for 1 year

\$199.00

only \$3.90 per issue

[Subscribe](#)

All prices are NET prices.
VAT will be added later in the checkout.
Tax calculation will be finalised during checkout.

Rent or Buy article

Get time limited or full article access on ReadCube.

from \$8.99

[Rent or Buy](#)

All prices are NET prices.

Additional access options:

- [Log in](#)
- [Access through your institution](#)
- [Learn about institutional subscriptions](#)

Fig. 1: Microstructures and tensile properties of FNAT-m-47h and FNAT-47h alloys.



Fig. 2: Microstructure analysis of the FNAT-47h and FNAT-4h alloys.

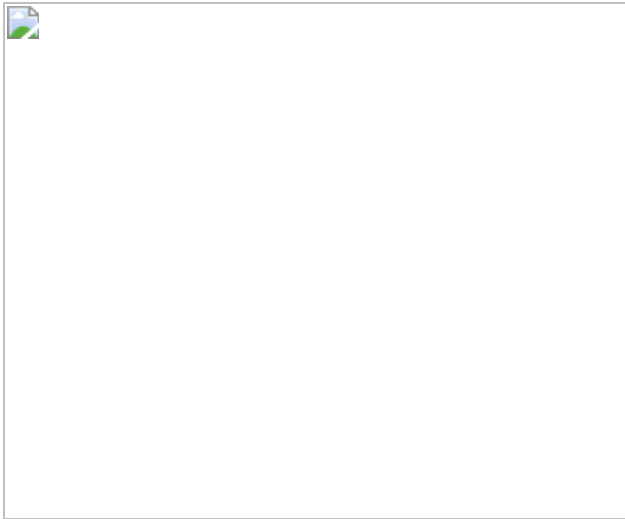


Fig. 3: Room-temperature mechanical properties and deformation mechanisms of FNAT alloys.



Fig. 4: Comparison of uniform elongation versus ultimate tensile strength at room temperature of the current MEAs (FNAT-47h, FNAT-8h, and FNAT-4h) with other HEAs and steels.



Data availability

All figures have associated raw data, available on request from Y.Y.

References

1. 1.

Gali, A. & George, E. P. Tensile properties of high- and medium-entropy alloys. *Intermetallics* **39**, 74–78 (2013).

[CAS](#) [Google Scholar](#)

2. 2.

Gludovatz, B. et al. Exceptional damage-tolerance of a medium-entropy alloy CrCoNi at cryogenic temperatures. *Nat. Commun.* **7**, 10602 (2016).

[ADS](#) [CAS](#) [PubMed](#) [PubMed Central](#) [Google Scholar](#)

3. 3.

Gludovatz, B. et al. A fracture-resistant high-entropy alloy for cryogenic applications. *Science* **345**, 1153–1158 (2014).

[ADS](#) [CAS](#) [PubMed](#) [PubMed Central](#) [Google Scholar](#)

4. 4.

Kumar, K., Van Swygenhoven, H. & Suresh, S. Mechanical behavior of nanocrystalline metals and alloys. *Acta Mater.* **51**, 5743–5774 (2003).

[ADS](#) [CAS](#) [Google Scholar](#)

5. 5.

Lu, L., Chen, X., Huang, X. & Lu, K. Revealing the maximum strength in nanotwinned copper. *Science* **323**, 607–610 (2009).

[ADS](#) [CAS](#) [PubMed](#) [PubMed Central](#) [Google Scholar](#)

6. 6.

Labusch, R. A statistical theory of solid solution hardening. *Phys. Status Solidi B* **41**, 659–669 (1970).

[ADS](#) [Google Scholar](#)

7. 7.

Gladman, T. Precipitation hardening in metals. *Mater. Sci. Technol.* **15**, 30–36 (1999).

[CAS](#) [Google Scholar](#)

8. 8.

Jiang, S. et al. Ultrastrong steel via minimal lattice misfit and high-density nanoprecipitation. *Nature* **544**, 460 (2017).

[ADS](#) [CAS](#) [PubMed](#) [PubMed Central](#) [Google Scholar](#)

9. 9.

Yang, T. et al. Multicomponent intermetallic nanoparticles and superb mechanical behaviors of complex alloys. *Science* **362**, 933–937 (2018).

[ADS](#) [CAS](#) [PubMed](#) [PubMed Central](#) [Google Scholar](#)

10. 10.

He, B. et al. High dislocation density-induced large ductility in deformed and partitioned steels. *Science* **357**, 1029–1032 (2017).

[ADS](#) [CAS](#) [PubMed](#) [PubMed Central](#) [Google Scholar](#)

11. 11.

Lu, K., Lu, L. & Suresh, S. Strengthening materials by engineering coherent internal boundaries at the nanoscale. *Science* **324**, 349–352 (2009).

[ADS](#) [CAS](#) [PubMed](#) [PubMed Central](#) [Google Scholar](#)

12. 12.

La Roca, P., Baruj, A., Sobrero, C. E., Malarria, J. A. & Sade, M. Nanoprecipitation effects on phase stability of Fe-Mn-Al-Ni alloys. *J. Alloys Compd.* **708**, 422–427 (2017).

[Google Scholar](#)

13. 13.

Luo, H., Shan, F., Huo, Y. & Wang, Y. Effect of precipitates on phase transformation behavior of Ti-49 at.% Ni film. *Thin Solid Films* **339**, 305–308 (1999).

[ADS](#) [CAS](#) [Google Scholar](#)

14. 14.

Kaufman, L. & Cohen, M. The martensitic transformation in the iron-nickel system. *JOM* **8**, 1393–1401 (1956).

[ADS](#) [CAS](#) [Google Scholar](#)

15. 15.

Liang, Y.-J. et al. High-content ductile coherent nanoprecipitates achieve ultrastrong high-entropy alloys. *Nat. Commun.* **9**, 4063 (2018).

[ADS](#) [PubMed](#) [PubMed Central](#) [Google Scholar](#)

16. 16.

Raabe, D., Ponge, D., Dmitrieva, O. & Sander, B. Nanoprecipitate-hardened 1.5 GPa steels with unexpected high ductility. *Scr. Mater.* **60**, 1141–1144 (2009).

[CAS](#) [Google Scholar](#)

17. 17.

Nishiyama, Z. X-ray investigation of the mechanism of the transformation from face centered cubic lattice to body centered cubic. *Sci. Rep. Tohoku Univ.* **23**, 637 (1934).

[CAS](#) [Google Scholar](#)

18. 18.

Fisher, J., Hollomon, J. & Turnbull, D. Kinetics of the austenite → martensite transformation. *Metals Trans.* **185**, 691–700 (1949).

[Google Scholar](#)

19. 19.

Jimenez-Melero, E. et al. Martensitic transformation of individual grains in low-alloyed TRIP steels. *Scr. Mater.* **56**, 421–424 (2007).

[CAS](#) [Google Scholar](#)

20. 20.

Yang, H.-S. & Bhadeshia, H. Austenite grain size and the martensite-start temperature. *Scr. Mater.* **60**, 493–495 (2009).

[CAS](#) [Google Scholar](#)

21. 21.

Jin, S., Morris, J., Chen, Y., Thomas, G. & Jaffee, R. An investigation of transformation strengthening in precipitation-hardened Fe-Ni austenite. *Metall. Trans. A* **9**, 1625–1633 (1978).

[Google Scholar](#)

22. 22.

Wang, T. et al. Co-introduction of precipitate hardening and TRIP in a TWIP high-entropy alloy using friction stir alloying. *Sci. Rep.* **11**, 1–10 (2021).

[CAS](#) [Google Scholar](#)

23. 23.

Kaufman, L. & Bernstein, H. *Computer Calculation of Phase Diagrams. With Special Reference to Refractory Metals* (Academic Press, 1970).

24. 24.

Cao, W. et al. PANDAT software with PanEngine, PanOptimizer and PanPrecipitation for multi-component phase diagram calculation and materials property simulation. *Calphad* **33**, 328–342 (2009).

[CAS](#) [Google Scholar](#)

25. 25.

Yeh, J. W., Chen, Y. L., Lin, S. J. & Chen, S. K. in *Materials Science Forum* Vol. 560 (eds Balmori-Ramirez, H. et al.) 1–9 (Trans Tech Publ, 2007).

26. 26.

Cacciamani, G. et al. Critical evaluation of the Fe–Ni, Fe–Ti and Fe–Ni–Ti alloy systems. *Intermetallics* **14**, 1312–1325 (2006).

[CAS](#) [Google Scholar](#)

27. 27.

Borgenstam, A. & Hillert, M. Massive transformation in the Fe–Ni system. *Acta Mater.* **48**, 2765–2775 (2000).

[ADS](#) [CAS](#) [Google Scholar](#)

28. 28.

Nishiyama, Z. *Martensitic Transformation* (Elsevier, 2012).

29. 29.

Ardell, A. J. Precipitation hardening. *Metall. Trans. A* **16**, 2131–2165 (1985).

[Google Scholar](#)

30. 30.

Gorbatov, O. I. et al. Effect of composition on antiphase boundary energy in Ni₃Al-based alloys: ab initio calculations. *Phys. Rev. B* **93**, 224106 (2016).

[ADS](#) [Google Scholar](#)

31. 31.

Rosenberg, J. & Piehler, H. Calculation of the Taylor factor and lattice rotations for bcc metals deforming by pencil glide. *Metall. Trans.* **2**, 257–259 (1971).

[CAS](#) [Google Scholar](#)

32. 32.

Zhang, M., Li, L., Fu, R., Krizan, D. & De Cooman, B. Continuous cooling transformation diagrams and properties of micro-alloyed TRIP steels. *Mater. Sci. Eng. A* **438–440**, 296–299 (2006).

[Google Scholar](#)

33. 33.

Zhao, J.-l., Yan, X., Wen, S. & Lin, L. Microstructure and mechanical properties of high manganese TRIP steel. *J. Iron Steel Res. Int.* **19**, 57–62 (2012).

[CAS](#) [Google Scholar](#)

34. 34.

Bouaziz, O., Zurob, H. & Huang, M. Driving force and logic of development of advanced high strength steels for automotive applications. *Steel Res. Int.* **84**, 937–947 (2013).

[CAS](#) [Google Scholar](#)

35. 35.

Boyer, H. E. *Atlas of Stress–Strain Curves* (ASM International, 1987).

36. 36.

Morris, J., Jr. Maraging steels: Making steel strong and cheap. *Nat. Mater.* **16**, 787 (2017).

[ADS](#) [CAS](#) [PubMed](#) [PubMed Central](#) [Google Scholar](#)

37. 37.

García-Mateo, C. & Caballero, F. G. The role of retained austenite on tensile properties of steels with bainitic microstructures. *Mater. Trans.* **46**, 1839–1846 (2005).

[Google Scholar](#)

38. 38.

Kim, S.-H., Kim, H. & Kim, N. J. Brittle intermetallic compound makes ultrastrong low-density steel with large ductility. *Nature* **518**, 77–79 (2015).

[ADS](#) [CAS](#) [PubMed](#) [PubMed Central](#) [Google Scholar](#)

39. 39.

De Moor, E., Speer, J. G., Matlock, D. K., Kwak, J.-H. & Lee, S.-B. Effect of carbon and manganese on the quenching and partitioning response of CMnSi steels. *ISIJ Int.* **51**, 137–144 (2011).

[Google Scholar](#)

40. 40.

Dong, X., Shen, Y., Yin, T., Misra, R. & Lin, G. Strengthening a medium-carbon steel to 2800 MPa by tailoring nanosized precipitates and the phase ratio. *Mater. Sci. Eng. A* **759**, 725–735 (2019).

[CAS](#) [Google Scholar](#)

41. 41.

Bouaziz, O., Barbier, D., Cugy, P. & Petigand, G. Effect of process parameters on a metallurgical route providing nano-structured single phase steel with high work-hardening. *Adv. Eng. Mater.* **14**, 49–51 (2012).

[CAS](#) [Google Scholar](#)

42. 42.

Wang, H., Tao, N. & Lu, K. Strengthening an austenitic Fe–Mn steel using nanotwinned austenitic grains. *Acta Mater.* **60**, 4027–4040

(2012).

[ADS](#) [CAS](#) [Google Scholar](#)

43. 43.

Otto, F. et al. The influences of temperature and microstructure on the tensile properties of a CoCrFeMnNi high-entropy alloy. *Acta Mater.* **61**, 5743–5755 (2013).

[ADS](#) [CAS](#) [Google Scholar](#)

44. 44.

Wu, Z., Bei, H., Pharr, G. M. & George, E. P. Temperature dependence of the mechanical properties of equiatomic solid solution alloys with face-centered cubic crystal structures. *Acta Mater.* **81**, 428–441 (2014).

[CAS](#) [Google Scholar](#)

45. 45.

He, J. et al. A precipitation-hardened high-entropy alloy with outstanding tensile properties. *Acta Mater.* **102**, 187–196 (2016).

[ADS](#) [CAS](#) [Google Scholar](#)

46. 46.

Li, Z., Pradeep, K. G., Deng, Y., Raabe, D. & Tasan, C. C. Metastable high-entropy dual-phase alloys overcome the strength–ductility trade-off. *Nature* **534**, 227 (2016).

[ADS](#) [CAS](#) [PubMed](#) [PubMed Central](#) [Google Scholar](#)

47. 47.

Wignall, G. D. et al. The 40 m general purpose small-angle neutron scattering instrument at Oak Ridge National Laboratory. *J. Appl. Cryst.* **45**, 990–998 (2012).

[CAS](#) [Google Scholar](#)

48. 48.

Kotlarchyk, M. & Chen, S. H. Analysis of small angle neutron scattering spectra from polydisperse interacting colloids. *J. Chem. Phys.* **79**, 2461–2469 (1983).

[ADS](#) [CAS](#) [Google Scholar](#)

49. 49.

Thompson, K. et al. In situ site-specific specimen preparation for atom probe tomography. *Ultramicroscopy* **107**, 131–139 (2007).

[CAS](#) [PubMed](#) [PubMed Central](#) [Google Scholar](#)

50. 50.

Soven, P. Coherent-potential model of substitutional disordered alloys. *Phys. Rev.* **156**, 809 (1967).

[ADS](#) [CAS](#) [Google Scholar](#)

51. 51.

Taylor, D. Vibrational properties of imperfect crystals with large defect concentrations. *Phys. Rev.* **156**, 1017 (1967).

[ADS](#) [CAS](#) [Google Scholar](#)

52. 52.

Stocks, G., Temmerman, W. & Gyorffy, B. Complete solution of the Korringa–Kohn–Rostoker coherent-potential-approximation equations:

Cu–Ni alloys. *Phys. Rev. Lett.* **41**, 339 (1978).

[ADS](#) [CAS](#) [Google Scholar](#)

53. 53.

Ebert, H., Koedderitzsch, D. & Minar, J. Calculating condensed matter properties using the KKR–Green’s function method—recent developments and applications. *Rep. Prog. Phys.* **74**, 096501 (2011).

[ADS](#) [Google Scholar](#)

54. 54.

Perdew, J. P., Burke, K. & Ernzerhof, M. Generalized gradient approximation made simple. *Phys. Rev. Lett.* **77**, 3865 (1996).

[ADS](#) [CAS](#) [PubMed](#) [Google Scholar](#)

55. 55.

Togo, A. & Tanaka, I. First principles phonon calculations in materials science. *Scr. Mater.* **108**, 1–5 (2015).

[ADS](#) [CAS](#) [Google Scholar](#)

56. 56.

Giannozzi, P. et al. QUANTUM ESPRESSO: a modular and open-source software project for quantum simulations of materials. *J. Phys. Condens. Matter* **21**, 395502 (2009).

[PubMed](#) [PubMed Central](#) [Google Scholar](#)

57. 57.

Liechtenstein, A. I., Katsnelson, M., Antropov, V. & Gubanov, V. Local spin density functional approach to the theory of exchange

interactions in ferromagnetic metals and alloys. *J. Magn. Magn. Mater.* **67**, 65–74 (1987).

[ADS](#) [CAS](#) [Google Scholar](#)

58. 58.

Vaks, V. & Zein, N. Theory of phase transitions in solid solutions. *J. Exp. Theor. Phys.* **40**, 537 (1975).

[ADS](#) [Google Scholar](#)

59. 59.

Vaks, V. & Samolyuk, G. On accuracy of different cluster models used in describing ordering phase transitions in fcc alloys. *J. Exp. Theor. Phys.* **88**, 89–100 (1999).

[ADS](#) [CAS](#) [Google Scholar](#)

60. 60.

Chuang, Y.-Y., Chang, Y. A., Schmid, R. & Lin, J.-C. Magnetic contributions to the thermodynamic functions of alloys and the phase equilibria of Fe–Ni system below 1200 K. *Metall. Trans. A* **17**, 1361–1372 (1986).

[Google Scholar](#)

61. 61.

Edwards, D. The paramagnetic state of itinerant electron systems with local magnetic moments. I. Static properties. *J. Phys. F Met. Phys.* **12**, 1789 (1982).

[ADS](#) [CAS](#) [Google Scholar](#)

62. 62.

Rappe, A. M., Rabe, K. M., Kaxiras, E. & Joannopoulos, J. Optimized pseudopotentials. *Phys. Rev. B* **41**, 1227 (1990).

[ADS](#) [CAS](#) [Google Scholar](#)

63. 63.

Ramer, N. J. & Rappe, A. M. Virtual-crystal approximation that works: locating a compositional phase boundary in $\text{Pb}(\text{Zr}_{1-x}\text{Ti}_x)\text{O}_3$. *Phys. Rev. B* **62**, R743 (2000).

[ADS](#) [CAS](#) [Google Scholar](#)

64. 64.

Kurdjumov, G. & Sachs, G. Crystallographic orientation relationship between α -and γ -Fe. *Ann. Phys.* **64**, 325 (1930).

[Google Scholar](#)

65. 65.

American Iron and Steel Institute. *High-Temperature Characteristics of Stainless Steel* A Designer's Handbook Report No. 9004 (Nickel Development Institute, 1979);

https://nickelinstitute.org/media/1699/high_temperaturecharacteristics_ofstainlesssteel_9004_.pdf

66. 66.

Warlimont, H. & Martienssen, W. *Springer Handbook of Materials Data* (Springer, 2018).

[Download references](#)

Acknowledgements

This research was supported by the US Department of Energy, Office of Science, Basic Energy Sciences, Materials Sciences and Engineering Division (testing and analysis of mechanical properties and responsible deformation mechanisms, TEM characterization of the FNAT-4h alloy, and writing of the manuscript) and by the Laboratory Directed Research and Development programme of Oak Ridge National Laboratory (ORNL) (microstructural characterization and first-principles calculations), managed by UT-Battelle, LLC, for the US Department of Energy. Y.Y. acknowledges CompuTherm for providing the phase diagram calculation software Pandat. Resources at ORNL's High Flux Isotope Reactor for small-angle neutron scattering, Spallation Neutron Source for neutron diffraction, and Center for Nanophase Materials Sciences for atom probe tomography were used in this study, which are US DOE Office of Science User Facilities.

Author information

Author notes

1. Tianyi Chen

Present address: Oregon State University, Corvallis, OR, USA

Affiliations

1. Materials Science and Technology Division, Oak Ridge National Laboratory, Oak Ridge, TN, USA

Ying Yang, Tianyi Chen, Lizhen Tan, Yanli Wang, German D. Samolyuk & Easo P. George

2. Center for Nanophase Materials Sciences, Oak Ridge National Laboratory, Oak Ridge, TN, USA

Jonathan D. Poplawsky, Andrew R. Lupini & Albina Borisevich

3. Neutron Scattering Division, Oak Ridge National Laboratory, Oak Ridge, TN, USA

Ke An & Ken Littrell

4. Materials Science and Engineering Department, University of Tennessee, Knoxville, TN, USA

Easo P. George

Authors

1. Ying Yang

[View author publications](#)

You can also search for this author in [PubMed](#) [Google Scholar](#)

2. Tianyi Chen

[View author publications](#)

You can also search for this author in [PubMed](#) [Google Scholar](#)

3. Lizhen Tan

[View author publications](#)

You can also search for this author in [PubMed](#) [Google Scholar](#)

4. Jonathan D. Poplawsky

[View author publications](#)

You can also search for this author in [PubMed](#) [Google Scholar](#)

5. Ke An

[View author publications](#)

You can also search for this author in [PubMed](#) [Google Scholar](#)

6. Yanli Wang

[View author publications](#)

You can also search for this author in [PubMed](#) [Google Scholar](#)

7. German D. Samolyuk

[View author publications](#)

You can also search for this author in [PubMed](#) [Google Scholar](#)

8. Ken Littrell

[View author publications](#)

You can also search for this author in [PubMed](#) [Google Scholar](#)

9. Andrew R. Lupini

[View author publications](#)

You can also search for this author in [PubMed](#) [Google Scholar](#)

10. Albina Borisevich

[View author publications](#)

You can also search for this author in [PubMed](#) [Google Scholar](#)

11. Easo P. George

[View author publications](#)

You can also search for this author in [PubMed](#) [Google Scholar](#)

Contributions

Y.Y. conceived the study, designed the alloy and supervised the project. T.C., A.R.L., A.B. and L.T. performed the TEM and STEM analyses. L.T. performed EBSD analysis. K.A. performed neutron diffraction and phase analysis. Y.W. performed and analysed tensile tests with DIC. J.D.P. performed the APT analysis. G.D.S. performed the first-principles calculations. K.L. performed the SANS analysis. Y.Y. and E.P.G. analysed and interpreted the mechanical properties and deformation mechanisms and wrote the manuscript. All authors reviewed and commented on the manuscript.

Corresponding authors

Correspondence to [Ying Yang](#) or [Easo P. George](#).

Ethics declarations

Competing interests

The authors declare no competing interests.

Additional information

Peer review information *Nature* thanks the anonymous reviewers for their contribution to the peer review of this work.

Publisher's note Springer Nature remains neutral with regard to jurisdictional claims in published maps and institutional affiliations.

Extended data figures and tables

[Extended Data Fig. 1 Temperature dependence of phase equilibria and composition calculated using the CALPHAD approach, and the free energy from first-principles calculations.](#)

a, Mole fraction of equilibrium phases in FNAT. **b**, Compositions of elements (at%) in the fcc phase. **c**, Free energy of fcc and bcc phases that have the same composition (Fe-23Ni-3.5Al-0.5Ti, at%) as the matrix of FNAT.

[Extended Data Fig. 2 Information for estimating yield strength of FNAT-47h.](#)

a, Room-temperature tensile stress-strain curve of FNAT after solutionizing at 1,100 °C and water quenching showing yield strength of ~325 MPa. **b**, STEM bright-field image showing dislocations cutting particles (yellow

arrows) in the matrix of a plastically deformed FNAT sample. **c**, Corresponding HAADF image of **b**.

Extended Data Fig. 3 TEM/STEM analyses of interface between precipitate and matrix of the FNAT-47h alloy.

a, b, HAADF lattice images before deformation (from tab section of tensile specimen). **a**, A lattice image of L₁₂/bcc interface displays the Nishiyama–Wasserman orientation $\langle\{1\bar{1}1\}\{L1\}\{2\}\rangle$ parallel $\langle\{0\bar{1}1\}\{bcc\}\rangle$ and $\langle\{110\}\{L1\}\{2\}\rangle$ parallel $\langle[100]\{bcc\}\rangle$, where the interplanar spacings, $d\langle\{1\bar{1}1\}\{L1\}\{2\}\rangle = 0.2072 \text{ nm}$ and $d\langle\{0\bar{1}1\}\{bcc\}\rangle = 0.2027 \text{ nm}$, result in a mismatch of ~2.2% and a semi-coherent interface. **b**, A lattice image of L₁₂/fcc interface region exhibits full cube-on-cube lattice coherency with $\langle(\bar{1}11)\{L1\}\{2\}\rangle$ parallel $\langle(\bar{1}11)\{fcc\}\rangle$ and $\langle\{110\}\{L1\}\{2\}\rangle$ parallel $\langle[110]\{fcc\}\rangle$, where the interplanar spacings, $d\langle\{1\bar{1}1\}\{L1\}\{2\}\rangle = 0.2072 \text{ nm}$ and $d\langle\{1\bar{1}1\}\{fcc\}\rangle = 0.2074 \text{ nm}$, result in a small mismatch of ~0.1%. **c–e**, TEM and HAADF lattice images after deformation (from gauge section of tensile specimen). **c**, Dark-field TEM image showing L₁₂ precipitates, some containing streaks (marked by arrowheads), embedded in a deformation-induced bcc grain after deformation. **d**, HAADF lattice image showing a stacking fault with a Burgers vector of $\langle\frac{1}{6}<112>\rangle$ formed in one of the L₁₂ precipitates containing streaks. Labels A, B, C in the inset denote alternating {111} planes in the L₁₂ structure. **e**, HAADF lattice image showing semi-coherent L₁₂/bcc interface with the Kurdjumov–Sachs orientation relationship⁶⁴, namely, $\langle(\bar{1}11)\{L1\}\{2\}\rangle$ parallel $\langle(\bar{1}10)\{bcc\}\rangle$ and $\langle\{110\}\{L1\}\{2\}\rangle$ parallel $\langle[111]\{bcc\}\rangle$ and a lattice mismatch of ~2.2%. The slip-transfer mechanism in **c–e** is common when dislocations move from fcc matrix to L₁₂ precipitate, but is rarely seen when the matrix is bcc.

Extended Data Fig. 4 STEM HAADF image, corresponding FFT diffractogram and inverse FFT image of the as-quenched FNAT-4h alloy sample tilted to [110] zone axis condition.

a, HR STEM image. **b**, FFT diffractogram. **c**, the inverse FFT generated using the blue-circled 'extra spots' in **b**. The diffuse spatial distribution of the bright features in **c** indicates that the extra spots in **b** are caused by small variable local misorientations due to local internal strains as opposed to any nano-domains of a different matrix phase.

Extended Data Fig. 5 Ultimate tensile strength versus Ni or (Ni + Co) content at room temperature and 700 °C.

Open symbols, room temperature (RT); filled symbols, 700 °C. The FNAT alloy is compared with different materials whose data sources are Fe-based heat-resistant alloys including 410, 430, 302, 309, 310, 316, 321, 347⁶⁵ A286 and Incoloy 800⁶⁶; Ni-based super alloys⁶⁶ including Inconel 706, Inconel 718, Nimonic 80A, PE 16, Inconel 625, Inconel 600, Hastelloy S, Hastelloy X, Udimet 630; and Ni–Co-based super alloys⁶⁶ including Incoloy 909, Nimonic 90, Nimonic 115, Waspaloy, Udimet 720, Udimet 500, Rene 41, Rene 95, Astroloy, Inconel 617 and Haynes 230.

Extended Data Fig. 6 Textures of FNAT-47h and FNAT-m-47h after hot-rolling and annealing.

a, b, EBSD pole figures for FNAT-47h, **c, d**, EBSD pole figures for FNAT-m-47h. The normal direction (ND) in each case is at the centre of the circle and is either 001 or 111 as marked. TD in **a–d** refers to the transverse direction. **e**, Neutron diffraction spectra of FNAT-47h along the rolling direction (RD) and the normal direction (ND). Note that we have shifted the RD and ND spectra horizontally with respect to each other to facilitate comparison (otherwise the peaks would overlap). Both EBSD (**a, b**) and ND (**e**) results show that FNAT-47h has negligible texture.

Extended Data Fig. 7 Fracture analysis of tensile-tested FNAT-m-47h and FNAT-47h alloys.

a, FNAT-m-47h: fractograph and stress–strain curve showing considerable necking before fracture, and DIC strain maps showing strain localization in the region where fracture eventually occurs. **b**, FNAT-47h: fractograph and stress–strain curve showing minimal necking before fracture, and DIC strain maps showing relatively diffuse strain distribution throughout the gauge section with no evidence of localization near the fracture plane.

Extended Data Table 1 Precipitate parameters calculated from different fits to APT data

[Full size table](#)

Extended Data Table 2 Parameters of precipitates in deformed and undeformed bcc and fcc grains

[Full size table](#)

Rights and permissions

[Reprints and Permissions](#)

About this article



Check for
updates

Cite this article

Yang, Y., Chen, T., Tan, L. *et al.* Bifunctional nanoprecipitates strengthen and ductilize a medium-entropy alloy. *Nature* **595**, 245–249 (2021).
<https://doi.org/10.1038/s41586-021-03607-y>

[Download citation](#)

- Received: 26 August 2019

- Accepted: 04 May 2021
- Published: 07 July 2021
- Issue Date: 08 July 2021
- DOI: <https://doi.org/10.1038/s41586-021-03607-y>

Comments

By submitting a comment you agree to abide by our [Terms](#) and [Community Guidelines](#). If you find something abusive or that does not comply with our terms or guidelines please flag it as inappropriate.

[Access through your institution](#)

[Change institution](#)

[Buy or subscribe](#)

Advertisement

This article was downloaded by **calibre** from <https://www.nature.com/articles/s41586-021-03607-y>.

| [Section menu](#) | [Main menu](#) |

Supply chain diversity buffers cities against food shocks

[Download PDF](#)

- Article
- [Published: 07 July 2021](#)

Supply chain diversity buffers cities against food shocks

- [Michael Gomez](#) [ORCID: orcid.org/0000-0002-5906-6819¹](#),
- [Alfonso Mejia](#) [ORCID: orcid.org/0000-0003-3891-1822¹](#),
- [Benjamin L. Ruddell](#) [ORCID: orcid.org/0000-0003-2967-9339²](#) &
- [Richard R. Rushforth²](#)

Nature volume 595, pages 250–254 (2021) [Cite this article](#)

- 155 Altmetric
- [Metrics details](#)

Subjects

- [Civil engineering](#)
- [Hydrology](#)
- [Sustainability](#)
- [Urban ecology](#)

Abstract

Food supply shocks are increasing worldwide^{1,2}, particularly the type of shock wherein food production or distribution loss in one location propagates through the food supply chain to other locations^{3,4}. Analogous to biodiversity buffering ecosystems against external shocks^{5,6}, ecological theory suggests that food supply chain diversity is crucial for managing the risk of food shock to human populations^{7,8}. Here we show that boosting a city's food supply chain diversity increases the resistance of a city to food shocks of mild to moderate severity by up to 15 per cent. We develop an intensity–duration–frequency model linking food shock risk to supply chain diversity. The empirical–statistical model is based on annual food inflow

observations from all metropolitan areas in the USA during the years 2012 to 2015, years when most of the country experienced moderate to severe droughts. The model explains a city's resistance to food shocks of a given frequency, intensity and duration as a monotonically declining function of the city's food inflow supply chain's Shannon diversity. This model is simple, operationally useful and addresses any kind of hazard. Using this method, cities can improve their resistance to food supply shocks with policies that increase the food supply chain's diversity.

[Download PDF](#)

Main

Food supply shock is a pressing issue that may be increasing worldwide^{1,2}. Extreme-weather events, possibly exacerbated by climate change^{9,10}, are a main driver of food supply shocks¹¹. The risk of simultaneous global breadbasket failure is also probably rising¹², posing a threat to systemic and catastrophic food production losses¹³.

Geopolitical crises and policy changes are also responsible for a large proportion of shocks to different food systems¹. Moreover, threats to public health can disrupt food supply chains, as shown by the coronavirus disease 2019 pandemic in several national economies around the world¹⁴. Global and national food supply chains increase exposure to shocks compared with local food supply chains^{4,7,15,16}, but also add diversity and resilience^{15,17}.

Network topological diversity and connectivity are key attributes of resilient social–ecological^{7,18} systems. Food supply chains, along with other material inflows such as water and energy, are a close analogy to an ecological food web^{19,20}.

Resilience to shock has “three R’s”^{21,22}: resistance to changing food inflows, robustness to a wide range of hazards and recovery or reorganization time after a shock. Therefore, from ecological and resilience theory^{23,24}, a food shock resilience model should relate the diversity and/or connectivity of the food supply chain network to explain a city's resistance to food shocks. Supply chain diversity provides adaptive options for the city to exploit when some of its supply chains suffer shock^{25,26,27}, thus boosting resilience to shock. The methods in this paper measure resistance to food supply shock, which is a specific subtype of resilience²¹.

If cities, companies and nations had access to a model estimating their ability to buffer food supply chain shocks, this model could be used in policy and management to optimize supply chains and control the risk of shocks^{26,28}. The ideal model should be simple, quantitative, accurate, operationally useful, applicable at the scale of cities (which consume and process most food)²⁹, ‘hazard agnostic’ for all causes of shocks, and would explain shock risk as a function of factors that a city, company or nation

can control. We are skilled at modelling hazard-specific risk management, but general hazard-agnostic models of resilience are better because they can potentially handle unexpected extreme events that continue to threaten our human systems. Here, we propose a statistical–empirical model meeting these ideal criteria, explaining the resistance of USA cities to food supply shocks as a function of the topological diversity of the city’s food supplier network.

Results

Using annual timescale food inflow supply networks (crops, live animals, feed and meat) for the cities of the USA, we extracted the annual intranational food inflow subgraph of each metropolitan area for the period 2012–2015, which is the period with available data³⁰ and when food production systems were substantially affected by drought and agricultural production shocks on the Great Plains and in the western USA^{31,32}. In this model a shock occurs when food inflows drop by more than the intensity threshold (ranging from 3% to 15%) for a duration of a year, with the drop measured against the average inflows of the four-year time period.

Using observations of thousands of food inflows to hundreds of USA cities across four years and four types of food, we calculate the probability (or frequency) of exceeding a given shock intensity for an annual duration for each USA city. The resistance of a city to food shocks is the complement to the probability of the shock. We find that resistance relates positively to the Shannon diversity of a city’s food inflows. This assumes that all cities’ supply chains were exposed to shocks of many intensities during the study period. This is a justified assumption in the USA for the study period of 2012–2015, because in 2012 the USA Great Plains experienced an exceptionally severe drought³³ and in 2012–2013 the western USA experienced a severe drought⁹, both with widespread losses reported in crops and livestock^{33,34}.

The resulting model takes the operationally useful form of an intensity–duration–frequency (IDF) relationship that is widely used for risk and hazard engineering and as a basis for design codes and policies of risk³⁵. This model provides an all-hazards or ‘hazard agnostic’ approach, because—although the empirically observed shocks underlying our analysis are mostly due to drought affecting food suppliers—the model is valid in principle for all kinds of shocks to the city’s food supply network.

Food shocks and supply chain diversity

For cities in the USA, the probability of an annual food supply shock S being greater than a shock intensity s , $P(S > s)$ (see [Methods](#)), declines as the diversity D of a city’s

food inflows supply chain increases (Fig. 1a). Our measure of supply chain diversity is calculated using the Shannon diversity of a city's supply chain network of intranational trading partners based on a combination of five different indicators (Methods). Using data for 284 cities and 4 food sectors, the annual probabilities of food supply shocks are calculated by measuring, for each city and food sector, the maximum food supply departure from the annual average during 2012–2015 (Methods). We utilize a total of 4,884 buyer–supplier subgraphs and 1,221 time series to calculate $P(S > s)$ and D .

Fig. 1: Relationship between the probability of shock and supply chain diversity.

 figure1



a, b, Empirical (**a**) and modelled (**b**) relationship between the probability of food supply chain shock $P(S > s)$ and supply chain diversity D for different shock intensities s . Food systems—each food system consists of the supply chain for one of the cities' four food sectors—are classified into 6 bins of supply chain diversity (limits 0, 0.395, 0.497, 0.585, 0.665, 0.755 and 0.92) with 204, 202, 204, 203, 206 and 202 observations in each bin. These 6 bins each have an average (with standard error given in parentheses) supply chain diversity of 0.28 (0.007), 0.45 (0.002), 0.54 (0.002), 0.62 (0.002), 0.71 (0.002) and 0.81 (0.002), respectively. The probability of food supply chain shock in each bin is calculated as the number of food systems with shocks larger than a shock intensity s divided by the total number of food systems in the bin (Methods). For clarity, panel **a** shows the probabilities of food supply chain shock for $\{s \in \{3, 5, 10, 15\}\}$ (for other s values see Supplementary Fig. 1). For each s value, the empirical value of $P(S > s)$ is fitted against D using a constrained exponential function (curves in **a**). The confidence bounds represent ± 1 s.d. of the fitted curves (degrees of freedom = 4). The parameter values and goodness-of-fit results for these exponential fits are shown in Extended Data Table 1. With the exponential fit of the

empirical relationship, the curves in panel **b** are obtained by relating the parameters from the exponential fits to the shock intensity s using linear regression (Extended Data Fig. 1a, b). The parameter values and goodness-of-fit results for these linear fits are shown in Extended Data Table 2.

[Full size image](#)

Our results indicate that with greater supply chain diversity D , cities are more likely to avoid or resist shocks of increasing intensity (3%, 5%, 10% and 15%; Fig. 1a). The shock intensity is quantified as the occurrence of a food supply loss greater than a specified percentage threshold s . On average, 1 in 4 cities (probability of shock 0.25; Fig. 1a) with D of 0.20 experience a supply shock greater than 15% in any of their food sectors, while for the same threshold, cities with D values of 0.45, 0.54, 0.63, 0.71 and 0.83 experience food supply shocks 1 out of 6, 8, 14, 17 and 202 times, respectively (probabilities of 0.18, 0.12, 0.07, 0.06 and 0.004, respectively; Fig. 1a). The same trend is observed for shock intensities greater than 3%, 5% and 10% (Fig. 1a). The relationship in Fig. 1a holds when controlling for changes in demand using population or food inflows as proxy for demand (Methods). It also holds when the analysis is performed using the original food flow data with 69 cities rather than the 284 cities in Fig. 1a (Methods). In addition, although the five indicators used to calculate diversity have a varied influence on the relationship in Fig. 1a, the inclusion of all indicators in the supply chain diversity measure increases the Pearson correlation between the data in Fig. 1a (Methods).

We use the observed empirical relationship between $P(S > s)$ and D to build a statistical IDF model of food supply shocks. Letting $\{F\}_{s}(D) = \ln(P(S > s))$, the model takes the following form

$$\{F\}_{s}(D) = -k_s(D - D_{0,s}) \quad (1)$$

where k_s and $D_{0,s}$ are fitting parameters that depend on the shock intensity s . The parameters are estimated using nonlinear least squares. The exponential function in equation (1) provides a good fit to the data ($R^2 \geq 0.73$; Extended Data Table 1) and it has the desirable characteristics of being simple to implement and bounded at $P(S > s) \in [0,1]$ and $D \in [0,1]$.

Many different (social, economic, infrastructural and environmental) urban indicators of city functioning have been shown to scale with the city size at the metropolitan level^{36,37}, where population is typically used to quantify city size. Hence, we evaluate whether D varies in a systematic way with the city size. For all food sectors, D shows a very weak positive trend with population (Supplementary Fig. 2). Since larger cities

tend to have slightly more diverse supply chains (Supplementary Fig. 2), they are slightly less likely to experience shocks of increasing intensity.

A general model of food shocks to cities

We use the model parameters fitted using equation (1) to derive and extrapolate a family of IDF curves covering a wide range of shock intensities. The model parameters k_s and $D_{0,s}$ are each linearly regressed against the shock intensity s to obtain parameter values for different intensities (Extended Data Fig. 1a,b). The fitted linear regressions show good performance ($R^2 \geq 0.80$; Extended Data Table 2). Using these regressed parameter values in equation (1), we obtain the IDF curves in Fig. 1b. The probability of shock equations for different shock intensity values are included in Extended Data Table 3. For example, assuming a design frequency of $P = 0.25$ per year (a ‘four-year’ shock), a city with $D = 0.2$ can expect to experience at least one food shock of 15% or greater. If the same city increased its food supply chain diversity to $D = 0.8$, the same 15% shock occurs less often, with frequency $P = 0.05$ (a ‘twenty-year’ shock). The curves in Fig. 1b are valid for food supply chain shock to USA cities and regions at roughly the metropolitan area scale during the period 2012–2015, but may possibly be valid for other regions, time periods and supply chain types as well.

In the standard engineering design application³⁵, design codes or standards will set the maximum tolerable frequency and shock intensity (for example, annual $P < 0.01$ and $s < 5\%$), and the city would enact policies and investments to modify D to bring the expected frequency and intensity below that level of risk. Insurance and emergency management strategies would then be developed to cover the remaining risk. These IDF curves can be directly employed by engineers, insurers, policymakers and planners to measure and control the risk of shock to the food supply chain and to design solutions that reduce the risk of shock.

Using the IDF curves to create a map of the so-called ‘100-year’ shock with a 1% annual exceedance probability (frequency F is $P(S > s) = 0.01$, duration D is 1 year), we find that the expected shock intensity s varies from 22% to 32% in cities and rural regions across the USA (Fig. 2). The narrow 10% range of variability is due to the relative similarity of food supply chain structure and diversity across USA communities. The cities with the highest expected 100-year shock intensities are: Grand Junction, Colorado; Corpus Christi, Texas; Beaumont, Texas; and Steamboat Springs, Colorado (Fig. 2); and the cities with the lowest expected intensities are: Florence, South Carolina; Cleveland, Ohio; Roanoke, Virginia; and Columbus, Ohio. The shock intensities are on average greater in the western USA (west of the 100th meridian) than in the eastern USA (Fig. 2), with an average shock intensity of $26.3 \pm 1.9\%$ (average ± 1 standard deviation) versus $24.8 \pm 1.5\%$, respectively. In addition, some cities show a lower shock intensity than their neighbouring cities. For

example, Los Angeles has a lower shock intensity compared to other cities in the state of California, with a shock intensity of 23.5% versus $27.2 \pm 0.9\%$, respectively. The lower expected shock intensity of Los Angeles is due to its unusually diversified (with $D = 0.69$) food supply chain. Spatial patterns for shocks with other frequencies are similar.

Fig. 2: Map of expected shock intensities of an annual duration food supply chain shock with annual occurrence probability of 1%.

 [figure2](#)

The shock intensities are represented as a fraction of the average annual inflows. The annual occurrence probability of 1% is also known as a 100-year food supply shock.

[Full size image](#)

Co-occurrence of food shocks

The model in equation (1) is valid if only one food sector is shocked. However, food supply shocks to multiple sectors (for example, crops, live animals) can and do co-occur¹, meaning that shocks from different sectors can be simultaneously experienced by a city or region. Shock co-occurrence is due to multiple factors, such as the tendency of droughts to affect large areas and of industries to collocate and to form strong interdependencies^{31,32}. Even though drought and extreme heat may have a more immediate impact on crop and pasture losses, those losses can quickly propagate to other food sectors, for example, by reducing the crop inputs required to produce animal feed and by inducing livestock culling^{31,32}. The contextual details of a cascading shock are difficult to predict, making it important that the model consider both single and also co-occurring shocks.

In our dataset, shock co-occurrence is widespread, with most cities in the study period 2012–2015 experiencing at least one shock co-occurrence of 2 or more food sectors (Extended Data Fig. 2). Accounting for shock co-occurrence, we find that the probability $P'(S > s)$ of an annual food supply shock S exceeding intensity threshold s declines with increasing D (Fig. 3a). For example, on average 1 in 4 cities (that is, $P(S > s) = 0.25$), with D of 0.20 experience food supply shocks of $s > 10\%$ in more than one food sector simultaneously. Our empirical results suggest that supply chain diversity can also boost the resistance of cities to rarer but more dangerous co-occurring shocks.

Fig. 3: Relationship between the probability of co-occurring shocks and supply chain diversity.

 figure3

a, b, Empirical (**a**) and modelled (**b**) relationship between the probability of co-occurring food supply chain shock $P'(S > s)$ and supply chain diversity D for different shock intensities s . Food systems are classified into 6 bins of supply chain diversity (limits 0, 0.395, 0.497, 0.585, 0.665, 0.755 and 0.92) with 204, 202, 204, 203, 206 and 202 observations in each bin. These 6 bins each have an average (with standard error given in parentheses) supply chain diversity of 0.28 (0.007), 0.45 (0.002), 0.54 (0.002), 0.62 (0.002), 0.71 (0.002) and 0.81 (0.002), respectively. The probability of co-occurring food supply chain shocks in each bin is calculated as the number of cities with shocks larger than a shock intensity s to 2 or more food sectors divided by the total number of cities in the bin (Methods). For each s , the empirical value of $P'(S > s)$ is fitted against D using a constrained exponential function (curves in panel **a**). The parameter values and goodness-of-fit results for these exponential fits are shown in Extended Data Table 4. With the exponential fit of the empirical relationship, the curves in panel **b** are obtained by relating the parameters from the exponential fits to

the shock intensity s using linear regression (Extended Data Fig. 1c, d). The parameter values and goodness-of-fit results for these linear fits are shown in Extended Data Table 5. Panel b shows the curves for $(s \in \{3, 5, 10, 15\})$; for other s values see Supplementary Fig. 3.

[Full size image](#)

To consider the effect of shock co-occurrence on the IDF curves, we modify the model in equation (1) as follows:

$$\text{Equation (2)}: F(s)^{\prime} = -k_s^{\prime}(D - D_0 s^{\prime})$$

where the fitting parameters k_s^{\prime} and D_0 now account for the effect of co-occurrence on the probabilities of food supply shock to a city. The parameters are estimated using nonlinear least squares (Extended Data Table 4). Each of the estimated parameters is related to the shock intensity s using linear regression (Extended Data Fig. 1c, d and Extended Data Table 5), which are in turn used, together with equation (2), to create a family of IDF curves that account for co-occurrence effects (Fig. 3b).

For a given intensity, the model expects co-occurring food supply shocks to be less frequent than single food supply shocks (Figs. 1b and 3b). For example, when neglecting co-occurrence, for an annual-duration shock intensity of 10%, a city with $D = 0.2$ has a frequency of shock of $P = 0.45$, whereas for co-occurring shocks the expected frequency decreases to $P = 0.29$. For example, the frequency with which San Diego ($D = 0.35$), California, expects a single shock of 10% intensity is $P = 0.36$, but for two or more co-occurring shocks, $P = 0.22$.

Discussion

Analogous to biodiversity buffering ecosystems against external shocks^{5,6}, our results show that cities with a greater diversity of food suppliers have a lower probability of suffering a food supply shock for any reason. This method aims at operationalizing ecological theory and network theory to form a valid engineering operations risk management framework for supply chains, grounded in empirical science. This study is a step towards quantifying, explaining and managing the risk faced by cities and regions. The all-hazard nature of the method is important, because it promises the ability to build resilience in the face of the unpredictable events that increasingly characterize hazards in our fast-paced and highly connected world. This method also holds promise for managing supply chain shock risk and resilience at the scales of

companies, neighbourhoods and nations, as well as for other kinds of supply chains beyond food.

Approaches aimed at reducing or avoiding food supply shocks have been extensively explored at the national level^{15,16,38}, and the method presented in this paper corroborates—partially—prior national-scale findings, while presenting a simpler answer that applies at finer and more manageable scales. Food supply shocks are most harmful to vulnerable populations within cities, so boosting food supply resilience in cities—and especially in vulnerable neighbourhoods of cities—is an important policy goal. Although food insecurity is on average low in developed countries, approximately 10–12% in the USA³⁹, it can be high for marginalized groups in cities and in rural areas; 20–40% in the USA³⁹. Food insecurity is positively related to food price variability across American cities⁴⁰. Food supply shocks may increase food prices and price variability⁴¹. Therefore, it seems plausible that higher food supply diversity could reduce food insecurity. Because of the varied socioeconomic geography of the USA, our dataset includes cities and regions with markedly different population, density, wealth, race, culture and climate characteristics. Therefore, our results may be directly relevant for a wide range of cities, cultures, timeframes and nations.

Pimm et al.⁴² emphasize the need to test and utilize empirical measures to operationalize resilience concepts. Our empirical model, linking supply chain diversity to the probability of shock, contributes to that operational goal. Cities need a multifaceted and adaptive approach to manage risk from multiple forms of shocks and to build resilience. In an era of expanding urbanization and connectivity, cities have a key role in global sustainability⁴³. Cities will need to actively manage their supply chain connections to deal with the causes and consequences of shocks to their critical lifelines, such as food. Using this method to guide the policy objective of diversification of supply chains, cities and communities can engage in demand-side policies that scientifically manage risk and build resilience into their supply chains. The IDF framing of this method makes it directly applicable using the design-code framework that is already broadly employed by policymakers to manage risk by design.

A city's food supply chains—like most supply chains—represent the agglomeration of efforts by many independent companies and logistics operations that grow, manufacture, ship, distribute, store and retail food products. It is a complex supply chain with many parts⁴⁴. Translating the high-level design framework inherent to our proposed IDF model into actionable steps and effective regulations for individual operators remains a challenge for the future. Diversity by design, at the level of communities, will take coordination, and possibly regulation, among many parties.

Food businesses (for example, grocers, restaurants and distributors) and—to a lesser extent, individuals—can voluntarily contribute to a resilient food policy by intentionally favouring a diverse supply chain where possible, and by maintaining slightly larger food inventories in locales that are known to be at higher risk of food shock (for example, southern Utah). Local, state, and federal governments and mission agencies can collect data on the diversity of their businesses’ suppliers, can set policy targets to achieve minimum supply chain diversity, and can create regulations or incentives to achieve those minimums. In the USA, this could be relevant to several government-sponsored programmes aimed at reducing food insecurity, such as the Supplementary Nutrition Assistance Program⁴⁵ and the National School Lunch Program⁴⁶.

Insurers can price in shock risk where appropriate to incentivize diversity and resilience, and a niche business sector could emerge to mitigate that risk by managing supply chains or building buffers. Large agribusiness can reduce the supply-side risk by diversifying its supply chains. Governments can scientifically size and locate food buffers (stockpiles) to fill the gap between the IDF food security risk metrics presented in this paper and the desired level of food security—or can prioritize emergency recovery assets to higher-risk locations. The precise and actionable statistics in this model form a basis for scientifically designed food security and risk management systems that fit neatly within the existing risk management and design paradigm already used by insurers, engineers, emergency managers and policymakers.

Methods

Dataset of food flow networks

We derive annual, intranational food flow networks for the USA using the Freight Analysis Framework version 4 (FAF4) database³⁰. The derived networks are for different food sectors and include all metropolitan areas in the USA. The FAF4 database consists of annual commodity flows during 2012–2015 for 115 geographic areas in the USA and 43 different sectors. We focus on the following four food sectors in the FAF4 database: crops, live animals, animal feed and meat. The 115 geographic areas in the FAF4 database cover the entire contiguous USA, including 69 metropolitan statistical areas and 46 remainders of states (the remainder is the area of a state that is not part of a FAF4 metropolitan area).

To obtain food flows for all metropolitan areas in the USA, we disaggregate the FAF4 database from 115 to 329 areas (Supplementary Fig. 4), out of which 284 are metropolitan or combined statistical areas (120 metropolitan and 164 combined statistical areas). The disaggregation is performed using different socioeconomic and agricultural-related variables as attractors of supply and demand. For each food sector,

a flow with origin o and destination d in the FAF4 database is disaggregated to a metropolitan-level flow with origin o' and destination d' using a disaggregation variable a as the best attractor of supply or demand.

The disaggregation is performed in two stages. In the first stage, the supply U of each FAF4 remainder of state is disaggregated to include all the metropolitan areas in that remainder of state as follows:

$$\frac{\{U\}_{o'} \{d\}^c}{\{a\}_{o'} \{d\}^c} = \frac{\{U\}_{od} \{c\}}{\{a\}_o \{c\}}, \quad (3)$$

where $\{U\}_{o'} \{d\}^c$ (in tons per year) is the disaggregated supply for food sector c in origin o' that satisfies demand at the FAF4 destination d , $\{U\}_{od} \{c\}$ (in tons per year) is the FAF4 food flow for sector c between areas o and d , and $\{a\}_{o'} \{d\}^c$ and a_o are the attractor variables for the new origin o' and FAF4 origin o , respectively. In the second stage, $\{U\}_{o'} \{d\}^c$ is further disaggregated into demand E using:

$$\frac{\{E\}_{d'} \{d\}^c}{\{a\}_{d'} \{d\}^c} = \frac{\{U\}_{o'} \{d\}^c}{\{a\}_o \{d\}^c}, \quad (4)$$

where $\{E\}_{d'} \{d\}^c$ (in tons per year) is the demand at destination d' for food sector c supplied by origin o' , while $\{a\}_{d'} \{d\}^c$ and $\{a\}_o \{d\}^c$ are the attractor variables at the disaggregated destination d' and FAF4 destination d , respectively.

The FAF4 database includes food flow data at both the state level (48 states) and metropolitan level (115 areas including 69 metropolitan areas). Prior to performing the disaggregation, we jointly use the FAF4 state data and the FAF4 metropolitan data to select the best performing attractor variables. That is, we first use equations (3) and (4) to disaggregate the FAF4 state-level data to the metropolitan-level for the metropolitan and remainder-of-state areas in FAF4. By comparing the performance of our disaggregated flow data against the empirical FAF4 metropolitan-level data, we select the best attractor variable for each food sector. The following attractor variables are considered: population⁴⁷, employment⁴⁸, wages⁴⁸, number of establishments⁴⁸ and cropland area⁴⁹. These variables are selected on the basis of previous analysis and data availability⁵⁰.

To assess the performance of the attractor variables, we use the Pearson correlation coefficient between the empirical FAF4 flows and the disaggregated flows for the metropolitan areas and remainder-of-state areas in FAF4 (Extended Data Fig. 3). The

performance is high with correlation values greater than 0.87 and an average of 0.95. Using the best-performing disaggregation variables, we build the food flow networks employed in this study. The nodes in the networks represent metropolitan and remainder-of-state areas, and the weighted links represent annual food flows during 2012–2015 for crops, live animals, feed and meat (Supplementary Fig. 5).

The FAF4 metropolitan and remainder-of-state areas we used to select the attractor variables span a wide range of populations, cropland areas, and number of establishments, since these FAF4 areas include the largest cities in the USA and a broad range of medium-size cities. The values of the attractor variables used in the disaggregation are within the ranges implied by the FAF4 metropolitan data (Supplementary Fig. 6), indicating that the variables are reliable. The exception to this is population, which is only used to disaggregate meat demand. Population, however, has a high disaggregation performance with a correlation coefficient of 0.97 (Extended Data Fig. 3). In addition, the use of population to disaggregate meat demand is consistent with previous scaling results for metropolitan areas in the USA⁵¹ that have shown that metropolitan-level variables that are related to resource consumption scale approximately linearly with population.

Food inflows supply chain diversity

To determine annual supply chain diversity, we extract the annual food buyer–supplier subgraph of each city and food sector from the food flow networks¹⁹. We refer to each of these subgraphs as a food system. The food buyer–supplier subgraph of a city i consists of all the supply chain interactions with its trading partners or neighbours j for a specific food sector. Our measure of supply chain diversity is based on the notion of functional distance⁵². We compute the functional distance d between i and any of its trading partners j by combining five different indicators: physical distance, climate correlation, urban classification, economic specialization and network modularity. The indicators are described below in the ‘Functional distance indicators’ section of the Methods. We also perform statistical analyses to evaluate the influence of the attractor variables on these indicators (Methods). The indicators represent stable characteristics of cities and therefore tend to remain fairly constant during our study period.

The functional distance $\langle d_{ij}^r \rangle$ for an indicator r between any pair of connected nodes (i, j) is calculated as

$$\langle d_{ij}^r \rangle = N^{-1} |r_k - r_i|, \quad (5)$$

where the normalization constant N is determined as the maximum value of $|r_k - r_i|$ between any node k in the network and i . In equation (5), \langle

$(\{d\}_{ij}^r = 0)$ for functionally similar nodes and $(\{d\}_{ij}^r = 1)$ for dissimilar nodes.

For each city's buyer–supplier subgraph and food sector, any pair of connected nodes has 5 different functional distance indicators associated with it. To combine these distance indicators into a single measure, we calculate the average functional distance indicator $\langle \{d\}_{ij}^r \rangle$ as the arithmetic average of the 5 functional distance indicators for any pair (i, j) of connected nodes. We use the discrete probability distribution of food inflows binned by $\langle \{d\}_{ij}^r \rangle$ categories, together with Shannon entropy⁵³, to calculate the supply chain diversity $\langle D \rangle_{i,c}^t$ of node i and sector c at year t :

$$\langle D \rangle_{i,c}^t = \frac{-\sum_{k=1}^K Y_{i,c}^t(k) \ln(Y_{i,c}^t(k)/K)}{\log K}. \quad (6)$$

For sector c and year t , $\langle Y_{i,c}^t(k) \rangle$ is the proportion of food inflows to node i within bin k . The k bin is obtained by binning all the $\langle d_{ij}^r \rangle$ values for node i into a total number of K bins.

$\langle D \rangle_{i,c}^t$ is sensitive to the total number of bins K . Thus, for each node in our food flow networks, we tested the sensitivity of $\langle D \rangle_{i,c}^t$ to the total number of bins K . For $K = 15$, D values stabilize (Supplementary Fig. 7); therefore, we used 15 bins when performing all calculations of functional diversity.

Functional distance indicators

The average functional distance between a city and its trading partners is based on the following five indicators:

1. (1)

Physical distance indicator (PDI). The PDI is obtained by calculating the Euclidean distance from the centroid of each geographic area to the centroid of all other areas. The geometric centroids of all geographical areas are calculated using the GIS software ArcMap (<https://desktop.arcgis.com/en/arcmap/>).

2. (2)

Climate indicator (CI). To account for different climates in cities across the USA, the Palmer Drought Severity Index (PDSI) is used⁵⁴. The monthly PDSI is obtained from the National Oceanic and Atmospheric Administration for the years 1895–2015 at the climate division geographic level. An area-weighted

average is performed to aggregate the PDSI data to the metropolitan level. The CI is obtained by calculating the monthly correlation between an area and all other areas.

3. (3)

Urban classification indicator (UCI). To identify the urbanization level of a geographical area, the Urban-Rural Classification indicator of the National Center for Health Statistics is employed⁵⁵. This indicator classifies counties using a scale from 1 to 6, where a value of 1 indicates the county is highly rural and a value of 6 means highly urban. The UCI is obtained at the metropolitan level using an area-weighted average of the county-level values.

4. (4)

Network modularity indicator (NMI). This indicator identifies geographical areas (network nodes) that belong to the same community. A community is a group of nodes whose strength interactions are stronger than with the rest of the network. To identify the network's communities, we aggregate the flows from the four food sectors (crops, live animals, feed and meat) into a single-layer network. The communities are identified by maximizing the modularity measure of Newman^{56,57} using the greedy optimization algorithm of Blondel et al.^{58,59}. Network nodes that lie in the same community are assigned a NMI of 1 and 0 otherwise.

5. (5)

Economic specialization indicator (ESI). Each geographical area is assigned a score based on its dominant economic supply sector. Supply is quantified using the FAF4 intranational commodity flows³⁰. Areas with a dominant meat sector are assigned an ESI of 1, crops an ESI of 2, fruits and vegetables an ESI of 3, animal feed an ESI of 4, live animals an ESI of 5, milled grains an ESI of 6, and industrial products an ESI of 7.

Probabilities of food supply chain shock

The annual probability of food supply chain shock is calculated as the probability that food inflows to a city fall below a percentage of the average inflows for that city during 2012–2015⁸. To compute this probability, we group all nodes from the 4 food flow networks (1,221 observations) into 6 diversity bins ordered from lowest to highest functional diversity D . The bin size is selected to obtain bins with similar number of observations, approximately 204 observations in each bin. For each city i and food sector c in a bin, we calculate the food supply chain shock $\langle\{S\}_{\{i\}^{\{c\}}}\rangle$ as

$$\text{Equation 7: } \text{\$}\$\{S\}_{i}^c = \left[1 - \frac{\min(\{I\}_{i}^c)}{\langle I \rangle_{i}^c} \right] \times 100$$

(7)

where $\langle I \rangle_{i}^c$ is the time series of total food inflows to node i for sector c during 2012–2015, and $\min(\{I\}_{i}^c)$ and $\langle I \rangle_{i}^c$ are the minimum and average values of the time series $\{I\}_{i}^c$, respectively.

For each diversity bin b , we count the number of observations n_b that meet the criteria $\{S\}_{i}^c > s$ for $s \in \{3, 4, 5, \dots, 15\}$, with s being the shock intensity threshold. The probability of a food supply shock S being greater than s in bin b is calculated as:

$$\text{Equation 8: } \text{\$}\$\{P\}_{b}(S > s) = \frac{n_b}{N_b},$$

(8)

where N_b is the total number of observations in bin b . Thus, for each shock intensity s , we obtain a set of probabilities of food supply chain shock,

$$\text{Equation 9: } \text{\$}\$\{P(S > s)\}_{b} = \{P\}_{b}(S > s), \quad b = \{1, \dots, 6\}.$$

(9)

Furthermore, we adapt equations (8) and (9) to calculate the probability of a food supply chain shock S being greater than s , $P'(S > s)$, under co-occurrence conditions. We define co-occurrence as any city that experiences a shock to 2 or more food sectors during 2012–2015. With this definition, $P'(S > s)$ is calculated in a fashion similar to that described above. We bin the network's nodes into 6 groups from lowest to highest diversity and determine the percentage of food supply chain shock with equation (7). Letting $\{n\}_b^{\prime}$ be the total number of cities for which $\{S\}_{i}^c > s$ holds for 2 or more food sectors, the probability of a food supply chain shock S being greater than the shock intensity s in bin b is now

$$\text{Equation 10: } \text{\$}\$\{P\}_{b}^{\prime}(S > s) = \frac{\{n\}_b^{\prime}}{N_b},$$

(10)

where $\{N\}_b^{\prime}$ is the total number of cities in bin b . Thus, under co-occurrence conditions, the new set of probabilities for each shock intensity s is

$$\text{Equation 11: } \text{\$}\$\{P'_{b}(S > s)\}_{b} = \{P\}_{b}^{\prime}(S > s), \quad b = \{1, \dots, 6\}.$$

(11)

Statistical analyses

We use the disaggregated food flow data to calculate both the probability of food supply chain shock and supply chain diversity. Therefore, we perform two complementary analyses to test whether the attractor variables used in the disaggregation are causing a circularity issue in the empirical relationship between the probability of food supply chain shock and supply chain diversity. For the first analysis, we determine the Pearson correlation between the functional distance indicators (PDI, CI, UCI, NMI and ESI) and the attractor variables (Supplementary Fig. 8). We find that the attractor variables are weakly correlated with the functional distance indicators (Supplementary Table 1). For the second analysis, we determine the Pearson correlation between the food supply chain shock intensities and attractor variables for the 4 food sectors (Supplementary Fig. 9). The attractor variables are also weakly correlated with the food supply chain shock intensities (Supplementary Table 2). Thus, circularity is not unduly influencing the empirical relationship between the probability of shock and supply chain diversity.

We also evaluate whether the empirical relationship between the probability of food supply chain shock and supply chain diversity is driven by the disaggregation of the original FAF4 data. For this, we recalculate the probability of shock and supply chain diversity using the FAF4 data. For the FAF4 data, the probability of shock also declines with rising supply chain diversity (Supplementary Fig. 10), similar to the reduction observed using the disaggregated food flow data (Fig. 1a), suggesting that the latter data are not driving the relationship.

Furthermore, we test whether the relationship between the probability of food supply chain shock and supply chain diversity holds for different demand levels. To control for demand, we stratify all the data into low, medium and high demand levels using population or food inflows as proxies for demand. For both stratifications, the bounds are chosen so that each level has approximately the same number of data points. Using the stratified data, we recalculate the Pearson correlation between the probability of shock at 3%, 5%, 10% and 15% shock intensities and supply chain diversity for each level of population or food inflows (Supplementary Table 3). We find that the relationship between the probability of food supply chain shock and supply chain diversity holds for these different demand levels (Supplementary Table 3). Using the same exponential model in equation (1) to fit the relationship for the stratified data (Supplementary Fig. 11), we determine the exponential model parameters k_s and $D_{0,s}$ for each demand level (Extended Data Table 6). These parameters fall within the 95% confidence interval of the parameters of the exponential model in the main text (Extended Data Table 1), indicating that the model is robust.

We perform two different sensitivity analyses to assess the influence of the five distance indicators on the empirical relationship between the probability of food supply chain shock and supply chain diversity. The first analysis compares single-indicator diversity measures against the multi-indicator diversity measure calculated using all 5 indicators. Five different single-indicator diversity measures are compared, one measure for each of the 5 indicators: PDI, CI, UCI, NMI and ESI. For the second sensitivity analysis, we leave out one indicator at a time to calculate diversity using the 4 remaining indicators, which results in another 5 different diversity measures. The diversity measures for the sensitivity analyses are all calculated following the approach in the ‘Food inflows supply chain diversity’ section of the Methods. To perform the sensitivity analyses, we plot the empirical relationship between the probability of food supply chain shock and each diversity measure (Supplementary Figs. 12 and 13), and calculate the Pearson correlation of the data (Extended Data Table 7). The correlation coefficients are used to quantify the influence of the distance indicators on the relationship between the probability of food supply chain shock and supply chain diversity (Extended Data Table 7). The probabilities of food supply chain shock are calculated following the approach in the ‘Probabilities of food supply chain shock’ section of the Methods. We find that the five indicators have a varied influence on the relationship between the probability of food supply chain shock and supply chain diversity (Extended Data Table 7). The inclusion of all 5 indicators, however, in the supply chain diversity measure increases the Pearson correlation between the probability of food supply chain shock and supply chain diversity (Extended Data Table 7).

Data availability

The commodity flows data are from the Freight Analysis Framework version 4 dataset, prepared by the Federal Highway Administration of the United States Department of Transportation (https://ops.fhwa.dot.gov/freight/freight_analysis/faf/). The socioeconomic and agricultural data used are all publicly available at <https://www.census.gov/programs-surveys/popest.html> (population), <https://www.bls.gov/cew/downloadable-data-files.htm> (employment and wages), and <https://www.fsa.usda.gov/news-room/efoia/electronic-reading-room/frequently-requested-information/crop-acreage-data/index> (cropland area). Additional data used for the functional distance indicators are available at <https://www.ncdc.noaa.gov/temp-and-precip/drought/historical-palmers/> (Palmer drought severity index) and https://www.cdc.gov/nchs/data_access/urban_rural.htm (urban–rural classification). Calculated metropolitan level food flows and functional diversity are published in the HydroShare data repository at <https://doi.org/10.4211/hs.caebbbb68cce49f2bbf351f28d865794>. The base map of the USA is from the United States Census Bureau TIGER/Line database (<https://www.census.gov/cgi-bin/geo/shapefiles/index.php>).

Code availability

Requests for code related to the analyses performed can be directed to M.G. (michael_gomezs@hotmail.com).

References

1. 1.

Cottrell, R. S. et al. Food production shocks across land and sea. *Nat. Sustainability* **2**, 130–137 (2019).

[Google Scholar](#)

2. 2.

Wenz, L. & Levermann, A. Enhanced economic connectivity to foster heat stress-related losses. *Sci. Adv.* **2**, e1501026 (2016).

[ADS](#) [PubMed](#) [PubMed Central](#) [Google Scholar](#)

3. 3.

Bren d'Amour, C., Wenz, L., Kalkuhl, M., Christoph Steckel, J. & Creutzig, F. Teleconnected food supply shocks. *Environ. Res. Lett.* **11**, 035007 (2016).

[ADS](#) [Google Scholar](#)

4. 4.

Tu, C., Suweis, S. & D'Odorico, P. Impact of globalization on the resilience and sustainability of natural resources. *Nat. Sustainability* **2**, 283–289 (2019).

[Google Scholar](#)

5. 5.

Isbell, F. et al. Biodiversity increases the resistance of ecosystem productivity to climate extremes. *Nature* **526**, 574–577 (2015).

[ADS](#) [CAS](#) [Google Scholar](#)

6. 6.

Bennett, J. A. et al. Resistance of soil biota and plant growth to disturbance increases with plant diversity. *Ecol. Lett.* **23**, 119–128 (2020).

[Google Scholar](#)

7. 7.

Nyström, M. et al. Anatomy and resilience of the global production ecosystem. *Nature* **575**, 98–108 (2019).

[ADS](#) [Google Scholar](#)

8. 8.

Renard, D. & Tilman, D. National food production stabilized by crop diversity. *Nature* **571**, 257–260 (2019).

[ADS](#) [CAS](#) [Google Scholar](#)

9. 9.

Diffenbaugh, N. S., Swain, D. L. & Touma, D. Anthropogenic warming has increased drought risk in California. *Proc. Natl Acad. Sci. USA* **112**, 3931–3936 (2015).

[ADS](#) [CAS](#) [PubMed](#) [PubMed Central](#) [Google Scholar](#)

10. 10.

Naumann, G. et al. Global changes in drought conditions under different levels of warming. *Geophys. Res. Lett.* **45**, 3285–3296 (2018).

[ADS](#) [Google Scholar](#)

11. 11.

Lesk, C., Rowhani, P. & Ramankutty, N. Influence of extreme weather disasters on global crop production. *Nature* **529**, 84–87 (2016).

[ADS](#) [CAS](#) [Google Scholar](#)

12. 12.

Gaupp, F., Hall, J., Hochrainer-Stigler, S. & Dadson, S. Changing risks of simultaneous global breadbasket failure. *Nat. Clim. Change* **10**, 54–57 (2020).

[ADS](#) [Google Scholar](#)

13. 13.

Mehrabi, Z. Food system collapse. *Nat. Clim. Change* **10**, 16–17 (2020).

[ADS](#) [Google Scholar](#)

14. 14.

Scheelbeek, P. F. D. et al. United Kingdom's fruit and vegetable supply is increasingly dependent on imports from climate-vulnerable producing countries. *Nat. Food* **1**, 705–712 (2020).

[Google Scholar](#)

15. 15.

Puma, M. J., Bose, S., Chon, S. Y. & Cook, B. I. Assessing the evolving fragility of the global food system. *Environ. Res. Lett.* **10**, 024007 (2015).

[ADS](#) [Google Scholar](#)

16. 16.

Suweis, S., Carr, J. A., Maritan, A., Rinaldo, A. & D'Odorico, P. Resilience and reactivity of global food security. *Proc. Natl Acad. Sci. USA* **112**, 6902–6907 (2015).

[ADS](#) [CAS](#) [PubMed](#) [PubMed Central](#) [Google Scholar](#)

17. 17.

Marchand, P. et al. Reserves and trade jointly determine exposure to food supply shocks. *Environ. Res. Lett.* **11**, 095009 (2016).

[ADS](#) [Google Scholar](#)

18. 18.

Folke, C. et al. Regime shifts, resilience, and biodiversity in ecosystem management. *Annu. Rev. Ecol. Evol. Syst.* **35**, 557–581 (2004).

[Google Scholar](#)

19. 19.

Rushforth, R. & Ruddell, B. The vulnerability and resilience of a city's water footprint: the case of Flagstaff, Arizona, USA. *Wat. Resour. Res.* **52**, 2698–2714 (2016).

[ADS](#) [Google Scholar](#)

20. 20.

Vallina, S. M. & Le Quéré, C. Stability of complex food webs: resilience, resistance and the average interaction strength. *J. Theor. Biol.* **272**, 160–173 (2011).

[ADS](#) [MathSciNet](#) [MATH](#) [Google Scholar](#)

21. 21.

Allen, C. R., Angeler, D. G., Chaffin, B. C., Twidwell, D. & Garmestani, A. Resilience reconciled. *Nat. Sustainability* **2**, 898–900 (2019).

[Google Scholar](#)

22. 22.

Helpgott, A. Operationalising systemic resilience. *Eur. J. Oper. Res.* **268**, 852–864 (2018).

[Google Scholar](#)

23. 23.

Arese Lucini, F., Morone, F., Tomassone, M. S. & Makse, H. A. Diversity increases the stability of ecosystems. *PLoS ONE* **15**, e0228692 (2020).

[CAS](#) [PubMed](#) [PubMed Central](#) [Google Scholar](#)

24. 24.

Gao, J., Barzel, B. & Barabási, A.-L. Universal resilience patterns in complex networks. *Nature* **530**, 307–312 (2016).

[ADS](#) [CAS](#) [Google Scholar](#)

25. 25.

Bai, X., Nagendra, H., Shi, P. & Liu, H. Cities: build networks and share plans to emerge stronger from COVID-19. *Nature* **584**, 517–520 (2020).

[ADS](#) [CAS](#) [Google Scholar](#)

26. 26.

Garnett, P., Doherty, B. & Heron, T. Vulnerability of the United Kingdom's food supply chains exposed by COVID-19. *Nat. Food* **1**, 315–318 (2020).

[Google Scholar](#)

27. 27.

Rotz, S. & Fraser, E. D. G. Resilience and the industrial food system: analyzing the impacts of agricultural industrialization on food system vulnerability. *J. Environ. Stud. Sci.* **5**, 459–473 (2015).

[Google Scholar](#)

28. 28.

Gomez, M., Garcia, S., Rajtmajer, S., Grady, C. & Mejia, A. Fragility of a multilayer network of intranational supply chains. *Appl. Netw. Sci.* **5**, 71 (2020).

[PubMed](#) [PubMed Central](#) [Google Scholar](#)

29. 29.

Davies, E. G. R. Cities drive food and water security. *Nat. Sustainability* **1**, 120–121 (2018).

[Google Scholar](#)

30. 30.

Hwang, H. et al. *The Freight Analysis Framework Version 4 (FAF4)* ORNL/TM-2016/489 (Oak Ridge National Laboratory, 2016).

31. 31.

Countryman, A. M., Paarlberg, P. L. & Lee, J. G. Dynamic effects of drought on the U.S. beef supply chain. *Agric. Resour. Econ. Rev.* **45**, 459–484 (2016).

[Google Scholar](#)

32. 32.

Leister, A. M., Paarlberg, P. L. & Lee, J. G. Dynamic effects of drought on U.S. crop and livestock sectors. *J. Agric. Appl. Econ.* **47**, 261–284 (2015).

[Google Scholar](#)

33. 33.

Rippey, B. R. The U.S. drought of 2012. *Weather Clim. Extrem.* **10**, 57–64 (2015).

[Google Scholar](#)

34. 34.

Schnoor, J. L. The U.S. drought of 2012. *Environ. Sci. Technol.* **46**, 10480 (2012).

[ADS](#) [CAS](#) [Google Scholar](#)

35. 35.

Mays, L. *Water Resources Engineering* 3rd edn (Wiley, 2019).

36. 36.

Bettencourt, L. M. A. The origins of scaling in cities. *Science* **340**, 1438–1441 (2013).

[ADS](#) [MathSciNet](#) [CAS](#) [MATH](#) [Google Scholar](#)

37. 37.

Mahjabin, T., Garcia, S., Grady, C. & Mejia, A. Large cities get more for less: water footprint efficiency across the US. *PLoS ONE* **13**, e0202301 (2018).

[PubMed](#) [PubMed Central](#) [Google Scholar](#)

38. 38.

Seekell, D. et al. Resilience in the global food system. *Environ. Res. Lett.* **12**, 025010 (2017).

[ADS](#) [PubMed](#) [PubMed Central](#) [Google Scholar](#)

39. 39.

Coleman-Jensen, A., Rabbitt, M. P., Gregory, C. A. & Singh, A. *Household Food Security in the United States in 2015*.

<https://www.ers.usda.gov/webdocs/publications/79761/err-215.pdf?v=9349.1>

(Economic Research Service, U.S. Department of Agriculture, 2016).

40. 40.

Gregory, C. A. & Coleman-Jensen, A. Do high food prices increase food insecurity in the United States? *Appl. Econ. Perspect. Policy* **35**, 679–707 (2013).

[Google Scholar](#)

41. 41.

Gilbert, C. L. & Morgan, C. W. Food price volatility. *Phil. Trans. R. Soc. Lond. B* **365**, 3023–3034 (2010).

[CAS Google Scholar](#)

42. 42.

Pimm, S. L., Donohue, I., Montoya, J. M. & Loreau, M. Measuring resilience is essential to understand it. *Nat. Sustainability* **2**, 895–897 (2019).

[Google Scholar](#)

43. 43.

Elmqvist, T. et al. Sustainability and resilience for transformation in the urban century. *Nat. Sustainability* **2**, 267–273 (2019).

[Google Scholar](#)

44. 44.

Davis, K. F., Downs, S. & Gephart, J. A. Towards food supply chain resilience to environmental shocks. *Nat. Food* **2**, 54–65 (2021).

[Google Scholar](#)

45. 45.

United States Department of Agriculture, Food and Nutrition Service.
Supplemental Nutrition Assistance Program (SNAP)
<https://www.fns.usda.gov/snap/supplemental-nutrition-assistance-program>
(USDA).

46. 46.

United States Department of Agriculture, Food and Nutrition Service. *National School Lunch Program* <https://www.fns.usda.gov/nslp> (USDA).

47. 47.

Annual Resident Population Estimates 2010–2016. <https://www.census.gov/programs-surveys/popest.html> (United States Census Bureau, Population Division, 2017).

48. 48.

Quarterly Census Of Employment And Wages 2012. <https://www.bls.gov/cew/downloadable-data-files.htm> (United States Bureau of Labor Statistics, 2015).

49. 49.

Crop Acreage Data Reported To The Farm Service Agency 2012. <https://www.fsa.usda.gov/news-room/efoia/electronic-reading-room/frequently-requested-information/crop-acreage-data/index> (United States Department of Agriculture, Farm Service Agency, 2013).

50. 50.

Rushforth, R. R. & Ruddell, B. L. The hydro-economic interdependency of cities: virtual water connections of the Phoenix, Arizona metropolitan area. *Sustainability* **7**, 8522–8547 (2015).

[Google Scholar](#)

51. 51.

Bettencourt, L. M. A., Lobo, J., Helbing, D., Kühnert, C. & West, G. B. Growth, innovation, scaling, and the pace of life in cities. *Proc. Natl Acad. Sci. USA* **104**, 7301–7306 (2007).

[ADS](#) [CAS](#) [PubMed](#) [PubMed Central](#) [Google Scholar](#)

52. 52.

Walker, B., Kinzig, A. & Langridge, J. Plant attribute diversity, resilience, and ecosystem function: the nature and significance of dominant and minor species. *Ecosystems* **2**, 95–113 (1999).

[Google Scholar](#)

53. 53.

Shannon, C. E. A mathematical theory of communication. *Bell Syst. Tech. J.* **27**, 379–423 (1948).

[MathSciNet](#) [MATH](#) [Google Scholar](#)

54. 54.

United States National Oceanic and Atmospheric Administration *Historical Palmer Drought Indices*. <https://www.ncdc.noaa.gov/temp-and-precip/drought/historical-palmers/> (NOAA).

55. 55.

Ingram, D. & Franco, S. *NCHS Urban–Rural Classification Scheme for Counties*. https://www.cdc.gov/nchs/data_access/urban_rural.htm (National Center for Health Statistics, 2013).

56. 56.

Newman, M. E. J. Modularity and community structure in networks. *Proc. Natl Acad. Sci. USA* **103**, 8577 (2006).

[ADS](#) [CAS](#) [PubMed](#) [PubMed Central](#) [Google Scholar](#)

57. 57.

Girvan, M. & Newman, M. E. J. Community structure in social and biological networks. *Proc. Natl Acad. Sci. USA* **99**, 7821–7826 (2002).

[ADS](#) [MathSciNet](#) [CAS](#) [PubMed](#) [PubMed Central](#) [MATH](#) [Google Scholar](#)

58. 58.

Blondel, V. D., Guillaume, J. P., Lambiotte, R. & Lefebvre, E. Fast unfolding of communities in large networks. *J. Stat. Mech.* **2008**, P10008 (2008).

[MATH](#) [Google Scholar](#)

59. 59.

Garcia, S. & Mejia, A. Characterizing and modeling subnational virtual water networks of US agricultural and industrial commodity flows. *Adv. Water Resour.* **130**, 314–324 (2019).

[ADS](#) [Google Scholar](#)

[Download references](#)

Acknowledgements

We thank S. Spencer for advising on the form of exponent to use in the model. Computations for this research were performed on the Pennsylvania State University's Institute for Computational and Data Sciences' Roar supercomputer. This material is based upon work supported by the National Science Foundation (NSF) under grant ACI-1639529. Any opinions, findings, and conclusions or recommendations expressed in this material are those of the authors and do not necessarily reflect the view of the NSF.

Author information

Affiliations

1. Department of Civil and Environmental Engineering, The Pennsylvania State University, University Park, PA, USA

Michael Gomez & Alfonso Mejia

2. School of Informatics, Computing, and Cyber Systems, Northern Arizona University, Flagstaff, AZ, USA

Benjamin L. Ruddell & Richard R. Rushforth

Authors

1. Michael Gomez

[View author publications](#)

You can also search for this author in [PubMed](#) [Google Scholar](#)

2. Alfonso Mejia

[View author publications](#)

You can also search for this author in [PubMed](#) [Google Scholar](#)

3. Benjamin L. Ruddell

[View author publications](#)

You can also search for this author in [PubMed](#) [Google Scholar](#)

4. Richard R. Rushforth

[View author publications](#)

You can also search for this author in [PubMed](#) [Google Scholar](#)

Contributions

M.G. carried out the data analysis and generated the results with input from A.M. and B.L.R. All authors devised the research, contributed to the analysis of results, and wrote the manuscript.

Corresponding author

Correspondence to [Alfonso Mejia](#).

Ethics declarations

Competing interests

The authors declare no competing interests.

Additional information

Peer review information *Nature* thanks Zia Mehrabi and the other, anonymous, reviewer(s) for their contribution to the peer review of this work. Peer reviewer reports are available.

Publisher's note Springer Nature remains neutral with regard to jurisdictional claims in published maps and institutional affiliations.

Extended data figures and tables

[Extended Data Fig. 1 Shock intensity versus exponential regression parameters.](#)

Relationship between the supply chain shock intensity s and the exponential regression parameters k_s and $\langle\{D\}_{0,s}\rangle$ for single (**a, b**) and $\langle\{k\}_s\rangle^{\{\prime\}}$ and $\langle\{\boldsymbol{D}\}_s\rangle^{\{0,\boldsymbol{s}\}^{\{\prime\}}}$ for co-occurring shocks (**c, d**). The lines are linear regression fits. The goodness-of-fit results for single and co-occurring shocks are summarized in Extended Data Tables [1](#) and [4](#), respectively.

[Extended Data Fig. 2 Level of co-occurrence of food supply chain shocks across the USA.](#)

For a given shock intensity (3%, 5%, 10% and 15%), the co-occurrence level is measured as the number of food supply chain shocks from different food sectors to a geographic location during 2012–2015, out of a possible maximum of 4 shocks. The maps show the level of co-occurrence for different shock intensities. The overall co-occurrence level across the USA tends to decline as the threshold increases, meaning that co-occurrence becomes less likely for higher shock intensities.

[Extended Data Fig. 3 Performance of food flow disaggregation approach.](#)

Comparison between observed and disaggregated food supply (**a–d**) and demand (**e–h**) flows for crops (**a, e**), live animals (**b, f**), feed (**c, g**), and meat (**d, h**) based on the FAF4 metropolitan and remainder-of-state areas. Different socioeconomic and agricultural variables (Methods) were tested and those that resulted in the highest values of the Pearson correlation coefficient r were used in the disaggregation. For the crop sector, disaggregated flows using cropland area as an attractor yielded the highest r between observed and disaggregated flows for both supply and demand. For the live animals and feed sector, the flows disaggregated by number of establishments resulted in the highest r for both supply and demand. For the meat sector, the number of establishments resulted in the highest r value for supply and population for demand.

Extended Data Table 1 Goodness-of-fit results for the exponential regression between the probability of food supply chain shock and supply chain diversity for shock intensities s ranging from 3 to 15%

[Full size table](#)

Extended Data Table 2 Goodness-of-fit results for the linear regression between the parameters k_s and $D_{0,s}$ and the supply chain shock intensity s

[Full size table](#)

Extended Data Table 3 Probability of shock equations for different shock intensities s

[Full size table](#)

Extended Data Table 4 Goodness of fit results for the exponential regression between the probability of co-occurring food supply chain shocks and supply chain diversity

[Full size table](#)

Extended Data Table 5 Goodness-of-fit results for the linear regression between the parameters $\{\boldsymbol{k}\}_{\{\boldsymbol{s}\}}^{\prime}$ and $\{\boldsymbol{D}\}_{0,\{\boldsymbol{s}\}}^{\prime}$ and the supply chain shock intensity s

[Full size table](#)

Extended Data Table 6 Exponential fit parameters k_s and $D_{0,s}$ for the relationship between the probability of food supply chain shock and supply chain diversity at different demand levels and shock intensities

[Full size table](#)

Extended Data Table 7 Sensitivity of the supply chain diversity results to different configurations of the basket of indicators

[Full size table](#)

Supplementary information

[Supplementary Information](#)

This file contains Supplementary Figures 1-13, Supplementary Tables 1-3 and Supplementary References.

[Peer Review File](#)

Rights and permissions

[Reprints and Permissions](#)

About this article



Cite this article

Gomez, M., Mejia, A., Ruddell, B.L. *et al.* Supply chain diversity buffers cities against food shocks. *Nature* **595**, 250–254 (2021). <https://doi.org/10.1038/s41586-021-03621-0>

[Download citation](#)

- Received: 12 October 2020
- Accepted: 07 May 2021
- Published: 07 July 2021
- Issue Date: 08 July 2021
- DOI: <https://doi.org/10.1038/s41586-021-03621-0>

Comments

By submitting a comment you agree to abide by our [Terms](#) and [Community Guidelines](#). If you find something abusive or that does not comply with our terms or guidelines please flag it as inappropriate.

[Download PDF](#)

Associated Content

[How to buffer against an urban food shortage](#)

- Zia Mehrabi

Advertisement

| [Section menu](#) | [Main menu](#) |

- Article
- [Published: 07 July 2021](#)

Fluid-rich subducting topography generates anomalous forearc porosity

- [Christine Chesley](#) [ORCID: orcid.org/0000-0001-5077-8142¹](#),
- [Samer Naif](#) [ORCID: orcid.org/0000-0003-3579-5379²](#),
- [Kerry Key](#) [ORCID: orcid.org/0000-0003-1169-6683¹](#) &
- [Dan Bassett](#) [ORCID: orcid.org/0000-0001-6351-0284³](#)

Nature volume **595**, pages 255–260 (2021) [Cite this article](#)

- 72 Altmetric
- [Metrics details](#)

Subjects

- [Geology](#)
- [Geophysics](#)
- [Hydrogeology](#)
- [Seismology](#)
- [Tectonics](#)

Abstract

The role of subducting topography on the mode of fault slip—particularly whether it hinders or facilitates large megathrust earthquakes—remains a controversial topic in subduction dynamics^{1,2,3,4,5}. Models have illustrated

the potential for subducting topography to severely alter the structure, stress state and mechanics of subduction zones^{4,6}; however, direct geophysical imaging of the complex fracture networks proposed and the hydrology of both the subducting topography and the associated upper plate damage zones remains elusive. Here we use passive and controlled-source seafloor electromagnetic data collected at the northern Hikurangi Margin, New Zealand, to constrain electrical resistivity in a region of active seamount subduction. We show that a seamount on the incoming plate contains a thin, low-porosity basaltic cap that traps a conductive matrix of porous volcaniclastics and altered material over a resistive core, which allows 3.2 to 4.7 times more water to subduct, compared with normal, unfaulted oceanic lithosphere. In the forearc, we image a sediment-starved plate interface above a subducting seamount with similar electrical structure to the incoming plate seamount. A sharp resistive peak within the subducting seamount lies directly beneath a prominent upper plate conductive anomaly. The coincidence of this upper plate anomaly with the location of burst-type repeating earthquakes and seismicity associated with a recent slow slip event⁷ directly links subducting topography to the creation of fluid-rich damage zones in the forearc that alter the effective normal stress at the plate interface by modulating the fluid overpressure. In addition to severely modifying the structure and physical conditions of the upper plate, subducting seamounts represent an underappreciated mechanism for transporting a considerable flux of water to the forearc and deeper mantle.

Access options

Subscribe to Journal

Get full journal access for 1 year

\$199.00

only \$3.90 per issue

[Subscribe](#)

All prices are NET prices.
VAT will be added later in the checkout.
Tax calculation will be finalised during checkout.

Rent or Buy article

Get time limited or full article access on ReadCube.

from \$8.99

[Rent or Buy](#)

All prices are NET prices.

Additional access options:

- [Log in](#)
- [Access through your institution](#)
- [Learn about institutional subscriptions](#)

Fig. 1: Tectonic setting and HT-RESIST survey area.



Fig. 2: Preferred resistivity model and porosity.

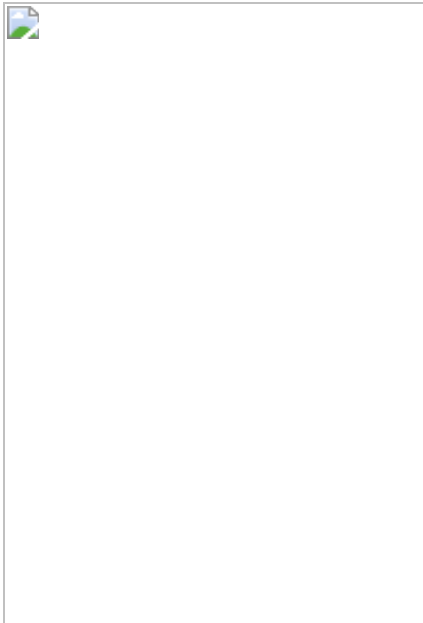
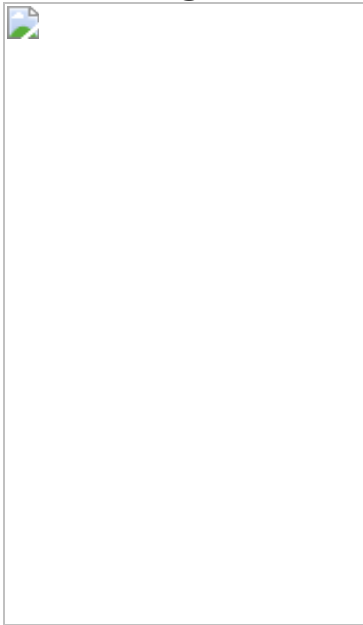


Fig. 3: Schematic of fluid transfer from subducting topography to the overthrusting forearc during a slow slip cycle.



Data availability

All electromagnetic data that were inverted and analysed in this study are available at <https://doi.org/10.5281/zenodo.4721384> and as Source data provided with this paper. The seismic reflection data overlain on the

resistivity models are available at <https://doi.org/10.21420/62C1-GS40>. [Source data](#) are provided with this paper.

Code availability

A version of the MARE2DEM code used to invert the data is available at <http://mare2dem.bitbucket.io>.

References

1. 1.

Cloos, M. Thrust-type subduction-zone earthquakes and seamount asperities: a physical model for seismic rupture. *Geology* **20**, 601–604 (1992).

[ADS](#) [Google Scholar](#)

2. 2.

Scholz, C. H. & Small, C. The effect of seamount subduction on seismic coupling. *Geology* **25**, 487–490 (1997).

[ADS](#) [Google Scholar](#)

3. 3.

Singh, S. C. et al. Aseismic zone and earthquake segmentation associated with a deep subducted seamount in Sumatra. *Nat. Geosci.* **4**, 308–311 (2011).

[ADS](#) [CAS](#) [Google Scholar](#)

4. 4.

Wang, K. & Bilek, S. L. Do subducting seamounts generate or stop large earthquakes? *Geology* **39**, 819–822 (2011).

[ADS](#) [Google Scholar](#)

5. 5.

Bassett, D. & Watts, A. B. Gravity anomalies, crustal structure, and seismicity at subduction zones: 1. Seafloor roughness and subducting relief. *Geochem. Geophys. Geosyst.* **16**, 1508–1540 (2015).

[ADS](#) [Google Scholar](#)

6. 6.

Dominguez, S., Lallemand, S. E., Malavieille, J. & Von Huene, R. Upper plate deformation associated with seamount subduction. *Tectonophysics* **293**, 207–224 (1998).

[ADS](#) [Google Scholar](#)

7. 7.

Shaddox, H. R. & Schwartz, S. Y. Subducted seamount diverts shallow slow slip to the forearc of the northern Hikurangi subduction zone, New Zealand. *Geology* **47**, 415–418 (2019).

[ADS](#) [CAS](#) [Google Scholar](#)

8. 8.

Barker, D. H. N. et al. Geophysical constraints on the relationship between seamount subduction, slow slip, and tremor at the North Hikurangi subduction zone, New Zealand. *Geophys. Res. Lett.* **45**, 804–813 (2018).

[Google Scholar](#)

9. 9.

Davidson, S. R. et al. Conjugate strike-slip faulting across a subduction front driven by incipient seamount subduction. *Geology* **48**,

493–498 (2020).

[ADS](#) [Google Scholar](#)

10. 10.

Wallace, L. M. et al. Characterizing the seismogenic zone of a major plate boundary subduction thrust: Hikurangi Margin, New Zealand. *Geochem. Geophys. Geosyst.* **10**, Q10006 (2009).

[ADS](#) [Google Scholar](#)

11. 11.

Barnes, P. M. et al. Slow slip source characterized by lithological and geometric heterogeneity. *Sci. Adv.* **6**, eaay3314 (2020).

[ADS](#) [CAS](#) [PubMed](#) [PubMed Central](#) [Google Scholar](#)

12. 12.

Evans, R. L. Constraints on the large-scale porosity and permeability structure of young oceanic crust from velocity and resistivity data. *Geophys. J. Int.* **119**, 869–879 (1994).

[ADS](#) [Google Scholar](#)

13. 13.

Naif, S., Key, K., Constable, S. & Evans, R. L. Water-rich bending faults at the Middle America Trench. *Geochem. Geophys. Geosyst.* **16**, 2582–2597 (2015).

[ADS](#) [Google Scholar](#)

14. 14.

Naif, S., Key, K., Constable, S. & Evans, R. L. Porosity and fluid budget of a water-rich megathrust revealed with electromagnetic data

at the Middle America Trench. *Geochem. Geophys. Geosyst.* **17**, 4495–4516 (2016).

[ADS](#) [Google Scholar](#)

15. 15.

Johansen, S. E. et al. Deep electrical imaging of the ultraslow-spreading Mohns Ridge. *Nature* **567**, 379–383 (2019).

[ADS](#) [CAS](#) [PubMed](#) [PubMed Central](#) [Google Scholar](#)

16. 16.

Chesley, C., Key, K., Constable, S., Behrens, J. & Macgregor, L. Crustal cracks and frozen flow in oceanic lithosphere inferred from electrical anisotropy. *Geochem. Geophys. Geosyst.* **20**, 5979–5999 (2019).

[ADS](#) [Google Scholar](#)

17. 17.

Barker, D. H. N., Sutherland, R., Henrys, S. & Bannister, S. Geometry of the Hikurangi subduction thrust and upper plate, North Island, New Zealand. *Geochem. Geophys. Geosyst.* **10**, Q02007 (2009).

[ADS](#) [Google Scholar](#)

18. 18.

Wallace, L. M. et al. Hikurangi subduction margin coring, logging, and observatories. In *Proc. International Ocean Discovery Program Vol. 372B/375* (eds Wallace L. M. et al.) (International Ocean Discovery Program, 2019); <https://doi.org/10.14379/iodp.proc.372B375.2019>

19. 19.

Wallace, L. M. et al. Slow slip near the trench at the Hikurangi subduction zone, New Zealand. *Science* **352**, 701–704 (2016).

[ADS](#) [CAS](#) [PubMed](#) [PubMed Central](#) [Google Scholar](#)

20. 20.

Taylor, B. The single largest oceanic plateau: Ontong Java–Manihiki–Hikurangi. *Earth Planet. Sci. Lett.* **241**, 372–380 (2006).

[ADS](#) [CAS](#) [Google Scholar](#)

21. 21.

Key, K. MARE2DEM: a 2-D inversion code for controlled-source electromagnetic and magnetotelluric data. *Geophys. J. Int.* **207**, 571–588 (2016).

[ADS](#) [CAS](#) [Google Scholar](#)

22. 22.

Davy, B., Hoernle, K. & Werner, R. Hikurangi Plateau: Crustal structure, rifted formation, and Gondwana subduction history. *Geochem. Geophys. Geosyst.* **9**, Q07004 (2008).

[ADS](#) [Google Scholar](#)

23. 23.

Wallace, L. M. et al. Site U1526. In *Proc. International Ocean Discovery Program Vol. 372B/375* (eds Wallace, L. M. et al.) (International Ocean Discovery Program, 2019);
<https://doi.org/10.14379/iodp.proc.372B375.106.2019>

24. 24.

Pezard, P. A. Electrical properties of mid-ocean ridge basalt and implications for the structure of the upper oceanic crust in hole 504B.

J. Geophys. Res. **95**, 9237–9264 (1990).

[ADS](#) [Google Scholar](#)

25. 25.

Antriasian, A. et al. Thermal regime of the Northern Hikurangi Margin, New Zealand. *Geophys. J. Int.* **216**, 1177–1190 (2018).

[ADS](#) [Google Scholar](#)

26. 26.

Fisher, A. T. & Wheat, C. G. Seamounts as conduits for massive fluid, heat, and solute fluxes on ridge flanks. *Oceanography* **23**, 74–87 (2010).

[Google Scholar](#)

27. 27.

Archie, G. E. The electrical resistivity log as an aid in determining some reservoir characteristics. *Trans. AIME* **146**, 54–62 (1942).

[Google Scholar](#)

28. 28.

Becker, K. Large-scale electrical resistivity and bulk porosity of the upper oceanic crust at hole 395A. In *Proc. Ocean Drilling Program Scientific Results* Vol. 106/109 (eds Detrick, R. et al.) 205–212 (Ocean Drilling Program, 1990);

<https://doi.org/10.2973/odp.proc.sr.106109.145.1990>

29. 29.

Barnes, P. M. et al. Site U1520. in *Proc. International Ocean Discovery Program* Vol. 372B/375 (eds Wallace, L. M. et al.)

(International Ocean Discovery Program, 2019);
<https://doi.org/10.14379/iodp.proc.372B375.105.2019>

30. 30.

Barnes, P. M. et al. Site U1519. in *Proc. International Ocean Discovery Program* Vol. 372B/375 (eds Wallace, L. M. et al.) (International Ocean Discovery Program, 2019);
<https://doi.org/10.14379/iodp.proc.372B375.104.2019>

31. 31.

Bell, R. et al. Seismic reflection character of the Hikurangi subduction interface, New Zealand, in the region of repeated Gisborne slow slip events. *Geophys. J. Int.* **180**, 34–48 (2010).

[ADS](#) [Google Scholar](#)

32. 32.

Watson, S. J. et al. Focused fluid seepage related to variations in accretionary wedge structure, Hikurangi Margin, New Zealand. *Geology* **48**, 56–61 (2020).

[ADS](#) [Google Scholar](#)

33. 33.

Arai, R. et al. Three-dimensional P-wave velocity structure of the northern Hikurangi Margin from the NZ3D experiment: evidence for fault-bound anisotropy. *J. Geophys. Res. Solid Earth* **125**, e2020JB020433 (2020).

[ADS](#) [Google Scholar](#)

34. 34.

Sun, T., Saffer, D. & Ellis, S. Mechanical and hydrological effects of seamount subduction on megathrust stress and slip. *Nat. Geosci.* **13**,

249–255 (2020).

[ADS](#) [CAS](#) [Google Scholar](#)

35. 35.

Zal, H. J. et al. Temporal and spatial variations in seismic anisotropy and V_P/V_S ratios in a region of slow slip. *Earth Planet. Sci. Lett.* **532**, 115970 (2020).

[CAS](#) [Google Scholar](#)

36. 36.

Warren-Smith, E. et al. Episodic stress and fluid pressure cycling in subducting oceanic crust during slow slip. *Nat. Geosci.* **12**, 475–481 (2019).

[ADS](#) [CAS](#) [Google Scholar](#)

37. 37.

Bonnet, G., Agard, P., Angiboust, S., Fournier, M. & Omrani, J. No large earthquakes in fully exposed subducted seamount. *Geology* **47**, 407–410 (2019).

[ADS](#) [CAS](#) [Google Scholar](#)

38. 38.

Nakajima, J. & Uchida, N. Repeated drainage from megathrusts during episodic slow slip. *Nat. Geosci.* **11**, 351–356 (2018).

[ADS](#) [CAS](#) [Google Scholar](#)

39. 39.

Sibson, R. H. Stress switching in subduction forearcs: implications for overpressure containment and strength cycling on megathrusts.

Tectonophysics **600**, 142–152 (2013).

[ADS](#) [Google Scholar](#)

40. 40.

Park, J. O. et al. A low-velocity zone with weak reflectivity along the Nankai subduction zone. *Geology* **38**, 283–286 (2010).

[ADS](#) [Google Scholar](#)

41. 41.

Bell, R., Holden, C., Power, W., Wang, X. & Downes, G. Hikurangi Margin tsunami earthquake generated by slow seismic rupture over a subducted seamount. *Earth Planet. Sci. Lett.* **397**, 1–9 (2014).

[ADS](#) [CAS](#) [Google Scholar](#)

42. 42.

Li, J. et al. Connections between subducted sediment, pore-fluid pressure, and earthquake behavior along the Alaska megathrust. *Geology* **46**, 299–302 (2018).

[ADS](#) [CAS](#) [Google Scholar](#)

43. 43.

van Rijsingen, E., Funiciello, F., Corbi, F. & Lallemand, S. Rough subducting seafloor reduces interseismic coupling and mega-earthquake occurrence: insights from analogue models. *Geophys. Res. Lett.* **46**, 3124–3132 (2019).

[ADS](#) [Google Scholar](#)

44. 44.

Wallace, L. M. Slow slip events in New Zealand. *Annu. Rev. Earth Planet. Sci.* **48**, 175–203 (2020).

[ADS](#) [CAS](#) [Google Scholar](#)

45. 45.

Conrad, C. P., Selway, K., Hirschmann, M. M., Ballmer, M. D. & Wessel, P. Constraints on volumes and patterns of asthenospheric melt from the space-time distribution of seamounts. *Geophys. Res. Lett.* **44**, 7203–7210 (2017).

[ADS](#) [Google Scholar](#)

46. 46.

Constable, S. Review paper: Instrumentation for marine magnetotelluric and controlled source electromagnetic sounding. *Geophys. Prospect.* **61**, 505–532 (2013).

[ADS](#) [Google Scholar](#)

47. 47.

Myer, D., Constable, S. & Key, K. Broad-band waveforms and robust processing for marine CSEM surveys. *Geophys. J. Int.* **184**, 689–698 (2011).

[ADS](#) [Google Scholar](#)

48. 48.

Key, K. & Constable, S. Inverted long-baseline acoustic navigation of deep-towed CSEM transmitters and receivers. *Mar. Geophys. Res.* **42**, 6 (2021).

[Google Scholar](#)

49. 49.

Myer, D., Constable, S., Key, K., Glinsky, M. E. & Liu, G. Marine CSEM of the Scarborough gas field, Part 1: Experimental design and data uncertainty. *Geophysics* **77**, E281–E299 (2012).

[ADS](#) [Google Scholar](#)

50. 50.

Egbert, G. D. Robust multiple-station magnetotelluric data processing. *Geophys. J. Int.* **130**, 475–496 (1997).

[ADS](#) [Google Scholar](#)

51. 51.

Wheelock, B., Constable, S. & Key, K. The advantages of logarithmically scaled data for electromagnetic inversion. *Geophys. J. Int.* **201**, 1765–1780 (2015).

[ADS](#) [Google Scholar](#)

52. 52.

Constable, S., Key, K. & Lewis, L. Mapping offshore sedimentary structure using electromagnetic methods and terrain effects in marine magnetotelluric data. *Geophys. J. Int.* **176**, 431–442 (2009).

[ADS](#) [Google Scholar](#)

53. 53.

Saffer, D. M. et al. Site U1518. in *Proc. International Ocean Discovery Program Vol. 372B/375* (eds Wallace, L. M. et al.) (International Ocean Discovery Program, 2019);
<https://doi.org/10.14379/iodp.proc.372B375.103.2019>

54. 54.

Schwalenberg, K., Rippe, D., Koch, S. & Scholl, C. Marine-controlled source electromagnetic study of methane seeps and gas hydrates at Opouawe Bank, Hikurangi Margin, New Zealand. *J. Geophys. Res. Solid Earth* **122**, 3334–3350 (2017).

[ADS](#) [CAS](#) [Google Scholar](#)

55. 55.

van Keken, P. E., Hacker, B. R., Syracuse, E. M. & Abers, G. A. Subduction factory: 4. Depth-dependent flux of H₂O from subducting slabs worldwide. *J. Geophys. Res. Solid Earth* **116**, B01401 (2011).

[ADS](#) [Google Scholar](#)

56. 56.

Park, J. & Rye, D. M. Broader impacts of the metasomatic underplating hypothesis. *Geochem. Geophys. Geosyst.* **20**, 4810–4829 (2019).

[ADS](#) [Google Scholar](#)

[Download references](#)

Acknowledgements

We acknowledge that this work was partially carried out on the lands of the Te Āti Awa. We thank Scripps Institution of Oceanography for providing the instrumentation necessary to collect the electromagnetic data used in this study, the New Zealand government for permission to work in their exclusive economic zone, and the captains (W. Hill and D. Murline) and crew of the R/V *Revelle* expeditions RR1817 and RR1903. We thank S. Constable and the Scripps Marine EM Lab (C. Armerding, J. Lemire, J. Perez and J. Souders) and the HT-RESIST science party (A. Adams, J. Alvarez-Aramberri, C. Armerding, E. Attias, E.A. Bertrand, D. Blatter, G. Boren, G. Franz, C. Gustafson, W. Heise, Y. Li, B. Oryan, N. Palmer, J.

Perez, J. Sherman, K. Woods and A. Yates). We thank the National Institute of Water and Atmospheric Research (NIWA; <https://niwa.co.nz/>) for providing high-resolution bathymetry data. This work was supported by the National Science Foundation grant OCE-1737328. C.C. acknowledges funding support by the Department of Defense (DoD) through the National Defense Science and Engineering Graduate Fellowship (NDSEG) Program. D.B. was supported by a Royal Society of New Zealand Marsden Fund grant (MFP-GNS1902); by the MBIE Endeavour Grant: Diagnosing peril posed by the Hikurangi subduction zone; and by public research funding from the Government of New Zealand Strategic Science Investment Fund to GNS Science. We acknowledge computing resources from Columbia University's Shared Research Computing Facility project, which is supported by NIH Research Facility Improvement Grant 1G20RR030893-01, and associated funds from the New York State Empire State Development, Division of Science Technology and Innovation (NYSTAR) Contract C090171, both awarded 15 April 2010.

Author information

Affiliations

1. Lamont-Doherty Earth Observatory, Columbia University, Palisades, NY, USA

Christine Chesley & Kerry Key

2. School of Earth and Atmospheric Sciences, Georgia Institute of Technology, Atlanta, GA, USA

Samer Naif

3. GNS Science, Lower Hutt, New Zealand

Dan Bassett

Authors

1. Christine Chesley
[View author publications](#)

You can also search for this author in [PubMed](#) [Google Scholar](#)

2. Samer Naif
[View author publications](#)

You can also search for this author in [PubMed](#) [Google Scholar](#)

3. Kerry Key
[View author publications](#)

You can also search for this author in [PubMed](#) [Google Scholar](#)

4. Dan Bassett
[View author publications](#)

You can also search for this author in [PubMed](#) [Google Scholar](#)

Contributions

S.N. and K.K. designed the experiment. S.N. and C.C. collected the data. C.C. and S.N. processed the data. C.C. modelled the data. All authors contributed to writing the manuscript.

Corresponding author

Correspondence to [Christine Chesley](#).

Ethics declarations

Competing interests

The authors declare no competing interests.

Additional information

Peer review information *Nature* thanks Martyn Unsworth and the other anonymous, reviewer(s) for their contribution to the peer review of this work. Peer reviewer reports are available.

Publisher's note Springer Nature remains neutral with regard to jurisdictional claims in published maps and institutional affiliations.

Extended data figures and tables

[Extended Data Fig. 1 Preferred inversion model \(vertical resistivity component \$\rho_y\$ \) with high-resolution bathymetry.](#)

Seafloor receivers used in the inversion are grey cubes with station numbers. See Extended Data Fig. 6 for the horizontal resistivity and anisotropy. **a**, **b**, Northeast-facing (**a**) and southwest-facing (**b**) views of the bathymetry. High-resolution bathymetry were provided courtesy of the National Institute of Water and Atmospheric Research (<https://niwa.co.nz/>).

[Extended Data Fig. 2 Porosity conversion of the preferred resistivity model using a range of Archie's law cementation exponents.](#)

a, $m = 1.6$. **b**, $m = 2$. **c**, $m = 2.4$ (same as Fig. 2b). **d**, $m = 2.8$.

[Extended Data Fig. 3 Resolution test of key model features.](#)

a, Model used to generate synthetic data. **b**, Model recovered from inversion of the synthetic data.

[Source data](#)

[Extended Data Fig. 4 Example of CSEM data and model responses from this survey.](#)

Amplitude (top) and phase (bottom) data (circles) and preferred model response (line) at 0.75 Hz for station 7 (green) and station 26 (blue) are shown. The rapid attenuation seen at station 7 and the much slower decay at station 26 are due to their respective locations on the conductive forearc and resistive Tūranganui Knoll.

Extended Data Fig. 5 MT impedance polar diagrams shown as a function of period and station ID.

Red and blue lines show the diagonal, $|Z_{xx}|$, and off-diagonal, $|Z_{xy}|$, components of the impedance tensor, respectively, as a function of geographic rotation, with north pointing up. The black arrow in the white circle is the strike direction for this survey. Grey shading masks the periods and stations where data are omitted from our 2D analysis due to 3D effects in the polar diagram shapes.

Extended Data Fig. 6 Vertical anisotropy of the preferred resistivity model.

a, Horizontal resistivity (ρ_h). **b**, Anisotropy ratio (ρ_v/ρ_h). The model has minimal anisotropy.

Extended Data Fig. 7 Preferred model r.m.s misfit breakdown.

a, b, Normalized r.m.s for CSEM data (**a**) and MT data (**b**). The blue dots and red dots in **a** are normalized residuals for all inline electric field amplitude and phase, respectively, at a given transmitter position. The bars in **b** are r.m.s. misfit for impedance tensor components of each MT receiver: blue, transverse electric (TE) mode apparent resistivity; green, TE phase; orange, transverse magnetic (TM) mode apparent resistivity; purple, TM phase.

Extended Data Fig. 8 CSEM data and response matrices.

CSEM data (top), model fits (middle) and residuals (bottom) for the highest power harmonics as a function of distance from the Hikurangi Margin and

transmitter–receiver offset. The dashed box indicates data collected at 1/6 Hz. All other data were collected at 1/4 Hz. **a**, Fundamental frequency. **b**, Third harmonic. **c**, Seventh harmonic.

Extended Data Fig. 9 MT data and model responses.

Fit of the preferred resistivity model (lines) to all MT data (circles) used in this study. TE mode is blue and TM mode is red.

Extended Data Fig. 10 Sensitivity to forearc conductors C1f, C2f and C3f.

a, b, Change in model fit between the preferred model and forward models testing the sensitivity to the forearc conductors for the CSEM data (**a**) and the MT data (**b**). To generate the top row of each panel, the resistivity of each conductor was individually increased to 5 Ω m. The resistivity was increased to 10 Ω m in the bottom panel. The blue dots and red dots in **a** are the change in r.m.s. for all inline electric field amplitudes and phases, respectively, at a given transmitter position. In **b**, the bars are the change in r.m.s. misfit for impedance tensor components of each MT receiver: blue, TE apparent resistivity; green, TE phase; orange, TM apparent resistivity; purple, TM phase.

[Source data](#)

Extended Data Fig. 11 Sensitivity to subducting seamount, R1f.

Change in model fit between the preferred model and forward models testing the sensitivity to the subducting seamount for the MT data (CSEM data are insensitive to R1f). To generate the top, middle and bottom panels, the resistivity of the subducting seamount was decreased to 20 Ω m, 10 Ω m and 7 Ω m, respectively. The bars are the change in r.m.s. misfit for impedance tensor components of each MT receiver: blue, TE apparent resistivity; green, TE phase; orange, TM apparent resistivity; purple, TM phase.

[Source data](#)

Supplementary information

[Peer Review File](#)

Source data

[Source Data Fig. 2](#)

[Source Data Extended Data Fig. 3](#)

[Source Data Extended Data Fig. 10](#)

[Source Data Extended Data Fig. 11](#)

Rights and permissions

[Reprints and Permissions](#)

About this article



Check for
updates

Cite this article

Chesley, C., Naif, S., Key, K. *et al.* Fluid-rich subducting topography generates anomalous forearc porosity. *Nature* **595**, 255–260 (2021).
<https://doi.org/10.1038/s41586-021-03619-8>

[Download citation](#)

- Received: 02 October 2020

- Accepted: 07 May 2021
- Published: 07 July 2021
- Issue Date: 08 July 2021
- DOI: <https://doi.org/10.1038/s41586-021-03619-8>

Comments

By submitting a comment you agree to abide by our [Terms](#) and [Community Guidelines](#). If you find something abusive or that does not comply with our terms or guidelines please flag it as inappropriate.

[Access through your institution](#)

[Change institution](#)

[Buy or subscribe](#)

Associated Content

[Fluid-rich extinct volcanoes cause small earthquakes beneath New Zealand](#)

- Catherine A. Rychert
- Nicholas Harmon

Advertisement

This article was downloaded by **calibre** from <https://www.nature.com/articles/s41586-021-03619-8>

- Article
- [Published: 16 June 2021](#)

GluD1 is a signal transduction device disguised as an ionotropic receptor

- [Jinye Dai](#) [ORCID: orcid.org/0000-0002-8497-3154^{1,2}](#),
- [Christopher Patzke](#) [ORCID: orcid.org/0000-0001-7293-8936²](#) nAff³,
- [Kif Liakath-Ali](#) [ORCID: orcid.org/0000-0001-9047-7424²](#),
- [Erica Seigneur²](#) &
- [Thomas C. Südhof](#) [ORCID: orcid.org/0000-0003-3361-9275^{1,2}](#)

[Nature](#) volume **595**, pages 261–265 (2021) [Cite this article](#)

- 3379 Accesses
- 23 Altmetric
- [Metrics details](#)

Subjects

- [Autism spectrum disorders](#)
- [Cellular neuroscience](#)
- [Molecular neuroscience](#)
- [Neurophysiology](#)
- [Schizophrenia](#)

Abstract

Ionotropic glutamate delta receptors 1 (GluD1) and 2 (GluD2) exhibit the molecular architecture of postsynaptic ionotropic glutamate receptors, but assemble into trans-synaptic adhesion complexes by binding to secreted cerebellins that in turn interact with presynaptic neurexins^{1,2,3,4}. It is unclear whether neurexin–cerebellin–GluD1/2 assemblies serve an adhesive synapse-formation function or mediate trans-synaptic signalling. Here we show in hippocampal synapses, that binding of presynaptic neurexin–cerebellin complexes to postsynaptic GluD1 controls glutamate receptor activity without affecting synapse numbers. Specifically, neurexin-1–cerebellin-2 and neurexin-3–cerebellin-2 complexes differentially regulate NMDA (*N*-methyl-d-aspartate) receptors and AMPA (α -amino-3-hydroxy-5-methyl-4-isoxazole propionic acid) receptors by activating distinct postsynaptic GluD1 effector signals. Of note, minimal GluD1 and GluD2 constructs containing only their N-terminal cerebellin-binding and C-terminal cytoplasmic domains, joined by an unrelated transmembrane region, fully control the levels of NMDA and AMPA receptors. The distinct signalling specificity of presynaptic neurexin-1 and neurexin-3^{5,6} is encoded by their alternatively spliced splice site 4 sequences, whereas the regulatory functions of postsynaptic GluD1 are mediated by conserved cytoplasmic sequence motifs spanning 5–13 residues. Thus, Gluds are signalling molecules that regulate NMDA and AMPA receptors by an unexpected transduction mechanism that bypasses their ionotropic receptor architecture and directly converts extracellular neurexin–cerebellin signals into postsynaptic receptor responses.

Access options

Subscribe to Journal

Get full journal access for 1 year

\$199.00

only \$3.90 per issue

[Subscribe](#)

All prices are NET prices.
VAT will be added later in the checkout.
Tax calculation will be finalised during checkout.

Rent or Buy article

Get time limited or full article access on ReadCube.

from \$8.99

[Rent or Buy](#)

All prices are NET prices.

Additional access options:

- [Log in](#)
- [Access through your institution](#)
- [Learn about institutional subscriptions](#)

Fig. 1: GluD1 controls AMPARs and NMDARs without altering synapse numbers.

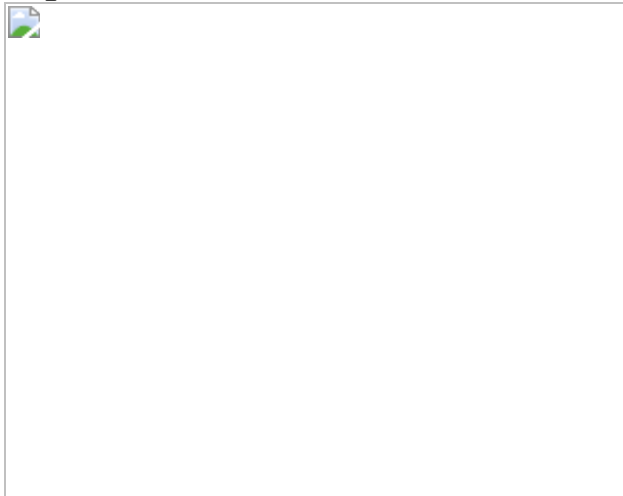


Fig. 2: GluD1 controls postsynaptic AMPAR EPSCs and NMDAR EPSCs by a CBLN2-dependent mechanism.

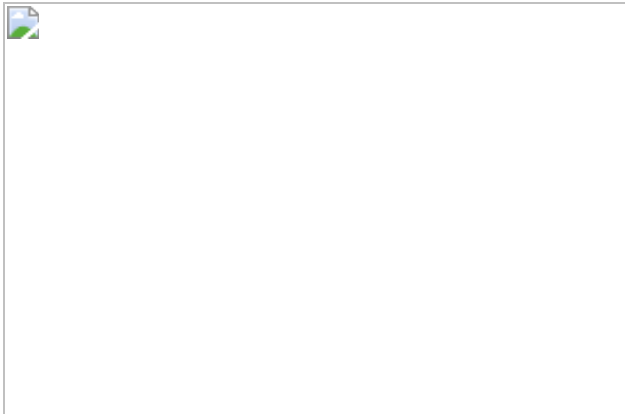


Fig. 3: GluD1 transduces both the NRXN1^{SS4+} signal that enhances NMDAR EPSCs and the NRXN3^{SS4+} signal that suppresses AMPAR EPSCs.

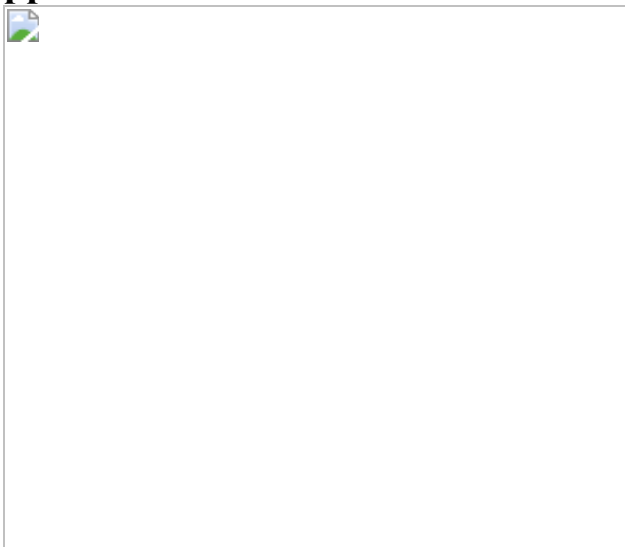


Fig. 4: Distinct cytoplasmic GluD1 sequences regulate AMPARs and NMDARs independent of the GluD1 ionotropic receptor transmembrane architecture.

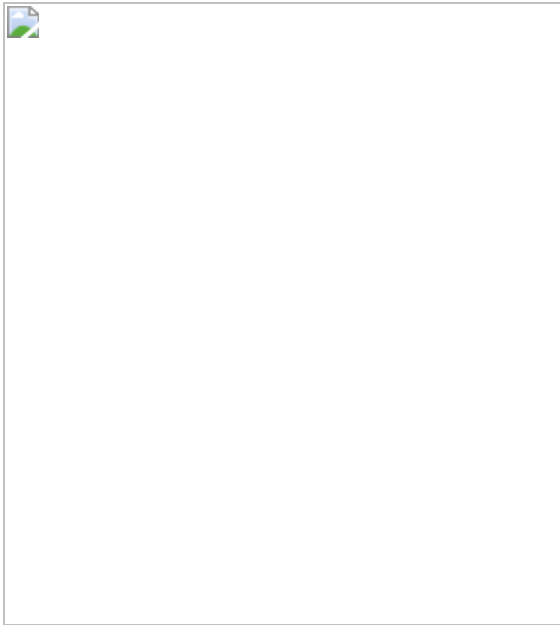
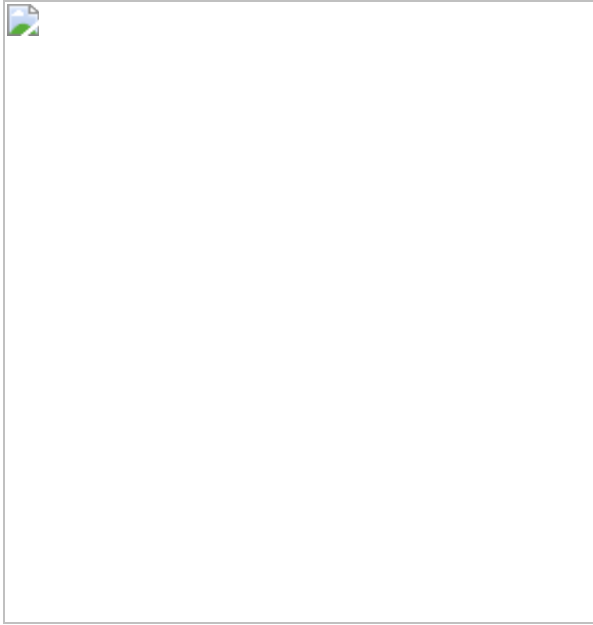


Fig. 5: Short GluD1 cytoplasmic sequence motifs transduce presynaptic neurexin signals into postsynaptic AMPAR and NMDAR responses.



Data availability

Exact P values are included with the source data. [Source data](#) are provided with this paper.

References

1. 1.

Uemura, T. et al. Trans-synaptic interaction of GluR δ 2 and Neurexin through Cbln1 mediates synapse formation in the cerebellum. *Cell* **141**, 1068–1079 (2010).

[CAS](#) [Article](#) [Google Scholar](#)

2. 2.

Joo, J. Y. et al. Differential interactions of cerebellin precursor protein (Cbln) subtypes and neurexin variants for synapse formation of cortical neurons. *Biochem. Biophys. Res. Commun.* **406**, 627–632 (2011).

[CAS](#) [Article](#) [Google Scholar](#)

3. 3.

Matsuda, K. et al. Cbln1 is a ligand for an orphan glutamate receptor δ 2, a bidirectional synapse organizer. *Science* **328**, 363–368 (2010).

[CAS](#) [Article](#) [ADS](#) [Google Scholar](#)

4. 4.

Yuzaki, M. & Aricescu, A. R. A GluD coming-of-age story. *Trends Neurosci.* **40**, 138–150 (2017).

[CAS](#) [Article](#) [Google Scholar](#)

5. 5.

Dai, J., Aoto, J. & Südhof, T. C. Alternative splicing of presynaptic neurexins differentially controls postsynaptic NMDA and AMPA receptor responses. *Neuron* **102**, 993–1008.e5 (2019).

[CAS](#) [Article](#) [Google Scholar](#)

6. 6.

Aoto, J., Martinelli, D. C., Malenka, R. C., Tabuchi, K. & Südhof, T. C. Presynaptic neurexin-3 alternative splicing trans-synaptically controls postsynaptic AMPA receptor trafficking. *Cell* **154**, 75–88 (2013).

[CAS](#) [Article](#) [Google Scholar](#)

7. 7.

Zhu, F., et al. Architecture of the mouse brain synaptome. *Neuron* **99**, 781–799 (2018).

[CAS](#) [Article](#) [Google Scholar](#)

8. 8.

Nusser, Z. Creating diverse synapses from the same molecules. *Curr. Opin. Neurobiol.* **51**, 8–15 (2018).

[CAS](#) [Article](#) [Google Scholar](#)

9. 9.

Huganir, R. L. & Nicoll, R. A. AMPARs and synaptic plasticity: the last 25 years. *Neuron* **80**, 704–717 (2013).

[CAS](#) [Article](#) [Google Scholar](#)

10. 10.

Nakazawa, K. & Sapkota, K. The origin of NMDA receptor hypofunction in schizophrenia. *Pharmacol. Ther.* **205**, 107426 (2020).

[CAS](#) [Article](#) [Google Scholar](#)

11. 11.

Singh, T., Neale, B. M., & Daly, M. J. Exome sequencing identifies rare coding variants in 10 genes which confer substantial risk for schizophrenia. Preprint at <https://doi.org/10.1101/2020.09.18.20192815> (2020)

12. 12.

Südhof, T. C. Synaptic neurexin complexes: a molecular code for the logic of neural circuits. *Cell* **171**, 745–769 (2017).

[Article](#) [Google Scholar](#)

13. 13.

Gomez, A. M., Traunmüller, L. & Scheiffele, P. Neurexins: molecular codes for shaping neuronal synapses. *Nat. Rev. Neurosci.* **22**, 137–151 (2021).

[CAS](#) [Article](#) [Google Scholar](#)

14. 14.

Hu, Z., Xiao, X., Zhang, Z. & Li, M. Genetic insights and neurobiological implications from NRXN1 in neuropsychiatric disorders. *Mol. Psychiatry* **24**, 1400–1414 (2019).

[Article](#) [Google Scholar](#)

15. 15.

Elegrheert, J. et al. Structural basis for integration of GluD receptors within synaptic organizer complexes. *Science* **353**, 295–299 (2016).

[CAS](#) [Article](#) [ADS](#) [Google Scholar](#)

16. 16.

Zhu, S. & Gouaux, E. Structure and symmetry inform gating principles of ionotropic glutamate receptors. *Neuropharmacology* **112**, 11–15

(2017).

[CAS](#) [Article](#) [Google Scholar](#)

17. 17.

Nakamoto, C. et al. Expression mapping, quantification, and complex formation of GluD1 and GluD2 glutamate receptors in adult mouse brain. *J. Comp. Neurol.* **528**, 1003–1027 (2020).

[CAS](#) [Article](#) [Google Scholar](#)

18. 18.

Platt, R. J. et al. CRISPR–Cas9 knockin mice for genome editing and cancer modeling. *Cell* **159**, 440–455 (2014).

[CAS](#) [Article](#) [Google Scholar](#)

19. 19.

Seigneur, E. & Südhof, T. C. Cerebellins are differentially expressed in selective subsets of neurons throughout the brain. *J. Comp. Neurol.* **525**, 3286–3311 (2017).

[CAS](#) [Article](#) [Google Scholar](#)

20. 20.

Torashima, T. et al. Rescue of abnormal phenotypes in $\delta 2$ glutamate receptor-deficient mice by the extracellular N-terminal and intracellular C-terminal domains of the $\delta 2$ glutamate receptor. *Eur. J. Neurosci.* **30**, 355–365 (2009).

[Article](#) [Google Scholar](#)

21. 21.

Hrvatin, S. et al. Single-cell analysis of experience-dependent transcriptomic states in the mouse visual cortex. *Nat. Neurosci.* **21**, 120–129 (2018).

[CAS](#) [Article](#) [Google Scholar](#)

22. 22.

Hirai, H. Ca²⁺-dependent regulation of synaptic δ2 glutamate receptor density in cultured rat Purkinje neurons. *Eur. J. Neurosci.* **14**, 73–82 (2001).

[CAS](#) [Article](#) [Google Scholar](#)

23. 23.

Sando, R., Jiang, X. & Südhof, T. C. Latrophilin GPCRs direct synapse specificity by coincident binding of FLRTs and teneurins. *Science* **363**, eaav7969 (2019).

[CAS](#) [Article](#) [Google Scholar](#)

24. 24.

Khalaj, A. J. et al. Deorphanizing FAM19A proteins as pan-neurexin ligands with an unusual biosynthetic binding mechanism. *J. Cell Biol.* **219**, e202004164 (2020).

[CAS](#) [Article](#) [Google Scholar](#)

25. 25.

Trotter, J. H. et al. Synaptic neurexin-1 assembles into dynamically regulated active zone nanoclusters. *J. Cell Biol.* **218**, 2677–2698 (2019).

[CAS](#) [Article](#) [Google Scholar](#)

26. 26.

Patzke, C., et al. Neuromodulator signaling bidirectionally controls vesicle numbers in human synapses. *Cell* **179**, 498–513 (2019).

[CAS Article](#) [Google Scholar](#)

27. 27.

Dai, J., Chen, P., Tian, H. & Sun, J. Spontaneous vesicle release is not tightly coupled to voltage-gated calcium channel-mediated Ca^{2+} influx and is triggered by a Ca^{2+} sensor other than synaptotagmin-2 at the juvenile mice calyx of held synapses. *J. Neurosci.* **35**, 9632–9637 (2015).

[CAS Article](#) [Google Scholar](#)

28. 28.

Jiang, X., Sando, R. & Südhof, T. C. Multiple signaling pathways are essential for synapse formation induced by synaptic adhesion molecules. *Proc. Natl Acad. Sci. USA* **118**, e2000173118 (2021).

[CAS Article](#) [Google Scholar](#)

29. 29.

Zhang, B. et al. Neuroligins sculpt cerebellar Purkinje-cell circuits by differential control of distinct classes of synapses. *Neuron* **87**, 781–796 (2015).

[CAS Article](#) [Google Scholar](#)

30. 30.

Zhang, R. S., Liakath-Ali, K. & Südhof, T. C. Latrophilin-2 and latrophilin-3 are redundantly essential for parallel-fiber synapse function in cerebellum. *eLife* **9**, e54443 (2020).

[CAS Article](#) [Google Scholar](#)

31. 31.

Kakegawa, W. et al. Differential regulation of synaptic plasticity and cerebellar motor learning by the C-terminal PDZ-binding motif of GluR δ 2. *J. Neurosci.* **28**, 1460–1468 (2008).

[CAS](#) [Article](#) [Google Scholar](#)

32. 32.

Uemura, T., Mori, H. & Mishina, M. Direct interaction of GluR δ 2 with Shank scaffold proteins in cerebellar Purkinje cells. *Mol. Cell. Neurosci.* **26**, 330–341 (2004).

[CAS](#) [Article](#) [Google Scholar](#)

[Download references](#)

Acknowledgements

We thank L. Chen for advice and the laboratory of H. Hirai for plasmids. This study was supported by a grant from the NIMH (MH052804 to T.C.S.) and fellowships to K.L.-A. from the European Molecular Biology Organization (ALTF 803-2017) and the Larry L. Hillblom Foundation (2020-A-016-FEL).

Author information

Author notes

1. Christopher Patzke

Present address: Boler-Parseghian Center for Rare and Neglected Diseases, Department of Biological Sciences, University of Notre Dame, Notre Dame, IN, USA

Affiliations

1. Howard Hughes Medical Institute, Stanford University, Stanford, CA, USA

Jinye Dai & Thomas C. Südhof

2. Department of Molecular and Cellular Physiology, Stanford University, Stanford, CA, USA

Jinye Dai, Christopher Patzke, Kif Liakath-Ali, Erica Seigneur & Thomas C. Südhof

Authors

1. Jinye Dai

[View author publications](#)

You can also search for this author in [PubMed](#) [Google Scholar](#)

2. Christopher Patzke

[View author publications](#)

You can also search for this author in [PubMed](#) [Google Scholar](#)

3. Kif Liakath-Ali

[View author publications](#)

You can also search for this author in [PubMed](#) [Google Scholar](#)

4. Erica Seigneur

[View author publications](#)

You can also search for this author in [PubMed](#) [Google Scholar](#)

5. Thomas C. Südhof

[View author publications](#)

You can also search for this author in [PubMed](#) [Google Scholar](#)

Contributions

J.D. performed all experiments and analysed all data except for the immunoblotting and *in situ* hybridization experiments, which were performed by C.P. and K. L.-A., respectively. E.S. contributed mouse husbandry and genotyping. J.D. and T.C.S. conceptualized the project, designed the experiments, analysed the data and wrote the manuscript with input from all authors.

Corresponding authors

Correspondence to [Jinye Dai](#) or [Thomas C. Südhof](#).

Ethics declarations

Competing interests

The authors declare no competing interests.

Additional information

Peer review information *Nature* thanks Zoltan Nusser and the other, anonymous, reviewer(s) for their contribution to the peer review of this work. Peer reviewer reports are available.

Publisher's note Springer Nature remains neutral with regard to jurisdictional claims in published maps and institutional affiliations.

Extended data figures and tables

[**Extended Data Fig. 1 CRISPR-mediated deletion and synaptic localization of GluD1 in cultured hippocampal neurons, and the effect on synapse numbers and synaptic function.**](#)

a, Quantitative RT–PCR demonstrating robust GluD1 but weak GluD2 expression in cultured hippocampal neurons, providing the rationale for targeting GluD1 over GluD2. **b**, Experimental strategy for the CRISPR-

mediated GluD1 deletion. Hippocampal cultures from Cas9-expressing transgenic¹⁸ mice were infected at DIV4-5 with lentiviruses expressing only mCherry or co-expressing mCherry with GluD1-directed sgRNAs, and were analysed at DIV15-17. **c**, Screening of five sgRNAs for the GluD1 KO efficacy in hippocampal cultures from Cas9-expressing transgenic mice¹⁸. GluD1 mRNA levels were analysed by quantitative RT-PCR in neurons as described in **a**. sgRNA sequences: sgRNA1, 5'-GCCGACTCCATCATCCACAT-3'; sgRNA2, 5'-GTAACGCAGTGGCATATCCA-3'; sgRNA3, 5'-GGCCAATAATCCGTTCCAGG-3'; sgRNA4, 5'-GAACGCAGCCAAGGACGACA-3'; sgRNA5, 5'-CTTCGAGGAGAACGCAGCCA-3'. sgRNA1 was used for all subsequent experiments. **d**, GluD1 deletion using sgRNA1 in hippocampal cultures from Cas9-expressing transgenic mice abolishes most GluD1 protein expression by the time of analysis used in the current experiments. Protein levels were quantified using immunoblots (see Fig. [1b](#)) with fluorescent secondary antibodies. **e**, Representative images of more than 3 experiments of hippocampal neurons cultured from Cas9-expressing transgenic mice and infected with a control lentivirus or a lentivirus expressing sgRNA1 targeting GluD1 (CRISPR). Neurons were stained for MAP2 and DAPI; the mCherry signal is from the lentiviruses). **f**, Representative images of hippocampal neurons cultured from Cas9-expressing transgenic mice and infected with a control lentivirus or a lentivirus expressing sgRNA1 targeting GluD1 (CRISPR, used as a negative control for GluD1 staining). Neurons were stained for vGluT1, MAP2 and GluD1 (left and middle panels) or Homer1 (right panels). **g**, Co-localization quantifications indicate that the GluD1 and the Homer1 signals are both adjacent to vGluT1 signals and are highly correlated with each other (Pearson correlation test). For minimum distance quantification, the range of 0.1-4 μm was analysed for distances between presynaptic vGluT1 and postsynaptic GluD1 or Homer1. **h**, CRISPR-mediated deletion of GluD1 has no effect on excitatory synapse numbers in hippocampal neurons, independently confirming the experiments shown in Fig. [1](#) using double labelling for pre- and postsynaptic excitatory synapse markers (vGluT1 and Homer1, respectively). Only puncta positive for both markers were quantified (left, representative images of neurons stained for vGluT1, Homer1 and MAP2; right, summary graphs of the density of double-positive for vGluT1 and

Homer1 synaptic puncta). **i**, CRISPR-mediated GluD1 deletion does not alter EPSC kinetics (left, AMPAR-EPSC rise time (20–80%); middle, AMPAR-EPSC decay constants at -70 mV fitted with double-exponential function; NMDAR-EPSC decay constants at $+40$ mV fitted with double-exponential function. Data for **i** and **j** are from the experiments of Fig. [1g–i](#). **j, k**, CRISPR-mediated GluD1 deletion does not alter the coefficient of variation (**j**; left, representative traces; right, summary graph of coefficient of variation), or the PPR of AMPAR-EPSCs (**k**; top, sample traces; bottom, summary plots of the PPRs as a function of interstimulus intervals (ISIs)). Data are means \pm s.e.m. (number of independent experiments (data points) is indicated in the bars of **a–d**, regions of interests/independent experiments is listed in **h**, and number of neurons/ independent experiments is indicated in **i–k**). Statistical significance was assessed by two-tailed Student's *t*-test or two-way ANOVA (* $P \leq 0.05$, ** $P \leq 0.01$, and *** $P \leq 0.001$; for numerical P values, see source data; non-significant comparisons are not indicated).

[Source data](#)

[**Extended Data Fig. 2 Effects of the CRISPR-mediated deletion of GluD1 and Cre-mediated deletion of Cbln2 in vivo.**](#)

a, b, Experimental strategy for CRISPR-mediated sparse GluD1 deletion in neurons of the subiculum in the hippocampal formation. Mice were bilaterally infected at P21 by stereotactic injections of lentiviruses co-expressing sgRNA directed against GluD1 and mCherry. Mice were sacrificed at P42-P49, and subiculum sections were analysed by acute slice physiology comparing adjacent infected mCherry-positive GluD1-deficient neurons with non-infected control neurons (strategy outline (**a**); diagram of stereotactic injections (**b**)). **c**, Image of a subiculum section from a stereotactically infected mouse (representative of 6 experiments). Arrows identify sparsely infected mCherry-positive neurons. **d**, CRISPR-mediated GluD1 deletion does not alter the coefficient of variation of AMPAR-EPSCs (left, representative traces; right, summary graph of coefficient of variation). **e**, CRISPR-mediated GluD1 deletion does not alter the EPSC kinetics (left, EPSC rise time (20–80%); middle, EPSC decay constants at -70 mV fitted with double-exponential function; EPSC decay constants at $+40$ mV fitted with double-exponential function). Data in this panel and

panel d were from the experiments in Fig. 11. f, g, RNA in situ hybridization analyses reveal that cerebellin-1 (Cbln1) is poorly expressed in the hippocampal formation, cerebellin-2 (Cbln2) is detectable only in subiculum neurons, and cerebellin-4 (Cbln4) is found only in a subset of interneurons (overview of the hippocampal formation hybridized for Cbln1, Cbln2, and Cbln4 mRNAs (f); representative images for each cerebellin (g)). Images are representative of multiple brain sections, and match those obtained by the Allen Brain Institute (<https://mouse.brain-map.org>). h, Experimental strategy for analysis of conditional Cbln2 deletions *in vivo* using Cbln2 cKO mice¹⁹. Mice were bilaterally infected at P21 by stereotactic injections of AAVs expressing ΔCre-eGFP (control) or Cre-eGFP, and subiculum neurons were analysed in acute slices 2–3 weeks later. In this and all following experiments, ΔCre refers to the expression of a mutant inactive Cre that is otherwise indistinguishable from Cre. i, Conditional Cbln2 deletion from subiculum neurons does not impair excitatory synapse numbers (representative images complementing those shown in Fig. 2a). j, Summary graph of the EPSC success rate during minimal stimulation experiments (Fig. 2d). k, Conditional Cbln2 deletion does not alter the coefficient of variation of AMPAR-EPSCs (left, representative traces; right, summary graph of coefficient of variation). l, Image of an acute slice of the hippocampal formation from a mouse infected with AAVs expressing Cre-eGFP (green), and illustration of the electrophysiological recording configuration. m, Conditional Cbln2 deletion does not alter the EPSC kinetics (left, EPSC rise time (20–80%); middle, EPSC decay constants at −70 mV fitted with double-exponential function; EPSC decay constants at +40 mV fitted with double-exponential function). Data in this panel and panel k were from the experiments shown in Fig. 2c. n, Constitutive Cbln2 deletion does not alter the AMPA/NMDA EPSC ratio at CA3-CA1 Schaffer collateral synapses (left, representative traces; right, summary graph). Both conditional and constitutive Cbln2 deletions cause a massive change in this ratio when analysed in subiculum synapses (see Fig. 2). o, Cumulative probability plots show that the conditional Cbln2 deletion in subiculum significantly shifts the distribution of AMPAR-EPSC amplitudes to the right and of NMDAR-EPSC amplitudes to the left, as analysed during minimal stimulation experiments. Data are means ± s.e.m. (number of neurons/mice is indicated in the bars of d, e, j, k, m, n). Statistical significance was assessed by two-tailed Student's *t*-test

or two sample K-S test ($*P \leq 0.05$, $**P \leq 0.01$, and $***P \leq 0.001$; for exact P values, see source data; non-significant relations are not indicated).

[Source data](#)

Extended Data Fig. 3 Double deletion of GluD1 and Cbln2 produces the same phenotype as individual deletions of GluD1 and Cbln2 in hippocampal cultures.

a, Experimental strategy. Hippocampal cultures from newborn mice expressing Cas9 on the Cbln2 cKO background (*cas9* and *Cbln2^{f/f}*) were infected with lentiviruses and analysed as indicated. Immunoblots on the right show that expression of the GluD1-directed sgRNA suppressed GluD1 protein levels with Δ Cre or Cre co-expression (for additional data, please also see Supplementary Fig. 1b). **b**, Quantifications of GluD1 levels show that CRISPR-mediated deletion of GluD1 is efficient even after Cre-mediated deletion of Cbln2. GluD1 protein levels were measured by quantitative immunoblotting using fluorescent secondary antibodies in neurons of the indicated genotypes. **c**, Representative images of neurons stained for vGluT1 and MAP2. Merged images and analyses of synaptic properties are shown in Fig. 2h. **d**, Summary graphs of vGluT1 puncta size and vGluT1 staining intensity as a function of the Cbln2-GluD1 double deletion (additional analyses for Fig. 2h). **e, f**, Conditional Cbln2 deletion has no effect on excitatory synapse numbers in hippocampal neurons as analysed in independent experiments complementing those of Fig. 2, but using double labelling for a presynaptic (vGluT1) and postsynaptic marker (Homer1). Only double-positive puncta were quantified (representative images of neurons stained for vGluT1, Homer1 and MAP2 (e); summary graph of the density of vGluT1 & Homer1 double-positive synaptic puncta(f)). **g**, Double GluD1 and Cbln2 deletion does not alter the coefficient of variation of AMPAR-EPSCs (left, representative traces; right, summary graph of coefficient of variation). **h**, Double GluD1 and Cbln2 deletion does not alter EPSC kinetics (left, EPSC rise time (20–80%); middle, AMPAR-EPSC decay constants at -70 mV fitted with a double-exponential function; right, NMDAR-EPSC decay constants at $+40$ mV fitted with a double-exponential function). Data in g and h were from the experiments of Fig. 2i–l. **i**, Measurements of PPRs of evoked AMPAR-

EPSCs show that the double GluD1 and Cbln2 deletion does not significantly alter PPRs (left, representative traces; right, summary plot of PPRs as a function of ISIs). Data are means \pm s.e.m. (n's in **b**, independent experiments (data points) are shown in bars; in **d** and **f**, dendrites/independent experiments; in **g–i**, neurons/independent experiments are listed). Statistical significance was assessed by two-tailed Student's *t*-test or two-way ANOVA (***P* \leq 0.01, and ****P* \leq 0.001; for numerical *P* values, see source data; non-significant comparisons are not indicated).

[Source data](#)

[Extended Data Fig. 4 Mechanism of Nrxn1 \$\beta^{SS4+}\$ and Nrxn3 \$\beta^{SS4+}\$ regulation of NMDARs and AMPARs.](#)

a, Experimental strategy for testing the effect of the CRISPR-mediated GluD1 deletion on Nrxn1 β^{SS4+} - and Nrxn3 β^{SS4+} -mediated signalling in hippocampal cultures. Neurons cultured from Cas9 mice were infected at DIV4-5 with lentiviruses expressing only mCherry or co-expressing mCherry and GluD1-sgRNA, and again at DIV 6-7 with lentiviruses expressing various Nrxn1 β or Nrxn3 β constructs. Neurons were analysed at DIV15-17. **b**, Nrxn1 β^{SS4-} , Nrxn1 β^{SS4+} , Nrxn3 β^{SS4-} , and Nrxn3 β^{SS4+} are similarly expressed in hippocampal cultures (top, sample blots; bottom, quantification of protein levels using Flag-tag antibodies; for additional data, please also see Supplementary Fig. [1c](#)). **c**, Quantifications of Nrxn1 β^{SS4-} , Nrxn1 β^{SS4+} , Nrxn3 β^{SS4-} , and Nrxn3 β^{SS4+} surface levels show that all constructs are efficiently transported to the cell-surface (left, representative images; right, summary graphs of the staining intensity of surface Flag-tagged proteins). Neurons were prepared as described in **a**. **d–h**, Nrxn1 β^{SS4-} , Nrxn1 β^{SS4+} , Nrxn3 β^{SS4-} , and Nrxn3 β^{SS4+} expression and GluD1 deletions, alone or in combination, did not change the kinetics of AMPAR- and NMDAR-EPSCs or the PPRs of AMPAR-EPSCs (AMPAR-EPSC rise time (20–80%) (**d**); AMPAR-EPSC decay constants at -70 mV fitted with double-exponential function [top, fast component; bottom, slow component] (**e**); NMDAR-EPSC decay constants at $+40$ mV fitted with double-exponential function [top, fast component; bottom, slow

component] (**f**); representative PPR traces (**g**); summary graphs of PPRs as a function of inter-stimulus intervals (**h**)). Data are from experiments in Fig. [3](#). **i**, Sequences of the alternatively spliced inserts of $\text{Nrnxn1}\beta^{\text{SS4}+}$ and $\text{Nrnxn3}\beta^{\text{SS4}+}$ and of the ‘swap’ mutants of these alternatively spliced inserts, referred to as $\text{Nrnxn1}\beta^{\text{N3-SS4}+}$ and $\text{Nrnxn3}\beta^{\text{N1-SS4}+}$, in which the SS4+ sequence of $\text{Nrnxn1}\beta^{\text{SS4}+}$ is introduced into $\text{Nrnxn3}\beta^{\text{SS4}+}$, and vice versa. **j, k**, Same as **b** and **c**, but with expression of $\text{Nrnxn1}\beta^{\text{N3-SS4}+}$ and $\text{Nrnxn3}\beta^{\text{N1-SS4}+}$ (for additional data, please also see Supplementary Fig. [1d](#)). **l–p**, $\text{Nrnxn1}\beta^{\text{N3-SS4}+}$ and $\text{Nrnxn3}\beta^{\text{N1-SS4}+}$, alone or in combination with the GluD1 KO, do not change the kinetics of AMPAR- and NMDAR-EPSCs or the paired-pulse ratio of AMPAR-EPSCs (AMPAR-EPSC rise time (20–80%) (**l**); AMPAR-EPSC decay constants at -70 mV fitted with a double-exponential function (**m**); NMDAR-EPSC decay constants at $+40$ mV fitted with a double-exponential function (**n**); representative PPR traces (**o**); summary graphs of PPRs as a function of inter-stimulus intervals (**p**)). Data are from experiments in Fig. [3](#). Data are means \pm s.e.m.; independent experiments (data points) are shown in bars (**b, j**); numbers of sections/independent experiments are shown in bars (**c, k**); neurons/independent experiments are listed (**d–f, h, l–n, p**). Please see source data for details.

[Source data](#)

[Extended Data Fig. 5 Design of GluD1 mutant proteins and of minimal GluD1-CD4 and GluD2-CD4 proteins.](#)

a, Alignment of the C-terminal sequences of mouse GluD1 and GluD2 to illustrate the location of cytoplasmic tail mutations in GluD1 and the positions where GluD sequences were fused to the CD4 transmembrane region in the GluD1-CD4^{TMR} and GluD2-CD4^{TMR} constructs (dotted lines indicate sequence not shown; ATD, amino-terminal domain; TMR 3, third transmembrane region that is followed by the cytoplasmic tail). The five highly conserved sequence motifs in the cytoplasmic C-terminal sequence that were mutated in rescue constructs are highlighted and labelled. In mutants #1–#4, the four internal sequence motifs #1–#4 were replaced by the same GQGHG sequences. The consensus sequence for type 1 PDZ domains at the very C terminus of GluD1 and GluD2 (GTSI) was replaced

with a consensus sequence for type 2 PDZ domains (EYYV). This replacement blocks the interaction of the C-terminal PDZ-domain binding sequence of GluD1 with type 1 PDZ-domain proteins, an interaction that has a well documented essential function for GluD2 in cerebellar long-term synaptic plasticity^{31,32}. **b**, List and description of all GluD1 and GluD2 mutants analysed. In the hybrid GluD1-CD4^{TMR} and GluD2-CD4^{TMR} constructs, all GluD1 and GluD2 sequences from the end of the ATD (that is, the beginning of the presumptive glutamate-binding domain) until the end of the last (3rd) TMR (for GluD1, residues 437–851; for GluD2, residues 441–851) were replaced by a linker and the TMR of CD4 (see shown sequences). As a result, GluD-CD4^{TMR} hybrid proteins lack the TMRs and presumptive glutamate-binding domain of Gluds. In addition, GluD1-CD4^{TMR} and GluD2-CD4^{TMR} contain a shortened cytoplasmic tail with only 59 GluD1 residues, lacking the juxta-membranous part of the cytoplasmic tail. The minimal GluD1-CD4^{TMR} constructs contain only short sequence motifs (5–13 residues) that are mutated in mutants #3 or #4.

Extended Data Fig. 6 GluD1 mutants and GluD1-CD4^{TMR} and GluD2-CD4^{TMR} constructs express well on the neuronal cell surface.

a, Experimental strategy for rescue experiments with GluD1 and GluD2 rescue constructs in GluD1-deficient hippocampal cultures from Cas9 mice. Cells were infected at DIV4–5 with lentiviruses expressing mCherry only or mCherry together with the GluD1 sgRNA, and again at DIV 6–7 with lentiviruses expressing the wild-type and mutant GluD1 and GluD2 constructs. Neurons were analysed at DIV15–17. **b–d**, Most mutant GluD1 and GluD2 proteins are similarly expressed in hippocampal cultures (representative immunoblots (for additional data, please also see Supplementary Fig. 1e–g) (**b, c**); quantification of GluD1 and GluD2 expression using GluD1 antibodies [top] or HA-antibodies recognizing the HA-epitope tag that was added to the N terminus of the rescue proteins [bottom] (**d**)). Note that although some constructs do not express as well as others (for example, mutant #5), all constructs were overexpressed compared to endogenous GluD1 protein levels. **e, f**, Quantifications of the surface levels of GluD1 and GluD2 rescue proteins reveal efficient transport

of all proteins to the cell-surface. Surface exposure was measured using staining of non-permeabilized fixed neurons with antibodies to extracellular epitopes (representative images (**e**); summary graphs of the staining intensity of internal HA-tagged proteins (top of panel), of surface HA-tagged proteins (middle of panel) and the ratio of surface/total proteins (bottom of panel) (**f**)). Neurons were stained first for surface HA before permeabilization, and then for internal HA after permeabilization using different HA antibodies. Data are means \pm s.e.m. (independent experiments (data points) are shown in bars for **d**, sections/independent experiments are shown in the bars for **f**. Please see source data for details.

[Source data](#)

[Extended Data Fig. 7 Analysis of EPSC kinetics and PPRs in various rescue experiments with cultured GluD1-deficient neurons.](#)

a–i, Quantification of EPSC kinetics for measurements of evoked EPSCs under various GluD1 KO and rescue conditions as indicated, demonstrating that the EPSC kinetics do not change with any experimental manipulation (EPSC rise time (20–80%) (**a, d, g**); AMPAR-EPSC decay constants recorded at -70 mV and fitted with a double-exponential function (top, fast component; bottom, slow component (**b, e, h**); NMDAR-EPSC decay constants recorded at $+40$ mV and fitted with a double-exponential function (top, fast component; bottom, slow component (**c, f, i**))). Data are from the experiments described in Figs. 4c–e, n–p, 5c–e. **j**, Representative traces of PPR recordings in cultured neurons under the indicated conditions. **k**, Summary graphs of the PPRs as a function of the inter-stimulus intervals under the indicated conditions. Data are means \pm s.e.m. (for **a–i**, *n* values are shown in Figs. 4c–e, n–p, 5c–e; for **j, k**, neurons/independent experiments are shown in **k**). Statistical significance was assessed by two-tailed Student's *t*-test or two-way ANOVA. No statistically significant differences were observed. Please see source data for details.

[Source data](#)

Extended Data Fig. 8 Analysis of wild-type and mutant GluD1^N-CD4^{TMR}-GluD1^{935–993} proteins.

a, Design of wild-type and mutant GluD1^N-CD4^{TMR}-GluD1^{935–993} constructs, corresponding to the GluD1-CD4^{TMR} construct (Fig. 4l) with a greatly shortened C-terminal tail. In the Mut3 and Mut4 constructs, the internal sequence motifs were replaced by the same ‘GQGHG’ sequence, and the C-terminal ‘GTSI’ sequence was mutated to ‘EYYV’ (Extended Data Fig. 5). **b, c**, Immunoblotting analyses show that most mutant GluD1 proteins are similarly expressed in hippocampal cultures (representative immunoblots (**b**); quantification of GluD1 expression using the HA-epitope tag that was added to the N terminus of the rescue proteins (**c**); for additional data, please also see Supplementary Fig. 1h). **d, e**, Quantifications of GluD1 rescue protein surface levels show that wild-type and Mut3- and Mut4-mutant GluD1^N-CD4^{TMR}-GluD1^{935–993} proteins are efficiently transported to the cell-surface (representative images (**d**); summary graphs of the staining intensity of internal HA-tagged proteins (left), of surface HA-tagged proteins (middle) and the ratio of surface/total proteins (right) (**e**)). Surface exposure was measured by staining neurons first for surface HA before permeabilization, and then for internal HA after permeabilization using different HA antibodies. **f**, Representative traces of evoked AMPAR- and NMDAR-EPSCs recorded in hippocampal cultures without or with the GluD1 deletion and rescue with WT, Mut3, and Mut4 GluD1^N-CD4^{TMR}-GluD1^{935–993} constructs. **g**, Summary graphs of the AMPA/NMDA ratio illustrating that the GluD1 deletion enhances the AMPA/NMDA ratio ~300%, that the WT GluD1^N-CD4^{TMR}-GluD1^{935–993} construct fully rescues this phenotype, but that Mut3- and Mut4-mutant GluD1^N-CD4^{TMR}-GluD1^{935–993} constructs only partly rescue. Neurons were infected with lentiviruses encoding mCherry without or with the GluD1 sgRNA at DIV4–5, re-infected with lentiviruses encoding various GluD1 constructs at DIV6–7, and analysed at DIV15–17. **h, i**, Summary graphs of the amplitudes of AMPAR-EPSCs (**h**) and NMDAR-EPSCs (**i**) demonstrating that the GluD1 deletion increases AMPARs (~150%) but decreases NMDARs (~40%), and that WT GluD1^N-CD4^{TMR}-GluD1^{935–993} fully rescues both phenotypes, whereas Mut3-mutant GluD1^N-CD4^{TMR}-GluD1^{935–993} rescues only the AMPAR but not the NMDAR phenotype and

Mut4-mutant GluD1^N-CD4^{TMR}-GluD1^{935–993} rescues only the NMDAR but not the AMPAR phenotype. **j**, None of the GluD1 manipulations affects the PPR of AMPAR-EPSCs (left, representative traces of PPR recordings; right, summary graphs of PPRs as a function of the inter-stimulus intervals). Data are means \pm s.e.m. (n values are shown in bars: independent experiments (data points) (**c**); sections/independent experiments (**e**); neurons/independent experiments (**g, j**)). Statistical significance was assessed by two-tailed Student's *t*-test or two-way ANOVA (* $P \leq 0.05$, ** $P \leq 0.01$, and *** $P \leq 0.001$; for numerical P values, see source data; non-significant comparisons are not indicated).

Source data

Extended Data Fig. 9 Validation of minimal GluD1-CD4^{TMR} proteins containing only short cytoplasmic GluD1 sequence motifs.

a, b, Minimal GluD1-CD4^{TMR} proteins containing only short cytoplasmic GluD1 sequence motifs proteins are expressed at similar levels in cultured hippocampal neurons (representative immunoblots (**a**); quantification of GluD1 expression using the N-terminal HA-epitope tag of rescue proteins (**b**); for additional data, please also see Supplementary Fig. 1*i*). See Extended Data Fig. 5 for an explanation of the constructs used. **c**, Surface quantifications show that all minimal GluD1-CD4^{TMR} proteins are efficiently transported to the cell-surface (left, representative images; right, summary graphs of the staining intensity of internal HA-tagged proteins (top), of surface HA-tagged proteins (middle) and of the ratio of surface/total proteins (bottom panel)). Surface exposure was measured by staining neurons first for surface HA before permeabilization, and then for internal HA after permeabilization using different HA antibodies. Controls demonstrated that fixed non-permeabilized cells are impermeant to antibodies. **d–f**, Summary graphs demonstrating that minimal GluD1-CD4^{TMR} proteins do not change the NMDAR- or AMPAR-EPSC kinetics (AMPAR-EPSC rise times (20–80%) (**d**); AMPAR-EPSC decay constants at -70 mV fitted with a double-exponential function (top, fast component; bottom, slow component) (**e**); NMDAR-EPSC decay constants at $+40$ mV

fitted with a double-exponential function (top, fast component; bottom, slow component) (f)). Data are from the experiments in Fig. 5g-i. g, h, The GluD1 deletion without or with expression of minimal GluD1-CD4^{TMR} rescue constructs does not change the paired-pulse ratio (PPR) of AMPAR-EPSCs (representative traces (g); summary graphs of PPRs as a function of the inter-stimulus intervals under the indicated conditions (h)). Data are means ± s.e.m. (number in bars: independent experiments (data points) (b); sections/independent experiments (c); neurons/independent experiments (h); numbers of cells/independent experiments for d–f are given in Fig. 5). Statistical significance was assessed by two-tailed Student's *t*-test or two-way ANOVA. No statistically significant differences were observed. Please see source data for details.

[Source data](#)

Extended Data Fig. 10 Mechanistic model of NrXn1^{SS4+}→Cbln2→GluD1→NMDAR and NrXn3^{SS4+}→Cbln2→GluD1→AMPAR signalling pathways.

The model, based on the present data, proposes that NrXn1- and NrXn3-alternative splicing at SS4 regulates the postsynaptic content of AMPARs and NMDARs at hippocampal synapses in the subiculum but not the CA1 region by binding to Cbln2, which in turn binds to GluD1 (see Figs. 1 and 2). Surprisingly, binding to the same GluD1-Cbln2 complex enables NrXn1^{SS4+} to enhance NMDARs but not AMPARs, whereas binding of NrXn3^{SS4+} to the GluD1-Cbln2 complex suppresses AMPARs but not NMDARs (see Fig. 3). Signal transduction by the NrXn1^{SS4+}-Cbln2-GluD1 and NrXn3^{SS4+}-Cbln2-GluD1 assemblies is mediated by distinct cytoplasmic GluD1 sequences (HRSPN for AMPAR regulation by NrXn3^{SS4+}, SRTLS for NMDAR regulation by NrXn1^{SS4+}), suggesting that GluD1 couples NrXn1^{SS4+} and NrXn3^{SS4+} signals to distinct effector sequences (see Figs. 4 and 5). Since GluD1 and GluD2 constructs lacking the native GluD1 transmembrane architecture are fully active (see Fig. 4 and 5), binding of NrXn1^{SS4+}-Cbln2 and NrXn3^{SS4+}-Cbln2 complexes to the

ATD of GluD1 (and of GluD2) activates a transmembrane signal without inducing a conformational change in the transmembrane regions of GluDs.

Supplementary information

[Supplementary Figure](#)

Original full-sized immunoblots for all protein level analyses.

[Reporting Summary](#)

[Peer Review File](#)

Source data

[Source Data Fig. 1](#)

[Source Data Fig. 2](#)

[Source Data Fig. 3](#)

[Source Data Fig. 4](#)

[Source Data Fig. 5](#)

[Source Data Extended Data Fig. 1](#)

[Source Data Extended Data Fig. 2](#)

[Source Data Extended Data Fig. 3](#)

[Source Data Extended Data Fig. 4](#)

[Source Data Extended Data Fig. 6](#)

[**Source Data Extended Data Fig. 7**](#)

[**Source Data Extended Data Fig. 8**](#)

[**Source Data Extended Data Fig. 9**](#)

Rights and permissions

[Reprints and Permissions](#)

About this article



Check for
updates

Cite this article

Dai, J., Patzke, C., Liakath-Ali, K. *et al.* GluD1 is a signal transduction device disguised as an ionotropic receptor. *Nature* **595**, 261–265 (2021). <https://doi.org/10.1038/s41586-021-03661-6>

[Download citation](#)

- Received: 09 August 2020
- Accepted: 20 May 2021
- Published: 16 June 2021
- Issue Date: 08 July 2021
- DOI: <https://doi.org/10.1038/s41586-021-03661-6>

Comments

By submitting a comment you agree to abide by our [Terms](#) and [Community Guidelines](#). If you find something abusive or that does not comply with our terms or guidelines please flag it as inappropriate.

[Access through your institution](#)

[Change institution](#)

[Buy or subscribe](#)

Advertisement

This article was downloaded by **calibre** from <https://www.nature.com/articles/s41586-021-03661-6>

| [Section menu](#) | [Main menu](#) |

- Article
- [Published: 23 June 2021](#)

Obesity accelerates hair thinning by stem cell-centric converging mechanisms

- [Hironobu Morinaga¹](#),
- [Yasuaki Mohri¹](#),
- [Marina Grachtchouk²](#),
- [Kyosuke Asakawa¹](#),
- [Hiroyuki Matsumura¹](#),
- [Motohiko Oshima³](#),
- [Naoya Takayama⁴](#),
- [Tomoki Kato¹](#),
- [Yuriko Nishimori¹](#),
- [Yuriko Sorimachi⁵](#),
- [Keiyo Takubo ORCID: orcid.org/0000-0002-1736-7592⁵](#),
- [Takayoshi Saganami⁶](#),
- [Atsushi Iwama³](#),
- [Yoichiro Iwakura ORCID: orcid.org/0000-0002-9934-5775⁷](#),
- [Andrzej A. Dlugosz²](#) &
- [Emi K. Nishimura ORCID: orcid.org/0000-0002-5767-8045^{1,8,9}](#)

[Nature](#) volume 595, pages 266–271 (2021) [Cite this article](#)

- 6822 Accesses
- 490 Altmetric
- [Metrics details](#)

Subjects

- [Skin stem cells](#)
- [Stem-cell differentiation](#)

Abstract

Obesity is a worldwide epidemic that predisposes individuals to many age-associated diseases, but its exact effects on organ dysfunction are largely unknown¹. Hair follicles—mini-epithelial organs that grow hair—are miniaturized by ageing to cause hair loss through the depletion of hair follicle stem cells (HFSCs)². Here we report that obesity-induced stress, such as that induced by a high-fat diet (HFD), targets HFSCs to accelerate hair thinning. Chronological gene expression analysis revealed that HFD feeding for four consecutive days in young mice directed activated HFSCs towards epidermal keratinization by generating excess reactive oxygen species, but did not reduce the pool of HFSCs. Integrative analysis using stem cell fate tracing, epigenetics and reverse genetics showed that further feeding with an HFD subsequently induced lipid droplets and NF-κB activation within HFSCs via autocrine and/or paracrine IL-1R signalling. These integrated factors converge on the marked inhibition of Sonic hedgehog (SHH) signal transduction in HFSCs, thereby further depleting lipid-laden HFSCs through their aberrant differentiation and inducing hair follicle miniaturization and eventual hair loss. Conversely, transgenic or pharmacological activation of SHH rescued HFD-induced hair loss. These data collectively demonstrate that stem cell inflammatory signals induced by obesity robustly represses organ regeneration signals to accelerate the miniaturization of mini-organs, and suggests the importance of daily prevention of organ dysfunction.

Access options

Subscribe to Journal

Get full journal access for 1 year

\$199.00

only \$3.90 per issue

[Subscribe](#)

All prices are NET prices.

VAT will be added later in the checkout.

Tax calculation will be finalised during checkout.

Rent or Buy article

Get time limited or full article access on ReadCube.

from \$8.99

[Rent or Buy](#)

All prices are NET prices.

Additional access options:

- [Log in](#)
- [Access through your institution](#)
- [Learn about institutional subscriptions](#)

Fig. 1: Obesity accelerates hair loss through fate switching and depletion of HFSCs.

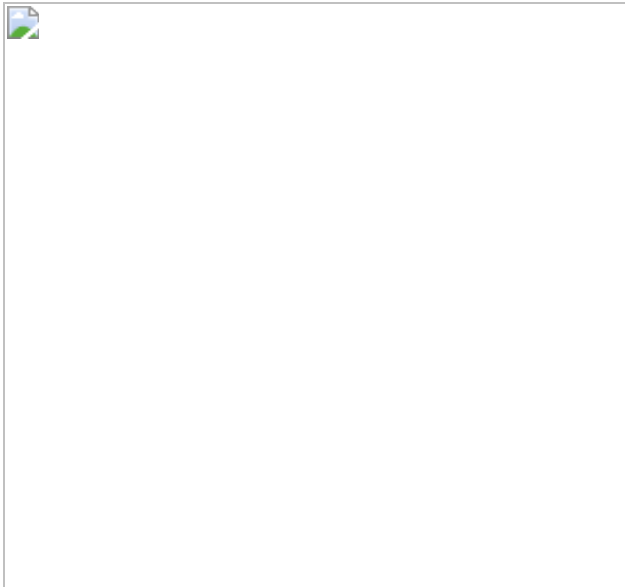


Fig. 2: An HFD inhibits the SHH pathway to promote fate switching of HFSCs towards epidermal differentiation.



Fig. 3: HFD-induced stem cell inflammageing with oxidative stress accelerates HFSC depletion and resultant hair loss through inhibition of SHH signalling.

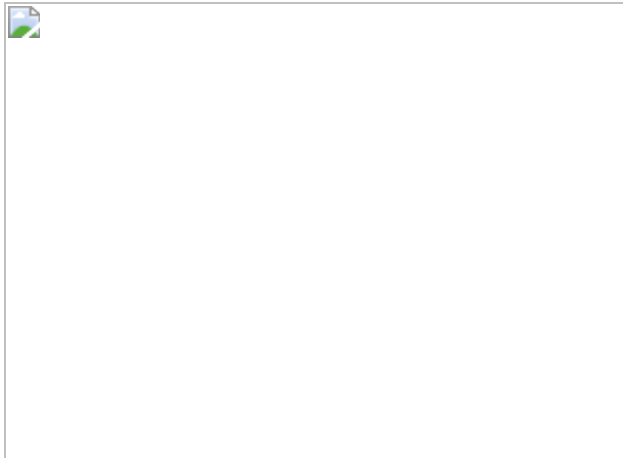
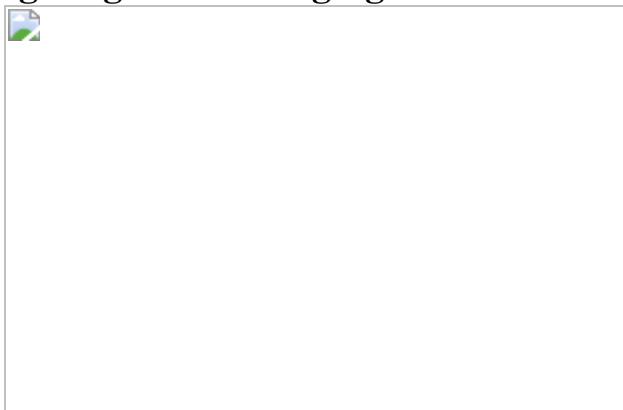


Fig. 4: SHH activation in HFSCs prevents HFD-induced hair loss by targeting the converging roots of HFSCs.



Data availability

Microarray data have been deposited in the GEO database (accession number [GSE131958](#)). RNA-seq data have been deposited in the GEO public database (accession number [GSE169173](#)). All ATAC data have been deposited in the DNA Databank of Japan (DDBJ) database (<https://www.ddbj.nig.ac.jp>; accession number DRA008515) [Source data](#) are provided with this paper.

References

1. 1.

Novak, J. S. S., Baksh, S. C. & Fuchs, E. Dietary interventions as regulators of stem cell behavior in homeostasis and disease. *Genes Dev.* **35**, 199–211 (2021).

[CAS](#) [Article](#) [Google Scholar](#)

2. 2.

Matsumura, H. et al. Hair follicle aging is driven by transepidermal elimination of stem cells via COL17A1 proteolysis. *Science* **351**, aad4395 (2016).

[Article](#) [Google Scholar](#)

3. 3.

Calle, E. E., Rodriguez, C., Walker-Thurmond, K. & Thun, M. J. Overweight, obesity, and mortality from cancer in a prospectively studied cohort of U.S. adults. *N. Engl. J. Med.* **348**, 1625–1638 (2003).

[Article](#) [Google Scholar](#)

4. 4.

Sakaue, S. et al. Trans-biobank analysis with 676,000 individuals elucidates the association of polygenic risk scores of complex traits with human lifespan. *Nat. Med.* **26**, 542–548 (2020).

[CAS](#) [Article](#) [Google Scholar](#)

5. 5.

Aune, D. et al. BMI and all cause mortality: systematic review and non-linear dose-response meta-analysis of 230 cohort studies with 3.74 million deaths among 30.3 million participants. *Br. Med. J.* **353**, i2156 (2016).

[Article](#) [Google Scholar](#)

6. 6.

Ambrosi, T. H. et al. Adipocyte accumulation in the bone marrow during obesity and aging impairs stem cell-based hematopoietic and bone regeneration. *Cell Stem Cell* **20**, 771–784.e6 (2017).

[CAS Article](#) [Google Scholar](#)

7. 7.

Beyaz, S. et al. High-fat diet enhances stemness and tumorigenicity of intestinal progenitors. *Nature* **531**, 53–58 (2016).

[CAS Article](#) [ADS](#) [Google Scholar](#)

8. 8.

Inomata, K. et al. Genotoxic stress abrogates renewal of melanocyte stem cells by triggering their differentiation. *Cell* **137**, 1088–1099 (2009).

[CAS Article](#) [Google Scholar](#)

9. 9.

Oh, J., Lee, Y. D. & Wagers, A. J. Stem cell aging: mechanisms, regulators and therapeutic opportunities. *Nat. Med.* **20**, 870–880 (2014).

[CAS Article](#) [Google Scholar](#)

10. 10.

Flach, J. et al. Replication stress is a potent driver of functional decline in ageing haematopoietic stem cells. *Nature* **512**, 198–202 (2014).

[CAS Article](#) [ADS](#) [Google Scholar](#)

11. 11.

Matsumura, H. et al. Distinct types of stem cell divisions determine organ regeneration and aging in hair follicles. *Nat. Aging* **1**, 190–204 (2021).

[Article](#) [Google Scholar](#)

12. 12.

Matilainen, V., Koskela, P. & Keinänen-Kiukaanniemi, S. Early androgenetic alopecia as a marker of insulin resistance. *Lancet* **356**, 1165–1166 (2000).

[CAS](#) [Article](#) [Google Scholar](#)

13. 13.

Driskell, R. R. et al. Distinct fibroblast lineages determine dermal architecture in skin development and repair. *Nature* **504**, 277–281 (2013).

[CAS](#) [Article](#) [ADS](#) [Google Scholar](#)

14. 14.

Salzer, M. C. et al. Identity noise and adipogenic traits characterize dermal fibroblast aging. *Cell* **175**, 1575–1590.e22 (2018).

[CAS](#) [Article](#) [Google Scholar](#)

15. 15.

Chen, C. C., Plikus, M. V., Tang, P. C., Widelitz, R. B. & Chuong, C. M. The modulatable stem cell niche: tissue interactions during hair and feather follicle regeneration. *J. Mol. Biol.* **428**, 1423–1440 (2016).

[CAS](#) [Article](#) [Google Scholar](#)

16. 16.

Festa, E. et al. Adipocyte lineage cells contribute to the skin stem cell niche to drive hair cycling. *Cell* **146**, 761–771 (2011).

[CAS](#) [Article](#) [Google Scholar](#)

17. 17.

Rompolas, P. & Greco, V. Stem cell dynamics in the hair follicle niche. *Semin. Cell Dev. Biol.* **25-26**, 34–42 (2014).

[Article](#) [Google Scholar](#)

18. 18.

Nakajima, T. et al. Roles of MED1 in quiescence of hair follicle stem cells and maintenance of normal hair cycling. *J. Invest. Dermatol.* **133**, 354–360 (2013).

[CAS](#) [Article](#) [Google Scholar](#)

19. 19.

Greco, V. et al. A two-step mechanism for stem cell activation during hair regeneration. *Cell Stem Cell* **4**, 155–169 (2009).

[CAS](#) [Article](#) [Google Scholar](#)

20. 20.

Xing, L. et al. Alopecia areata is driven by cytotoxic T lymphocytes and is reversed by JAK inhibition. *Nat. Med.* **20**, 1043–1049 (2014).

[CAS](#) [Article](#) [Google Scholar](#)

21. 21.

St-Jacques, B. et al. Sonic hedgehog signaling is essential for hair development. *Curr. Biol.* **8**, 1058–1068 (1998).

[CAS](#) [Article](#) [Google Scholar](#)

22. 22.

Ouspenskaia, T., Matos, I., Mertz, A. F., Fiore, V. F. & Fuchs, E. WNT-SHH antagonism specifies and expands stem cells prior to niche formation. *Cell* **164**, 156–169 (2016).

[CAS](#) [Article](#) [Google Scholar](#)

23. 23.

Hsu, Y. C., Li, L. & Fuchs, E. Transit-amplifying cells orchestrate stem cell activity and tissue regeneration. *Cell* **157**, 935–949 (2014).

[CAS](#) [Article](#) [Google Scholar](#)

24. 24.

Ermilov, A. N. et al. Maintenance of taste organs is strictly dependent on epithelial hedgehog/GLI signaling. *PLoS Genet.* **12**, e1006442 (2016).

[Article](#) [Google Scholar](#)

25. 25.

Furukawa, S. et al. Increased oxidative stress in obesity and its impact on metabolic syndrome. *J. Clin. Invest.* **114**, 1752–1761 (2004).

[CAS](#) [Article](#) [Google Scholar](#)

26. 26.

Lichti, U., Anders, J. & Yuspa, S. H. Isolation and short-term culture of primary keratinocytes, hair follicle populations and dermal cells from newborn mice and keratinocytes from adult mice for in vitro analysis and for grafting to immunodeficient mice. *Nat. Protocols* **3**, 799–810 (2008).

[CAS](#) [Article](#) [Google Scholar](#)

27. 27.

Wang, Y. et al. Interleukin-1 β induces blood-brain barrier disruption by downregulating Sonic hedgehog in astrocytes. *PLoS ONE* **9**, e110024 (2014).

[Article](#) [ADS](#) [Google Scholar](#)

28. 28.

Horai, R. et al. Production of mice deficient in genes for interleukin (IL)-1 α , IL-1 β , IL-1 α/β , and IL-1 receptor antagonist shows that IL-1 β is crucial in turpentine-induced fever development and glucocorticoid secretion. *J. Exp. Med.* **187**, 1463–1475 (1998).

[CAS](#) [Article](#) [Google Scholar](#)

29. 29.

Tanaka, Y. et al. NF-E2-related factor 2 inhibits lipid accumulation and oxidative stress in mice fed a high-fat diet. *J. Pharmacol. Exp. Ther.* **325**, 655–664 (2008).

[CAS](#) [Article](#) [Google Scholar](#)

30. 30.

Grachtchouk, M. et al. Basal cell carcinomas in mice arise from hair follicle stem cells and multiple epithelial progenitor populations. *J. Clin. Invest.* **121**, 1768–1781 (2011).

[CAS](#) [Article](#) [Google Scholar](#)

31. 31.

Ito, M. et al. Stem cells in the hair follicle bulge contribute to wound repair but not to homeostasis of the epidermis. *Nat. Med.* **11**, 1351–

1354 (2005).

[CAS](#) [Article](#) [Google Scholar](#)

32. 32.

Taniyama, Y. et al. Beneficial effect of intracoronary verapamil on microvascular and myocardial salvage in patients with acute myocardial infarction. *J. Am. Coll. Cardiol.* **30**, 1193–1199 (1997).

[CAS](#) [Article](#) [Google Scholar](#)

33. 33.

Itoh, K. et al. An Nrf2/small Maf heterodimer mediates the induction of phase II detoxifying enzyme genes through antioxidant response elements. *Biochem. Biophys. Res. Commun.* **236**, 313–322 (1997).

[CAS](#) [Article](#) [Google Scholar](#)

34. 34.

Nishie, W. et al. Humanization of autoantigen. *Nat. Med.* **13**, 378–383 (2007).

[CAS](#) [Article](#) [Google Scholar](#)

35. 35.

Yang, R. L., Li, W., Shi, Y. H. & Le, G. W. Lipoic acid prevents high-fat diet-induced dyslipidemia and oxidative stress: a microarray analysis. *Nutrition* **24**, 582–588 (2008).

[Article](#) [Google Scholar](#)

36. 36.

Fujiwara, H. et al. The basement membrane of hair follicle stem cells is a muscle cell niche. *Cell* **144**, 577–589 (2011).

[CAS](#) [Article](#) [Google Scholar](#)

37. 37.

Jensen, K. B., Driskell, R. R. & Watt, F. M. Assaying proliferation and differentiation capacity of stem cells using disaggregated adult mouse epidermis. *Nat. Protocols* **5**, 898–911 (2010).

[CAS](#) [Article](#) [Google Scholar](#)

38. 38.

Ba, X. & Boldogh, I. 8-Oxoguanine DNA glycosylase 1: beyond repair of the oxidatively modified base lesions. *Redox Biol.* **14**, 669–678 (2018).

[CAS](#) [Article](#) [Google Scholar](#)

39. 39.

Solanas, G. et al. Aged stem cells reprogram their daily rhythmic functions to adapt to stress. *Cell* **170**, 678–692.e20 (2017).

[CAS](#) [Article](#) [Google Scholar](#)

[Download references](#)

Acknowledgements

We thank R. Yajima, H. Katagiri, I. Manabe, S. Wakana and Y. Nabeshima for technical support, and DASS Manuscript for editing. E.K.N. is supported by an AMED Project for Elucidating and Controlling Mechanisms of Ageing and Longevity (JP17gm5010002–JP21gm5010002), Scientific Research on Innovative Areas ‘Stem Cell Aging and Disease’ (26115003) and by Aderans Co Ltd. H. Morinaga is supported by a JSPS Grant-in-Aid for Young Scientists (B) (17K15663). A.A.D is supported by an NIH grant (R01 AR045973) and Cancer Center Support grant (P30 CA046592).

Author information

Affiliations

1. Department of Stem Cell Biology, Medical Research Institute, Tokyo Medical and Dental University, Tokyo, Japan

Hironobu Morinaga, Yasuaki Mohri, Kyosuke Asakawa, Hiroyuki Matsumura, Tomoki Kato, Yuriko Nishimori & Emi K. Nishimura

2. Department of Dermatology, University of Michigan Medical School, Ann Arbor, MI, USA

Marina Grachtchouk & Andrzej A. Dlugosz

3. Division of Stem Cell and Molecular Medicine, Center for Stem Cell Biology and Regenerative Medicine, The Institute of Medical Science, The University of Tokyo, Tokyo, Japan

Motohiko Oshima & Atsushi Iwama

4. Department of Regenerative Medicine, Graduate School of Medicine, Chiba University, Chiba, Japan

Naoya Takayama

5. Department of Stem Cell Biology, Research Institute National Center for Global Health and Medicine, Tokyo, Japan

Yuriko Sorimachi & Keiyo Takubo

6. Department of Molecular Medicine and Metabolism, Research Institute of Environmental Medicine, Nagoya University, Nagoya, Japan

Takayoshi Saganami

7. Centre for Animal Disease Models, Research Institute for Biomedical Sciences, Tokyo University of Science, Chiba, Japan

Yoichiro Iwakura

8. Division of Aging and Regeneration, Institute of Medical Science, The University of Tokyo, Tokyo, Japan

Emi K. Nishimura

9. Division of Stem Cell Aging Medicine, Center for Stem Cell Biology and Regenerative Medicine, The Institute of Medical Science, The University of Tokyo, Tokyo, Japan

Emi K. Nishimura

Authors

1. Hironobu Morinaga

[View author publications](#)

You can also search for this author in [PubMed](#) [Google Scholar](#)

2. Yasuaki Mohri

[View author publications](#)

You can also search for this author in [PubMed](#) [Google Scholar](#)

3. Marina Grachtchouk

[View author publications](#)

You can also search for this author in [PubMed](#) [Google Scholar](#)

4. Kyosuke Asakawa

[View author publications](#)

You can also search for this author in [PubMed](#) [Google Scholar](#)

5. Hiroyuki Matsumura

[View author publications](#)

You can also search for this author in [PubMed](#) [Google Scholar](#)

6. Motohiko Oshima

[View author publications](#)

You can also search for this author in [PubMed](#) [Google Scholar](#)

7. Naoya Takayama

[View author publications](#)

You can also search for this author in [PubMed](#) [Google Scholar](#)

8. Tomoki Kato

[View author publications](#)

You can also search for this author in [PubMed](#) [Google Scholar](#)

9. Yuriko Nishimori

[View author publications](#)

You can also search for this author in [PubMed](#) [Google Scholar](#)

10. Yuriko Sorimachi

[View author publications](#)

You can also search for this author in [PubMed](#) [Google Scholar](#)

11. Keiyo Takubo

[View author publications](#)

You can also search for this author in [PubMed](#) [Google Scholar](#)

12. Takayoshi Saganami

[View author publications](#)

You can also search for this author in [PubMed](#) [Google Scholar](#)

13. Atsushi Iwama

[View author publications](#)

You can also search for this author in [PubMed](#) [Google Scholar](#)

14. Yoichiro Iwakura

[View author publications](#)

You can also search for this author in [PubMed](#) [Google Scholar](#)

15. Andrzej A. Dlugosz

[View author publications](#)

You can also search for this author in [PubMed](#) [Google Scholar](#)

16. Emi K. Nishimura

[View author publications](#)

You can also search for this author in [PubMed](#) [Google Scholar](#)

Contributions

H. Morinaga performed the majority of experiments with support from Y.M., K.A., H. Matsumura, Y.N., T.S., T.K. and A.I. M.G. and A.A.D. prepared *Gli2ΔC* and *Gli2ΔN* mice. M.O., N.T. and A.I. performed and analysed ATAC-seq. Y.I. prepared *Il1ra* knockout and *Il1a;Il1b* knockout mice. Y.S. and K.T. helped to perform the OCR assay. H. Morinaga and E.K.N designed the study and wrote the manuscript.

Corresponding author

Correspondence to [Emi K. Nishimura](#).

Ethics declarations

Competing interests

E.K.N. is an inventor on a patent application (in preparation) related to this manuscript, which will be filed by the Tokyo Medical and Dental University. The other authors declare no competing interests.

Additional information

Peer review information *Nature* thanks Ömer Yilmaz and the other, anonymous, reviewer(s) for their contribution to the peer review of this work.

Publisher's note Springer Nature remains neutral with regard to jurisdictional claims in published maps and institutional affiliations.

Extended data figures and tables

Extended Data Fig. 1 Obesity accelerates hair loss with repeated hair cycle induction.

a, Experimental design for **a**, **f**, **g**, and representative images of mice fed an ND or an HFD as indicated ($n = 4$). **b**, Experimental design for **c–e**, **h**. **c–e**, Representative images of genetically obese mice fed an ND with hair cycle induction at the indicated times ($n = 4$ mice each for control and obese). **f**, Representative images of C57BL/6J mice fed an ND or an HFD ($n = 3$). **g**, Representative images of female mice fed an ND or an HFD ($n = 4$). **h–j**, Representative images (**h**), fasting blood glucose levels (**i**) and body weights (**j**) of streptozocin-induced diabetic mice (ND, $n = 4$; HFD, $n = 4$; STZ-treated mice, $n = 8$; two-tailed Dunnett's test, $^{**}P < 0.05$; for exact P values see Source Data). **k**, Representative images of mice fed an ND or a high-sucrose diet (HSD; $n = 4$). **l**, Representative cross-section images of hair follicles from three ND-fed and three HFD-fed mice. Bulge and basal layer stained with COL17A1 and K14, respectively. **m–o**, Whole-mount images and bulge numbers for *ob/ob* mice ($n = 3$, two-tailed unpaired t -test) or HFD-fed female mice ($n = 4$, two-tailed unpaired t -test). Scale bars, 60 μm . **p**, Correlation between the degree of obesity and hair follicle number or the number of hair follicles without a bulge (sebaceous gland only) after five months' treatment with HFD or ND with monthly hair

depilation by plucking. Two-tailed Pearson's correlation coefficient. ns, not significant; wo, without. Data shown as mean \pm s.d.

[Source data](#)

Extended Data Fig. 2 An HFD prematurely accelerates hair cycle progression.

a, Representative images of zigzag hairs (left) and maximum hair diameters of zigzag and awl hairs (right) from 6-month-old mice (4 months of treatment with ND or HFD). $n = 4$, two-tailed unpaired *t*-test. **b**, Lengths of hairs of 6-month-old mice ($n = 4$, two-tailed unpaired *t*-test). **c**, HE staining (left) and interfollicular epidermis (IFE) thickness (right) of skin from ND- or HFD-fed 6-month-old mice ($n = 3$, two-tailed unpaired *t*-test). Scale bar, 100 μ m. **d**, Assay of anagen induction of HFD-fed mice; the HFD was started from 4 weeks of age and hair was shaved at 6 weeks of age. Anagen onset was judged by skin colour change ($n = 4$). **e**, HE staining of hair follicles from telogen to catagen of 5-month-old mice (3 months of treatment with ND or HFD). Representative images from three mice at each hair stage. Hair depilation by hair plucking was conducted at telogen and samples were observed on the indicated days after depilation. Scale bar, 100 μ m. **f**, Proportions of catagen and telogen hair follicles 20 days after anagen induction. **g, h**, Whole-mount imaging (**g**) and section imaging (**h**) of endothelial cells ($CD31^+$) and neural cells ($TUJ1^+$). Representative images from three mice. Anagen induction was performed by hair depilation using hair plucking. Scale bar, 30 μ m. Data shown as mean \pm s.d.

[Source data](#)

Extended Data Fig. 3 HFD feeding causes HFSCs to prematurely commit to epidermal differentiation.

a, The locations of GFP^+ cells in *K15CrePR;Rosa-H2BGFP* mice after recombination ($n = 2$). *K15CrePR;Rosa-H2BGFP* mice were treated or not treated with Ru486 (representative images, left) and the locations of GFP^+ cells were recorded in Ru486-treated mice (right). Scale bar, 50 μ m. **b**,

Representative immunostaining for GFP and the suprabasal marker K1 from three mice. Some GFP⁺ cells, which had been HFSCs at the timing of Ru486 treatment, expressed K1 when they moved up to the epidermis. Anagen induction was performed by hair depilation using hair plucking. Scale bar, 50 µm (left), 30 µm (bottom right). Top right, timing of experiment. **c**, Representative whole-mount staining for K14 and K1 of hair follicles from three mice. K1 expression was higher in anagen hair follicles of HFD-fed mice than in anagen hair follicles of ND-fed mice. Scale bar, 60 µm. **d**, FACS analysis of dorsal skin; the CD34^{high}ITGA6^{high}SCA1⁻ population was used as HFSCs for qPCR, microarray analyses and ATAC-seq analysis. **e**, qPCR analysis for *Krt1* in HFSCs from ND- or HFD-fed mice. $n = 4$ mice, two-tailed unpaired *t*-test. **f**, Left, immunostaining for activated CASP3, a marker for apoptosis, and K15 in dorsal skin after hair plucking (pk) or hair removal cream. Right, quantification of hair follicles (HF). $n = 3$ mice, two-tailed unpaired *t*-test. **g**, Whole-mount staining of physiological anagen hair follicles (without any experimental treatment to induce anagen) for K1 and K14. Scale bar, 60 µm. Images are representative of mice aged 25 d (P25; $n = 3$), 10 m ($n = 2$) or 24 m ($n = 1$). Dotted lines show bulge regions. **h**, Representative cross-section staining of anagen hair follicles from three HFD-fed *K15crePR;Rosa-H2B-GFP* mice for K1 and GFP. Anagen induction was performed by hair depilation using hair plucking. Scale bar, 50 µm. Arrows in **g**, **h** indicate ectopic expression of K1. Data shown as mean ± s.d.

[Source data](#)

[**Extended Data Fig. 4 SHH signalling is inhibited specifically in HFSCs from HFD-fed mice.**](#)

a, *Col17a1* mRNA expression in telogen HFSCs from young, old, ND-fed and HFD-fed mice without depilation (3-month feeding, $n = 3$, two-tailed unpaired *t*-test) derived from microarray data. **b**, Motif analysis of ATAC-seq data with binomial *P* values. TF, transcription factor. **c–e**, RNA-seq analysis of anagen HFSCs from 6-month-old HFD-fed (4 months) and ND-fed mice ($n = 2$). **c**, Pathways downregulated in anagen HFSCs from HFD-fed mice were analysed with GSEA by choosing c2.cp.biocarta.v7.2 (curated gene sets) as the gene set correlation. All pathways with GSEA

$P < 0.05$ are shown. **d**, Enrichment plot for the SHH pathway Biocarta gene set. **e**, Heatmap of the Biocarta SHH pathway gene set core signature (red to dark blue, high to low expression in the space of the analysed gene set). **f**, qPCR analysis for *Gli1* and *Ptch1* of HFSCs from 7-week-old *ob/ob* and *db/db* mice ($n = 4$, two-tailed unpaired *t*-test). ctrl, control t, telogen; a, anagen. Data shown as mean \pm s.d.

[Source data](#)

Extended Data Fig. 5 SHH inhibition causes hair loss after one hair cycle.

a, Study design and all images of male *Gli2ΔC* mice (control, $n = 5$; *Gli2ΔC*, $n = 6$). **b**, Images of female *Gli2ΔC* and control mice ($n = 2$). **c**, Representative HE staining of the dorsal skin from two control or *Gli2ΔC* mice. Scale bar, 100 μ m. **d**, Representative images of whole-mount staining from one *K15crePR; Rosa-H2BEGFP* (ctrl) mice and one *K15crePR; Rosa-rtTA; TetO-Gli2ΔC; Rosa-H2BEGFP* mouse 5 days after hair depilation. Seven-week-old mice were treated with Ru486 five times and Dox treatment was started in 8-week-old mice simultaneously with hair cycle induction by a hair depilation cream. Scale bar, 60 μ m.

Extended Data Fig. 6 Intrafollicular inflammatory milieu in HFSCs from HFD-fed mice coordinately inhibits the SHH pathway and promotes the epidermal commitment of HFSCs.

a, Pathways upregulated in telogen HFSCs from HFD-fed mice ($n = 3$) analysed with GSEA by choosing C2 (curated gene sets) as the gene set correlation. All pathways with GSEA $P < 0.1$ are shown. **b**, GSEA profiles for telogen HFSCs from HFD-fed mice ($n = 3$) compared with ND-fed mice. **c**, Left, immunostaining for NF κ B and ITGA6. Scale bar, 10 μ m. Right, the relative intensity of NF κ B translocation was calculated in the nuclei of HFSCs from 6-month-old mice fed an HFD for 4 months ($n = 3$, two-tailed unpaired *t*-test). **d**, qPCR analysis for *Il1b* using whole skin cells from 7-week-old *ob/ob* or *db/db* mice ($n = 4$, two-tailed unpaired *t*-test). **e**, Representative images of 8-oxoguanine (8G) and K15 staining of skin from

three mice after 3 months of ND or HFD. **f**, Representative images of neutral lipid staining by lipidtox in telogen HFSCs from 2-month-old or 5-month-old mice ($n = 3$ mice). mo, months old. Scale bar, 30 μ m. **g**, Representative images of neutral lipid staining of anagen HFSCs from 6-month-old *K15crePR;RosaH2BGFP* mice fed ND or HFD ($n = 3$ mice). Scale bar, 20 μ m. **h**, Immunostaining for Lipidtox, survivin and COL17A1 in the hair follicle bulge and germ on anagen day 3. Representative images from three mice are shown. Five-month-old mice were depilated by plucking to induce anagen. Scale bar, 20 μ m. **i**, qPCR analysis of *Gli1*, *Gli2* and *Ptch1* after treatment of mouse neonatal skin with IL6 or TNF ($n = 4$, one-way ANOVA followed by two-tailed Dunnett's test). **j**, Local administration of recombinant IL-1 β activates IL-1R signalling and inhibits SHH signalling, especially in aged mice. Left, an atelocollagen sponge impregnated with 1 μ g IL-1 β or PBS was implanted subcutaneously; qPCR analysis of HFSCs was conducted 1 day after implantation. $n = 4$ or $n = 2$ for 7-week- or 17-month-old mice, respectively. Middle, right, relative expression (two-tailed unpaired *t*-test; see [Methods](#)). **k**, Representative images of 6-month-old *Il1ra* knockout mice. **l**, Representative whole-mount staining of skin from three control or *Il1ra* knockout mice. Scale bar, 60 μ m. **m**, Hair follicle numbers for 6-month-old control or *Il1ra* knockout mice ($n = 3$, two-tailed unpaired *t*-test). Data shown as mean \pm s.d.; for exact *P* values, see Source Data.

[Source data](#)

[**Extended Data Fig. 7 Low-grade inflammatory milieu in HFD-fed mice stimulates IL-1 \$\beta\$ signalling in HFSCs.**](#)

a, Ratio of total immune cells ($CD45^+$), macrophages ($CD45^+CD11b^+F4/80^+$), T cells ($CD45^+CD3^+$) and MHC2 $^+$ cells ($CD45^+MHC2^+$) in the dermis analysed by FACS for 6-month-old mice fed ND or HFD. Ratio of total immune cells ($CD45^+$), T cells ($CD45^+CD3^+$) and MHC2 $^+$ cells ($CD45^+MHC2^+$) in the epidermis analysed by FACS for the same mice ($n = 3$ mice, two-tailed unpaired *t*-test; for exact *P* values see Source Data). **b**, **c**, Immunostaining (left) and quantification (right) of MHC2 (**b**) and CD3 (**c**) ($n = 3$, two-tailed unpaired *t*-test) in hair follicles

from 6-month-old mice fed ND or HFD. Scale bars, 30 µm. **d**, qPCR analysis of *Il1b* in the indicated populations ($n = 3$). ND, not detected. **e**, qPCR analysis of *Il1b* in anagen HFSCs from ND-fed or HFD-fed mice. Representative results from four mice. Nt, normal diet telogen; Ht, high fat diet telogen; Na, normal diet anagen; Ha, high fat diet anagen. Data shown as mean ± s.d.

[Source data](#)

Extended Data Fig. 8 Short-term HFD feeding promotes epidermal commitment of HFSCs through the generation of ROS.

a, Total intracellular ROS contents and mitochondrial superoxide production were analysed using DCFDA and MitoSOX, respectively, in telogen or anagen HFSCs from 7-week-old ND- or HFD-fed mice (dorsal skin collected 4 days after treatment; $n = 4$). MFI, mean fluorescence intensity. **b**, Representative images (left) and quantification (right) of 8G in skin from ND-fed or HFD-fed mice ($n = 3$, two-tailed unpaired *t*-test). Scale bar, 30 µm. **c**, OCR of total epidermis measured using lipid mixture or palmitate and sequential injection of oligomycin, FCCP and rotenone/antimycin (left). Basal and maximum OCR levels are shown on the right. LM, lipid mixture. PA, palmitic acid ($n = 6$, one-way ANOVA followed by two-tailed Dunnett's test). **d**, Immunostaining for Tom20, a mitochondria marker, in hair follicles from 8-week-old mice with or without short-term exposure to HFD. Representative images from two mice. **e**, Principal component (PC) analysis of HFSCs after short-term (4 days) or long-term (3 months) treatment with HFD. **f**, BioCarta pathway enrichment analysis by DAVID using anagen HFSCs after short-term (4 days) treatment with HFD (fold change ≥ 2.0 or < 0.5 , $n = 1$). **g**, Immunostaining showed that three days of treatment of mouse dorsal skin with 1% H₂O₂ or one treatment with 5% H₂O₂ increased the expression of K1 in anagen HFSCs. Scale bar, 50 µm. **h**, qPCR showed that three days of treatment with H₂O₂ increased the expression of *K1* ($n = 3$, two-tailed unpaired *t*-test) but not *Gli1* or *Ptch1* in anagen HFSCs. Anagen induction was performed by hair depilation using hair plucking. Data shown as mean ± s.d.

[Source data](#)

[Extended Data Fig. 9 SHH signal activation partially rescues HFD-induced hair thinning.](#)

a, Experimental design. **b, c**, Representative images of *Tnf* knockout ($n = 3$) and *Il1a Il1b* double-knockout mice ($n = 3$). **d**, Representative images of HFD-fed mice treated with α -lipoic acid ($n = 4$, see [Methods](#)). **e**, Representative images of HFD-fed *Nrf2* knockout mice ($n = 3$). **f**, Representative images of HFD-fed *COL17A1* transgenic (Tg) mice (Tg, $n = 4$; control, $n = 3$). **g**, Ki67 staining of hair follicles from *Gli2ΔN* mice. Three days after onset of the hair cycle, the number of proliferating HFSCs in *Gli2ΔN* mice was higher than in control mice. Anagen induction was performed by hair depilation (dp) using hair plucking. Scale bar, 30 μ m. **h**, Hair width of zigzag hairs in ND-fed, HFD-fed or SAG-treated HFD-fed mice ($n = 4$, one-way ANOVA followed by two-tailed Tukey's test). **i**, A single treatment with SAG after three months (top) did not rescue HFD-induced hair loss (bottom; $n = 3$). **j**, Treatment with SAG every week after hair depilation (top) rescued HFD-induced hair loss (bottom; $n = 7$, one-way ANOVA followed by two-tailed Tukey's test; for exact P values see Source Data). **k**, Treatment of aged mice with SAG for one week did not rescue age-associated hair loss. Top left, timeline; bottom left, representative images of mice; middle, whole-mount images of hair follicles; right, quantification of bulges ($n = 4$, two-tailed unpaired t -test). Data shown as means \pm s.d.

[Source data](#)

[Extended Data Fig. 10 Similarities and differences between ageing-induced and obesity-induced hair loss.](#)

Chronological ageing and obesity induce or accelerate hair follicle miniaturization through stem cell depletion that is based on distinct molecular mechanisms. Age-associated repetition of hair cycles causes a sustained DNA damage response in HFSCs to reduce their expression of *COL17A1*; this results in hemidesmosomal instability, which causes the repetition of atypical stem cell divisions that induce the epidermal

differentiation of HFSCs and eventually detach HFSCs from the basement membrane. By sharp contrast, short-term exposure of HFSCs to an HFD causes the accumulation of ROS, and long-term exposure causes lipid droplets in HFSCs, activates IL-1R signalling and inhibits SHH signalling, which induces epidermal and sebocyte differentiation and elimination of lipid-laden HFSCs upon hair cycle-coupled activation. In both cases, those aberrant fate changes occur in a small population of HFSCs upon their activation at early anagen, thereby diminishing the pool of HFSCs in those particular follicles and causing hair follicle miniaturization and hair thinning in a stepwise manner. Because the skin contains a densely arranged hair follicle bulge (niche) that contains abundant HFSC pools, and the expression of the hair thinning phenotype appears with a time delay because of the long duration of the hair cycle, HFSC depletion proceeds in a latent manner and manifests the hair thinning and loss phenotype only after several rounds of hair cycles.

Supplementary information

Supplementary Figures

This file contains Supplementary Figures 1-4.

Reporting Summary

Source data

Source Data Fig. 1

Source Data Fig. 2

Source Data Fig. 3

Source Data Fig. 4

Source Data Extended Data Fig. 1

[Source Data Extended Data Fig. 2](#)

[Source Data Extended Data Fig. 3](#)

[Source Data Extended Data Fig. 4](#)

[Source Data Extended Data Fig. 6](#)

[Source Data Extended Data Fig. 7](#)

[Source Data Extended Data Fig. 8](#)

[Source Data Extended Data Fig. 9](#)

Rights and permissions

[Reprints and Permissions](#)

About this article



Check for
updates

Cite this article

Morinaga, H., Mohri, Y., Grachtchouk, M. *et al.* Obesity accelerates hair thinning by stem cell-centric converging mechanisms. *Nature* **595**, 266–271 (2021). <https://doi.org/10.1038/s41586-021-03624-x>

[Download citation](#)

- Received: 07 November 2019
- Accepted: 07 May 2021

- Published: 23 June 2021
- Issue Date: 08 July 2021
- DOI: <https://doi.org/10.1038/s41586-021-03624-x>

Comments

By submitting a comment you agree to abide by our [Terms](#) and [Community Guidelines](#). If you find something abusive or that does not comply with our terms or guidelines please flag it as inappropriate.

[Access through your institution](#)

[Change institution](#)

[Buy or subscribe](#)

Advertisement

This article was downloaded by **calibre** from <https://www.nature.com/articles/s41586-021-03624-x>

| [Section menu](#) | [Main menu](#) |

- Article
- [Published: 23 June 2021](#)

Caloric restriction disrupts the microbiota and colonization resistance

- [Reiner Jumpertz von Schwartzenberg](#)^{1,2,3 na1},
- [Jordan E. Bisanz](#) [ORCID: orcid.org/0000-0002-8649-1706](#)^{4 na1},
- [Svetlana Lyalina](#)⁵,
- [Peter Spanogiovannopoulos](#)⁴,
- [Qi Yan Ang](#) [ORCID: orcid.org/0000-0002-9788-1283](#)⁴,
- [Jingwei Cai](#)⁶,
- [Sophia Dickmann](#)¹,
- [Marie Friedrich](#)¹,
- [Su-Yang Liu](#)⁷,
- [Stephanie L. Collins](#)⁶,
- [Danielle Ingebrigtsen](#)⁸,
- [Steve Miller](#)⁸,
- [Jessie A. Turnbaugh](#)⁴,
- [Andrew D. Patterson](#) [ORCID: orcid.org/0000-0003-2073-0070](#)⁶,
- [Katherine S. Pollard](#) [ORCID: orcid.org/0000-0002-9870-6196](#)^{5,9,10,11,12},
- [Knut Mai](#)^{1,2},
- [Joachim Spranger](#) [ORCID: orcid.org/0000-0002-8900-4467](#)^{1,2,3 na2}
&
- [Peter J. Turnbaugh](#) [ORCID: orcid.org/0000-0002-0888-2875](#)^{4 na2}

[Nature](#) volume 595, pages 272–277 (2021) [Cite this article](#)

- 9685 Accesses
- 610 Altmetric
- [Metrics details](#)

Subjects

- [Metabolic syndrome](#)
- [Microbiome](#)
- [Nutrition](#)

Abstract

Diet is a major factor that shapes the gut microbiome¹, but the consequences of diet-induced changes in the microbiome for host pathophysiology remain poorly understood. We conducted a randomized human intervention study using a very-low-calorie diet (NCT01105143). Although metabolic health was improved, severe calorie restriction led to a decrease in bacterial abundance and restructuring of the gut microbiome. Transplantation of post-diet microbiota to mice decreased their body weight and adiposity relative to mice that received pre-diet microbiota. Weight loss was associated with impaired nutrient absorption and enrichment in *Clostridioides difficile*, which was consistent with a decrease in bile acids and was sufficient to replicate metabolic phenotypes in mice in a toxin-dependent manner. These results emphasize the importance of diet–microbiome interactions in modulating host energy balance and the need to understand the role of diet in the interplay between pathogenic and beneficial symbionts.

Access options

Subscribe to Journal

Get full journal access for 1 year

\$199.00

only \$3.90 per issue

[Subscribe](#)

All prices are NET prices.

VAT will be added later in the checkout.

Tax calculation will be finalised during checkout.

Rent or Buy article

Get time limited or full article access on ReadCube.

from \$8.99

[Rent or Buy](#)

All prices are NET prices.

Additional access options:

- [Log in](#)
- [Access through your institution](#)
- [Learn about institutional subscriptions](#)

Fig. 1: Very low-calorie diets alter microbiota composition and activity.

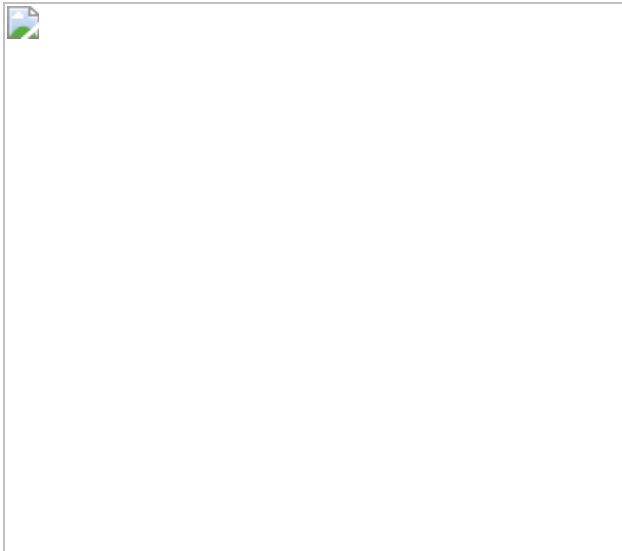


Fig. 2: Weight loss and improved metabolic health are transmissible via the gut microbiome.

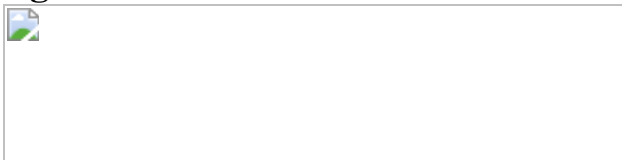


Fig. 3: Endogenous *C. difficile* is unrestricted by the post-diet microbiota and contributes to weight loss in a toxin-dependent manner.

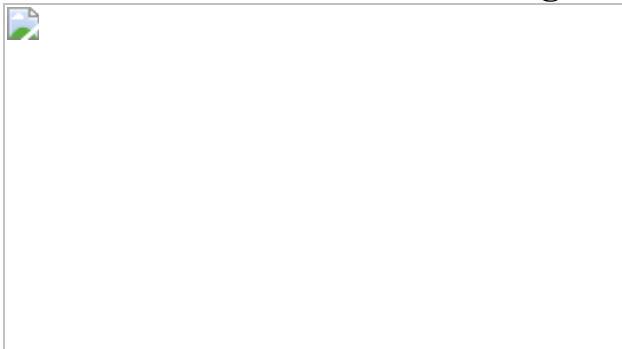


Fig. 4: Caloric restriction is associated with an expansion of *C. difficile* and altered bile acid pools.



Data availability

16S rRNA gene and metagenomic sequencing reads have been deposited in the SRA under BioProject [PRJNA412411](#). The genome of *C. difficile* JBZPo1 has been deposited under BioProject [PRJNA503906](#). The following public databases were used: The Genome Taxonomy Database (<https://gtdb.ecogenomic.org/>), DADA2 Taxonomic Training Sets (<http://benjineb.github.io/dada2/assign.html>), CAZy (<http://www.cazy.org/>), and KEGG (<https://www.genome.jp/kegg/>). [Source data](#) are provided with this paper.

References

1. 1.

David, L. A. et al. Diet rapidly and reproducibly alters the human gut microbiome. *Nature* **505**, 559–563 (2014).

[CAS](#) [PubMed](#) [ADS](#) [Google Scholar](#)

2. 2.

Johansson, K., Neovius, M. & Hemmingsson, E. Effects of anti-obesity drugs, diet, and exercise on weight-loss maintenance after a very-low-calorie diet or low-calorie diet: a systematic review and meta-analysis of randomized controlled trials. *Am. J. Clin. Nutr.* **99**, 14–23 (2014).

[CAS](#) [PubMed](#) [Google Scholar](#)

3. 3.

Louis, S., Tappu, R. M., Damms-Machado, A., Huson, D. H. & Bischoff, S. C. Characterization of the gut microbial community of obese patients following a weight-loss intervention using whole metagenome shotgun sequencing. *PLoS ONE* **11**, e0149564 (2016).

[PubMed](#) [PubMed Central](#) [Google Scholar](#)

4. 4.

Heinsen, F.-A. et al. Beneficial effects of a dietary weight loss intervention on human gut microbiome diversity and metabolism are not sustained during weight maintenance. *Obes. Facts* **9**, 379–391 (2016).

[CAS](#) [PubMed](#) [PubMed Central](#) [Google Scholar](#)

5. 5.

Spranger, L. et al. Thrifty energy phenotype predicts weight regain — results of a randomized controlled trial. Preprint at <https://www.medrxiv.org/content/10.1101/2021.03.25.21254300v1> (2021).

6. 6.

Kohl, K. D., Amaya, J., Passemant, C. A., Dearing, M. D. & McCue, M. D. Unique and shared responses of the gut microbiota to prolonged fasting: a comparative study across five classes of vertebrate hosts. *FEMS Microbiol. Ecol.* **90**, 883–894 (2014).

[CAS](#) [PubMed](#) [Google Scholar](#)

7. 7.

Zarrinpar, A., Chaix, A., Yooseph, S. & Panda, S. Diet and feeding pattern affect the diurnal dynamics of the gut microbiome. *Cell Metab.* **20**, 1006–1017 (2014).

[CAS](#) [PubMed](#) [PubMed Central](#) [Google Scholar](#)

8. 8.

Harris, J. K. et al. Specific microbiome changes in a mouse model of parenteral nutrition associated liver injury and intestinal inflammation. *PLoS ONE* **9**, e110396 (2014).

[PubMed](#) [PubMed Central](#) [ADS](#) [Google Scholar](#)

9. 9.

van Passel, M. W. et al. The genome of *Akkermansia muciniphila*, a dedicated intestinal mucin degrader, and its use in exploring intestinal metagenomes. *PLoS ONE* **6**, e16876 (2011).

[PubMed](#) [PubMed Central](#) [ADS](#) [Google Scholar](#)

10. 10.

Morrison, D. J. & Preston, T. Formation of short chain fatty acids by the gut microbiota and their impact on human metabolism. *Gut Microbes* **7**, 189–200 (2016).

[PubMed](#) [PubMed Central](#) [Google Scholar](#)

11. 11.

Uchiyama, T., Irie, M., Mori, H., Kurokawa, K. & Yamada, T. FuncTree: functional analysis and visualization for large-scale omics data. *PLoS ONE* **10**, e0126967 (2015).

[PubMed](#) [PubMed Central](#) [Google Scholar](#)

12. 12.

Lombard, V., Golaconda Ramulu, H., Drula, E., Coutinho, P. M. & Henrissat, B. The carbohydrate-active enzymes database (CAZy) in 2013. *Nucleic Acids Res.* **42**, D490–D495 (2014).

[CAS](#) [PubMed](#) [Google Scholar](#)

13. 13.

Langille, M. G. et al. Predictive functional profiling of microbial communities using 16S rRNA marker gene sequences. *Nat. Biotechnol.* **31**, 814–821 (2013).

[CAS](#) [PubMed](#) [PubMed Central](#) [Google Scholar](#)

14. 14.

Bäckhed, F. et al. The gut microbiota as an environmental factor that regulates fat storage. *Proc. Natl Acad. Sci. USA* **101**, 15718–15723 (2004).

[PubMed](#) [PubMed Central](#) [ADS](#) [Google Scholar](#)

15. 15.

Cani, P. D. et al. Microbial regulation of organismal energy homeostasis. *Nat. Metab.* **1**, 34–46 (2019).

[CAS](#) [PubMed](#) [Google Scholar](#)

16. 16.

Hunt, J. J. & Ballard, J. D. Variations in virulence and molecular biology among emerging strains of *Clostridium difficile*. *Microbiol. Mol. Biol. Rev.* **77**, 567–581 (2013).

[PubMed](#) [PubMed Central](#) [Google Scholar](#)

17. 17.

Bauer, M. P. et al. *Clostridium difficile* infection in Europe: a hospital-based survey. *Lancet* **377**, 63–73 (2011).

[PubMed](#) [Google Scholar](#)

18. 18.

Kuehne, S. A. et al. The role of toxin A and toxin B in *Clostridium difficile* infection. *Nature* **467**, 711–713 (2010).

[CAS](#) [PubMed](#) [ADS](#) [Google Scholar](#)

19. 19.

Wüst, J., Sullivan, N. M., Hardegger, U. & Wilkins, T. D. Investigation of an outbreak of antibiotic-associated colitis by various typing methods. *J. Clin. Microbiol.* **16**, 1096–1101 (1982).

[PubMed](#) [PubMed Central](#) [Google Scholar](#)

20. 20.

Buffie, C. G. et al. Precision microbiome reconstitution restores bile acid mediated resistance to *Clostridium difficile*. *Nature* **517**, 205–208 (2015).

[CAS](#) [PubMed](#) [ADS](#) [Google Scholar](#)

21. 21.

Sorg, J. A. & Sonenshein, A. L. Bile salts and glycine as cogerminants for *Clostridium difficile* spores. *J. Bacteriol.* **190**, 2505–2512 (2008).

[CAS](#) [PubMed](#) [PubMed Central](#) [Google Scholar](#)

22. 22.

Festi, D. et al. Gallbladder motility and gallstone formation in obese patients following very low calorie diets. Use it (fat) to lose it (well). *Int. J. Obes. Relat. Metab. Disord.* **22**, 592–600 (1998).

[CAS](#) [PubMed](#) [Google Scholar](#)

23. 23.

Carmody, R. N. et al. Cooking shapes the structure and function of the gut microbiome. *Nat. Microbiol.* **4**, 2052–2063 (2019).

[PubMed](#) [PubMed Central](#) [Google Scholar](#)

24. 24.

Fang, F. C., Polage, C. R. & Wilcox, M. H. Point-counterpoint: what is the optimal approach for detection of *Clostridium difficile* infection? *J. Clin. Microbiol.* **55**, 670–680 (2017).

[PubMed](#) [PubMed Central](#) [Google Scholar](#)

25. 25.

Furuya-Kanamori, L. et al. Asymptomatic *Clostridium difficile* colonization: epidemiology and clinical implications. *BMC Infect. Dis.* **15**, 516 (2015).

[PubMed](#) [PubMed Central](#) [Google Scholar](#)

26. 26.

Zacharioudakis, I. M., Zervou, F. N., Pliakos, E. E., Ziakas, P. D. & Mylonakis, E. Colonization with toxinogenic *C. difficile* upon hospital admission, and risk of infection: a systematic review and meta-analysis. *Am. J. Gastroenterol.* **110**, 381–390, quiz 391 (2015).

[PubMed](#) [Google Scholar](#)

27. 27.

Caporaso, J. G. et al. Ultra-high-throughput microbial community analysis on the Illumina HiSeq and MiSeq platforms. *ISME J.* **6**, 1621–1624 (2012).

[CAS](#) [PubMed](#) [PubMed Central](#) [Google Scholar](#)

28. 28.

Callahan, B. J. et al. DADA2: High-resolution sample inference from Illumina amplicon data. *Nat. Methods* **13**, 581–583 (2016).

[CAS](#) [PubMed](#) [PubMed Central](#) [Google Scholar](#)

29. 29.

Wang, Q., Garrity, G. M., Tiedje, J. M. & Cole, J. R. Naive Bayesian classifier for rapid assignment of rRNA sequences into the new bacterial taxonomy. *Appl. Environ. Microbiol.* **73**, 5261–5267 (2007).

[CAS](#) [PubMed](#) [PubMed Central](#) [ADS](#) [Google Scholar](#)

30. 30.

Fernandes, A. D., Macklaim, J. M., Linn, T. G., Reid, G. & Gloor, G. B. ANOVA-like differential expression (ALDEx) analysis for mixed population RNA-seq. *PLoS ONE* **8**, e67019 (2013).

[CAS](#) [PubMed](#) [PubMed Central](#) [ADS](#) [Google Scholar](#)

31. 31.

Fernandes, A. D. et al. Unifying the analysis of high-throughput sequencing datasets: characterizing RNA-seq, 16S rRNA gene sequencing and selective growth experiments by compositional data analysis. *Microbiome* **2**, 15 (2014).

[PubMed](#) [PubMed Central](#) [Google Scholar](#)

32. 32.

Langmead, B. & Salzberg, S. L. Fast gapped-read alignment with Bowtie 2. *Nat. Methods* **9**, 357–359 (2012).

[CAS](#) [PubMed](#) [PubMed Central](#) [Google Scholar](#)

33. 33.

Kanehisa, M., Goto, S., Sato, Y., Furumichi, M. & Tanabe, M. KEGG for integration and interpretation of large-scale molecular data sets. *Nucleic Acids Res.* **40**, D109–D114 (2012).

[CAS](#) [PubMed](#) [Google Scholar](#)

34. 34.

Zhao, Y., Tang, H. & Ye, Y. RAPSearch2: a fast and memory-efficient protein similarity search tool for next-generation sequencing data. *Bioinformatics* **28**, 125–126 (2012).

[CAS](#) [PubMed](#) [Google Scholar](#)

35. 35.

Nayfach, S. & Pollard, K. S. Average genome size estimation improves comparative metagenomics and sheds light on the functional ecology of the human microbiome. *Genome Biol.* **16**, 51 (2015).

[PubMed](#) [PubMed Central](#) [Google Scholar](#)

36. 36.

Law, C. W., Chen, Y., Shi, W. & Smyth, G. K. voom: precision weights unlock linear model analysis tools for RNA-seq read counts. *Genome Biol.* **15**, R29 (2014).

[PubMed](#) [PubMed Central](#) [Google Scholar](#)

37. 37.

Wu, D. et al. ROAST: rotation gene set tests for complex microarray experiments. *Bioinformatics* **26**, 2176–2182 (2010).

[CAS](#) [PubMed](#) [PubMed Central](#) [Google Scholar](#)

38. 38.

Buchfink, B., Xie, C. & Huson, D. H. Fast and sensitive protein alignment using DIAMOND. *Nat. Methods* **12**, 59–60 (2015).

[CAS](#) [PubMed](#) [Google Scholar](#)

39. 39.

Menzel, P., Ng, K. L. & Krogh, A. Fast and sensitive taxonomic classification for metagenomics with Kaiju. *Nat. Commun.* **7**, 11257 (2016).

[CAS](#) [PubMed](#) [PubMed Central](#) [ADS](#) [Google Scholar](#)

40. 40.

Wood, D. E., Lu, J. & Langmead, B. Improved metagenomic analysis with Kraken 2. *Genome Biol.* **20**, 257 (2019).

[CAS](#) [PubMed](#) [PubMed Central](#) [Google Scholar](#)

41. 41.

Chaumeil, P.-A., Mussig, A. J., Hugenholtz, P. & Parks, D. H. GTDB-Tk: a toolkit to classify genomes with the Genome Taxonomy Database. *Bioinformatics* **36**, 1925–1927 (2019).

[PubMed](#) [PubMed Central](#) [Google Scholar](#)

42. 42.

Edwards, U., Rogall, T., Blöcker, H., Emde, M. & Böttger, E. C. Isolation and direct complete nucleotide determination of entire genes. Characterization of a gene coding for 16S ribosomal RNA. *Nucleic Acids Res.* **17**, 7843–7853 (1989).

[CAS](#) [PubMed](#) [PubMed Central](#) [Google Scholar](#)

43. 43.

Sarafian, M. H. et al. Bile acid profiling and quantification in biofluids using ultra-performance liquid chromatography tandem mass spectrometry. *Anal. Chem.* **87**, 9662–9670 (2015).

[CAS](#) [PubMed](#) [Google Scholar](#)

44. 44.

Cai, J. et al. Orthogonal comparison of GC-MS and ^1H NMR spectroscopy for short chain fatty acid quantitation. *Anal. Chem.* **89**, 7900–7906 (2017).

[CAS](#) [PubMed](#) [PubMed Central](#) [Google Scholar](#)

45. 45.

Zheng, X. et al. A targeted metabolomic protocol for short-chain fatty acids and branched-chain amino acids. *Metabolomics* **9**, 818–827 (2013).

[CAS](#) [PubMed](#) [PubMed Central](#) [Google Scholar](#)

46. 46.

Erben, U. et al. A guide to histomorphological evaluation of intestinal inflammation in mouse models. *Int. J. Clin. Exp. Pathol.* **7**, 4557–4576 (2014).

[PubMed](#) [PubMed Central](#) [Google Scholar](#)

47. 47.

Chen, E. Z. & Li, H. A two-part mixed-effects model for analyzing longitudinal microbiome compositional data. *Bioinformatics* **32**, 2611–2617 (2016).

[CAS](#) [PubMed](#) [PubMed Central](#) [Google Scholar](#)

48. 48.

Turnbaugh, P. J. et al. The effect of diet on the human gut microbiome: a metagenomic analysis in humanized gnotobiotic mice. *Sci. Transl. Med.* **1**, 6ra14 (2009).

[PubMed](#) [PubMed Central](#) [Google Scholar](#)

49. 49.

Fouladi, F. et al. Sequence variant analysis reveals poor correlations in microbial taxonomic abundance between humans and mice after gnotobiotic transfer. *ISME J.* **14**, 1809–1820 (2020).

[CAS](#) [PubMed](#) [PubMed Central](#) [Google Scholar](#)

50. 50.

Persson, S., Torpdahl, M. & Olsen, K. E. New multiplex PCR method for the detection of *Clostridium difficile* toxin A (tcdA) and toxin B (tcdB) and the binary toxin (cdtA/cdtB) genes applied to a Danish strain collection. *Clin. Microbiol. Infect.* **14**, 1057–1064 (2008).

[CAS](#) [PubMed](#) [Google Scholar](#)

51. 51.

Kubota, H. et al. Longitudinal investigation of carriage rates, counts, and genotypes of toxigenic *Clostridium difficile* in early infancy. *Appl. Environ. Microbiol.* **82**, 5806–5814 (2016).

[CAS](#) [PubMed](#) [PubMed Central](#) [ADS](#) [Google Scholar](#)

52. 52.

Li, D., Liu, C.-M., Luo, R., Sadakane, K. & Lam, T.-W. MEGAHIT: an ultra-fast single-node solution for large and complex metagenomics assembly via succinct de Bruijn graph. *Bioinformatics* **31**, 1674–1676 (2015).

[CAS](#) [PubMed](#) [PubMed Central](#) [Google Scholar](#)

53. 53.

Alneberg, J. et al. Binning metagenomic contigs by coverage and composition. *Nat. Methods* **11**, 1144–1146 (2014).

[CAS](#) [PubMed](#) [Google Scholar](#)

54. 54.

Uritskiy, G. V., DiRuggiero, J. & Taylor, J. MetaWRAP—a flexible pipeline for genome-resolved metagenomic data analysis. *Microbiome* **6**, 158 (2018).

[PubMed](#) [PubMed Central](#) [Google Scholar](#)

55. 55.

Parks, D. H., Imelfort, M., Skennerton, C. T., Hugenholtz, P. & Tyson, G. W. CheckM: assessing the quality of microbial genomes recovered from isolates, single cells, and metagenomes. *Genome Res.* **25**, 1043–1055 (2015).

[CAS](#) [PubMed](#) [PubMed Central](#) [Google Scholar](#)

56. 56.

Bolger, A. M., Lohse, M. & Usadel, B. Trimmomatic: a flexible trimmer for Illumina sequence data. *Bioinformatics* **30**, 2114–2120

(2014).

[CAS](#) [PubMed](#) [PubMed Central](#) [Google Scholar](#)

57. 57.

Bankevich, A. et al. SPAdes: a new genome assembly algorithm and its applications to single-cell sequencing. *J. Comput. Biol.* **19**, 455–477 (2012).

[MathSciNet](#) [CAS](#) [PubMed](#) [PubMed Central](#) [Google Scholar](#)

58. 58.

Pritchard, L., Glover, R. H., Humphris, S., Elphinstone, J. G. & Toth, I. K. Genomics and taxonomy in diagnostics for food security: soft-rotting enterobacterial plant pathogens. *Anal. Methods* **8**, 12–24 (2015).

[Google Scholar](#)

59. 59.

Segata, N., Börnigen, D., Morgan, X. C. & Huttenhower, C. PhyloPhlAn is a new method for improved phylogenetic and taxonomic placement of microbes. *Nat. Commun.* **4**, 2304 (2013).

[PubMed](#) [ADS](#) [Google Scholar](#)

60. 60.

Wattam, A. R. et al. Improvements to PATRIC, the all-bacterial Bioinformatics Database and Analysis Resource Center. *Nucleic Acids Res.* **45**, D535–D542 (2017).

[CAS](#) [PubMed](#) [Google Scholar](#)

61. 61.

Kuznetsova, A., Brockhoff, P. B. & Christensen, R. H. B. lmerTest package: tests in linear mixed effects models. *J. Stat. Softw.* **82**, 1–26 (2017).

[Google Scholar](#)

62. 62.

Wickham, H. *ggplot2: Elegant Graphics for Data Analysis* (Springer, 2016).

63. 63.

Brouns, F. et al. Glycaemic index methodology. *Nutr. Res. Rev.* **18**, 145–171 (2005).

[CAS](#) [PubMed](#) [ADS](#) [Google Scholar](#)

[Download references](#)

Acknowledgements

We thank the UCSF Gnotobiotic Core Facility, and the Lynch lab (UCSF) for technical support; S. Brachs from the Spranger Lab for technical and scientific support with the animal experiments; and P. B. Smith in the Metabolomics Facility of Penn State. The Turnbaugh lab was supported by the National Institutes of Health (R01HL122593; R21CA227232; P30DK098722; 1R01AR074500; 1R01DK114034) and the Sugar, Stress, Environment, and Weight (SSEW) Center. P.J.T. was a Chan Zuckerberg Biohub investigator and a Nadia’s Gift Foundation Innovator supported, in part, by the Damon Runyon Cancer Research Foundation (DRR-42-16), the UCSF Program for Breakthrough Biomedical Research (partially funded by the Sandler Foundation), and the Searle Scholars Program. J.E.B. was the recipient of a Natural Sciences and Engineering Research Council of Canada Postdoctoral Fellowship and received support from the National Institute of Allergy and Infectious Diseases (K99AI147165). P.S. was supported by the Canadian Institutes of Health Research Fellowship

program. Q.Y.A. was the recipient of a graduate fellowship from A*STAR (Agency for Science, Technology and Research), Singapore. Funding was also provided by the Berlin Institute of Health (J.S., R.J.v.S., K.M.) and the German Research Foundation (DFG) to J.S. (CRC/TR 296 Locotact, CRG192 and CRG218) as well as the DZHK (German Centre for Cardiovascular Research) partner site Berlin (R.J.v.S., J.S.), DZD (German Centre for Diabetes Research) partner site Berlin (J.S.), and the BMBF (German Ministry of Education and Research) (K.M., J.S.). R.J.v.S. was a participant in the BIH Charité Clinician Scientist Program funded by the Charité-Universitätsmedizin Berlin and the Berlin Institute of Health. Further funding was provided by the Einstein Foundation Berlin via the Einstein Center for Regenerative Therapies (R.J.v.S.) and the Institute for Diabetes Research and Metabolic Diseases (IDM) of the Helmholtz Center Munich, Germany (R.J.v.S.). Funding support was also provided via the Gladstone Institutes and NSF grant DMS-1850638 (K.S.P.).

Author information

Author notes

1. These authors contributed equally: Reiner Jumpertz von Schwartzenberg, Jordan E. Bisanz
2. These authors jointly supervised this work: Joachim Spranger, Peter J. Turnbaugh

Affiliations

1. Charité Universitätsmedizin Berlin, Department of Endocrinology and Metabolic Diseases, Berlin, Germany

Reiner Jumpertz von Schwartzenberg, Sophia Dickmann, Marie Friedrich, Knut Mai & Joachim Spranger

2. Berlin Institute of Health (BIH), Berlin, Germany

Reiner Jumpertz von Schwartzenberg, Knut Mai & Joachim Spranger

3. DZHK (German Centre for Cardiovascular Research), partner site
Berlin, Center for Cardiovascular Research (CCR), Berlin, Germany

Reiner Jumpertz von Schwartzenberg & Joachim Spranger

4. Department of Microbiology & Immunology, University of California
San Francisco, San Francisco, CA, USA

Jordan E. Bisanz, Peter Spanogiannopoulos, Qi Yan Ang, Jessie A.
Turnbaugh & Peter J. Turnbaugh

5. Gladstone Institutes, San Francisco, CA, USA

Svetlana Lyalina & Katherine S. Pollard

6. Center for Molecular Toxicology and Carcinogenesis, Department of
Veterinary and Biomedical Sciences, The Pennsylvania State
University, University Park, PA, USA

Jingwei Cai, Stephanie L. Collins & Andrew D. Patterson

7. Department of Pathology, University of California San Francisco, San
Francisco, CA, USA

Su-Yang Liu

8. Department of Laboratory Medicine, University of California San
Francisco, San Francisco, CA, USA

Danielle Ingebrigtsen & Steve Miller

9. Department of Epidemiology & Biostatistics, University of California
San Francisco, San Francisco, CA, USA

Katherine S. Pollard

10. Institute for Human Genetics, University of California San Francisco,
San Francisco, CA, USA

Katherine S. Pollard

11. Institute for Computational Health Sciences, University of California San Francisco, San Francisco, CA, USA

Katherine S. Pollard

12. Chan Zuckerberg Biohub, San Francisco, CA, USA

Katherine S. Pollard

Authors

1. Reiner Jumpertz von Schwartzenberg

[View author publications](#)

You can also search for this author in [PubMed](#) [Google Scholar](#)

2. Jordan E. Bisanz

[View author publications](#)

You can also search for this author in [PubMed](#) [Google Scholar](#)

3. Svetlana Lyalina

[View author publications](#)

You can also search for this author in [PubMed](#) [Google Scholar](#)

4. Peter Spanogiannopoulos

[View author publications](#)

You can also search for this author in [PubMed](#) [Google Scholar](#)

5. Qi Yan Ang

[View author publications](#)

You can also search for this author in [PubMed](#) [Google Scholar](#)

6. Jingwei Cai

[View author publications](#)

You can also search for this author in [PubMed](#) [Google Scholar](#)

7. Sophia Dickmann

[View author publications](#)

You can also search for this author in [PubMed](#) [Google Scholar](#)

8. Marie Friedrich

[View author publications](#)

You can also search for this author in [PubMed](#) [Google Scholar](#)

9. Su-Yang Liu

[View author publications](#)

You can also search for this author in [PubMed](#) [Google Scholar](#)

10. Stephanie L. Collins

[View author publications](#)

You can also search for this author in [PubMed](#) [Google Scholar](#)

11. Danielle Ingebrigtsen

[View author publications](#)

You can also search for this author in [PubMed](#) [Google Scholar](#)

12. Steve Miller

[View author publications](#)

You can also search for this author in [PubMed](#) [Google Scholar](#)

13. Jessie A. Turnbaugh

[View author publications](#)

You can also search for this author in [PubMed](#) [Google Scholar](#)

14. Andrew D. Patterson

[View author publications](#)

You can also search for this author in [PubMed](#) [Google Scholar](#)

15. Katherine S. Pollard

[View author publications](#)

You can also search for this author in [PubMed](#) [Google Scholar](#)

16. Knut Mai

[View author publications](#)

You can also search for this author in [PubMed](#) [Google Scholar](#)

17. Joachim Spranger

[View author publications](#)

You can also search for this author in [PubMed](#) [Google Scholar](#)

18. Peter J. Turnbaugh

[View author publications](#)

You can also search for this author in [PubMed](#) [Google Scholar](#)

Contributions

Manuscript preparation with input from all authors: J.E.B., R.J.v.S., J.S., and P.J.T. Human cohort study design and execution: R.J.v.S., K.M., and J.S. Microbiome transplantation experiment design and execution: J.E.B., R.J.v.S., P.S., Q.Y.A., S.D., M.F., J.A.T., J.S., and P.J.T. 16S rRNA gene sequencing and analysis: J.E.B., R.J.v.S., and P.S. Metagenomic sequencing and analysis: J.E.B., S.L., R.J.v.S., and K.S.P. Metabolomic quantification and analysis: J.C., J.E.B., S.L.C., and A.D.P. *C. difficile* in vitro and gnotobiotic experiments: J.E.B., J.A.T., and P.J.T. Histological scoring: S.-Y.L. *C. difficile* testing: J.E.B., D.I., and S.M. Statistical analysis and data presentation: J.E.B., R.J.v.S., S.L., K.S.P., and P.J.T. Supervision and funding: R.J.v.S., A.D.P., K.S.P., K.M., J.S., and P.J.T.

Corresponding authors

Correspondence to [Joachim Spranger](#) or [Peter J. Turnbaugh](#).

Ethics declarations

Competing interests

P.J.T. is on the scientific advisory boards for Kaleido, Pendulum, Seres, and SNIPRbiome; there is no direct overlap between the current study and these consulting duties. All other authors declare no competing interests.

Additional information

Peer review information *Nature* thanks Daniel Tancredi and the other, anonymous, reviewer(s) for their contribution to the peer review of this work.

Publisher's note Springer Nature remains neutral with regard to jurisdictional claims in published maps and institutional affiliations.

Extended data figures and tables

[Extended Data Fig. 1 MMS diet intervention study.](#)

- a**, CONSORT diagram describing enrolment, allocation, and data analysis.
- b**, Per time point group sizes and timing of data collection. Participants in the diet group underwent 2 months of a very-low calorie liquid diet followed by an additional month of a conventional low-calorie diet. During the fourth month, they were instructed to maintain a stable weight. During all diet periods individuals were counselled by clinical nutritionists. Time points with data collection are shown for both diet and control participants.
- c, e**, Daily consumption of macronutrients measured by mass (**c**) and percentage of daily energy intake (**e**) in diet group ($n_{\text{baseline}} = 34$, $n_{\text{VLCD}} = 34$, $n_{\text{CONVD}} = 30$, $n_{\text{MAINT}} = 32$ participants). **d**, Total daily caloric

intake during diet phases ($n_{\text{intervention}}$ as in **c**, **e**, control group $n_{\text{baseline}} = 30$, $n_{\text{CONVD}} = 22$, $n_{\text{MAINT}} = 24$ participants). **f**, Decreases in relative body fat are observed in the intervention group ($n_{\text{baseline}} = 40$, $n_{\text{CONVD}} = 36$, $n_{\text{MAINT}} = 33$ participants) relative to the control group ($n_{\text{baseline}} = 40$, $n_{\text{CONVD}} = 24$, $n_{\text{MAINT}} = 26$ participants). **g**, Diet leads to improvement in glucose tolerance as measured by OGTT within and between diet ($n_{\text{baseline}} = 40$, $n_{\text{CONVD}} = 36$, $n_{\text{MAINT}} = 35$ participants) and control ($n_{\text{baseline}} = 40$, $n_{\text{CONVD}} = 25$, $n_{\text{MAINT}} = 26$ participants) groups. LMM with Tukey's two-sided all-pair comparison. In boxplots: centre line, median; box, first and third quartiles; whiskers, $1.5 \times$ interquartile range (IQR) with outliers individually plotted.

[Source data](#)

Extended Data Fig. 2 Reproducible and reversible shifts are observed in the gut microbiota as a result of caloric restriction in both 16S rRNA amplicon and shotgun metagenomic sequencing data.

a, Concentration of faecal DNA reveals decreased microbiota abundances in response to VLCD contrasting within diet group ($n_{\text{baseline}} = 21$, $n_{\text{VLCD}} = 16$, $n_{\text{CONVD}} = 17$, $n_{\text{MAINT}} = 7$ participants) and between diet and control groups ($n_{\text{baseline}} = 19$, $n_{\text{CONVD}} = 5$, $n_{\text{MAINT}} = 7$ participants). Microbiota determined by 16S rRNA gene sequencing revert to a state more closely resembling baseline samples after VLCD ($n = 19–33$ per group per time point; Supplementary Table 3) by both Bray–Curtis dissimilarity (**b**) and Jensen Shannon divergence (**c**; also $P < 0.001$, $R^2 = 0.031$ by ADONIS with Participant ID as stratum). **d**, Reproducible shifts in community membership are observed across individuals on the second principal coordinate in response to diet followed by reversion during conventional diet and maintenance (Unweighted UniFrac). Each series of connected points represents a single individual in the study with the number representing the time point of the study in months. **e**, Genera whose abundances were altered by VLCD demonstrate rapid reversion during the conventional diet (30 most important genera by GINI coefficient displayed,

Random Forest, *FDR $Q < 0.1$ ALDEx2). **f**, Shannon diversity is significantly decreased after conventional diet ($P = 0.047$, $n = 29$, mean difference = 0.149 (0.002–0.296 95% CI), paired Welch's two-sided t -test). **g**, Microbiota revert to a state more closely resembling baseline samples after VLCD, as measured through species-level metagenomic assignments ($P = 0.012$, $n = 15$ –29 per group per time point; Supplementary Table 3, two-sided Wilcoxon signed rank test). **h**, Metagenomic species whose abundances are altered by VLCD demonstrate rapid reversion during the conventional diet and maintenance phases (30 most important genera by GINI coefficient displayed). **i**, Volcano plots of differentially abundant KOs by contrast in metagenome data. VLCD demonstrates the largest effect size with apparent reversion when contrasted against CONVD. Effects of CONVD compared to baseline and cross-group comparisons yield minimal significant results. Statistical analysis was conducted using Limma. **j**, The BCAAs leucine and isoleucine are significantly reduced during VLCD ($n_{\text{intervention}} = 18$, $n_{\text{control}} = 10$ participants per time point, Wilcoxon signed-rank test). **k**, The butanoyl-CoA:acetoacetate CoA-transferase α -subunit, an enzyme that catalyses the final step in the production of butyrate, is increased in relative abundance during VLCD (FDR $Q = 0.032$, Limma; Supplementary Table 4). **l**, Normalizing relative abundance of butanoyl-CoA:acetoacetate CoA-transferase with qPCR quantification of 16S rRNA gene copies to infer the absolute number of genome equivalents (GE) in the sample demonstrates a decrease in the absolute abundance of the enzyme family ($P = 0.017$, LMM with Tukey two-sided all-pair comparison).

Sample size in number of participants for **k**, **l**: $n_{\text{baseline}} = 29$, $n_{\text{VLCD}} = 24$, $n_{\text{CONVD}} = 29$, $n_{\text{MAINT}} = 28$. In boxplots: centre line, median; box, first and third quartiles; whiskers, $1.5 \times$ interquartile range (IQR) with outliers individually plotted.

Extended Data Fig. 3 Diet-dependent changes in the microbiome are maintained following transplantation to GF mice.

a, Distribution of weight loss in diet intervention participants identified the five individuals that lost the most weight for transplantation of stool samples to GF C57BL/6J mice. **b**, Experiment design and microbiota

sampling times. **c**, Differential 16S rRNA ASV abundances in human donors and recipient mice demonstrate 58 candidate effectors of the weight-loss phenotype (zero-inflated beta regression model with random effects (ZIBR), FDR $Q < 0.1$, Supplementary Table 6). Note: taxonomy assigned using SILVA 123 with *Peptoclostridium difficile* synonymous for *C. difficile*. **d**, Functional differences between pre- and post-diet recipient communities by enrichment of KEGG functional pathways based on inferred gene content from amplicon sequencing (PICRUSt, Supplementary Table 7). Comparison of groups predicts altered amino acid, carbohydrate, and SCFA metabolic function. Central nodes represent KEGG pathways significantly enriched by their constituent significant differentially abundant KOs, shown with fold-change (colour) and FDR value (size) indicated (FDR $Q < 0.1$, LMM). **e**, Detection of *C. difficile* and TcdA/TcdB by endpoint PCR, ELISA, and selective and differential culture demonstrates active toxin production in post-diet mice at time of death.

Extended Data Fig. 4 Replication microbiome transplantation experiments.

a, Replication of experiment with transplantation of stool samples from five participants who lost most weight during conventional diet demonstrates significant differences in body weight between mice that received pre-diet and post-diet samples (Fig. 2b); there are no significant differences in body fat (**b**) or food consumption (**c**; $n_{\text{pre-diet}} = 7$, $n_{\text{post-diet}} = 8$ mice, LMM). Each point in **c** represents the measurement for a single mouse on a single day. **d**, Transplantation of pooled faecal samples from five participants who lost most weight during VLCD reveals significantly more weight loss in post-diet sample recipient mice (LMM). **e**, **f**, Post-diet recipient mice also show a trend towards reduced body fat (**e**) and improved OGTT (**f**; $P = 0.18$ and $P = 0.43$ respectively, two-sided Mann–Whitney U test). In **d–f**, $n_{\text{pre-diet}} = 5$, $n_{\text{post-diet}} = 6$ mice. **g**, Food intake was not significantly different between pre- and post-diet recipient mice over time or between groups ($P = 0.70$, LMM $n_{\text{post-diet}} = 6$, $n_{\text{pre-diet}} = 5$ mice measured over 16 time points as in **d**). **h**, **i**, Transplantation of pooled faecal samples from the median four weight losers revealed a small but significant effect on weight gain in recipient mice (**h**; LMM, $n_{\text{pre-diet}} = 13$, $n_{\text{post-diet}} = 12$ mice per time point) with an

associated reduction in body fat as measured by epididymal fat pad weight (**i**; $P = 0.036$, one-tailed Welch's t -test). **j**, This cohort showed no significant differences in OGTT results (AUC, $P = 0.650$, two-sided Mann–Whitney U test). Data shown as mean \pm s.e.m. where relevant. TcdA/B ELISA demonstrates a lack of stable *C. difficile* colonization in **k** (CONVD) and **l** (VLCD) replication experiments (ELISA reactions shown for individual animals at days 4 and 20 after colonization, respectively). LMM with participant as random effect and Tukey two-sided all-pair comparison unless otherwise noted. In boxplots: centre line, median; box, first and third quartiles; whiskers, $1.5 \times$ interquartile range (IQR) with outliers individually plotted.

Source data

Extended Data Fig. 5 Characterization of *C. difficile* JBZPo1.

a, JBZPo1 was assembled with 255-fold coverage (Illumina MiSeq 250) into 120 contigs (inner grey track; N50 = 87,201 bp) with an average GC content of 28.6% (green–purple centre track showing GC content), and 3,777 coding sequences (outer red and blue tracks displaying positive and negative strands, respectively). **b**, The *C. difficile* pathogenicity locus (PaLoc) encodes both toxin A (*tcdA*) and B (*tcdB*). **c**, The binary toxin (*cdt*) locus (CdtLoc) does not encode intact binary toxin. **d**, Phylogenetic tree of 717 *C. difficile* genomes and associated virulence factor carriage places JBZPo1 flanked by Ribotype 014-20 strains and separate from the hypervirulent epidemic NAP1/B1/027 strains (for example, R20291).

Extended Data Fig. 6 Extended data relating to *C. difficile* sufficiency experiments.

a, Experimental design relating to JBZPo1 transplantation experiment (Fig. 3b). **b**, Establishment of colonization with *C. difficile* JBZPo1 did not lead to dehydration as determined by hydration ratio (hydration ratio = [total body water – free water]/lean mass; $P = 0.59$, two-sided Mann–Whitney U test). Centre line, median; box, first and third quartiles; whiskers, $1.5 \times$ interquartile range (IQR) with outliers individually plotted. **c**, Body composition analysis revealed a significant difference between humanized

vehicle control and *C. difficile* colonized mice at the end of the experiment ($P < 0.001$, LMM with Tukey's two-sided all-pair comparison, $n = 6$ mice per group), which suggests that *C. difficile* caused increased adiposity. **d**, Quantification of JBZPo1 in recipient mice ($P = 0.003\text{--}0.006$, $n = 6$ mice per group per time point except $n = 5$ mice at 8 days in humanized control owing to missing sample; two-sided Mann–Whitney U test). Data shown as mean \pm s.e.m. **e**, ELISA of caecal contents from recipient mice confirmed production of TcdA/TcdB only in JBZPo1 recipient mice at end of experiment. **f**, Blinded pathological analysis revealed minor neutrophil infiltration with reactive changes (two-sided Mann–Whitney U test, $n = 6$ mice per group).

[Source data](#)

Extended Data Fig. 7 Diet-induced changes in microbiota influence *C. difficile*-associated weight loss and Toxin B expression.

a, Experimental design. **b**, Weight loss over time demonstrates a significant effect of diet of donor ($n = 7\text{--}8$ mice per group per day as in **a**; $P = 5.9 \times 10^{-5}$, estimate $= -4.6\%$ (-6.6 to -2.7 95% CI) for VLCD, $P = 1.5 \times 10^{-7}$, estimate $= -6.6\%$ (-8.5 to -4.6 95% CI) for CONVD). **c**, Mice colonized with stool samples from donors on CONVD showed an increase in TcdB expression over baseline 2 days after colonization ($P = 0.003$, $n = 7\text{--}8$ mice per group as in **a**, Kruskal–Wallis with two-sided Dunn's test). **d**, *C. difficile* carriage did not differ significantly among groups (suggesting no modulation of virulence), with the exception of 8 days after colonization in CONVD-recipient mice ($P = 0.017$ CONVD versus baseline; $n = 7\text{--}8$ mice per group as in **a**; two-sided Mann–Whitney U test). Data shown as mean \pm s.e.m. in **c**, **d**. **e**, Concentrations of key bile acids in P50 in response to diet ($n = 1$ participant per time point). LMM with participant as random effect and Tukey two-sided all-pair comparison unless otherwise noted.

[Source data](#)

Extended Data Fig. 8 Extended Data relating to necessity of Toxins A and B in metabolic phenotypes.

a, Experimental design relating to *C. difficile* 630 toxin-deficient mutant transplantation experiment (Fig. 3g). **b**, Colonization with TcdA/B⁺ strains does not lead to dehydration in GF animals and increases hydration in humanized animals ($P = 0.06$ and $P = 0.0016$ respectively, Kruskal–Wallis with two-sided Dunn’s test). **c**, Caecal *C. difficile* colonization level is not significantly different between strains ($P = 0.37$ and $P = 0.11$ for GF and humanized mice, respectively, Kruskal–Wallis with two-sided Dunn’s test), but is altered in mono-colonization versus humanized mice. **d**, ELISA of caecal contents confirms production of toxin only in *C. difficile* 630 Δerm mutants. **e**, Dense neutrophil and lymphocyte infiltration along with moderate epithelial hyperplasia and goblet cell loss due to TcdA⁺ TcdB⁺ *C. difficile* irrespective of colonization background (Kruskal–Wallis test with two-sided Dunn’s post hoc test). In b–e, $n = 5\text{--}6$ mice per group as in a.

Source data

Extended Data Fig. 9 Metabolomic profiling of the five participants who lost the most weight supports a working model for the effect of caloric restriction on colonization resistance.

a, b, BCAAs (a) and SCFAs (b) were decreased during VLCD and CONVD relative to baseline in the five participants who lost the most weight ($n = 5$ individuals per time point; mean \pm s.e.m.). **c**, Significant differences in bile acid levels between baseline and VCLD phases in these individuals implicate altered bile acid profiles in permissibility to *C. difficile* ($n = 5$ individuals per time point). **a–c**, LMM with Tukey’s two-sided all-pair comparison. **d**, Working model for the complex interactions between caloric restriction, the gut microbiome, and *C. difficile*. We propose that caloric restriction decreases host production of primary bile acids, including cholic acid, while also lowering total gut microbial colonization and altering the gut microbial community structure. Together, these effects lead to decreased production of the *C. difficile*-inhibitory

deoxycholic acid, which allows expansion of *C. difficile*, which, in turn, disrupts host energy balance. Notably, our data also support the existence of *C. difficile*-independent mechanisms for weight loss owing to the restructuring of the gut microbiome following caloric restriction. e, Representative culture plate showing presumptive *C. difficile* colonies with characteristic yellow appearance and filamentous edges.

Supplementary information

Supplementary Information

This file contains the Human Study Protocol.

Reporting Summary

Supplementary Tables

This file contains supplementary Tables 1-9.

Source data

Source Data Fig. 1

Source Data Fig. 2

Source Data Fig. 3

Source Data Fig. 4

Source Data Extended Data Fig. 1

Source Data Extended Data Fig. 4

Source Data Extended Data Fig. 6

[**Source Data Extended Data Fig. 7**](#)

[**Source Data Extended Data Fig. 8**](#)

Rights and permissions

[Reprints and Permissions](#)

About this article



Check for
updates

Cite this article

von Schwartzenberg, R.J., Bisanz, J.E., Lyalina, S. *et al.* Caloric restriction disrupts the microbiota and colonization resistance. *Nature* **595**, 272–277 (2021). <https://doi.org/10.1038/s41586-021-03663-4>

[Download citation](#)

- Received: 28 November 2017
- Accepted: 21 May 2021
- Published: 23 June 2021
- Issue Date: 08 July 2021
- DOI: <https://doi.org/10.1038/s41586-021-03663-4>

Comments

By submitting a comment you agree to abide by our [Terms](#) and [Community Guidelines](#). If you find something abusive or that does not comply with our terms or guidelines please flag it as inappropriate.

[Access through your institution](#)

[Change institution](#)

[Buy or subscribe](#)

Advertisement

This article was downloaded by **calibre** from <https://www.nature.com/articles/s41586-021-03663-4>

| [Section menu](#) | [Main menu](#) |

Nanobodies from camelid mice and llamas neutralize SARS-CoV-2 variants

[Download PDF](#)

- Article
- Open Access
- [Published: 07 June 2021](#)

Nanobodies from camelid mice and llamas neutralize SARS-CoV-2 variants

- [Jianliang Xu](#) [ORCID: orcid.org/0000-0003-4154-4322](#)¹ na1,
- [Kai Xu](#)² na1 nAff12,
- [Seolkyoung Jung](#)¹,
- [Andrea Conte](#)¹,
- [Jenna Lieberman](#)¹,
- [Frauke Muecksch](#) [ORCID: orcid.org/0000-0002-0132-5101](#)³,
- [Julio Cesar Cetrulo Lorenzi](#) [ORCID: orcid.org/0000-0003-2492-3961](#)⁴,
- [Solji Park](#)¹,
- [Fabian Schmidt](#)³,
- [Zijun Wang](#)⁴,
- [Yaoxing Huang](#) [ORCID: orcid.org/0000-0001-6270-1644](#)⁵,
- [Yang Luo](#)⁵,
- [Manoj S. Nair](#) [ORCID: orcid.org/0000-0002-5994-3957](#)⁵,
- [Pengfei Wang](#)⁵,
- [Jonathan E. Schulz](#)⁶,
- [Lino Tessarollo](#)⁷,
- [Tatsiana Bylund](#)²,
- [Gwo-Yu Chuang](#)²,
- [Adam S. Olia](#)²,
- [Tyler Stephens](#)⁸,
- [I-Ting Teng](#)²,
- [Yaroslav Tsybovsky](#)⁸,
- [Tongqing Zhou](#)²,
- [Vincent Munster](#) [ORCID: orcid.org/0000-0002-2288-3196](#)⁶,
- [David D. Ho](#) [ORCID: orcid.org/0000-0003-1627-149X](#)⁵,
- [Theodora Hatzioannou](#) [ORCID: orcid.org/0000-0002-7889-0766](#)³,

- [Paul D. Bieniasz](#) ORCID: [orcid.org/0000-0002-2368-3719^{3,9}](https://orcid.org/0000-0002-2368-3719),
- [Michel C. Nussenzweig](#) ORCID: [orcid.org/0000-0003-0592-8564^{4,9}](https://orcid.org/0000-0003-0592-8564),
- [Peter D. Kwong](#) ORCID: [orcid.org/0000-0003-3560-232X^{2 na1}](https://orcid.org/0000-0003-3560-232X) &
- [Rafael Casellas](#) ORCID: [orcid.org/0000-0001-9282-2287^{1,10,11 na1}](https://orcid.org/0000-0001-9282-2287)

Nature volume **595**, pages 278–282 (2021) [Cite this article](#)

- 16k Accesses
- 270 Altmetric
- [Metrics details](#)

Subjects

- [Antimicrobial responses](#)
- [Infectious diseases](#)
- [SARS-CoV-2](#)

Abstract

Since the start of the COVID-19 pandemic, SARS-CoV-2 has caused millions of deaths worldwide. Although a number of vaccines have been deployed, the continual evolution of the receptor-binding domain (RBD) of the virus has challenged their efficacy. In particular, the emerging variants B.1.1.7, B.1.351 and P.1 (first detected in the UK, South Africa and Brazil, respectively) have compromised the efficacy of sera from patients who have recovered from COVID-19 and immunotherapies that have received emergency use authorization^{1,2,3}. One potential alternative to avert viral escape is the use of camelid VHVs (variable heavy chain domains of heavy chain antibody (also known as nanobodies)), which can recognize epitopes that are often inaccessible to conventional antibodies⁴. Here, we isolate anti-RBD nanobodies from llamas and from mice that we engineered to produce VHVs cloned from alpacas, dromedaries and Bactrian camels. We identified two groups of highly neutralizing nanobodies. Group 1 circumvents antigenic drift by recognizing an RBD region that is highly conserved in coronaviruses but rarely targeted by human antibodies. Group 2 is almost exclusively focused to the RBD–ACE2 interface and does not neutralize SARS-CoV-2 variants that carry E484K or N501Y substitutions. However, nanobodies in group 2 retain full neutralization activity against these variants when expressed as homotrimers, and—to our knowledge—rival the most potent antibodies against SARS-CoV-2 that have been produced to date. These findings suggest that multivalent nanobodies overcome SARS-CoV-2 mutations through two separate mechanisms: enhanced avidity for the ACE2-binding domain and recognition of conserved epitopes

that are largely inaccessible to human antibodies. Therefore, although new SARS-CoV-2 mutants will continue to emerge, nanobodies represent promising tools to prevent COVID-19 mortality when vaccines are compromised.

[Download PDF](#)

Main

In contrast to mouse and human antibody binding domains (which are about 50 kDa in size), camelid VHJs retain full antigen specificity at about 15 kDa. This feature—along with extended complementarity determining regions (CDRs)—enables nanobodies to bind epitopes that are not normally accessible to conventional antibodies⁴, such as conserved viral domains that are often masked by glycan shields. Nanobodies can be readily humanized⁵ and in recent clinical trials they appeared safe and of low immunogenicity⁶. Despite these advantages, nanobodies are not widely used. One reason is that camelids are large animals that are not suitable for academic facilities. There are also few reagents available to isolate antigen-specific memory B cells from immunized camelids⁷. To bypass these hurdles, we sought to produce nanobodies in mice by combining 18 alpaca, 7 dromedary and 5 Bactrian camel VHJ genes in a 25-kb insertion cassette (Fig. 1a). Each gene was fused to a VH promoter, leader exons and recombination signal sequences to ensure physiological expression and recombination (Extended Data Fig. 1). Using CRISPR–Cas9, we inserted the VHJ cassette in lieu of the VH locus in mouse embryonic stem cells (Fig. 1a).

Fig. 1: Production of nanomice.

 **figure1**

a, Thirty VHJs selected from alpaca, dromedary and Bactrian camel were inserted via CRISPR–Cas9 in lieu of the 2.5-Mb mouse VH locus. CH1 exons from C μ and C γ 1 were also deleted to avoid misfolding of the antibody heavy chain. **b**, Flow cytometry analysis of splenic B220 $^{+}$ B cells from wild-type (WT) mice or heterozygous nanomice. IgM $^{+}$ Ig κ^{+} cells express conventional heavy–light chain antibodies, whereas IgM $^{+}$ Ig κ^{-} cells are mostly Ig λ^{+} in wild-type mice (not shown) or single-chain-antibody B cells in nanomice. **c**, Flow cytometry analysis of splenic cells from unimmunized and immunized nanomice and controls stained with CD95 and IgG1. **d**, Pie charts showing VHH somatic hypermutation in unimmunized and immunized nanomice. Pie segments are proportional to the VHH sequences carrying the mutations indicated on the periphery of the chart. The middle circle shows the total number of sequences, and mutation frequency is given below.

[Full size image](#)

Camelid nanobodies are expressed only in conjunction with dedicated IgG2 and IgG3, which splice out the CH1 exon during transcription⁴. In conventional antibodies, the hydrophobic surface of CH1 helps to pair heavy and light chain constant domains. To recapitulate this configuration in the mouse genome, we deleted CH1 from both *Ighm* and *Ighg1* in the embryonic stem cells (Fig. 1a). The targeted allele was germline-transmitted from mouse chimeras to F₁ offspring (hereafter referred to as ‘nanomice’).

As expected, about 85% of splenic B220⁺ B cells in wild-type mice were IgM⁺Igκ⁺ (Fig. 1b, left). By contrast, 72% of splenic B220⁺ B cells in heterozygous nanomice displayed an IgM⁺Igκ⁻ phenotype (Fig. 1b, right) and of these less than 2% were IgM⁺Igλ⁺ (Extended Data Fig. 2a), which implies that a large fraction of nanomouse B cells develop expressing single-chain antibodies. We confirmed this observation by amplifying VHH–DJ joining events using gene-specific primers. We found that all 30 VHHS were recombined to downstream JHs in bone marrow and spleen samples (Extended Data Fig. 2b). We performed a deep-sequencing analysis, which confirmed that all VHH genes undergo V(D)J recombination and are thus potentially available for expansion during the immune response (Extended Data Fig. 2c).

In VHH-homozygous nanomice, the B cell compartment was largely normal and displayed all developmental stages, including B1, B2 and marginal-zone B cells (Extended Data Fig. 3a). One difference was an increased number of IgM⁺ transitional and immature B cells in the bone marrow and spleen, respectively, indicative of enhanced selection as cells transition from the short- to the long-lived CD23^{high}CD21^{low} compartment, which in nanomice was reduced 1.7-fold relative to wild-type mice (Extended Data Fig. 3a). Another distinct feature was the absence of IgD (Extended Data Fig. 3b). This phenotype probably results from differential mRNA splicing owing to CH1 deletion at *Ighm*, because IgD was also absent in mice that are homozygous for deletion of the *Ighm* CH1 only (in which VHs and *Ighg1* CH1 are intact) (Extended Data Fig. 3b). Taken together, these data show that mouse B cells can mature expressing single-chain antibodies.

Activation and hypermutation in nanomice

To probe activation, splenic B cells were isolated and cultured in the presence of lipopolysaccharide and interleukin-4. Under these conditions, VHH-expressing cells underwent proliferation and switch recombination to IgG1 (Extended Data Fig. 3b,c). To examine activation in vivo, we performed intraperitoneal immunizations with keyhole limpet haemocyanin. Twelve days after immunization, nanomice showed numbers of B220⁺CD95^{high}IgG1⁺ germinal-centre B cells equivalent to those of controls (Fig. 1c).

To study affinity maturation against a specific antigen, we immunized nanomice with human immunodeficiency virus-1 (HIV-1) envelope trimer (BG505 DS-SOSIP)⁸ (Extended Data Fig. 3d). Hypermutation of VHH genes was increased relative to unimmunized controls (1.1×10^{-2} versus 7.5×10^{-4}) (Fig. 1d). The mutation spectra revealed an enrichment in G-to-A and C-to-T transitions (Extended Data Fig. 3e), consistent with activation-induced cytidine deaminase catalysis⁹.

To measure the antibody response against BG505 DS-SOSIP, we characterized 16 nanobodies that were enriched for HIV-1 trimer recognition. Sequence analysis showed CDR3s to be highly diverse in this group in terms of JH use, mutations and size (9–16 amino acids) (Extended Data Fig. 4a). To measure binding kinetics, we applied biolayer interferometry. The analysis identified four VHH9 variants, which displayed dissociation constants (K_{DS}) that ranged from 2 to 13 nM—demonstrating that they represent high-affinity binders (Extended Data Fig. 4b, Supplementary Table 1). We conclude that mouse B cells that express single-chain antibodies can undergo affinity maturation and produce highly specific nanobodies upon immunization.

SARS-CoV-2 neutralizing nanobodies

We next sought to produce neutralizing nanobodies against SARS-CoV-2. To this end, we immunized three nanomice and one llama with RBD and the stabilized prefusion spike of SARS-CoV-2 (Fig. 2a). We isolated peripheral blood mononuclear cells after immunization, and amplified and cloned VHHs into a phagemid vector. Following phage display, we enriched RBD-specific nanobodies using an enzyme-linked immunosorbent assay-based binding screen. Our deep-sequencing analysis identified, on average, 26,000 nanobody variants per library, which represents a total of 192 and 199 unique CDR3s for llama and nanomice, respectively (Extended Data Fig. 5a). We then clustered the nanobodies by CDR3s (Methods), isolated representative clones from each subgroup and tested them for blocking RBD binding to the ACE2 receptor *in vitro*¹⁰. We selected six llama and six nanomouse nanobodies using this method.

Fig. 2: Isolation of nanobodies against SARS-CoV-2.

 **figure2**

a, Immunization of llama and nanomice to obtain high-affinity nanobodies against SARS-CoV-2 RBD. **b**, Biolayer interferometry (BLI) analysis of difference concentrations of Nb17 monomer (left) and trimer (right) binding to immobilized RBD. Red trace represents the raw data; the kinetic fit is shown in grey underneath. Equilibrium (K_D) constants are provided. **c**, Table summarizing pseudovirus neutralization potency (IC_{50}) of selected nanobodies. Values are provided in molarity (left) or as ng ml^{-1} (right). **d**, Diagrams showing nanobodies used in neutralization assays as monomers, bivalent or trimers (the last two fused to human IgG1 Fc via the human or llama IgG2a hinge domain). **e**, Neutralization of SARS-CoV-2 pseudovirus by the 20 nanobodies shown in **c**. Nb12 monomer (red), bivalent (cyan) and trimer (magenta), as well as Nb19 trimer (blue), are highlighted. Data are representative of two independent experiments and the error bars are mean \pm s.d. of triplicates.

[Full size image](#)

To refine the list of candidates, we measured RBD-binding affinity by biolayer interferometry. This analysis identified 4 nanobodies from llama (designed nanobody (Nb) 15, Nb17, Nb19 and Nb56) and 2 nanobodies from nanomouse (Nb12 and Nb30) with dissociation constants below 30 nM (Fig. 2b, Extended Data Fig. 5b–d, Supplementary Table 1). The off-rate varied from $7.1 \times 10^{-3} \text{ s}^{-1}$ to $1.1 \times 10^{-3} \text{ s}^{-1}$, demonstrating slow dissociation for all nanobodies (Extended Data Fig. 5e). We next explored neutralization in vitro using lentiviral particles pseudotyped with the SARS-CoV-2 spike¹¹. The nanobody monomers displayed nanomolar and sub-nanomolar half-maximal inhibitory concentration (IC_{50}) values that ranged from 11.7 nM (168.5 ng ml^{-1}) for Nb12 to 0.335 nM (4.6 ng ml^{-1}) for Nb19 (Fig. 2c).

A crucial advantage of nanobodies over conventional antibodies is that they can be easily assembled into multimers, which often results in marked avidity^{12,13}. To explore this property, we fused nanobodies as trimers using flexible GGGGS($\times 3$) linkers and connected them to human IgG1 Fc via the human hinge domain or its much longer, flexible llama counterpart (Fig. 2d). We also created bivalent antibodies by fusing two VHJs to IgG1 Fc (Fig. 2d). We found that neutralization increased with the number of linked monomers, from 3-fold for Nb15 to 180-fold for Nb12 (Fig. 2c,e). Notably, the four most potent multimeric nanobodies (Nb12, Nb17, Nb19 and Nb56) reached IC_{50} values in the picomolar range (from 65 to 9 pM) (Fig. 2c,e). To our knowledge, these values rank among the best reported to date for anti-SARS-CoV-2 nanobodies¹⁴.

Nanobodies overcome SARS-CoV-2 mutants

With the worldwide spread of SARS-CoV-2, several variants that carry RBD mutations have emerged that increase transmissibility or allow escape from antibody neutralization. Of particular interest is the B.1.1.7 variant (which contains an N501Y substitution) that caused an upsurge in COVID-19 cases in the UK¹⁵. A second variant of concern is B.1.351, which combines N501Y with two additional RBD substitutions (K417N and E484K). P.1, a third variant that spread rapidly in Brazil, shows changes similar to those of B.1.1.7 and B.1.351: N501Y, K417T and E484K¹⁶. All of these mutations have been shown to reduce the efficacy of serum antibodies elicited by the Moderna and Pfizer–BioNTech vaccines^{1,2}.

We first explored whether our leading nanobodies could neutralize virus pseudotyped with SARS-CoV-2 spike carrying the RBD mutations. The R683G substitution, which increases infectivity in vitro¹⁷ was included as a control. In contrast to their efficacy against the wild-type virus, Nb17, Nb19 and Nb56 were unable to neutralize viruses carrying the E484K substitution alone or in combination with K417N and N501Y

(Fig. 3a). Similarly, Nb15 was ineffective against N501Y. However, with the exception of Nb17, the nanobodies all remained highly potent binders and neutralizers in bivalent or trivalent forms (Fig. 3a, Extended Data Figs. 5e, 6a). In the case of Nb15 and Nb56 trimers, IC₅₀ values reached 30 pM and 14 pM, respectively. Thus, the E484K and N501Y substitutions enable viral escape from monomeric, but not multimeric, nanobodies.

Fig. 3: Neutralization of wild-type and mutant SARS-CoV-2.

 figure3

a, Neutralization assays (IC₅₀ values) of pseudoviruses carrying wild-type or mutant SARS-CoV-2 spike. Colour gradient indicates values ranging from 0 (blue) to 50,000 pM (red). Pseudotyped viruses containing E484K or K417N, E484K and N501Y (KEN) also contain the R683G substitution. **b**, Neutralization assay showing the sensitivity of SARS-CoV-2 B.1.351 to different concentrations of trivalent Nb15, Nb56 and Nb12, and bivalent Nb30. Data are representative of two independent

experiments and the error bars are mean \pm s.d. of triplicates. **c**, Schematics summarizing the BLI competition assay, in which nanobody–RBD immunocomplexes attached to a biosensor are incubated with different nanobodies to measure binding. **d–g**, Binding of nanobodies to Nb12–RBD (**d**), Nb30–RBD (**e**), Nb15–RBD (**f**) and Nb56–RBD (**g**) immunocomplexes.

[Full size image](#)

In contrast to llama nanobodies, the neutralization potencies of nanomouse Nb12 and Nb30 were largely unaltered by RBD mutations (Fig. [3a](#)), which suggests that they recognize a region that is different from the receptor-binding motif. To explore whether multimeric nanobodies function against authentic virus, we repeated the neutralization assay with trivalent Nb15, Nb56 and Nb12, and bivalent Nb30, using SARS-CoV-2 WA1 and the B1.1.7, B1.351 and P.1 variants. The results closely recapitulated the pseudovirus findings, showing neutralization of wild type and the three variants by all four nanobodies (Fig. [3b](#), Extended Data Fig. [6b](#)). Of note, these nanobodies were most effective against the B1.1.7 variant, with IC₅₀ values that ranged between 4 pM (for Nb15) and 538 pM (for Nb30), and were relatively less effective against the B.1.351 variant, showing a range of 18 pM (for Nb56) to 2,755 pM (for Nb30) (Extended Data Fig. [6c](#)). Neutralization of the P.1 variant was intermediate (Extended Data Fig. [6b, c](#)).

The fact that llama and nanomouse nanobodies are differentially affected by the variants suggests that they recognize different RBD epitopes. To test this idea, we applied biolayer interferometry using a preformed nanobody–RBD immunocomplex that was incubated with a second nanobody (Fig. [3c](#)). We found that all four llama nanobodies, but not Nb30, could bind the Nb12–RBD immunocomplex (Fig. [3d](#)). Similarly, Nb30–RBD interfered with Nb12 binding, whereas llama nanobodies bound freely to it (Fig. [3e](#)). At the same time, Nb12 and Nb30 recognized all combinations of llama nanobody–RBD complexes, whereas llama nanobodies could not (Fig. [3f, g](#), Extended Data Fig. [6d](#)). Thus, nanomouse and llama nanobodies recognize two distinct neutralizing RBD regions.

As is often the case with single-chain antibodies, both llama and nanomouse nanobodies were largely thermostable and could be aerosolized with commercially available mesh nebulizers without losing neutralization activity (Extended Data Fig. [6e–g](#)).

Nanobody structures

To define the region bound by nanomouse nanobodies, we collected single-particle cryo-electron microscopy data on a Titian Krios for Nb12 and Nb30 in complex with

HexaPro¹⁰, a prefusion construct of the SARS-CoV-2 spike (Extended Data Figs. 7, 8, Supplementary Table 2). In both cases, we used particle subtraction, classification and local refinement to enhance the resolution of the nanobody–spike interface.

The structure of the Nb12–spike complex revealed Nb12 to induce a two-RBD-up, one-RBD-down spike conformation, with Nb12 recognizing a region towards the middle of the RBD, outside of the ACE2-binding region and distal from the residues (417, 484 and 501) affected in emerging variants of concern (Fig. 4a, Extended Data Fig. 9a). The structure of the Nb30–spike complex revealed Nb30 to induce a three-RBD-up conformation, with Nb30 recognizing a region at the opposite end of RBD from the ACE2-binding motif and residues affected by escape mutations (Fig. 4b, Extended Data Fig. 9b).

Fig. 4: Structures of leading nanobodies in complex with SARS-CoV-2 spike.



a, Cryo-electron microscopy structure of Nb12 in complex with SARS-CoV-2 spike. **b**, As in a, for Nb30. **c**, Interface between nanobodies and spike. **d**, Surface properties

of RBD, including sequence diversity (dark purple indicates diversity among sarbecoviruses), and prevalence of RBD-recognized regions by human antibodies (dark raspberry indicates high prevalence) and binding site for ACE2 (cyan).

[Full size image](#)

To understand how the two nanomouse nanobodies neutralized despite recognizing surfaces outside the ACE2-binding domain, we superimposed the structure of the ACE2–RBD complex^{18,19,20} with those of Nb12 and Nb30 (Extended Data Fig. 9c). We observed a substantial portion of Nb12 domain clashing with ACE2, which indicates that Nb12 and ACE2 binding are sterically incompatible. With Nb30, we observed a subtler clash with glycan N322 on ACE2, which nonetheless also indicated that Nb30 and ACE2 binding are sterically incompatible.

To obtain a structural understanding of the neutralizing regions recognized by nanomouse and llama nanobodies, we also determined 3D negative-stain electron microscopy reconstructions of each of the nanobodies in complex with HexaPro. These reconstructions revealed that llama nanobodies uniformly target the ACE2-binding interface, with Nb17, Nb19 and Nb56 inducing a one-RBD-up conformation, whereas Nb15 associates with all-RBD-down spikes (Extended Data Fig. 9d–h). By contrast, both nanomouse Nb12 and Nb30 recognize RBD at a surface outside the ACE2-binding site (Fig. 4c).

RBD regions recognized by mouse nanobodies

To provide insight into the prevalence of regions on RBD recognized by nanomouse versus human antibodies, we superimposed 51 RBD-directed human neutralizing antibodies in the Protein Data Bank and quantified the recognition prevalence at the residue level (Fig. 4d, Supplementary Table 3). Although recognition extended over much of the RBD, the prevalence of human antibody recognition was much higher in the ACE2-binding region in which the residues affected by emerging mutations reside. By contrast, the regions recognized by Nb12 and Nb30 were conserved in sarbecoviruses and displayed a substantially lower prevalence of human antibody recognition. The epitope of Nb12 overlaps considerably with those recognized by previous nanobodies specific for SARS-CoV²¹ and SARS-CoV-2^{13,22}, which raises the possibility that these nanobodies might also block the new SARS-CoV-2 variants. However, the Nb30 binding footprint is farther away from the ACE2 RBD motif and covers a surface area that is 79% conserved among sarbecoviruses, including SARS-CoV, SARS-CoV-2 and bat coronaviruses (compared to 54% for Nb12 and, on average, 23% for human antibodies) (Fig. 4c,d, Supplementary Table 3). Consistent with these findings, we found that Nb12 and Nb30 bind to the RBD of SARS-CoV and of the bat coronavirus WIV16 and neutralize HIV-1-based pseudoviruses that carry

their spike, whereas Nb56 does not (Extended Data Fig. [10a, b](#)). We observed similar neutralization patterns with vesicular stomatitis virus-based pseudoviruses carrying spike proteins from pangolin and six additional bat coronaviruses (Extended Data Fig. [10c](#)). We conclude that nanomouse VHVs circumvent RBD antigenic drift by recognizing a sarbecoviral conserved region outside the ACE2-binding motif.

Discussion

A key contribution of our study is the creation of nanobody-producing mice. Previous work has explored the transgenic expression of a limited number of llama VHVs^{[23](#)}. In our model, the 30 VHVs replace the entire VH domain, which leads to physiological recombination and selection during ontogeny. Although our nanomice are capable of producing high-affinity nanobodies, they can be improved further by increasing the number of available VHVs. This could be done by engineering a second allele carrying VHVs from llamas, vicuñas and guanacos (the three camelids that are not represented in our insertion cassette). We anticipate that this and similar improvements in animal models will help to popularize the development of nanobodies against infectious diseases or for basic applications.

As a proof of principle, we used nanomice to produce highly specific nanobodies against SARS-CoV-2 RBD. To date, numerous monoclonal antibodies isolated from patients with COVID-19 or from humanized mice have been shown to block the RBD–ACE2 interface. Unsurprisingly, immunotherapies that involve such antibodies are vulnerable to escape variants that carry mutations at or around the ACE2-binding motif^{[1,2,3](#)}. The anti-RBD nanobodies we isolated overcome this limitation in two important ways. First, similar to human antibodies, llama nanobodies (Nb15 and Nb56) hinder ACE2 binding to the spike of the original virus, but they are ineffective against viruses that carry E484K or N501Y substitutions. However, in multimeric form, these nanobodies overcome the block and display marked neutralization potency. This reversal is probably the result of increased avidity for the trimeric spike, or possibly the simultaneous cross-linking of multiple spikes on the viral membrane. Another possibility is that trimers occlude ACE2 access to the RBD. Second, nanobodies isolated from nanomice (Nb12 and Nb30) associate with an RBD region that is highly conserved among sarbecoviruses^{[21](#)}, but remains inaccessible to most human antibodies. As this region lies outside the ACE2-binding motif, nanobody–RBD contacts are unaffected by the E484K or N501Y substitutions. Importantly, even though the conserved domain does not overlap with the ACE2-binding motif, our structural studies suggest that nanobodies of this class sterically interfere with ACE2–RBD associations. On the basis of these features, we propose that our leading nanobodies may provide valuable tools for passive immunotherapy or pulmonary delivery against current or future SARS-CoV-2 variants of concern.

Methods

Data reporting

No statistical methods were used to predetermine sample size. The experiments were not randomized and the investigators were not blinded to allocation during experiments and outcome assessment.

Construction of exchange-cassette and VHH minigene

To replace the entire mouse VH locus (mm10, chromosome 12: 113,567,224–116,010,427) we assembled a targeting vector (pLH28-exchange-cassette) and a VHH minigene. The targeting vector was built by inserting a selection cassette composed of pEF1a-Puro-TK-2A-EGFP in between wtLoxP and LoxP257 sites within the pLH28 exchange vector²⁴. As homology arms, 1-kb and 0.8-kb fragments flanking the VH deletion domain were cloned 5' and 3' of the LoxP sites. To build the VHH minigene, VHH genes (18 from alpaca, 7 from dromedary and 5 from Bactrian camel) were selected on the basis of published sequences^{25,26,27}. Thirty mouse VH promoters (250 bp) were next chosen on the basis of their expression as measured by GRO-seq in resting and activated mouse B cells. VHHs were codon-optimized and complemented with mouse leading exons, introns and recombination signal sequences. The 30 units were pieced together by Gibson assembly (NEB) into the pBeloBAC11 vector.

Embryonic stem cell targeting

E14 cells were cultured in Glasgow's MEM (Thermo Fisher Scientific, 11710035) supplemented with 10% FBS (ATCC, SCRR-03-2020), Glutamax, sodium pyruvate, non-essential amino acids (NEAA), penicillin (50 units per ml)–streptomycin (50 µg ml⁻¹) and β-mercaptoethanol (Thermo Fisher Scientific, 35050061, 11360070, 11140050, 15140122, 21985023, respectively) at 37 °C and 5% CO₂. mLIF (GeminiBio, 400-495, 10,000×), MEKi (Stemgent, 0400602, 10,000×) and GSKi (Stemgent, 0400402, 3,333×) were added to the medium before use. Dishes and plates were coated with 0.1% glycine for 15 min at room temperature before use. To delete the CH1 exon of Cμ, sgRNAs targeting the flanking introns were cloned into the CRISPR–Cas9 plasmid pX458 (Addgene, 48138). A 100-nt-long single-stranded oligonucleotide (ODN) donor (100 µM, 3 µl) was co-transfected with the two Cas9 sgRNA plasmids (2 µg each) into embryonic stem (ES) cells (2 million cells) with the Amaxa nucleofection kit (Lonza, VPH-1001, programme A030). After 24 h of culture, GFP^{high} ES cells were FACS-sorted and cultured in 10-cm dishes at a concentration of 2,000 cells per dish. Seven days later, colonies were transferred into 96-well plates and cultured for an additional 3 days. Genomic DNA was then extracted and genotyped for

$C\mu$ exon deletion. Clones with homozygous deletions were selected to next delete the $C\gamma 1$ exon with the same strategy. To delete the entire VH locus, sgRNAs targeting sequences upstream of *Ighv1-86* (first Igkv) and downstream of *Ighv5-1* (last Igkv), respectively, were cloned into pX458. Selected ES cells (2 million cells) were co-transfected with the two Cas9 sgRNA plasmids (1.5 μ g each) and the pLH28-exchange-cassette plasmid (1.5 μ g) and then cultured in 10-cm dishes. Twenty-four h later, cells were selected with puromycin (0.8 μ g ml $^{-1}$) for 10 days and individual colonies were picked for expansion and genotyping by long-range PCR. Positive clones (2 million cells) were co-transfected with VHH minigene vector (3 μ g) and a Cre-expressing plasmid (1 μ g) and cultured in 10-cm dish for 3 days. Cells were then selected with ganciclovir (2 μ g ml $^{-1}$) for 7 days before individual colonies were picked for expansion and genotyping. sgRNAs and ODN primers are listed in Supplementary Table 4.

Generation of nanomice

Two modified ES cell clones with normal karyotype were injected into C57BL/6 blastocysts, which were then transferred to the uteri of pseudopregnant C56BL/6 recipients. High-percentage chimeras were mated to C57BL/6 mice and offspring were genotyped for VHH minigene knock-in and $C\mu$ and $C\gamma 1$ exon deletion. One out of three chimeras produced F₁ offspring that showed germline transmission. Three F₁ male mice were backcrossed with C57BL/6 mice. F₂ heterozygous mice were inbred to produce mice homozygous for all three modifications. Two F₁ offspring from the same chimera were null for Ch1 of *Ighm* but wild type for VH and CH1 exon of $C\gamma 1$. These mice were used as controls for Extended Data Fig. 3b.

FACS analysis

B cells were activated by culturing them in RPMI 1640 supplemented with 10% FBS, HEPES, sodium pyruvate, NEAA, penicillin-streptomycin and β -mercaptoethanol at 37 °C and 5% CO₂ in the presence of lipopolysaccharide (LPS, Sigma, L2630, 50 μ g ml $^{-1}$), interleukin-4 (IL-4, Sigma, I1020, 2.5 ng ml $^{-1}$) and anti-CD180 (1:2,000, BD Pharmingen, 552128) antibody for 72 h. For proliferation assays, cells were stained with CellTracer Violet (Thermo Fisher Scientific, C34557) at room temperature for 20 min before culturing for 96 h. For all FACS staining, cells were incubated in FACS buffer (phosphate-buffered saline (PBS), 2% FBS) at 4 °C for 20 min. Antibodies used for staining were: anti-B220-PerCP-Cy5.5 (1:500, eBioscience, 45-045-82), anti-B220-APC (1:500, Invitrogen, 17-0452-83), anti-IgM-APC (1:500, eBioscience, 17-5790-82), anti-Ig κ -PE (1:500, BD Pharmingen, 559940), anti-Ig κ -FITC (1:500, BD Pharmingen, 550003), anti-Ig λ -FITC (1:200, BD Pharmingen, 553434), anti-IgG1-PE (1:200, BD Pharmingen, 550083), anti-IgG1-APC (1:200, BD Pharmingen, 550874),

anti-IgD–FITC (1:200, BD Pharmingen, 553439), anti-CD95–PE (1:200, BD Pharmingen, 554258), anti-CD43–PE (1:200, BD Pharmingen, 553271), anti-CD23–PE (1:200, BD Pharmingen, 553139), anti-CD21–FITC (1:200, Biolegend, 123408) and Viability Dye eFluor506 (1:1000, Invitrogen, 1923275). Data were acquired using BD FACSCanto and FACSDiva software and analysed with FlowJo software. Gating strategy is shown in Extended Data Fig. [10d](#).

Analysis of VHH(D)J recombination

Genomic DNA from bone marrow or splenic samples was extracted with the DNeasy Blood & Tissue kit (Qiagen, 69506). VHH(D)J joints were PCR-amplified from 100 ng of DNA with a framework primer unique for each of the 30 VHHs, and a common downstream JH4 primer. PCR products were loaded onto 1% agarose gel to resolved them by size. Primers are listed in Supplementary Table [4](#).

VHH(D)J recombinants phagemid library construction

VHH(D)J phagemid libraries from unimmunized mice were constructed by first extracting RNA from nanomouse splenic samples with Trizol (Thermo Fisher Scientific, 15596026) and reverse-transcribed to cDNA with SuperScript III (Thermo Fisher Scientific, 18080400) according to the manufacturer’s instructions with some modifications. Ten µg of total RNA was denatured and annealed with gene-specific primers corresponding to CH2 of *Ighm*. After elongation at 50 °C for 50 min, template-switching oligonucleotide (TSO) (3'-propyl modified) linker was added to the reaction and the first strand cDNA was elongated for another 90 min at 42 °C. The reaction was inactivated at 85 °C for 5 min and 2 µl of cDNA was used as template for VHH(D)J amplification by two-step PCR with HiFi PCR Premix (Takara, 639298). For the first-step PCR, unmodified TSO and *Ighm*-CH2-specific oligonucleotides were used. Thirty ng of the first-step PCR product was then amplified with a primer mix of 30 forward primers corresponding to framework (FR1) of 30 VHH genes and 4 reverse primers corresponding to JH1~JH4. pMES4 phagemid (Addgene, 98223) was amplified with primers to introduce SfiI sites on both ends. VHH(D)J and pMES4 fragments were then digested with SfiI (NEB, R0123L) and ligated (100 and 200 ng, respectively) with T4 ligase (NEB, M0202L) at 16 °C overnight. Ligation product was purified with DNA Clean & Concentrator (Zymo Research, D4014) and eluted into 12 µl of water. Three µl of DNA was electroporated into 60 µl of TG1 cells (Lucigen, 60502-2) in 1.0-mm cuvette (HARVARD Apparatus, 450134) with BTX electroporation system ECM 630 at the setting of 25 µF, 200 ohms, 1,600 volts. After 1 h recovery in 37 °C in shaker incubator, TG1 cells were plated on 5 of 10-cm LB agar plates supplemented with 100 µg ml⁻¹ carbenicillin (KD Medical, BPL-2400). Plates were placed in 37 °C bacteria incubator overnight, bacteria were scraped off

plates and phagemid library was DNA-extracted with Zymo Plasmid Miniprep kit (Zymo Research, D4054). Primers are listed in Supplementary Table 4.

Sanger sequencing for somatic hypermutation analysis

VHH(D)J recombinants from splenic cells of two nanomice were PCR-amplified as described in ‘VHH(D)J recombinants phagemid library construction’, and then cloned directly into pCR-Blunt II-TOPO vector (Thermo Fisher Scientific, 450245) and transformed into Stab13 competent *Escherichia coli* (Thermo Fisher Scientific, C737303). Ninety-six colonies were randomly picked for Sanger sequencing. TG1 cells from BG505 DS-SOSIP immunized nanomouse phagemid library were plated onto carbenicillin-containing plates and 50 colonies picked for Sanger sequencing. Sequence alignment was performed using Snapgene software.

Immunizations

All animal-related procedures were performed by following our NIAMS ACUC protocol. To monitor the germinal centre reaction, three nanomice and two C57BL/6 mice were immunized intraperitoneally with 50 µg of keyhole limpet haemocyanin (KLH) in the presence of complete Freund’s adjuvant (CFA). A boost injection was performed in the footpads with 25 µg of KLH in the presence of incomplete Freund’s adjuvant (IFA) on day 6. Spleen samples were collected on day 12 for analysis.

To isolate nanobodies recognizing HIV-1 envelope trimer, one nanomouse was immunized intraperitoneally with 50 µg of BG505 DS-SOSIP in the presence of CFA on day 0, and boost immunized with 25 µg of BG505 DS-SOSIP in the presence of IFA or PBS on day 22 and 44, respectively. Bone marrow, spleen and blood were collected on day 48.

To isolate neutralizing nanobodies against SARS-CoV-2, a llama (Capralogics) was immunized subcutaneously with 1 mg of recombinant RBD protein in the presence of CFA at day 0, and boost immunized with 0.5 mg of RBD protein in the presence of IFA on days 14, 28 and 42. Two more boost immunizations with 0.5 mg of recombinant spike protein in the presence of IFA were performed on day 56 and 70. On day 80, 500 ml of whole blood were collected for library preparation.

To isolate SARS-CoV-2 neutralizing nanobodies from nanomice, two groups of mice (five for group 1 and six for group 2) were immunized with RBD and/or spike protein and bleeds were collected after a 62-day immunization protocol. Mice were immunized intraperitoneally with 50 µg of RBD protein (group 1) or spike protein (group 2) in the presence of CFA on day 0, and boost immunized intraperitoneally with 25 µg of RBD protein (group 1) or spike protein (group 2) in the presence of IFA

on days 14, 28 and 42. Mice were further immunized with 25 µg of spike protein in PBS on day 56 and 59, intraperitoneally and intravenously, respectively. Bone marrow, spleen and blood samples were collected on day 62. The best responders—nanomouse 1 (group 1) and nanomice 2 and 3 (group 2)—were selected for phage library construction.

Llama and nanomouse phage library construction

The llama phage library was constructed as previously described²⁸ with some modifications. In brief, 300 ml of whole blood was collected from llama and peripheral blood mononuclear cells (PBMCs) were enriched using Ficoll-Paque plus (GE Healthcare, 17-1440-03). Fifty µg of extracted RNA was reverse-transcribed to cDNA with random hexamers and 2.5 µl of cDNA was used for first round RT–PCR with gene-specific primers CALL001 and CALL002. The PCR reaction was repeated in 12 individual tubes with cDNA added into reactions separately. PCR fragments of about 700-bp long were gel-purified and used as template (30 ng for each reaction, repeated in 12 individual tubes) for second round PCR with nested primers VHH-Back and VHH-For. PCR product from individual reactions were pooled and gel-purified. Nanobody fragments and pMES4 phagemid were digested with PstI-HF and BstEII-HF restriction enzymes (NEB: R3140L, R3162L) and ligated (1 µg and 2 µg respectively) with T4 ligase at 16 °C overnight. Ligation product was column-purified (into 12 µl of H₂O) and electroporated into 360 µl of TG1 cells. After 1 h of recovery at 37 °C in a shaker incubator, cells were plated on 6 of 245 × 245-mm dish (Thermo Fisher Scientific, 431301) containing 2-YT agar supplemented with 100 µg ml⁻¹ carbenicillin and 2% (w/v) glucose. Plates were placed in a 37 °C bacteria incubator overnight and then bacteria were scraped off of plates and archived as glycerol stocks. Cells were infected with VCSM13 helper phage (Agilent Technologies, 200251) followed by precipitation of culture supernatant with 20% polyethylene glycol 8000 (Sigma, 89510) in 2.5 M sodium chloride on ice to purify the nanobody phage particles. Phage particles were resuspended in 1 ml PBS, 300 µl were used for screening immediately and the remaining phages were stored at –80 °C in the presence of 10% glycerol.

Nanomouse nanobody phage libraries were constructed the same way as nanomouse VHH(D)J region phagemid library construction with some modifications. In brief, total RNA was extracted from splenic cells, bone marrow cells and PBMCs of immunized mice and processed separately until the TG1 cell electroporation step. RNA from splenic cells, bone marrow and PBMCs (50 µg, 50 µg and all, respectively) were reversed-transcribed to cDNA with *Ighg1*-CH2-specific primer in separate tubes. Two µl of cDNA was used as template for PCR variable domain amplification (12 reactions each), using unmodified TSO and *Ighg1*-CH2-specific oligonucleotide as primers. Second PCR was repeated in 12 reactions using 30 ng of the first-step PCR

product as template and 30 FR1 and 4 JH oligonucleotide mix as primers. PCR products were gel-purified, digested with SfiI and ligated with pMES4 (200 ng and 400 ng, respectively). Ligation products from splenic cells, bone marrow and PBMC samples were pooled and column-purified (into 12 µl of water) and electroporated into 360 µl of TG1 cells and phage libraries prepared as described in ‘VHH(D)J recombinants phagemid library construction’. Primers are listed in Supplementary Table 4.

Library construction for Illumina MiSeq deep sequencing

Phagemid DNA extracted from TG1 cell libraries was used as starting material for constructing MiSeq libraries to measure VHH use and nanobody diversity. In brief, 1.2 µg of phagemid DNA was used as template and VHH(D)J inserts were amplified with primers recognizing the pMES4 backbone using CloneAmp HiFi PCR Premix (Takara, 639298) in a 50-µl reaction (9 cycles). To avoid MiSeq failure owing to low complexity at initial cycles and to enable multiplex sequencing, 1–9-nt-long staggers were introduced into forward primers. Without purification, 5 µl of the first PCR product were used as template for a second PCR (9 cycles) to add Illumina P5 and P7 primers on both ends. PCR product was then loaded onto a 2% agarose gel and the approximately 580-bp size band was purified with Zymoclean Gel DNA Recovery Kit (Zymo Research, D4002). DNA concentration was determined by Qubit 4 Fluorometer (Thermo Fisher Scientific, Q33238) and average DNA size was determined by TapeStation 4150 (Agilent). DNA was then adjusted to 2 nM in elution buffer containing 0.1% Tween-20. For unimmunized nanomice VHH(D)J library, DNA (2 nM) from 3 mice was mixed at a 1:1:1 ratio and loaded for MiSeq run. For immunized llama and nanomice nanobody diversity analysis, DNA (2 nM) of pre-selection and post-selection libraries were mixed at 10:1 ratio first and then samples from individual animals were pooled at 1:1 ratio before loading for MiSeq sequencing. Primers are listed in Supplementary Table 4.

Deep-sequencing analysis

For unimmunized nanomouse VHH use analysis, pooled library from 3 mice was sequenced by MiSeq (pair end, 270 cycles × 2). Pair-end reads were merged with NGmerge²⁹ with default settings. Nucleotides corresponding to pMES4 were trimmed using pTrimmer program³⁰, leaving clean VHH(D)J sequences in the merged reads. Reads with undetermined N nucleotides, low quality sequence or less than 300 nt in length were removed with the fastp program³¹. Fastq format sequences were converted to .fasta format for further analysis. To calculate VHH use, a BLAST database was built from a .fasta format file (vhh.exon.fa) containing the exon sequence of all 30 VHH genes, using BLAST+. VHH(D)Js were then aligned to VHH genes using

igblast program³². The alignment output file was simplified to retain only sequence identifier and VHH(D)J recombination information.

For immunized llama and nanomouse nanobody diversity analysis, in total 8 libraries (pre- and post-selection) were sequenced by MiSeq (pair end, 300 cycles × 2). The 3'-end low-quality sequences were trimmed using the Sickle program (v1.33, available at <https://github.com/najoshi/sickle>). For different libraries, the minimum length of trimmed sequence was adjusted on the basis of the length of staggers in the primers used for library construction. Paired sequences were merged by flash program (v.1.2.11)³³ and translated. To extract nanobody sequences and to locate CDR3 regions, we used ANARCI program³⁴ to annotate VHH genes with IMGT numbering. Protein sequences with greater than or equal to 100 amino acids in total and greater than or equal to 1 amino acid in the CDR3 region were extracted for further analysis. Enrichment of individual sequences were calculated by comparing their frequencies in pre- and post-selection libraries. Sequences that were enriched more than 10 times and had greater than or equal to 5×10^{-5} frequency were selected for CDR3 clustering using cd-hit program (v.4.6.8)³⁵.

Expression and purification of BG505 DS-SOSIP and SARS-CoV-2 proteins

BG505 DS-SOSIP protein was expressed and purified as previously described³⁶. The spike protein of SARS-CoV-2 and its RBD were expressed and purified as previously described^{37,38} with some modifications. In brief, 1 mg of pCAGGS-Spike or pCAGGS-RBD plasmid was transfected into 1 l of Expi293 cells (Thermo Fisher Scientific, A14528) with Turbo293 transfection reagent (Speed Biosystem, PXX1002). Supernatants from transfected cells were collected on day 4 after transfection by centrifugation of the culture at 12,000g for 15 min. Supernatant was then filtered through 0.2 m aPES filter (Thermo Fisher Scientific, 5670020) and incubated with 10 ml of cOmplete His-tag purification resin (Roche, 05893801001) for 1 h at room temperature. Next, His-tag resin was collected through gravity flow columns (BioRad, 9704652), washed with 100 ml of washing buffer (15 mM imidazole, 50 mM TrisHCl, 300 mM NaCl) and eluted with 25 ml of elution buffer (300 mM imidazole, 50 mM TrisHCl, 300 mM NaCl). Eluate was concentrated in 10-kDa Amicon Centrifugal Units (EMD Millipore, UFC901024) and then dialysed in PBS using Slide-A-Lyzer dialysis cassette (Thermo Fisher Scientific, 66381). Proteins were analysed by NuPAGE gel (Thermo Fisher Scientific, NP0336BOX) and visualized by InstantBlue staining (Abcam, ab119211). Soluble spike trimers or monomeric RBD proteins were aliquoted, snap-frozen by liquid nitrogen and stored at -80°C before being used for immunization. RBD and spike (HexaPro) proteins used for phage screening, BLI,

negative-stain electron microscopy and cryo-electron microscopy (cryo-EM) were done as previously described^{[10,39](#)}.

Phage screening for BG505 DS-SOSIP, RBD and spike binding nanobodies

RBD, spike and BG505 DS-SOSIP were coated by different methods onto MaxiSorp 96-well plate (Thermo Fisher Scientific, 439454) for phage screening. For RBD screening, two wells were coated with 50 µl of RBD protein (100 µg ml⁻¹ in PBS) at 4 °C overnight. Another well with 50 µl of PBS was used as an non-coated control. Wells were washed with PBS with 0.1% Tween-20 three times and blocked with 5% non-fat milk in PBS at room temperature for 1 h. For spike or BG505 DS-SOSIP screening, three wells were coated with 50 µl of lectin (EMD Millipore, L8275, 100 µg ml⁻¹ in PBS) at 4 °C overnight. Wells were washed and blocked with 10% non-fat milk in room temperature for 1 h. After three washes, 50 µl of 100 µg ml⁻¹ of BG505 DS-SOSIP or spike were added to 2 wells, incubated at room temperature for 2 h and washed. A third well contained PBS and served as a non-coated control. Three hundred µl of phage particles was mixed with 300 µl of 10% non-fat milk and rotated gently at room temperature for 1 h. One hundred and fifty µl of blocked phage particles was then added into each well and incubated in room temperature for 2 h with gentle shaking. After 15 washes, phages were eluted with TrypLE Express Enzyme (Thermo Fisher Scientific, 12605010) by shaking plates at 700 rpm at room temperature for 30 min and used immediately for selection efficiency estimation (10 µl of phage eluate) and recovery infection (the remaining eluate) as previously described^{[28](#)}. Anti-RBD libraries were selected with RBD protein once, and libraries constructed from BG505 DS-SOSIP or spike immunized animals were selected with BG505 DS-SOSIP or spike (HexaPro) proteins twice.

Enzyme-linked immunosorbent assay selection of anti-BG505 DS-SOSIP and anti-RBD nanobodies

After one or two rounds of selection, recovered TG-1 cells were plated and colonies were picked to prepare periplasmic extracts containing crude nanobodies for enzyme-linked immunosorbent assay (ELISA). In brief, individual colonies were picked and grown in 96 deep-well plates (Thermo Fisher Scientific, 278743) in 2YT medium supplemented with 100 µg ml⁻¹ of carbenicillin and 0.1% glucose. IPTG (final 1 mM) was added when optical density at 600 nm (OD₆₀₀) reached 1 and protein expression was induced in 30 °C for 16 h. Periplasmic extracts were prepared by resuspending bacteria pellet in 200 µl of PBS and rapidly frozen in liquid nitrogen. Frozen cells were thawed slowly at room temperature and centrifuged at 4,100g for 15 min. Maxisorp plates were coated with lectin (2 µg ml⁻¹) followed by BG505 DS-SOSIP (2

$\mu\text{g ml}^{-1}$) or with RBD ($2 \mu\text{g ml}^{-1}$). After blocking, 100 μl of nanobody-containing supernatant were transferred to the plates and incubated for 2 h at room temperature. Plates were washed and then incubated with horse radish peroxidase (HRP) conjugated goat anti-alpaca VHH domain specific antibody (Jackson ImmunoResearch, 128-035-232) for 1 h at room temperature. Plates were washed and then developed by addition of 50 μl of tetramethylbenzidine (TMB) (Thermo Fisher Scientific, 34028) for 10 min, then the reaction was stopped by adding 50 μl of 1 M H_2SO_4 . Absorbance at 450 nm was measured with Synergy microplate reader (BioTek Gen5).

Expression and purification of nanobodies

Phagemids from lead candidates identified by ELISA were extracted from TG-1 cells and transformed into WK6 cells (ATCC, 47078). Cultures were grown in 30 ml of 2YT medium ($100 \mu\text{g ml}^{-1}$ of carbenicillin and 0.1% glucose) at 37°C and 220 rpm until OD_{600} reached 1. Protein expression was induced by 1 mM IPTG at 30°C for 16 h and then pelleted at 4,100g for 15 min. The resulting pellets were resuspended in 1 ml of PBS plus 30 μl of 0.5 MU ml^{-1} polymyxin B (Sigma, P1004) and incubated at 37°C with shaking for 1 h. Cell debris were pelleted at 12,000g for 5 min and nanobodies in the supernatant were purified using Capturem His-tagged purification kit (Takara, 635710). For larger-scale nanobody production (0.2 to 1 l of culture), nanobodies in the supernatant were purified by cOmplete His-tag purification resin and dialysed in PBS as described in ‘Expression and purification of BG505 DS-SOSIP and SARS-CoV-2 proteins’. Proteins were filtered sterile by 0.22- μm PVDF membrane (EMD Millipore, UFC30GVNB) before being used for downstream assays.

Expression and purification of Fc conjugated nanobodies and RBD in Expi293 cells

Monomeric or trimeric nanobody sequences were fused to the Fc region of human IgG1 with 6 \times His tag at the C-terminal end and cloned into the pVRC8400 vector. In trimeric form, nanobody units were connected through (GGGGS) \times 3 flexible linkers. In some cases, llama IgG2a hinge region was used in lieu of human IgG1 hinge. The Fc fusion constructs were expressed in Expi293 cells as described in ‘Expression and purification of BG505 DS-SOSIP and SARS-CoV-2 proteins’ at 33°C from day 2 to day 4. Antibodies in the supernatant were purified using either cOmplete His-tag purification resin or protein A (Thermo Fisher Scientific, A26457). When protein A resin was used, antibodies were eluted by IgG elution buffer (Thermo Fisher Scientific, 21009) and brought to neutral pH by adding 1/10 volume of Tris-HCl (1M, pH 8). Antibodies were concentrated, dialysed and filtered. Nanobody–Fc yields were up to 100 mg l^{-1} . RBD region of SARS-CoV, SARS-CoV-2 and bat coronavirus

WIV16 spike protein were fused to the Fc region of human IgG1 and cloned into pVRC8400 vector. RBD–Fc proteins were expressed in Expi293 cells and purified with protein A.

SARS-CoV-2 surrogate virus neutralization test

RBD–ACE2 interaction blocking potential of nanobodies was tested using the SARS-CoV-2 surrogate virus neutralization test (sVNT) kit (Genscript, L00847) according to the manufacturer’s instructions. In brief, HRP–RBD was diluted and incubated with specified concentrations of nanobodies for 30 min at 37 °C. Samples were then transferred onto ACE2-coated plates and incubated for 15 min at 37 °C. Plates were washed, and the assay was developed using TMB reagent and quenched with stop solution. Absorbance at 450 nm was measured with a Synergy microplate reader (BioTek Gen5). Inhibition rate was calculated and plotted using Microsoft Excel according to manufacturer’s instruction of the sVNT kit.

Pseudotyped virus neutralization assay

A panel of plasmids expressing RBD-mutant SARS-CoV-2 spike proteins in the context of pSARS-CoV-2-SD19 have previously been described^{1,40}. The mutants E484K and KEN (K417N, E484K and N501Y) were constructed in the context of a pSARS-CoV-2-S_{Δ19} variant with a substitution in the furin cleavage site (R683G). The IC₅₀ of these pseudotypes were compared to a wild-type SARS-CoV-2 spike sequence carrying R683G in the subsequent analyses, as appropriate. Generation of SARS-CoV-2 pseudotyped HIV-1 particles and pseudovirus neutralization assay was performed as previously described¹¹. In brief, 293T cells were transfected with pNL4-3DEnv-nanoluc and pSARS-CoV-2-SD19 and pseudotyped virus stocks were collected 48 h after transfection, filtered and stored at –80 °C. Serially diluted nanobodies were incubated with the pseudotyped virus for 1 h at 37 °C. The mixture was added to 293T_{ACE2}¹¹ (for analysis of wild-type neutralization activity) (Fig. 2) or HT1080Ace2 cl.14¹⁷ cells (for analysis of spike mutant panel) (Fig. 3), and after 48 h cells were washed with PBS and lysed with Luciferase Cell Culture Lysis 5x reagent (Promega). Nanoluc luciferase activity in lysates was measured using the Nano-Glo Luciferase Assay System (Promega) with Modulus II Microplate Reader User interface (TURNER BioSystems). The relative luminescence units were normalized to those derived from cells infected with SARS-CoV-2 pseudotyped virus in the absence of antibodies. Neutralization of HIV-1-based SARS-CoV-1 and bat coronavirus WIV16 pseudotypes were performed in HT1080/ACE2cl.14 cells as previously described⁴¹. The IC₅₀ for nanobodies was determined using four-parameter nonlinear regression (GraphPad Prism).

Recombinant Indiana vesicular stomatitis virus (rVSV) expressing different coronavirus spikes (SARS-CoV-2, RaTG13, GDPangolin, GXPangolin, SARS-CoV, WIV1, SHC014, LYRa11, Rs7327, Rs4084 and Rs4231) were generated as previously described^{2,42,43}. In brief, HEK293T cells were grown to 80% confluence before transfection with the spike gene using Lipofectamine 3000 (Invitrogen). Cells were cultured overnight at 37 °C with 5% CO₂, and VSV-G pseudo-typed ΔG-luciferase (G*ΔG-luciferase, Kerafast) was used to infect the cells in DMEM at a multiplicity of infection (MOI) of 3 for 2 h before washing the cells with 1× DPBS three times. The next day, the transfection supernatant was collected and clarified by centrifugation at 300g for 10 min. Each viral stock was then incubated with 20% I1 hybridoma (anti-VSV-G, ATCC: CRL-2700) supernatant for 1 h at 37 °C to neutralize contaminating VSV-G pseudo-typed ΔG-luciferase virus before measuring titres and making aliquots to be stored at -80 °C. Neutralization assays were performed by incubating pseudoviruses with serial dilutions of antibodies and scored by the reduction in luciferase gene expression as previously described^{2,42,43}. In brief, 293T_{ACE2} cells were seeded in 96-well plates (2×10^4 cells per well). Pseudoviruses were incubated with serial dilutions of the antibodies in triplicate for 30 min at 37 °C. The mixture was added to cultured cells and incubated for an additional 16 h. Luminescence was measured using Luciferase Assay System (Promega), and IC₅₀ was defined as the dilution at which the relative light units were reduced by 50% compared with the virus control wells (virus + cells) after subtraction of the background in the control groups with cells only. The IC₅₀ values were calculated using a five-parameter dose-response curve in GraphPad Prism.

Authentic SARS-CoV-2 microplate neutralization

The SARS-CoV-2 viruses USA-WA1/2020 (WA1), USA/CA_CDC_5574/2020 (B.1.1.7), hCoV-19/South Africa/KRISP-EC-K005321/2020 (B.1.351) and hCoV-19/Japan/TY7-503/2021 (P.1) were obtained from BEI Resources (NIAID, NIH) and propagated for one passage using Vero E6 cells. Virus infectious titre was determined by an end-point dilution and cytopathic effect (CPE) assay on Vero E6 cells as previously described⁴². An end-point dilution microplate neutralization assay was performed to measure the neutralization activity of nanobodies. In brief, nanobodies were subjected to successive fivefold dilutions starting from 10 µg ml⁻¹. Triplicates of each dilution were incubated with SARS-CoV-2 at an MOI of 0.1 in EMEM with 7.5% inactivated fetal calf serum for 1 h at 37 °C. After incubation, the virus–nanobody mixture was transferred onto a monolayer of Vero E6 cells grown overnight. The cells were incubated with the mixture for about 70 h. CPE of viral infection was visually scored for each well in a blinded fashion by two independent observers. The results were then reported as percentage of neutralization at a given nanobody dilution.

The IC₅₀ for nanobodies was determined using nonlinear regression (normalized response, variable slope) in GraphPad Prism.

Nanobody stability studies

Nanobody was nebulized with a portable mesh nebulizer (Philips, InnoSpire Go) producing 2–5 µm particles at a final concentration of 0.4 mg ml⁻¹. The resulting aerosol was collected by condensation into a 50-ml tube cooled on ice. Pre- and post-nebulization samples were analysed by NuPAGE gel and visualized by InstantBlue staining. SARS-CoV-2 surrogate virus neutralization test was also performed to compare the neutralization potency of pre- and post-nebulization samples. For thermostability tests, nanobodies supplemented with loading buffer (Thermo Fisher Scientific, NP0007) and β-mercaptoethanol were heated at 98 °C for 10 min and then analysed on a NuPAGE gel and visualized by InstantBlue staining.

BLI assay to measure nanobody affinity

The BLI assay was performed using a fortéBio Octet Red384 instrument to determine the affinity of nanobodies to RBD. In brief, biotinylated-RBD was immobilized onto streptavidin-coated biosensors and then dipped into a solution containing the nanobody for 30 s followed by dissociation for 2–3 min. To assay the binding of nanobodies to RBD–Fc (SARS-CoV, SARS-CoV-2 and WIV16), 6×His-tagged nanobody was immobilized onto Ni-NTA coated biosensors and then dip into RBD–Fc solution for association for 1 min followed by dissociation for 1 min. Sensorgrams of the concentration series were corrected with corresponding blank curves and fitted globally with Octet evaluation software using a 1:1 Langmuir model of binding.

Nanobody–RBD binding competition assay

Nanobody–RBD binding competition assay was performed using a fortéBio Octet Red384 instrument. Biotinylated-RBD was first immobilized onto streptavidin coated biosensors and allowed to associate with one of the six nanobodies, then dipped into a solution contained a second nanobody.

Negative-staining electron microscopy analysis for the structure of nanobody–spike complex

Nanobody–spike complexes were prepared by mixing the two proteins at a 1:1 weight ratio, then diluted with a buffer containing 10 mM HEPES, pH 7.4, 150 mM NaCl, adsorbed to a freshly glow-discharged carbon-coated copper grid, washed with the above buffer, and stained with 0.75% uranyl formate. Images were collected at a

magnification of 57,000 using EPU on a Thermo Fisher Talos F200C microscope equipped with a 4k × 4k CETA 16 M camera and operated at 200 kV. The pixel size was 2.5 Å for the CETA camera. Particle picking, reference-free 2D classification, 3D reconstruction and refinement were performed using cryoSPARC.

Cryo-EM data collection and processing

Nanobody–spike complexes (Nb12–S6P and Nb30–S6P) were prepared by manual mixture of the two proteins in a 1:1 weight ratio, then diluted to a final concentration of 0.5 mg ml⁻¹. Samples (2.7 µl) were applied to a glow-discharged Quantifoil R 2/2 gold grids and vitrified using a Vitrobot Mark IV with a blot time of 3 s before the grid was plunged into liquid ethane. Data were acquired using the Leginon system installed on Titan Krios electron microscopes operating at 300 kV and equipped with a K3-BioQuantum direct detection device. The dose was fractionated over 40 raw frames and collected over a 2-s exposure time. Motion correction, CTF estimation, particle picking, 2D classifications, ab initio model generation, heterogeneous refinements, 3D variability analysis and homogeneous 3D refinements were carried out with cryoSPARC. Local refinement was performed to resolve the RBD–nanobody interface by using a mask encompassing one copy of the RBD–nanobody complex for refinement, after removing the rest of the density by particle subtraction.

Cryo-EM model fitting

For initial fits to the cryo-EM reconstructed maps, we used the coordinates of the SARS-CoV-2 spike from Protein Data Bank (PDB) code 7JZL, and a nanobody model predicted by the ABodyBuilder server⁴⁴. These initial models were docked into the cryo-EM maps using Chimera. The coordinates were then fit to the electron density more precisely through an iterative process of manual fitting using Coot and real space refinement within Phenix, Molprobity and EMRinger were used to check geometry and evaluate structures at each iteration step. Figures were generated in UCSF ChimeraX and PyMOL (<https://pymol.org>). Map-fitting cross correlations were calculated using Fit-in-Map feature in UCSF Chimera. Overall and local resolution of cryo-EM maps was determined using cryoSPARC.

Informatics analysis

Sequence entropy are based on nine strains with the following UniProt identifiers: SARS-CoV-2: P0DTD1, B.1.1.7 and B.1.351; SARS-CoV: A7J8L4, Q202E5 and P59594; and bat SARS-like coronavirus: MG772933, WIV16 (A0A0U2IWM2) and RsSHC014 (U5WLK5). The entropy was calculated for each residue based on aligned sequences with the formula:

$$-\sum_{i=1}^{21} p(x_i) \log(p(x_i))$$

In which x_i are standard amino acids, plus gap.

The buried surface area on the RBD were calculated for 51 human antibody–SARS-CoV-2 RBD complexes using the Naccess program.

Data presentation

Figures arranged in Adobe Illustrator 2020.

Reporting summary

Further information on research design is available in the [Nature Research Reporting Summary](#) linked to this paper.

Data availability

Raw data and original images are provided in Supplementary Table 5 and Supplementary Fig. 1. The accession numbers for the deep-sequencing data reported in this Article can be found at [GSE167310](#). Coordinates and maps for reported cryo-EM structures have been deposited in the Electron Microscopy Data Bank and PDB at [EMD-24078](#) and [EMD-24077](#), and [7MY3](#) and [7MY2](#), respectively. Any other relevant data are available from the corresponding authors upon reasonable request.

References

1. 1.

Wang, Z. et al. mRNA vaccine-elicited antibodies to SARS-CoV-2 and circulating variants. *Nature* **592**, 616–622 (2021).

[ADS](#) [CAS](#) [Article](#) [Google Scholar](#)

2. 2.

Wang, P. et al. Antibody resistance of SARS-CoV-2 variants B.1.351 and B.1.1.7. *Nature* **593**, 130–135 (2021).

[ADS](#) [CAS](#) [Article](#) [Google Scholar](#)

3. 3.

Wu, K. et al. mRNA-1273 vaccine induces neutralizing antibodies against spike mutants from global SARS-CoV-2 variants. Preprint at <https://doi.org/10.1101/2021.01.25.427948> (2021).

4. 4.

Muyldermans, S. Nanobodies: natural single-domain antibodies. *Annu. Rev. Biochem.* **82**, 775–797 (2013).

[CAS](#) [Article](#) [Google Scholar](#)

5. 5.

Muyldermans, S. Applications of nanobodies. *Annu. Rev. Anim. Biosci.* **9**, 401–421 (2021).

[CAS](#) [Article](#) [Google Scholar](#)

6. 6.

Scully, M. et al. Caplacizumab treatment for acquired thrombotic thrombocytopenic purpura. *N. Engl. J. Med.* **380**, 335–346 (2019).

[CAS](#) [Article](#) [Google Scholar](#)

7. 7.

Hussen, J. & Schuberth, H. J. Recent advances in camel immunology. *Front. Immunol.* **11**, 614150 (2021).

[Article](#) [Google Scholar](#)

8. 8.

Kong, R. et al. Antibody lineages with vaccine-induced antigen-binding hotspots develop broad HIV neutralization. *Cell* **178**, 567–584 (2019).

[CAS](#) [Article](#) [Google Scholar](#)

9. 9.

Pham, P., Bransteitter, R., Petruska, J. & Goodman, M. F. Processive AID-catalysed cytosine deamination on single-stranded DNA simulates somatic hypermutation. *Nature* **424**, 103–107 (2003).

[ADS](#) [CAS](#) [Article](#) [Google Scholar](#)

10. 10.

Hsieh, C. L. et al. Structure-based design of prefusion-stabilized SARS-CoV-2 spikes. *Science* **369**, 1501–1505 (2020).

[ADS](#) [CAS](#) [Article](#) [Google Scholar](#)

11. 11.

Robbiani, D. F. et al. Convergent antibody responses to SARS-CoV-2 in convalescent individuals. *Nature* **584**, 437–442 (2020).

[ADS](#) [CAS](#) [Article](#) [Google Scholar](#)

12. 12.

Schoof, M. et al. An ultrapotent synthetic nanobody neutralizes SARS-CoV-2 by stabilizing inactive Spike. *Science* **370**, 1473–1479 (2020).

[ADS](#) [CAS](#) [PubMed](#) [PubMed Central](#) [Google Scholar](#)

13. 13.

Xiang, Y. et al. Versatile and multivalent nanobodies efficiently neutralize SARS-CoV-2. *Science* **370**, 1479–1484 (2020).

[ADS](#) [CAS](#) [PubMed](#) [PubMed Central](#) [Google Scholar](#)

14. 14.

Saelens, X. & Schepens, B. Single-domain antibodies make a difference. *Science* **371**, 681–682 (2021).

[ADS](#) [CAS](#) [Article](#) [Google Scholar](#)

15. 15.

Kupferschmidt, K. Fast-spreading U.K. virus variant raises alarms. *Science* **371**, 9–10 (2021).

[ADS](#) [CAS](#) [Article](#) [Google Scholar](#)

16. 16.

Faria, N. R. et al. Genomics and epidemiology of a novel SARS-CoV-2 lineage in Manaus, Brazil. Preprint at <https://doi.org/10.1101/2021.02.26.21252554> (2021).

17. 17.

Schmidt, F. et al. Measuring SARS-CoV-2 neutralizing antibody activity using pseudotyped and chimeric viruses. *J. Exp. Med.* **217**, e20201181 (2020).

[Article](#) [Google Scholar](#)

18. 18.

Benton, D. J. et al. Receptor binding and priming of the spike protein of SARS-CoV-2 for membrane fusion. *Nature* **588**, 327–330 (2020).

[ADS](#) [CAS](#) [Article](#) [Google Scholar](#)

19. 19.

Lan, J. et al. Structure of the SARS-CoV-2 spike receptor-binding domain bound to the ACE2 receptor. *Nature* **581**, 215–220 (2020).

[ADS](#) [CAS](#) [Article](#) [Google Scholar](#)

20. 20.

Zhou, T. et al. Cryo-EM structures of SARS-CoV-2 spike without and with ACE2 reveal a pH-dependent switch to mediate endosomal positioning of receptor-binding domains. *Cell Host Microbe* **28**, 867–879 (2020).

[CAS](#) [Article](#) [Google Scholar](#)

21. 21.

Wrapp, D. et al. Structural basis for potent neutralization of betacoronaviruses by single-domain camelid antibodies. *Cell* **181**, 1004–1015 (2020).

[CAS](#) [Article](#) [Google Scholar](#)

22. 22.

Koenig, P. A. et al. Structure-guided multivalent nanobodies block SARS-CoV-2 infection and suppress mutational escape. *Science* **371**, eabe6230 (2021).

[CAS](#) [Article](#) [Google Scholar](#)

23. 23.

Janssens, R. et al. Generation of heavy-chain-only antibodies in mice. *Proc. Natl Acad. Sci. USA* **103**, 15130–15135 (2006).

[ADS](#) [CAS](#) [Article](#) [Google Scholar](#)

24. 24.

Han, L., Masani, S. & Yu, K. Overlapping activation-induced cytidine deaminase hotspot motifs in Ig class-switch recombination. *Proc. Natl Acad. Sci. USA* **108**, 11584–11589 (2011).

[ADS](#) [CAS](#) [Article](#) [Google Scholar](#)

25. 25.

Achour, I. et al. Tetrameric and homodimeric camelid IgGs originate from the same IgH locus. *J. Immunol.* **181**, 2001–2009 (2008).

[CAS](#) [Article](#) [Google Scholar](#)

26. 26.

The Bactrian Camels Genome Sequencing and Analysis Consortium. Genome sequences of wild and domestic bactrian camels. *Nat. Commun.* **3**, 1202 (2012).

[ADS](#) [CAS](#) [Article](#) [Google Scholar](#)

27. 27.

Wu, H. et al. Camelid genomes reveal evolution and adaptation to desert environments. *Nat. Commun.* **5**, 5188 (2014).

[ADS](#) [CAS](#) [Article](#) [Google Scholar](#)

28. 28.

Pardon, E. et al. A general protocol for the generation of nanobodies for structural biology. *Nat. Protocols* **9**, 674–693 (2014).

[CAS](#) [Article](#) [Google Scholar](#)

29. 29.

Gaspar, J. M. NGmerge: merging paired-end reads via novel empirically-derived models of sequencing errors. *BMC Bioinformatics* **19**, 536 (2018).

[CAS](#) [Article](#) [Google Scholar](#)

30. 30.

Zhang, X. et al. pTrimmer: an efficient tool to trim primers of multiplex deep sequencing data. *BMC Bioinformatics* **20**, 236 (2019).

[Article](#) [Google Scholar](#)

31. 31.

Chen, S., Zhou, Y., Chen, Y. & Gu, J. fastp: an ultra-fast all-in-one FASTQ preprocessor. *Bioinformatics* **34**, i884–i890 (2018).

[Article](#) [Google Scholar](#)

32. 32.

Ye, J., Ma, N., Madden, T. L. & Ostell, J. M. IgBLAST: an immunoglobulin variable domain sequence analysis tool. *Nucleic Acids Res.* **41**, W34–W40 (2013).

[Article](#) [Google Scholar](#)

33. 33.

Magoč, T. & Salzberg, S. L. FLASH: fast length adjustment of short reads to improve genome assemblies. *Bioinformatics* **27**, 2957–2963 (2011).

[Article](#) [Google Scholar](#)

34. 34.

Dunbar, J. & Deane, C. M. ANARCI: antigen receptor numbering and receptor classification. *Bioinformatics* **32**, 298–300 (2016).

[CAS](#) [Google Scholar](#)

35. 35.

Li, W. & Godzik, A. Cd-hit: a fast program for clustering and comparing large sets of protein or nucleotide sequences.

Bioinformatics **22**, 1658–1659 (2006).

[CAS](#) [Article](#) [Google Scholar](#)

36. 36.

Chuang, G. Y. et al. Structure-based design of a soluble prefusion-closed HIV-1 env trimer with reduced CD4 affinity and improved immunogenicity. *J. Virol.* **91**, e02268-16 (2017).

[Article](#) [Google Scholar](#)

37. 37.

Amanat, F. et al. A serological assay to detect SARS-CoV-2 seroconversion in humans. *Nat. Med.* **26**, 1033–1036 (2020).

[CAS](#) [Article](#) [Google Scholar](#)

38. 38.

Stadlbauer, D. et al. SARS-CoV-2 seroconversion in humans: a detailed protocol for a serological assay, antigen production, and test setup. *Curr. Protoc. Microbiol.* **57**, e100 (2020).

[CAS](#) [Article](#) [Google Scholar](#)

39. 39.

Zhou, T. et al. Structure-based design with tag-based purification and in-process biotinylation enable streamlined development of SARS-CoV-2 spike molecular probes. *Cell Rep.* **33**, 108322 (2020).

40. 40.

Weisblum, Y. et al. Escape from neutralizing antibodies by SARS-CoV-2 spike protein variants. *eLife* **9**, e61312 (2020).

[CAS](#) [Article](#) [Google Scholar](#)

41. 41.

Muecksch, F. et al. Development of potency, breadth and resilience to viral escape mutations in SARS-CoV-2 neutralizing antibodies. Preprint at <https://doi.org/10.1101/2021.03.07.434227> (2021).

42. 42.

Liu, L. et al. Potent neutralizing antibodies against multiple epitopes on SARS-CoV-2 spike. *Nature* **584**, 450–456 (2020).

[CAS](#) [Article](#) [Google Scholar](#)

43. 43.

Wang, P. et al. SARS-CoV-2 neutralizing antibody responses are more robust in patients with severe disease. *Emerg. Microbes Infect.* **9**, 2091–2093 (2020).

[CAS](#) [Article](#) [Google Scholar](#)

44. 44.

Leem, J., Dunbar, J., Georges, G., Shi, J. & Deane, C. M. ABODYBuilder: automated antibody structure prediction with data-driven accuracy estimation. *Mabs* **8**, 1259–1268 (2016).

[CAS](#) [Article](#) [Google Scholar](#)

[Download references](#)

Acknowledgements

We thank S. Dell'Orso for assistance with deep sequencing; J. Simone, K. Tinsley and J. Lay for sorting; M. Laycock for proofreading the manuscript; P. and N.-Y. Wilson for plasmids and reagents; E. Tyler for camelid and mouse drawings; N. Wong for ES cell karyotyping; E. Sounthor for ES cell injections; the Vaccine Production Program of the Vaccine Research Center

for BG505 DS-SOSIP; members of the structural biology section (Vaccine Research Center) for discussions and manuscript feedback. and U. Baxa, A. Wier, M. Hutchison and T. Edwards of the National CryoEM Facility (NCEF) for collecting cryo-EM data and for technical assistance with cryo-EM data processing. This work was supported by NIAMS and NCI funding and the NIH Helix Systems (<http://helix.nih.gov>). This work was supported by the intramural research programme of the Vaccine Research Center, National Institute of Allergy and Infectious Diseases (NIAID) and federal funds from the Frederick National Laboratory for Cancer Research under contract HHSN261200800001E (T.S. and Y.T.). Cryo-EM datasets were collected at the NCEF of the NCI under contract HSSN261200800001E. M.C.N. and P.D.B. are HHMI Investigators.

Author information

Author notes

1. Kai Xu

Present address: Department of Veterinary Biosciences, College of Veterinary Medicine, The Ohio State University, Columbus, OH, USA

2. These authors contributed equally: Jianliang Xu, Kai Xu, Peter D. Kwong, Rafael Casellas

Affiliations

1. Lymphocyte Nuclear Biology, NIAMS, NIH, Bethesda, MD, USA

Jianliang Xu, Seolkyoung Jung, Andrea Conte, Jenna Lieberman, Solji Park & Rafael Casellas

2. Vaccine Research Center, NIAID, NIH, Bethesda, MD, USA

Kai Xu, Tatsiana Bylund, Gwo-Yu Chuang, Adam S. Olia, I-Ting Teng, Tongqing Zhou & Peter D. Kwong

3. Laboratory of Retrovirology, The Rockefeller University, New York, NY, USA

Frauke Muecksch, Fabian Schmidt, Theodora Hatzioannou & Paul D. Bieniasz

4. Laboratory of Molecular Immunology, The Rockefeller University, New York, NY, USA

Julio Cesar Cetrulo Lorenzi, Zijun Wang & Michel C. Nussenzweig

5. Aaron Diamond AIDS Research Center, Columbia University Vagelos College of Physicians and Surgeons, New York, NY, USA

Yaoxing Huang, Yang Luo, Manoj S. Nair, Pengfei Wang & David D. Ho

6. Laboratory of Virology, Division of Intramural Research, NIAID, NIH, Rocky Mountain Laboratories, Hamilton, MT, USA

Jonathan E. Schulz & Vincent Munster

7. Mouse Cancer Genetics Program, CCR, NCI, NIH, Frederick, MD, USA

Lino Tessarollo

8. Electron Microscopy Laboratory, Cancer Research Technology Program, Frederick National Laboratory for Cancer Research sponsored by the National Cancer Institute, Frederick, MD, USA

Tyler Stephens & Yaroslav Tsybovsky

9. Howard Hughes Medical Institute, The Rockefeller University, New York, NY, USA

Paul D. Bieniasz & Michel C. Nussenzweig

10. The NIH Regulome Project, NIH, Bethesda, MD, USA

Rafael Casellas

11. Center for Cancer Research, NCI, NIH, Bethesda, MD, USA

Rafael Casellas

Authors

1. Jianliang Xu

[View author publications](#)

You can also search for this author in [PubMed](#) [Google Scholar](#)

2. Kai Xu

[View author publications](#)

You can also search for this author in [PubMed](#) [Google Scholar](#)

3. Seolkyoung Jung

[View author publications](#)

You can also search for this author in [PubMed](#) [Google Scholar](#)

4. Andrea Conte

[View author publications](#)

You can also search for this author in [PubMed](#) [Google Scholar](#)

5. Jenna Lieberman

[View author publications](#)

You can also search for this author in [PubMed](#) [Google Scholar](#)

6. Frauke Muecksch

[View author publications](#)

You can also search for this author in [PubMed](#) [Google Scholar](#)

7. Julio Cesar Cetrulo Lorenzi

[View author publications](#)

You can also search for this author in [PubMed](#) [Google Scholar](#)

8. Solji Park

[View author publications](#)

You can also search for this author in [PubMed](#) [Google Scholar](#)

9. Fabian Schmidt

[View author publications](#)

You can also search for this author in [PubMed](#) [Google Scholar](#)

10. Zijun Wang

[View author publications](#)

You can also search for this author in [PubMed](#) [Google Scholar](#)

11. Yaxing Huang

[View author publications](#)

You can also search for this author in [PubMed](#) [Google Scholar](#)

12. Yang Luo

[View author publications](#)

You can also search for this author in [PubMed](#) [Google Scholar](#)

13. Manoj S. Nair

[View author publications](#)

You can also search for this author in [PubMed](#) [Google Scholar](#)

14. Pengfei Wang

[View author publications](#)

You can also search for this author in [PubMed](#) [Google Scholar](#)

15. Jonathan E. Schulz

[View author publications](#)

You can also search for this author in [PubMed](#) [Google Scholar](#)

16. Lino Tessarollo

[View author publications](#)

You can also search for this author in [PubMed](#) [Google Scholar](#)

17. Tatsiana Bylund

[View author publications](#)

You can also search for this author in [PubMed](#) [Google Scholar](#)

18. Gwo-Yu Chuang

[View author publications](#)

You can also search for this author in [PubMed](#) [Google Scholar](#)

19. Adam S. Olia

[View author publications](#)

You can also search for this author in [PubMed](#) [Google Scholar](#)

20. Tyler Stephens

[View author publications](#)

You can also search for this author in [PubMed](#) [Google Scholar](#)

21. I-Ting Teng

[View author publications](#)

You can also search for this author in [PubMed](#) [Google Scholar](#)

22. Yaroslav Tsybovsky

[View author publications](#)

You can also search for this author in [PubMed](#) [Google Scholar](#)

23. Tongqing Zhou

[View author publications](#)

You can also search for this author in [PubMed](#) [Google Scholar](#)

24. Vincent Munster

[View author publications](#)

You can also search for this author in [PubMed](#) [Google Scholar](#)

25. David D. Ho

[View author publications](#)

You can also search for this author in [PubMed](#) [Google Scholar](#)

26. Theodora Hatzioannou

[View author publications](#)

You can also search for this author in [PubMed](#) [Google Scholar](#)

27. Paul D. Bieniasz

[View author publications](#)

You can also search for this author in [PubMed](#) [Google Scholar](#)

28. Michel C. Nussenzweig

[View author publications](#)

You can also search for this author in [PubMed](#) [Google Scholar](#)

29. Peter D. Kwong

[View author publications](#)

You can also search for this author in [PubMed](#) [Google Scholar](#)

30. Rafael Casellas

[View author publications](#)

You can also search for this author in [PubMed](#) [Google Scholar](#)

Contributions

J.X., K.X., A.C., J.L., F.M., J.C.C.L., S.P., F.S., Z.W., Y.H., Y.L., M.S.N., P.W. and J.E.S. performed experiments. T.B., G.-Y.C., J.X. and S.J. performed bioinformatic analyses. A.S.O., I-T.T. and T.Z. contributed critical reagents. T.S. and Y.T. assisted with cryo-EM samples and data collection. L.T., J.X., K.X., V.M., D.D.H., T.H., P.D.B., M.C.N., P.D.K. and R.C. designed experiments and discussed results. J.X., K.X., P.D.K. and R.C. wrote the manuscript.

Corresponding authors

Correspondence to [Jianliang Xu](#) or [Michel C. Nussenzweig](#) or [Peter D. Kwong](#) or [Rafael Casellas](#).

Ethics declarations

Competing interests

The National Institutes of Health has filed a provisional patent application in connection with this work on which J.X. and R.C. are inventors (US patent 63-151,530).

Additional information

Peer review information *Nature* thanks Patrick Wilson and the other, anonymous, reviewer(s) for their contribution to the peer review of this work.

Publisher's note Springer Nature remains neutral with regard to jurisdictional claims in published maps and institutional affiliations.

Extended data figures and tables

Extended Data Fig. 1 VHH genes used in the array and gene unit assembly.

Alignment of the 30 VHH genes, highlighting the 100% amino acid conservation (in red) and the 4 hydrophilic amino acids in framework (FR) 2 (in blue). In VH proteins, these latter four amino acids are hydrophobic and mediate the interaction with light chains. Schematics below show the configuration of VHH gene units, composed of a mouse VH promoter (250 bp, containing the octamer and TATA box); mouse leader exons–intron (about 150 bp) encoding the signal peptide cleaved off during heavy chain processing in the endoplasmic reticulum; the camelid VHH open reading frame (about 300 bp); and mouse downstream sequences (100 bp) containing the recombination signal sequences (RSSs).

Extended Data Fig. 2 Igλ expression and recombination frequency of VHH genes.

a, Flow cytometry analysis of Igλ expression in B220⁺IgM⁺ splenic B cells from wild type and heterozygous nanomice. **b**, VHH–DJ recombination was monitored by genomic PCR in bone marrow and spleen samples using an FR1 VHH-specific primer and a second primer downstream of JH4. The expected PCR products for each recombination event between a given VHH and JH1, JH2, JH3 or JH4 are provided. Data are representative of two independent experiments. **c**, Bar graph showing VHH percentage use among splenic B cells in three nanomouse littermates.

Extended Data Fig. 3 B cell development in nanomice.

a, Flow cytometry analysis of bone marrow (left two columns), spleen (third and fourth columns) and peritoneal cavity B cells (last column) in wild-type controls and nanomice. First column shows the percentage of B220-gated CD43⁺IgM⁻ proB and CD43⁻IgM⁺ immature B cells. Second column shows percentage of IgM and Igκ within the B220-gated population. Third column denotes the total number of B220⁺ B cells in the spleen. The y axis shows viability staining with eFluor506 (eBiosciences). The fourth column shows the percentage of B220-gated CD23^{low}CD21^{low}

immature, CD23^{high}CD21^{low} follicular, and CD23^{low}CD21^{high} marginal-zone splenic, cells in the two strains. The last column shows the percentage of B1 (IgM^{high}B220^{low}) and B2 (IgM^{low}B220^{high}) cells in the peritoneal cavity. Examples of gating for bone marrow and splenic B cells is provided in Extended Data Fig. 10d. **b**, Histograms depicting the percentage of Igκ (left), IgD (middle) and IgG1 (right row) in wild-type, nanomice, and *Ighm*-CH1^{-/-} mice. The latter measured in ex vivo cultures treated with LPS, IL-4 and anti-CD180. Population gates are represented with a line and the percentage of total cells is provided. **c**, Proliferation assay of nanomouse and control B cells cultured for 96 h with LPS, IL-4 and anti-CD180. **d**, Immunization regimen. Nanomice were immunized with 50 µg HIV-1 envelope trimer at the indicated dates. **e**, Per cent nucleotide substitutions (adjusted for base composition) observed in nanobodies isolated from immunized nanomice. Phage library was selected for binding to HIV-1 envelope trimer.

Extended Data Fig. 4 Nanomouse immune response to HIV-1 envelope trimer.

a, Top table shows nanobody and JH use for the 16 VHH clones isolated from immunized nanomice. Middle graph shows protein alignment for VHHs isolated from HIV-1 trimer immunized nanomice. CDRs are boxed. Bottom table shows hypermutation profiles for VHH, D and J domains of selected nanobodies. **b**, Left, BLI analysis of BG505 DS-SOSIP binding to immobilized VHH9-1. Red trace represents the raw data, and the kinetic fit is shown in grey underneath. Right, table showing the kinetic constants for association (k_{on}), dissociation (k_{off}) and equilibrium (K_D) for all four VHH9 nanobody variants.

Extended Data Fig. 5 Isolation of anti-SARS-CoV-2 RBD nanobodies.

a, Table indicating (1) the total number of unique nanobody genes identified from llama and three nanomice phage display libraries following selection for RBD binding; (2) the number of nanobodies enriched at least tenfold after selection; (3) the number of nanobodies with a unique CRD3; and (4)

the different clusters of nanobodies that share similar CDR3 s (with no more than 2 amino acid differences). **b**, Table showing in vitro neutralization results for the six leading nanobodies using the sVNT kit of GenScript. **c**, Dot plot depicting the extent of enrichment (y axis) and frequency (x axis) of unique nanobodies after RBD selection of llama (left) or nanomouse 1 (right) libraries. Green circles represent nanobodies that block ACE2–RBD interactions in vitro, black circles are nanobodies that do not efficiently block ACE2–RBD interactions, and grey dots represent untested nanobodies. **d**, Top graph shows protein alignment of the six nanobodies isolated from llama and nanomice immunized with SARS-CoV-2 spike and RBD. Bottom table shows detailed information of the VHH, D and J domains of nanomouse nanobodies. **e**, Table depicting equilibrium (K_D), association (K_{on}) and dissociation (K_{off}) constants obtained for each nanobody as a monomer (black) or trimer (red) form.

Extended Data Fig. 6 Neutralization of pseudo and authentic SARS-CoV-2 viruses.

a, Comparison of neutralization activities of leading nanobodies in monovalent, bivalent or trivalent form (results for monovalent and trivalent reproduced from Fig. [3a](#)). **b**, Neutralization assays for wild-type (WA1) and SARS-CoV-2 variants B.1.1.7 and P.1 for trivalent Nb56, Nb15, Nb12 and bivalent Nb30. Data are representative of two independent experiments. Data are mean \pm s.d. of triplicates. **c**, IC₅₀ neutralization values for experiments shown in Fig. [3b](#) and **b**. Top table values are in pM, lower table values are in ng ml⁻¹. **d**, Related to Fig. [3c–f](#). Immunocomplexes used were Nb17–RBD (left) and Nb19–RBD (right). **e**, Coomassie staining showing nanobody integrity following nebulization. With the exception of Nb30 (bivalent), all nanobodies were fused to Fcs as trimers. Data are representative of two independent experiments. **f**, Bar graph showing in vitro neutralization (percentage) of RBD–ACE2 interactions by the different trivalent nanobody (bivalent for Nb30) before and after nebulization at two different concentrations (0.1 µg ml⁻¹ (blue) and 0.02 µg ml⁻¹ (orange)). **g**, Coomassie staining showing integrity of nanobody monomers (left) or multimers (right) following heat treatment (98 °C for 10 min). Data are representative of two independent experiments.

Extended Data Fig. 7 Cryo-EM data processing and validation for Nb12–spike complex.

a, A representative cryo-EM micrograph showing Nb12–spike complex embedded in vitreous ice. **b**, A contrast-transfer function (CTF) fit of the micrograph. **c**, Representative 2D average classes. **d**, Overall resolution estimation (Fourier shell correlation (FSC) of 0.143). **e**, Local resolution estimation of the cryo-EM map. **f**, Cryo-EM density and models for an interface region between RBD and Nb12 after local refinement.

Extended Data Fig. 8 Cryo-EM data processing and validation for Nb30–spike complex.

a, A representative cryo-EM micrograph showing Nb30–spike complex embedded in vitreous ice. **b**, A CTF fit of the micrograph. **c**, Representative 2D average classes. **d**, Overall resolution estimation (FSC of 0.143). **e**, Local resolution estimation of the cryo-EM map. **f**, Cryo-EM density and models for an interface region between RBD and Nb30 after local refinement.

Extended Data Fig. 9 Structural analysis of nanomice and llama nanobody interface with the SARS-CoV-2 spike.

a, Structure of Nb12 and RBD region (inset, interface between Nb12 and RBD with contact residues shown in stick representation). **b**, Structure of Nb30 and RBD region (inset, interface between Nb30 and RBD with contact residues shown as stick representation). **c**, Cryo-EM defined structures of nanomouse nanobodies recognize regions on RBD distal from residues 417, 484 and 501 (affected by mutations in emerging variants). **d**, SARS-CoV-2 spike (HexaPro) structure in two perpendicular views. **e**, Spike–Nb15 (red) complex structure in two perpendicular views. **f**, Spike–Nb17 (light green) complex structure in two perpendicular views. **g**, Spike–Nb19 (dark green) complex structure in two perpendicular views. **h**, Spike–Nb56 (purple) complex structure in two perpendicular views.

Extended Data Fig. 10 Binding and neutralization of sarbecoviruses by nanomouse nanobodies and gating strategy for nanomouse and wild-type B cells.

a, Neutralization using trivalent Nb56 and Nb12, and bivalent Nb30, against pseudoviruses carrying SARS-CoV (left) or bat coronavirus WIV16 (right) spikes. Data are representative of two independent experiments and the error bars are mean \pm s.d. of triplicates. **b**, BLI analysis of trivalent Nb56 and Nb12, and bivalent Nb30, binding to immobilized RBD from SARS-CoV-2 (left), SARS-CoV (middle) and bat coronavirus WIV16 (right). Equilibrium (K_D) constants are provided. **c**, IC₅₀ (pM) values for neutralization in culture assays, showing the sensitivity of HIV-1 and VSV pseudotyped viruses containing 13 sarbecoviral spike proteins. **d**, Analysis of bone marrow (top) or splenic (bottom) B cells was done by gating lymphocytes (first plot), avoiding aggregates (plots 2 and 3), B220⁺apoptotic⁻ gating (plot 4), and visualization with cell-surface makers as indicated (plots 5 and 6).

Supplementary information

Supplementary Figure 1

Original, uncropped images of the gels used in Extended Data Fig. 2b and Extended Data Fig. 7.

Reporting Summary

Supplementary Table 1

Raw data used to calculate SHM pre- and post-immunization (shown in Fig. 1d) and numbers of VHVs obtained by deep-sequencing used to create the bar graph shown in Extended Data Fig. 2c.

Supplementary Table 2

Data collection and refinement statistics for cryoEM experiments.

Supplementary Table 3

Surface area of RBD residues buried by 51 human antibodies.

Supplementary Table 4

A list of all oligos used in the current study.

Supplementary Table 5

The raw data used to calculate SHM pre- and post-immunization (shown in Fig. 1d) and numbers of VHVs obtained by deep-sequencing used to create the bar graph shown in Extended Data Fig. 2c.

Rights and permissions

Open Access This article is licensed under a Creative Commons Attribution 4.0 International License, which permits use, sharing, adaptation, distribution and reproduction in any medium or format, as long as you give appropriate credit to the original author(s) and the source, provide a link to the Creative Commons license, and indicate if changes were made. The images or other third party material in this article are included in the article's Creative Commons license, unless indicated otherwise in a credit line to the material. If material is not included in the article's Creative Commons license and your intended use is not permitted by statutory regulation or exceeds the permitted use, you will need to obtain permission directly from the copyright holder. To view a copy of this license, visit <http://creativecommons.org/licenses/by/4.0/>.

Reprints and Permissions

About this article



Cite this article

Xu, J., Xu, K., Jung, S. *et al.* Nanobodies from camelid mice and llamas neutralize SARS-CoV-2 variants. *Nature* **595**, 278–282 (2021).
<https://doi.org/10.1038/s41586-021-03676-z>

[Download citation](#)

- Received: 04 March 2021
- Accepted: 27 May 2021
- Published: 07 June 2021
- Issue Date: 08 July 2021
- DOI: <https://doi.org/10.1038/s41586-021-03676-z>

Comments

By submitting a comment you agree to abide by our [Terms](#) and [Community Guidelines](#). If you find something abusive or that does not comply with our terms or guidelines please flag it as inappropriate.

[Download PDF](#)

Associated Content

Collection

[Coronavirus](#)

Engineered single-domain antibodies tackle COVID variants

- James E. Voss

Advertisement

This article was downloaded by **calibre** from <https://www.nature.com/articles/s41586-021-03676-z>

| [Section menu](#) | [Main menu](#) |

Diverse functional autoantibodies in patients with COVID-19

[Download PDF](#)

- Article
- [Published: 19 May 2021](#)

Diverse functional autoantibodies in patients with COVID-19

- [Eric Y. Wang](#) [ORCID: orcid.org/0000-0002-6120-5136¹](#),
[Tianyang Mao](#) [ORCID: orcid.org/0000-0001-9251-8592¹](#),
- [Jon Klein](#) [ORCID: orcid.org/0000-0002-3552-7684¹](#),
- [Yile Dai](#) [ORCID: orcid.org/0000-0002-7761-3361¹](#),
- [John D. Huck¹](#),
- [Jillian R. Jaycox¹](#),
- [Feimei Liu](#) [ORCID: orcid.org/0000-0003-2663-6544¹](#),
- [Ting Zhou](#) [ORCID: orcid.org/0000-0001-8783-8380¹](#),
- [Benjamin Israelow¹](#),
- [Patrick Wong¹](#),
- [Andreas Coppi²](#),
- [Carolina Lucas](#) [ORCID: orcid.org/0000-0003-4590-2756¹](#),
- [Julio Silva](#) [ORCID: orcid.org/0000-0001-8212-7440¹](#),
- [Ji Eun Oh](#) [ORCID: orcid.org/0000-0003-2511-7064¹](#),
- [Eric Song](#) [ORCID: orcid.org/0000-0001-5448-5865¹](#),
- [Emily S. Perotti¹](#),
- [Neil S. Zheng¹](#),
- [Suzanne Fischer¹](#),
- [Melissa Campbell³](#),
- [John B. Fournier³](#),
- [Anne L. Wyllie](#) [ORCID: orcid.org/0000-0001-6015-0279⁴](#),
- [Chantal B. F. Vogels⁴](#),
- [Isabel M. Ott⁴](#),
- [Chaney C. Kalinich⁴](#),
- [Mary E. Petrone⁴](#),
- [Anne E. Watkins⁴](#),
- [Yale IMPACT Team](#),

- [Charles Dela Cruz](#) ORCID: [orcid.org/0000-0002-5258-1797⁵](https://orcid.org/0000-0002-5258-1797),
- [Shelli F. Farhadian](#) ORCID: [orcid.org/0000-0001-7230-1409³](https://orcid.org/0000-0001-7230-1409),
- [Wade L. Schulz](#) ORCID: [orcid.org/0000-0002-2048-4028^{2,6}](https://orcid.org/0000-0002-2048-4028),
- [Shuangge Ma⁷](#),
- [Nathan D. Grubaugh⁴](#),
- [Albert I. Ko](#) ORCID: [orcid.org/0000-0001-9023-2339^{3,4}](https://orcid.org/0000-0001-9023-2339),
- [Akiko Iwasaki](#) ORCID: [orcid.org/0000-0002-7824-9856^{1,4,8}](https://orcid.org/0000-0002-7824-9856) &
- [Aaron M. Ring](#) ORCID: [orcid.org/0000-0003-3699-2446^{1,9}](https://orcid.org/0000-0003-3699-2446)

Nature volume 595, pages 283–288 (2021)[Cite this article](#)

- 47k Accesses
- 1 Citations
- 795 Altmetric
- [Metrics details](#)

Subjects

- [Applied immunology](#)
- [Autoimmunity](#)
- [SARS-CoV-2](#)
- [Viral infection](#)

Abstract

COVID-19 manifests with a wide spectrum of clinical phenotypes that are characterized by exaggerated and misdirected host immune responses^{1,2,3,4,5,6}. Although pathological innate immune activation is well-documented in severe disease¹, the effect of autoantibodies on disease progression is less well-defined. Here we use a high-throughput autoantibody discovery technique known as rapid extracellular antigen profiling⁷ to screen a cohort of 194 individuals infected with SARS-CoV-2, comprising 172 patients with COVID-19 and 22 healthcare workers with mild disease or asymptomatic infection, for autoantibodies against 2,770 extracellular and secreted proteins (members of the exoproteome). We found that patients with COVID-19 exhibit marked increases in autoantibody reactivities as compared to uninfected individuals, and show a high prevalence of autoantibodies against immunomodulatory proteins (including cytokines, chemokines, complement components and cell-surface proteins). We established that these autoantibodies

perturb immune function and impair virological control by inhibiting immunoreceptor signalling and by altering peripheral immune cell composition, and found that mouse surrogates of these autoantibodies increase disease severity in a mouse model of SARS-CoV-2 infection. Our analysis of autoantibodies against tissue-associated antigens revealed associations with specific clinical characteristics. Our findings suggest a pathological role for exoproteome-directed autoantibodies in COVID-19, with diverse effects on immune functionality and associations with clinical outcomes.

[Download PDF](#)

Main

Humoral immunity has dichotomous roles in COVID-19. Although neutralizing antibodies protect against SARS-CoV-2 infection^{8,9}, growing evidence suggests that dysregulated humoral immunity also contributes to the characteristic immunopathology of COVID-19^{10,11,12,13,14,15,16}. Recent reports have identified isolated autoantibody reactivities in patients with COVID-19, including reactivities that are characteristic of systemic autoimmune diseases^{11,12,13,14,15}. Importantly, some autoantibodies—particularly neutralizing autoantibodies against type I interferons (IFNs)—appear to directly contribute to COVID-19 pathophysiology by antagonizing innate antiviral responses^{11,12}. Although notable examples of disease-modifying autoantibody responses have previously been described, the full breadth of autoantibody reactivities in COVID-19 remains undetermined, as does their immunological and clinical effects.

A particularly important class of autoantibodies are those that target the exoproteome. Exoproteome-targeting autoantibodies can exert a wide range of functional effects, such as the perturbation of cell signalling (as with the case of autoantibodies against type I IFNs^{11,12}) and targeted killing of specific cell populations via Fc receptors (FcR) and/or complement. We thus sought to identify functional autoantibody responses in patients with COVID-19 by screening for autoantibody reactivities against the human exoproteome.

Widespread autoantibody increases in COVID-19

To discover functional autoantibodies that could influence the outcome of COVID-19, we used a high-throughput autoantibody discovery method known as rapid extracellular antigen profiling (REAP)⁷. REAP enables the highly multiplexed detection of antibody reactivities through the biopanning of IgG from patients against a genetically barcoded library of 2,770 human extracellular proteins displayed on the surface of yeast, converting an antibody–antigen binding event into a quantitative

sequencing readout (the REAP score) on the basis of the enrichment of the barcodes of each protein (Extended Data Fig. 1a). To allow for the detection of antibodies against coronavirus proteins, we additionally included the receptor-binding domain (RBD) of SARS-CoV-2 and other common coronaviruses in the library (a full antigen list is provided in Supplementary Table 1).

We used REAP to screen samples from patients infected with SARS-CoV-2 who were prospectively followed as part of the ‘Yale Implementing Medical and Public Health Action Against Coronavirus CT’ (IMPACT) study (Extended Data Fig. 1b). This cohort includes 172 patients who were seen at Yale–New Haven Hospital with a range of clinical severities (as previously reported¹) and 22 healthcare workers who had mild illness or asymptomatic infection. We screened longitudinal samples for a subset of the cohort. As a control, we screened 30 healthcare workers who tested negative for SARS-CoV-2 by qPCR with reverse transcription (RT–qPCR) throughout their follow-up period in the IMPACT study. Patient demographics can be found in Extended Data Table 1. To validate the performance of REAP, we compared antibody reactivity to SARS-CoV-2 RBD using REAP to that evaluated using enzyme-linked immunosorbent assays (ELISAs) (Extended Data Fig. 1c), and also compared IL-6R REAP reactivity in patients who received anti-IL-6R therapeutic antibodies with those who did not (Extended Data Fig. 1d). We found a strong concordance between REAP scores for SARS-CoV-2 RBD and ELISA positivity for SARS-CoV-2 RBD, as well as between IL-6R REAP scores and anti-IL-6R treatment.

Next, we examined the total degree of autoreactivity in patients by quantifying the number of autoantibodies at different REAP score thresholds. Irrespective of the REAP score cut off we used, patients with COVID-19 had a greater number of reactivities compared to uninfected individuals, and the highest scoring reactivities were preferentially enriched in patients with severe disease (Fig. 1a,b, Extended Data Fig. 2a). There was not a statistically significant difference in days from symptom onset between patients with severe or moderate COVID-19 (Extended Data Fig. 2b), which suggests that the effects of temporal confounding were minimal. As sex differences in the immune response to SARS-CoV-2 have previously been reported¹⁷, we compared the number of autoantibody reactivities between men and women with COVID-19 and found no significant differences in reactivity numbers at any score cut off (Extended Data Fig. 2c). Finally, in a comparison with the REAP profiles of patients with systemic lupus erythematosus (SLE) or autoimmune polyendocrinopathy–candidiasis–ectodermal dystrophy (APECED), patients with COVID-19 had greater numbers of reactivities than did individuals with SLE but fewer numbers of reactivities than did individuals with APECED (Extended Data Fig. 2d). The demographics and clinical characteristics of patients with SLE or APECED have previously been described⁷. Altogether, these results indicate that autoantibodies that target the exoproteome are increased in COVID-19.

Fig. 1: Immune-targeting autoantibodies are increased in patients with COVID-19.

 figure1

a. Heat map of REAP scores for immune-related proteins and RBDs of the indicated coronaviruses, across all patient samples and stratified by disease severity. CSF, cerebrospinal fluid; gran., granulocyte; mono./lympho., monocytes and lymphocytes;

NK, natural killer. **b**, **c**, Number of positive (REAP score ≥ 6) total reactivities (**b**) and immune-targeting reactivities (**c**) in samples from patients with severe disease ($n = 66$), moderate disease ($n = 160$) or mild or asymptomatic disease ($n = 36$), and uninfected individuals (negative) ($n = 54$). Dashed lines indicate medians; dotted lines indicate first and third quartiles. NS, not significant. **d**, Score plot of principal component (PC) analysis performed on immune-targeting reactivities in samples from patients who were hospitalized with COVID-19 ($n = 226$), coloured by clinical score (CS). **e**, Loadings for the first (left) and second (right) principal components from **d** in descending order. In **b–d**, n values include longitudinal samples from the same patient. Significance in **b**, **c** was determined using a linear mixed model with correction for multiple comparisons (Methods).

[Source data](#)

[Full size image](#)

To investigate the temporal nature of these reactivities relative to the progression of COVID-19, we assessed longitudinal REAP score dynamics. Although definitive assignment was not possible owing to lack of pre-infection samples, we inferred reactivities as ‘likely pre-existing’, ‘newly acquired’ or ‘waning’ on the basis of REAP score trajectories plotted against days from symptom onset and the development of anti-spike S1 IgG. We found that some reactivities were present with high REAP scores within 10 days of symptom onset and before the development of anti-spike S1 IgG responses, which suggests that they were probably pre-existing (Extended Data Fig. [3a, d](#)). Others increased in score and tracked with increasing anti-spike S1 IgG levels, which indicates that they were newly acquired after infection (Extended Data Fig. [3b, e](#)). Finally, some reactivities decreased in REAP score over time while anti-spike S1 IgG increased or remained high, which suggests waning autoantibody titres (Extended Data Fig. [3c, f](#)).

To further explore the potential cellular sources of the increased autoantibody reactivities in patients with COVID-19, we examined B cell phenotypes in peripheral blood mononuclear cells that matched the REAP plasma samples. Similar to previous reports^{[10](#)}, we found that extrafollicular double-negative B cells are expanded in patients with moderate or severe COVID-19, as compared to uninfected individuals (Extended Data Fig. [2f](#)).

Autoantibodies target immune-related proteins

Our analysis of the specific reactivities detected by REAP indicated that autoantibodies targeting immune-related proteins were increased in patients with severe COVID-19 (Fig. [1a, c](#), Extended Data Fig. [2e](#)). These proteins included those

involved in lymphocyte function and activation, leukocyte trafficking, the type I and type III IFN responses, type II immunity and the acute phase response. Confirming a previous report¹¹, we identified autoantibodies against type I IFNs in 5.2% of patients who were hospitalized with COVID-19. Using an ELISA, we orthogonally validated a subset of 22 autoantibodies that target cytokines, chemokines, growth factors, complement factors and cell-surface proteins (Extended Data Fig. 4a–d). These results demonstrate that patients with COVID-19 possess autoantibodies that may affect a wide range of immunological functions.

To uncover the low-dimensional features in immune-targeting reactivities, we performed a principal component analysis (Fig. 1d,e, Extended Data Fig. 4e). We found that the first principal component was primarily composed of autoantibody reactivities against type I IFNs (Fig. 1e) and separated a distinct cluster of samples from individuals with a severe disease phenotype (Fig. 1d), consistent with a previous report¹¹. The second principal component comprised autoantibody reactivities against cytokines, chemokines and the type III IFNs IFNλ2 and IFNλ3 (Fig. 1e). Notably, the severity of COVID-19 disease was a significant predictor of second principal component score (Extended Data Fig. 4f,g). These findings suggest that autoantibodies against cytokines and chemokines may contribute to disease severity in COVID-19.

Virological and immunological autoantibody effects

Because autoantibodies in patients may influence circulating concentrations of their target proteins, we examined the plasma concentrations of cytokines and chemokines in patients with autoantibodies against these proteins. In some cases, autoantibodies were associated with apparent increases in their autoantigen targets (Extended Data Fig. 5b,f,j,m), whereas in other cases they correlated with apparent decreases (Extended Data Fig. 5k,l).

To more directly assess potential immunomodulatory effects of cytokine- and chemokine-targeting autoantibodies in patients with COVID-19, we assessed the in vitro activity of selected autoantibodies. We found that IgG from patients with anti-GM-CSF, anti-CXCL1 or anti-CXCL7 autoantibodies could antagonize the signalling of GM-CSF, CXCL1 and CXCL7, respectively (Fig. 2a,b). In addition, we found that plasma or IgG from patients with anti-CD38 or anti-CD3ε autoantibodies led to increased antibody-dependent cellular phagocytosis by macrophages of Raji B cells or Jurkat T cells, respectively (Fig. 2c, Extended Data Fig. 4h,i). These results demonstrate that immune-targeting autoantibodies in patients with COVID-19 can directly inhibit the activity of cytokines and chemokines, and engage FcR effector functions that could lead to immune-cell depletions in affected patients.

Fig. 2: Immune-targeting autoantibodies in patients with COVID-19 have functional effects.

 figure2

a, GM-CSF signalling assay performed with IgG from a patient with COVID-19 who was positive for anti-GM-CSF autoantibody (pink circles) and two uninfected healthcare workers (grey squares). Results are averages of technical duplicates from one experiment. **b**, CXCL1 (left) and CXCL7 (right) signalling assays performed with IgG from patients with COVID-19 who were positive for anti-CXCL1 or anti-CXCL7 autoantibody (AAb) and from healthcare workers (HCWs). Results are averages of three technical replicates or duplicates. RLU, relative luminescence unit. **c**, Macrophage phagocytosis assay performed with Raji (left) or Jurkat (right) cells, using plasma or IgG from patients with COVID-19 who were positive for anti-CD38 or anti-CD3 ε autoantibody, respectively, anti-CD38 or anti-CD3 ε monoclonal antibodies (positive controls), and plasma or IgG from healthcare workers, respectively ($n = 1$ for all groups). Technical replicates are shown. Results in **b**, **c** are representative of two independent experiments. **d**, Longitudinal comparisons of SARS-CoV-2 viral load between patients with (positive) and without (negative) autoantibodies against type I IFNs. Linear regressions (solid lines) and 95% confidence bands (shaded areas) for each group are displayed. d, day. n values include longitudinal samples from the same patient. **e–g**, Average per cent B cells (**e**), relative proportions of classical, intermediate and nonclassical monocytes (**f**) and average per cent CD4 $^+$ T cells (**g**) among peripheral leukocytes in healthcare workers and patients with COVID-19 stratified by disease severity and positive REAP reactivity (autoantibody-positive) (REAP score ≥ 2) against B-cell-displayed proteins (CD38, Fc μ R and FCRL3) (**e**),

proteins preferentially displayed on classical and intermediate monocytes (CCR2, CCRL2, FFAR4, SYND4 and CPAMD8) (**f**) and CD3 ε (**g**), respectively. Gating strategies for **e–g** are shown in Extended Data Fig. [8](#). Data from **e, g** are presented as box plots with the first quartile, median, third quartile, whiskers (minimum and maximum values within the first or third quartiles $\pm 1.5 \times$ the interquartile range), and individual data points indicated. Significance was determined using a generalized linear mixed model (**d**) (Methods) or a two-sided Wilcoxon rank-sum test (**e**). In **b, c, e–g**, *n* values indicate samples from unique patients. All error bars represent s.d.

[Source data](#)

[Full size image](#)

To investigate the potential virological effects of cytokine- and chemokine-targeting autoantibodies, we examined a subset of patients with COVID-19 with autoantibodies against type I IFNs. Consistent with previous reports^{[11](#)}, we found that these autoantibodies can neutralize the signalling activity of type I IFNs in vitro (Extended Data Fig. [4j, k](#)). To further assess the functional effects of these autoantibodies, we compared longitudinal composite viral loads in patients who had autoantibodies against type I IFNs to those who did not. After controlling for the contributions of age, sex, days from symptom onset and anti-SARS-CoV-2 IgG responses, patients with autoantibodies against type I IFNs had significantly increased average viral loads relative to patients who lacked these autoantibodies (Fig. [2d](#), Extended Data Fig. [4l](#)). We also found that patients with autoantibodies against type I IFNs had extended durations of hospital admission relative to those who did not (Extended Data Fig. [4m](#)). These results indicate that autoantibodies against type I IFNs impair virological clearance in patients with COVID-19.

To investigate the *in vivo* effects of autoantibodies against immune-cell surface proteins in COVID-19, we looked for associations between these autoantibodies and blood leukocyte composition. First, we focused on two groups of antigens: those expressed on B cells (CD38, Fc μ R and FcRL3) and those preferentially expressed on classical and intermediate monocytes (CCR2, CCRL2, FFAR4, SYND4 and CPAMD8, which we identified from a public RNA-sequencing dataset^{[18](#)}). We found that patients with autoantibodies against B cell or classical- and intermediate-monocyte antigens had lower frequencies of B cells (Fig. [2e](#)) and anti-SARS-CoV-2-RBD IgM (Extended Data Fig. [6a](#)) or classical and intermediate monocytes (Fig. [2f](#), Extended Data Fig. [6b](#)), respectively, as compared to patients who were matched for disease severity but negative for these autoantibodies. Looking at individual reactivities, we found that a patient with anti-CD3 ε autoantibodies had intact B and natural killer cell compartments but markedly reduced levels of CD4 $^+$, CD8 $^+$ and natural killer T cells (Fig. [2g](#), Extended Data Fig. [6c, d](#)). Similarly, a patient with anti-CD38 autoantibodies exhibited a lower frequency of natural killer cells and activated

CD4⁺ or CD8⁺ T cells, all of which also express CD38 (Extended Data Fig. 6f). Of note, we found that IgG or plasma from these patients could mediate antibody-dependent cellular phagocytosis against Jurkat or Raji cells, respectively, in vitro (Fig. 2c). In aggregate, these data show that autoantibodies that target immune-cell surface proteins may lead to the depletion of specific immune-cell populations in patients with COVID-19.

Autoantibodies increase disease severity in mice

To directly assess the effect of cytokine-targeting autoantibodies in the pathogenesis of COVID-19 in vivo, we used mice that transgenically express human ACE2 under the human keratin 18 promoter (K18-hACE2 mice) to recapitulate aspects of COVID-19 pathogenesis in humans upon SARS-CoV-2 infection^{19,20,21}. Given the enrichment of autoantibodies targeting type I IFNs in patients with severe COVID-19, we first examined the effect of antibody-mediated blockade of type I IFNs in vivo. We found that mice that were pretreated with neutralizing antibodies against IFNAR (the interferon- α/β receptor) were more susceptible to SARS-CoV-2 infection; they had increased weight loss (Fig. 3a) and reduced survival (Fig. 3b). Additionally, compared to mice infected with SARS-CoV-2 that were treated with phosphate-buffered saline (PBS), infected mice treated with anti-IFNAR exhibited impaired monocyte recruitment, maturation and proinflammatory macrophage differentiation in the lungs (Extended Data Fig. 7b–d), as well as marked decreases in the relative frequency and absolute number of activated (CD44⁺CD69⁺) natural killer cells and CD4⁺, CD8⁺ and $\gamma\delta$ T cells (Extended Data Fig. 7e,f). Collectively, these findings demonstrate that the early blockade of type I IFN signalling by antibodies (which mimics the effects of pre-existing autoantibodies targeting type I IFNs) results in exacerbated disease and interferes with myeloid and lymphoid activation in response to SARS-CoV-2 infection.

Fig. 3: Immune-targeting autoantibodies increase disease severity in a mouse model of COVID-19.

 **figure3**

a–g, K18-hACE2 mice were intranasally infected with a sublethal dose (**b, c**) or median lethal dose (**d–g**) of SARS-CoV-2 (USA-WA1/2020 isolate), and treated with indicated antibodies (administered intraperitoneally at the indicated dose per mouse at the time points indicated in **a**). **b, c**, Normalized body weight (**b**) and survival defined as 10% weight loss or mortality (**c**) of K18-hACE2 mice treated with PBS or anti-IFNAR from day 1 to 14 after infection. **d–g**, Survival defined as 20% weight loss or mortality of K18-hACE2 mice treated with anti-IL-18 (**d**), anti-IL-1 β (**e**), anti-IL-21R (**f**), anti-GM-CSF (**g**) or PBS-treated from day 1 to 14 after infection. Significance in **c–g** was determined using log-rank (Mantel–Cox) test. All error bars are s.e.m. All *n* values indicate biologically independent mice, examined over two independent experiments.

[Source data](#)

[Full size image](#)

Beyond type I IFNs, we identified patients with COVID-19 with autoantibodies that target components of the interleukin-18 (IL-18) pathway (in particular, IL-18R β) (Extended Data Fig. [4d](#)), which has a critical role in antiviral responses of natural killer and CD8 $^{+}$ T cells^{[22,23](#)}. To examine the effect of disruptions to the IL-18 pathway in SARS-CoV-2 infection, we administered neutralizing anti-IL-18 antibodies to K18-hACE2 mice immediately before infection. We found that IL-18 blockade greatly enhanced susceptibility of these mice to SARS-CoV-2 infection (Fig. [3d](#), Extended

Data Fig. 7k), resulted in a significantly higher viral burden (Extended Data Fig. 7g, h) and led to a decreased frequency and number of effector natural killer cells with enhanced cytotoxic properties (CD11b⁺ or KLRG1⁺) (Extended Data Fig. 7i, j). These results highlight the disruptive role that autoantibody-mediated blockade of IL-18 can have in the immune response to SARS-CoV-2.

Furthermore, we identified IL-1 β , IL-21 and GM-CSF as cytokine autoantibody targets in patients with COVID-19. IL-1 β and IL-21 both participate directly in host antiviral defence^{24,25}, and IL-21 is a major contributor to the second principal component in our principal component analysis of immune-targeting autoantibodies in COVID-19 (Fig. 1e). GM-CSF has a critical role in augmenting innate antiviral defence mediated by alveolar macrophages²⁶. Consistent with the antiviral properties of these three cytokines, we found that mice that received anti-IL-1 β , anti-IL-21R or anti-GM-CSF antibodies became substantially more susceptible to SARS-CoV-2 infection, as they had significantly decreased survival (Fig. 3e–g) and lost more weight (Extended Data Fig. 7l–n) upon SARS-CoV-2 infection than did mice treated with PBS.

Tissue-targeting autoantibody correlations

In addition to immune-targeting autoantibodies, we also observed a high prevalence of tissue-associated autoantibodies in patients with COVID-19 (Fig. 4a). These autoantibodies were directed against vascular cells, coagulation factors and platelets, connective tissue, extracellular matrix components and various organ systems, including lung, the central nervous system compartment, skin, gastrointestinal tract and other tissues. To assess whether any of these putative autoantigens were associated with significant perturbations in clinical phenotype, we performed exploratory data analysis using a common, generalized linear mixed-effects model (Extended Data Fig. 9). We found that some of the autoantigens (such as NXPH1, PCSK1, SLC2A10 and DCD) significantly correlated with clinical markers that are known to be associated with an increased severity of COVID-19 disease (such as d-dimer, ferritin, C-reactive protein and lactate)^{27,28}. Given the extent of autoantigens specific to the central nervous system that we identified in our REAP screen, and previous reports on the potential for SARS-CoV-2 neuroinvasion²⁹, we further examined whether any of the autoantibodies correlated with the Glasgow Coma Scale scores of any of the patients. We found that ten patients with COVID-19 developed autoantibodies against HCRTR2, which is an orexin receptor that is enriched in the hypothalamus. We noted a marked negative correlation between levels of HCRTR2 autoantibodies in these patients and exceptionally low Glasgow coma scale scores, encompassing the time of sample collection (Fig. 4b). Furthermore, we validated the presence of these autoantibodies in two patients using an ELISA (Fig. 4c) and, using an in vitro orexin

signalling assay, found that HCRTR2 autoantibodies in one patient antagonized HCRTR2 activity (Fig. 4d).

Fig. 4: Autoantibodies against tissue-associated antigens are prevalent and functional in patients with COVID-19.

 figure4



a, Heat map of tissue-associated REAP scores stratified by disease severity. CNS, central nervous system; coag., coagulation factors; GI, gastrointestinal; pleio., pleiotropic. **b**, Correlation of HCRTR2 REAP scores with Glasgow Coma Scale (GCS) scores in patients with COVID-19 ($n = 89$, Spearman's $\rho = -0.20$, $P = 0.052$).

Linear regression (solid lines) and 95% confidence bands (shaded areas) are displayed. Patients are coloured by clinical score. Significance of Spearman's correlation was determined via asymptotic *t*-approximation with a two-sided test. **c**, Single-point pan-IgG HCRTR2 autoantibody ELISA conducted with 1:50 plasma dilution. Dotted line represents average of uninfected individuals (healthcare workers) + 3 s.d. Results are averages of technical duplicates from one experiment. OD, optical density. **d**, Orexin signalling assay performed with IgG from patients with COVID-19 who were positive for anti-HCRTR2 autoantibody and from healthcare workers. Results are averages of three technical replicates from one experiment. All *n* values indicate samples from unique patients. All error bars represent s.d.

[Source data](#)

[Full size image](#)

Discussion

The extent of autoantibody reactivities seen in patients with COVID-19 suggests that humoral immunopathology is an intrinsic aspect of the pathogenesis of COVID-19. Screening patient samples with the REAP platform, we have identified and validated numerous protein targets across a wide range of tissues and immunological and physiological functions. These autoantibodies had potent functional activities and could be directly correlated with various virological, immunological and clinical parameters *in vivo* within samples from patients with COVID-19. Our analysis of REAP score trajectories and comparisons to SARS-CoV-2 humoral responses suggest that some of these autoantibodies probably predated infection, whereas others were induced after infection. Furthermore, mouse surrogates of these autoantibodies led to increased disease severity in a mouse model of SARS-CoV-2 infection. These results provide evidence that autoantibodies are capable of altering the course of COVID-19 by perturbing the immune response to SARS-CoV-2 and tissue homeostasis.

The diversity of autoantibody responses in patients with COVID-19 also underscores the importance of high-throughput and unbiased proteome-scale surveys for autoantibody targets. Beyond validating the biologically compelling example of autoantibodies targeting type I IFNs in COVID-19, our studies implicated numerous other immune pathways that are targeted by autoantibodies in COVID-19. We also detected autoantibodies against various tissue-associated antigens and identified correlations between these autoantibodies and inflammatory clinical markers such as d-dimer, ferritin, C-reactive protein and lactate in patients with COVID-19. Many of the tissue autoantibodies that we identified were also present across diverse physiological compartments that have frequently been implicated in post-COVID-19 syndrome³⁰. For example, we identified autoantibodies against the orexin receptor

HCRTR2 that—ex vivo—could inhibit orexin signalling, which has an important role in regulating wakefulness and appetite³¹. Ultimately, whether the specific autoantibodies identified here have a role in the establishment of post-COVID-19 syndrome, and whether they persist beyond the acute phase of COVID-19, warrants further investigation.

In summary, our analyses have revealed an expansive autoantibody landscape in patients with COVID-19 and identified distinct autoantibodies that exerted notable immunological and clinical outcomes. These results implicate previously underappreciated immunological pathways in the aetiology of COVID-19 and suggest therapeutic paradigms that are centred around modulating these pathways—as well as attenuating the autoantibodies themselves. Finally, our findings provide a strong rationale for the wider investigation of autoantibodies in the pathogenesis of infectious diseases.

Methods

No statistical methods were used to predetermine sample size. For research performed on human samples, randomization was not performed as these studies were observational in nature. For experiments involving mice, age- and sex-matched mice were randomly assigned to experimental groups. For the REAP screen, human peripheral blood mononuclear cell flow cytometry measurements and plasma cytokine measurements, investigators were blinded to patients' clinical information and clinical scores until after data collection and analysis. For all other experiments, investigators were not blinded to patients' clinical information and clinical scores during data collection and analysis.

Ethics statement

This study was approved by Yale Human Research Protection Program Institutional Review Boards (FWA00002571, protocol ID 2000027690). Informed consent was obtained from all enrolled patients and healthcare workers.

Patients

As previously described¹ and reproduced here for accessibility, 197 patients admitted to Yale New Haven Hospital with COVID-19 between 18 March and 5 May 2020 were included in this study. No statistical methods were used to predetermine sample size. Nasopharyngeal and saliva samples were collected as previously described³², approximately every four days, for SARS-CoV-2 reverse-transcription qPCR analysis when clinically feasible. Paired whole blood for flow cytometry analysis was collected

simultaneously in sodium-heparin-coated vacutainers and kept on gentle agitation until processing. All blood was processed on the day of collection. Patients were scored for COVID-19 disease severity through review of electronic medical records at each longitudinal time point. Scores were assigned by a clinical infectious disease physician according to a custom-developed disease severity scale. Moderate disease status (clinical score 1–3) was defined as: SARS-CoV-2 infection requiring hospitalization without supplementary oxygen (1); infection requiring noninvasive supplementary oxygen ($<3\text{ l min}^{-1}$ to maintain $\text{SpO}_2 > 92\%$) (2); and infection requiring noninvasive supplementary oxygen ($>3\text{ l min}^{-1}$ to maintain $\text{SpO}_2 > 92\%$, or $>2\text{ l min}^{-1}$ to maintain $\text{SpO}_2 > 92\%$ and had a high-sensitivity C-reactive protein (CRP) >70) and received tocilizumab (3). Severe disease status (clinical score 4 or 5) was defined as infection meeting all criteria for clinical score 3, and also requiring admission to the intensive care unit and $>6\text{ l min}^{-1}$ supplementary oxygen to maintain $\text{SpO}_2 > 92\%$ (4); or infection requiring invasive mechanical ventilation or extracorporeal membrane oxygenation in addition to glucocorticoid or vasopressor administration (5). Clinical score 6 was assigned for deceased patients. For all patients, days from symptom onset were estimated as follows: (1) highest priority was given to explicit onset dates provided by patients; (2) next highest priority was given to the earliest reported symptom by a patient; and (3) in the absence of direct information regarding symptom onset, we estimated a date through manual assessment of the electronic medical records by an independent clinician. Demographic information was aggregated through a systematic and retrospective review of patient electronic medical records and was used to construct Extended Data Table 1. The clinical data were collected using EPIC EHR and REDCap 9.3.6 software. At the time of sample acquisition and processing, investigators were unaware of the conditions of the patients. Blood acquisition was performed and recorded by a separate team. Information about the conditions of the patients was not available until after processing and analysis of raw data by flow cytometry and ELISA. A clinical team, separate from the experimental team, performed chart reviews to determine relevant statistics. Cytokines and fluorescence-activated cell sorting analyses were performed blinded. Patients' clinical information and clinical score coding were revealed only after data collection.

Clinical data acquisition

Clinical data for patients and healthcare workers were extracted from the Yale–New Haven Health computational health platform^{33,34} in the Observational Medical Outcomes Partnership data model. For each research specimen, summary statistics including minimum, mean, median and maximum values were obtained for relevant clinical measurements, including the Glasgow coma scale, within ± 1 day of biospecimen collection. Disease severity end points, including admission,

supplementary oxygen use and invasive ventilation, were validated as previously described^{[35](#)}.

Viral RNA measurements from human nasopharyngeal samples

RNA concentrations were measured from human nasopharyngeal samples by RT-qPCR as previously described^{[32](#)}. In brief, total nucleic acid was extracted from 300 µl of viral transport medium (nasopharyngeal swab) using the MagMAX Viral/Pathogen Nucleic Acid Isolation kit (ThermoFisher) and eluted into 75 µl elution buffer. For SARS-CoV-2 RNA detection, 5 µl of RNA template was tested as previously described^{[36](#)}, using the US Centers for Disease Control and Prevention real-time RT-PCR primer/probe sets 2019-nCoV_N1 and 2019-nCoV_N2, as well as the human RNase P as an extraction control. Virus RNA copies were quantified using a tenfold dilution standard curve of RNA transcripts that was previously generated. If the RNA concentration was lower than the limit of detection (ND) that was previously determined, the value was set to 0 and used for the analyses.

Yeast induction

All yeast were induced as previously described^{[7](#)}. In brief, one day before induction, yeast were expanded in synthetic dextrose medium lacking uracil (SDO –Ura) at 30 °C. The following day, yeast were induced by resuspension at an optical density of 1 in synthetic galactose medium lacking uracil (SGO –Ura) supplemented with 10% SDO –Ura and culturing at 30 °C for approximately 18 h.

REAP

IgG antibody isolation for REAP was performed as previously described^{[7](#)}. In brief, Triton X-100 and RNase A were added to plasma samples at final concentrations of 0.5% and 0.5 mg ml⁻¹, respectively, and incubated at room temperature for 30 min before use to reduce risk from any potential virus in plasma. Twenty µl protein G magnetic resin (Lytic Solutions) was washed with sterile PBS, resuspended in 75 µl sterile PBS, and added to 25 µl plasma. Plasma–resin mixture was incubated overnight at 4 °C with shaking. Resin was washed with sterile PBS, resuspended in 90 µl 100 mM glycine pH 2.7, and incubated for five min at room temperature. Supernatant was extracted and added to 10 µl sterile 1M Tris pH 8.0. At this point, IgG concentration was measured using a NanoDrop 8000 Spectrophotometer (Thermo Fisher Scientific). To generate yeast-depleted IgG for use in REAP, purified IgG was added to 10⁸ induced empty vector (pDD003) yeast and incubated for 3 h at 4 °C with shaking. Yeast–IgG mixtures were placed into 96-well 0.45-µm filter plates (Thomas Scientific)

and yeast-depleted IgG was eluted into sterile 96-well plates by centrifugation at 3,000g for 3 min.

Yeast library selection for REAP was performed as previously described⁷. In brief, 400 µl of the induced yeast library was set aside to allow for comparison to post-selection libraries. Then, 10⁸ induced yeast were added to wells of a sterile 96-well v-bottom microtitre plate, resuspended in 100 µl PBE (PBS with 0.5% BSA and 0.5 mM EDTA) containing 10 µg patient-derived antibody, and incubated with shaking for 1 h at 4 °C. Yeast were washed twice with PBE, resuspended in 100 µl PBE with a 1:100 dilution of biotin anti-human IgG Fc antibody (clone HP6017, BioLegend), and incubated with shaking for 1 h at 4 °C. Yeast were washed twice with PBE, resuspended in 100 µl PBE with a 1:20 dilution of Streptavidin MicroBeads (Miltenyi Biotec), and incubated with shaking for 30 min at 4 °C. All following steps were carried out at room temperature. Multi-96 Columns (Miltenyi Biotec) were placed into a MultiMACS M96 Separator (Miltenyi Biotec) in positive selection mode and the columns were equilibrated with 70% ethanol and degassed PBE. Yeast were resuspended in 200 µl degassed PBE and placed into the columns. The columns were washed three times with degassed PBE. To elute the selected yeast, columns were removed from the separator and placed over 96-well deep well plates. Then, 700 µl degassed PBE was added to each well of the column and the column and deep-well plate were centrifuged briefly. This process was repeated three times. Yeast were recovered in 1 ml SDO –Ura at 30 °C.

DNA was extracted from yeast libraries using Zymoprep-96 Yeast Plasmid Miniprep kits or Zymoprep Yeast Plasmid Miniprep II kits (Zymo Research) according to standard manufacturer protocols. A first round of PCR was used to amplify a DNA sequence containing the protein display barcode on the yeast plasmid. PCR reactions were conducted using 1 µl plasmid DNA, 159_DIF2 and 159_DIR2 primers, and the following PCR settings: 98 °C denaturation, 58 °C annealing, 72 °C extension, 25 rounds of amplification. A second round of PCR was conducted using 1 µl first round PCR product, Nextera i5 and i7 dual-index library primers (Illumina) along with dual-index primers containing custom indices, and the following PCR settings: 98 °C denaturation, 58 °C annealing, 72 °C extension, 25 rounds of amplification. PCR products were pooled and run on a 1% agarose gel. The band corresponding to 257 base pairs was cut out and DNA (NGS library) was extracted using a QIAquick Gel Extraction Kit (Qiagen) according to standard manufacturer protocols. NGS library was sequenced using an Illumina NextSeq 500 and NextSeq 500/550 75 cycle High Output Kit v2.5 with 75 base pair single-end sequencing according to standard manufacturer protocols. A minimum of 50,000 reads per sample was collected and the preselection library was sampled at ten times greater depth than other samples.

REAP data analysis

REAP score was calculated as previously described⁷. First, barcode counts were extracted from raw NGS data using custom codes. Next, aggregate and clonal enrichment was calculated using edgeR³⁷ and custom codes. For aggregate enrichment, barcode counts across all unique barcodes associated with a given protein were summed, library sizes across samples were normalized using default edgeR parameters, common and tagwise dispersion were estimated using default edgeR parameters, and exact tests comparing each sample to the preselection library were performed using default edgeR parameters. Aggregate enrichment is thus the log₂-transformed fold change values from these exact tests with zeroes in the place of negative fold changes. log₂-transformed fold change values for clonal enrichment were calculated in an identical manner, but barcode counts across all unique barcodes associated with a given protein were not summed. Clonal enrichment for a given reactivity was defined as the fraction of clones out of total clones that were enriched (log₂-transformed fold change ≥ 2). Thus, the clonal enrichment metric progressively penalizes proteins with lower fractions of clones enriched. This metric was implemented because a true reactivity should theoretically enrich all yeast clones displaying a given protein.

Aggregate (E_a) and clonal enrichment (E_c) for a given protein, a scaling factor (β_u) on the basis of the number of unique yeast clones (yeast that have a unique DNA barcode) displaying a given protein, and a scaling factor (β_f) on the basis of the overall frequency of yeast in the library displaying a given protein were used as inputs to calculate the REAP score, which is defined as REAP score = $E_a \times (E_c)^2 \times \beta_u \times \beta_f$. β_u and β_f are logarithmic scaling factors that progressively penalize the REAP score of proteins with low numbers of unique barcodes or low frequencies in the library. β_u is applied to proteins with ≤ 5 unique yeast clones in the library and β_f is applied to proteins with a frequency of ≤ 0.0001 in the library. β_f was implemented to mitigate spurious enrichment signals from low-frequency proteins, which could occur owing to sequencing errors or stochasticity in the selection process. β_u was implemented because the clonal enrichment metric is less valid for proteins with low numbers of unique yeast clones, decreasing confidence in the validity of the reactivity. β_u is defined as $\beta_u = \ln(x_u + 0.5)/1.705$ and β_f is defined as $\beta_f = \ln(x_f + 7.1)/1.16$, in which x_u is the number of unique yeast clones for a given protein and x_f is the log₁₀-transformed frequency of a given protein in the library. Antigens (excluding coronavirus RBDs and IL-6R) with an average REAP score greater than 0.5 across all samples were defined as ‘sticky’ and excluded from further analysis. Antigens defined as immune-targeting and tissue-associated were manually identified.

Autoantibody ELISA measurement

In brief, 200 ng of purchased or independently produced recombinant protein in 100 µl of PBS pH 7.0 was added to 96-well flat-bottom Immulon 2HB plates (Thermo Fisher Scientific) and placed at 4 °C overnight. Plates were washed once with 225 µl ELISA wash buffer (PBS + 0.05% Tween 20) and 150 µl ELISA blocking buffer (PBS + 2% human serum albumin) was added to the well. Plates were incubated for 2 h at room temperature. ELISA blocking buffer was removed from the wells and appropriate dilutions of sample plasma in 100 µl ELISA blocking buffer were added to each well. Plates were incubated for 2 h at room temperature. Plates were washed 6 times with 225 µl ELISA wash buffer and 1:5,000 goat anti-human IgG HRP (Millipore Sigma) or anti-human IgG isotype-specific HRP (Southern Biotech; IgG1: clone HP6001, IgG2: clone 31-7-4, IgG3: clone HP6050, IgG4: clone HP6025) in 100 µl ELISA blocking buffer was added to the wells. Plates were incubated for 1 h at room temperature. Plates were washed 6 times with 225 µl ELISA wash buffer. Then, 50 µl TMB substrate (BD Biosciences) was added to the wells and plates were incubated for 20–30 min in the dark at room temperature. Next, 50 µl 1 M sulfuric acid was added to the wells and absorbance at 450 nm was measured in a Synergy HTX Multi-Mode Microplate Reader (BioTek). Proteins used are as follows: ACKR1–mIgG2a-Fc (produced in-house), BAMBI (Sino Biological, 10890-H08H-20), C1qB (Sino Biological, 10941-H08B-20), CCL15 (PeproTech, 300-43), CCL16 (PeproTech, 300-44), CNPY3 (produced in-house), CNPY4 (produced in-house), CST5 (produced in-house), CD38 (R&D Systems, 2404-AC-010), GM-CSF (produced in-house), CXCL1 (PeproTech, 300-11), CXCL3 (PeproTech, 300-40), CXCL7 (PeproTech, 300-14), Fc μ R (R&D Systems, 9494-MU-050), HCRT2–mIgG2a-Fc (produced in-house), IFN ω (PeproTech, 300-02J), IL-13 (PeproTech, 200-13), IL-1 α (RayBiotech, 228-10846-1), IL-6 (produced in-house), leptin (R&D Systems, 398-LP-01M), SLC2A12–mIgG2a-Fc (produced in-house), TSLP (PeproTech, 300-62) and IL-18R β (produced in-house).

SARS-CoV-2-specific antibody ELISA measurement

SARS-CoV-2-specific antibodies were measured as previously described³⁸. In brief, plasma samples were first treated with 0.5% Triton X-100 and 0.5 mg ml⁻¹ RNase A at room temperature for 30 min to inactivate potentially infectious viruses. Meanwhile, recombinant SARS-CoV-2 S1 protein (ACRO Biosystems, S1N-C52H3) or recombinant SARS-CoV-2 RBD protein (ACRO Biosystems, SPD-C82E9) was used to coat 96-well MaxiSorp plates (Thermo Scientific) at a concentration of 2 µg ml⁻¹ in PBS in 50 µl per well, followed by overnight incubation at 4 °C. The coating buffer was removed, and plates were incubated for 1 h at room temperature with 200 µl of blocking solution (PBS with 0.1% Tween-20 and 3% milk powder). Plasma was diluted 1:50 in dilution solution (PBS with 0.1% Tween-20 and 1% milk powder) and 100 µl of diluted serum was added for 2 h at room temperature. Plates were washed three times with PBS-T (PBS with 0.1% Tween-20) and 50 µl of HRP anti-human IgG

antibody at 1:5,000 dilution (GenScript) or anti-human IgM-peroxidase antibody at 1:5,000 dilution (Sigma-Aldrich) in dilution solution were added to each well. After 1 h of incubation at room temperature, plates were washed six times with PBS-T. Plates were developed with 100 µl of TMB Substrate Reagent Set (BD Biosciences 555214) and the reaction was stopped after 12 minutes by the addition of 100 µl of 2 N sulfuric acid. Plates were then read at a wavelength of 450 nm and 570 nm. The cut-off values for seropositivity were determined as 0.392, 0.436 and 0.341 for anti-S1-IgG, anti-S1 IgM and anti-RBD IgG, respectively. Eighty and sixty-nine pre-pandemic plasma samples were assayed to establish the negative baselines for the S1 and RBD antigens, respectively. These values were statistically determined with a confidence level of 99%.

Functional validation of anti-GM-CSF autoantibody and autoantibodies targeting type I IFNs

TF-1 cells (ATCC, CRL-2003) were cultured in RPMI (+ 10% heat inactivated FBS, 10 U ml⁻¹ penicillin, 100 mg ml⁻¹ streptomycin, 1 mM sodium pyruvate, 2 ng ml⁻¹ GM-CSF (PeproTech, 300-03)) and incubated at 37 °C, 5% CO₂. THP-1 cells (ATCC, TIB-202) were cultured in RPMI (+ 10% heat inactivated FBS, 10 U ml⁻¹ penicillin, 100 mg ml⁻¹ streptomycin) and incubated at 37 °C, 5% CO₂. For validation of GM-CSF autoantibodies, TF-1 cells were starved of recombinant GM-CSF 18 h before experiments. GM-CSF at 200 pg ml⁻¹ was incubated with dilutions of purified IgG for 15 min at room temperature and then used to stimulate TF-1 cells in a 96-well plate (2×10^5 cells per well) in a final volume of 100 µl (final concentration of 100 pg ml⁻¹). For validation of IFN autoantibodies, IFN α 2 (R&D Systems, 11100-1) and IFN ω (Peprotech, 300-02J) at 1,500 pg ml⁻¹ and 2,000 pg ml⁻¹, respectively, were incubated with dilutions of purified IgG for 15 min at room temperature and then used to stimulate THP-1 cells in a 96-well plate (3.5×10^5 cells per well) in a final volume of 100 µl (final concentrations of 750 and 1,000 pg ml⁻¹, respectively). IgG was purified from plasma using protein G magnetic beads (Lytic Solutions) as previously described⁷. After 15 min of stimulation, cells were fixed in 4% paraformaldehyde for 30 min, washed with PBS and permeabilized in 100% methanol on ice for 45 min. Cells were then washed twice with PBE and stained with PE-conjugated anti-STAT5 pY694 (1:50) (BD Biosciences, 562077) or anti-STAT1 pY701 (1:50) (BD Biosciences, 612564) and human TruStain FcX (1:100) (Biolegend, 422302) for 1 h at room temperature. Cells were washed with PBE and acquired on a SONY SA3800 flow cytometer. Data were analysed using FlowJo software version 10.6 software (Tree Star). pSTAT signal was measured as a function of mean fluorescence intensity (MFI). Per cent maximum signal was calculated by subtracting background MFI and calculating values as a percentage of cytokine-induced pSTAT MFI in the absence of IgG. Curves were fit using a sigmoidal four-parameter logistic curve. TF-1 and THP-1

cells were purchased commercially and were not authenticated by us. TF-1 and THP-1 cells were not tested for mycoplasma contamination.

Functional validation of anti-CXCL1, anti-CXCL7 and anti-HCRT2 autoantibodies

CXCL1, CXCL7 and orexin signalling was assayed using the PRESTO-TANGO system³⁹. HTLA cells, a HEK293-derived cell line that stably expresses β-arrestin-TEV and tTA-luciferase, were seeded in wells of a sterile tissue-culture-grade flat-bottom 96-well plate (35,000 cells per well) in 100 µl DMEM (+ 10% FBS, 1% penicillin–streptomycin) and incubated at 37 °C, 5% CO₂. At 18–24 h after seeding (approximately 80–90% cell confluence), 200 ng CXCR2-Tango or HCTR2-Tango plasmid in 20 µl DMEM and 600 ng polyethylenimine-max (Polysciences, 24765-1) in 20 µl DMEM were mixed, incubated at room temperature for 20 min and added to each well. At 18–24 h after transfection, medium was replaced with 100 µl DMEM (+ 1% penicillin–streptomycin, 10 mM HEPES) containing 10 ng CXCL7 (Peprotech, 300-14) or CXCL1 (PeproTech, 300-46), or 100 nM orexin A (Millipore Sigma, O6012) and 5 µg isolated IgG. IgG was purified from plasma using protein G magnetic beads (Lytic Solutions) as previously described⁷. At 18–24 h after stimulation, supernatant was replaced with 50 µl Bright-Glo solution (Promega) diluted 20-fold with PBS with 20 mM HEPES. The plate was incubated at room temperature for 20 min in the dark and luminescence was quantified using a Synergy HTX Multi-Mode Microplate Reader (BioTek). HTLA cells were a gift from N. Palm and were derived as previously described³⁹. HTLA cells were authenticated based on their performance in PRESTO-TANGO and were not tested for mycoplasma contamination. Tango plasmids were a gift from B. Roth (Addgene plasmid no. 66260)

Functional validation of anti-CD38 and anti-CD3ε autoantibodies

Bone marrow stem cells were isolated from the femur and tibia of 8-week-old C57BL/6 mice. Cells were plated in RPMI (+ 10% heat inactivated FBS, 10 U ml⁻¹ penicillin, 100 mg ml⁻¹ streptomycin (cRPMI)) with 30% (v/v) L929 fibroblast conditioned medium as a source of M-CSF and incubated at 37 °C, 5% CO₂. On day 3 after isolation, 10 ml L929 fibroblast conditioned medium was added to plates. Two hundred thousand bone-marrow-derived macrophages (7 days after isolation) were plated on non-TC treated 6-well plates in cRPMI + 10% L929 medium. The following day, Raji (ATCC, CCL-86) or Jurkat (ATCC, TIB-152) cells were labelled using CellTrace Far Red (Thermo Fisher) according to standard manufacturer protocols. For the T cell antibody-dependent cellular phagocytosis assay, labelled Jurkat cells were incubated with 100 µg ml⁻¹ healthy control IgG or CD3ε autoantibody⁺ patient IgG for 30 min on ice. Mouse IgG2a anti-human CD3ε (clone OKT3, Biolegend) was used

at 5 µg ml⁻¹ as a positive control. Jurkat cells were washed with 10 ml PBS. One million Jurkat cells were added to each well and incubated for 3 h. For the B cell antibody-dependent cellular phagocytosis assay, Raji cells were incubated with complement inactivated patient plasma at 1:50 dilution in PBS for 30 min on ice. Mouse IgG2a anti-human CD38 (clone MAB2404, R&D systems) was used at 5 µg ml⁻¹ as a positive control. Raji cells were washed with 10 ml PBS once. Five hundred thousand Raji cells were added to each well and incubated for 3 h at 37 °C, 5% CO₂. Bone marrow-derived macrophages were detached from the plate after a 3-h incubation using 10 mM EDTA PBS and stained with anti-mouse CD45–Pacific blue (clone 30-F11, Biolegend) for 30 min at 4 °C. Samples were acquired on a CytoFLEX flow cytometer (Beckman Coulter). Raji and Jurkat cells were purchased commercially and were not authenticated by us. Raji and Jurkat cells were not tested for mycoplasma contamination.

Mice

B6.Cg-Tg(K18-ACE2)2Prlmn/J (K18-hACE2) mice (stock no. 034860) and C57BL/6 mice (stock no. 000664) were purchased from the Jackson Laboratories and were subsequently bred and housed at Yale University. Six- to ten-week-old mixed-sex mice were used throughout the study. All mice were housed as groups of 5 to 6 mice per cage and maintained on a 12-h light/dark cycle (lights on at 07:00) at 22–25 °C and 30–70% relative humidity under specific-pathogen-free conditions. All procedures used in this study (sex-matched and age-matched) complied with federal guidelines and the institutional policies of the Yale School of Medicine Animal Care and Use Committee. All infection studies were performed in animal biosafety level 3 facilities at Yale University in accordance with approved institutional protocols.

SARS-CoV-2 mouse infections and antibody treatments

Before infection, mice were anaesthetized using 30% (v/v) isoflurane diluted in propylene glycol. Then, 50 µl of SARS-CoV-2 isolate USA-WA1/2020 (NR-52281; BEI Resources) at 2 × 10⁴ or 6 × 10⁴ plaque-forming units (PFU) per ml was delivered intranasally to mice, equivalent of 1,000 (sublethal dose) or 3,000 (median lethal dose) PFU per mouse, respectively. Following infection, weight loss and survival were monitored daily. Mice reported as ‘dead’ in this study were found dead, moribund or euthanized at 90% or 80% of their starting body weight. For IFNAR blockade, mice were treated intraperitoneally once with 2 mg of blocking antibodies one day before infection (clone MAR1-5A3). For IL-18 blockade, mice were treated intraperitoneally three times each with 0.5 mg of blocking antibodies at 0, 2 and 4 days after infection (clone YIGIF74-1G7). For blockade of IL-1β, GM-CSF or IL-21R, mice were treated intraperitoneally three times each with 0.2 mg of blocking antibodies at 0, 2 and 4 days after infection (anti-IL-1β: clone B122; anti-GM-CSF: clone MP1-22E9; and

anti-IL-21R: clone 4A9). The first injection of anti-IL18, anti-IL-1 β , anti-GM-CSF or anti-IL-21R antibodies was given at least 8 to 10 h before infection. All blocking antibodies were purchased from BioXCell.

Statistical analysis

Details of linear models and principal component analysis can be found in the [Supplementary Methods](#). Specific details of other statistical analysis are found in the figure legends. Data analysis was performed using MATLAB, GraphPad Prism, R, and the following R packages: ggplot2, edgeR, tidyverse, dplyr, stringr, forcats, lme4, emmeans and ggpubr.

Reporting summary

Further information on research design is available in the [Nature Research Reporting Summary](#) linked to this paper.

Data availability

The previously published RNA-sequencing dataset is publicly available in the Gene Expression Omnibus under accession number [GSE107011](#). All data analysed in this study are available in the Article and [Supplementary Information](#). Data that are not available within the manuscript are available from the corresponding authors upon reasonable request. [Source data](#) are provided with this paper.

Code availability

Custom codes used for analysis in this study are available publicly at https://github.com/ring-lab/COVID-19_REAP_nature_2021.

References

1. 1.

Lucas, C. et al. Longitudinal analyses reveal immunological misfiring in severe COVID-19. *Nature* **584**, 463–469 (2020).

[CAS Article](#) [Google Scholar](#)

2. 2.

Maucourant, C. et al. Natural killer cell immunotypes related to COVID-19 disease severity. *Sci. Immunol.* **5**, eabd6832 (2020).

[CAS](#) [Article](#) [Google Scholar](#)

3. 3.

Mann, E. R. et al. Longitudinal immune profiling reveals key myeloid signatures associated with COVID-19. *Sci. Immunol.* **5**, eabd6197 (2020).

[Article](#) [Google Scholar](#)

4. 4.

Lee, J. S. et al. Immunophenotyping of COVID-19 and influenza highlights the role of type I interferons in development of severe COVID-19. *Sci. Immunol.* **5**, eabd1554 (2020).

[CAS](#) [Article](#) [Google Scholar](#)

5. 5.

Rodrigues, T. S. et al. Inflammasomes are activated in response to SARS-CoV-2 infection and are associated with COVID-19 severity in patients. *J. Exp. Med.* **218**, e20201707 (2021).

[CAS](#) [Article](#) [Google Scholar](#)

6. 6.

Vabret, N. et al. Immunology of COVID-19: current state of the science. *Immunity* **52**, 910–941 (2020).

[CAS](#) [Article](#) [Google Scholar](#)

7. 7.

Wang, E. Y. et al. REAP: a platform to identify autoantibodies that target the human exoproteome. Preprint at <https://doi.org/10.1101/2021.02.11.430703> (2021).

8. 8.

Hassan, A. O. et al. A SARS-CoV-2 infection model in mice demonstrates protection by neutralizing antibodies. *Cell* **182**, 744–753.e4 (2020).

[CAS](#) [Article](#) [Google Scholar](#)

9. 9.

Garcia-Beltran, W. F. et al. COVID-19 neutralizing antibodies predict disease severity and survival. *Cell* **184**, 476–488 (2021).

[CAS](#) [Article](#) [Google Scholar](#)

10. 10.

Woodruff, M. C. et al. Extrafollicular B cell responses correlate with neutralizing antibodies and morbidity in COVID-19. *Nat. Immunol.* **21**, 1506–1516 (2020).

[Article](#) [Google Scholar](#)

11. 11.

Bastard, P. et al. Autoantibodies against type I IFNs in patients with life-threatening COVID-19. *Science* **370**, eabd4585 (2020).

[CAS](#) [Article](#) [Google Scholar](#)

12. 12.

Combes, A. J. et al. Global absence and targeting of protective immune states in severe COVID-19. *Nature* **591**, 124–130 (2021).

[ADS](#) [CAS](#) [Article](#) [Google Scholar](#)

13. 13.

Zuo, Y. et al. Prothrombotic autoantibodies in serum from patients hospitalized with COVID-19. *Sci. Transl. Med.* **12**, eabd3876 (2020).

[CAS](#) [Article](#) [Google Scholar](#)

14. 14.

Woodruff, M. C., Ramonell, R. P., Lee, F. E.-H. & Sanz, I. Clinically identifiable autoreactivity is common in severe SARS-CoV-2 infection. Preprint at <https://doi.org/10.1101/2020.10.21.20216192> (2020).

15. 15.

Zhou, Y. et al. Clinical and autoimmune characteristics of severe and critical cases of COVID-19. *Clin. Transl. Sci.* **13**, 1077–1086 (2020).

[CAS](#) [Article](#) [Google Scholar](#)

16. 16.

Chang, S. E. et al. New-onset IgG autoantibodies in hospitalized patients with COVID-19. Preprint at <https://doi.org/10.1101/2021.01.27.21250559> (2021).

17. 17.

Takahashi, T. et al. Sex differences in immune responses that underlie COVID-19 disease outcomes. *Nature* **588**, 315–320 (2020).

[ADS](#) [CAS](#) [Article](#) [Google Scholar](#)

18. 18.

Monaco, G. et al. RNA-seq signatures normalized by mRNA abundance allow absolute deconvolution of human immune cell types. *Cell Rep.* **26**, 1627–1640.e7 (2019).

[CAS](#) [Article](#) [Google Scholar](#)

19. 19.

McCray, P. B., Jr et al. Lethal infection of K18-hACE2 mice infected with severe acute respiratory syndrome coronavirus. *J. Virol.* **81**, 813–821 (2007).

[CAS](#) [Article](#) [Google Scholar](#)

20. 20.

Zheng, J. et al. COVID-19 treatments and pathogenesis including anosmia in K18-hACE2 mice. *Nature* **589**, 603–607 (2021).

[ADS](#) [CAS](#) [Article](#) [Google Scholar](#)

21. 21.

Winkler, E. S. et al. SARS-CoV-2 infection of human ACE2-transgenic mice causes severe lung inflammation and impaired function. *Nat. Immunol.* **21**, 1327–

1335 (2020).

[CAS](#) [Article](#) [Google Scholar](#)

22. 22.

Mantovani, A., Dinarello, C. A., Molgora, M. & Garlanda, C. Interleukin-1 and related cytokines in the regulation of inflammation and immunity. *Immunity* **50**, 778–795 (2019).

[CAS](#) [Article](#) [Google Scholar](#)

23. 23.

Zhou, T. et al. IL-18BP is a secreted immune checkpoint and barrier to IL-18 immunotherapy. *Nature* **583**, 609–614 (2020).

[ADS](#) [CAS](#) [Article](#) [Google Scholar](#)

24. 24.

Orzalli, M. H. et al. An antiviral branch of the IL-1 signaling pathway restricts immune-evasive virus replication. *Mol. Cell* **71**, 825–840.e6 (2018).

[CAS](#) [Article](#) [Google Scholar](#)

25. 25.

Spolski, R. & Leonard, W. J. Interleukin-21: a double-edged sword with therapeutic potential. *Nat. Rev. Drug Discov.* **13**, 379–395 (2014).

[CAS](#) [Article](#) [Google Scholar](#)

26. 26.

Trapnell, B. C. & Whitsett, J. A. GM-CSF regulates pulmonary surfactant homeostasis and alveolar macrophage-mediated innate host defense. *Annu. Rev. Physiol.* **64**, 775–802 (2002).

[CAS](#) [Article](#) [Google Scholar](#)

27. 27.

Wang, G. et al. C-reactive protein level may predict the risk of COVID-19 aggravation. *Open Forum Infect. Dis.* **7**, ofaa153 (2020).

[Article](#) [Google Scholar](#)

28. 28.

Cheng, L. et al. Ferritin in the coronavirus disease 2019 (COVID-19): a systematic review and meta-analysis. *J. Clin. Lab. Anal.* **34**, e23618 (2020).

[CAS](#) [PubMed](#) [PubMed Central](#) [Google Scholar](#)

29. 29.

Song, E. et al. Neuroinvasion of SARS-CoV-2 in human and mouse brain. *J. Exp. Med.* **218**, e20202135 (2021).

[CAS](#) [Article](#) [Google Scholar](#)

30. 30.

Nalbandian, A. et al. Post-acute COVID-19 syndrome. *Nat. Med.* **27**, 601–615 (2021).

[CAS](#) [Article](#) [Google Scholar](#)

31. 31.

Nixon, J. P. et al. Sleep disorders, obesity, and aging: the role of orexin. *Ageing Res. Rev.* **20**, 63–73 (2015).

[CAS](#) [Article](#) [Google Scholar](#)

32. 32.

Wyllie, A. L. et al. Saliva or nasopharyngeal swab specimens for detection of SARS-CoV-2. *N. Engl. J. Med.* **383**, 1283–1286 (2020).

[Article](#) [Google Scholar](#)

33. 33.

McPadden, J. et al. Health care and precision medicine research: analysis of a scalable data science platform. *J. Med. Internet Res.* **21**, e13043 (2019).

[Article](#) [Google Scholar](#)

34. 34.

Schulz, W. L., Durant, T. J. S., Torre, C. J., Jr, Hsiao, A. L. & Krumholz, H. M. Agile health care analytics: enabling real-time disease surveillance with a computational health platform. *J. Med. Internet Res.* **22**, e18707 (2020).

[Article](#) [Google Scholar](#)

35. 35.

McPadden, J. et al. Clinical characteristics and outcomes for 7,995 patients with SARS-CoV-2 infection. Preprint at <https://doi.org/10.1101/2020.07.19.20157305> (2020).

36. 36.

Vogels, C. B. F. et al. Analytical sensitivity and efficiency comparisons of SARS-CoV-2 RT-qPCR primer-probe sets. *Nat. Microbiol.* **5**, 1299–1305 (2020).

[CAS](#) [Article](#) [Google Scholar](#)

37. 37.

Robinson, M. D., McCarthy, D. J. & Smyth, G. K. edgeR: a Bioconductor package for differential expression analysis of digital gene expression data. *Bioinformatics* **26**, 139–140 (2010).

[CAS](#) [Article](#) [Google Scholar](#)

38. 38.

Amanat, F. et al. A serological assay to detect SARS-CoV-2 seroconversion in humans. *Nat. Med.* **26**, 1033–1036 (2020).

[CAS](#) [Article](#) [Google Scholar](#)

39. 39.

Kroeze, W. K. et al. PRESTO-Tango as an open-source resource for interrogation of the druggable human GPCRome. *Nat. Struct. Mol. Biol.* **22**, 362–369 (2015).

[CAS](#) [Article](#) [Google Scholar](#)

[Download references](#)

Acknowledgements

We thank all members of the laboratories of A.M.R. and A.I., as well as E. Meffre, J. Craft and K. O'Connor, for helpful conversation and technical assistance; M. Linehan and H. Dong for logistical assistance; H. P. Young for technical assistance with data management; N. K. Savalia and T. J. Shelby for discussion regarding statistical techniques; and L. Steinman for helpful discussions about autoantibodies to HCRTR2. This work was supported by the Mathers Family Foundation (to A.M.R. and A.I.), the Ludwig Family Foundation (to A.M.R. and A.I.), a supplement to the Yale Cancer Center Support Grant 3P30CA016359-40S4 (to A.M.R.), the Beatrice Neuwirth Foundation, Yale Schools of Medicine and Public Health and NIAID grant U19 AI08992. IMPACT received support from the Yale COVID-19 Research Resource Fund. A.M.R. is additionally supported by an NIH Director's Early Independence Award (DP5OD023088), a Pew-Stewart Award, and the Robert T. McCluskey Foundation. T.M. and Y.D. are supported by the Yale Interdisciplinary Immunology Training Program T32AI007019. J.K. and J.R.J. are supported by the Yale Medical Scientist Training Program T32GM007205. Schematics in Fig. 3a, Extended Data Figs. 1a, 7a were created with Biorender.com.

Author information

Author notes

1. These authors contributed equally: Eric Y. Wang, Tianyang Mao, Jon Klein, Yile Dai

Affiliations

1. Department of Immunobiology, Yale School of Medicine, New Haven, CT, USA

Eric Y. Wang, Tianyang Mao, Jon Klein, Yile Dai, John D. Huck, Jillian R. Jaycox, Feimei Liu, Ting Zhou, Benjamin Israelow, Patrick Wong, Carolina Lucas, Julio Silva, Ji Eun Oh, Eric Song, Emily S. Perotti, Neil S. Zheng, Suzanne Fischer, Alice Lu-Culligan, Anjelica Martin, Daniel Kim, Eriko Kudo, Melissa Linehan, Nicole Sonnert, Tyler Rice, William Khoury-Hanold, Yixin Yang, Yiyun Cao, Akiko Iwasaki & Aaron M. Ring

2. Center for Outcomes Research and Evaluation, Yale–New Haven Hospital, New Haven, CT, USA

Andreas Coppi & Wade L. Schulz

3. Department of Internal Medicine (Infectious Diseases), Yale School of Medicine, New Haven, CT, USA

Melissa Campbell, John B. Fournier, Camila D. Odio, Rick Martinello, Rupak Datta, Shelli F. Farhadian & Albert I. Ko

4. Department of Epidemiology of Microbial Diseases, Yale School of Public Health, New Haven, CT, USA

Anne L. Wyllie, Chantal B. F. Vogels, Isabel M. Ott, Chaney C. Kalinich, Mary E. Petrone, Anne E. Watkins, Adam J. Moore, Arnau Casanovas-Massana, Christina A. Harden, Cole Jensen, Elizabeth B. White, Kristina Brower, Nathan D. Grubaugh, Albert I. Ko & Akiko Iwasaki

5. Department of Medicine, Section of Pulmonary and Critical Care Medicine, Yale School of Medicine, New Haven, CT, USA

Charles Dela Cruz

6. Department of Laboratory Medicine, Yale School of Medicine, New Haven, CT, USA

Wade L. Schulz

7. Department of Biostatistics, Yale School of Public Health, New Haven, CT, USA

Shuangge Ma

8. Howard Hughes Medical Institute, Chevy Chase, MD, USA

Akiko Iwasaki

9. Department of Pharmacology, Yale School of Medicine, New Haven, CT, USA

Aaron M. Ring

10. Yale School of Medicine, New Haven, CT, USA

Abeer Obaid, Allison Nelson, Angela Nunez, Bertie Geng, Codruta Todeasa, David McDonald, Denise Shepard, Erin Silva, Giuseppe DeIuliis, Harold Rahming, Hong-Jai Park, Irene Matos, Jessica Nouws, Jordan Valdez, Kadi-Ann Rose, Laura Glick, Lokesh Sharma, Lorenzo Sewanan, Lynda Knaggs, Maksym Minasyan, Maria Batsu, Maura Nakahata, Michael Simonov, Mikhail Smolgovsky, Nida Naushad, Pavithra Vijayakumar, Ryan Handoko, Santos Bermejo, Xiaohua Peng & Yvette Strong

11. Department of Biochemistry and of Molecular Biology, Yale University School of Medicine, New Haven, CT, USA
Edward Courchaine & Sean Bickerton
12. Yale Viral Hepatitis Program, Yale University School of Medicine, New Haven, CT, USA
Joseph Lim
13. Yale Center for Clinical Investigation, Yale University School of Medicine, New Haven, CT, USA
Kelly Anastasio & Maxine Kuang
14. Department of Neurology, Yale University School of Medicine, New Haven, CT, USA
Michael H. Askenase & Sofia Velazquez
15. Department of Molecular, Cellular and Developmental Biology, Yale University School of Medicine, New Haven, CT, USA
Sarah Prophet

Authors

1. Eric Y. Wang
[View author publications](#)

You can also search for this author in [PubMed](#) [Google Scholar](#)

2. Tianyang Mao
[View author publications](#)

You can also search for this author in [PubMed](#) [Google Scholar](#)

3. Jon Klein
[View author publications](#)

You can also search for this author in [PubMed](#) [Google Scholar](#)

4. Yile Dai
[View author publications](#)

You can also search for this author in [PubMed](#) [Google Scholar](#)

5. John D. Huck

[View author publications](#)

You can also search for this author in [PubMed](#) [Google Scholar](#)

6. Jillian R. Jaycox

[View author publications](#)

You can also search for this author in [PubMed](#) [Google Scholar](#)

7. Feimei Liu

[View author publications](#)

You can also search for this author in [PubMed](#) [Google Scholar](#)

8. Ting Zhou

[View author publications](#)

You can also search for this author in [PubMed](#) [Google Scholar](#)

9. Benjamin Israelow

[View author publications](#)

You can also search for this author in [PubMed](#) [Google Scholar](#)

10. Patrick Wong

[View author publications](#)

You can also search for this author in [PubMed](#) [Google Scholar](#)

11. Andreas Coppi

[View author publications](#)

You can also search for this author in [PubMed](#) [Google Scholar](#)

12. Carolina Lucas

[View author publications](#)

You can also search for this author in [PubMed](#) [Google Scholar](#)

13. Julio Silva

[View author publications](#)

You can also search for this author in [PubMed](#) [Google Scholar](#)

14. Ji Eun Oh

[View author publications](#)

You can also search for this author in [PubMed](#) [Google Scholar](#)

15. Eric Song

[View author publications](#)

You can also search for this author in [PubMed](#) [Google Scholar](#)

16. Emily S. Perotti

[View author publications](#)

You can also search for this author in [PubMed](#) [Google Scholar](#)

17. Neil S. Zheng

[View author publications](#)

You can also search for this author in [PubMed](#) [Google Scholar](#)

18. Suzanne Fischer

[View author publications](#)

You can also search for this author in [PubMed](#) [Google Scholar](#)

19. Melissa Campbell

[View author publications](#)

You can also search for this author in [PubMed](#) [Google Scholar](#)

20. John B. Fournier

[View author publications](#)

You can also search for this author in [PubMed](#) [Google Scholar](#)

21. Anne L. Wyllie

[View author publications](#)

You can also search for this author in [PubMed](#) [Google Scholar](#)

22. Chantal B. F. Vogels

[View author publications](#)

You can also search for this author in [PubMed](#) [Google Scholar](#)

23. Isabel M. Ott

[View author publications](#)

You can also search for this author in [PubMed](#) [Google Scholar](#)

24. Chaney C. Kalinich

[View author publications](#)

You can also search for this author in [PubMed](#) [Google Scholar](#)

25. Mary E. Petrone

[View author publications](#)

You can also search for this author in [PubMed](#) [Google Scholar](#)

26. Anne E. Watkins

[View author publications](#)

You can also search for this author in [PubMed](#) [Google Scholar](#)

27. Charles Dela Cruz

[View author publications](#)

You can also search for this author in [PubMed](#) [Google Scholar](#)

28. Shelli F. Farhadian

[View author publications](#)

You can also search for this author in [PubMed](#) [Google Scholar](#)

29. Wade L. Schulz

[View author publications](#)

You can also search for this author in [PubMed](#) [Google Scholar](#)

30. Shuangge Ma

[View author publications](#)

You can also search for this author in [PubMed](#) [Google Scholar](#)

31. Nathan D. Grubaugh

[View author publications](#)

You can also search for this author in [PubMed](#) [Google Scholar](#)

32. Albert I. Ko

[View author publications](#)

You can also search for this author in [PubMed](#) [Google Scholar](#)

33. Akiko Iwasaki

[View author publications](#)

You can also search for this author in [PubMed](#) [Google Scholar](#)

34. Aaron M. Ring

[View author publications](#)

You can also search for this author in [PubMed](#) [Google Scholar](#)

Consortia

Yale IMPACT Team

- Abeer Obaid
- , Adam J. Moore
- , Arnau Casanovas-Massana
- , Alice Lu-Culligan
- , Allison Nelson
- , Angela Nunez
- , Anjelica Martin
- , Bertie Geng
- , Camila D. Odio
- , Christina A. Harden
- , Codruta Todeasa
- , Cole Jensen
- , Daniel Kim
- , David McDonald
- , Denise Shepard
- , Edward Courchaine
- , Elizabeth B. White
- , Erin Silva
- , Eriko Kudo
- , Giuseppe DeIuliis
- , Harold Rahming
- , Hong-Jai Park

- , Irene Matos
- , Jessica Nouws
- , Jordan Valdez
- , Joseph Lim
- , Kadi-Ann Rose
- , Kelly Anastasio
- , Kristina Brower
- , Laura Glick
- , Lokesh Sharma
- , Lorenzo Sewanan
- , Lynda Knaggs
- , Maksym Minasyan
- , Maria Batsu
- , Maxine Kuang
- , Maura Nakahata
- , Melissa Linehan
- , Michael H. Askenase
- , Michael Simonov
- , Mikhail Smolgovsky
- , Nicole Sonnert
- , Nida Naushad
- , Pavithra Vijayakumar
- , Rick Martinello
- , Rupak Datta
- , Ryan Handoko
- , Santos Bermejo
- , Sarah Prophet
- , Sean Bickerton
- , Sofia Velazquez
- , Tyler Rice
- , William Khoury-Hanold
- , Xiaohua Peng
- , Yexin Yang
- , Yiyun Cao
- & Yvette Strong

Contributions

E.Y.W., T.M., J.K., Y.D., J.D.H., J.R.J., A.I. and A.M.R. designed experiments. E.Y.W. and Y.D. performed the REAP assay. E.Y.W., Y.D., J.D.H., J.R.J., F.L., E.S.P. and S.F. performed biochemical and functional validations. T.M., B.I. and E. Song performed mouse experiments. C.L., P.W., J.K., J.S., T.M. and J.E.O. defined parameters for flow

cytometry experiments, and collected and processed peripheral blood mononuclear cell samples from patients. A.L.W., C.B.F.V., I.M.O., C.C.K., M.E.P. and A.E.W. performed the virus RNA concentration assays. N.D.G. supervised the virus RNA concentration assays. B.I. and J.K. collected epidemiological and clinical data. C.D.C., S.F., A.I.K., M.C. and J.B.F. assisted in designing, recruiting and following in-patient and healthcare worker cohorts. A.C. performed clinical data aggregation and management. W.L.S. supervised clinical data aggregation and management. E.Y.W., T.M., J.K., N.S.Z., Y.D., J.D.H., J.R.J., A.I. and A.M.R. analysed data. S.M. supervised the statistical analysis. E.Y.W., T.M., J.K., A.I. and A.M.R. wrote the paper. A.M.R. and A.I. supervised the research. Authors from the Yale IMPACT Research Team contributed to collection and storage of patient samples, as well as the collection of the patients' epidemiological and clinical data.

Corresponding authors

Correspondence to [Akiko Iwasaki](#) or [Aaron M. Ring](#).

Ethics declarations

Competing interests

A.M.R., E.Y.W. and Y.D. are inventors of a pending US patent application (PCT/US21/23521) filed by Yale University describing the REAP technology used in this Article. A.M.R. is the founder of Seranova Bio, the commercial licensee of the REAP technology. A.I. serves as a consultant for Spring Discovery, Boehringer Ingelheim and Adaptive Biotechnologies.

Additional information

Peer review information *Nature* thanks Petter Brodin, Karl Dane Wittrup and the other, anonymous, reviewer(s) for their contribution to the peer review of this work. Peer reviewer reports are available.

Publisher's note Springer Nature remains neutral with regard to jurisdictional claims in published maps and institutional affiliations.

Extended data figures and tables

[Extended Data Fig. 1 REAP screen of patients with COVID-19.](#)

a, A simplified schematic of REAP. Antibodies are incubated with a barcoded yeast library displaying members of the exoproteome. Antibody-bound yeast are enriched by magnetic-column-based sorting and enrichment is quantified by next-generation sequencing. **b**, Heat map of all profiled reactivities across all patient samples stratified by disease severity and using the same colour scale as in Fig. [1a](#). Sticky antigens (as defined in Methods) were removed from the heat map. **c**, SARS-CoV-2 RBD REAP scores for samples from patients with COVID-19 stratified by positive or negative ELISA RBD reactivity. **d**, IL-6R REAP scores for samples from patients with COVID-19 stratified by treatment with an anti-IL-6R biologic therapy (tocilizumab or sarilumab). Samples collected at least one day after

infusion were considered treated. Samples collected on the day of infusion were excluded from analysis owing to uncertainty in the timing of sample collection. Significance in **c**, **d** was determined using a linear mixed model (Methods). In **c**, **d**, *n* values include longitudinal samples from the same patient.

Source data

Extended Data Fig. 2 Comparisons of reactivities and clinical or immunological parameters between patient groups.

a, Number of positive reactivities per sample at various REAP score cut offs, stratified by disease severity. **b**, Days from symptom onset (DFSO) in samples from patients with severe or moderate COVID-19. Days from symptom onset data were not available for a limited number of samples from each group and were not available for any samples from individuals with mild COVID-19 or no symptoms. The median (solid line) and first and third quartile (dashed lines) are shown. **c**, Number of positive reactivities per sample at various REAP score cut offs, stratified by patient sex. **d**, Number of positive reactivities in samples from patients with COVID-19, SLE or APECED at various score cut offs. Patients with SLE or APECED were screened as previously described⁷. Owing to the smaller size of the yeast exoproteome library used to screen the samples from patients with SLE or APECED, reactivities in samples from patients with COVID-19 against proteins that were not in the previously described yeast exoproteome library were removed from these analyses. **e**, Number of positive immune-targeting reactivities per sample at various REAP score cut offs, stratified by disease severity. **f**, Average percentages of double-negative ($\text{IgD}^- \text{CD27}^-$) B cells among peripheral leukocytes in patients with COVID-19 stratified by disease severity and uninfected controls (neg.). In **a–e**, *n* values include longitudinal samples from the same patient. In **f**, *n* values indicate samples from unique patients. Significance was determined using linear mixed models (**a–e**) (Methods) or a Kruskal–Wallis test followed by a two-sided Dunn’s test (**f**). Medians are represented by a dashed line and first and third quartiles are represented by dotted lines for all plots in this figure.

[Source data](#)

Extended Data Fig. 3 Autoantibodies exhibit varied developmental kinetics in patients with COVID-19.

a, Percentage of reactivities (REAP score greater than score cut off) in patients with COVID-19 present within 10 days of symptom onset at various score cut offs. **b**, Percentage of reactivities in patients with COVID-19 that had a REAP score less than the score cut off (using various score cut offs) at the first time point sampled and an increase in REAP score of at least 1 at the last time point. **c**, Percentage of reactivities in patients with COVID-19 that had a REAP score greater than the score cut off (using various score cut offs) at the first time point sampled and a decrease in REAP score of at least 1 at the last time point. For **a–c**, all patients with COVID-19 with longitudinal samples available ($n = 77$ patients) were included in calculations. **d–f**, Plots of longitudinal changes in REAP score for ‘likely pre-existing’ (**d**), ‘newly acquired’ (**e**) and ‘waning’ (**f**) REAP reactivities in individual patients alongside scaled anti-spike S1 ELISA values in the same patients. Scaled ELISA values are defined as anti-spike S1 ELISA optical density (450–570 nm) values multiplied by four. In each plot, unique patients are represented by uniquely coloured lines. For a given patient, solid lines connect REAP scores of reactivities against respective antigens at various time points and dashed lines connect scaled anti-spike S1 ELISA values at those same time points. The dotted grey line indicates the scaled ELISA positivity cut off value (Methods).

[Source data](#)

Extended Data Fig. 4 Biochemical and functional validation of autoantibodies in patients with COVID-19.

a, Single-point pan-IgG autoantibody ELISAs conducted with 1:25 or 1:50 plasma dilution (indicated in graph titles). Dotted line represents the uninfected individual (healthcare worker) average plus 3 s.d. For controls, results (averages of technical duplicates) from biologically independent samples are displayed in the same column (n indicated below each column). For patients with COVID-19, results from one patient are displayed in each

column and technical duplicates are depicted as distinct points. **b–d**, GM-CSF (**b**), CD38 (**c**) and IL-18R β (**d**) pan-IgG autoantibody ELISAs conducted with serial dilutions of plasma from patients with COVID-19 or uninfected individuals. Results are averages of two technical replicates. Curves were fit using a sigmoidal four-parameter logistic curve. Experiments in **a–d** were performed once. **e**, Per cent of variance explained for principal components from the principal component analysis in Fig. [1d](#). **f**, Second principal component scores of samples from patients with COVID-19 stratified by clinical score. Solid black lines depict group means. **g**, Fixed-effects model fits from a generalized linear mixed effects model with second principal component score as the dependent variable (Methods). **h, i**, Flow cytometry gating for the Raji (**h**) and Jurkat (**i**) macrophage phagocytosis assay in Fig. [2c](#). **j, k**, IFN α 2 (**j**) and IFN ω (**k**) signalling assay performed with IgG from patients with COVID-19 who were positive for anti-IFN α 2 or anti-IFN ω autoantibody or from uninfected individuals. Results are averages of two technical replicates from one experiment. **l**, Fixed-effects model fits for the generalized linear mixed-effects model in Fig. [2d](#) (Methods). **m**, Hospital stay length in patients with and without autoantibodies targeting type I IFNs, stratified by disease severity. Significance in **m** was determined using a two-sided Wilcoxon rank-sum test. In **f**, *n* values include longitudinal samples from the same patient. All other *n* values in this figure indicate samples from unique patients.

[Source data](#)

[**Extended Data Fig. 5 Effects of anti-cytokine autoantibodies on corresponding cytokine plasma concentrations.**](#)

a–t, Average concentration of plasma CCL11 (**a**), CCL15 (**b**), CCL2 (**c**), CCL26 (**d**), CCL8 (**e**), CXCL1 (**f**), CXCL12 (**g**), CXCL13 (**h**), FLT3LG (**i**), IFN α 2 (**j**), IL-1A (**k**), IL-1B (**l**), IL-13 (**m**), IL-16 (**n**), IL-21 (**o**), IL-22 (**p**), IL6 (**q**), PDGFA (**r**), TGF α (**s**) and TSLP (**t**) measured by a Luminex assay in patients stratified by COVID-19 disease severity and REAP reactivity (autoantibody positive) (REAP score ≥ 2 at any time point) against the corresponding cytokine. Data are presented as box plots with the first quartile, median, third quartile, whiskers (minimum and maximum values

within the first and third quartiles $\pm 1.5 \times$ the interquartile range), and individual data points indicated. Significance was determined using two-sided, Wilcoxon rank-sum tests. All n values in this figure indicate samples from unique patients.

[Source data](#)

Extended Data Fig. 6 Additional correlations between autoantibodies targeting immune-cell surface proteins.

a, Average anti-SARS-CoV-2 RBD IgM reactivity as measured by ELISA in patients stratified by COVID-19 disease severity and REAP reactivity against B-cell-displayed proteins (as defined in Fig. 2e). **b**, Average percentage among total monocytes of classical monocytes, intermediate monocytes and nonclassical monocytes in patients stratified by COVID-19 disease severity and REAP reactivity against proteins preferentially displayed on classical and intermediate monocytes (as defined in Fig. 2f). **c**, Average per cent CD8⁺ T cells, natural killer T (NKT) cells and natural killer cells among peripheral leukocytes in patients stratified by COVID-19 disease severity and REAP reactivity against CD3ε. **d**, Average CD4⁺ T cell-to-natural killer cell ratio, CD8⁺ T cell-to-natural killer cell ratio and natural killer T cell-to-natural killer cell ratio among peripheral leukocytes in patients stratified by COVID-19 disease severity and REAP reactivity against CD3ε. **e**, Representative flow plot of T cells (CD3⁺), natural killer cells (CD56⁺) and natural killer T cells (CD3⁺CD56⁺) for c, d. **f**, Average per cent B cells, natural killer cells, activated CD4⁺ T cells and activated CD8⁺ T cells among peripheral leukocytes in patients stratified by COVID-19 disease severity and REAP reactivity against CD38. **g**, Representative flow plot of B cells (CD19⁺HLA-DR⁺) for f. **h**, Representative flow plot of activated CD8⁺ T cells (CD38⁺HLA-DR⁺) for f. Significance in a was determined using a two-sided Wilcoxon rank-sum test. All n values in this figure indicate samples from unique patients. All box plots are presented with the median, first and third quartile, whiskers (minimum and maximum values within the first and third quartiles $\pm 1.5 \times$ the interquartile range), and individual data points indicated.

[Source data](#)

Extended Data Fig. 7 Additional immunological and clinical characterization of autoantibody effects in a mouse model of COVID-19.

a–n, Schematic of experiment (**a**) in which K18-hACE2 mice were intranasally infected with a sublethal (**b–f**) or median lethal (**g–n**) dose of SARS-CoV-2 (USA-WA1/2020 isolate) and treated with indicated antibodies. **b, c**, Relative frequency (**b**) and absolute number (**c**) of lung Ly6C⁺CD11b⁺CD64⁺ macrophages from mock-infected, SARS-CoV-2-infected and PBS-treated, and SARS-CoV-2-infected and anti-IFNAR-treated K18-hACE2 mice. **d**, Expression of CD64 on lung-infiltrating CD11b⁺Ly6C^{high} monocytes. **e, f**, Relative frequency (**e**) and absolute number (**f**) of CD44⁺CD69⁺ lymphocytes (CD4⁺ T cells, CD8⁺ T cells, NK1.1⁺ cells and $\gamma\delta$ T cells). **g, h**, Viral RNA loads (**g**) and infectious titres (**h**) from lung tissue homogenates of mock-infected, SARS-CoV-2-infected and PBS-treated, and SARS-CoV-2-infected and anti-IL-18-treated mice measured by reverse-transcription qPCR and plaque assay, respectively. **i, j**, Relative frequency (**i**) or absolute number (**j**) of CD11b⁺ and KLRG1⁺NK1.1⁺ cells in lung tissues of PBS- and anti-IL-18-treated mice. **k–n**, Normalized body weight of anti-IL-18- (**k**), anti-IL-1 β - (**l**), anti-IL-21R- (**m**), anti-GM-CSF- (**n**) and PBS-treated, SARS-CoV-2-infected K18-hACE2 mice from day 1 to 14 after infection. Significance was determined using one-way analysis of variance followed by Tukey correction (**b–f, g**), and unpaired two-tailed *t*-tests (**i, j**). All *n* values in this figure represent biologically independent mice examined over two independent experiments.

[Source data](#)

Extended Data Fig. 8 Flow cytometry gating strategies for immunophenotyping experiments.

a, Gating strategy to identify the B cells described in Fig. 2e, monocytes described in Fig. 2f, Extended Data Fig. 6b, and T cells, natural killer T

cells and natural killer cells described in Fig. 2g, Extended Data Fig. 6c,d, f, in human peripheral blood mononuclear cells. b, Gating strategy to identify CD11b⁺Ly6C^{high} monocytes and Ly6C⁺CD11b⁺CD64⁺ macrophages in mouse lung tissues described in Extended Data Fig. 7b–d. c, Gating strategy to identify CD44⁺CD69⁺ lymphocytes in mouse lung tissues described in Extended Data Fig. 7e,f. d, Gating strategy to identify KLRG1⁺ and CD11b⁺ natural killer cells described in Extended Data Fig. 7i,j.

Extended Data Fig. 9 Tissue-associated autoantibodies are correlated with clinical parameters in patients with COVID-19.

Heat map of pairwise, $-\log_{10}$ -transformed REAP protein *P* values from generalized linear model fits accounting for age, sex and maximum REAP score in estimating average or minimum clinical values from hospital admission. A total of 135 samples from unique patients were included in this analysis ($n = 135$). Intensity represents *P* values and colour indicates directionality of gene-parameter pairs (red indicates positive change, blue indicates negative change). Grey columns indicate genes excluded from analysis due to insufficient patient number ($n < 2$). Asterisks denote pairwise relationships that were significant after correction for multiple comparisons (false-discovery rate). Specific details of the generalized linear models can be found in the Methods. Proteins were classified as in Fig. 4a.

[Source data](#)

Extended Data Table 1 Demographics and clinical characteristics for patients in the IMPACT cohort

[Full size table](#)

Supplementary information

Supplementary Information

This file contains the Supplementary Methods.

Reporting Summary

Supplementary Table 1

The full antigen list.

Peer Review File

Source data

Source Data Fig. 1

Source Data Fig. 2

Source Data Fig. 3

Source Data Fig. 4

Source Data Extended Data Fig. 1

Source Data Extended Data Fig. 2

Source Data Extended Data Fig. 3

Source Data Extended Data Fig. 4

Source Data Extended Data Fig. 5

Source Data Extended Data Fig. 6

Source Data Extended Data Fig. 7

Source Data Extended Data Fig. 9

Rights and permissions

[Reprints and Permissions](#)

About this article



Cite this article

Wang, E.Y., Mao, T., Klein, J. *et al.* Diverse functional autoantibodies in patients with COVID-19. *Nature* **595**, 283–288 (2021).
<https://doi.org/10.1038/s41586-021-03631-y>

[Download citation](#)

- Received: 04 December 2020
- Accepted: 11 May 2021
- Published: 19 May 2021
- Issue Date: 08 July 2021
- DOI: <https://doi.org/10.1038/s41586-021-03631-y>

Comments

By submitting a comment you agree to abide by our [Terms](#) and [Community Guidelines](#). If you find something abusive or that does not comply with our terms or guidelines please flag it as inappropriate.

[Download PDF](#)

Associated Content

Collection

[Coronavirus](#)

Advertisement

This article was downloaded by **calibre** from <https://www.nature.com/articles/s41586-021-03631-y>.

| [Section menu](#) | [Main menu](#) |

- Article
- [Published: 30 June 2021](#)

Two chemoattenuated PfSPZ malaria vaccines induce sterile hepatic immunity

- [Agnes Mwakingwe-Omari](#)¹ ORCID: orcid.org/0000-0003-3078-6094 Affl6,
- [Sara A. Healy](#) ORCID: orcid.org/0000-0003-3078-6094¹ ORCID: orcid.org/0000-0003-3078-6094 Affl1,
- [Jacquelyn Lane](#)¹,
- [David M. Cook](#)¹,
- [Sahand Kalhori](#)¹,
- [Charles Wyatt](#)¹,
- [Aarti Kolluri](#)¹,
- [Omely Marte-Salcedo](#)¹,
- [Alemush Imeru](#)¹,
- [Martha Nason](#) ORCID: orcid.org/0000-0002-0110-881X²,
- [Lei K. Ding](#)¹,
- [Hope Decederfelt](#)³,
- [Junhui Duan](#)¹,
- [Jillian Neal](#)¹,
- [Jacob Raiten](#)¹,
- [Grace Lee](#)¹,
- [Jen C. C. Hume](#)¹,
- [Jihyun E. Jeon](#)³,
- [Ijeoma Ikpeama](#)⁴,
- [Natasha KC](#)^{5,6},
- [Sumana Chakravarty](#)⁵,
- [Tooba Murshedkar](#)⁵,
- [L. W. Preston Church](#)⁵,

- [Anita Manoj⁵](#),
- [Anusha Gunasekera⁵](#),
- [Charles Anderson¹](#),
- [Sean C. Murphy](#) [ORCID: orcid.org/0000-0002-2048-0131](#)^{7,8,9,10},
- [Sandra March¹¹](#),
- [Sangeeta N. Bhatia](#) [ORCID: orcid.org/0000-0002-1293-2097](#)^{11,12,13,14,15},
- [Eric R. James⁵](#),
- [Peter F. Billingsley⁵](#),
- [B. Kim Lee Sim^{5,6}](#),
- [Thomas L. Richie](#) [ORCID: orcid.org/0000-0002-2946-5456](#)⁵,
- [Irfan Zaidi^{1 na2}](#),
- [Stephen L. Hoffman^{5 na2}](#) &
- [Patrick E. Duffy](#) [ORCID: orcid.org/0000-0002-4483-5005](#)¹

[Nature](#) volume **595**, pages 289–294 (2021) [Cite this article](#)

- 526 Accesses
- 1 Citations
- 477 Altmetric
- [Metrics details](#)

Subjects

- [Adaptive clinical trial](#)
- [Live attenuated vaccines](#)
- [Malaria](#)

Abstract

The global decline in malaria has stalled¹, emphasizing the need for vaccines that induce durable sterilizing immunity. Here we optimized regimens for chemoprophylaxis vaccination (CVac), for which aseptic,

purified, cryopreserved, infectious *Plasmodium falciparum* sporozoites (PfSPZ) were inoculated under prophylactic cover with pyrimethamine (PYR) (Sanaria PfSPZ-CVac(PYR)) or chloroquine (CQ) (PfSPZ-CVac(CQ))—which kill liver-stage and blood-stage parasites, respectively—and we assessed vaccine efficacy against homologous (that is, the same strain as the vaccine) and heterologous (a different strain) controlled human malaria infection (CHMI) three months after immunization (<https://clinicaltrials.gov/>, NCT02511054 and NCT03083847). We report that a fourfold increase in the dose of PfSPZ-CVac(PYR) from 5.12×10^4 to 2×10^5 PfSPZs transformed a minimal vaccine efficacy (low dose, two out of nine (22.2%) participants protected against homologous CHMI), to a high-level vaccine efficacy with seven out of eight (87.5%) individuals protected against homologous and seven out of nine (77.8%) protected against heterologous CHMI. Increased protection was associated with V δ 2 $\gamma\delta$ T cell and antibody responses. At the higher dose, PfSPZ-CVac(CQ) protected six out of six (100%) participants against heterologous CHMI three months after immunization. All homologous (four out of four) and heterologous (eight out of eight) infectivity control participants showed parasitaemia. PfSPZ-CVac(CQ) and PfSPZ-CVac(PYR) induced a durable, sterile vaccine efficacy against a heterologous South American strain of *P. falciparum*, which has a genome and predicted CD8 T cell immunome that differs more strongly from the African vaccine strain than other analysed African *P. falciparum* strains.

Access options

Subscribe to Journal

Get full journal access for 1 year

\$199.00

only \$3.90 per issue

[Subscribe](#)

All prices are NET prices.
VAT will be added later in the checkout.
Tax calculation will be finalised during checkout.

Rent or Buy article

Get time limited or full article access on ReadCube.

from \$8.99

[Rent or Buy](#)

All prices are NET prices.

Additional access options:

- [Log in](#)
- [Access through your institution](#)
- [Learn about institutional subscriptions](#)

Fig. 1: Parasitaemia detected by qPCR after the first, second and third dose of 2×10^5 PfSPZ for the PfSPZ-CVac high-dose study and PYR activity against liver-stage parasites.

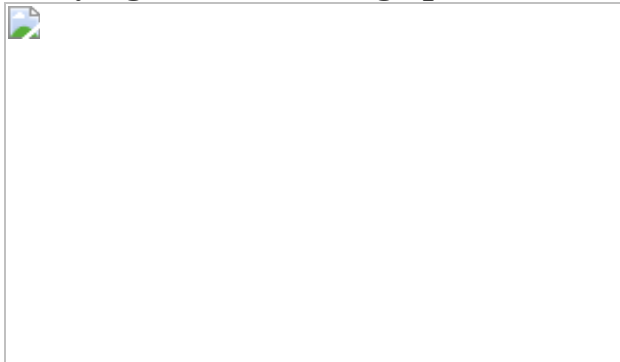


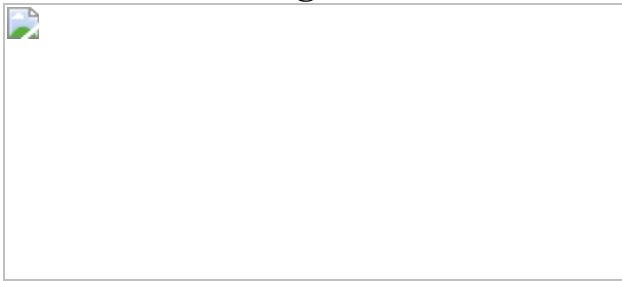
Fig. 2: Vaccine efficacy of PfSPZ-CVac(PYR) against homologous and heterologous CHMI and PfSPZ-CVac(CQ) against heterologous CHMI, 3 months after the last immunization.



Fig. 3: V δ 2 $\gamma\delta$ T cells related to protective immunity.



Fig. 4: Anti-PfCSP IgG levels by ELISA in vaccinated participants of the low-dose and high-dose studies.



Data availability

The data supporting the findings of this study are available within the Article and its Supplementary Information and from the corresponding author upon reasonable request.

References

1. 1.

WHO. *World Malaria Report 2019* (World Health Organization, 2019).

2. 2.

The RTS,S Clinical Trials Partnership. Efficacy and safety of the RTS,S/AS01 malaria vaccine during 18 months after vaccination: a phase 3 randomized, controlled trial in children and young infants at 11 African sites. *PLoS Med.* **11**, e1001685 (2014).

[Google Scholar](#)

3. 3.

RTS,S Clinical Trials Partnership. Efficacy and safety of RTS,S/AS01 malaria vaccine with or without a booster dose in infants and children in Africa: final results of a phase 3, individually randomised, controlled trial. *Lancet* **386**, 31–45 (2015).

[Google Scholar](#)

4. 4.

The RTS,S Clinical Trials Partnership. A phase 3 trial of RTS,S/AS01 malaria vaccine in African infants. *N. Engl. J. Med.* **367**, 2284–2295 (2012).

[Google Scholar](#)

5. 5.

Epstein, J. E. et al. Protection against *Plasmodium falciparum* malaria by PfSPZ vaccine. *JCI Insight* **2**, e89154 (2017).

[PubMed](#) [PubMed Central](#) [Google Scholar](#)

6. 6.

Jongo, S. A. et al. Safety, immunogenicity, and protective efficacy against controlled human malaria infection of *Plasmodium falciparum* sporozoite vaccine in Tanzanian adults. *Am. J. Trop. Med. Hyg.* **99**, 338–349 (2018).

[CAS](#) [PubMed](#) [PubMed Central](#) [Google Scholar](#)

7. 7.

Lyke, K. E. et al. Attenuated PfSPZ vaccine induces strain-transcending T cells and durable protection against heterologous controlled human malaria infection. *Proc. Natl Acad. Sci. USA* **114**, 2711–2716 (2017).

[CAS](#) [PubMed](#) [PubMed Central](#) [Google Scholar](#)

8. 8.

Seder, R. A. et al. Protection against malaria by intravenous immunization with a nonreplicating sporozoite vaccine. *Science* **341**, 1359–1365 (2013).

[ADS](#) [CAS](#) [Google Scholar](#)

9. 9.

Sissoko, M. S. et al. Safety and efficacy of PfSPZ vaccine against *Plasmodium falciparum* via direct venous inoculation in healthy malaria-exposed adults in Mali: a randomised, double-blind phase 1 trial. *Lancet Infect. Dis.* **17**, 498–509 (2017).

[CAS](#) [PubMed](#) [PubMed Central](#) [Google Scholar](#)

10. 10.

Sissoko, M. S. et al. Three dose regimen of PfSPZ vaccine protects adult Malians against *Plasmodium falciparum* through an intense transmission season: a randomised, controlled phase I trial. *Lancet Infect. Dis.* (in the press).

11. 11.

Butler, N. S. et al. Superior antimalarial immunity after vaccination with late liver stage-arresting genetically attenuated parasites. *Cell*

Host Microbe **9**, 451–462 (2011).

[CAS](#) [PubMed](#) [PubMed Central](#) [Google Scholar](#)

12. 12.

Kublin, J. G. et al. Complete attenuation of genetically engineered sporozoites in human subjects. *Sci. Transl. Med.* **9**, eaad9099 (2017).

13. 13.

Roestenberg, M. et al. A double-blind, placebo-controlled phase 1/2a trial of the genetically attenuated malaria vaccine PfSPZ-GA1. *Sci. Transl. Med.* **12**, eaa5629 (2020).

[CAS](#) [Google Scholar](#)

14. 14.

Roestenberg, M. et al. Protection against a malaria challenge by sporozoite inoculation. *N. Engl. J. Med.* **361**, 468–477 (2009).

[CAS](#) [Google Scholar](#)

15. 15.

Bijker, E. M. et al. Sporozoite immunization of human volunteers under mefloquine prophylaxis is safe, immunogenic and protective: a double-blind randomized controlled clinical trial. *PLoS ONE* **9**, e112910 (2014).

[ADS](#) [PubMed](#) [PubMed Central](#) [Google Scholar](#)

16. 16.

Sahu, T. et al. Chloroquine neither eliminates liver stage parasites nor delays their development in a murine chemoprophylaxis vaccination model. *Front. Microbiol.* **6**, 283 (2015).

[PubMed](#) [PubMed Central](#) [Google Scholar](#)

17. 17.

Hoffman, S. L. et al. Protection of humans against malaria by immunization with radiation-attenuated *Plasmodium falciparum* sporozoites. *J. Infect. Dis.* **185**, 1155–1164 (2002).

[Google Scholar](#)

18. 18.

Mordmüller, B. et al. Sterile protection against human malaria by chemoattenuated PfSPZ vaccine. *Nature* **542**, 445–449 (2017).

[ADS](#) [Google Scholar](#)

19. 19.

Schats, R. et al. Heterologous protection against malaria after immunization with *Plasmodium falciparum* sporozoites. *PLoS ONE* **10**, e0124243 (2015).

[PubMed](#) [PubMed Central](#) [Google Scholar](#)

20. 20.

Walk, J. et al. Modest heterologous protection after *Plasmodium falciparum* sporozoite immunization: a double-blind randomized controlled clinical trial. *BMC Med.* **15**, 168 (2017).

[PubMed](#) [PubMed Central](#) [Google Scholar](#)

21. 21.

Friesen, J., Borrman, S. & Matuschewski, K. Induction of antimalaria immunity by pyrimethamine prophylaxis during exposure to sporozoites is curtailed by parasite resistance. *Antimicrob. Agents Chemother.* **55**, 2760–2767 (2011).

[CAS](#) [PubMed](#) [PubMed Central](#) [Google Scholar](#)

22. 22.

Friesen, J. & Matuschewski, K. Comparative efficacy of pre-erythrocytic whole organism vaccine strategies against the malaria parasite. *Vaccine* **29**, 7002–7008 (2011).

[CAS](#) [Google Scholar](#)

23. 23.

Healy, S. A. et al. Chemoprophylaxis vaccination: phase I study to explore stage-specific immunity to *Plasmodium falciparum* in US adults. *Clin. Infect. Dis.* **71**, 1481–1490 (2020).

[CAS](#) [Google Scholar](#)

24. 24.

Epstein, J. E. & Richie, T. L. The whole parasite, pre-erythrocytic stage approach to malaria vaccine development: a review. *Curr. Opin. Infect. Dis.* **26**, 420–428 (2013).

[CAS](#) [Google Scholar](#)

25. 25.

March, S. et al. A microscale human liver platform that supports the hepatic stages of *Plasmodium falciparum* and *vivax*. *Cell Host Microbe* **14**, 104–115 (2013).

[CAS](#) [PubMed](#) [PubMed Central](#) [Google Scholar](#)

26. 26.

March, S. et al. Micropatterned coculture of primary human hepatocytes and supportive cells for the study of hepatotropic pathogens. *Nat. Protocols* **10**, 2027–2053 (2015).

[CAS](#) [Google Scholar](#)

27. 27.

Gural, N. et al. In vitro culture, drug sensitivity, and transcriptome of *Plasmodium vivax* hypnozoites. *Cell Host Microbe* **23**, 395–406.e4 (2018).

[CAS](#) [PubMed](#) [PubMed Central](#) [Google Scholar](#)

28. 28.

White, N. J. Clinical pharmacokinetics of antimalarial drugs. *Clin. Pharmacokinet.* **10**, 187–215 (1985).

[CAS](#) [Google Scholar](#)

29. 29.

Ishizuka, A. S. et al. Protection against malaria at 1 year and immune correlates following PfSPZ vaccination. *Nat. Med.* **22**, 614–623 (2016).

[CAS](#) [Google Scholar](#)

30. 30.

Zaidi, I. et al. $\gamma\delta$ T cells are required for the induction of sterile immunity during irradiated sporozoite vaccinations. *J. Immunol.* **199**, 3781–3788 (2017).

[CAS](#) [Google Scholar](#)

31. 31.

Nahrendorf, W., Scholzen, A., Sauerwein, R. W. & Langhorne, J. Cross-stage immunity for malaria vaccine development. *Vaccine* **33**, 7513–7517 (2015).

[CAS](#) [PubMed](#) [PubMed Central](#) [Google Scholar](#)

32. 32.

Nahrendorf, W. et al. Blood-stage immunity to *Plasmodium chabaudi* malaria following chemoprophylaxis and sporozoite immunization. *eLife* **4**, e05165 (2015).

[PubMed](#) [PubMed Central](#) [Google Scholar](#)

33. 33.

Moser, K. A. et al. Strains used in whole organism *Plasmodium falciparum* vaccine trials differ in genome structure, sequence, and immunogenic potential. *Genome Med.* **12**, 6 (2020).

[CAS](#) [PubMed](#) [PubMed Central](#) [Google Scholar](#)

34. 34.

Bijker, E. M. et al. Protection against malaria after immunization by chloroquine prophylaxis and sporozoites is mediated by preerythrocytic immunity. *Proc. Natl Acad. Sci. USA* **110**, 7862–7867 (2013).

[ADS](#) [CAS](#) [PubMed](#) [PubMed Central](#) [Google Scholar](#)

35. 35.

Belouye, E. et al. Protective T cell immunity against malaria liver stage after vaccination with live sporozoites under chloroquine treatment. *J. Immunol.* **172**, 2487–2495 (2004).

[CAS](#) [Google Scholar](#)

36. 36.

Lyke, K. E. et al. Multidose priming and delayed boosting improve *Plasmodium falciparum* sporozoite vaccine efficacy against

heterologous *P. falciparum* controlled human malaria infection. *Clin. Infect. Dis.* ciaa1294 (2020).

37. 37.

Hoffman, S. L. & Doolan, D. L. Malaria vaccines-targeting infected hepatocytes. *Nat. Med.* **6**, 1218–1219 (2000).

[CAS](#) [Google Scholar](#)

38. 38.

Epstein, J. E. et al. Live attenuated malaria vaccine designed to protect through hepatic CD8⁺ T cell immunity. *Science* **334**, 475–480 (2011).

[ADS](#) [CAS](#) [Google Scholar](#)

39. 39.

Issiaka, D. et al. Impact of seasonal malaria chemoprevention on hospital admissions and mortality in children under 5 years of age in Ouelessebougou, Mali. *Malar. J.* **19**, 103 (2020).

[PubMed](#) [PubMed Central](#) [Google Scholar](#)

40. 40.

Jongo, S. A. et al. Safety and differential antibody and T-cell responses to the *Plasmodium falciparum* sporozoite malaria vaccine, PfSPZ vaccine, by age in Tanzanian adults, adolescents, children, and infants. *Am. J. Trop. Med. Hyg.* **100**, 1433–1444 (2019).

[CAS](#) [PubMed](#) [PubMed Central](#) [Google Scholar](#)

41. 41.

Sulyok, Z. et al. Heterologous protection against malaria by a simple chemoattenuated PfSPZ vaccine regimen in a randomized trial. *Nat. Commun.* **12**, 2518 (2021)

42. 42.

Spring, M. et al. First-in-human evaluation of genetically attenuated *Plasmodium falciparum* sporozoites administered by bite of *Anopheles* mosquitoes to adult volunteers. *Vaccine* **31**, 4975–4983 (2013).

[Google Scholar](#)

43. 43.

Goswami, D. et al. A replication-competent late liver stage-attenuated human malaria parasite. *JCI Insight* **5**, e135589 (2020).

[PubMed](#) [PubMed Central](#) [Google Scholar](#)

44. 44.

Roestenberg, M. et al. Controlled human malaria infections by intradermal injection of cryopreserved *Plasmodium falciparum* sporozoites. *Am. J. Trop. Med. Hyg.* **88**, 5–13 (2013).

45. 45.

Mordmüller, B. et al. Direct venous inoculation of *Plasmodium falciparum* sporozoites for controlled human malaria infection: a dose-finding trial in two centres. *Malaria J.* **14**, 117 (2015).

46. 46.

Laurens, M. B. et al. Dose-dependent infectivity of aseptic, purified, cryopreserved *Plasmodium falciparum* 7G8 sporozoites in malaria-naïve adults. *J. Infect. Dis.* **220**, 1962–1966 (2019).

47. 47.

Divis, P. C., Shokoples, S. E., Singh, B. & Yanow, S. K. A TaqMan real-time PCR assay for the detection and quantitation of *Plasmodium knowlesi*. *Malar. J.* **9**, 344 (2010).

[CAS](#) [PubMed](#) [PubMed Central](#) [Google Scholar](#)

48. 48.

Seilie, A. M. et al. Beyond blood smears: qualification of *Plasmodium* 18S rRNA as a biomarker for controlled human malaria infections. *Am. J. Trop. Med. Hyg.* **100**, 1466–1476 (2019).

[PubMed](#) [PubMed Central](#) [Google Scholar](#)

49. 49.

Luethy, P. M. et al. Diagnostic challenges of prolonged post-treatment clearance of *Plasmodium* nucleic acids in a pre-transplant autosplenectomized patient with sickle cell disease. *Malar. J.* **17**, 23 (2018).

[PubMed](#) [PubMed Central](#) [Google Scholar](#)

50. 50.

Rougemont, M. et al. Detection of four *Plasmodium* species in blood from humans by 18S rRNA gene subunit-based and species-specific real-time PCR assays. *J. Clin. Microbiol.* **42**, 5636–5643 (2004).

[CAS](#) [PubMed](#) [PubMed Central](#) [Google Scholar](#)

51. 51.

Gabriel, E. E., Nason, M., Fay, M. P. & Follmann, D. A. A boundary-optimized rejection region test for the two-sample binomial problem. *Stat. Med.* **37**, 1047–1058 (2018).

[MathSciNet](#) [Google Scholar](#)

[Download references](#)

Acknowledgements

We thank the participants of the vaccine trial for their contribution and commitment to vaccine research. This work was supported by the Intramural Research Program of the National Institute of Allergy and Infectious Diseases (NIAID), National Institutes of Health and by the NIAID grants U01AI109700-01 and 2R44AI058375-11 to Sanaria for vaccine manufacture and trial execution. S.N.B. is a Howard Hughes Medical Institute Investigator. We thank the Sanaria and Protein Potential legal, administrative, manufacturing, quality, logistics, pharmaceutical operations, regulatory and clinical teams for their support of this project; T. Bauch, U. Desai, M. Mahoney, L. Walker, L. Williams of the Department of Laboratory Medicine, NIH CC for performing the malaria PCR diagnostic tests; N. Nerurkar for establishing and infecting the micropatterned co-cultures of hepatocytes; the LMIV and NIH CC clinical, pharmacy, immunology, laboratory, data, sample and project management teams and, in particular, NIH CC Outpatient Clinic 8 and Day Hospital Staffing; and J. Patrick Gorres for coordinating the preparation of the manuscript.

Author information

Author notes

1. Agnes Mwakingwe-Omari

Present address: Center for Vaccine Research, GlaxoSmithKline,
Rockville, MD, USA

2. These authors contributed equally: Agnes Mwakingwe-Omari, Sara A. Healy
3. These authors jointly supervised this work: Stephen L. Hoffman, Patrick E. Duffy

Affiliations

1. Laboratory of Malaria Immunology and Vaccinology, National Institute of Allergy and Infectious Diseases, National Institutes of Health, Bethesda, MD, USA

Agnes Mwakingwe-Omari, Sara A. Healy, Jacquelyn Lane, David M. Cook, Sahand Kalhori, Charles Wyatt, Aarti Kolluri, Omely Marte-Salcedo, Alemush Imeru, Lei K. Ding, Junhui Duan, Jillian Neal, Jacob Raiten, Grace Lee, Jen C. C. Hume, Charles Anderson, Irfan Zaidi & Patrick E. Duffy

2. Biostatistical Research Branch, National Institute of Allergy and Infectious Diseases, Rockville, MD, USA

Martha Nason

3. Clinical Center Pharmacy Department, National Institutes of Health, Bethesda, MD, USA

Hope Decederfelt & Jihyun E. Jeon

4. Department of Laboratory Medicine, Clinical Center, National Institutes of Health, Bethesda, MD, USA

Ijeoma Ikpeama

5. Sanaria, Rockville, MD, USA

Natasha KC, Sumana Chakravarty, Tooba Murshedkar, L. W. Preston Church, Anita Manoj, Anusha Gunasekera, Eric R. James, Peter F. Billingsley, B. Kim Lee Sim, Thomas L. Richie & Stephen L. Hoffman

6. Protein Potential, Rockville, MD, USA

Natasha KC & B. Kim Lee Sim

7. Department of Laboratory Medicine and Pathology, University of Washington, Seattle, WA, USA

Sean C. Murphy

8. Department of Microbiology, University of Washington, Seattle, WA, USA

Sean C. Murphy

9. Seattle Malaria Clinical Trials Center, Fred Hutch Cancer Research Center, Seattle, WA, USA

Sean C. Murphy

10. Center for Emerging and Re-emerging Infectious Diseases, University of Washington, Seattle, WA, USA

Sean C. Murphy

11. Institute for Medical Engineering and Science, Massachusetts Institute of Technology, Cambridge, MA, USA

Sandra March & Sangeeta N. Bhatia

12. Koch Institute for Integrative Cancer Research, Cambridge, MA, USA

Sangeeta N. Bhatia

13. Broad Institute, Cambridge, MA, USA

Sangeeta N. Bhatia

14. Howard Hughes Medical Institute, Chevy Chase, MD, USA

Sangeeta N. Bhatia

15. Department of Medicine, Brigham and Women's Hospital, Boston, MA, USA

Sangeeta N. Bhatia

Authors

1. Agnes Mwakingwe-Omari
[View author publications](#)

You can also search for this author in [PubMed](#) [Google Scholar](#)

2. Sara A. Healy

[View author publications](#)

You can also search for this author in [PubMed](#) [Google Scholar](#)

3. Jacquelyn Lane

[View author publications](#)

You can also search for this author in [PubMed](#) [Google Scholar](#)

4. David M. Cook

[View author publications](#)

You can also search for this author in [PubMed](#) [Google Scholar](#)

5. Sahand Kalhori

[View author publications](#)

You can also search for this author in [PubMed](#) [Google Scholar](#)

6. Charles Wyatt

[View author publications](#)

You can also search for this author in [PubMed](#) [Google Scholar](#)

7. Aarti Kolluri

[View author publications](#)

You can also search for this author in [PubMed](#) [Google Scholar](#)

8. Omely Marte-Salcedo

[View author publications](#)

You can also search for this author in [PubMed](#) [Google Scholar](#)

9. Alemush Imeru

[View author publications](#)

You can also search for this author in [PubMed](#) [Google Scholar](#)

10. Martha Nason

[View author publications](#)

You can also search for this author in [PubMed](#) [Google Scholar](#)

11. Lei K. Ding

[View author publications](#)

You can also search for this author in [PubMed](#) [Google Scholar](#)

12. Hope Decederfelt

[View author publications](#)

You can also search for this author in [PubMed](#) [Google Scholar](#)

13. Junhui Duan

[View author publications](#)

You can also search for this author in [PubMed](#) [Google Scholar](#)

14. Jillian Neal

[View author publications](#)

You can also search for this author in [PubMed](#) [Google Scholar](#)

15. Jacob Raiten

[View author publications](#)

You can also search for this author in [PubMed](#) [Google Scholar](#)

16. Grace Lee

[View author publications](#)

You can also search for this author in [PubMed](#) [Google Scholar](#)

17. Jen C. C. Hume

[View author publications](#)

You can also search for this author in [PubMed](#) [Google Scholar](#)

18. Jihyun E. Jeon

[View author publications](#)

You can also search for this author in [PubMed](#) [Google Scholar](#)

19. Ijeoma Ikpeama

[View author publications](#)

You can also search for this author in [PubMed](#) [Google Scholar](#)

20. Natasha KC

[View author publications](#)

You can also search for this author in [PubMed](#) [Google Scholar](#)

21. Sumana Chakravarty

[View author publications](#)

You can also search for this author in [PubMed](#) [Google Scholar](#)

22. Tooba Murshedkar

[View author publications](#)

You can also search for this author in [PubMed](#) [Google Scholar](#)

23. L. W. Preston Church

[View author publications](#)

You can also search for this author in [PubMed](#) [Google Scholar](#)

24. Anita Manoj

[View author publications](#)

You can also search for this author in [PubMed](#) [Google Scholar](#)

25. Anusha Gunasekera

[View author publications](#)

You can also search for this author in [PubMed](#) [Google Scholar](#)

26. Charles Anderson

[View author publications](#)

You can also search for this author in [PubMed](#) [Google Scholar](#)

27. Sean C. Murphy

[View author publications](#)

You can also search for this author in [PubMed](#) [Google Scholar](#)

28. Sandra March

[View author publications](#)

You can also search for this author in [PubMed](#) [Google Scholar](#)

29. Sangeeta N. Bhatia

[View author publications](#)

You can also search for this author in [PubMed](#) [Google Scholar](#)

30. Eric R. James

[View author publications](#)

You can also search for this author in [PubMed](#) [Google Scholar](#)

31. Peter F. Billingsley

[View author publications](#)

You can also search for this author in [PubMed](#) [Google Scholar](#)

32. B. Kim Lee Sim

[View author publications](#)

You can also search for this author in [PubMed](#) [Google Scholar](#)

33. Thomas L. Richie

[View author publications](#)

You can also search for this author in [PubMed](#) [Google Scholar](#)

34. Irfan Zaidi

[View author publications](#)

You can also search for this author in [PubMed](#) [Google Scholar](#)

35. Stephen L. Hoffman

[View author publications](#)

You can also search for this author in [PubMed](#) [Google Scholar](#)

36. Patrick E. Duffy

[View author publications](#)

You can also search for this author in [PubMed](#) [Google Scholar](#)

Contributions

S.A.H., S.L.H. and P.E.D. conceived and designed the study. A.M.-O., S.A.H., J.L., D.M.C., S.K., C.W., A.K., O.M.-S., A.I., L.K.D., H.D. and J.E.J. executed the clinical trials, with safety oversight by L.W.C.P. and T.L.R. T.M., A.M., A.G., B.K.L.S., P.F.B. and E.R.J. prepared the investigational product and coordinated regulatory affairs. M.N. analysed the clinical trial results. J.D., J.N., J.R., G.L., J.C.C.H., N.K., S.C., I.I., C.A., S.C.M., S.M., S.N.B. and I.Z. designed and performed laboratory studies. A.M.-O., S.L.H. and P.E.D. prepared the initial manuscript draft; all authors reviewed and edited the manuscript. A.M.-O. and S.A.H. supervised the trials and S.L.H. and P.E.D. supervised the study teams.

Corresponding author

Correspondence to [Patrick E. Duffy](#).

Ethics declarations

Competing interests

T.M., L.W.P.C., A.M., A.G., B.K.L.S., N.K.C., S.C., P.F.B., E.R.J., T.L.R. and S.L.H. are salaried, full-time employees of Sanaria, the developer and sponsor of Sanaria PfSPZ Vaccine. S.L.H. and B.K.L.S. also have financial interests in Sanaria. B.K.L.S. and S.L.H. are inventors on patents and patent applications that have been assigned to Sanaria. All other authors declare no competing interests.

Additional information

Peer review information *Nature* thanks Stefan Kappe and Laurent Renia for their contribution to the peer review of this work. Peer reviewer reports are available.

Publisher's note Springer Nature remains neutral with regard to jurisdictional claims in published maps and institutional affiliations.

Extended data figures and tables

[Extended Data Fig. 1 Trial profile for PfSPZ-CVac low-dose study.](#)

^aOne participant was treated at day 16 after CHMI although that participant did complete the end-of-study visit. ^bThe serious adverse event (SAE) and adverse event (AE) in the PYR/CQ group were encephalopathy and eye irritation, respectively. The non-compliance incidents include a participant's unwillingness to remain on pregnancy prevention (PYR/CQ group) and a work conflict preventing the participant from attending scheduled visits (CQ group).

[Extended Data Fig. 2 Detection of parasitaemia in volunteers by qPCR after low-dose PfSPZ-CVac.](#)

Parasitaemia was measured in participants on days 6–10 after each PfSPZ-CVac dose. The median parasitaemia is displayed for positive participants and error bars indicate the IQR. Vax, PfSPZ Challenge + CQ or PYR/CQ

administration and follow-up until day 14 after PfSPZ Challenge 1 and day 10 after PfSPZ Challenge doses 2 and 3. The table shows (from left to right in each cell): the number of participants who were positive by qPCR/the injected number of participants; the median peak parasite density of positive participants (parasites per ml); and the average day of peak parasite density after each dose of PfSPZ-CVac. ND, not detected; n/a, not applicable.

Extended Data Fig. 3 Protective efficacy of PfSPZ-CVac(CQ) and PfSPZ-CVac(PYR + CQ) against homologous PfSPZ CHMI in the PfSPZ-CVac low-dose study.

Participants were followed for 27 days after CHMI, and a survival curve is presented displaying the number of participants that remained protected throughout follow-up after homologous CHMI. To assess vaccine efficacy, the unvaccinated group was compared with the vaccine group for time to first detectable parasitaemia after the final challenge using a log-rank test, and the presence or absence of parasitaemia using a two-tailed Barnard's test. In the pilot PfSPZ-CVac(PYR + CQ) group (to test safety), 0/2 participants were protected; in the main PfSPZ-CVac(PYR+CQ) group, 2/9 (22.2%, $P = 0.8$) participants were protected; in the PfSPZ-CVac(CQ) group, 4/5 (80%, $P = 0.048$; 95% confidence interval, 1–99%) participants were protected.

Extended Data Fig. 4 Trial profile for the PfSPZ-CVac high-dose study.

^aOther, 15 withdrew consent, 6 deemed eligible after study was fully enrolled, 3 lost to follow-up, 2 schedule conflict, 1 withdrawn before randomization. ^bOne individual enrolled in the PYR group was withdrawn before receiving the first vaccination owing to acute illness, and enrolled in the control group. This person is counted twice. ^cBoth participants were withdrawn before receiving vaccination 1. ^dThe two serious adverse events in the CQ group were mental status change and pneumothorax.

Extended Data Fig. 5 V δ 2 $\gamma\delta$ T cells at baseline in protected and infected individuals who received the vaccine.

Filled circles indicate vaccinated participants in the high-dose study, and open circles indicate vaccinated participants in the low-dose study. Median values are displayed and error bars indicate the IQR. For protected individuals in the high-dose study, $n = 20$; for protected individuals in the low-dose study, $n = 6$. For infected individuals in the high-dose study, $n = 3$; for infected individuals in the low-dose study, $n = 8$.

Extended Data Fig. 6 Anti-PfCSP IgM antibodies in vaccinated participants in the PfSPZ-CVac high-dose study analysed using ELISA.

IgM antibodies against PfCSP (net OD 1.0) 2 weeks after the third dose of PfSPZ-CVac(PYR) and PfSPZ-CVac(CQ); and immediately before CHMI. Median values are displayed and error bars indicate the IQR. At both time points, sample sizes for the PYR high-dose study, $n = 14$ for protected and $n = 3$ for infected vaccinated participants; for the CQ high-dose study, $n = 6$ for protected vaccinated individuals at 2 weeks after the third CVac and $n = 5$ for protected vaccinated individuals at before CHMI. No vaccinated participants were infected in the CQ high-dose study.

Extended Data Fig. 7 Antibody responses in vaccinated participants of the PfSPZ-CVac low-dose and PfSPZ-CVac high-dose studies analysed using automated immunofluorescence and automated inhibition of sporozoite invasion assays.

For each panel, filled circles are protected participants, open circles are infected participants who received homologous CHMI, filled triangles are uninfected (protected) participants and open triangles are infected participants who received heterologous CHMI. Median values are displayed and error bars indicate the IQR. P values were calculated using two-sided Wilcoxon–Mann–Whitney tests and group differences with $P > 0.07$ are not

indicated. **a, b**, Antibodies against PfCSP by automated immunofluorescence assay were analysed 2 weeks after the third dose of PfSPZ-CVac(PYR) and PfSPZ-CVac(CQ) (**a**) and immediately before CHMI (**b**). **c, d**, Antibodies against PfCSP by automated inhibition of sporozoite invasion were analysed 2 weeks after the third dose of PfSPZ-CVac(PYR) and PfSPZ-CVac(CQ) (**c**) and immediately before CHMI (**d**). At both time points, sample sizes for the PYR low-dose study, $n = 2$ for protected and $n = 7$ for infected vaccinated participants; for the PYR high-dose study, $n = 14$ for protected and $n = 3$ for infected vaccinated participants; for the CQ low-dose study, $n = 4$ for protected and $n = 1$ for infected vaccinated participants; for the CQ high-dose study, $n = 6$ for protected participants in **a** and **c** (2 weeks after the third CVac), and $n = 5$ for protected participants in **b** and **d** (before CHMI). No vaccinated participants were infected in the CQ high-dose study. Anti-PfCSP antibodies at both 2 weeks after the last dose (high-dose 1,941 versus low-dose 382, $P = 0.043$) and immediately before CHMI (high-dose 1,149 versus low-dose 95, $P = 0.009$) were significantly higher in the high-dose PfSPZ-CVac(PYR) participants compared with the low-dose PfSPZ-CVac(PYR) participants. In PfPSZ-CVac(CQ) participants, the anti-PfSPZ antibodies were higher but not significant (2 weeks after the third dose, 300 versus 4,272, $P = 0.176$; before CHMI, 245 versus 910, $P = 0.310$). The inhibition of sporozoite invasion assay showed a statistically significant increase after vaccination for the high-dose PfSPZ-CVac(PYR) versus low-dose PfSPZ-CVac(PYR) when measured 2 weeks after the third dose (45.00 versus 3.81, $P < 0.001$) and immediately before CHMI (39.87 versus 1.00, $P < 0.001$). In PfPSZ-CVac(CQ) participants, the anti-PfCSP antibodies were significantly higher in the high-dose group when measured 2 weeks after the third dose (29.79 versus 8.79, $P = 0.054$) but not significantly different before CHMI (5.67 versus 7.32, $P = 0.671$).

Extended Data Fig. 8 Detection of parasitaemia by qPCR in each individual after the first, second and third dose of PfSPZ-CVac in the high-dose study.

Parasitaemia was measured in participants on days 6–10 after each PfSPZ-CVac dose. Vax, PfSPZ Challenge + CQ or PYR administration and follow-

up until day 14 after PfSPZ Challenge 1 and day 10 after PfSPZ Challenge doses 2 and 3.

Extended Data Fig. 9 In vitro PYR activity against liver-stage parasites.

PYR was added to the cultures (blue) at three concentrations (1 μ M, 10 μ M and 100 μ M), starting 2 days after infection and replaced with daily medium changes until day 4, at which point the cultures were fixed. The diameter of representative parasites of each group on day 4 are shown. Ctl, control. Statistical significance was determined by one-sided ANOVA. *** $P < 0.001$ (exact $P = 0.0006$); **** $P < 0.0001$; ns, not significant (exact $P = 0.2335$).

Extended Data Fig. 10 Flow cytometry gating strategy used to enumerate T cell subsets using flow cytometry ex vivo staining of whole blood.

The FSC/SSC parameters were used to define the lymphocyte gate as the first gate in the whole blood ex vivo assay. Within the lymphocyte gate, CD3-Alexa-700-positive events (T cell gate) were gated against CD56-PE-Cy7-positive events (NK cells). In the T cell gate, plotting V δ 2-FITC versus gdTCR-PE identified discrete V δ 2 $^+$, V δ 2 $^-$ and CD3 $^+$ γ δ TCR $^-$ populations. The T cell gate was used to further delineate CD4- and CD8-positive events.

Supplementary information

Supplementary Information

This file contains notes on the clinical trial design for the first low-dose study, Supplementary Methods and Results and Supplementary Tables 1-4.

Reporting Summary

Supplementary Data

Raw data showing Vd2 results.

Peer Review File

Rights and permissions

Reprints and Permissions

About this article



Check for
updates

Cite this article

Mwakingwe-Omari, A., Healy, S.A., Lane, J. *et al.* Two chemoattenuated PfSPZ malaria vaccines induce sterile hepatic immunity. *Nature* **595**, 289–294 (2021). <https://doi.org/10.1038/s41586-021-03684-z>

Download citation

- Received: 29 December 2020
- Accepted: 01 June 2021
- Published: 30 June 2021
- Issue Date: 08 July 2021
- DOI: <https://doi.org/10.1038/s41586-021-03684-z>

Further reading

- [Vaccine made of live malaria parasites shows early success](#)

- Heidi Ledford

Nature (2021)

Comments

By submitting a comment you agree to abide by our [Terms](#) and [Community Guidelines](#). If you find something abusive or that does not comply with our terms or guidelines please flag it as inappropriate.

[Access through your institution](#)

[Change institution](#)

[Buy or subscribe](#)

Associated Content

[Malaria vaccine gets a parasite boost in the liver](#)

- Nana K. Minkah
- Stefan H. I. Kappe

Advertisement

This article was downloaded by **calibre** from <https://www.nature.com/articles/s41586-021-03684-z>

- Article
- [Published: 02 June 2021](#)

Base editing of haematopoietic stem cells rescues sickle cell disease in mice

- [Gregory A. Newby](#)^{1,2,3 na1},
- [Jonathan S. Yen](#) [ORCID: orcid.org/0000-0002-9432-9450](#)^{4 na1},
- [Kaitly J. Woodard](#) [ORCID: orcid.org/0000-0002-5622-8069](#)^{4 na1},
- [Thiyagaraj Mayuranathan](#)^{4 na1},
- [Cicera R. Lazzarotto](#) [ORCID: orcid.org/0000-0003-1093-0175](#)⁴,
- [Yichao Li](#) [ORCID: orcid.org/0000-0001-5791-096X](#)⁴,
- [Heather Sheppard-Tillman](#) [ORCID: orcid.org/0000-0002-9623-2812](#)⁵,
- [Shaina N. Porter](#)⁶,
- [Yu Yao](#)⁴,
- [Kalin Mayberry](#)⁴,
- [Kelcee A. Everette](#)^{1,2,3},
- [Yoonjeong Jang](#)⁴,
- [Christopher J. Podracky](#)^{1,2,3},
- [Elizabeth Thaman](#)⁷,
- [Christophe Lechauve](#)⁴,
- [Akshay Sharma](#) [ORCID: orcid.org/0000-0003-3281-2081](#)⁸,
- [Jordana M. Henderson](#)⁹,
- [Michelle F. Richter](#)^{1,2,3},
- [Kevin T. Zhao](#) [ORCID: orcid.org/0000-0003-3440-2094](#)^{1,2,3},
- [Shannon M. Miller](#)^{1,2,3},
- [Tina Wang](#)^{1,2,3},
- [Luke W. Koblan](#) [ORCID: orcid.org/0000-0003-2814-4412](#)^{1,2,3},
- [Anton P. McCaffrey](#)⁹,

- [John F. Tisdale¹⁰](#),
- [Theodosia A. Kalfa](#) ORCID: orcid.org/0000-0002-0426-9686^{7,11},
- [Shondra M. Pruett-Miller](#) ORCID: orcid.org/0000-0002-3793-585X⁶,
- [Shengdar Q. Tsai](#) ORCID: orcid.org/0000-0001-9161-3993⁴,
- [Mitchell J. Weiss](#) ORCID: orcid.org/0000-0003-2460-3036⁴ &
- [David R. Liu](#) ORCID: orcid.org/0000-0002-9943-7557^{1,2,3}

[Nature](#) volume **595**, pages 295–302 (2021) [Cite this article](#)

- 10k Accesses
- 482 Altmetric
- [Metrics details](#)

Subjects

- [Genetic engineering](#)
- [Haematological diseases](#)

Abstract

Sickle cell disease (SCD) is caused by a mutation in the β -globin gene *HBB*¹. We used a custom adenine base editor (ABE8e-NRCH)^{2,3} to convert the SCD allele (*HBB^S*) into Makassar β -globin (*HBB^G*), a non-pathogenic variant^{4,5}. Ex vivo delivery of mRNA encoding the base editor with a targeting guide RNA into haematopoietic stem and progenitor cells (HSPCs) from patients with SCD resulted in 80% conversion of *HBB^S* to *HBB^G*. Sixteen weeks after transplantation of edited human HSPCs into immunodeficient mice, the frequency of *HBB^G* was 68% and hypoxia-induced sickling of bone marrow reticulocytes had decreased fivefold, indicating durable gene editing. To assess the physiological effects of *HBB^S* base editing, we delivered ABE8e-NRCH and guide RNA into HSPCs from a humanized SCD mouse⁶ and then transplanted these cells into irradiated mice. After sixteen weeks, Makassar β -globin represented 79% of β -globin protein in blood, and hypoxia-induced sickling was reduced threefold. Mice

that received base-edited HSPCs showed near-normal haematological parameters and reduced splenic pathology compared to mice that received unedited cells. Secondary transplantation of edited bone marrow confirmed that the gene editing was durable in long-term haematopoietic stem cells and showed that *HBB^S*-to-*HBB^G* editing of 20% or more is sufficient for phenotypic rescue. Base editing of human HSPCs avoided the p53 activation and larger deletions that have been observed following Cas9 nuclease treatment. These findings point towards a one-time autologous treatment for SCD that eliminates pathogenic *HBB^S*, generates benign *HBB^G*, and minimizes the undesired consequences of double-strand DNA breaks.

Access options

Subscribe to Journal

Get full journal access for 1 year

\$199.00

only \$3.90 per issue

[Subscribe](#)

All prices are NET prices.

VAT will be added later in the checkout.

Tax calculation will be finalised during checkout.

Rent or Buy article

Get time limited or full article access on ReadCube.

from \$8.99

[Rent or Buy](#)

All prices are NET prices.

Additional access options:

- [Log in](#)
- [Access through your institution](#)
- [Learn about institutional subscriptions](#)

Fig. 1: Adenine base editing converts SCD β -globin gene (HBB^S) to benign Makassar β -globin gene (HBB^G) in patient CD34 $^{+}$ HSPCs.



Fig. 2: Engraftment of ABE8e-NRCH mRNA-treated SCD CD34 $^{+}$ HSPCs after transplantation into immunodeficient mice.

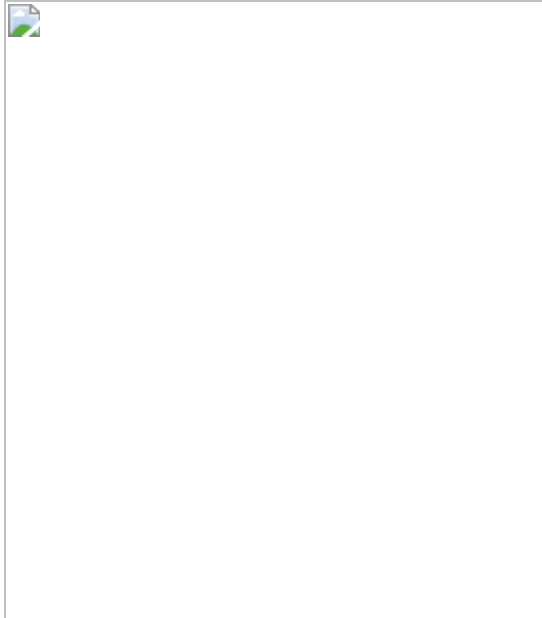


Fig. 3: HBB^S -to- HBB^G base editing alleviates pathology in a mouse model of SCD.

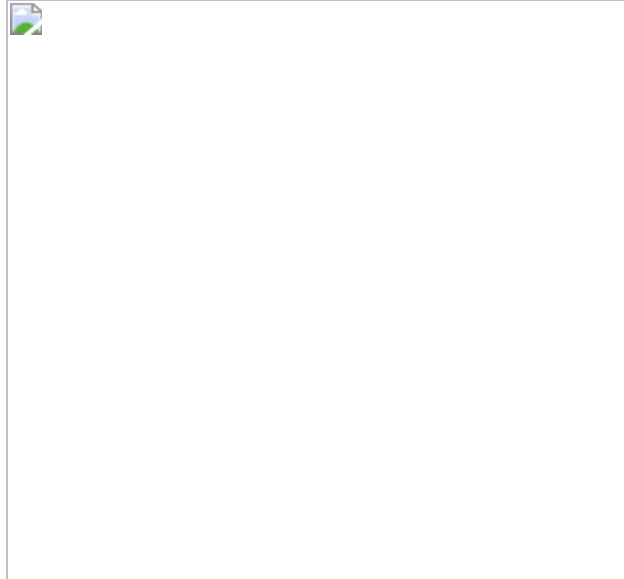
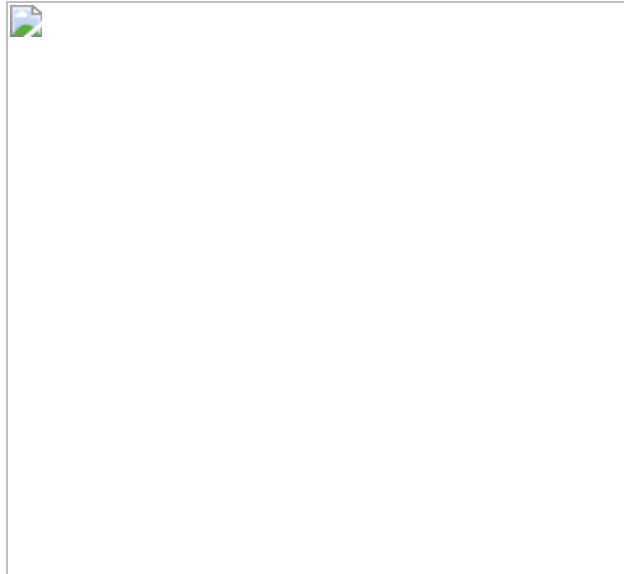


Fig. 4: Secondary transplantation reveals HBB^S -to- HBB^G base editing requirements for haematological correction.



Data availability

HTS sequencing files can be accessed using the NCBI Sequence Read Archive ([PRJNA725249](#)).

Code availability

The code used to conduct off-target quantification and the statistical analysis is available at https://github.com/tsailabSJ/MKSR_off_targets.

References

1. 1.

Piel, F. B., Steinberg, M. H. & Rees, D. C. Sickle cell disease. *N. Engl. J. Med.* **377**, 305 (2017).

[PubMed](#) [Google Scholar](#)

2. 2.

Richter, M. F. et al. Phage-assisted evolution of an adenine base editor with improved Cas domain compatibility and activity. *Nat. Biotechnol.* **38**, 883–891 (2020).

[CAS](#) [PubMed](#) [PubMed Central](#) [Google Scholar](#)

3. 3.

Miller, S. M. et al. Continuous evolution of SpCas9 variants compatible with non-G PAMs. *Nat. Biotechnol.* **38**, 471–481 (2020).

[CAS](#) [PubMed](#) [PubMed Central](#) [Google Scholar](#)

4. 4.

Sangkitporn, S., Rerkamnuaychoke, B., Sangkitporn, S., Mitrakul, C. & Sutivigit, Y. Hb G Makassar (β 6:Glu-Ala) in a Thai family. *J. Med. Assoc. Thai.* **85**, 577–582 (2002).

[PubMed](#) [Google Scholar](#)

5. 5.

Blackwell, R. Q., Oemijati, S., Pribadi, W., Weng, M. I. & Liu, C. S. Hemoglobin G Makassar: β 6 Glu \rightarrow Ala. *Biochim. Biophys. Acta* **214**, 396–401 (1970).

[CAS](#) [PubMed](#) [Google Scholar](#)

6. 6.

Wu, L. C. et al. Correction of sickle cell disease by homologous recombination in embryonic stem cells. *Blood* **108**, 1183–1188 (2006).

[CAS](#) [PubMed](#) [PubMed Central](#) [Google Scholar](#)

7. 7.

Leonard, A., Tisdale, J. & Abraham, A. Curative options for sickle cell disease: haploidentical stem cell transplantation or gene therapy? *Br. J. Haematol.* **189**, 408–423 (2020).

[PubMed](#) [Google Scholar](#)

8. 8.

Magrin, E., Miccio, A. & Cavazzana, M. Lentiviral and genome-editing strategies for the treatment of β -hemoglobinopathies. *Blood* **134**, 1203–1213 (2019).

[PubMed](#) [Google Scholar](#)

9. 9.

Zeng, J. et al. Therapeutic base editing of human hematopoietic stem cells. *Nat. Med.* **26**, 535–541 (2020).

[CAS](#) [PubMed](#) [PubMed Central](#) [Google Scholar](#)

10. 10.

Ribeil, J. A. et al. Gene therapy in a patient with sickle cell disease. *N. Engl. J. Med.* **376**, 848–855 (2017).

[CAS](#) [PubMed](#) [Google Scholar](#)

11. 11.

Esrick, E. B. et al. Post-transcriptional genetic silencing of *BCL11A* to treat sickle cell disease. *N. Engl. J. Med.* **384**, 205–215 (2021).

[CAS](#) [PubMed](#) [Google Scholar](#)

12. 12.

Frangoul, H. et al. CRISPR-Cas9 gene editing for sickle cell disease and β -thalassemia. *N. Engl. J. Med.* **384**, 252–260 (2021).

[CAS](#) [PubMed](#) [Google Scholar](#)

13. 13.

Zuccaro, M. V. et al. Allele-specific chromosome removal after Cas9 cleavage in human embryos. *Cell* **183**, 1650–1664.e15 (2020).

[CAS](#) [PubMed](#) [Google Scholar](#)

14. 14.

Song, Y. et al. Large-fragment deletions induced by Cas9 cleavage while not in the BEs system. *Mol. Ther. Nucleic Acids* **21**, 523–526 (2020).

[CAS](#) [PubMed](#) [PubMed Central](#) [Google Scholar](#)

15. 15.

Kosicki, M., Tomberg, K. & Bradley, A. Repair of double-strand breaks induced by CRISPR-Cas9 leads to large deletions and complex rearrangements. *Nat. Biotechnol.* **36**, 765–771 (2018).

[CAS](#) [PubMed](#) [PubMed Central](#) [Google Scholar](#)

16. 16.

Haapaniemi, E., Botla, S., Persson, J., Schmierer, B. & Taipale, J. CRISPR-Cas9 genome editing induces a p53-mediated DNA damage response. *Nat. Med.* **24**, 927–930 (2018).

[CAS](#) [PubMed](#) [Google Scholar](#)

17. 17.

Ihry, R. J. et al. p53 inhibits CRISPR-Cas9 engineering in human pluripotent stem cells. *Nat. Med.* **24**, 939–946 (2018).

[CAS](#) [PubMed](#) [Google Scholar](#)

18. 18.

Enache, O. M. et al. Cas9 activates the p53 pathway and selects for p53-inactivating mutations. *Nat. Genet.* **52**, 662–668 (2020).

[CAS](#) [PubMed](#) [PubMed Central](#) [Google Scholar](#)

19. 19.

Wilkinson, A. C. et al. Cas9-AAV6 gene correction of beta-globin in autologous HSCs improves sickle cell disease erythropoiesis in mice. *Nat. Commun.* **12**, 686 (2021).

[ADS](#) [CAS](#) [PubMed](#) [PubMed Central](#) [Google Scholar](#)

20. 20.

Dever, D. P. et al. CRISPR/Cas9 β-globin gene targeting in human haematopoietic stem cells. *Nature* **539**, 384–389 (2016).

[ADS](#) [CAS](#) [PubMed](#) [PubMed Central](#) [Google Scholar](#)

21. 21.

Viprakasit, V., Wiriyasateinkul, A., Sattayasevana, B., Miles, K. L. & Laosombat, V. Hb G-Makassar [β 6(A3)Glu \rightarrow Ala; codon 6 (GAG \rightarrow GCG)]: molecular characterization, clinical, and hematological effects. *Hemoglobin* **26**, 245–253 (2002).

[CAS](#) [PubMed](#) [Google Scholar](#)

22. 22.

Chu, S. H. et al. Rationally designed base editors for precise editing of the sickle cell disease mutation. *CRISPR J.* **4**, 169–177 (2021).

[CAS](#) [PubMed](#) [Google Scholar](#)

23. 23.

Bae, S., Park, J. & Kim, J. S. Cas-OFFinder: a fast and versatile algorithm that searches for potential off-target sites of Cas9 RNA-guided endonucleases. *Bioinformatics* **30**, 1473–1475 (2014).

[CAS](#) [PubMed](#) [PubMed Central](#) [Google Scholar](#)

24. 24.

Tsai, S. Q. et al. CIRCLE-seq: a highly sensitive in vitro screen for genome-wide CRISPR-Cas9 nuclease off-targets. *Nat. Methods* **14**, 607–614 (2017).

[CAS](#) [PubMed](#) [PubMed Central](#) [Google Scholar](#)

25. 25.

McIntosh, B. E. et al. Nonirradiated NOD,B6.SCID $Il2r\gamma^{-/-}$ $Kit^{W41/W41}$ (NBSGW) mice support multilineage engraftment of human hematopoietic cells. *Stem Cell Reports* **4**, 171–180 (2015).

[CAS](#) [PubMed](#) [PubMed Central](#) [Google Scholar](#)

26. 26.

.Alanis-Lobato, G. et al. Frequent loss-of-heterozygosity in CRISPR-Cas9-edited early human embryos. *Proc. Natl Acad. Sci. USA* <https://doi.org/10.1073/pnas.2004832117> (2021).

27. 27.

Demirci, S. et al. β T87Q-globin gene therapy reduces sickle hemoglobin production, allowing for *ex vivo* anti-sickling activity in human erythroid cells. *Mol. Ther. Methods Clin. Dev.* **17**, 912–921 (2020).

[CAS](#) [PubMed](#) [PubMed Central](#) [Google Scholar](#)

28. 28.

Wu, Y. et al. Highly efficient therapeutic gene editing of human hematopoietic stem cells. *Nat. Med.* **25**, 776–783 (2019).

[CAS](#) [PubMed](#) [PubMed Central](#) [Google Scholar](#)

29. 29.

Anzalone, A. V., Koblan, L. W. & Liu, D. R. Genome editing with CRISPR-Cas nucleases, base editors, transposases and prime editors. *Nat. Biotechnol.* **38**, 824–844 (2020).

[CAS](#) [PubMed](#) [Google Scholar](#)

30. 30.

Komor, A. C., Kim, Y. B., Packer, M. S., Zuris, J. A. & Liu, D. R. Programmable editing of a target base in genomic DNA without double-stranded DNA cleavage. *Nature* **533**, 420–424 (2016).

[ADS](#) [CAS](#) [PubMed](#) [PubMed Central](#) [Google Scholar](#)

31. 31.

Gaudelli, N. M. et al. Programmable base editing of A•T to G•C in genomic DNA without DNA cleavage. *Nature* **551**, 464–471 (2017).

[ADS](#) [CAS](#) [PubMed](#) [PubMed Central](#) [Google Scholar](#)

32. 32.

Huang, T. P., Newby, G. A. & Liu, D. R. Precision genome editing using cytosine and adenine base editors in mammalian cells. *Nat. Protoc.* **16**, 1089–1128 (2021).

[CAS](#) [PubMed](#) [Google Scholar](#)

33. 33.

Clement, K. et al. CRISPResso2 provides accurate and rapid genome editing sequence analysis. *Nat. Biotechnol.* **37**, 224–226 (2019).

[CAS](#) [PubMed](#) [PubMed Central](#) [Google Scholar](#)

34. 34.

Vaidyanathan, S. et al. Uridine depletion and chemical modification increase Cas9 mRNA activity and reduce immunogenicity without HPLC purification. *Mol. Ther. Nucleic Acids* **12**, 530–542 (2018).

[CAS](#) [PubMed](#) [PubMed Central](#) [Google Scholar](#)

35. 35.

Rees, H. A. et al. Improving the DNA specificity and applicability of base editing through protein engineering and protein delivery. *Nat. Commun.* **8**, 15790 (2017).

[ADS](#) [CAS](#) [PubMed](#) [PubMed Central](#) [Google Scholar](#)

36. 36.

Doman, J. L., Raguram, A., Newby, G. A. & Liu, D. R. Evaluation and minimization of Cas9-independent off-target DNA editing by cytosine base editors. *Nat. Biotechnol.* **38**, 620–628 (2020).

[CAS](#) [PubMed](#) [PubMed Central](#) [Google Scholar](#)

37. 37.

Zuris, J. A. et al. Cationic lipid-mediated delivery of proteins enables efficient protein-based genome editing in vitro and in vivo. *Nat. Biotechnol.* **33**, 73–80 (2015).

[CAS](#) [PubMed](#) [Google Scholar](#)

38. 38.

Rees, H. A. & Liu, D. R. Base editing: precision chemistry on the genome and transcriptome of living cells. *Nat. Rev. Genet.* **19**, 770–788 (2018).

[CAS](#) [PubMed](#) [PubMed Central](#) [Google Scholar](#)

39. 39.

Vakulskas, C. A. et al. A high-fidelity Cas9 mutant delivered as a ribonucleoprotein complex enables efficient gene editing in human hematopoietic stem and progenitor cells. *Nat. Med.* **24**, 1216–1224 (2018).

[CAS](#) [PubMed](#) [PubMed Central](#) [Google Scholar](#)

40. 40.

Hendel, A. et al. Chemically modified guide RNAs enhance CRISPR-Cas genome editing in human primary cells. *Nat. Biotechnol.* **33**, 985–989 (2015).

[CAS](#) [PubMed](#) [PubMed Central](#) [Google Scholar](#)

41. 41.

Connelly, J. P. & Pruett-Miller, S. M. CRIS.py: a versatile and high-throughput analysis program for CRISPR-based genome editing. *Sci. Rep.* **9**, 4194 (2019).

[ADS](#) [PubMed](#) [PubMed Central](#) [Google Scholar](#)

42. 42.

Hu, J. et al. Isolation and functional characterization of human erythroblasts at distinct stages: implications for understanding of normal and disordered erythropoiesis in vivo. *Blood* **121**, 3246–3253 (2013).

[CAS](#) [PubMed](#) [PubMed Central](#) [Google Scholar](#)

43. 43.

Traxler, E. A. et al. A genome-editing strategy to treat β -hemoglobinopathies that recapitulates a mutation associated with a benign genetic condition. *Nat. Med.* **22**, 987–990 (2016).

[CAS](#) [PubMed](#) [PubMed Central](#) [Google Scholar](#)

44. 44.

Lazzarotto, C. R. et al. Defining CRISPR-Cas9 genome-wide nuclease activities with CIRCLE-seq. *Nat. Protoc.* **13**, 2615–2642 (2018).

[CAS](#) [PubMed](#) [PubMed Central](#) [Google Scholar](#)

45. 45.

Hwang, G. H., Kim, J. S. & Bae, S. Web-based CRISPR toolkits: Cas-OFFinder, Cas-Designer, and Cas-Analyzer. *Methods Mol. Biol.* **2162**, 23–33 (2021).

[CAS](#) [PubMed](#) [Google Scholar](#)

46. 46.

Heinz, S. et al. Simple combinations of lineage-determining transcription factors prime cis-regulatory elements required for macrophage and B cell identities. *Mol. Cell* **38**, 576–589 (2010).

[CAS](#) [PubMed](#) [PubMed Central](#) [Google Scholar](#)

47. 47.

Kumar, S. & Geiger, H. HSC niche biology and HSC expansion ex vivo. *Trends Mol. Med.* **23**, 799–819 (2017).

[PubMed](#) [PubMed Central](#) [Google Scholar](#)

48. 48.

Leonard, A. et al. Low-dose busulfan reduces human CD34⁺ cell doses required for engraftment in c-kit mutant immunodeficient mice. *Mol. Ther. Methods Clin. Dev.* **15**, 430–437 (2019).

[CAS](#) [PubMed](#) [PubMed Central](#) [Google Scholar](#)

49. 49.

Karimian, A., Ahmadi, Y. & Yousefi, B. Multiple functions of p21 in cell cycle, apoptosis and transcriptional regulation after DNA damage. *DNA Repair* **42**, 63–71 (2016).

[CAS](#) [PubMed](#) [Google Scholar](#)

50. 50.

Kim, H. S., Jeong, Y. K., Hur, J. K., Kim, J. S. & Bae, S. Adenine base editors catalyze cytosine conversions in human cells. *Nat. Biotechnol.* **37**, 1145–1148 (2019).

[CAS](#) [PubMed](#) [Google Scholar](#)

[Download references](#)

Acknowledgements

We thank the SCD patients who contributed samples for this study; D. Gao and other members of our laboratories for discussions; and M. O'Reilly for assistance with Adobe Illustrator. This work was supported by US National Institutes of Health awards U01 AI142756, RM1 HG009490, R01 EB031172, R35 GM118062 (D.R.L.), R01R01HL156647 (M.J.W. and D.R.L), U01AI157189 (S.Q.T.), and P01 HL053749 (M.J.W. and S.Q.T.), the Bill and Melinda Gates Foundation (D.R.L.), the Howard Hughes Medical Institute (D.R.L.), the St. Jude Collaborative Research Consortium (D.R.L, S.M.P.-M., S.Q.T and M.J.W.), the Doris Duke Foundation (for aspects of this study that did not use mice; M.J.W., S.Q.T. and A.S.), the American Lebanese Syrian Associated Charities (A.S. and M.J.W.) and the Assisi Foundation of Memphis (M.J.W.). G.A.N. was supported by a Helen Hay Whitney Postdoctoral Fellowship and the HHMI. A.S. was supported by a Scholar Award from the American Society of Hematology. L.W.K. and K.A.E. acknowledge NSF GRFP fellowships. The content is solely the responsibility of the authors and does not necessarily represent the official views of the National Institutes of Health.

Author information

Author notes

1. These authors contributed equally: Gregory A. Newby, Jonathan S. Yen, Kaitly J. Woodard, Thiagaraj Mayuranathan

Affiliations

1. Merkin Institute of Transformative Technologies in Healthcare, Broad Institute of Harvard and MIT, Cambridge, MA, USA

Gregory A. Newby, Kelcee A. Everette, Christopher J. Podracky, Michelle F. Richter, Kevin T. Zhao, Shannon M.

Miller, Tina Wang, Luke W. Koblan & David R. Liu

2. Department of Chemistry and Chemical Biology, Harvard University, Cambridge, MA, USA

Gregory A. Newby, Kelcee A. Everette, Christopher J. Podracky, Michelle F. Richter, Kevin T. Zhao, Shannon M. Miller, Tina Wang, Luke W. Koblan & David R. Liu

3. Howard Hughes Medical Institute, Harvard University, Cambridge, MA, USA

Gregory A. Newby, Kelcee A. Everette, Christopher J. Podracky, Michelle F. Richter, Kevin T. Zhao, Shannon M. Miller, Tina Wang, Luke W. Koblan & David R. Liu

4. Department of Hematology, St. Jude Children's Research Hospital, Memphis, TN, USA

Jonathan S. Yen, Kaitly J. Woodard, Thiagaraj Mayuranathan, Cicera R. Lazzarotto, Yichao Li, Yu Yao, Kalin Mayberry, Yoonjeong Jang, Christophe Lechauve, Shengdar Q. Tsai & Mitchell J. Weiss

5. Department of Pathology, St. Jude Children's Research Hospital, Memphis, TN, USA

Heather Sheppard-Tillman

6. Department of Cell and Molecular Biology, St. Jude Children's Research Hospital, Memphis, TN, USA

Shaina N. Porter & Shondra M. Pruett-Miller

7. Division of Hematology, Cancer and Blood Diseases Institute, Cincinnati Children's Hospital Medical Center, Cincinnati, OH, USA

Elizabeth Thaman & Theodosia A. Kalfa

8. Department of Bone Marrow Transplantation and Cellular Therapy, St Jude Children's Research Hospital, Memphis, TN, USA

Akshay Sharma

9. TriLink BioTechnologies, San Diego, CA, USA

Jordana M. Henderson & Anton P. McCaffrey

10. Cellular and Molecular Therapeutics Branch, National Heart, Lung, and Blood Institute and National Institute of Diabetes and Digestive and Kidney Diseases, Bethesda, MD, USA

John F. Tisdale

11. Department of Pediatrics, University of Cincinnati College of Medicine, Cincinnati, OH, USA

Theodosia A. Kalfa

Authors

1. Gregory A. Newby

[View author publications](#)

You can also search for this author in [PubMed](#) [Google Scholar](#)

2. Jonathan S. Yen

[View author publications](#)

You can also search for this author in [PubMed](#) [Google Scholar](#)

3. Kaitly J. Woodard

[View author publications](#)

You can also search for this author in [PubMed](#) [Google Scholar](#)

4. Thiagaraj Mayuranathan

[View author publications](#)

You can also search for this author in [PubMed](#) [Google Scholar](#)

5. Cicera R. Lazzarotto

[View author publications](#)

You can also search for this author in [PubMed](#) [Google Scholar](#)

6. Yichao Li

[View author publications](#)

You can also search for this author in [PubMed](#) [Google Scholar](#)

7. Heather Sheppard-Tillman

[View author publications](#)

You can also search for this author in [PubMed](#) [Google Scholar](#)

8. Shaina N. Porter

[View author publications](#)

You can also search for this author in [PubMed](#) [Google Scholar](#)

9. Yu Yao

[View author publications](#)

You can also search for this author in [PubMed](#) [Google Scholar](#)

10. Kalin Mayberry

[View author publications](#)

You can also search for this author in [PubMed](#) [Google Scholar](#)

11. Kelcee A. Everette

[View author publications](#)

You can also search for this author in [PubMed](#) [Google Scholar](#)

12. Yoonjeong Jang

[View author publications](#)

You can also search for this author in [PubMed](#) [Google Scholar](#)

13. Christopher J. Podracky
[View author publications](#)

You can also search for this author in [PubMed](#) [Google Scholar](#)

14. Elizabeth Thaman
[View author publications](#)

You can also search for this author in [PubMed](#) [Google Scholar](#)

15. Christophe Lechauve
[View author publications](#)

You can also search for this author in [PubMed](#) [Google Scholar](#)

16. Akshay Sharma
[View author publications](#)

You can also search for this author in [PubMed](#) [Google Scholar](#)

17. Jordana M. Henderson
[View author publications](#)

You can also search for this author in [PubMed](#) [Google Scholar](#)

18. Michelle F. Richter
[View author publications](#)

You can also search for this author in [PubMed](#) [Google Scholar](#)

19. Kevin T. Zhao
[View author publications](#)

You can also search for this author in [PubMed](#) [Google Scholar](#)

20. Shannon M. Miller
[View author publications](#)

You can also search for this author in [PubMed](#) [Google Scholar](#)

21. Tina Wang
[View author publications](#)

You can also search for this author in [PubMed](#) [Google Scholar](#)

22. Luke W. Koblan
[View author publications](#)

You can also search for this author in [PubMed](#) [Google Scholar](#)

23. Anton P. McCaffrey
[View author publications](#)

You can also search for this author in [PubMed](#) [Google Scholar](#)

24. John F. Tisdale
[View author publications](#)

You can also search for this author in [PubMed](#) [Google Scholar](#)

25. Theodosia A. Kalfa
[View author publications](#)

You can also search for this author in [PubMed](#) [Google Scholar](#)

26. Shondra M. Pruett-Miller
[View author publications](#)

You can also search for this author in [PubMed](#) [Google Scholar](#)

27. Shengdar Q. Tsai
[View author publications](#)

You can also search for this author in [PubMed](#) [Google Scholar](#)

28. Mitchell J. Weiss
[View author publications](#)

You can also search for this author in [PubMed](#) [Google Scholar](#)

29. David R. Liu

[View author publications](#)

You can also search for this author in [PubMed](#) [Google Scholar](#)

Contributions

G.A.N., J.S.Y., K.J.W., T.M., C.R.L., Y.L., H.S.-T., S.N.P., Y.Y., K.M., K.A.E., Y.J., C.J.P., E.T., C.L., and A.S. conducted experiments and analysed data. J.M.H., M.F.R., K.T.Z., S.M.M., T.W., L.W.K., and J.F.T. prepared materials and provided conceptual assistance, G.A.N., J.S.Y., K.J.W., M.J.W., and D.R.L. wrote the manuscript with input from all authors. J.S.Y., A.P.M., T.A.K., S.Q.T., S.M.P.-M., M.J.W., and D.R.L. supervised this study.

Corresponding authors

Correspondence to [Jonathan S. Yen](#) or [Mitchell J. Weiss](#) or [David R. Liu](#).

Ethics declarations

Competing interests

G.A.N., K.A.E., M.F.R., K.T.Z., S.M.M., T.W., L.W.K., and D.R.L. have filed patent applications on aspects of base editing through the Broad Institute. D.R.L. is a consultant and equity owner of Beam Therapeutics, Prime Medicine, and Pairwise Plants (companies that use genome editing). M.J.W. is on advisory boards for Cellarity Inc., Novartis, and Forma Therapeutics, and is an equity owner of Beam Therapeutics. A.S. is a consultant for Spotlight Therapeutics and his institution receives clinical trial support for the conduct of sickle cell disease gene editing trials from Vertex Pharmaceuticals, CRISPR Therapeutics, and Novartis. J.S.Y. is an equity owner of Beam Therapeutics. The authors declare no non-financial competing interests.

Additional information

Peer review information *Nature* thanks the anonymous reviewers for their contribution to the peer review of this work.

Publisher's note Springer Nature remains neutral with regard to jurisdictional claims in published maps and institutional affiliations.

Extended data figures and tables

[Extended Data Fig. 1 Optimization in HEK293T cells, viability and recovery following human SCD HSPC editing, and allelic editing outcomes.](#)

a, Plasmids encoding the *HBB^S*-targeting sgRNA and either ABE7.10-NRCH or ABE8e-NRCH were transfected by lipofection into HEK293T cells. Editing efficiency was measured after 3 days by HTS. Unedited cells were not lipofected. **b**, Two days after electroporation into human SCD HSPCs of base editor mRNA and sgRNA, or electroporation of ribonucleoprotein (RNP), cell number and viability were measured using a Chemometec Nucleocounter-3000. Acridine orange was used to stain the total cell number and DAPI was used to stain dead, permeabilized cells. The percentage viability was calculated as the DAPI-stained cells divided by the acridine orange cells within each sample. The percentage recovery was normalized to the cell count of the unedited sample. Unedited cells were not electroporated. **c**, Six days after electroporation of SCD HSPCs, genomic DNA was extracted and the target *HBB* locus was PCR amplified and sequenced using an Illumina instrument. The sequencing analysis program CRIS.py was used to identify and quantify the resulting alleles. All alleles above a threshold of 0.2% frequency are shown. Below this threshold, variant alleles appeared with greatest frequency in the untreated control sample, suggesting they do not arise from base editor treatment. Nucleotides altered from the endogenous sequence are shown in blue. Rare cytosine base editing was observed at a frequency of less than 1%, as has been previously described as a possible outcome from adenine base editing⁵⁰. Data shown as mean ± s.d., $n = 3$.

Extended Data Fig. 2 Erythroid differentiation of edited SCD CD34 $^{\pm}$ HSPCs.

Representative, immuno-flow cytometry for erythroid maturation stage markers^{42,43} at culture days 7 and 14. Top, gating strategy to identify single cells expressing the erythroid marker hCD235a. Bottom, gating strategy to track the progress of erythroid maturation based on expression of CD49D and BAND3 in hCD235a $^{+}$ cells. SSC-A, side scatter area; SSC-W, side scatter width; FSC-A, forward scatter area.

Extended Data Fig. 3 Reverse-phase HPLC analysis of erythroid cells derived from in vitro differentiation of edited SCD CD34 $^{\pm}$ HSPCs.

Reverse-phase HPLC chromatograms of erythroid cell lysates at culture day 18, with β -like globins and their associated fractions marked near the associated peak. Data from the most efficiently edited donor cells are shown. Red arrows indicate the start and end of globin chain peaks.

Extended Data Fig. 4 Off-target base editing associated with ABE8e-NRCH conversion of *HBB* S to *HBB* G Makassar in SCD CD34 $^{\pm}$ HSPCs.

CIRCLE-seq read counts obtained for each verified off-target site and the alignment of each site to the guide sequence are shown. Bar graphs show the percentage of sequencing reads containing A•T-to-G•C mutations within protospacer positions 4–10 at on- and off-target sites in genomic DNA samples from patient CD34 $^{+}$ HSPCs treated with ABE8e-NRCH mRNA, protein, or untreated controls ($n = 4$). Note that the mutation frequency shown is summed across all reads with one or more A•T-to-G•C mutations in this window. Sequencing errors therefore accumulate in control samples compared to standard sequencing error frequencies for a single nucleotide. Data shown as mean \pm s.d.

Extended Data Fig. 5 Off-target indel formation associated with ABE8e-NRCH conversion of *HBB*^S to *HBB*^G Makassar in SCD CD34⁺ HSPCs.

Bar graph showing the percentage of sequencing reads containing alleles harbouring indels at on- and off-target sites in genomic DNA samples from patient CD34⁺ HSPCs treated with ABE8e-NRCH mRNA, protein, or untreated controls ($n = 4$). Data shown as mean \pm s.d.

Extended Data Fig. 6 Flow cytometry analysis of human donor-derived erythroid CD235a⁺ cells after transplantation.

Human CD235a⁺ erythroid cells were purified by immuno-magnetic bead selection and analysed by flow cytometry for the indicated erythroid maturation markers^{42,43}.

Extended Data Fig. 7 Engraftment of ABE8e-NRCH RNP-treated SCD CD34⁺ HSPCs after transplantation into immunodeficient mice.

CD34⁺ HSPCs from three *HBB*^{S/S} patients with SCD were electroporated with ABE8e-NRCH RNP using an sgRNA targeting the SCD mutant codon, followed by transplantation of $2–5 \times 10^5$ treated cells into NBSGW mice via tail-vein injection. Mice were euthanized and analysed 16 weeks after transplantation. **a**, Experimental workflow. **b**, Engraftment measured by the percentage of human donor CD45⁺ cells (hCD45⁺ cells) in recipient mouse bone marrow. **c**, Human B cells (hCD19⁺), myeloid cells (hCD33⁺), and T cells (hCD3⁺) in recipient mouse bone marrow, shown as percentages of the total hCD45⁺ population. **d**, Human erythroid precursors (hCD235a⁺) in recipient mouse bone marrow, shown as a percentage of total human and mouse CD45⁻ cells. **e**, On-target (A7, Fig. 1a) editing efficiencies in human donor CD34⁺ cell-derived lineages purified from recipient bone marrow by FACS. Erythroid, myeloid, B cell, and HSPC human lineages were collected using antibodies against hCD235a, hCD33, hCD19, and hCD34,

respectively. Statistical significance was assessed by one-way ANOVA to compare groups; ns, not significant. **f**, Percentages of β -like globin proteins determined by reverse-phase HPLC analysis of human donor-derived reticulocytes isolated from recipient mouse bone marrow. **g**, Representative phase contrast images of human reticulocytes purified from bone marrow and incubated for 8 h with 2% oxygen. Nine images of more than 50 cells per image were collected per sample. Scale bars, 50 μm . **h**, Quantification of sickled cells calculated by counting images after incubation for 8 h in 2% oxygen as in **g**. More than 300 randomly selected cells per sample were counted by a blinded observer. $n = 14$ total mice analysed (**b–f**); triangle, square, and circle symbols represent samples from three different donors with SCD. Negative control data are shared with Fig. 2. Data shown as mean \pm s.d. Statistical significance between treated and untreated samples was assessed using two-tailed Student's *t*-test.

Extended Data Fig. 8 Engraftment of transplanted Townes mouse HSPCs, clonality of editing outcomes, and oxygen binding affinity of blood.

a, Donor cell engraftment measured by flow cytometry assessing the percentage of CD45.2 $^{+}$ cells among PBMCs. **b**, Bone marrow from three mice transplanted with edited Townes mouse HSPCs was plated at low density in methylcellulose. After 12 days of culture, 30 to 35 individual colonies per mouse were picked into cell lysis buffer and the edited locus was amplified by PCR and sequenced by HTS. Colonies were categorized by whether they contained no editing, a monoallelic edit, or a biallelic edit. **c**, Blood was drawn from mice at week 14 after transplantation. Haemoglobin oxygenation was measured using a Hemox Analyzer (TCS Scientific) across a continuous declining gradient of oxygen pressure to assess whether *HBB^S*-to-*HBB^G* editing led to altered haemoglobin–oxygen binding. Data shown as mean \pm s.d.

Extended Data Fig. 9 Adenine base editing of the SCD β -globin allele (*HBB^S*) to the Makassar variant (*HBB^G*) reduces erythrocyte sickling and splenic pathology in mice.

Mice were treated as described in Fig. 3a. Blood and spleen were analysed 16 weeks after transplantation of Lin⁻ mouse HSPCs containing human *HBB* alleles. **a**, Representative images of blood smears. One blood smear image was collected per mouse. Scale bars, 25 µm. **b**, Representative phase contrast images of peripheral blood incubated for 8 h with 2% oxygen. Nine images of more than 50 cells per image were collected per sample. Scale bars, 50 µm. **c**, Quantification of sickled cells. More than 300 randomly selected cells per condition were counted by a blinded observer. **d**, Mass of dissected spleens. **e**, Histological sections of spleens of recipient mice 16 weeks after transplantation. Splenic pathologies in mice that received unedited donor *HBB*^{S/S} HSCs include excessive extramedullary erythropoiesis and vascular congestion indicated by RBC pooling (bright red colour) resulting in expansion of red pulp (RP), reduction in white pulp (WP), and splenomegaly. Images were taken at 10× magnification and were processed, stained and photographed at the same time under identical conditions. Three images of each spleen were collected from different parts of the organ for each mouse. Scale bars, 100 µm. Unedited *HBB*^{S/S}, $n = 6$ mice; edited *HBB*^{S/S}, $n = 6$ mice; *HBB*^{A/S}, $n = 2$ mice. Data shown as mean ± s.d., with individual values as dots. Statistical significance was assessed using one-way ANOVA with Šidák's multiple comparisons test of the edited *HBB*^{S/S} values compared to each other group to calculate *P* values.

Extended Data Fig. 10 Comparison of DNA damage response and loss of target allele amplification consistent with large deletion or DNA rearrangement in HSPCs following treatment with Cas9 nuclease or with ABE.

HSPCs from a healthy human donor were electroporated in triplicate with Cas9 nuclease RNP targeting the *BCL11A* erythroid-specific enhancer, ABE8e-NRCH mRNA and an sgRNA targeting the wild-type *HBB* locus, or no cargo as a control. An additional set of control cells was not electroporated. **a**, *CDKN1* transcription levels, a measure of the p53-mediated DNA damage response⁴⁹, were quantified by ddPCR after reverse transcription, and were normalized to *CDKN1* levels before electroporation ($n = 3$). **b**, Editing efficiencies at the targeted genomic loci in HSPCs were

measured by HTS 6 days after electroporation. Adenine base editing at the synonymous bystander position 9 of the *HBB* protospacer is shown for ABE8e-NRCH. **c, d**, The indicated target sites were amplified and quantified by ddPCR to measure the fraction of missing alleles consistent with larger deletions, translocations, or other chromosomal rearrangements that result in loss of the ability to be amplified by PCR. PCR amplification of a non-targeted *ACTB* site was used to normalize each sample. Each DNA sample was assessed in triplicate ($n = 9$). Data shown as mean \pm s.d., with individual values in bar graphs shown as dots. Statistical significance between edited and unedited samples was assessed by a two-tailed Student's *t*-test; ns, not significant.

Supplementary information

Supplementary Information

This file contains a Supplementary Discussion, Supplementary Fig. 1, Supplementary Table 1, Supplementary References.

Reporting Summary

Supplementary Table 2

Off-target sites and primer sequences used for their amplification.

Supplementary Table 3

Complete blood counts from SCD model mice. Complete blood counts were collected from transplanted animals using a FORCYTE veterinary hematology analyzer 16 weeks after the transplantation. Blood counts from untransplanted Townes SCD mice with $HBB^{S/S}$, $HBB^{A/S}$, and $HBB^{A/A}$ genotypes were also measured as controls at 4-6 months of age. Data are shown as mean values \pm SD.

Rights and permissions

[Reprints and Permissions](#)

About this article



Check for
updates

Cite this article

Newby, G.A., Yen, J.S., Woodard, K.J. *et al.* Base editing of haematopoietic stem cells rescues sickle cell disease in mice. *Nature* **595**, 295–302 (2021).
<https://doi.org/10.1038/s41586-021-03609-w>

[Download citation](#)

- Received: 10 January 2021
- Accepted: 04 May 2021
- Published: 02 June 2021
- Issue Date: 08 July 2021
- DOI: <https://doi.org/10.1038/s41586-021-03609-w>

Comments

By submitting a comment you agree to abide by our [Terms](#) and [Community Guidelines](#). If you find something abusive or that does not comply with our terms or guidelines please flag it as inappropriate.

[Access through your institution](#)

[Change institution](#)

[Buy or subscribe](#)

Advertisement

This article was downloaded by **calibre** from <https://www.nature.com/articles/s41586-021-03609-w>

| [Section menu](#) | [Main menu](#) |

- Article
- [Published: 09 June 2021](#)

NORAD-induced Pumilio phase separation is required for genome stability

- [Mahmoud M. Elguindy](#) ORCID: [orcid.org/0000-0001-9151-1751^{1,2}](https://orcid.org/0000-0001-9151-1751) &
- [Joshua T. Mendell](#) ORCID: [orcid.org/0000-0001-8479-2284^{1,3,4,5}](https://orcid.org/0000-0001-8479-2284)

[Nature](#) volume **595**, pages 303–308 (2021) [Cite this article](#)

- 6982 Accesses
- 163 Altmetric
- [Metrics details](#)

Subjects

- [Chromosomes](#)
- [Genomic instability](#)
- [Intrinsically disordered proteins](#)
- [Long non-coding RNAs](#)
- [RNA](#)

Abstract

Liquid–liquid phase separation is a major mechanism of subcellular compartmentalization^{1,2}. Although the segregation of RNA into phase-separated condensates broadly affects RNA metabolism^{3,4}, whether and

how specific RNAs use phase separation to regulate interacting factors such as RNA-binding proteins (RBPs), and the phenotypic consequences of such regulatory interactions, are poorly understood. Here we show that RNA-driven phase separation is a key mechanism through which a long noncoding RNA (lncRNA) controls the activity of RBPs and maintains genomic stability in mammalian cells. The lncRNA *NORAD* prevents aberrant mitosis by inhibiting Pumilio (PUM) proteins^{5,6,7,8}. We show that *NORAD* can out-compete thousands of other PUM-binding transcripts to inhibit PUM by nucleating the formation of phase-separated PUM condensates, termed NP bodies. Dual mechanisms of PUM recruitment, involving multivalent PUM–*NORAD* and PUM–PUM interactions, enable *NORAD* to competitively sequester a super-stoichiometric amount of PUM in NP bodies. Disruption of *NORAD*-driven PUM phase separation leads to PUM hyperactivity and genome instability that is rescued by synthetic RNAs that induce the formation of PUM condensates. These results reveal a mechanism by which RNA-driven phase separation can regulate RBP activity and identify an essential role for this process in genome maintenance. The repetitive sequence architecture of *NORAD* and other lncRNAs^{9,10,11} suggests that phase separation may be a widely used mechanism of lncRNA-mediated regulation.

Access options

Subscribe to Journal

Get full journal access for 1 year

\$199.00

only \$3.90 per issue

[Subscribe](#)

All prices are NET prices.

VAT will be added later in the checkout.

Tax calculation will be finalised during checkout.

Rent or Buy article

Get time limited or full article access on ReadCube.

from \$8.99

[Rent or Buy](#)

All prices are NET prices.

Additional access options:

- [Log in](#)
- [Access through your institution](#)
- [Learn about institutional subscriptions](#)

Fig. 1: NORAD and PUM co-localize in cytoplasmic foci.

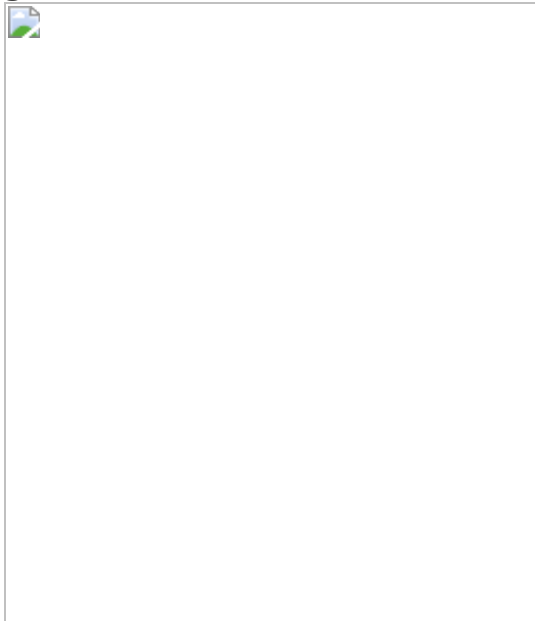


Fig. 2: NORAD induces PUM phase separation through multivalent RNA binding.

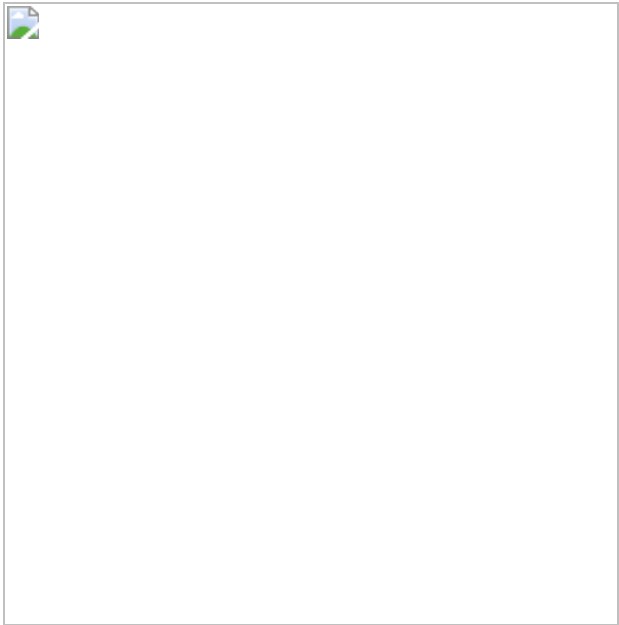


Fig. 3: Competitive, IDR-driven recruitment of PUM into *NORAD*–PUM condensates.

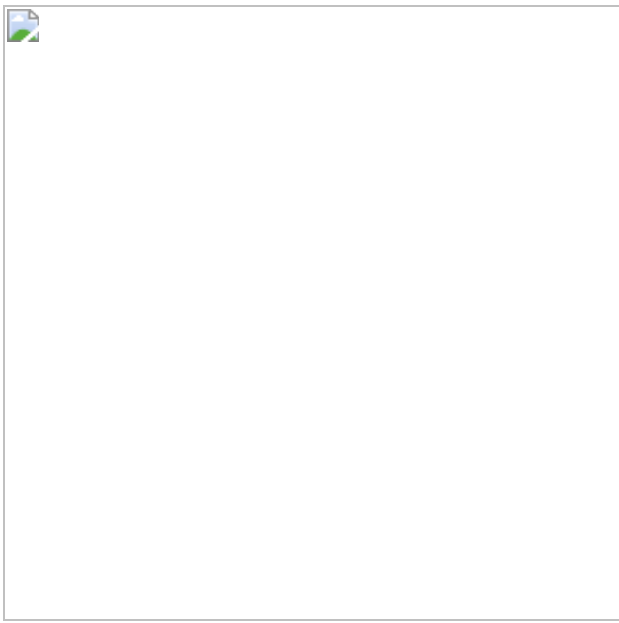


Fig. 4: PUM condensate-inducing RNAs limit PUM activity and rescue genomic instability in *NORAD*-deficient cells.



Data availability

All data needed to evaluate the conclusions of this Article are presented in the main text or supplementary materials. RNA-seq data for circPRE-expressing HCT116 cells (Fig. 4c) is available in the GEO under accession number [GSE154812](#). HCT116 cell RNA-seq data used to estimate the total number of PREs expressed in mRNAs per cell is available in the GEO under accession number [GSE75440](#). [Source data](#) are provided with this paper.

References

1. 1.

Banani, S. F., Lee, H. O., Hyman, A. A. & Rosen, M. K. Biomolecular condensates: organizers of cellular biochemistry. *Nat. Rev. Mol. Cell Biol.* **18**, 285–298 (2017).

[CAS](#) [Article](#) [Google Scholar](#)

2. 2.

Hyman, A. A., Weber, C. A. & Jülicher, F. Liquid–liquid phase separation in biology. *Annu. Rev. Cell Dev. Biol.* **30**, 39–58 (2014).

[CAS](#) [Article](#) [Google Scholar](#)

3. 3.

Corbet, G. A. & Parker, R. RNP granule formation: lessons from P-bodies and stress granules. *Cold Spring Harb. Symp. Quant. Biol.* **84**, 203–215 (2019).

[Article](#) [Google Scholar](#)

4. 4.

Roden, C. & Gladfelter, A. S. RNA contributions to the form and function of biomolecular condensates. *Nat. Rev. Mol. Cell Biol.* **22**, 183–195 (2021).

[CAS](#) [Article](#) [Google Scholar](#)

5. 5.

Elguindy, M. M. et al. PUMILIO, but not RBMX, binding is required for regulation of genomic stability by noncoding RNA *NORAD*. *eLife* **8**, e48625 (2019).

[CAS](#) [Article](#) [Google Scholar](#)

6. 6.

Kopp, F. et al. PUMILIO hyperactivity drives premature aging of *Norad*-deficient mice. *eLife* **8**, e42650 (2019).

[Article](#) [Google Scholar](#)

7. 7.

Lee, S. et al. Noncoding RNA *NORAD* regulates genomic stability by sequestering PUMILIO proteins. *Cell* **164**, 69–80 (2016).

[CAS](#) [Article](#) [Google Scholar](#)

8. 8.

Tichon, A. et al. A conserved abundant cytoplasmic long noncoding RNA modulates repression by Pumilio proteins in human cells. *Nat. Commun.* **7**, 12209 (2016).

[ADS](#) [CAS](#) [Article](#) [Google Scholar](#)

9. 9.

Pandya-Jones, A. et al. A protein assembly mediates *Xist* localization and gene silencing. *Nature* **587**, 145–151 (2020).

[ADS](#) [CAS](#) [Article](#) [Google Scholar](#)

10. 10.

Hacisuleyman, E., Shukla, C. J., Weiner, C. L. & Rinn, J. L. Function and evolution of local repeats in the *Firre* locus. *Nat. Commun.* **7**, 11021 (2016).

[ADS](#) [CAS](#) [Article](#) [Google Scholar](#)

11. 11.

Yamazaki, T. et al. Functional domains of *NEAT1* architectural lncRNA induce paraspeckle assembly through phase separation. *Mol. Cell* **70**, 1038–1053.e7 (2018).

[CAS](#) [Article](#) [Google Scholar](#)

12. 12.

Lin, Y., Protter, D. S., Rosen, M. K. & Parker, R. Formation and maturation of phase-separated liquid droplets by RNA-binding proteins. *Mol. Cell* **60**, 208–219 (2015).

[CAS](#) [Article](#) [Google Scholar](#)

13. 13.

Quinn, J. J. & Chang, H. Y. Unique features of long non-coding RNA biogenesis and function. *Nat. Rev. Genet.* **17**, 47–62 (2016).

[CAS](#) [Article](#) [Google Scholar](#)

14. 14.

Kopp, F. & Mendell, J. T. Functional classification and experimental dissection of long noncoding RNAs. *Cell* **172**, 393–407 (2018).

[CAS](#) [Article](#) [Google Scholar](#)

15. 15.

Yao, R. W., Wang, Y. & Chen, L. L. Cellular functions of long noncoding RNAs. *Nat. Cell Biol.* **21**, 542–551 (2019).

[CAS](#) [Article](#) [Google Scholar](#)

16. 16.

Goldstrohm, A. C., Hall, T. M. T. & McKenney, K. M. Post-transcriptional regulatory functions of mammalian Pumilio proteins. *Trends Genet.* **34**, 972–990 (2018).

[CAS](#) [Article](#) [Google Scholar](#)

17. 17.

Khong, A. et al. The stress granule transcriptome reveals principles of mRNA accumulation in stress granules. *Mol. Cell* **68**, 808–820.e5 (2017).

[CAS](#) [Article](#) [Google Scholar](#)

18. 18.

Namkoong, S., Ho, A., Woo, Y. M., Kwak, H. & Lee, J. H. Systematic characterization of stress-induced RNA granulation. *Mol. Cell* **70**, 175–187.e8 (2018).

[CAS](#) [Article](#) [Google Scholar](#)

19. 19.

Zhang, H. et al. RNA controls polyQ protein phase transitions. *Mol. Cell* **60**, 220–230 (2015).

[CAS](#) [Article](#) [Google Scholar](#)

20. 20.

Edwards, T. A., Pyle, S. E., Wharton, R. P. & Aggarwal, A. K. Structure of Pumilio reveals similarity between RNA and peptide binding motifs. *Cell* **105**, 281–289 (2001).

[CAS](#) [Article](#) [Google Scholar](#)

21. 21.

Litke, J. L. & Jaffrey, S. R. Highly efficient expression of circular RNA aptamers in cells using autocatalytic transcripts. *Nat. Biotechnol.* **37**, 667–675 (2019).

[CAS](#) [Article](#) [Google Scholar](#)

22. 22.

Gennarino, V. A. et al. A mild PUM1 mutation is associated with adult-onset ataxia, whereas haploinsufficiency causes developmental delay and seizures. *Cell* **172**, 924–936.e11 (2018).

[CAS](#) [Article](#) [Google Scholar](#)

23. 23.

Gennarino, V. A. et al. Pumilio1 haploinsufficiency leads to SCA1-like neurodegeneration by increasing wild-type Ataxin1 levels. *Cell* **160**, 1087–1098 (2015).

[CAS](#) [Article](#) [Google Scholar](#)

24. 24.

D'Amico, D. et al. The RNA-binding protein PUM2 impairs mitochondrial dynamics and mitophagy during aging. *Mol. Cell* **73**, 775–787.e10 (2019).

[Article](#) [Google Scholar](#)

25. 25.

Klosin, A. et al. Phase separation provides a mechanism to reduce noise in cells. *Science* **367**, 464–468 (2020).

[ADS](#) [CAS](#) [Article](#) [Google Scholar](#)

26. 26.

Islam, S. et al. Characterization of the single-cell transcriptional landscape by highly multiplex RNA-seq. *Genome Res.* **21**, 1160–1167 (2011).

[CAS](#) [Article](#) [Google Scholar](#)

27. 27.

Marinov, G. K. et al. From single-cell to cell-pool transcriptomes: stochasticity in gene expression and RNA splicing. *Genome Res.* **24**, 496–510 (2014).

[CAS](#) [Article](#) [Google Scholar](#)

28. 28.

Shapiro, E., Biezuner, T. & Linnarsson, S. Single-cell sequencing-based technologies will revolutionize whole-organism science. *Nat. Rev. Genet.* **14**, 618–630 (2013).

[CAS](#) [Article](#) [Google Scholar](#)

29. 29.

Golden, R. J. et al. An Argonaute phosphorylation cycle promotes microRNA-mediated silencing. *Nature* **542**, 197–202 (2017).

[ADS](#) [CAS](#) [Article](#) [Google Scholar](#)

30. 30.

Randolph, L. N., Bao, X., Zhou, C. & Lian, X. An all-in-one, Tet-On 3G inducible PiggyBac system for human pluripotent stem cells and derivatives. *Sci. Rep.* **7**, 1549 (2017).

[ADS](#) [Article](#) [Google Scholar](#)

31. 31.

Mito, M., Kawaguchi, T., Hirose, T. & Nakagawa, S. Simultaneous multicolor detection of RNA and proteins using super-resolution microscopy. *Methods* **98**, 158–165 (2016).

[CAS](#) [Article](#) [Google Scholar](#)

32. 32.

Bolte, S. & Cordelières, F. P. A guided tour into subcellular colocalization analysis in light microscopy. *J. Microsc.* **224**, 213–232 (2006).

[MathSciNet](#) [CAS](#) [Article](#) [Google Scholar](#)

33. 33.

Costes, S. V. et al. Automatic and quantitative measurement of protein-protein colocalization in live cells. *Biophys. J.* **86**, 3993–4003 (2004).

[ADS](#) [CAS](#) [Article](#) [Google Scholar](#)

34. 34.

Wheeler, J. R., Matheny, T., Jain, S., Abrisch, R. & Parker, R. Distinct stages in stress granule assembly and disassembly. *eLife* **5**, e18413 (2016).

[Article](#) [Google Scholar](#)

35. 35.

Frankish, A. et al. GENCODE reference annotation for the human and mouse genomes. *Nucleic Acids Res.* **47**, D766–D773 (2019).

[CAS](#) [Article](#) [Google Scholar](#)

36. 36.

Dobin, A. et al. STAR: ultrafast universal RNA-seq aligner. *Bioinformatics* **29**, 15–21 (2013).

[CAS](#) [Article](#) [Google Scholar](#)

37. 37.

Liao, Y., Smyth, G. K. & Shi, W. featureCounts: an efficient general purpose program for assigning sequence reads to genomic features. *Bioinformatics* **30**, 923–930 (2014).

[CAS](#) [Article](#) [Google Scholar](#)

38. 38.

McCarthy, D. J., Chen, Y. & Smyth, G. K. Differential expression analysis of multifactor RNA-seq experiments with respect to

biological variation. *Nucleic Acids Res.* **40**, 4288–4297 (2012).

[CAS Article](#) [Google Scholar](#)

39. 39.

Hafner, M. et al. Transcriptome-wide identification of RNA-binding protein and microRNA target sites by PAR-CLIP. *Cell* **141**, 129–141 (2010).

[CAS Article](#) [Google Scholar](#)

[Download references](#)

Acknowledgements

We thank M. Rosen, D. Trono, S. Qi, J. Weissman, F. Zhang, X. Lian, and S. Jaffrey for plasmids; H. Zhang for bioinformatics support; S. Nakagawa for technical assistance with RNA FISH; M. Rosen, W. Peeples, J. Han, and B. Sabari for discussions; K. Jancynzka for experimental assistance; A. Mobley and UTSW Flow Cytometry Core for assistance with FACS; and K. O'Donnell, Y. Meleis, and members of the Mendell laboratory for comments on the manuscript. This work was supported by grants from the NIH (R35CA197311 to J.T.M.; P30CA142543 to J.T.M.; and P50CA196516 to J.T.M.) and the Welch Foundation (I-1961 to J.T.M.). J.T.M. is an Investigator of the Howard Hughes Medical Institute.

Author information

Affiliations

1. Department of Molecular Biology, University of Texas Southwestern Medical Center, Dallas, TX, USA

Mahmoud M. Elguindy & Joshua T. Mendell

2. Medical Scientist Training Program, University of Texas Southwestern Medical Center, Dallas, TX, USA

Mahmoud M. Elguindy

3. Harold C. Simmons Comprehensive Cancer Center, University of Texas Southwestern Medical Center, Dallas, TX, USA

Joshua T. Mendell

4. Hamon Center for Regenerative Science and Medicine, University of Texas Southwestern Medical Center, Dallas, TX, USA

Joshua T. Mendell

5. Howard Hughes Medical Institute, University of Texas Southwestern Medical Center, Dallas, TX, USA

Joshua T. Mendell

Authors

1. Mahmoud M. Elguindy

[View author publications](#)

You can also search for this author in [PubMed](#) [Google Scholar](#)

2. Joshua T. Mendell

[View author publications](#)

You can also search for this author in [PubMed](#) [Google Scholar](#)

Contributions

M.M.E. and J.T.M designed experiments. M.M.E performed experiments. M.M.E. and J.T.M. wrote the manuscript.

Corresponding author

Correspondence to [Joshua T. Mendell](#).

Ethics declarations

Competing interests

The authors declare no competing interests.

Additional information

Peer review information *Nature* thanks Phillip A. Sharp and Igor Ulitsky for their contribution to the peer review of this work. Peer reviewer reports are available.

Publisher's note Springer Nature remains neutral with regard to jurisdictional claims in published maps and institutional affiliations.

Extended data figures and tables

[Extended Data Fig. 1 NORAD and PUM co-localize in cytoplasmic condensates.](#)

a, Left, confocal images of HCT116 cells co-stained for *NORAD* and PUM1 with or without treatment with camptothecin (Campto; 200 nM) for 24 h. Right, box plots of the mean fluorescence intensity and area of *NORAD* and PUM1 foci. *NORAD*, $n = 149$ foci; PUM1, $n = 58$ foci; *NORAD* + camptothecin, $n = 97$ foci; and PUM1 + camptothecin, $n = 67$ foci from at least two different fields analysed. Two-tailed *t*-test. **b**, Western blot of PUM1 or PUM2 in HCT116 cells of the indicated genotypes. Molecular weight in kDa shown on right. For gel source data, see Supplementary Fig. 1. **c**, Confocal images of PUM1 or PUM2 co-stained with P-body marker XRN1. **d**, Confocal images of PUM2 and stress granule marker G3BP1 with or without treatment with sodium arsenite (0.5 mM, 1 h incubation). **e**, Confocal images of *NORAD* and PUM localization in the indicated cell lines and genotypes. BJ-5ta cells are TERT-

immortalized human fibroblasts. **f**, Quantification of *NORAD* and PUM1 co-localization ($n = 20$ cells for each cell line). Mean co-localization shown above box plots. **a, f**, Middle line, median; box, 25th to 75th percentiles; whiskers, minimum to maximum.

[Source data](#)

[Extended Data Fig. 2 NP bodies are liquid-like condensates distinct from other known cytoplasmic granules.](#)

a, PUM1 western blot in HCT116 clones with GFP knock-in at the endogenous *PUM1* locus. Three genotype-confirmed wild-type and *NORAD*^{-/-} clones shown alongside parental wild-type and *NORAD*^{-/-} cells. Molecular weight in kDa shown on right. For gel source data, see Supplementary Fig. 1. **b**, Time-lapse images showing fusion of endogenous PUM1–GFP condensates in HCT116 cells. Scale bar, 5 μm . **c**, Representative 3D-reconstructed live cell confocal images used to estimate the volumes of NP bodies, P-bodies, and stress granules. Endogenously tagged PUM1–GFP HCT116 cells were used for NP body and stress granule measurements (the latter after treatment with 0.5 mM sodium arsenite for 1 h). The P-body marker DCP2–GFP was used to estimate the volume of P-bodies in HCT116 cells. **d**, Quantification of condensate volumes ($n = 1,072$ NP bodies from 20 cells, 51 P-bodies from 11 cells, and 62 stress granules from 10 cells). Average volumes shown above plots.

[Source data](#)

[Extended Data Fig. 3 Liquid-like properties of PUM droplets in vitro.](#)

a, Predicted disordered regions of PUM1 and PUM2, scored by PONDR VSL2. **b**, Schematic (top) and Coomassie stain (bottom) of purified MBP–SNAP-PUM–His proteins used for in vitro experiments. For gel source data, see Supplementary Fig. 1. **c**, PUM liquid droplet formation at 5 μM upon TEV-mediated cleavage of the solubilizing MBP tag. Proteins were fluorescently labelled with SNAP₄₈₈ and visualized by DIC or fluorescence

microscopy. Scale bar, 10 μ m. **d**, PUM1 liquid droplet formation at 5 μ M in the presence or absence of 10% PEG₃₃₅₀ after 1 h incubation. **e**, Confocal images (left) and quantification (right) of PUM1 droplet FRAP (5 μ M PUM1). Fluorescence intensities plotted relative to pre-bleach time point ($t = -5$ s). Data shown as mean \pm s.d. ($n = 3$ droplets). **f**, Time-lapse confocal images showing fusion of PUM1 droplets (5 μ M PUM1). **g**, DIC and fluorescence microscopy images of Cy3-labelled *NORAD* RNA (2.7 nM, red) after addition to preformed PUM1 or PUM2 droplets (5 μ M, green). **h**, Fluorescence microscopy images of PUM1 droplets (5 μ M, green) formed in the presence or absence of *NORAD* or PREmut RNA (2.7 nM, red). PREmut contains UGU to ACA mutations in all 18 *NORAD* PREs, which abolish PUM binding⁵. **i**, Images and analysis of PUM1–*NORAD* droplet FRAP. Droplets were formed with Cy3-labelled *NORAD* RNA (2 nM) and SNAP₄₈₈-labelled PUM1 (5 μ M). Data shown as mean \pm s.d. ($n = 3$ droplets).

[Source data](#)

[Extended Data Fig. 4 *NORAD*-induced PUM phase separation at physiological concentrations in vitro.](#)

a, Representative 3D-reconstructed confocal image of a PUM1-stained *NORAD*^{−/−} HCT116 cell used to estimate cytoplasmic volume. The length (l), width (w), and depth (d) of the entire cell and its nucleus were measured and used to calculate the total cellular and nuclear volumes using the ellipsoid volume formula. Cytoplasmic volume for each cell was determined by subtracting nuclear volume from total volume. **b**, Box-and-whisker plot of measured cytoplasmic volumes ($n = 20$ cells). Mean cytoplasmic volume shown on the right. Middle line, median; box, 25th to 75th percentiles; whiskers, minimum to maximum. **c**, Schematic of wild-type and mutant *NORAD* transcripts. Location of repeated *NORAD* domains (ND1–ND5) indicated with grey boxes and mammalian sequence conservation shown in green (UCSC Genome Browser hg38 PhastCons track). Locations of PREs indicated with red and yellow arrowheads. PREmut transcript contains 18 UGU to ACA mutations in PREs (grey arrowheads). ND4 represents the most conserved segment of *NORAD* and

contains 4 PREs. Figure modified from Elguindy et al.⁵. **d**, DIC and fluorescence microscopy images of PUM1 (150 nM, green) droplets in the presence or absence of *NORAD* (2 nM) or PEG₃₃₅₀.

[Source data](#)

Extended Data Fig. 5 PUM target transcripts do not induce PUM1 droplet formation in vitro at physiological concentrations.

a, Dot plot of PRE-containing mRNA copy numbers in HCT116 cells (estimated by RNA-seq; see [Methods](#)) versus the number of PREs in their 3' UTRs. Transcripts selected for in vitro assays labelled in blue with the number of PREs in their 3' UTRs in parentheses. Note that the selected mRNAs were also identified as PUM CLIP targets that were downregulated upon PUM overexpression^{7,39}. **b**, Plot of transcript PRE number multiplied by estimated copy number, highlighting the unique combination of *NORAD* abundance and PRE valency compared to other PRE-containing RNAs. **c**, qRT–PCR validation of copy numbers of the indicated transcripts in HCT116 cells. Mean copy number is shown above each bar. Data shown as mean ± s.d. $n = 3$ biological replicates. **d**, Approximate cytoplasmic concentration of each PUM target transcript in HCT116 cells. **e**, Confocal images of PUM1 droplets, formed with 150 nM PUM1 plus 2 nM *NORAD* or increasing concentrations of the indicated in vitro transcribed 3' UTR of each PUM target. Red boxes highlight assays performed at the estimated physiologic concentration of each transcript in HCT116 cells. The same PUM1 protein preparation was used for droplet formation assays with *NORAD* and 3' UTRs.

[Source data](#)

Extended Data Fig. 6 PUM target mRNAs weakly co-localize with PUM1 foci.

a, Confocal images of HCT116 cells co-stained for the indicated RNA and PUM1 by RNA FISH and immunofluorescence, respectively. **b**,

Quantification of the indicated PUM target mRNA and PUM1 co-localization ($n = 20$ cells for each RNA). Mean co-localization shown above box plots. Middle line, median; box, 25th to 75th percentiles; whiskers, minimum to maximum co-localization for each target mRNA.

[Source data](#)

Extended Data Fig. 7 Competitive, super-stoichiometric recruitment of PUM into RNA-induced droplets.

a, Quantification of the number of PUM1 molecules per PRE in droplets nucleated by *NORAD* (2 nM) or PRE₈ oligonucleotide (10 nM) and the indicated concentration of PUM1 in vitro. Black line represents the mean ($n = 101, 115, 113, 107, 114$, and 115 droplets for each condition from left to right). **b**, Quantification of PUM1 partition coefficients formed with 150 nM PUM1 and 10 nM PRE₈ RNA normalized to partition coefficient at 0 μ M competitor RNA (PRE₁ RNA). IC₅₀ represents concentration of PRE₁ RNA needed to reduce PUM1 partitioning by 50%. Data shown as mean \pm s.d. $n = 44$ or more droplets analysed for each data point. Each PRE in the PRE₈ RNA is approximately 9 times more efficient at PUM1 recruitment than a monovalent PRE.

[Source data](#)

Extended Data Fig. 8 Purification and characterization of PUM1^{HDmut} and IDR-deletion proteins.

a, Structure of the human PUM1 HD domain (PDB: 1M8X) in complex with PRE–RNA, showing mutated residues in PUM1^{HDmut} (pink). **b**, EMSA demonstrating loss of PUM1^{HDmut} RNA binding. **c**, Coomassie stain of purified MBP–SNAP–PUM1^{HDmut}–His protein used for in vitro experiments. **d**, Droplet formation by the indicated PUM proteins in the presence or absence of PRE₈ RNA oligonucleotide. **e**, Coomassie stain of purified MBP–SNAP–PUM1^{HD-WT} Δ IDR–His and MBP–SNAP–PUM1^{HDmut} Δ IDR–His proteins used for in vitro experiments. Gels were

cropped to remove irrelevant lanes where indicated with vertical lines. For gel source data, see Supplementary Fig. 1.

Extended Data Fig. 9 Recruitment of PUM proteins into pre-formed NORAD–PUM condensates independently of RNA binding.

a, Western blot analysis of PUM1 (left) and PUM2 (right) in HCT116 cells of the indicated genotypes transduced with lentiviruses expressing PUM^{WT}–GFP or PUM^{HDmut}–GFP. Molecular weight in kDa shown on right. For gel source data, see Supplementary Fig. 1. **b**, Time-lapse live-cell confocal images showing fusion of PUM1^{WT}–GFP or PUM1^{HDmut}–GFP condensates in wild-type HCT116 cells. Scale bar, 5 μm. **c, d**, Top, images of PUM1^{WT}–GFP and PUM1^{HDmut}–GFP FRAP (**c**) or PUM2^{WT}–GFP and PUM2^{HDmut}–GFP FRAP (**d**) in wild-type HCT116 cells. Puncta undergoing photobleaching shown in dashed boxes. Bottom, FRAP quantification with fluorescence intensities plotted relative to pre-bleach time point ($t = -5$ s). Data shown as mean ± s.d. (**c**; $n = 3$ puncta) or mean (**d**; $n = 2$ puncta). Scale bar, 5 μm. **e**, Confocal images of PUM2^{WT}–GFP (top) and PUM2^{HDmut}–GFP (bottom) in HCT116 cells of the indicated genotypes. **f**, Left, confocal images of GFP-tagged full-length or IDR-deleted PUM1^{WT} or PUM1^{HDmut} expressed in wild-type HCT116 cells. Right, quantification of PUM1 partition coefficients, defined as the intensity of PUM1–GFP inside condensates relative to the surrounding cytoplasm. Partition coefficients were calculated for $n = 175, 116, 36$, or 121 condensates from 5 different cells for each protein from left to right. Black bar depicts the mean partition coefficient. Two-tailed *t*-test comparing each PUM1 mutant to PUM1^{WT}. *** $P < 1 \times 10^{-15}$; n.s., not significant.

[Source data](#)

Extended Data Fig. 10 NORAD expression and PUM localization in circPRE-expressing cell lines.

a, Schematic of circPRE-producing constructs²¹, which encode the Broccoli aptamer and 0–8 PREs. **b**, Copy number analysis of circPRE-transcripts in

HCT116 CRISPRi cells expressing control or *NORAD*-targeting sgRNAs. Mean copy number in sg*NORAD* cell lines is shown above each bar. circPRE₄-low and circPRE₄-mid represent distinct cell populations sorted for different circPRE copy numbers. Data shown as mean ± s.d. $n = 3$ biological replicates. **c**, qRT–PCR analysis of *NORAD* expression in the indicated circPRE HCT116 CRISPRi cell lines expressing control or *NORAD*-targeting sgRNAs. Data shown as mean ± s.d. $n = 3$ technical replicates. **d**, **e**, Top, confocal images of PUM1 (**d**) or PUM2 (**e**) immunofluorescence in the indicated cell lines. Bottom, quantification of the number of PUM1 (**d**) or PUM2 (**e**) foci per cell in the indicated sgControl- or sg*NORAD*-infected cell lines ($n = 20$ cells for each cell line). Mean number of foci shown above each box plot. Middle line, median; box, 25th to 75th percentiles; whiskers, minimum to maximum.

[Source data](#)

Supplementary information

[Supplementary Figure 1](#)

Gel source data.

[Reporting Summary](#)

[Supplementary Table 1](#)

A list of oligonucleotides and antibodies used in this study.

[Peer Review File](#)

Source data

[Source Data Fig. 1](#)

[Source Data Fig. 2](#)

[Source Data Fig. 3](#)

[Source Data Fig. 4](#)

[Source Data Extended Data Fig. 1](#)

[Source Data Extended Data Fig. 2](#)

[Source Data Extended Data Fig. 3](#)

[Source Data Extended Data Fig. 4](#)

[Source Data Extended Data Fig. 5](#)

[Source Data Extended Data Fig. 6](#)

[Source Data Extended Data Fig. 7](#)

[Source Data Extended Data Fig. 9](#)

[Source Data Extended Data Fig. 10](#)

Rights and permissions

[Reprints and Permissions](#)

About this article



Check for
updates

[**Cite this article**](#)

Elguindy, M.M., Mendell, J.T. *NORAD*-induced Pumilio phase separation is required for genome stability. *Nature* **595**, 303–308 (2021).
<https://doi.org/10.1038/s41586-021-03633-w>

[Download citation](#)

- Received: 24 August 2020
- Accepted: 11 May 2021
- Published: 09 June 2021
- Issue Date: 08 July 2021
- DOI: <https://doi.org/10.1038/s41586-021-03633-w>

Comments

By submitting a comment you agree to abide by our [Terms](#) and [Community Guidelines](#). If you find something abusive or that does not comply with our terms or guidelines please flag it as inappropriate.

[Access through your institution](#)

[Change institution](#)

[Buy or subscribe](#)

Advertisement

This article was downloaded by **calibre** from <https://www.nature.com/articles/s41586-021-03633-w>

- Article
- [Published: 05 May 2021](#)

Epigenetic silencing by SETDB1 suppresses tumour intrinsic immunogenicity

- [Gabriel K. Griffin](#)^{1,2,3 na1},
- [Jingyi Wu](#)^{1,2 na1},
- [Arvin Iracheta-Vellve](#) ORCID: orcid.org/0000-0002-6635-3904^{1 na1},
- [James C. Patti](#) ORCID: orcid.org/0000-0002-1733-6702¹,
- [Jeffrey Hsu](#) ORCID: orcid.org/0000-0001-6065-4653¹,
- [Thomas Davis](#)¹,
- [Deborah Dele-Oni](#)¹,
- [Peter P. Du](#) ORCID: orcid.org/0000-0003-2652-0541¹,
- [Aya G. Halawi](#)¹,
- [Jeffrey J. Ishizuka](#)^{4 nAff8},
- [Sarah Y. Kim](#)¹,
- [Susan Klaeger](#) ORCID: orcid.org/0000-0002-0074-5163¹,
- [Nelson H. Knudsen](#) ORCID: orcid.org/0000-0002-0384-1097^{1,5},
- [Brian C. Miller](#) ORCID: orcid.org/0000-0001-5931-4184^{1,4,6,7},
- [Tung H. Nguyen](#)¹,
- [Kira E. Olander](#)¹,
- [Malvina Papanastasiou](#) ORCID: orcid.org/0000-0003-3378-6612¹,
- [Suzanna Rachimi](#)¹,
- [Emily J. Robitschek](#)^{1,4},
- [Emily M. Schneider](#) ORCID: orcid.org/0000-0001-5778-9119¹,
- [Mitchell D. Yeary](#)¹,
- [Margaret D. Zimmer](#)¹,
- [Jacob D. Jaffe](#) ORCID: orcid.org/0000-0001-9845-1210^{1 nAff9},

- [Steven A. Carr](#)¹,
- [John G. Doench](#) [ORCID: orcid.org/0000-0002-3707-9889](#)¹,
- [W. Nicholas Haining](#)^{1,4} nAff10,
- [Kathleen B. Yates](#)^{1,5},
- [Robert T. Manguso](#) [ORCID: orcid.org/0000-0003-1336-413X](#)^{1,5} na2
&
- [Bradley E. Bernstein](#) [ORCID: orcid.org/0000-0002-5726-6278](#)^{1,2} na2

[Nature](#) volume **595**, pages 309–314 (2021) [Cite this article](#)

- 17k Accesses
- 183 Altmetric
- [Metrics details](#)

Subjects

- [Cancer epigenetics](#)
- [Cancer immunotherapy](#)
- [Chromatin](#)
- [Tumour immunology](#)

Abstract

Epigenetic dysregulation is a defining feature of tumorigenesis that is implicated in immune escape^{1,2}. Here, to identify factors that modulate the immune sensitivity of cancer cells, we performed in vivo CRISPR–Cas9 screens targeting 936 chromatin regulators in mouse tumour models treated with immune checkpoint blockade. We identified the H3K9 methyltransferase SETDB1 and other members of the HUSH and KAP1 complexes as mediators of immune escape^{3,4,5}. We also found that amplification of *SETDB1* (1q21.3) in human tumours is associated with immune exclusion and resistance to immune checkpoint blockade. SETDB1 represses broad domains, primarily within the open genome compartment.

These domains are enriched for transposable elements (TEs) and immune clusters associated with segmental duplication events, a central mechanism of genome evolution⁶. SETDB1 loss derepresses latent TE-derived regulatory elements, immunostimulatory genes, and TE-encoded retroviral antigens in these regions, and triggers TE-specific cytotoxic T cell responses *in vivo*. Our study establishes SETDB1 as an epigenetic checkpoint that suppresses tumour-intrinsic immunogenicity, and thus represents a candidate target for immunotherapy.

Access options

Subscribe to Journal

Get full journal access for 1 year

\$199.00

only \$3.90 per issue

[Subscribe](#)

All prices are NET prices.

VAT will be added later in the checkout.

Tax calculation will be finalised during checkout.

Rent or Buy article

Get time limited or full article access on ReadCube.

from \$8.99

[Rent or Buy](#)

All prices are NET prices.

Additional access options:

- [Log in](#)

- [Access through your institution](#)
- [Learn about institutional subscriptions](#)

Fig. 1: In vivo chromatin regulator screens.

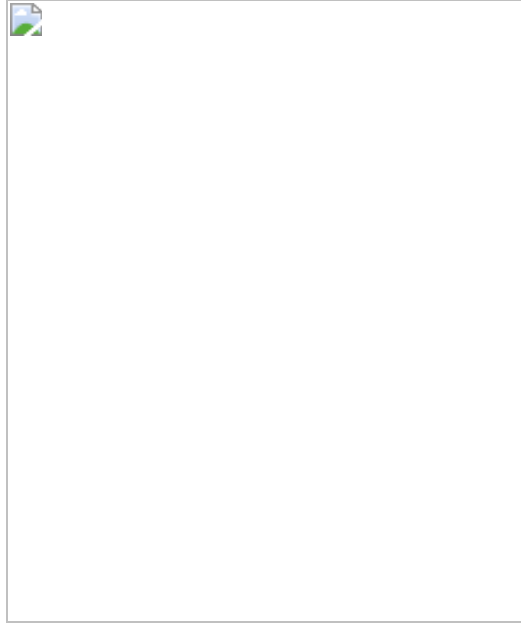


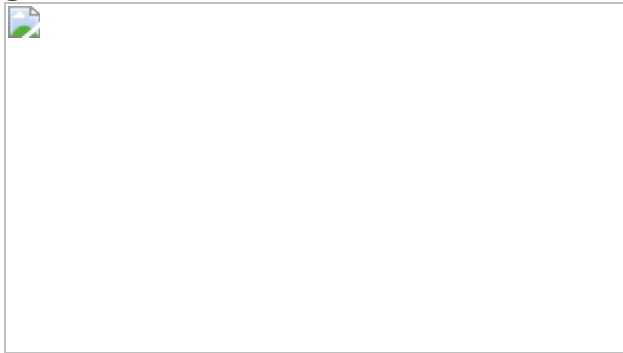
Fig. 2: *SETDB1* (1q21.3) amplification in human tumours.



Fig. 3: SETDB1 targets evolving genomic loci.



Fig. 4: SETDB1 loss induces TE-encoded viral antigens.



Data availability

All genomic sequencing data that support the findings of this study have been deposited in the Gene Expression Omnibus database with the accession code [GSE155972](#). The original mass spectra for all experiments, and the protein sequence database used for searches have been deposited in the public proteomics repository MassIVE (<https://massive.ucsd.edu>) and are accessible at <ftp://massive.ucsd.edu/MSV000086580/>. [Source data](#) are provided with this paper.

References

1. 1.

- Jones, P. A., Ohtani, H., Chakravarthy, A. & De Carvalho, D. D. Epigenetic therapy in immune-oncology. *Nat. Rev. Cancer* **19**, 151–161 (2019).

[CAS](#) [PubMed](#) [Google Scholar](#)

2. 2.

Topper, M. J., Vaz, M., Marrone, K. A., Brahmer, J. R. & Baylin, S. B. The emerging role of epigenetic therapeutics in immuno-oncology. *Nat. Rev. Clin. Oncol.* **17**, 75–90 (2020).

[PubMed](#) [Google Scholar](#)

3. 3.

Matsui, T. et al. Proviral silencing in embryonic stem cells requires the histone methyltransferase ESET. *Nature* **464**, 927–931 (2010).

[ADS](#) [CAS](#) [PubMed](#) [Google Scholar](#)

4. 4.

Rowe, H. M. et al. KAP1 controls endogenous retroviruses in embryonic stem cells. *Nature* **463**, 237–240 (2010).

[ADS](#) [CAS](#) [PubMed](#) [Google Scholar](#)

5. 5.

Tchasovnikarova, I. A. et al. Epigenetic silencing by the HUSH complex mediates position-effect variegation in human cells. *Science* **348**, 1481–1485 (2015).

[ADS](#) [CAS](#) [PubMed](#) [PubMed Central](#) [Google Scholar](#)

6. 6.

Dennis, M. Y. & Eichler, E. E. Human adaptation and evolution by segmental duplication. *Curr. Opin. Genet. Dev.* **41**, 44–52 (2016).

[CAS](#) [PubMed](#) [PubMed Central](#) [Google Scholar](#)

7. 7.

Sharma, P., Hu-Lieskován, S., Wargo, J. A. & Ribas, A. Primary, adaptive, and acquired resistance to cancer immunotherapy. *Cell* **168**, 707–723 (2017).

[CAS](#) [PubMed](#) [PubMed Central](#) [Google Scholar](#)

8. 8.

Spranger, S. & Gajewski, T. F. Mechanisms of tumor cell–intrinsic immune evasion. *Annu. Rev. Cancer Biol.* **2**, 213–228 (2018).

[Google Scholar](#)

9. 9.

Galluzzi, L., Chan, T. A., Kroemer, G., Wolchok, J. D. & López-Soto, A. The hallmarks of successful anticancer immunotherapy. *Sci. Transl. Med.* **10**, eaat7807 (2018).

[PubMed](#) [Google Scholar](#)

10. 10.

Wei, S. C., Duffy, C. R. & Allison, J. P. Fundamental mechanisms of immune checkpoint blockade therapy. *Cancer Discov.* **8**, 1069–1086 (2018).

[PubMed](#) [Google Scholar](#)

11. 11.

Baumeister, S. H., Freeman, G. J., Dranoff, G. & Sharpe, A. H. Coinhibitory pathways in immunotherapy for cancer. *Annu. Rev. Immunol.* **34**, 539–573 (2016).

[CAS](#) [PubMed](#) [Google Scholar](#)

12. 12.

Sheng, W. et al. LSD1 ablation stimulates anti-tumor immunity and enables checkpoint blockade. *Cell* **174**, 549–563.e19 (2018).

[CAS](#) [PubMed](#) [PubMed Central](#) [Google Scholar](#)

13. 13.

Miao, D. et al. Genomic correlates of response to immune checkpoint therapies in clear cell renal cell carcinoma. *Science* **359**, 801–806 (2018).

[ADS](#) [CAS](#) [PubMed](#) [PubMed Central](#) [Google Scholar](#)

14. 14.

Burr, M. L. et al. An evolutionarily conserved function of polycomb silences the MHC class I antigen presentation pathway and enables immune evasion in cancer. *Cancer Cell* **36**, 385–401.e8 (2019).

[CAS](#) [PubMed](#) [PubMed Central](#) [Google Scholar](#)

15. 15.

Li, F. et al. *In vivo* epigenetic CRISPR screen identifies *Asfla* as an immunotherapeutic target in *Kras*-mutant lung adenocarcinoma. *Cancer Discov.* **10**, 270–287 (2020).

[PubMed](#) [Google Scholar](#)

16. 16.

Manguso, R. T. et al. *In vivo* CRISPR screening identifies Ptpn2 as a cancer immunotherapy target. *Nature* **547**, 413–418 (2017).

[CAS](#) [PubMed](#) [PubMed Central](#) [Google Scholar](#)

17. 17.

Jacobs, F. M. J. et al. An evolutionary arms race between KRAB zinc-finger genes ZNF91/93 and SVA/L1 retrotransposons. *Nature* **516**, 242–245 (2014).

[ADS](#) [CAS](#) [PubMed](#) [PubMed Central](#) [Google Scholar](#)

18. 18.

Ceol, C. J. et al. The histone methyltransferase SETDB1 is recurrently amplified in melanoma and accelerates its onset. *Nature* **471**, 513–517 (2011).

[ADS](#) [CAS](#) [PubMed](#) [PubMed Central](#) [Google Scholar](#)

19. 19.

Braun, D. A. et al. Interplay of somatic alterations and immune infiltration modulates response to PD-1 blockade in advanced clear cell renal cell carcinoma. *Nat. Med.* **26**, 909–918 (2020).

[CAS](#) [PubMed](#) [PubMed Central](#) [Google Scholar](#)

20. 20.

Lieberman-Aiden, E. et al. Comprehensive mapping of long-range interactions reveals folding principles of the human genome. *Science* **326**, 289–293 (2009).

[ADS](#) [CAS](#) [PubMed](#) [PubMed Central](#) [Google Scholar](#)

21. 21.

Azazi, D., Mudge, J. M., Odom, D. T. & Flieck, P. Functional signatures of evolutionarily young CTCF binding sites. *BMC Biol.* **18**, 132 (2020).

[CAS](#) [PubMed](#) [PubMed Central](#) [Google Scholar](#)

22. 22.

Cosman, D. et al. ULBPs, novel MHC class I-related molecules, bind to CMV glycoprotein UL16 and stimulate NK cytotoxicity through the NKG2D receptor. *Immunity* **14**, 123–133 (2001).

[CAS](#) [PubMed](#) [Google Scholar](#)

23. 23.

Cuellar, T. L. et al. Silencing of retrotransposons by SETDB1 inhibits the interferon response in acute myeloid leukemia. *J. Cell Biol.* **216**, 3535–3549 (2017).

[CAS](#) [PubMed](#) [PubMed Central](#) [Google Scholar](#)

24. 24.

Mehdipour, P. et al. Epigenetic therapy induces transcription of inverted SINEs and ADAR1 dependency. *Nature* **588**, 169–173 (2020).

[ADS](#) [CAS](#) [PubMed](#) [PubMed Central](#) [Google Scholar](#)

25. 25.

Takahashi, Y. et al. Regression of human kidney cancer following allogeneic stem cell transplantation is associated with recognition of an HERV-E antigen by T cells. *J. Clin. Invest.* **118**, 1099–1109 (2008).

[CAS](#) [PubMed](#) [PubMed Central](#) [Google Scholar](#)

26. 26.

Laumont, C. M. et al. Noncoding regions are the main source of targetable tumor-specific antigens. *Sci. Transl. Med.* **10**, eaau5516 (2018).

[CAS](#) [PubMed](#) [Google Scholar](#)

27. 27.

Kershaw, M. H. et al. Immunization against endogenous retroviral tumor-associated antigens. *Cancer Res.* **61**, 7920–7924 (2001).

[CAS](#) [PubMed](#) [PubMed Central](#) [Google Scholar](#)

28. 28.

White, H. D., Roeder, D. A. & Green, W. R. An immunodominant Kb-restricted peptide from the p15E transmembrane protein of endogenous ecotropic murine leukemia virus (MuLV) AKR623 that restores susceptibility of a tumor line to anti-AKR/Gross MuLV cytotoxic T lymphocytes. *J. Virol.* **68**, 897–904 (1994).

[CAS](#) [PubMed](#) [PubMed Central](#) [Google Scholar](#)

29. 29.

Jiang, Y. et al. The methyltransferase SETDB1 regulates a large neuron-specific topological chromatin domain. *Nat. Genet.* **49**, 1239–1250 (2017).

[CAS](#) [PubMed](#) [PubMed Central](#) [Google Scholar](#)

30. 30.

Adoue, V. et al. The histone methyltransferase SETDB1 controls T helper cell lineage integrity by repressing endogenous retroviruses. *Immunity* **50**, 629–644.e8 (2019).

[CAS](#) [PubMed](#) [Google Scholar](#)

31. 31.

Doench, J. G. et al. Rational design of highly active sgRNAs for CRISPR–Cas9-mediated gene inactivation. *Nat. Biotechnol.* **32**, 1262–1267 (2014).

[CAS](#) [PubMed](#) [PubMed Central](#) [Google Scholar](#)

32. 32.

Goldman, M. J. et al. Visualizing and interpreting cancer genomics data via the Xena platform. *Nat. Biotechnol.* **38**, 675–678 (2020).

[CAS](#) [PubMed](#) [PubMed Central](#) [Google Scholar](#)

33. 33.

Subramanian, A. et al. Gene set enrichment analysis: a knowledge-based approach for interpreting genome-wide expression profiles. *Proc. Natl Acad. Sci. USA* **102**, 15545–15550 (2005).

[ADS](#) [CAS](#) [PubMed](#) [PubMed Central](#) [Google Scholar](#)

34. 34.

Liberzon, A. et al. The Molecular Signatures Database (MSigDB) hallmark gene set collection. *Cell Syst.* **1**, 417–425 (2015).

[CAS](#) [PubMed](#) [PubMed Central](#) [Google Scholar](#)

35. 35.

Liberzon, A. et al. Molecular signatures database (MSigDB) 3.0. *Bioinformatics* **27**, 1739–1740 (2011).

[CAS](#) [PubMed](#) [PubMed Central](#) [Google Scholar](#)

36. 36.

Motzer, R. J. et al. Nivolumab versus everolimus in advanced renal-cell carcinoma. *N. Engl. J. Med.* **373**, 1803–1813 (2015).

[CAS](#) [PubMed](#) [PubMed Central](#) [Google Scholar](#)

37. 37.

van Galen, P. et al. A multiplexed system for quantitative comparisons of chromatin landscapes. *Mol. Cell* **61**, 170–180 (2016).

[PubMed](#) [Google Scholar](#)

38. 38.

D, L., Lauren, D., Van, P., Bradley, E. & Charles, B. Mint-ChIP3: A low-input ChIP-seq protocol using multiplexed chromatin and T7 amplification v1. *protocols.io*
<https://doi.org/10.17504/protocols.io.wbefaje> (2019).

39. 39.

Buenrostro, J. D., Giresi, P. G., Zaba, L. C., Chang, H. Y. & Greenleaf, W. J. Transposition of native chromatin for fast and sensitive epigenomic profiling of open chromatin, DNA-binding proteins and nucleosome position. *Nat. Methods* **10**, 1213–1218 (2013).

[CAS](#) [PubMed](#) [PubMed Central](#) [Google Scholar](#)

40. 40.

Dixon, J. R. et al. Chromatin architecture reorganization during stem cell differentiation. *Nature* **518**, 331–336 (2015).

[ADS](#) [CAS](#) [PubMed](#) [PubMed Central](#) [Google Scholar](#)

41. 41.

Bonev, B. et al. Multiscale 3D genome rewiring during mouse neural development. *Cell* **171**, 557–572.e24 (2017).

[CAS](#) [PubMed](#) [PubMed Central](#) [Google Scholar](#)

42. 42.

Heinz, S. et al. Simple combinations of lineage-determining transcription factors prime cis-regulatory elements required for

macrophage and B cell identities. *Mol. Cell* **38**, 576–589 (2010).

[CAS](#) [PubMed](#) [PubMed Central](#) [Google Scholar](#)

43. 43.

Mi, H., Muruganujan, A., Ebert, D., Huang, X. & Thomas, P. D. PANTHER version 14: more genomes, a new PANTHER GO-slim and improvements in enrichment analysis tools. *Nucleic Acids Res.* **47** (D1), D419–D426 (2019).

[CAS](#) [PubMed](#) [Google Scholar](#)

44. 44.

The Gene Ontology Consortium. Gene ontology: tool for the unification of biology. *Nat. Genet.* **25**, 25–29 (2000).

[PubMed Central](#) [Google Scholar](#)

45. 45.

The Gene Ontology Consortium. The Gene Ontology Resource: 20 years and still GOing strong. *Nucleic Acids Res.* **47** (D1), D330–D338 (2019).

[Google Scholar](#)

46. 46.

Huang, D. W., Sherman, B. T. & Lempicki, R. A. Systematic and integrative analysis of large gene lists using DAVID bioinformatics resources. *Nat. Protoc.* **4**, 44–57 (2009).

[CAS](#) [Google Scholar](#)

47. 47.

ENCODE Project Consortium. An integrated encyclopedia of DNA elements in the human genome. *Nature* **489**, 57–74 (2012).

[ADS](#) [Google Scholar](#)

48. 48.

Davis, C. A. et al. The Encyclopedia of DNA elements (ENCODE): data portal update. *Nucleic Acids Res.* **46** (D1), D794–D801 (2018).

[CAS](#) [PubMed](#) [Google Scholar](#)

49. 49.

Nakagawa, S. & Takahashi, M. U. gEVE: a genome-based endogenous viral element database provides comprehensive viral protein-coding sequences in mammalian genomes. *Database* **2016**, PMC4885607 (2016).

50. 50.

Evans, L. H., Morrison, R. P., Malik, F. G., Portis, J. & Britt, W. J. A neutralizable epitope common to the envelope glycoproteins of ecotropic, polytropic, xenotropic, and amphotropic murine leukemia viruses. *J. Virol.* **64**, 6176–6183 (1990).

[CAS](#) [PubMed](#) [PubMed Central](#) [Google Scholar](#)

51. 51.

Mertins, P. et al. Reproducible workflow for multiplexed deep-scale proteome and phosphoproteome analysis of tumor tissues by liquid chromatography-mass spectrometry. *Nat. Protoc.* **13**, 1632–1661 (2018).

[CAS](#) [PubMed](#) [PubMed Central](#) [Google Scholar](#)

52. 52.

Reynisson, B., Alvarez, B., Paul, S., Peters, B. & Nielsen, M. NetMHCpan-4.1 and NetMHCIIpan-4.0: improved predictions of MHC antigen presentation by concurrent motif deconvolution and integration of MS MHC eluted ligand data. *Nucleic Acids Res.* **48** (W1), W449–W454 (2020).

[CAS](#) [PubMed](#) [PubMed Central](#) [Google Scholar](#)

53. 53.

Abelin, J. G. et al. Mass spectrometry profiling of HLA-associated peptidomes in mono-allelic cells enables more accurate epitope prediction. *Immunity* **46**, 315–326 (2017).

[CAS](#) [PubMed](#) [PubMed Central](#) [Google Scholar](#)

54. 54.

Sarkizova, S. et al. A large peptidome dataset improves HLA class I epitope prediction across most of the human population. *Nat. Biotechnol.* **38**, 199–209 (2020).

[CAS](#) [PubMed](#) [Google Scholar](#)

55. 55.

Wolf, F. A., Angerer, P. & Theis, F. J. SCANPY: large-scale single-cell gene expression data analysis. *Genome Biol.* **19**, 15 (2018).

[PubMed](#) [PubMed Central](#) [Google Scholar](#)

56. 56.

Butler, A., Hoffman, P., Smibert, P., Papalexi, E. & Satija, R. Integrating single-cell transcriptomic data across different conditions, technologies, and species. *Nat. Biotechnol.* **36**, 411–420 (2018).

[CAS](#) [PubMed](#) [PubMed Central](#) [Google Scholar](#)

57. 57.

Ntranos, V., Yi, L., Melsted, P. & Pachter, L. A discriminative learning approach to differential expression analysis for single-cell RNA-seq. *Nat. Methods* **16**, 163–166 (2019).

[CAS](#) [PubMed](#) [Google Scholar](#)

58. 58.

Lun, A. T. L., Bach, K. & Marioni, J. C. Pooling across cells to normalize single-cell RNA sequencing data with many zero counts. *Genome Biol.* **17**, 75 (2016).

[PubMed](#) [Google Scholar](#)

[Download references](#)

Acknowledgements

This work was supported by funds from Calico Life Sciences, the Gene Regulation Observatory at the Broad Institute of MIT and Harvard, the Damon-Runyon Cancer Research Foundation (to G.K.G. and J.W.), the National Cancer Institute (NCI) Clinical Proteomic Tumor Analysis Consortium (NIH/NCI U24-CA210986 and NIH/NCI U01 CA214125 to S.A.C), the Wong Family Award (to B.C.M.), and the NCI/NIH Director's Fund (DP1CA216873 to B.E.B.). B.E.B. is the Bernard and Mildred Kayden Endowed MGH Research Institute Chair and an American Cancer Society Research Professor. The authors thank all members of the Bernstein and Manguso laboratories at MGH and the Broad Institute, E. Van Allen, N. Vokes, A. Sharpe, G. Poncet-Montange, D. McKinney, T. Sundberg, J. Grownay, D. Stokoe and A. Firestone for thoughtful discussions and feedback. Graphics in Fig. 1a were created with Biorender.com using a paid license.

Author information

Author notes

1. Jeffrey J. Ishizuka

Present address: Department of Internal Medicine (Oncology), Yale Cancer Center and Yale School of Medicine, New Haven, CT, USA

2. Jacob D. Jaffe

Present address: Inzen Therapeutics, Cambridge, MA, USA

3. W. Nicholas Haining

Present address: Merck, Boston, MA, USA

4. These authors contributed equally: Gabriel K. Griffin, Jingyi Wu, Arvin Iracheta-Vellve

5. These authors jointly supervised this work: Robert T. Manguso, Bradley E. Bernstein

Affiliations

1. Broad Institute of MIT and Harvard, Cambridge, MA, USA

Gabriel K. Griffin, Jingyi Wu, Arvin Iracheta-Vellve, James C. Patti, Jeffrey Hsu, Thomas Davis, Deborah Dele-Oni, Peter P. Du, Aya G. Halawi, Sarah Y. Kim, Susan Klaeger, Nelson H. Knudsen, Brian C. Miller, Tung H. Nguyen, Kira E. Olander, Malvina Papanastasiou, Suzanna Rachimi, Emily J. Robitschek, Emily M. Schneider, Mitchell D. Yeary, Margaret D. Zimmer, Jacob D. Jaffe, Steven A. Carr, John G. Doench, W. Nicholas Haining, Kathleen B. Yates, Robert T. Manguso & Bradley E. Bernstein

2. Department of Pathology and Center for Cancer Research, Massachusetts General Hospital and Harvard Medical School, Boston, MA, USA

Gabriel K. Griffin, Jingyi Wu & Bradley E. Bernstein

3. Department of Pathology, Brigham and Women's Hospital and Harvard Medical School, Boston, MA, USA

Gabriel K. Griffin

4. Department of Pediatric Oncology, Dana-Farber Cancer Institute and Harvard Medical School, Boston, MA, USA

Jeffrey J. Ishizuka, Brian C. Miller, Emily J. Robitschek & W. Nicholas Haining

5. Department of Medicine and Center for Cancer Research, Massachusetts General Hospital and Harvard Medical School, Boston, MA, USA

Nelson H. Knudsen, Kathleen B. Yates & Robert T. Manguso

6. Department of Medical Oncology, Dana-Farber Cancer Institute and Harvard Medical School, Boston, MA, USA

Brian C. Miller

7. Department of Immunology and Evergrande Center for Immunological Diseases, Harvard Medical School, Boston, MA, USA

Brian C. Miller

Authors

1. Gabriel K. Griffin

[View author publications](#)

You can also search for this author in [PubMed](#) [Google Scholar](#)

2. Jingyi Wu

[View author publications](#)

You can also search for this author in [PubMed](#) [Google Scholar](#)

3. Arvin Iracheta-Vellve

[View author publications](#)

You can also search for this author in [PubMed](#) [Google Scholar](#)

4. James C. Patti

[View author publications](#)

You can also search for this author in [PubMed](#) [Google Scholar](#)

5. Jeffrey Hsu

[View author publications](#)

You can also search for this author in [PubMed](#) [Google Scholar](#)

6. Thomas Davis

[View author publications](#)

You can also search for this author in [PubMed](#) [Google Scholar](#)

7. Deborah Dele-Oni

[View author publications](#)

You can also search for this author in [PubMed](#) [Google Scholar](#)

8. Peter P. Du

[View author publications](#)

You can also search for this author in [PubMed](#) [Google Scholar](#)

9. Aya G. Halawi

[View author publications](#)

You can also search for this author in [PubMed](#) [Google Scholar](#)

10. Jeffrey J. Ishizuka

[View author publications](#)

You can also search for this author in [PubMed](#) [Google Scholar](#)

11. Sarah Y. Kim

[View author publications](#)

You can also search for this author in [PubMed](#) [Google Scholar](#)

12. Susan Klaeger

[View author publications](#)

You can also search for this author in [PubMed](#) [Google Scholar](#)

13. Nelson H. Knudsen

[View author publications](#)

You can also search for this author in [PubMed](#) [Google Scholar](#)

14. Brian C. Miller

[View author publications](#)

You can also search for this author in [PubMed](#) [Google Scholar](#)

15. Tung H. Nguyen

[View author publications](#)

You can also search for this author in [PubMed](#) [Google Scholar](#)

16. Kira E. Olander

[View author publications](#)

You can also search for this author in [PubMed](#) [Google Scholar](#)

17. Malvina Papanastasiou

[View author publications](#)

You can also search for this author in [PubMed](#) [Google Scholar](#)

18. Suzanna Rachimi

[View author publications](#)

You can also search for this author in [PubMed](#) [Google Scholar](#)

19. Emily J. Robitschek

[View author publications](#)

You can also search for this author in [PubMed](#) [Google Scholar](#)

20. Emily M. Schneider

[View author publications](#)

You can also search for this author in [PubMed](#) [Google Scholar](#)

21. Mitchell D. Yeary

[View author publications](#)

You can also search for this author in [PubMed](#) [Google Scholar](#)

22. Margaret D. Zimmer

[View author publications](#)

You can also search for this author in [PubMed](#) [Google Scholar](#)

23. Jacob D. Jaffe

[View author publications](#)

You can also search for this author in [PubMed](#) [Google Scholar](#)

24. Steven A. Carr

[View author publications](#)

You can also search for this author in [PubMed](#) [Google Scholar](#)

25. John G. Doench

[View author publications](#)

You can also search for this author in [PubMed](#) [Google Scholar](#)

26. W. Nicholas Haining

[View author publications](#)

You can also search for this author in [PubMed](#) [Google Scholar](#)

27. Kathleen B. Yates

[View author publications](#)

You can also search for this author in [PubMed](#) [Google Scholar](#)

28. Robert T. Manguso

[View author publications](#)

You can also search for this author in [PubMed](#) [Google Scholar](#)

29. Bradley E. Bernstein

[View author publications](#)

You can also search for this author in [PubMed](#) [Google Scholar](#)

Contributions

Conception and experimental design: G.K.G., J.W., A.I.-V., J.G.D., J.D.J., S.A.C., W.N.H., K.B.Y., R.T.M. and B.E.B. Methodology and data acquisition: G.K.G., J.W., A.I.-V., J.C.P., J.H., D.D.-O., A.H., S.K., N.H.K., B.C.M., T.H.N., K.E.O., M.P., S.R., E.J.R., E.M.S., M.D.Y., M.D.Z., J.D.J., K.B.Y., R.T.M. and B.E.B. Analysis and interpretation of data: G.K.G., J.W., A.I.-V., J.C.P., J.H., T.D., D.D.-O., A.G.H., P.P.D., J.J.I., S.Y.K., S.K., N.H.K., B.C.M., T.H.N., K.E.O., M.P., S.R., E.J.R., M.D.Y., M.D.Z., J.D.J., W.N.H., K.B.Y., R.T.M. and B.E.B. Manuscript writing and revision: G.K.G., K.B.Y., R.T.M. and B.E.B. In addition to the equally contributing first authors, co-authors J.C.P., J.H. and T.D. each made critical and equal contributions to experimental and computational aspects of this study.

Corresponding authors

Correspondence to [Robert T. Manguso](#) or [Bradley E. Bernstein](#).

Ethics declarations

Competing interests

G.K.G. consults for Moderna Therapeutics. J.J.I. consults for Tango Therapeutics and Phenomic AI. B.C.M. consults for Rheos Medicines. J.G.D. consults for Agios, Foghorn Therapeutics, Maze Therapeutics, Merck and Pfizer. J.G.D. consults for and has equity in Tango Therapeutics. S.C.A. is a member of the scientific advisory boards of Kymera, PTM BioLabs and Seer and an ad hoc scientific advisor to Pfizer and Biogen. R.T.M. consults for Bristol Myers Squibb. B.E.B. declares outside interests in Fulcrum Therapeutics, Arsenal Biosciences, HiFiBio, Cell Signaling Technologies and Chroma Medicine. The remaining authors declare no competing interests.

Additional information

Peer review information *Nature* thanks Daniel De Carvalho, Lelia Delamarre and Didier Trono for their contribution to the peer review of this work.

Publisher's note Springer Nature remains neutral with regard to jurisdictional claims in published maps and institutional affiliations.

Extended data figures and tables

[Extended Data Fig. 1 Analysis of screening performance.](#)

a, Tumour volumes (mean \pm s.e.m.) of bilateral tumours ($n = 25$ mice, $n = 50$ individual tumours) in the LLC (top) and B16 (bottom) screens for the indicated treatment conditions on day 12 (LLC) and day 9 (B16) after tumour inoculation. Statistics by ANOVA with Tukey's test for multiple comparisons. **b**, Saturation analysis of animal replicates from the three *in vivo* screening conditions for LLC (top) and B16 (bottom). Pearson's correlations are calculated for the \log_2 guide abundance in one animal versus any other animal, then for two averaged animals versus any other two, and so on. Saturation approaches $r = 0.95$ for both screens. **c**, Depletion (negative ratios) or enrichment (positive ratios) of targeted

chromatin regulator genes in ICB-treated WT versus NSG mice in the LLC (*x*-axis) and B16 (*y*-axis) screens. Circle sizes reflect the significance ($-\log_{10}(P \text{ value})$) of depletion in the higher scoring model. Selected genes that scored uniquely in B16 (left) or LLC (right) are highlighted and coloured according to their associated chromatin regulator complexes.

d, RNA expression (FPKM) in LLC (*x*-axis) and B16 (*y*-axis) for the top 30 screening hits by STARS score in each cell line. Colours indicate whether the gene was depleted in LLC only (orange), B16 only (blue), or in both cell lines (red). One outlier value ($x = 11.7, y = 248.7$) for the B16-only hit, *Cdk2* is excluded for ease of visualization but is included in the calculation of the correlation coefficient. * $P < 0.05$; ** $P < 0.01$; *** $P < 0.001$; **** $P < 0.0001$.

[Source data](#)

Extended Data Fig. 2 Tumour growth and survival data for *Setdb1*, *Trim28*, and HUSH complex KO.

a, Tumour growth (mean \pm s.e.m.) in untreated WT mice (no ICB) inoculated with *Setdb1* ($n = 10$) *Tasor* ($n = 5$), *Mphosph8* ($n = 5$), or *Trim28* ($n = 5$) KO LLC cells, or *Setdb1* or *Trim28* KO B16 cells. Data are representative of 3 (*Setdb1*), 1 (*Tasor*), 1 (*Mphosph8*), 1 (*Trim28* in LLC), and 2 (*Trim28* in B16) experiments. Statistics by two-sided Student's *t*-test at the indicated time-points. **b**, Tumour growth (mean \pm s.e.m.) in WT mice treated with ICB inoculated with *Mphosph8* ($n = 20$) or *Trim28* ($n = 20$) KO LLC cells. Data represent 1 experiment. Statistics by two-sided Student's *t*-test at the indicated time-points. **c**, Overall survival for untreated (top) and ICB-treated (bottom) WT mice inoculated with B16 (left) or LLC (right) tumours and corresponding to Fig. 1d. Statistics by log-rank test. **d**, Tumour growth (top, mean \pm s.e.m.) and overall survival (bottom) for untreated NSG mice (no ICB) inoculated with *Setdb1* KO B16 (left, $n = 20$) or LLC (right, $n = 15$). Data represent 1 experiment. Statistics for tumour growth by two-sided Student's *t*-test at the indicated time-points. Statistics for overall survival by log-rank test. * $P < 0.05$; *** $P < 0.001$; **** $P < 0.0001$.

[Source data](#)

Extended Data Fig. 3 *SETDB1* (1q21.3) amplification in human TCGA and ICB-treated cohorts.

a, Running enrichment scores by GSEA for immune gene sets significantly (FDR <0.001) anti-correlated with *SETDB1* expression by Pearson's correlation across TCGA cohorts. **b**, Pearson's correlation between *SETDB1* expression and cytolytic score (geometric mean of *PRF1* and *GZMA* expression) in TCGA cohorts. Circle size indicates statistical significance ($-\log_{10}(P \text{ value})$) of the Pearson's correlation. Blue and red indicate negative and positive values, respectively. **c**, Bootstrap analysis plotting the rank of the correlation between cytolytic score and *SETDB1* expression (red lines) in each TCGA cohort, compared to 408 randomly selected control genes (grey lines). **d**, Kaplan–Meier curves for patients with renal cell carcinoma treated with PD-1 blockade (left, nivolumab) or mTOR inhibitor (right, everolimus). Overall survival curves are stratified according to *SETDB1* expression (top 50%, high expression; bottom 50%, low expression). Hazard ratios associated with *SETDB1* high expression are listed. The number of patients-at-risk are indicated for each time point. Statistics by log-rank test. **e**, Bootstrap analysis showing the impact of GISTIC2-defined copy-number alterations (CNA) on overall survival in patients treated with mTOR inhibitor (left, everolimus) or PD-1 blockade (right, nivolumab). Positive values indicate a CNA that has a harmful impact on survival with ICB or mTOR inhibitor, and negative values indicate a CNA that has a beneficial effect. 1q21.3 amplification (red) is highlighted alongside chromosomal regions previously reported as predictors of ICB response in RCC, including 10q23.31 deletion (associated with improved response) and 9p21.3 deletion (associated with poor response).

Extended Data Fig. 4 Identification of *SETDB1* domains.

a, Heat map of H3K9me3 peaks (rows, FPKM) in control and *Setdb1* KO LLC (left) and B16 (right) cells. Peaks are separated based on whether they were lost (top) or retained (bottom) in *Setdb1* KO cells, and annotated by whether they are located in the open compartment A of the genome. Statistics for compartment A enrichment by permutation testing. **b**, The

number of 100-kb windows containing the indicated numbers of SETDB1-dependent H3K9me3 peaks in B16 (left) or LLC (right) cells, compared to random control peaks. Statistics by Chi-square test. **c**, Workflow for annotation of SETDB1-domains from H3K9me3 ChIP-seq data in LLC and B16 cells. * $P < 0.05$; **** $P < 0.0001$.

Extended Data Fig. 5 TE-encoded regulatory elements in *Setdb1* KO LLC and B16 cells.

a, Proportion of chromatin accessible sites (ATAC-seq) gained in *Setdb1* KO LLC or B16 cells that are located within (red) or outside (grey) SETDB1 domains. **b**, Proportion of ATAC-seq sites gained in *Setdb1* KO LLC or B16 cells that coincide with promoters (light grey), distal TEs (red), or other promoter-distal sites (dark grey). Statistics by permutation testing. **c**, Proportion of gained ATAC-seq sites at distal TEs in *Setdb1* KO B16 cells that also gain H3K27 acetylation and resemble active enhancers. **d**, Coordinate gain of chromatin accessibility and H3K27 acetylation at an example TE-site in *Setdb1* KO B16 cells. **e**, Activation of genes near (<50 kb) gained ATAC-seq sites at distal TEs in *Setdb1* KO LLC or B16 cells compared to control genes. Statistics by permutation testing. **f–g**, Flow cytometry in control and *Setdb1* KO cells showing gating strategy (**f**), cell-surface expression (**g**) (y-axis, median fluorescence intensity (MFI)) for ULBP1 and RAET1 ligands in LLC (left), and MHC I expression in LLC and B16 (right) with or without induction with IFN γ (10 ng ml^{-1} , 24 h). Data are mean \pm s.e.m. and reflect 2 independent experiments with 4 biological replicates. Statistics by two-sided Student's *t*-test. * $P < 0.05$; ** $P < 0.01$.

Extended Data Fig. 6 Gene and TE expression in *Setdb1* KO LLC and B16 cells.

a, Distribution of TE types (top) and LTR subfamilies (bottom) induced in *Setdb1* KO LLC or B16 cells by RNA-seq. **b**, Heat map showing RNA expression (row normalized) of canonical interferon-stimulated genes in untreated and poly(I:C) stimulated (500 ng ml^{-1} , 48 h) control and *Setdb1* KO LLC and B16 cells. **c**, Percentage of TEs induced in *Setdb1* KO LLC or

B16 cells that retain intact viral ORFs, compared to control TEs. Statistics by Fisher's exact test. **d**, Flow cytometry for cell-surface expression of the MuLV envelope protein in *Setdb1* KO LLC and B16 cells. Gating strategy (left) and histograms (right) with mode-normalized cell counts are shown. Data are representative of $n = 3$ and $n = 2$ experiments in LLC and B16, respectively. **e**, Differential protein expression in B16 cells by whole-cell mass spectrometry. Tryptic protein sequences derived from TEs (red) or canonical proteins (grey) are highlighted. Fold-change (x -axis) and statistical significance (y -axis) for proteins in *Setdb1* KO versus control are shown. **f**, Venn diagrams showing the number of predicted, unique TE-encoded H2-K^b/H2-D^b binding peptides in LLC and B16 cells by GRCm38 RNA-seq analysis. Diagrams show the total number of predicted, TE-encoded MHC Class I peptides in LLC and B16 cells (left), and subsets showing (1) high expression in control cells and further induction upon *Setdb1* KO (middle), and (2) no detectable expression in control cells and strong induction only upon *Setdb1* KO (right). Several MuLV-encoded peptides known to be presented by H2-K^b or H2-D^b are highlighted.

*** $P < 0.001$. **** $P < 0.0001$.

Extended Data Fig. 7 TE expression in SETDB1 KO A375 cells.

a, Distribution of TE types (top) and LTR subfamilies (bottom) induced in *SETDB1* KO A375 cells by RNA-seq. **b**, Volcano plot of Hallmark IFN-alpha response genes in A375 cells by RNA-seq. Fold-change (x -axis) and statistical significance (y -axis) in *SETDB1* KO versus control are shown. **c**, Percentage of TEs induced in *Setdb1* KO A375 cells that retain intact viral ORFs compared to control TEs. Statistics by Fisher's exact test. **d**, Diagram showing the total number of predicted, unique TE-encoded MHCI peptides induced in *SETDB1* KO A375 cells by RNA-seq. Binding predictions are based on A375-specific HLA types (see [Methods](#)). Subsets of predicted TE-encoded MHCI peptides with (1) high expression in control cells and further induction upon *SETDB1* KO, or (2) no detectable expression in control cells and strong induction only upon *SETDB1* KO, are highlighted.

*** $P < 0.001$. **** $P < 0.0001$.

Extended Data Fig. 8 Gene expression and scRNA-seq analysis of immune infiltration in LLC tumours.

a–c, Transcriptional profiling with RNA-seq performed on bulk tumour tissue from control ($n = 8$ untreated and $n = 6$ ICB-treated) and *Setdb1* KO ($n = 10$ untreated and $n = 6$ ICB-treated) LLC tumours. Data represent 1 experiment. **a**, Running enrichment scores by GSEA for immune gene sets significantly (FDR <0.01) upregulated in *Setdb1* KO LLC tumours treated with ICB relative to controls. **b**, Volcano plot depicts expression fold-change (x-axis) and statistical significance (y-axis) of cytotoxicity genes (red) and all other genes (grey) in *Setdb1* KO LLC tumours treated with ICB relative to controls. **c**, TCR repertoire profiling with targeted sequencing of alpha and beta-chain variable regions from *Setdb1* KO LLC tumours (untreated and ICB-treated) relative to controls. Variation in clonotype abundance (skewing) is represented by the Gini index (left, higher number indicates greater skewness) and Shannon entropy (right, lower number indicates greater skewness). Data are mean \pm s.e.m. Statistics by two-sided Student's *t*-test. **d–h**, scRNA-seq (3') analysis of immune cells (CD45⁺ enrichment) from control ($n = 3$ untreated, $n = 4$ ICB-treated) or *Setdb1* KO ($n = 3$ untreated, $n = 4$ ICB-treated) LLC tumours. Data are from 1 experiment. **d**, UMAP plots highlight 4,497 cells and associated clusters identified in the lymphoid compartment. **e**, Representative marker genes used to identify and annotate cell clusters in **d**. **f**, Changes in lymphoid populations in ICB-treated tumours ($n = 4$ control, $n = 4$ *Setdb1* KO) as a proportion of the total lymphoid population. Data are mean \pm s.e.m. Statistics by two-sided Student's *t*-test. **g**, Ratio of NK-2 to NK-1 cells in ICB-treated samples. Data are mean \pm s.e.m. Statistics by Mann–Whitney *U* test. **h**, Differentially expressed genes ($\log_2(\text{fold-change})$) in NK-2 vs NK-1 cells. Circle sizes indicate statistical significance (FDR). * $P < 0.05$. *** $P < 0.0001$.

Extended Data Fig. 9 TCR profiling and scRNA-seq of p15E-specific T cells isolated from control and *Setdb1* KO LLC tumours.

a, Unique CDR3 sequences (*x*-axis) identified from TCR sequencing of flow-sorted p15E-tetramer-positive CD8⁺ T cells isolated from control LLC tumours. High-confidence CDR3 sequences (*n* = 377) are highlighted by brackets and identified based on strong statistical enrichment ($-\log_{10}(P$ value) > 46 cut-off indicated by dotted line, see [Methods](#)) within the p15E-tetramer-positive fraction. **b, c**, scRNA-seq (5') of 24,860 lymphoid cells (CD4⁺CD8⁺ enrichment) isolated from control (*n* = 4 untreated, *n* = 4 ICB-treated) and *Setdb1* KO (*n* = 3 untreated, *n* = 3 ICB-treated) LLC tumours. **b**, UMAP plot highlights cell populations identified among CD4⁺CD8⁺-enriched lymphoid cells. **c**, Representative marker genes used to identify and annotate cell clusters in **b**. **d**, Representative flow cytometry gating strategy for p15E-tetramer studies. Corresponds to Fig. [4e](#). **P* < 0.05.

[Extended Data Fig. 10 Survival data and functional studies evaluating MHCI ablation, CD8 depletion, and NK depletion in Setdb1 KO cells.](#)

a, Overall survival for ICB-treated WT mice inoculated with control and *Setdb1* KO B16 (left) or LLC (right) cells with intact (*B2m* WT) or deficient (*B2m* KO) MHCI, as detailed in Fig. [4f](#) and Methods. Statistics by log-rank test. **b**, Overall survival for ICB-treated WT mice inoculated with control or *Setdb1* KO B16 (left) or LLC (right) cells that received intraperitoneal injections with isotype (left), CD8-depleting (middle), or NK-depleting (right) antibodies starting on day -3 before tumour challenge and continuing every 3 days until day 18, as detailed in Fig. [4f](#) and Methods. Statistics by log-rank test. **P* < 0.05; ****P* < 0.001.

[Source data](#)

Supplementary information

[Reporting Summary](#)

[Supplementary Table 1](#)

List of chromatin regulator genes included in the CRISPR screening library.

Supplementary Table 2

sgRNA depletion and enrichment data for *in vivo* CRISPR screens in LLC and B16.

Supplementary Table 3

Enrichments for transposable elements and segmental duplications within SETDB1 domains.

Supplementary Table 4

Gene-ontology enrichments for segmental duplications within SETDB1 domains.

Supplementary Table 5

H2-K^b peptides detected by immunopeptidomics in control and *Setdb1* KO LLC cells.

Supplementary Table 6

High-confidence CDR3 regions identified by TCR sequencing of p15E-specific CD8⁺ T cells.

Supplementary Table 7

SRA accession numbers for public RNA-seq data of normal tissues.

Source data

Source Data Fig. 1

Source Data Fig. 4

Source Data Extended Data Fig. 1

Source Data Extended Data Fig. 2

Source Data Extended Data Fig. 10

Rights and permissions

Reprints and Permissions

About this article



Check for
updates

Cite this article

Griffin, G.K., Wu, J., Iracheta-Vellve, A. *et al.* Epigenetic silencing by SETDB1 suppresses tumour intrinsic immunogenicity. *Nature* **595**, 309–314 (2021). <https://doi.org/10.1038/s41586-021-03520-4>

Download citation

- Received: 14 August 2020
- Accepted: 07 April 2021
- Published: 05 May 2021
- Issue Date: 08 July 2021
- DOI: <https://doi.org/10.1038/s41586-021-03520-4>

Comments

By submitting a comment you agree to abide by our [Terms](#) and [Community Guidelines](#). If you find something abusive or that does not comply with our terms or guidelines please flag it as inappropriate.

[Access through your institution](#)

[Change institution](#)

[Buy or subscribe](#)

Advertisement

This article was downloaded by **calibre** from <https://www.nature.com/articles/s41586-021-03520-4>

| [Section menu](#) | [Main menu](#) |

- Article
- [Published: 16 June 2021](#)

Structural basis of omega-3 fatty acid transport across the blood–brain barrier

- [Rosemary J. Cater¹](#),
- [Geok Lin Chua²](#),
- [Satchal K. Erramilli](#) [ORCID: orcid.org/0000-0001-8694-7681³](#),
- [James E. Keener⁴](#),
- [Brendon C. Choy](#) [ORCID: orcid.org/0000-0001-7070-073X¹](#),
- [Piotr Tokarz³](#),
- [Cheen Fei Chin](#) [ORCID: orcid.org/0000-0001-6753-9228²](#),
- [Debra Q. Y. Quek²](#),
- [Brian Kloss](#) [ORCID: orcid.org/0000-0003-0130-8739⁵](#),
- [Joseph G. Pepe](#) [ORCID: orcid.org/0000-0003-2993-1872¹](#),
- [Giacomo Parisi¹](#),
- [Bernice H. Wong](#) [ORCID: orcid.org/0000-0001-8981-1376²](#),
- [Oliver B. Clarke](#) [ORCID: orcid.org/0000-0003-1876-196X^{1,6}](#),
- [Michael T. Marty](#) [ORCID: orcid.org/0000-0001-8115-1772⁴](#),
- [Anthony A. Kossiakoff³](#),
- [George Khelashvili](#) [ORCID: orcid.org/0000-0001-7235-8579^{7,8}](#),
- [David L. Silver](#) [ORCID: orcid.org/0000-0002-7289-9890²](#) &
- [Filippo Mancia](#) [ORCID: orcid.org/0000-0003-3293-2200¹](#)

[Nature](#) volume 595, pages 315–319 (2021) [Cite this article](#)

- 6173 Accesses

- 247 Altmetric
- [Metrics details](#)

Subjects

- [Computational biophysics](#)
- [Cryoelectron microscopy](#)
- [Membrane proteins](#)
- [Permeation and transport](#)

Abstract

Docosahexaenoic acid is an omega-3 fatty acid that is essential for neurological development and function, and it is supplied to the brain and eyes predominantly from dietary sources^{1,2,3,4,5,6}. This nutrient is transported across the blood–brain and blood–retina barriers in the form of lysophosphatidylcholine by major facilitator superfamily domain containing 2A (MFSD2A) in a Na⁺-dependent manner^{7,8}. Here we present the structure of MFSD2A determined using single-particle cryo-electron microscopy, which reveals twelve transmembrane helices that are separated into two pseudosymmetric domains. The transporter is in an inward-facing conformation and features a large amphipathic cavity that contains the Na⁺-binding site and a bound lysolipid substrate, which we confirmed using native mass spectrometry. Together with our functional analyses and molecular dynamics simulations, this structure reveals details of how MFSD2A interacts with substrates and how Na⁺-dependent conformational changes allow for the release of these substrates into the membrane through a lateral gate. Our work provides insights into the molecular mechanism by which this atypical major facility superfamily transporter mediates the uptake of lysolipids into the brain, and has the potential to aid in the delivery of neurotherapeutic agents.

Access options

Subscribe to Journal

Get full journal access for 1 year

\$199.00

only \$3.90 per issue

[Subscribe](#)

All prices are NET prices.

VAT will be added later in the checkout.

Tax calculation will be finalised during checkout.

Rent or Buy article

Get time limited or full article access on ReadCube.

from \$8.99

[Rent or Buy](#)

All prices are NET prices.

Additional access options:

- [Log in](#)
- [Access through your institution](#)
- [Learn about institutional subscriptions](#)

Fig. 1: Structure of MFSD2A in an inward-facing conformation.

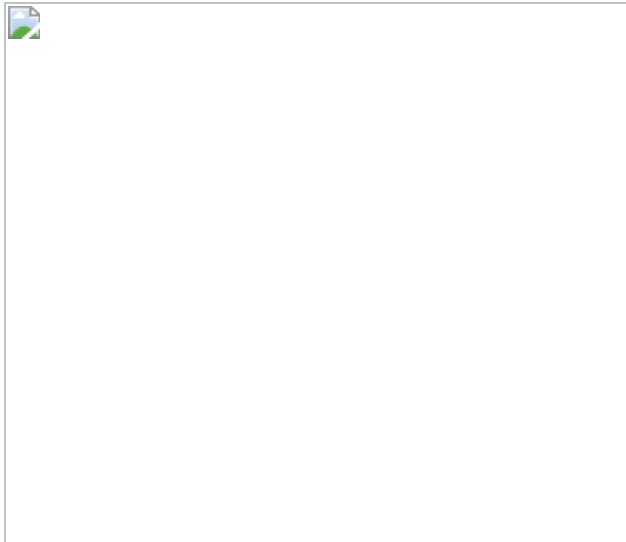


Fig. 2: The intracellular cavity of MFSD2A features the Na^+ - and lysolipid-binding sites.

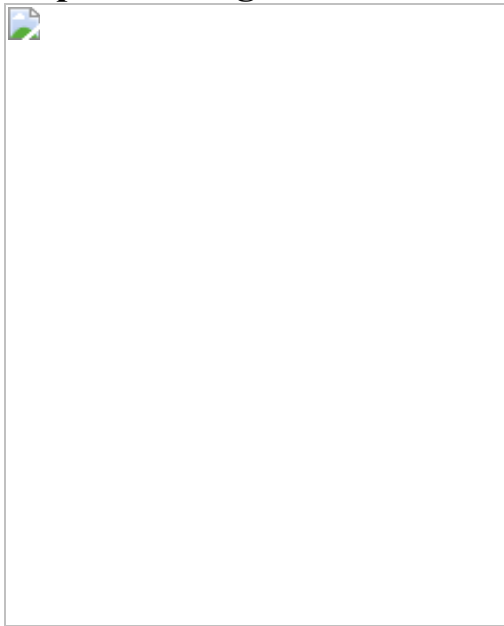


Fig. 3: Molecular dynamics simulations of MFSD2A reveal coupling between Na^+ binding and lysolipid movement through a dynamic intracellular gate.

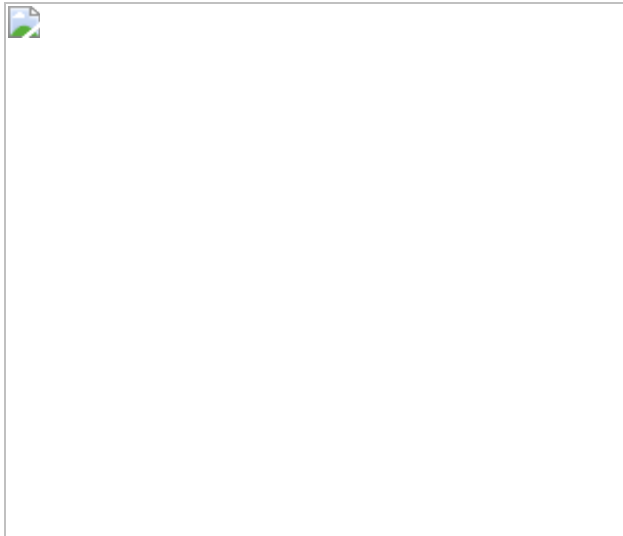
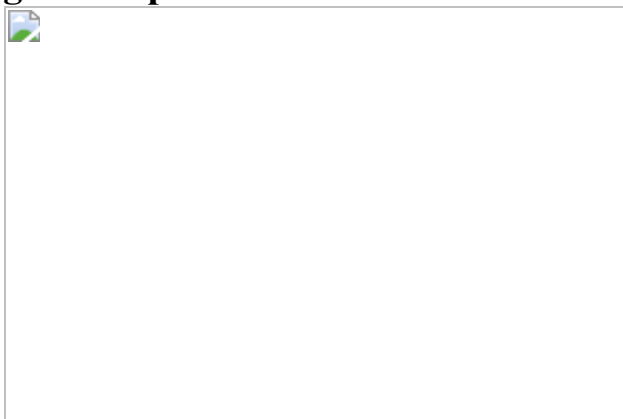


Fig. 4: Proposed mechanism of MFSD2A-mediated transport.



Data availability

All raw movie frames have been deposited into EMPIAR, with accession code EMPIAR-10698. The density map has been deposited into Electron Microscopy Data Bank, with accession code [EMD-23883](#). The model has been deposited in the PDB, with accession code [7MJS](#). All raw flow cytometry data and gels are available in the Article or its [Supplementary Information](#). Any additional data are available from the corresponding authors upon reasonable request.

References

1. 1.

Breckenridge, W. C., Gombos, G. & Morgan, I. G. The lipid composition of adult rat brain synaptosomal plasma membranes. *Biochim. Biophys. Acta* **266**, 695–707 (1972).

[CAS](#) [PubMed](#) [Google Scholar](#)

2. 2.

Connor, W. E. Importance of n-3 fatty acids in health and disease. *Am. J. Clin. Nutr.* **71**, 171S–175S (2000).

[CAS](#) [PubMed](#) [Google Scholar](#)

3. 3.

Horrocks, L. A. & Yeo, Y. K. Health benefits of docosahexaenoic acid (DHA). *Pharmacol. Res.* **40**, 211–225 (1999).

[CAS](#) [PubMed](#) [Google Scholar](#)

4. 4.

Innis, S. M. Dietary (n-3) fatty acids and brain development. *J. Nutr.* **137**, 855–859 (2007).

[CAS](#) [PubMed](#) [Google Scholar](#)

5. 5.

Kidd, P. M. Omega-3 DHA and EPA for cognition, behavior, and mood: clinical findings and structural-functional synergies with cell membrane phospholipids. *Altern. Med. Rev.* **12**, 207–227 (2007).

[PubMed](#) [Google Scholar](#)

6. 6.

Salem, N., Jr, Litman, B., Kim, H.-Y. & Gawrisch, K. Mechanisms of action of docosahexaenoic acid in the nervous system. *Lipids* **36**, 945–

959 (2001).

[CAS](#) [PubMed](#) [Google Scholar](#)

7. 7.

Nguyen, L. N. et al. Mfsd2a is a transporter for the essential omega-3 fatty acid docosahexaenoic acid. *Nature* **509**, 503–506 (2014).

[ADS](#) [CAS](#) [PubMed](#) [Google Scholar](#)

8. 8.

Wong, B. H. et al. Mfsd2a is a transporter for the essential ω-3 fatty acid docosahexaenoic acid (DHA) in eye and is important for photoreceptor cell development. *J. Biol. Chem.* **291**, 10501–10514 (2016).

[CAS](#) [PubMed](#) [PubMed Central](#) [Google Scholar](#)

9. 9.

Lobanova, E. S. et al. Disrupted blood–retina lysophosphatidylcholine transport impairs photoreceptor health but not visual signal transduction. *J. Neurosci.* **39**, 9689–9701 (2019).

[PubMed](#) [PubMed Central](#) [Google Scholar](#)

10. 10.

Andreone, B. J. et al. Blood-brain barrier permeability is regulated by lipid transport-dependent suppression of caveolae-mediated transcytosis. *Neuron* **94**, 581–594 (2017).

[CAS](#) [PubMed](#) [PubMed Central](#) [Google Scholar](#)

11. 11.

Chan, J. P. et al. The lysolipid transporter Mfsd2a regulates lipogenesis in the developing brain. *PLoS Biol.* **16**, e2006443 (2018).

[PubMed](#) [PubMed Central](#) [Google Scholar](#)

12. 12.

Alakbarzade, V. et al. A partially inactivating mutation in the sodium-dependent lysophosphatidylcholine transporter MFSD2A causes a non-lethal microcephaly syndrome. *Nat. Genet.* **47**, 814–817 (2015).

[CAS](#) [PubMed](#) [Google Scholar](#)

13. 13.

Razmara, E. et al. Novel neuroclinical findings of autosomal recessive primary microcephaly 15 in a consanguineous Iranian family. *Eur. J. Med. Genet.* **63**, 104096 (2020).

[PubMed](#) [Google Scholar](#)

14. 14.

Scala, M. et al. Biallelic *MFSD2A* variants associated with congenital microcephaly, developmental delay, and recognizable neuroimaging features. *Eur. J. Hum. Genet.* **28**, 1509–1519 (2020).

[CAS](#) [PubMed](#) [Google Scholar](#)

15. 15.

Harel, T. et al. Homozygous mutation in *MFSD2A*, encoding a lysolipid transporter for docosahexanoic acid, is associated with microcephaly and hypomyelination. *Neurogenetics* **19**, 227–235 (2018).

[PubMed](#) [Google Scholar](#)

16. 16.

Guemez-Gamboa, A. et al. Inactivating mutations in *MFSD2A*, required for omega-3 fatty acid transport in brain, cause a lethal microcephaly syndrome. *Nat. Genet.* **47**, 809–813 (2015).

[CAS](#) [PubMed](#) [PubMed Central](#) [Google Scholar](#)

17. 17.

Quistgaard, E. M., Löw, C., Guettou, F. & Nordlund, P. Understanding transport by the major facilitator superfamily (MFS): structures pave the way. *Nat. Rev. Mol. Cell Biol.* **17**, 123–132 (2016).

[CAS](#) [PubMed](#) [Google Scholar](#)

18. 18.

Yan, N. Structural biology of the major facilitator superfamily transporters. *Annu. Rev. Biophys.* **44**, 257–283 (2015).

[CAS](#) [PubMed](#) [Google Scholar](#)

19. 19.

Kawahara, A. et al. The sphingolipid transporter Spns2 functions in migration of zebrafish myocardial precursors. *Science* **323**, 524–527 (2009).

[ADS](#) [CAS](#) [PubMed](#) [Google Scholar](#)

20. 20.

Vu, T. M. et al. Mfsd2b is essential for the sphingosine-1-phosphate export in erythrocytes and platelets. *Nature* **550**, 524–528 (2017).

[ADS](#) [CAS](#) [PubMed](#) [Google Scholar](#)

21. 21.

Kobayashi, N. et al. MFSD2B is a sphingosine 1-phosphate transporter in erythroid cells. *Sci. Rep.* **8**, 4969 (2018).

[ADS](#) [PubMed](#) [PubMed Central](#) [Google Scholar](#)

22. 22.

Lin, Y., Deepak, R. N. V. K., Zheng, J. Z., Fan, H. & Zheng, L. A dual substrate-accessing mechanism of a major facilitator superfamily protein facilitates lysophospholipid flipping across the cell membrane. *J. Biol. Chem.* **293**, 19919–19931 (2018).

[CAS](#) [PubMed](#) [PubMed Central](#) [Google Scholar](#)

23. 23.

Quek, D. Q., Nguyen, L. N., Fan, H. & Silver, D. L. Structural insights into the transport mechanism of the human sodium-dependent lysophosphatidylcholine transporter Mfsd2a. *J. Biol. Chem.* **291**, 9383–9394 (2016).

[CAS](#) [PubMed](#) [PubMed Central](#) [Google Scholar](#)

24. 24.

Perez, C. et al. Structure and mechanism of an active lipid-linked oligosaccharide flippase. *Nature* **524**, 433–438 (2015).

[ADS](#) [CAS](#) [PubMed](#) [Google Scholar](#)

25. 25.

Renaud, J. P. et al. Cryo-EM in drug discovery: achievements, limitations and prospects. *Nat. Rev. Drug Discov.* **17**, 471–492 (2018).

[CAS](#) [PubMed](#) [Google Scholar](#)

26. 26.

Nygaard, R., Kim, J. & Mancia, F. Cryo-electron microscopy analysis of small membrane proteins. *Curr. Opin. Struct. Biol.* **64**, 26–33 (2020).

[CAS](#) [PubMed](#) [Google Scholar](#)

27. 27.

Choy, B. C., Cater, R. J., Mancia, F. & Pryor Jr., E. E. A 10-year meta-analysis of membrane protein structural biology: detergents, membrane mimetics, and structure determination techniques. *Biochim. Biophys. Acta* **1863**, 183533 (2021).

[CAS](#) [Google Scholar](#)

28. 28.

Dominik, P. K. et al. Conformational chaperones for structural studies of membrane proteins using antibody phage display with nanodiscs. *Structure* **24**, 300–309 (2016).

[CAS](#) [PubMed](#) [Google Scholar](#)

29. 29.

Dominik, P. K. & Kossiakoff, A. A. Phage display selections for affinity reagents to membrane proteins in nanodiscs. *Methods Enzymol.* **557**, 219–245 (2015).

[CAS](#) [PubMed](#) [Google Scholar](#)

30. 30.

Fellouse, F. A., Wiesmann, C. & Sidhu, S. S. Synthetic antibodies from a four-amino-acid code: a dominant role for tyrosine in antigen recognition. *Proc. Natl Acad. Sci. USA* **101**, 12467–12472 (2004).

[ADS](#) [CAS](#) [PubMed](#) [PubMed Central](#) [Google Scholar](#)

31. 31.

Ethayathulla, A. S. et al. Structure-based mechanism for Na^+ /melibiose symport by MelB. *Nat. Commun.* **5**, 3009 (2014).

[ADS](#) [PubMed](#) [Google Scholar](#)

32. 32.

Yardeni, E. H., Mishra, S., Stein, R. A., Bibi, E. & Mchaourab, H. S. The multidrug transporter MdfA deviates from the canonical model of alternating access of MFS transporters. *J. Mol. Biol.* **432**, 5665–5680 (2020).

[CAS](#) [PubMed](#) [Google Scholar](#)

33. 33.

Assur, Z., Hendrickson, W. A. & Mancia, F. Tools for coproducing multiple proteins in mammalian cells. *Methods Mol. Biol.* **801**, 173–187 (2012).

[CAS](#) [PubMed](#) [PubMed Central](#) [Google Scholar](#)

34. 34.

Kawate, T. & Gouaux, E. Fluorescence-detection size-exclusion chromatography for precrystallization screening of integral membrane proteins. *Structure* **14**, 673–681 (2006).

[CAS](#) [PubMed](#) [Google Scholar](#)

35. 35.

Gibson, D. G. et al. Enzymatic assembly of DNA molecules up to several hundred kilobases. *Nat. Methods* **6**, 343–345 (2009).

[CAS](#) [PubMed](#) [Google Scholar](#)

36. 36.

Miller, K. R. et al. T cell receptor-like recognition of tumor in vivo by synthetic antibody fragment. *PloS ONE* **7**, e43746 (2012).

[ADS](#) [CAS](#) [PubMed](#) [PubMed Central](#) [Google Scholar](#)

37. 37.

Rizk, S. S. et al. Allosteric control of ligand-binding affinity using engineered conformation-specific effector proteins. *Nat. Struct. Mol. Biol.* **18**, 437–442 (2011).

[CAS](#) [PubMed](#) [PubMed Central](#) [Google Scholar](#)

38. 38.

Paduch, M. & Kossiakoff, A. A. Generating conformation and complex-specific synthetic antibodies. *Methods Mol. Biol.* **1575**, 93–119 (2017).

[CAS](#) [PubMed](#) [Google Scholar](#)

39. 39.

Kim, J. et al. Structure and drug resistance of the *Plasmodium falciparum* transporter PfCRT. *Nature* **576**, 315–320 (2019).

[CAS](#) [PubMed](#) [PubMed Central](#) [Google Scholar](#)

40. 40.

Suloway, C. et al. Automated molecular microscopy: the new Legion system. *J. Struct. Biol.* **151**, 41–60 (2005).

[CAS](#) [PubMed](#) [Google Scholar](#)

41. 41.

Cheng, A. et al. High resolution single particle cryo-electron microscopy using beam-image shift. *J. Struct. Biol.* **204**, 270–275 (2018).

[CAS](#) [PubMed](#) [PubMed Central](#) [Google Scholar](#)

42. 42.

Rice, W. J. et al. Routine determination of ice thickness for cryo-EM grids. *J. Struct. Biol.* **204**, 38–44 (2018).

[CAS](#) [PubMed](#) [PubMed Central](#) [Google Scholar](#)

43. 43.

Punjani, A., Rubinstein, J. L., Fleet, D. J. & Brubaker, M. A. cryoSPARC: algorithms for rapid unsupervised cryo-EM structure determination. *Nat. Methods* **14**, 290–296 (2017).

[CAS](#) [PubMed](#) [Google Scholar](#)

44. 44.

Bepler, T. et al. Positive-unlabeled convolutional neural networks for particle picking in cryo-electron micrographs. *Nat. Methods* **16**, 1153–1160 (2019).

[CAS](#) [PubMed](#) [PubMed Central](#) [Google Scholar](#)

45. 45.

Guan, L., Mirza, O., Verner, G., Iwata, S. & Kaback, H. R. Structural determination of wild-type lactose permease. *Proc. Natl Acad. Sci. USA* **104**, 15294–15298 (2007).

[ADS](#) [CAS](#) [PubMed](#) [PubMed Central](#) [Google Scholar](#)

46. 46.

Stein, N. CHAINSAW: a program for mutating pdb files used as templates in molecular replacement. *J. Appl. Crystallogr.* **41**, 641–643 (2008).

[CAS](#) [Google Scholar](#)

47. 47.

Potterton, L. et al. CCP4i2: the new graphical user interface to the CCP4 program suite. *Acta Crystallogr. D* **74**, 68–84 (2018).

[CAS](#) [Google Scholar](#)

48. 48.

Pettersen, E. F. et al. UCSF Chimera—a visualization system for exploratory research and analysis. *J. Comput. Chem.* **25**, 1605–1612 (2004).

[CAS](#) [Google Scholar](#)

49. 49.

Emsley, P. & Cowtan, K. Coot: model-building tools for molecular graphics. *Acta Crystallogr. D* **60**, 2126–2132 (2004).

[Google Scholar](#)

50. 50.

Emsley, P., Lohkamp, B., Scott, W. G. & Cowtan, K. Features and development of Coot. *Acta Crystallogr. D* **66**, 486–501 (2010).

[CAS](#) [PubMed](#) [PubMed Central](#) [Google Scholar](#)

51. 51.

Casañal, A., Lohkamp, B. & Emsley, P. Current developments in Coot for macromolecular model building of electron cryo-microscopy and

crystallographic data. *Protein Sci.* **29**, 1055–1064 (2020).

[Google Scholar](#)

52. 52.

Slabinski, L. et al. XtalPred: a web server for prediction of protein crystallizability. *Bioinformatics* **23**, 3403–3405 (2007).

[CAS](#) [PubMed](#) [Google Scholar](#)

53. 53.

Ahuja, S. et al. Structural analysis of bacterial ABC transporter inhibition by an antibody fragment. *Structure* **23**, 713–723 (2015).

[CAS](#) [PubMed](#) [Google Scholar](#)

54. 54.

Adams, P. D. et al. PHENIX: a comprehensive Python-based system for macromolecular structure solution. *Acta Crystallogr. D* **66**, 213–221 (2010).

[CAS](#) [PubMed](#) [PubMed Central](#) [Google Scholar](#)

55. 55.

Kidmose, R. T. et al. Namdinator – automatic molecular dynamics flexible fitting of structural models into cryo-EM and crystallography experimental maps. *IUCrJ* **6**, 526–531 (2019).

[CAS](#) [PubMed](#) [PubMed Central](#) [Google Scholar](#)

56. 56.

Voss, N. R. & Gerstein, M. 3V: cavity, channel and cleft volume calculator and extractor. *Nucleic Acids Res.* **38**, W555–W562 (2010).

[CAS](#) [PubMed](#) [PubMed Central](#) [Google Scholar](#)

57. 57.

Edgar, R. C. MUSCLE: multiple sequence alignment with high accuracy and high throughput. *Nucleic Acids Res.* **32**, 1792–1797 (2004).

[CAS](#) [PubMed](#) [PubMed Central](#) [Google Scholar](#)

58. 58.

Townsend, J. A., Keener, J. E., Miller, Z. M., Prell, J. S. & Marty, M. T. Imidazole derivatives improve charge reduction and stabilization for native mass spectrometry. *Anal. Chem.* **91**, 14765–14772 (2019).

[CAS](#) [PubMed](#) [PubMed Central](#) [Google Scholar](#)

59. 59.

Marty, M. T. et al. Bayesian deconvolution of mass and ion mobility spectra: from binary interactions to polydisperse ensembles. *Anal. Chem.* **87**, 4370–4376 (2015).

[CAS](#) [PubMed](#) [PubMed Central](#) [Google Scholar](#)

60. 60.

Wersto, R. P. et al. Doublet discrimination in DNA cell-cycle analysis. *Cytometry* **46**, 296–306 (2001).

[CAS](#) [PubMed](#) [Google Scholar](#)

61. 61.

Das, R. & Baker, D. Macromolecular modeling with Rosetta. *Annu. Rev. Biochem.* **77**, 363–382 (2008).

[CAS](#) [PubMed](#) [Google Scholar](#)

62. 62.

Webb, B. & Sali, A. Comparative protein structure modeling using MODELLER. *Curr. Protoc. Protein Sci.* **86**, 2.9.1–2.9.37 (2016).

[Google Scholar](#)

63. 63.

Jo, S., Lim, J. B., Klauda, J. B. & Im, W. CHARMM-GUI membrane builder for mixed bilayers and its application to yeast membranes. *Biophys. J.* **97**, 50–58 (2009).

[ADS](#) [CAS](#) [PubMed](#) [PubMed Central](#) [Google Scholar](#)

64. 64.

Phillips, J. C. et al. Scalable molecular dynamics on CPU and GPU architectures with NAMD. *J. Chem. Phys.* **153**, 044130 (2020).

[CAS](#) [PubMed](#) [Google Scholar](#)

65. 65.

Eastman, P. et al. OpenMM 7: Rapid development of high performance algorithms for molecular dynamics. *PLoS Comput. Biol.* **13**, e1005659 (2017).

[PubMed](#) [PubMed Central](#) [Google Scholar](#)

66. 66.

Huang, J. et al. CHARMM36m: an improved force field for folded and intrinsically disordered proteins. *Nat. Methods* **14**, 71–73 (2017).

[CAS](#) [PubMed](#) [Google Scholar](#)

67. 67.

Venable, R. M., Luo, Y., Gawrisch, K., Roux, B. & Pastor, R. W. Simulations of anionic lipid membranes: development of interaction-specific ion parameters and validation using NMR data. *J. Phys. Chem. B* **117**, 10183–10192 (2013).

[CAS](#) [PubMed](#) [Google Scholar](#)

68. 68.

Pérez-Hernández, G., Paul, F., Giorgino, T., De Fabritiis, G. & Noé, F. Identification of slow molecular order parameters for Markov model construction. *J. Chem. Phys.* **139**, 015102 (2013).

[ADS](#) [PubMed](#) [Google Scholar](#)

69. 69.

Morra, G. et al. Mechanisms of lipid scrambling by the G protein-coupled receptor opsin. *Structure* **26**, 356–367.e3 (2018).

[CAS](#) [PubMed](#) [Google Scholar](#)

70. 70.

Razavi, A. M., Khelashvili, G. & Weinstein, H. How structural elements evolving from bacterial to human SLC6 transporters enabled new functional properties. *BMC Biol.* **16**, 31 (2018).

[PubMed](#) [PubMed Central](#) [Google Scholar](#)

71. 71.

Razavi, A. M., Khelashvili, G. & Weinstein, H. A Markov state-based quantitative kinetic model of sodium release from the dopamine transporter. *Sci. Rep.* **7**, 40076 (2017).

[ADS](#) [CAS](#) [PubMed](#) [PubMed Central](#) [Google Scholar](#)

72. 72.

Lee, B. C. et al. Gating mechanism of the extracellular entry to the lipid pathway in a TMEM16 scramblase. *Nat. Commun.* **9**, 3251 (2018).

[ADS](#) [PubMed](#) [PubMed Central](#) [Google Scholar](#)

73. 73.

Beauchamp, K. A. et al. MSMBuilder2: modeling conformational dynamics at the picosecond to millisecond scale. *J. Chem. Theory Comput.* **7**, 3412–3419 (2011).

[CAS](#) [PubMed](#) [PubMed Central](#) [Google Scholar](#)

74. 74.

Harrigan, M. P. et al. MSMBuilder: statistical models for biomolecular dynamics. *Biophys. J.* **112**, 10–15 (2017).

[ADS](#) [CAS](#) [PubMed](#) [PubMed Central](#) [Google Scholar](#)

75. 75.

Deuflhard, P. & Weber, M. Robust Perron cluster analysis in conformation dynamics. *Linear Algebra Appl.* **398**, 161–184 (2005).

[MathSciNet](#) [MATH](#) [Google Scholar](#)

76. 76.

Dijkstra, E. W. A note on two problems in connexion with graphs. *Numer. Math.* **1**, 269–271 (1959).

[MathSciNet](#) [MATH](#) [Google Scholar](#)

77. 77.

Berezhkovskii, A., Hummer, G. & Szabo, A. Reactive flux and folding pathways in network models of coarse-grained protein dynamics. *J.*

Chem. Phys. **130**, 05B614 (2009).

[Google Scholar](#)

78. 78.

Wu, T. T. & Kabat, E. A. An analysis of the sequences of the variable regions of Bence Jones proteins and myeloma light chains and their implications for antibody complementarity. *J. Exp. Med.* **132**, 211–250 (1970).

[CAS](#) [PubMed](#) [PubMed Central](#) [Google Scholar](#)

79. 79.

Waterhouse, A. M., Procter, J. B., Martin, D. M., Clamp, M. & Barton, G. J. Jalview Version 2—a multiple sequence alignment editor and analysis workbench. *Bioinformatics* **25**, 1189–1191 (2009).

[CAS](#) [PubMed](#) [PubMed Central](#) [Google Scholar](#)

[Download references](#)

Acknowledgements

We thank members of the laboratory of F.M., Columbia Cryo-EM facility and Iowa State University Protein Facility for their assistance; and E. Kots for generating the molecular dynamics trajectory video. This work was supported by NIH grants (R35 GM132120 and R21 MH125649 to F.M., R35 GM128624 to M.T.M. and R01 GM117372 to A.A.K.) and grants from the National Research Foundation and Ministry of Health, Singapore (NRF-NRFI2017-05 and MOH-000217 to D.L.S.). R.J.C. was supported by the Simons Society of Fellows (award number 578646). G.K. is supported by the HRH Prince Alwaleed Bin Talal Bin Abdulaziz Alsaud Institute of Computational Biomedicine at Weill Cornell Medical College through the 1923 Fund. C.F.C. and B.H.W. are supported by the Khoo Postdoctoral Research Fellowship. Some of the work was performed at the Center for Membrane Protein Production and Analysis (COMPPÅ; NIH P41

GM116799 to W. A. Hendrickson), and at the National Resource for Automated Molecular Microscopy at the Simons Electron Microscopy Center (P41 GM103310), both located at the New York Structural Biology Center. Molecular dynamics simulations were performed using the Oak Ridge Leadership Computing Facility (summit allocation BIP109) at the Oak Ridge National Laboratory (supported by the Office of Science of the US Department of Energy under contract number DE-AC05-00OR22725), and computational resources of the David A. Cofrin Center for Biomedical Information at Weill Cornell Medical College.

Author information

Affiliations

1. Department of Physiology and Cellular Biophysics, Columbia University, New York, NY, USA

Rosemary J. Cater, Brendon C. Choy, Joseph G. Pepe, Giacomo Parisi, Oliver B. Clarke & Filippo Mancia

2. Signature Research Program in Cardiovascular and Metabolic Disorders, Duke-NUS Medical School, Singapore, Singapore

Geok Lin Chua, Cheen Fei Chin, Debra Q. Y. Quek, Bernice H. Wong & David L. Silver

3. Department of Biochemistry and Molecular Biology, University of Chicago, Chicago, IL, USA

Satchal K. Erramilli, Piotr Tokarz & Anthony A. Kossiakoff

4. Department of Chemistry and Biochemistry, University of Arizona, Tucson, AZ, USA

James E. Keener & Michael T. Marty

5. Center on Membrane Protein Production and Analysis, New York
Structural Biology Center, New York, NY, USA

Brian Kloss

6. Department of Anesthesiology, Columbia University Irving Medical
Center, New York, NY, USA

Oliver B. Clarke

7. Department of Physiology and Biophysics, Weill Cornell Medical
College, Cornell University, New York, NY, USA

George Khelashvili

8. Institute for Computational Biomedicine, Weill Cornell Medical
College, Cornell University, New York, NY, USA

George Khelashvili

Authors

1. Rosemary J. Cater

[View author publications](#)

You can also search for this author in [PubMed](#) [Google Scholar](#)

2. Geok Lin Chua

[View author publications](#)

You can also search for this author in [PubMed](#) [Google Scholar](#)

3. Satchal K. Erramilli

[View author publications](#)

You can also search for this author in [PubMed](#) [Google Scholar](#)

4. James E. Keener

[View author publications](#)

You can also search for this author in [PubMed](#) [Google Scholar](#)

5. Brendon C. Choy

[View author publications](#)

You can also search for this author in [PubMed](#) [Google Scholar](#)

6. Piotr Tokarz

[View author publications](#)

You can also search for this author in [PubMed](#) [Google Scholar](#)

7. Cheen Fei Chin

[View author publications](#)

You can also search for this author in [PubMed](#) [Google Scholar](#)

8. Debra Q. Y. Quek

[View author publications](#)

You can also search for this author in [PubMed](#) [Google Scholar](#)

9. Brian Kloss

[View author publications](#)

You can also search for this author in [PubMed](#) [Google Scholar](#)

10. Joseph G. Pepe

[View author publications](#)

You can also search for this author in [PubMed](#) [Google Scholar](#)

11. Giacomo Parisi

[View author publications](#)

You can also search for this author in [PubMed](#) [Google Scholar](#)

12. Bernice H. Wong

[View author publications](#)

You can also search for this author in [PubMed](#) [Google Scholar](#)

13. Oliver B. Clarke

[View author publications](#)

You can also search for this author in [PubMed](#) [Google Scholar](#)

14. Michael T. Marty

[View author publications](#)

You can also search for this author in [PubMed](#) [Google Scholar](#)

15. Anthony A. Kossiakoff

[View author publications](#)

You can also search for this author in [PubMed](#) [Google Scholar](#)

16. George Khelashvili

[View author publications](#)

You can also search for this author in [PubMed](#) [Google Scholar](#)

17. David L. Silver

[View author publications](#)

You can also search for this author in [PubMed](#) [Google Scholar](#)

18. Filippo Mancia

[View author publications](#)

You can also search for this author in [PubMed](#) [Google Scholar](#)

Contributions

R.J.C. performed cloning with assistance from B.K., designed and performed expression screening experiments, produced baculovirus, and optimized protein expression and purification with assistance from B.C.C. Fabs were identified and purified by S.K.E., P.T. and A.A.K. Protein preparation for structural analysis was performed by R.J.C. who

also screened and optimized sample vitrification, and generated cryo-EM data with assistance from G.P. Cryo-EM data analysis and model building was performed by R.J.C. with guidance from O.B.C. Uptake studies and mutagenesis experiments were designed and performed by G.L.C., C.F.C., D.Q.Y.Q. and D.L.S. Molecular dynamics simulations were designed and performed by G.K., with input from R.J.C. and F.M. TLC analysis was performed by G.L.C. and B.H.W. Samples for native mass spectrometry were prepared by R.J.C. and J.G.P. Native mass spectrometry was performed by J.E.K. and M.T.M. The manuscript was written by R.J.C., F.M. and G.K. with input from G.L.C. and D.L.S. Figures were prepared by R.J.C., G.K., B.C.C. and G.L.C. Guidance and input at all stages of the project were provided by F.M. and D.L.S.

Corresponding authors

Correspondence to [George Khelashvili](#) or [David L. Silver](#) or [Filippo Mancia](#).

Ethics declarations

Competing interests

D.L.S. is a scientific founder and advisor of Travecta Therapeutics that has developed a drug delivery platform that uses MFSD2A transport. All other authors declare no competing interests.

Additional information

Peer review information *Nature* thanks Osamu Nureki, Diwakar Shukla and the other, anonymous, reviewer(s) for their contribution to the peer review of this work. Peer reviewer reports are available.

Publisher's note Springer Nature remains neutral with regard to jurisdictional claims in published maps and institutional affiliations.

Extended data figures and tables

Extended Data Fig. 1 Biochemical characterization, functional validation, nanodisc reconstitution and Fab complex formation of GgMFSD2A.

a, Chemical structure of LPC-DHA. **b**, Fluorescent size-exclusion chromatography elution profiles of seven MFSD2A orthologues fused to green fluorescent protein. Orthologues screened are from *D. rerio* (MFSD2A_DR) (NCBI BC085388), *X. tropicalis* (MFSD2A_XT) (NCBI BC123088), *B. taurus* (MFSD2A_BT) (NCBI BC149727), GgMFSD2A (MFSD2A_GG) (NCBI XM_417826), *C. lupus familiaris* (MFSD2A_CLF) (NCBI XP_532546), HsMFSD2A (MFSD2A_HS) (NCBI NM_032793) and *M. musculus* (MFSD2A_MM) (NCBI NM_029662). **c**, MFSD2A-mediated uptake of C¹⁴-LPC-18:1 into HEK293 cells transfected with either HsMFSD2A or GgMFSD2A wild-type and Na⁺-binding-deficient mutant constructs (D97A and D92A, respectively). Uptake is expressed as mean ± s.e.m.; $n = 3$ independent experiments. **d**, Complementarity-determining region (CDR) sequences of unique synthetic antigen binders (Fabs) panned for binding to iGgMFSD2A reconstituted in MSP1E3D1 nanodiscs. Enriched Tyr-Ser-Gly-Trp residues, which have an important role in antigen recognition, are highlighted in purple, blue, red and orange, respectively; other conserved residues are highlighted in green. Residues are numbered according to the Kabat system⁷⁸. **e**, EC₅₀ evaluation of purified Fabs 2AG1 (blue) (1.71 ± 0.03 nM), 2AG2 (red) (2.06 ± 0.08 nM), and 2AG3 (orange) (8.94 ± 0.08 nM) binding to GgMFSD2A incorporated into MSP1E3D1 nanodiscs. Data points represent mean ± s.d.; $n = 3$ independent experiments. **f**, Normalized high-performance liquid chromatography elution profiles of GgMFSD2A purified in DDM supplemented with CHS (black) and reconstituted in MSP1E3D1 nanodiscs without (blue) and with (green) 2AG3 Fab bound. **g**, Representative SDS-PAGE gel of purified GgMFSD2A reconstituted in MSP1E3D1 nanodiscs with 2AG3 Fab bound. For gel source data, see Supplementary Fig. 1.

Extended Data Fig. 2 Multiple sequence alignment of MFSD2A and MFSD2B.

Seven MFSD2A and six MFSD2B variants were aligned using MUSCLE⁵⁷ and visualized and coloured using Jalview with the ClustalX colour scheme⁷⁹. The sequences aligned for MFSD2A are from *D. rerio* (NCBI BC085388) (2A_DR), *X. tropicalis* (NCBI BC123088) (2A_XT), *B. taurus* (NCBI BC149727) (2A_BT), *G. gallus* (NCBI XM_417826) (2A_GG), *C. lupus familiaris* (NCBI XP_532546) (2A_CLF), *H. sapiens* (NCBI-NM_032793) (2A_HS) and *M. musculus* (NCBI-NM_029662) (2A_MM). The sequences aligned for MFSD2B are from *X. tropicalis* (UniProtKB A4IH46) (2B_XT), *B. taurus* (NCBI XM_010810291) (2B_BT), *G. gallus* (NCBI-XM_004935790) (2B_GG), *C. lupus familiaris* (NCBI XM_005630178) (2B_CLF), *H. sapiens* (NCBI NM_001346880) (2B_HS) and *M. musculus* (NCBI NM_001033488) (2B_MM). Secondary structural elements are shown as cylinders, labelled and coloured as in Fig. 1.

Residues discussed throughout the Article are indicated with circles of the same colour used to highlight them in figure panels showing the structure. Additionally, red diamonds denote known disease-causing human mutations^{12,14,15,16}, green hexagons denote glycosylation sites (in GgMFSD2A) and yellow triangles denote two cysteines that form a disulfide crosslink.

Extended Data Fig. 3 Cryo-EM workflow and analysis of the MFSD2A–Fab 2AG3 complex.

a, Flow chart outlining cryo-EM image acquisition and processing performed to obtain a structure of nanodisc-reconstituted GgMFSD2A in complex with the Fab 2AG3. A representative micrograph and 2D class averages are shown. Although 2D class averages of monomeric and dimeric GgMFSD2A with and without bound Fab were observed, only monomeric particles with bound Fab (green) were used for the final reconstruction; the others (red) were discarded. All processing was performed using CryoSPARC v.2.15⁴³ (Methods). **b**, Euler angle distribution plot of the final three-dimensional reconstruction of the GgMFSD2A–Fab 2AG3 complex. **c**, Fourier shell correlation (FSC) curves for the GgMFSD2A–Fab 2AG3

complex. **d**, Local resolution map of the *GgMFSD2A*–Fab 2AG3 complex, with an orthogonal view indicating the location of the clipping plane.

Extended Data Fig. 4 Fit of cryo-EM density with MFSD2A model.

Cryo-EM densities (semi-transparent surface) are superimposed on structural elements of *GgMFSD2A*, including TM1 to TM12, C207–C460 disulfide crosslink, N-linked glycans and bound LPC-18:3 in two possible conformations. TMs are rendered as a cartoon with residue side chains in stick representation and coloured as in Fig. 1; the other features are also shown in stick representation.

Extended Data Fig. 5 Characterization of an endogenous lysolipid bound to MFSD2A.

a, Native (left) and zero-charge deconvolved (right) mass spectra of *GgMFSD2A* in DDM. Peaks corresponding to glycosylated *GgMFSD2A* with no bound ligand are highlighted in orange, whereas peaks corresponding to glycosylated *GgMFSD2A* with a bound lysolipid (515 Da) are highlighted in purple. **b**, Single-cell uptake of the fluorescent substrate LPC–NBD by cells expressing wild-type and D97A (corresponding to D92 in *GgMFSD2A*) *HsMFSD2A*–mCherry fusion constructs analysed by fluorescence-activated cell sorting. LPC–NBD uptake was measured in the presence of increasing concentrations of LPC-18:3 (the number of cells analysed per condition was around 900). Left panels show output from flow cytometric analysis (Methods, Extended Data Fig. 6), and right panels show gated data normalized to mCherry expression and represented as a per cent of uptake by wild type in the absence of LPC-18:3 (denoted as WT_{max} on axis), collected in the same experiment ± s.e.m. **c**, TLC analysis of cells expressing wild-type and D97A *HsMFSD2A* showing intracellular conversion of LPC-18:3 to PC-18:3 as evidence for LPC-18:3 uptake⁷. Experiments were performed in triplicate and the quantified intensities of the PC bands are indicated for each lane. **d**, Native (left) and zero-charge deconvolved (right) mass spectra of *GgMFSD2A* in POPG-filled MSP1E3D1 nanodiscs. Apo and lysolipid-bound peaks are coloured as in **a**,

and those annotated with an asterisk correspond to an unassigned mass of 68,980 Da, which may be attributed to a glycan cleavage or truncation of the protein.

Extended Data Fig. 6 Flow cytometry analysis and concentration response for *HsMFSD2A*-mediated uptake of LPC–NBD.

a, Top panels, single-cell events were separated from doublets for wild-type and D97A *HsMFSD2A*–mCherry constructs via selection of populations through the area (*A*), width (*W*) and height (*H*) of the mCherry fluorescence intensities for forward (FSC) and sideward (SSC) scatter, performed in sequence as indicated by black arrows. Middle panels, selected single cells (indicated by ovals and rectangles at each stage in the top panels) were analysed for LPC–NBD and mCherry fluorescence, as well as viability. LPC–NBD fluorescence intensity is represented as a rainbow colour gradient from blue (low) to red (high). Viability was assessed by DAPI staining, and non-viable cells are annotated as ‘population d’ and number of non-viable cells is indicated in the top left corner of each respective plot. Gates for subsequent analyses were set as described in the Methods and are indicated by a black rectangle. The number of cells within each gate is indicated in the top left corner of each respective plot. Bottom, scatter plot of single-cell uptake of LPC–NBD by gated cells expressing wild-type (black) and D97A (red) *HsMFSD2A*–mCherry fusion constructs. LPC–NBD uptake was normalized to mCherry expression and represented as a per cent of wild type \pm s.e.m. Horizontal bar indicates the mean, and each point represents a single-cell event. The number of cells plotted is indicated in the top left corner of the respective plot in the middle panel. **b**, Top, uptake of increasing concentrations of LPC–NBD by single cells transfected with either wild-type or D97A *HsMFSD2A*–mCherry constructs. Data were analysed as in **a**, and the number of cells analysed per condition was about 1,000. Bottom, LPC–NBD concentration response curves for wild-type (black) and D97A (red) *HsMFSD2A*–mCherry fusion constructs. Hill coefficient (*n*) and concentration for half-maximal LPC–NBD uptake (EC_{50}) for wild type are indicated on the graph. **c**, Flow cytometric analysis of LPC–NBD and mCherry fluorescence for wild-type

and all analysed mutant *HsMFSD2A* constructs. LPC–NBD fluorescence intensity is represented as a rainbow colour gradient from blue (low) to red (high). Gates and indicated by a black rectangle and the number of cells within each gate is shown in the top left corner of each plot. **d**, Scatter plot of single-cell uptake of LPC–NBD by gated cells expressing wild-type and mutant *HsMFSD2A*–mCherry fusion constructs. LPC–NBD uptake was normalized to mCherry expression and represented as a per cent of wild type \pm s.e.m. Horizontal bar indicates the mean, and each point represents a single cell event. The *n* values for each construct assayed are in **c**. The colour coding matches that used in Fig. 2, Extended Data Fig. 11. In cases in which residue number or identity differ between *HsMFSD2A* and *GgMFSD2A*, the corresponding residue in *GgMFSD2A* is provided in parentheses.

Extended Data Fig. 7 tICA analysis identifies major conformational states sampled in molecular dynamics simulations and reveals their structural characteristics.

a, Two-dimensional (2D) landscape representing all molecular dynamics trajectories mapped with the tICA transformation in the space of the first two tICA eigenvectors (tIC1 and tIC2). Population distribution within the 2D space is indicated by a colour gradient with the red and blue shades representing the most and least populated regions of 2D space, respectively. Locations of 50 microstates obtained from *k*-means clustering analysis of the tICA space are shown as small black squares. **b**, Contribution of each tICA vector to the total fluctuation of the system. **c**, Contributions of the collective variables used as tICA parameters to tIC1 and tIC2. **d**, The 2D tICA space from **a**, highlighting 12 selected microstates (labelled 1 to 12) that describe structural properties of various conformational states of the system. The three shaded regions represent conformations of the protein with no ion bound (green shade), ion bound at D92 (red shade) and ion bound at E312 (blue shade). **e**, The 2D tICA space from **a**, redrawn to show the direction of change in the extent of lysolipid penetration and intracellular gate (IC-gate) opening along the landscape. **f**, Columns from left to right show probability distributions of the following collective variables in the 12 microstates selected from **d**: vertical distance (*Z*)

between lysolipid phosphorous atom (P_{lyso}) and E312 $C\alpha$, number of lysolipid atoms in the intracellular cavity, minimum distances between any ion in the system and D92, between any ion in the system and E312, between M182 and W403, between M182 and F399, between R85 and D88, between R85 and E312, and number of water oxygen atoms in the intracellular cavity. The ranges of collective variables were normalized such that the lowest and highest values for each variable correspond to 0 and 1, respectively. State numbers are provided on the lefthand side as (i)–(iv), which correspond to Fig. 3a–d, respectively.

Extended Data Fig. 8 Lipid penetration into the intracellular cavity of MFSD2A.

a, Snapshots depicting the position of phosphorus atoms (spheres) of POPC (orange), LPC-18:1 (purple), LPC-18:3 (teal) and LPC-DHA (lime) at the entrance to and inside the intracellular cavity during molecular dynamics simulations. **b**, Histograms representing the distance along the membrane-perpendicular z axis between the phosphorus atoms of the lipids in **a**, and the $C\alpha$ atom of a reference residue (E312, highlighted in **a**). **c**, Structure of LPC-18:3 highlighting the headgroup (green; O11, O12, O13, O14, P, C11, C12, N, C13, C14 and C15 in CHARMM nomenclature), backbone (blue; C31, O31, O32, C3, C2, O21 and C1), single-bonded hydrocarbon tail (pink; C32–C38), and double-bonded hydrocarbon tail (yellow; C39–C48) regions. **d**, Frequency of contacts between the LPC-18:3 headgroup, backbone, single-bonded and double-bonded tail regions, and GgMFSD2A residues. Results for top 20 contact residues are shown. Contacts were defined as distances less than 4 Å between non-hydrogen atoms of the protein and the substrate.

Extended Data Fig. 9 Sampling of the major conformational states is affected by the presence and absence of Na^+ and lysolipid substrate in the molecular dynamics simulations.

Projection (coloured dots) of each molecular dynamics trajectory from the three sets of simulations on the 2D tICA landscape (in pale colours) from Extended Data Fig. 7. **a–d**, Simulations of GgMFSD2A in a POPC bilayer

were performed in either Na^+Cl^- or Li^+Cl^- solution (**a**); Na^+Cl^- solution with a single LPC-18:1 at the interface of the intracellular gate and the inner leaflet of the membrane (**b**); Na^+Cl^- solution with a single LPC-18:3 at the interface of the intracellular gate and the inner leaflet of the membrane (**c**); and Na^+Cl^- solution with a single LPC-18:3 bound as in the cryo-EM structure (**d**). The colours of the dots indicate the timeframes in the evolution of the trajectory: blue and cyan represent the initial stages of the simulation, yellow and green correspond to the middle part of the trajectory, and red shows the last third of the trajectory. The yellow circle in **a** (trajectory 0) denotes the conformation of the system in which LPC-18:1, LPC-18:3 and LPC-DHA were introduced.

Extended Data Fig. 10 Pathways for opening of the intracellular gate and substrate entry.

- a**, The three main pathways for intracellular gate (IC-gate) opening and substrate penetration, identified from Markov state modelling and transition path theory analyses are shown on the tIC1 versus tIC2 landscape, represented as in Extended Data Fig. 7. We named the macrostates on these pathways A to H; each label is placed at the centre of the corresponding state. Arrows coloured in blue, red and green represent the three main pathways between macrostates, and their thickness indicates the relative magnitude of flux for each given pathway. Macrostates A, I, G and H correspond to states shown in Fig. 3a, 3b, 3c and 3d, respectively, and macrostate E corresponds to the cryo-EM structure. The remaining macrostates represent structural intermediates between these major states.
- b**, The percentage of total flux for the top three pathways shown in **a**. **c**, Structural representation of the key macrostates from **a**. Macrostates B, C, F and K have been omitted for simplicity, as they are structural intermediates between the major states presented (Extended Data Fig. 7). Helices in the N domain are in yellow; helices in the C domain are in green. Select residues are shown in stick representation and coloured as in Fig. 2. For visual clarity, TM1, TM3, TM4, TM6, TM9 and TM12 have been omitted, and TM5 is partially transparent.

Extended Data Fig. 11 Interdomain contacts on the extracellular side of MFSD2A.

a, Structure of *GgMFSD2A* in the plane of the membrane with inset highlighting a disulfide crosslink between C207 and C460 (salmon), a charged and polar network involving D68, Y321, R326 and Y455 (brown), and a hydrophobic plug comprising F60, F61, F329 and L333 (grey). TMs are coloured as in Fig. 1. **b**, Single-cell uptake of the fluorescent substrate LPC–NBD by cells expressing wild-type and mutant *HsMFSD2A*–mCherry fusion constructs. LPC–NBD uptake was normalized to mCherry expression and represented as a per cent of wild type collected in the same experiment \pm s.e.m. The colour coding matches that used in **a**. In cases in which residue number or identity differs between *HsMFSD2A* and *GgMFSD2A* the corresponding residue in *GgMFSD2A* is provided in parentheses. **c**, **d**, Snapshots from molecular dynamics simulations of wild-type (**c**) and F60A/F61A/F329A/L333A-mutant *GgMFSD2A* (**d**), showing water oxygens as purple spheres. Insets illustrate magnified views of the intracellular cavity. *GgMFSD2A* is represented as in Fig. 1, with plug residues labelled and coloured in grey. **e**, Number of water oxygens in the intracellular cavity derived from simulations of wild-type and F60A/F61A/F329A/L333A-mutant *GgMFSD2A*, in black and red, respectively. Water oxygens were considered in the intracellular cavity if within 5 Å of the following residues: 51, 55, 59, 63, 64, 68, 77, 81, 85, 89, 92, 181, 185, 189, 193, 197, 201, 316, 312, 309, 305, 398, 402, 428, 432, 436, 440 or 444. **f**, Single-cell uptake of the fluorescent substrate LPC–NBD by cells expressing wild-type and mutant *HsMFSD2A*–mCherry fusion constructs. Data were normalized and represented as in **b**. Extended Data Figure 6 provides the raw data and *n* values for each construct assayed in **b** and **f**.

Extended Data Table 1 Cryo-EM data

[Full size table](#)

Supplementary information

[Supplementary Information](#)

This file contains Supplementary Notes and Supplementary Fig. 1.

Reporting Summary

Supplementary Table 1

Raw Single Cell Flow Cytometry Data.

Peer Review File

Video 1

Molecular dynamics trajectory showing LPC-18:1 exploring the intracellular cavity of MFSD2A. The 18:1 aliphatic tail is coloured in white, whereas the phosphate and the amine groups are coloured in red and blue, respectively. TM5 and TM8 are shown in green, while the gate residues, M182 (on TM5) and W402/F399 (on TM10), are depicted in licorice. E312 and R85 within the central charged region are drawn in surface representation and are coloured in purple. When the LPC-18:1 comes within 4Å of E312 and R85, the colour of the atoms of these residues that become engaged with the lysolipid change from purple to orange. For this video, all 24 MD trajectories with LPC-18:1 were combined into a single trajectory and the resulting trajectory was smoothed using the “smooth” Pymol (Schrödinger) function applied to a window size of 2 (corresponding to a stride of 4ns).

Rights and permissions

Reprints and Permissions

About this article



Check for
updates

Cite this article

Cater, R.J., Chua, G.L., Erramilli, S.K. *et al.* Structural basis of omega-3 fatty acid transport across the blood–brain barrier. *Nature* **595**, 315–319 (2021). <https://doi.org/10.1038/s41586-021-03650-9>

[Download citation](#)

- Received: 07 February 2021
- Accepted: 17 May 2021
- Published: 16 June 2021
- Issue Date: 08 July 2021
- DOI: <https://doi.org/10.1038/s41586-021-03650-9>

Comments

By submitting a comment you agree to abide by our [Terms](#) and [Community Guidelines](#). If you find something abusive or that does not comply with our terms or guidelines please flag it as inappropriate.

[Access through your institution](#)

[Change institution](#)

[Buy or subscribe](#)

Advertisement

This article was downloaded by **calibre** from <https://www.nature.com/articles/s41586-021-03650-9>

- Matters Arising
- [Published: 07 July 2021](#)

Shark mortality cannot be assessed by fishery overlap alone

- [Hilario Murua](#) [ORCID: orcid.org/0000-0001-8577-5291](#)¹,
- [Shane P. Griffiths](#)²,
- [Alistair J. Hobday](#) [ORCID: orcid.org/0000-0002-3194-8326](#)^{3,4},
- [Shelley C. Clarke](#)⁵,
- [Enric Cortés](#)⁶,
- [Eric L. Gilman](#)⁷,
- [Josu Santiago](#)⁸,
- [Haritz Arizabalaga](#) [ORCID: orcid.org/0000-0002-3861-6316](#)⁸,
- [Paul de Bruyn](#)⁹,
- [Jon Lopez](#) [ORCID: orcid.org/0000-0002-4172-4094](#)²,
- [Alexandre M. Aires-da-Silva](#)² &
- [Victor Restrepo](#)¹

[Nature](#) volume 595, pages E4–E7 (2021) [Cite this article](#)

- 6 Altmetric
- [Metrics details](#)

Subjects

- [Environmental sciences](#)
- [Marine biology](#)

Matters Arising to this article was published on 07 July 2021

The Original Article was published on 24 July 2019

arising from N. Queiroz et al. *Nature* <https://doi.org/10.1038/s41586-019-1444-4> (2019)

Access options

Subscribe to Journal

Get full journal access for 1 year

\$199.00

only \$3.90 per issue

[Subscribe](#)

All prices are NET prices.

VAT will be added later in the checkout.

Tax calculation will be finalised during checkout.

Rent or Buy article

Get time limited or full article access on ReadCube.

from \$8.99

[Rent or Buy](#)

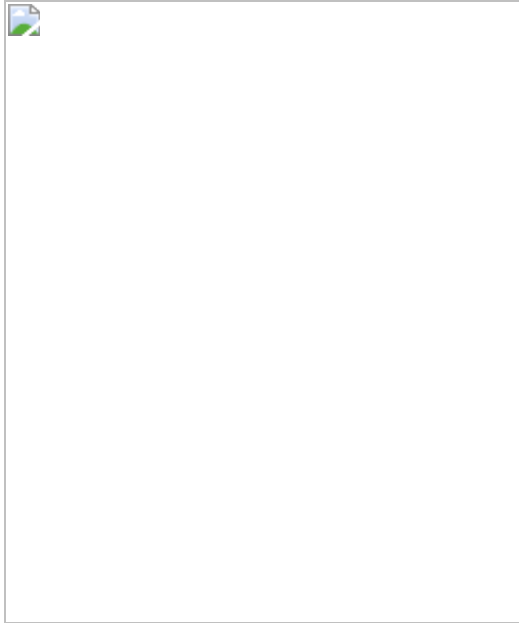
All prices are NET prices.

Additional access options:

- [Log in](#)

- [Access through your institution](#)
- [Learn about institutional subscriptions](#)

Fig. 1: Match or mismatch between FEI hotspots or shark density hotspots, and fishing effort hotspots.



Data availability

To prepare Table 1 and linear regressions between North Atlantic annual shark landings (FAO total capture production) and shark FEI as calculated by Queiroz et al.¹, FAO statistics available from <http://www.fao.org/fishery/statistics/global-capture-production/query/es> were used following the description of the data by Queiroz et al.¹. To produce Table 2 and Fig. 1, data from Queiroz et al.¹ were used from <https://github.com/GlobalSharkMovement/GlobalSpatialRisk>.

References

1. 1.

Queiroz, N. et al. Global spatial risk assessment of sharks under the footprint of fisheries. *Nature* **572**, 461–466 (2019).

[ADS](#) [CAS](#) [Article](#) [Google Scholar](#)

2. 2.

Hobday, A. J. et al. Ecological risk assessment for the effects of fishing. *Fish. Res.* **108**, 372–384 (2011).

[Article](#) [Google Scholar](#)

3. 3.

Gallagher, A. J., Kyne, P. M. & Hammerschlag, N. Ecological risk assessment and its application to elasmobranch conservation and management. *J. Fish Biol.* **80**, 1727–1748 (2012).

[CAS](#) [Article](#) [Google Scholar](#)

4. 4.

Hilborn, R. & Walters, C. J. *Quantitative Fisheries Stock Assessment, Choice, Dynamics and Uncertainty* (Chapman and Hall, 1992).

5. 5.

Weng, K. C. & Block, B. A. Diel vertical migration of the bigeye thresher shark (*Alopias superciliosus*), a species possessing orbital retia mirabilia. *Fish Bull.* **102**, 221–229 (2004).

[Google Scholar](#)

6. 6.

Queiroz, N., Humphries, N. E., Noble, L. R., Santos, A. M. & Sims, D. W. Short-term movements and diving behaviour of satellite-tracked blue sharks *Prionace glauca* in the northeastern Atlantic Ocean. *Mar. Ecol. Prog. Ser.* **406**, 265–279 (2010).

[ADS](#) [Article](#) [Google Scholar](#)

7. 7.

Cortés, E. et al. Expanded ecological risk assessment of pelagic sharks caught in Atlantic pelagic longline fisheries. *Collect. Vol. Sci. Pap. ICCAT* **71**, 2637–2688 (2015).

[Article](#) [Google Scholar](#)

8. 8.

Foster, D. G., Epperly, S. P., Shah, A. K. & Watson, J. W. Evaluation of hook and bait type on the catch rates in the Western North Atlantic Ocean pelagic longline fishery. *Bull. Mar. Sci.* **88**, 529–545 (2012).

[Article](#) [Google Scholar](#)

9. 9.

Cortés, E. et al. Ecological risk assessment of pelagic sharks caught in Atlantic pelagic longline fisheries. *Aquat. Living Resour.* **23**, 25–34 (2010).

[Article](#) [Google Scholar](#)

10. 10.

Ellis, J. R., McCully Phillips, S. R. & Poisson, F. A review of capture and post-release mortality of elasmobranchs. *J. Fish Biol.* **90**, 653–722 (2017).

[CAS](#) [Article](#) [Google Scholar](#)

11. 11.

Gallagher, A. J., Orbesen, E. S., Hammerschlag, N. & Serafy, J. E. Vulnerability of oceanic sharks as pelagic longline bycatch. *Glob. Ecol. Conserv.* **1**, 50–59 (2014).

[Article](#) [Google Scholar](#)

12. 12.

Pacourea, N. et al. Half a century of global decline in oceanic sharks and rays. *Nature* **589**, 567–571 (2021).

[ADS](#) [CAS](#) [Article](#) [Google Scholar](#)

13. 13.

Poisson, F. et al. Technical mitigation measures for sharks and rays in fisheries for tuna and tuna-like species: turning possibility into reality. *Aquat. Living Resour.* **29**, 402 (2016).

[Article](#) [Google Scholar](#)

14. 14.

Doherty, P. D. et al. Big catch, little sharks: insight into Peruvian small-scale longline fisheries. *Ecol. Evol.* **4**, 2375–2383 (2014).

[Article](#) [Google Scholar](#)

15. 15.

Alfaro-Shigueto, J. et al. Where small can have a large impact: structure and characterization of small-scale fisheries in Peru. *Fish. Res.* **106**, 8–17 (2010).

[Article](#) [Google Scholar](#)

16. 16.

R Core Team. *R: A language and environment for statistical computing*. <http://www.R-project.org/> (R Foundation for Statistical Computing, 2019).

[Download references](#)

Acknowledgements

We thank M. J. Williams for useful suggestions on a previous version of the Comment, which were very helpful in improving the manuscript. The views expressed by E.C. herein are those of the author and do not necessarily reflect those of the agency of E.C.

Author information

Affiliations

1. International Seafood Sustainability Foundation, Washington, DC, USA
Hilario Murua & Victor Restrepo
2. Inter-American Tropical Tuna Commission, La Jolla, CA, USA
Shane P. Griffiths, Jon Lopez & Alexandre M. Aires-da-Silva
3. CSIRO Oceans and Atmosphere, Hobart, Tasmania, Australia
Alistair J. Hobday
4. Centre for Marine Socioecology, University of Tasmania, Hobart, Tasmania, Australia
Alistair J. Hobday
5. Areas Beyond National Jurisdiction Tuna Project, Food and Agriculture Organization, Rome, Italy
Shelley C. Clarke
6. NOAA Fisheries Southeast Fisheries Science Center, Panama City Laboratory, Panama City, FL, USA

Enric Cortés

7. Pelagic Ecosystems Research Group, Hawaii Pacific University, Honolulu, HI, USA

Eric L. Gilman

8. AZTI, Marine Research, Basque Research and Technology Alliance (BRTA), Sukarrieta, Basque Country, Spain

Josu Santiago & Haritz Arrizabalaga

9. Indian Ocean Tuna Commission, Victoria, Seychelles

Paul de Bruyn

Authors

1. Hilario Murua

[View author publications](#)

You can also search for this author in [PubMed](#) [Google Scholar](#)

2. Shane P. Griffiths

[View author publications](#)

You can also search for this author in [PubMed](#) [Google Scholar](#)

3. Alistair J. Hobday

[View author publications](#)

You can also search for this author in [PubMed](#) [Google Scholar](#)

4. Shelley C. Clarke

[View author publications](#)

You can also search for this author in [PubMed](#) [Google Scholar](#)

5. Enric Cortés

[View author publications](#)

You can also search for this author in [PubMed](#) [Google Scholar](#)

6. Eric L. Gilman

[View author publications](#)

You can also search for this author in [PubMed](#) [Google Scholar](#)

7. Josu Santiago

[View author publications](#)

You can also search for this author in [PubMed](#) [Google Scholar](#)

8. Haritz Arrizabalaga

[View author publications](#)

You can also search for this author in [PubMed](#) [Google Scholar](#)

9. Paul de Bruyn

[View author publications](#)

You can also search for this author in [PubMed](#) [Google Scholar](#)

10. Jon Lopez

[View author publications](#)

You can also search for this author in [PubMed](#) [Google Scholar](#)

11. Alexandre M. Aires-da-Silva

[View author publications](#)

You can also search for this author in [PubMed](#) [Google Scholar](#)

12. Victor Restrepo

[View author publications](#)

You can also search for this author in [PubMed](#) [Google Scholar](#)

Contributions

H.M., S.P.G. and V.R. conceived the study; H.M., S.P.G., A.J.H., S.C.C., E.C. and E.L.G. wrote the manuscript with further input and revisions from all authors; H.M., S.P.G. and J.S. performed the data analyses and produced the figures and tables; all authors contributed to the interpretation and discussion of the manuscript.

Corresponding author

Correspondence to [Hilario Murua](#).

Ethics declarations

Competing interests

The authors declare no competing interests.

Additional information

Publisher's note Springer Nature remains neutral with regard to jurisdictional claims in published maps and institutional affiliations.

Supplementary information

[**Reporting Summary**](#)

Rights and permissions

[**Reprints and Permissions**](#)

About this article



Cite this article

Murua, H., Griffiths, S.P., Hobday, A.J. *et al.* Shark mortality cannot be assessed by fishery overlap alone. *Nature* **595**, E4–E7 (2021).
<https://doi.org/10.1038/s41586-021-03396-4>

[Download citation](#)

- Received: 04 December 2019
- Accepted: 25 February 2021
- Published: 07 July 2021
- Issue Date: 08 July 2021
- DOI: <https://doi.org/10.1038/s41586-021-03396-4>

Comments

By submitting a comment you agree to abide by our [Terms](#) and [Community Guidelines](#). If you find something abusive or that does not comply with our terms or guidelines please flag it as inappropriate.

[Access through your institution](#)

[Change institution](#)

[Buy or subscribe](#)

Advertisement

| [Section menu](#) | [Main menu](#) |

- Matters Arising
- [Published: 07 July 2021](#)

Reply to: Shark mortality cannot be assessed by fishery overlap alone

- [Nuno Queiroz^{1,2}](#),
- [Nicolas E. Humphries²](#),
- [Ana Couto¹](#),
- [Marisa Vedor^{1,3}](#),
- [Ivo da Costa¹](#),
- [Ana M. M. Sequeira^{4,5}](#),
- [Gonzalo Mucientes¹](#),
- [António M. Santos^{1,3}](#),
- [Francisco J. Abascal⁶](#),
- [Debra L. Abercrombie⁷](#),
- [Katya Abrantes⁸](#),
- [David Acuña-Marrero⁹](#),
- [André S. Afonso^{10,11}](#),
- [Pedro Afonso^{12,13,14}](#),
- [Darrell Anders¹⁵](#),
- [Gonzalo Araujo¹⁶](#),
- [Randall Arauz^{17,18,19}](#),
- [Pascal Bach²⁰](#),
- [Adam Barnett⁸](#),
- [Diego Bernal²¹](#),
- [Michael L. Berumen²²](#),
- [Sandra Bessudo Lion^{19,23}](#),
- [Natalia P. A. Bezerra¹⁰](#),
- [Antonin V. Blaison²⁰](#),

- Barbara A. Block²⁴,
- Mark E. Bond²⁵,
- Ramon Bonfil²⁶,
- Russell W. Bradford²⁷,
- Camrin D. Braun^{28,29},
- Edward J. Brooks³⁰,
- Annabelle Brooks^{30,31},
- Judith Brown³²,
- Barry D. Bruce²⁷,
- Michael E. Byrne^{33,34},
- Steven E. Campana³⁵,
- Aaron B. Carlisle³⁶,
- Demian D. Chapman²⁵,
- Taylor K. Chapple^{24 nAff109},
- John Chisholm³⁷,
- Christopher R. Clarke³⁸,
- Eric G. Clua³⁹,
- Jesse E. M. Cochran²²,
- Estelle C. Crochelet^{40,41},
- Laurent Dagorn²⁰,
- Ryan Daly^{42,43},
- Daniel Devia Cortés⁴⁴,
- Thomas K. Doyle^{45,46},
- Michael Drew⁴⁷,
- Clinton A. J. Duffy⁴⁸,
- Thor Erikson⁴⁹,
- Eduardo Espinoza^{19,50},
- Luciana C. Ferreira⁵¹,
- Francesco Ferretti⁵²,
- John D. Filmalter^{20,43},
- G. Chris Fischer⁵³,
- Richard Fitzpatrick⁸,
- Jorge Fontes^{12,13,14},
- Fabien Forget²⁰,

- Mark Fowler⁵⁴,
- Malcolm P. Francis⁵⁵,
- Austin J. Gallagher^{56,57},
- Enrico Gennari^{43,58,59},
- Simon D. Goldsworthy⁶⁰,
- Matthew J. Gollock⁶¹,
- Jonathan R. Green⁶²,
- Johan A. Gustafson⁶³,
- Tristan L. Guttridge⁶⁴,
- Hector M. Guzman⁶⁵,
- Neil Hammerschlag^{57,66},
- Luke Harman⁴⁵,
- Fábio H. V. Hazin¹⁰,
- Matthew Heard⁴⁷,
- Alex R. Hearn^{19,67,68},
- John C. Holdsworth⁶⁹,
- Bonnie J. Holmes^{70 nAff110},
- Lucy A. Howey⁷¹,
- Mauricio Hoyos^{19,72},
- Robert E. Hueter⁷³,
- Nigel E. Hussey⁷⁴,
- Charlie Huvaneers⁴⁷,
- Dylan T. Irion⁷⁵,
- David M. P. Jacoby⁷⁶,
- Oliver J. D. Jewell^{77,78},
- Ryan Johnson⁷⁹,
- Lance K. B. Jordan⁷¹,
- Warren Joyce⁵⁴,
- Clare A. Keating Daly⁴²,
- James T. Ketchum^{19,72},
- A. Peter Klimley^{19,80},
- Alison A. Kock^{43,81,82,83},
- Pieter Koen⁸⁴,
- Felipe Ladino²³,

- Fernanda O. Lana^{10,85},
- James S. E. Lea^{38,86},
- Fiona Llewellyn⁶¹,
- Warrick S. Lyon⁵⁵,
- Anna MacDonnell⁵⁴,
- Bruno C. L. Macena^{10,13},
- Heather Marshall^{21,87},
- Jaime D. McAllister⁸⁸,
- Michael A. Meyér¹⁵,
- John J. Morris⁷³,
- Emily R. Nelson⁵⁷,
- Yannis P. Papastamatiou²⁵,
- Cesar Peñaherrera-Palma^{19,89},
- Simon J. Pierce⁹⁰,
- Francois Poisson²⁰,
- Lina Maria Quintero²³,
- Andrew J. Richardson⁹¹,
- Paul J. Rogers⁶⁰,
- Christoph A. Rohner⁹⁰,
- David R. L. Rowat⁹²,
- Melita Samoilys⁹³,
- Jayson M. Semmens⁸⁸,
- Marcus Sheaves⁸,
- George Shillinger^{19,24,94},
- Mahmood Shivji³³,
- Sarika Singh¹⁵,
- Gregory B. Skomal³⁶,
- Malcolm J. Smale⁹⁵,
- Laurenne B. Snyders¹⁵,
- German Soler^{19,23,88},
- Marc Soria²⁰,
- Kilian M. Stehfest⁸⁸,
- Simon R. Thorrold²⁹,
- Mariana T. Tolotti²⁰,

- [Alison Towner](#)^{59,78},
- [Paulo Travassos](#)¹⁰,
- [John P. Tyminski](#)⁷³,
- [Frederic Vandeperre](#)^{12,13,14},
- [Jeremy J. Vaudo](#)³³,
- [Yuuki Y. Watanabe](#)^{96,97},
- [Sam B. Weber](#)⁹⁸,
- [Bradley M. Wetherbee](#)^{33,99},
- [Timothy D. White](#)²⁴,
- [Sean Williams](#)³⁰,
- [Patricia M. Zárate](#)¹⁰⁰,
- [Robert Harcourt](#)¹⁰¹,
- [Graeme C. Hays](#)¹⁰²,
- [Mark G. Meekan](#)⁵¹,
- [Michele Thums](#)⁵¹,
- [Xabier Irigoien](#)^{103,104},
- [Victor M. Eguiluz](#)¹⁰⁵,
- [Carlos M. Duarte](#)²²,
- [Lara L. Sousa](#)^{2,106},
- [Samantha J. Simpson](#)^{2,107},
- [Emily J. Southall](#)² &
- [David W. Sims](#) ORCID: orcid.org/0000-0002-0916-7363^{2,107,108}

[Nature](#) volume 595, pages E8–E16 (2021) [Cite this article](#)

- 45 Altmetric
- [Metrics details](#)

Subjects

- [Conservation biology](#)
- [Marine biology](#)

The [Original Article](#) was published on 07 July 2021

replying to H. Murua et al. *Nature* <https://doi.org/10.1038/s41586-021-03396-4> (2021)

Access options

Subscribe to Journal

Get full journal access for 1 year

\$199.00

only \$3.90 per issue

[Subscribe](#)

All prices are NET prices.

VAT will be added later in the checkout.

Tax calculation will be finalised during checkout.

Rent or Buy article

Get time limited or full article access on ReadCube.

from \$8.99

[Rent or Buy](#)

All prices are NET prices.

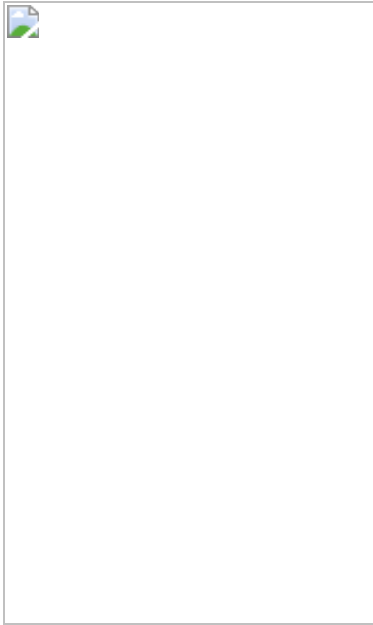
Additional access options:

- [Log in](#)
- [Access through your institution](#)
- [Learn about institutional subscriptions](#)

Fig. 1: Spatial distributions and overlap of sharks and longline fishing vessels.



Fig. 2: Effect of scale on the position and extent of FEI hotspots and areas free from AIS longline fishing effort.



Data availability

Data used in linear-regression modelling are available on GitHub (https://github.com/GlobalSharkMovement/GlobalSpatialRisk/tree/master/derived_data). Data used to prepare the maps (shark relative spatial density, longline-fishing effort and shark–longline-fishing overlap and FEI) are available on GitHub (<https://github.com/GlobalSharkMovement/GlobalSpatialRisk>).

Code availability

Code used to prepare the maps (shark relative spatial density, longline-fishing effort and shark–longline-fishing overlap and FEI) is available on GitHub (<https://github.com/GlobalSharkMovement/GlobalSpatialRisk>).

References

1. 1.

Queiroz, N. et al. Global spatial risk assessment of sharks under the footprint of fisheries. *Nature* **572**, 461–466 (2019).

[ADS](#) [CAS](#) [Article](#) [Google Scholar](#)

2. 2.

Murua, H. et al. Shark mortality cannot be assessed by fishery overlap alone. *Nature* <https://doi.org/10.1038/s41586-021-03396-4> (2021).

3. 3.

Cortés, E. et al. Ecological risk assessment of pelagic sharks caught in Atlantic pelagic longline fisheries. *Aquat. Living Resour.* **23**, 25–34 (2010).

[Article](#) [Google Scholar](#)

4. 4.

Cortés, E. et al. Expanded ecological risk assessment of pelagic sharks caught in Atlantic pelagic longline fisheries. *Collect. Vol. Sci. Pap. ICCAT* **71**, 2637–2688 (2015).

[Google Scholar](#)

5. 5.

Murua, H. et al. Updated Ecological Risk Assessment (ERA) for shark species caught in fisheries managed by the Indian Ocean Tuna Commission (IOTC). *21st Meeting of the Scientific Committee of the IOTC Document IOTC-2018-SC21-14* (Indian Ocean Tuna Commission, 2018).

6. 6.

Ward, P. & Myers, R. A. Inferring the depth distribution of catchability for pelagic fishes and correcting for variations in the depth of longline fishing gear. *Can. J. Fish. Aquat. Sci.* **62**, 1130–1142 (2005).

[Article](#) [Google Scholar](#)

7. 7.

Andrzejaczek, S., Gleiss, A. C., Pattiarratchi, C. B. & Meekan, M. G. Patterns and drivers of vertical movements of the large fishes of the epipelagic. *Rev. Fish Biol. Fish.* **29**, 335–354 (2019).

[Article](#) [Google Scholar](#)

8. 8.

International Commission for the Conservation of Atlantic Tunas. *Report of the 2018 ICCAT Intersessional Meeting of the Sharks Species Group* (2018).

9. 9.

Coelho, R., Fernandez-Carvalho, J., Lino, P. G. & Santos, M. N. An overview of the hooking mortality of elasmobranchs caught in a swordfish pelagic longline fishery in the Atlantic Ocean. *Aquat. Living Resour.* **25**, 311–319 (2012).

[Article](#) [Google Scholar](#)

10. 10.

Dapp, D. R., Walker, T. I., Huveneers, C. & Reina, R. D. Respiratory mode and gear type are important determinants of elasmobranch immediate and post-release mortality. *Fish Fish.* **17**, 507–524 (2016).

[Article](#) [Google Scholar](#)

11. 11.

Gallagher, A. J., Serafy, J. E., Cooke, S. J. & Hammerschlag, N. Physiological stress response, reflex impairment, and survival of five sympatric shark species following experimental capture and release. *Mar. Ecol. Prog. Ser.* **496**, 207–218 (2014).

[ADS](#) [Article](#) [Google Scholar](#)

12. 12.

Hutchinson, M. R., Itano, D. G., Muir, J. A. & Holland, K. N. Post-release survival of juvenile silky sharks captured in a tropical tuna purse seine fishery. *Mar. Ecol. Prog. Ser.* **521**, 143–154 (2015).

[ADS](#) [Article](#) [Google Scholar](#)

13. 13.

Worm, B. et al. Global catches, exploitation rates, and rebuilding options for sharks. *Mar. Policy* **40**, 194–204 (2013).

[Article](#) [Google Scholar](#)

14. 14.

McCauley, D. J. et al. Marine defaunation: animal loss in the global ocean. *Science* **347**, 1255641 (2015).

[Article](#) [Google Scholar](#)

15. 15.

Pacourea, N. et al. Half a century of global decline in oceanic sharks and rays. *Nature* **589**, 567–571 (2021).

[ADS](#) [CAS](#) [Article](#) [Google Scholar](#)

[Download references](#)

Acknowledgements

Funding support was provided by the Natural Environment Research Council (NERC) (NE/R00997/X/1), European Research Council (ERC-AdG-2019 883583 OCEAN DEOXYFISH) (D.W.S.), Australian Research Council (ARC DP210103091) (A.M.M.S. and D.W.S.), Fundação para a Ciência e a Tecnologia CECIND/02857/2018 (N.Q.), PTDC/BIA-COM/28855/2017 (M.V.) and a 2020 Pew Fellowship in Marine Conservation (A.M.M.S.). This research is part of the Global Shark Movement Project (<https://www.globalsharkmovement.org/>).

Author information

Author notes

1. Taylor K. Chapple

Present address: Hatfield Marine Science Center, Oregon State University, Newport, OR, USA

2. Bonnie J. Holmes

Present address: The University of the Sunshine Coast, Sippy Downs, Queensland, Australia

Affiliations

1. Centro de Investigação em Biodiversidade e Recursos Genéticos/Research Network in Biodiversity and Evolutionary Biology, Campus Agrário de Vairão, Universidade do Porto, Vairão, Portugal

Nuno Queiroz, Ana Couto, Marisa Vedor, Ivo da Costa, Gonzalo Mucientes & António M. Santos

2. Marine Biological Association of the United Kingdom, Plymouth, UK

Nuno Queiroz, Nicolas E. Humphries, Lara L. Sousa, Samantha J. Simpson, Emily J. Southall & David W. Sims

3. Departamento de Biologia, Faculdade de Ciências da Universidade do Porto, Porto, Portugal

Marisa Vedor & António M. Santos

4. UWA Oceans Institute, Indian Ocean Marine Research Centre, University of Western Australia, Crawley, Western Australia, Australia

Ana M. M. Sequeira

5. School of Biological Sciences, University of Western Australia, Crawley, Western Australia, Australia

Ana M. M. Sequeira

6. Spanish Institute of Oceanography, Santa Cruz de Tenerife, Spain

Francisco J. Abascal

7. Abercrombie and Fish, Port Jefferson Station, NY, USA

Debra L. Abercrombie

8. Marine Biology and Aquaculture Unit, College of Science and Engineering, James Cook University, Cairns, Queensland, Australia

Katya Abrantes, Adam Barnett, Richard Fitzpatrick & Marcus Sheaves

9. Institute of Natural and Mathematical Sciences, Massey University, Palmerston North, New Zealand

David Acuña-Marrero

10. Universidade Federal Rural de Pernambuco (UFRPE), Departamento de Pesca e Aquicultura, Recife, Brazil

André S. Afonso, Natalia P. A. Bezerra, Fábio H. V. Hazin, Fernanda O. Lana, Bruno C. L. Macena & Paulo Travassos

11. MARE, Marine and Environmental Sciences Centre, Instituto Politécnico de Leiria, Peniche, Portugal

André S. Afonso

12. MARE, Laboratório Marítimo da Guia, Faculdade de Ciências da Universidade de Lisboa, Cascais, Portugal

Pedro Afonso, Jorge Fontes & Frederic Vandeperre

13. Institute of Marine Research (IMAR), Departamento de Oceanografia e Pescas, Universidade dos Açores, Horta, Portugal

Pedro Afonso, Jorge Fontes, Bruno C. L. Macena & Frederic Vandeperre

14. Okeanos - Departamento de Oceanografia e Pescas, Universidade dos Açores, Horta, Portugal

Pedro Afonso, Jorge Fontes & Frederic Vandeperre

15. Department of Environmental Affairs, Oceans and Coasts Research, Cape Town, South Africa

Darrell Anders, Michael A. Meÿer, Sarika Singh & Laurenne B. Snyders

16. Large Marine Vertebrates Research Institute Philippines, Jagna, Philippines

Gonzalo Araujo

17. Fins Attached Marine Research and Conservation, Colorado Springs, CO, USA

Randall Arauz

18. Programa Restauración de Tortugas Marinas PRETOMA, San José, Costa Rica

Randall Arauz

19. MigraMar, Olema, CA, USA

Randall Arauz, Sandra Bessudo Lion, Eduardo Espinoza, Alex R. Hearn, Mauricio Hoyos, James T. Ketchum, A. Peter Klimley, Cesar Peñaherrera-Palma, George Shillinger & German Soler

20. Institut de Recherche pour le Développement, UMR MARBEC (IRD, Ifremer, Univ. Montpellier, CNRS), Sète, France

Pascal Bach, Antonin V. Blaison, Laurent Dagorn, John D. Filmalter, Fabien Forget, Francois Poisson, Marc Soria & Mariana T. Tolotti

21. Biology Department, University of Massachusetts Dartmouth, Dartmouth, MA, USA

Diego Bernal & Heather Marshall

22. Red Sea Research Center, Division of Biological and Environmental Science and Engineering, King Abdullah University of Science and Technology, Thuwal, Saudi Arabia

Michael L. Berumen, Jesse E. M. Cochran & Carlos M. Duarte

23. Fundación Malpelo y Otros Ecosistemas Marinos, Bogota, Colombia

Sandra Bessudo Lion, Felipe Ladino, Lina Maria Quintero & German Soler

24. Hopkins Marine Station of Stanford University, Pacific Grove, CA, USA

Barbara A. Block, Taylor K. Chapple, George Shillinger & Timothy D. White

25. Department of Biological Sciences, Florida International University,
North Miami, FL, USA

Mark E. Bond, Demian D. Chapman & Yannis P. Papastamatiou

26. Instituto de Ciências do Mar, Universidade Federal do Ceará,
Fortaleza, Brazil

Ramon Bonfil

27. CSIRO Oceans and Atmosphere, Hobart, Tasmania, Australia

Russell W. Bradford & Barry D. Bruce

28. School of Aquatic and Fishery Sciences, University of Washington,
Seattle, WA, USA

Camrin D. Braun

29. Biology Department, Woods Hole Oceanographic Institution, Woods
Hole, MA, USA

Camrin D. Braun & Simon R. Thorrold

30. Shark Research and Conservation Program, Cape Eleuthera Institute,
Eleuthera, Bahamas

Edward J. Brooks, Annabelle Brooks & Sean Williams

31. University of Exeter, Exeter, UK

Annabelle Brooks

32. South Atlantic Environmental Research Institute, Stanley, Falkland
Islands

Judith Brown

33. Department of Biological Sciences, The Guy Harvey Research Institute, Nova Southeastern University, Dania Beach, FL, USA
Michael E. Byrne, Mahmood Shivji, Jeremy J. Vaudo & Bradley M. Wetherbee
34. School of Natural Resources, University of Missouri, Columbia, MO, USA
Michael E. Byrne
35. Life and Environmental Sciences, University of Iceland, Reykjavik, Iceland
Steven E. Campana
36. School of Marine Science and Policy, University of Delaware, Lewes, DE, USA
Aaron B. Carlisle & Gregory B. Skomal
37. Massachusetts Division of Marine Fisheries, New Bedford, MA, USA
John Chisholm
38. Marine Research Facility, Jeddah, Saudi Arabia
Christopher R. Clarke & James S. E. Lea
39. PSL, Labex CORAIL, CRIOBE USR3278 EPHE-CNRS-UPVD, Papetoai, French Polynesia
Eric G. Clua
40. Agence de Recherche pour la Biodiversité à la Réunion (ARBRE), Réunion, Marseille, France
Estelle C. Crochelet

41. Institut de Recherche pour le Développement, UMR 228 ESPACE-DEV, Réunion, Marseille, France

Estelle C. Crochelet

42. Save Our Seas Foundation–D’Arros Research Centre (SOSF-DRC), Geneva, Switzerland

Ryan Daly & Clare A. Keating Daly

43. South African Institute for Aquatic Biodiversity (SAIAB), Grahamstown, South Africa

Ryan Daly, John D. Filmalter, Enrico Gennari & Alison A. Kock

44. Department of Fisheries Evaluation, Fisheries Research Division, Instituto de Fomento Pesquero (IFOP), Valparaíso, Chile

Daniel Devia Cortés

45. School of Biological, Earth and Environmental Sciences, University College Cork, Cork, Ireland

Thomas K. Doyle & Luke Harman

46. MaREI Centre, Environmental Research Institute, University College Cork, Cork, Ireland

Thomas K. Doyle

47. College of Science and Engineering, Flinders University, Adelaide, South Australia, Australia

Michael Drew, Matthew Heard & Charlie Huvaneers

48. Department of Conservation, Auckland, New Zealand

Clinton A. J. Duffy

49. South African Institute for Aquatic Biodiversity, Geological Sciences,
UKZN, Durban, South Africa

Thor Erikson

50. Direccion Parque Nacional Galapagos, Puerto Ayora, Galapagos,
Ecuador

Eduardo Espinoza

51. Australian Institute of Marine Science, Indian Ocean Marine Research
Centre (UWA), Crawley, Western Australia, Australia

Luciana C. Ferreira, Mark G. Meekan & Michele Thums

52. Department of Fish and Wildlife Conservation, Virginia Tech,
Blacksburg, VA, USA

Francesco Ferretti

53. OCEARCH, Park City, UT, USA

G. Chris Fischer

54. Bedford Institute of Oceanography, Dartmouth, Nova Scotia, Canada

Mark Fowler, Warren Joyce & Anna MacDonnell

55. National Institute of Water and Atmospheric Research, Wellington,
New Zealand

Malcolm P. Francis & Warrick S. Lyon

56. Beneath the Waves, Herndon, VA, USA

Austin J. Gallagher

57. Rosenstiel School of Marine and Atmospheric Science, University of
Miami, Miami, FL, USA

Austin J. Gallagher, Neil Hammerschlag & Emily R. Nelson

58. Oceans Research Institute, Mossel Bay, South Africa

Enrico Gennari

59. Department of Ichthyology and Fisheries Science, Rhodes University,
Grahamstown, South Africa

Enrico Gennari & Alison Towner

60. SARDI Aquatic Sciences, Adelaide, South Australia, Australia

Simon D. Goldsworthy & Paul J. Rogers

61. Zoological Society of London, London, UK

Matthew J. Gollock & Fiona Llewellyn

62. Galapagos Whale Shark Project, Puerto Ayora, Galapagos, Ecuador

Jonathan R. Green

63. Griffith Centre for Coastal Management, Griffith University School of
Engineering, Griffith University, Gold Coast, Queensland, Australia

Johan A. Gustafson

64. Saving the Blue, Cooper City, FL, USA

Tristan L. Guttridge

65. Smithsonian Tropical Research Institute, Panama City, Panama

Hector M. Guzman

66. Leonard and Jayne Abess Center for Ecosystem Science and Policy,
University of Miami, Coral Gables, FL, USA

Neil Hammerschlag

67. Galapagos Science Center, San Cristobal, Galapagos, Ecuador

Alex R. Hearn

68. Universidad San Francisco de Quito, Quito, Ecuador

Alex R. Hearn

69. Blue Water Marine Research, Tutukaka, New Zealand

John C. Holdsworth

70. University of Queensland, Brisbane, Queensland, Australia

Bonnie J. Holmes

71. Microwave Telemetry, Columbia, MD, USA

Lucy A. Howey & Lance K. B. Jordan

72. Pelagios-Kakunja, La Paz, Mexico

Mauricio Hoyos & James T. Ketchum

73. Mote Marine Laboratory, Center for Shark Research, Sarasota, FL,
USA

Robert E. Hueter, John J. Morris & John P. Tyminski

74. Biological Sciences, University of Windsor, Windsor, Ontario, Canada

Nigel E. Hussey

75. Cape Research and Diver Development, Simon's Town, South Africa

Dylan T. Irion

76. Institute of Zoology, Zoological Society of London, London, UK

David M. P. Jacoby

77. Centre for Sustainable Aquatic Ecosystems, Harry Butler Institute,
Murdoch University, Perth, Western Australia, Australia

Oliver J. D. Jewell

78. Dyer Island Conservation Trust, Western Cape, South Africa

Oliver J. D. Jewell & Alison Towner

79. Blue Wilderness Research Unit, Scottburgh, South Africa

Ryan Johnson

80. University of California Davis, Davis, CA, USA

A. Peter Klimley

81. Cape Research Centre, South African National Parks, Steenberg, South Africa

Alison A. Kock

82. Shark Spotters, Fish Hoek, South Africa

Alison A. Kock

83. Institute for Communities and Wildlife in Africa, Department of Biological Sciences, University of Cape Town, Rondebosch, South Africa

Alison A. Kock

84. Western Cape Department of Agriculture, Veterinary Services, Elsenburg, South Africa

Pieter Koen

85. Departamento de Biologia Marinha, Universidade Federal Fluminense (UFF), Niterói, Brazil

Fernanda O. Lana

86. Department of Zoology, University of Cambridge, Cambridge, UK

James S. E. Lea

87. Atlantic White Shark Conservancy, Chatham, MA, USA

Heather Marshall

88. Fisheries and Aquaculture Centre, Institute for Marine and Antarctic Studies, University of Tasmania, Hobart, Tasmania, Australia

Jaime D. McAllister, Jayson M. Semmens, German Soler & Kilian M. Stehfest

89. Pontificia Universidad Católica del Ecuador Sede Manabi, Portoviejo, Ecuador

Cesar Peñaherrera-Palma

90. Marine Megafauna Foundation, Truckee, CA, USA

Simon J. Pierce & Christoph A. Rohner

91. Conservation and Fisheries Department, Ascension Island Government, Georgetown, Ascension Island, UK

Andrew J. Richardson

92. Marine Conservation Society Seychelles, Victoria, Seychelles

David R. L. Rowat

93. CORDIO, East Africa, Mombasa, Kenya

Melita Samoilys

94. Upwell, Monterey, CA, USA

George Shillinger

95. Department of Zoology and Institute for Coastal and Marine Research,
Nelson Mandela University, Port Elizabeth, South Africa

Malcolm J. Smale

96. National Institute of Polar Research, Tachikawa, Tokyo, Japan

Yuuki Y. Watanabe

97. SOKENDAI (The Graduate University for Advanced Studies),
Tachikawa, Tokyo, Japan

Yuuki Y. Watanabe

98. Centre for Ecology and Conservation, University of Exeter, Penryn,
UK

Sam B. Weber

99. Department of Biological Sciences, University of Rhode Island,
Kingston, RI, USA

Bradley M. Wetherbee

100. Department of Oceanography and Environment, Fisheries Research
Division, Instituto de Fomento Pesquero (IFOP), Valparaíso, Chile

Patricia M. Zárate

101. Department of Biological Sciences, Macquarie University, Sydney,
New South Wales, Australia

Robert Harcourt

102. School of Life and Environmental Sciences, Deakin University,
Geelong, Victoria, Australia

Graeme C. Hays

103. AZTI - BRTA, Pasaia, Spain

Xabier Irigoien

104. IKERBASQUE, Basque Foundation for Science, Bilbao, Spain

Xabier Irigoien

105. Instituto de Fisica Interdisciplinar y Sistemas Complejos, Consejo Superior de Investigaciones Cientificas, University of the Balearic Islands, Palma de Mallorca, Spain

Victor M. Eguiluz

106. Wildlife Conservation Research Unit, Department of Zoology,
University of Oxford, Tubney, UK

Lara L. Sousa

107. Ocean and Earth Science, National Oceanography Centre
Southampton, University of Southampton, Southampton, UK

Samantha J. Simpson & David W. Sims

108. Centre for Biological Sciences, University of Southampton,
Southampton, UK

David W. Sims

Authors

1. Nuno Queiroz

[View author publications](#)

You can also search for this author in [PubMed](#) [Google Scholar](#)

2. Nicolas E. Humphries

[View author publications](#)

You can also search for this author in [PubMed](#) [Google Scholar](#)

3. Ana Couto

[View author publications](#)

You can also search for this author in [PubMed](#) [Google Scholar](#)

4. Marisa Vedor

[View author publications](#)

You can also search for this author in [PubMed](#) [Google Scholar](#)

5. Ivo da Costa

[View author publications](#)

You can also search for this author in [PubMed](#) [Google Scholar](#)

6. Ana M. M. Sequeira

[View author publications](#)

You can also search for this author in [PubMed](#) [Google Scholar](#)

7. Gonzalo Mucientes

[View author publications](#)

You can also search for this author in [PubMed](#) [Google Scholar](#)

8. António M. Santos

[View author publications](#)

You can also search for this author in [PubMed](#) [Google Scholar](#)

9. Francisco J. Abascal

[View author publications](#)

You can also search for this author in [PubMed](#) [Google Scholar](#)

10. Debra L. Abercrombie
[View author publications](#)

You can also search for this author in [PubMed](#) [Google Scholar](#)

11. Katya Abrantes
[View author publications](#)

You can also search for this author in [PubMed](#) [Google Scholar](#)

12. David Acuña-Marrero
[View author publications](#)

You can also search for this author in [PubMed](#) [Google Scholar](#)

13. André S. Afonso
[View author publications](#)

You can also search for this author in [PubMed](#) [Google Scholar](#)

14. Pedro Afonso
[View author publications](#)

You can also search for this author in [PubMed](#) [Google Scholar](#)

15. Darrell Anders
[View author publications](#)

You can also search for this author in [PubMed](#) [Google Scholar](#)

16. Gonzalo Araujo
[View author publications](#)

You can also search for this author in [PubMed](#) [Google Scholar](#)

17. Randall Arauz
[View author publications](#)

You can also search for this author in [PubMed](#) [Google Scholar](#)

18. Pascal Bach

[View author publications](#)

You can also search for this author in [PubMed](#) [Google Scholar](#)

19. Adam Barnett

[View author publications](#)

You can also search for this author in [PubMed](#) [Google Scholar](#)

20. Diego Bernal

[View author publications](#)

You can also search for this author in [PubMed](#) [Google Scholar](#)

21. Michael L. Berumen

[View author publications](#)

You can also search for this author in [PubMed](#) [Google Scholar](#)

22. Sandra Bessudo Lion

[View author publications](#)

You can also search for this author in [PubMed](#) [Google Scholar](#)

23. Natalia P. A. Bezerra

[View author publications](#)

You can also search for this author in [PubMed](#) [Google Scholar](#)

24. Antonin V. Blaison

[View author publications](#)

You can also search for this author in [PubMed](#) [Google Scholar](#)

25. Barbara A. Block

[View author publications](#)

You can also search for this author in [PubMed](#) [Google Scholar](#)

26. Mark E. Bond

[View author publications](#)

You can also search for this author in [PubMed](#) [Google Scholar](#)

27. Ramon Bonfil

[View author publications](#)

You can also search for this author in [PubMed](#) [Google Scholar](#)

28. Russell W. Bradford

[View author publications](#)

You can also search for this author in [PubMed](#) [Google Scholar](#)

29. Camrin D. Braun

[View author publications](#)

You can also search for this author in [PubMed](#) [Google Scholar](#)

30. Edward J. Brooks

[View author publications](#)

You can also search for this author in [PubMed](#) [Google Scholar](#)

31. Annabelle Brooks

[View author publications](#)

You can also search for this author in [PubMed](#) [Google Scholar](#)

32. Judith Brown

[View author publications](#)

You can also search for this author in [PubMed](#) [Google Scholar](#)

33. Barry D. Bruce

[View author publications](#)

You can also search for this author in [PubMed](#) [Google Scholar](#)

34. Michael E. Byrne

[View author publications](#)

You can also search for this author in [PubMed](#) [Google Scholar](#)

35. Steven E. Campana

[View author publications](#)

You can also search for this author in [PubMed](#) [Google Scholar](#)

36. Aaron B. Carlisle

[View author publications](#)

You can also search for this author in [PubMed](#) [Google Scholar](#)

37. Demian D. Chapman

[View author publications](#)

You can also search for this author in [PubMed](#) [Google Scholar](#)

38. Taylor K. Chapple

[View author publications](#)

You can also search for this author in [PubMed](#) [Google Scholar](#)

39. John Chisholm

[View author publications](#)

You can also search for this author in [PubMed](#) [Google Scholar](#)

40. Christopher R. Clarke

[View author publications](#)

You can also search for this author in [PubMed](#) [Google Scholar](#)

41. Eric G. Clua

[View author publications](#)

You can also search for this author in [PubMed](#) [Google Scholar](#)

42. Jesse E. M. Cochran

[View author publications](#)

You can also search for this author in [PubMed](#) [Google Scholar](#)

43. Estelle C. Crochelet

[View author publications](#)

You can also search for this author in [PubMed](#) [Google Scholar](#)

44. Laurent Dagorn

[View author publications](#)

You can also search for this author in [PubMed](#) [Google Scholar](#)

45. Ryan Daly

[View author publications](#)

You can also search for this author in [PubMed](#) [Google Scholar](#)

46. Daniel Devia Cortés

[View author publications](#)

You can also search for this author in [PubMed](#) [Google Scholar](#)

47. Thomas K. Doyle

[View author publications](#)

You can also search for this author in [PubMed](#) [Google Scholar](#)

48. Michael Drew

[View author publications](#)

You can also search for this author in [PubMed](#) [Google Scholar](#)

49. Clinton A. J. Duffy

[View author publications](#)

You can also search for this author in [PubMed](#) [Google Scholar](#)

50. Thor Erikson

[View author publications](#)

You can also search for this author in [PubMed](#) [Google Scholar](#)

51. Eduardo Espinoza

[View author publications](#)

You can also search for this author in [PubMed](#) [Google Scholar](#)

52. Luciana C. Ferreira

[View author publications](#)

You can also search for this author in [PubMed](#) [Google Scholar](#)

53. Francesco Ferretti

[View author publications](#)

You can also search for this author in [PubMed](#) [Google Scholar](#)

54. John D. Filmalter

[View author publications](#)

You can also search for this author in [PubMed](#) [Google Scholar](#)

55. G. Chris Fischer

[View author publications](#)

You can also search for this author in [PubMed](#) [Google Scholar](#)

56. Richard Fitzpatrick

[View author publications](#)

You can also search for this author in [PubMed](#) [Google Scholar](#)

57. Jorge Fontes

[View author publications](#)

You can also search for this author in [PubMed](#) [Google Scholar](#)

58. Fabien Forget

[View author publications](#)

You can also search for this author in [PubMed](#) [Google Scholar](#)

59. Mark Fowler

[View author publications](#)

You can also search for this author in [PubMed](#) [Google Scholar](#)

60. Malcolm P. Francis

[View author publications](#)

You can also search for this author in [PubMed](#) [Google Scholar](#)

61. Austin J. Gallagher

[View author publications](#)

You can also search for this author in [PubMed](#) [Google Scholar](#)

62. Enrico Gennari

[View author publications](#)

You can also search for this author in [PubMed](#) [Google Scholar](#)

63. Simon D. Goldsworthy

[View author publications](#)

You can also search for this author in [PubMed](#) [Google Scholar](#)

64. Matthew J. Gollock

[View author publications](#)

You can also search for this author in [PubMed](#) [Google Scholar](#)

65. Jonathan R. Green

[View author publications](#)

You can also search for this author in [PubMed](#) [Google Scholar](#)

66. Johan A. Gustafson

[View author publications](#)

You can also search for this author in [PubMed](#) [Google Scholar](#)

67. Tristan L. Guttridge

[View author publications](#)

You can also search for this author in [PubMed](#) [Google Scholar](#)

68. Hector M. Guzman

[View author publications](#)

You can also search for this author in [PubMed](#) [Google Scholar](#)

69. Neil Hammerschlag

[View author publications](#)

You can also search for this author in [PubMed](#) [Google Scholar](#)

70. Luke Harman

[View author publications](#)

You can also search for this author in [PubMed](#) [Google Scholar](#)

71. Fábio H. V. Hazin

[View author publications](#)

You can also search for this author in [PubMed](#) [Google Scholar](#)

72. Matthew Heard

[View author publications](#)

You can also search for this author in [PubMed](#) [Google Scholar](#)

73. Alex R. Hearn

[View author publications](#)

You can also search for this author in [PubMed](#) [Google Scholar](#)

74. John C. Holdsworth

[View author publications](#)

You can also search for this author in [PubMed](#) [Google Scholar](#)

75. Bonnie J. Holmes

[View author publications](#)

You can also search for this author in [PubMed](#) [Google Scholar](#)

76. Lucy A. Howey

[View author publications](#)

You can also search for this author in [PubMed](#) [Google Scholar](#)

77. Mauricio Hoyos

[View author publications](#)

You can also search for this author in [PubMed](#) [Google Scholar](#)

78. Robert E. Hueter

[View author publications](#)

You can also search for this author in [PubMed](#) [Google Scholar](#)

79. Nigel E. Hussey

[View author publications](#)

You can also search for this author in [PubMed](#) [Google Scholar](#)

80. Charlie Huvaneers

[View author publications](#)

You can also search for this author in [PubMed](#) [Google Scholar](#)

81. Dylan T. Irion

[View author publications](#)

You can also search for this author in [PubMed](#) [Google Scholar](#)

82. David M. P. Jacoby

[View author publications](#)

You can also search for this author in [PubMed](#) [Google Scholar](#)

83. Oliver J. D. Jewell

[View author publications](#)

You can also search for this author in [PubMed](#) [Google Scholar](#)

84. Ryan Johnson

[View author publications](#)

You can also search for this author in [PubMed](#) [Google Scholar](#)

85. Lance K. B. Jordan

[View author publications](#)

You can also search for this author in [PubMed](#) [Google Scholar](#)

86. Warren Joyce

[View author publications](#)

You can also search for this author in [PubMed](#) [Google Scholar](#)

87. Clare A. Keating Daly

[View author publications](#)

You can also search for this author in [PubMed](#) [Google Scholar](#)

88. James T. Ketchum

[View author publications](#)

You can also search for this author in [PubMed](#) [Google Scholar](#)

89. A. Peter Klimley

[View author publications](#)

You can also search for this author in [PubMed](#) [Google Scholar](#)

90. Alison A. Kock

[View author publications](#)

You can also search for this author in [PubMed](#) [Google Scholar](#)

91. Pieter Koen

[View author publications](#)

You can also search for this author in [PubMed](#) [Google Scholar](#)

92. Felipe Ladino

[View author publications](#)

You can also search for this author in [PubMed](#) [Google Scholar](#)

93. Fernanda O. Lana

[View author publications](#)

You can also search for this author in [PubMed](#) [Google Scholar](#)

94. James S. E. Lea

[View author publications](#)

You can also search for this author in [PubMed](#) [Google Scholar](#)

95. Fiona Llewellyn

[View author publications](#)

You can also search for this author in [PubMed](#) [Google Scholar](#)

96. Warrick S. Lyon

[View author publications](#)

You can also search for this author in [PubMed](#) [Google Scholar](#)

97. Anna MacDonnell

[View author publications](#)

You can also search for this author in [PubMed](#) [Google Scholar](#)

98. Bruno C. L. Macena

[View author publications](#)

You can also search for this author in [PubMed](#) [Google Scholar](#)

99. Heather Marshall

[View author publications](#)

You can also search for this author in [PubMed](#) [Google Scholar](#)

100. Jaime D. McAllister

[View author publications](#)

You can also search for this author in [PubMed](#) [Google Scholar](#)

101. Michael A. Meÿer

[View author publications](#)

You can also search for this author in [PubMed](#) [Google Scholar](#)

102. John J. Morris

[View author publications](#)

You can also search for this author in [PubMed](#) [Google Scholar](#)

103. Emily R. Nelson

[View author publications](#)

You can also search for this author in [PubMed](#) [Google Scholar](#)

104. Yannis P. Papastamatiou

[View author publications](#)

You can also search for this author in [PubMed](#) [Google Scholar](#)

105. Cesar Peñaherrera-Palma

[View author publications](#)

You can also search for this author in [PubMed](#) [Google Scholar](#)

106. Simon J. Pierce

[View author publications](#)

You can also search for this author in [PubMed](#) [Google Scholar](#)

107. Francois Poisson

[View author publications](#)

You can also search for this author in [PubMed](#) [Google Scholar](#)

108. Lina Maria Quintero

[View author publications](#)

You can also search for this author in [PubMed](#) [Google Scholar](#)

109. Andrew J. Richardson

[View author publications](#)

You can also search for this author in [PubMed](#) [Google Scholar](#)

110. Paul J. Rogers

[View author publications](#)

You can also search for this author in [PubMed](#) [Google Scholar](#)

111. Christoph A. Rohner

[View author publications](#)

You can also search for this author in [PubMed](#) [Google Scholar](#)

112. David R. L. Rowat

[View author publications](#)

You can also search for this author in [PubMed](#) [Google Scholar](#)

113. Melita Samoilys

[View author publications](#)

You can also search for this author in [PubMed](#) [Google Scholar](#)

114. Jayson M. Semmens

[View author publications](#)

You can also search for this author in [PubMed](#) [Google Scholar](#)

115. Marcus Sheaves

[View author publications](#)

You can also search for this author in [PubMed](#) [Google Scholar](#)

116. George Shillinger

[View author publications](#)

You can also search for this author in [PubMed](#) [Google Scholar](#)

117. Mahmood Shivji

[View author publications](#)

You can also search for this author in [PubMed](#) [Google Scholar](#)

118. Sarika Singh

[View author publications](#)

You can also search for this author in [PubMed](#) [Google Scholar](#)

119. Gregory B. Skomal

[View author publications](#)

You can also search for this author in [PubMed](#) [Google Scholar](#)

120. Malcolm J. Smale

[View author publications](#)

You can also search for this author in [PubMed](#) [Google Scholar](#)

121. Laurenne B. Snyders

[View author publications](#)

You can also search for this author in [PubMed](#) [Google Scholar](#)

122. German Soler

[View author publications](#)

You can also search for this author in [PubMed](#) [Google Scholar](#)

123. Marc Soria

[View author publications](#)

You can also search for this author in [PubMed](#) [Google Scholar](#)

124. Kilian M. Stehfest

[View author publications](#)

You can also search for this author in [PubMed](#) [Google Scholar](#)

125. Simon R. Thorrold

[View author publications](#)

You can also search for this author in [PubMed](#) [Google Scholar](#)

126. Mariana T. Tolotti

[View author publications](#)

You can also search for this author in [PubMed](#) [Google Scholar](#)

127. Alison Towner

[View author publications](#)

You can also search for this author in [PubMed](#) [Google Scholar](#)

128. Paulo Travassos

[View author publications](#)

You can also search for this author in [PubMed](#) [Google Scholar](#)

129. John P. Tyminski

[View author publications](#)

You can also search for this author in [PubMed](#) [Google Scholar](#)

130. Frederic Vandeperre

[View author publications](#)

You can also search for this author in [PubMed](#) [Google Scholar](#)

131. Jeremy J. Vaudo

[View author publications](#)

You can also search for this author in [PubMed](#) [Google Scholar](#)

132. Yuuki Y. Watanabe

[View author publications](#)

You can also search for this author in [PubMed](#) [Google Scholar](#)

133. Sam B. Weber

[View author publications](#)

You can also search for this author in [PubMed](#) [Google Scholar](#)

134. Bradley M. Wetherbee

[View author publications](#)

You can also search for this author in [PubMed](#) [Google Scholar](#)

135. Timothy D. White

[View author publications](#)

You can also search for this author in [PubMed](#) [Google Scholar](#)

136. Sean Williams

[View author publications](#)

You can also search for this author in [PubMed](#) [Google Scholar](#)

137. Patricia M. Zárate

[View author publications](#)

You can also search for this author in [PubMed](#) [Google Scholar](#)

138. Robert Harcourt

[View author publications](#)

You can also search for this author in [PubMed](#) [Google Scholar](#)

139. Graeme C. Hays

[View author publications](#)

You can also search for this author in [PubMed](#) [Google Scholar](#)

140. Mark G. Meekan

[View author publications](#)

You can also search for this author in [PubMed](#) [Google Scholar](#)

141. Michele Thums

[View author publications](#)

You can also search for this author in [PubMed](#) [Google Scholar](#)

142. Xabier Irigoien

[View author publications](#)

You can also search for this author in [PubMed](#) [Google Scholar](#)

143. Victor M. Eguiluz

[View author publications](#)

You can also search for this author in [PubMed](#) [Google Scholar](#)

144. Carlos M. Duarte

[View author publications](#)

You can also search for this author in [PubMed](#) [Google Scholar](#)

145. Lara L. Sousa

[View author publications](#)

You can also search for this author in [PubMed](#) [Google Scholar](#)

146. Samantha J. Simpson

[View author publications](#)

You can also search for this author in [PubMed](#) [Google Scholar](#)

147. Emily J. Southall

[View author publications](#)

You can also search for this author in [PubMed](#) [Google Scholar](#)

148. David W. Sims

[View author publications](#)

You can also search for this author in [PubMed](#) [Google Scholar](#)

Contributions

N.Q. and D.W.S. planned the data analysis. N.Q. led the data analysis with contributions from M.V., A.M.M.S. and D.W.S. N.E.H. contributed analysis tools. A.M.M.S. undertook linear-regression modelling. D.W.S. led the manuscript writing with contributions from N.Q., N.E.H., A.M.M.S and all authors. Six of the original authors were not included in the Reply authorship; two authors retired from science and the remaining four, although supportive of our Reply, declined to join the authorship due to potential conflicts of interest with the authors of the Comment and/or their institutions.

Corresponding author

Correspondence to [David W. Sims](#).

Ethics declarations

Competing interests

The authors declare no competing interests.

Additional information

Publisher's note Springer Nature remains neutral with regard to jurisdictional claims in published maps and institutional affiliations.

Extended data figures and tables

Extended Data Table 1 Global and regional drivers of FEI hotspots

[Full size table](#)

Extended Data Table 2 Examples of global and regional drivers of FEI hotspots for individual shark species

[Full size table](#)

Extended Data Table 3 Spatial refuge of pelagic sharks in ABNJs

[Full size table](#)

Extended Data Table 4 Comparison of spatial refuge estimated with AIS data 2012–2016 and 2012–2018

[Full size table](#)

Supplementary information

[Supplementary Information](#)

This file contains Supplementary Methods and Supplementary Tables 1-16.

[Reporting Summary](#)

Rights and permissions

[Reprints and Permissions](#)

About this article



Check for
updates

Cite this article

Queiroz, N., Humphries, N.E., Couto, A. *et al.* Reply to: Shark mortality cannot be assessed by fishery overlap alone. *Nature* **595**, E8–E16 (2021). <https://doi.org/10.1038/s41586-021-03397-3>

[Download citation](#)

- Published: 07 July 2021
- Issue Date: 08 July 2021
- DOI: <https://doi.org/10.1038/s41586-021-03397-3>

Comments

By submitting a comment you agree to abide by our [Terms](#) and [Community Guidelines](#). If you find something abusive or that does not comply with our terms or guidelines please flag it as inappropriate.

[Access through your institution](#)

[Change institution](#)

[Buy or subscribe](#)

Associated Content

Global spatial risk assessment of sharks under the footprint of fisheries

- Nuno Queiroz
- Nicolas E. Humphries
- David W. Sims

Advertisement

This article was downloaded by **calibre** from <https://www.nature.com/articles/s41586-021-03397-3>

| [Section menu](#) | [Main menu](#) |

- Matters Arising
- [Published: 07 July 2021](#)

Caution over the use of ecological big data for conservation

- [Alastair V. Harry](#) ORCID: orcid.org/0000-0002-9905-7909^{1,2} &
- [J. Matias Braccini](#)¹

[Nature](#) volume 595, pages E17–E19 (2021)[Cite this article](#)

- 17 Altmetric
- [Metrics details](#)

Subjects

- [Conservation biology](#)
- [Research data](#)

[Matters Arising](#) to this article was published on 07 July 2021

The [Original Article](#) was published on 24 July 2019

arising from N. Queiroz et al. *Nature* <https://doi.org/10.1038/s41586-019-1444-4> (2019)

Access options

[Subscribe to Journal](#)

Get full journal access for 1 year

\$199.00

only \$3.90 per issue

[Subscribe](#)

All prices are NET prices.

VAT will be added later in the checkout.

Tax calculation will be finalised during checkout.

Rent or Buy article

Get time limited or full article access on ReadCube.

from \$8.99

[Rent or Buy](#)

All prices are NET prices.

Additional access options:

- [Log in](#)
- [Access through your institution](#)
- [Learn about institutional subscriptions](#)

Fig. 1: Machine-learning-classified fishing effort data ($0.1^\circ \times 0.1^\circ$ grid cells) used to evaluate the risk to sharks from pelagic longline and purse seine fishing in waters under Australian jurisdiction.



Data availability

The results of the manual vessel review are available on GitHub (<https://github.com/alharry/sharkMA>).

References

1. 1.

Cheruvilil, K. S. & Soranno, P. A. Data-intensive ecological research is catalyzed by open science and team science. *Bioscience* **68**, 813–822 (2018).

[Article](#) [Google Scholar](#)

2. 2.

Kelling, S. et al. Data-intensive science: a new paradigm for biodiversity studies. *Bioscience* **59**, 613–620 (2009).

[Article](#) [Google Scholar](#)

3. 3.

Queiroz, N. et al. Global spatial risk assessment of sharks under the footprint of fisheries. *Nature* **572**, 461–466 (2019).

[ADS](#) [CAS](#) [Article](#) [Google Scholar](#)

4. 4.

Clarke, R. Big data, big risks. *Inf. Syst. J.* **26**, 77–90 (2016).

[Article](#) [Google Scholar](#)

5. 5.

Kroodsma, D. A. et al. Tracking the global footprint of fisheries. *Science* **359**, 904–908 (2018).

[ADS](#) [CAS](#) [Article](#) [Google Scholar](#)

6. 6.

Braccini, M., Molony, B. & Blay, N. Patterns in abundance and size of sharks in northwestern Australia: cause for optimism. *ICES J. Mar. Sci.* **77**, 72–82 (2020).

[Article](#) [Google Scholar](#)

7. 7.

Larcombe, J., Caton, A., Williams, D. M. & Speare, P. *Western Tuna and Billfish Fisheries Research* (Bureau of Resource Sciences, Canberra 1997).

8. 8.

Larcombe, J. & Begg, G. *Fishery Status Reports 2007. Status of Fish Stocks Managed by the Australian Government* (Bureau of Rural Sciences, Canberra 2007).

9. 9.

Hobsbawm, P. I., Patterson, H. M. & Blake, S. A. P. *Australian National Report to the Scientific Committee of the Indian Ocean Tuna Commission* (ABARES, Canberra 2020).

10. 10.

Kaplan, R. M., Chambers, D. A. & Glasgow, R. E. Big data and large sample size: a cautionary note on the potential for bias. *Clin. Transl. Sci.* **7**, 342–346 (2014).

[Article](#) [Google Scholar](#)

11. 11.

Bayraktarov, E. et al. Do big unstructured biodiversity data mean more knowledge? *Front. Ecol. Evol.* **6**, 239 (2019).

[Article](#) [Google Scholar](#)

12. 12.

Braccini, M., Blay, N., Hesp, A. & Molony, B. *Resource Assessment Report Temperate Demersal Elasmobranch Resource of Western Australia*. Fisheries Research Report No. 294 (Department of Primary Industries and Regional Development, Perth, 2018).

13. 13.

Roff, G., Brown, C. J., Priest, M. A. & Mumby, P. J. Decline of coastal apex shark populations over the past half century. *Commun. Biol.* **1**, 223 (2018).

[Article](#) [Google Scholar](#)

14. 14.

Hampton, S. E. et al. Big data and the future of ecology. *Front. Ecol. Environ.* **11**, 156–162 (2013).

[Article](#) [Google Scholar](#)

15. 15.

R Core Team. R: A language and environment for statistical computing. <http://www.R-project.org/> (R Foundation for Statistical

Computing, 2020).

[Download references](#)

Acknowledgements

We thank P. Orange and the WAFMRL Library for assistance in researching historical fishing records.

Author information

Affiliations

1. Fisheries & Agriculture Resource Management, Department of Primary Industries and Regional Development Western Australia, Hillarys, Western Australia, Australia

Alastair V. Harry & J. Matias Braccini

2. Centre for Sustainable Aquatic Ecosystems, Harry Butler Institute, Murdoch University, Murdoch, Western Australia, Australia

Alastair V. Harry

Authors

1. Alastair V. Harry

[View author publications](#)

You can also search for this author in [PubMed](#) [Google Scholar](#)

2. J. Matias Braccini

[View author publications](#)

You can also search for this author in [PubMed](#) [Google Scholar](#)

Contributions

A.V.H. carried out the analysis and wrote the first draft. A.V.H. and J.M.B. conceived the idea, interpreted the results, and edited and revised the final manuscript.

Corresponding author

Correspondence to [Alastair V. Harry](#).

Ethics declarations

Competing interests

The authors declare no competing interests.

Additional information

Publisher's note Springer Nature remains neutral with regard to jurisdictional claims in published maps and institutional affiliations.

Supplementary information

[Supplementary Information](#)

This file contains Supplementary Methods, Supplementary Figure 1, and Supplementary References.

[Reporting Summary](#)

Rights and permissions

[Reprints and Permissions](#)

About this article



Check for
updates

Cite this article

Harry, A.V., Braccini, J.M. Caution over the use of ecological big data for conservation. *Nature* **595**, E17–E19 (2021). <https://doi.org/10.1038/s41586-021-03463-w>

[Download citation](#)

- Received: 06 November 2019
- Accepted: 16 March 2021
- Published: 07 July 2021
- Issue Date: 08 July 2021
- DOI: <https://doi.org/10.1038/s41586-021-03463-w>

Comments

By submitting a comment you agree to abide by our [Terms](#) and [Community Guidelines](#). If you find something abusive or that does not comply with our terms or guidelines please flag it as inappropriate.

[Access through your institution](#)

[Change institution](#)

[Buy or subscribe](#)

Advertisement

| [Section menu](#) | [Main menu](#) |

- Matters Arising
- [Published: 07 July 2021](#)

Reply to: Caution over the use of ecological big data for conservation

- [Nuno Queiroz^{1,2}](#),
- [Nicolas E. Humphries²](#),
- [Ana Couto¹](#),
- [Marisa Vedor^{1,3}](#),
- [Ivo da Costa¹](#),
- [Ana M. M. Sequeira^{4,5}](#),
- [Gonzalo Mucientes¹](#),
- [António M. Santos^{1,3}](#),
- [Francisco J. Abascal⁶](#),
- [Debra L. Abercrombie⁷](#),
- [Katya Abrantes⁸](#),
- [David Acuña-Marrero⁹](#),
- [André S. Afonso^{10,11}](#),
- [Pedro Afonso^{12,13,14}](#),
- [Darrell Anders¹⁵](#),
- [Gonzalo Araujo¹⁶](#),
- [Randall Arauz^{17,18,19}](#),
- [Pascal Bach²⁰](#),
- [Adam Barnett⁸](#),
- [Diego Bernal²¹](#),
- [Michael L. Berumen²²](#),
- [Sandra Bessudo Lion^{19,23}](#),
- [Natalia P. A. Bezerra¹⁰](#),
- [Antonin V. Blaison²⁰](#),

- Barbara A. Block²⁴,
- Mark E. Bond²⁵,
- Ramon Bonfil²⁶,
- Camrin D. Braun^{27,28},
- Edward J. Brooks²⁹,
- Annabelle Brooks^{29,30},
- Judith Brown³¹,
- Michael E. Byrne^{32,33},
- Steven E. Campana³⁴,
- Aaron B. Carlisle³⁵,
- Demian D. Chapman²⁵,
- Taylor K. Chapple^{24 nAff108},
- John Chisholm³⁶,
- Christopher R. Clarke³⁷,
- Eric G. Clua³⁸,
- Jesse E. M. Cochran²²,
- Estelle C. Crochelet^{39,40},
- Laurent Dagorn²⁰,
- Ryan Daly^{41,42},
- Daniel Devia Cortés⁴³,
- Thomas K. Doyle^{44,45},
- Michael Drew⁴⁶,
- Clinton A. J. Duffy⁴⁷,
- Thor Erikson⁴⁸,
- Eduardo Espinoza^{19,49},
- Luciana C. Ferreira⁵⁰,
- Francesco Ferretti⁵¹,
- John D. Filmalter^{20,42},
- G. Chris Fischer⁵²,
- Richard Fitzpatrick⁸,
- Jorge Fontes^{12,13,14},
- Fabien Forget²⁰,
- Mark Fowler⁵³,
- Malcolm P. Francis⁵⁴,

- Austin J. Gallagher^{55,56},
- Enrico Gennari^{42,57,58},
- Simon D. Goldsworthy⁵⁹,
- Matthew J. Gollock⁶⁰,
- Jonathan R. Green⁶¹,
- Johan A. Gustafson⁶²,
- Tristan L. Guttridge⁶³,
- Hector M. Guzman⁶⁴,
- Neil Hammerschlag^{56,65},
- Luke Harman⁴⁴,
- Fábio H. V. Hazin¹⁰,
- Matthew Heard⁴⁶,
- Alex R. Hearn^{19,66,67},
- John C. Holdsworth⁶⁸,
- Bonnie J. Holmes^{69 nAff109},
- Lucy A. Howey⁷⁰,
- Mauricio Hoyos^{19,71},
- Robert E. Hueter⁷²,
- Nigel E. Hussey⁷³,
- Charlie Huvaneers⁴⁶,
- Dylan T. Irion⁷⁴,
- David M. P. Jacoby⁷⁵,
- Oliver J. D. Jewell^{76,77},
- Ryan Johnson⁷⁸,
- Lance K. B. Jordan⁷⁰,
- Warren Joyce⁵³,
- Clare A. Keating Daly⁴¹,
- James T. Ketchum^{19,71},
- A. Peter Klimley^{19,79},
- Alison A. Kock^{42,80,81,82},
- Pieter Koen⁸³,
- Felipe Ladino²³,
- Fernanda O. Lana^{10,84},
- James S. E. Lea^{37,85},

- Fiona Llewellyn⁶⁰,
- Warrick S. Lyon⁵⁴,
- Anna MacDonnell⁵³,
- Bruno C. L. Macena^{10,13},
- Heather Marshall^{21,86},
- Jaime D. McAllister⁸⁷,
- Michael A. Meÿer¹⁵,
- John J. Morris⁷²,
- Emily R. Nelson⁵⁶,
- Yannis P. Papastamatiou²⁵,
- Cesar Peñaherrera-Palma^{19,88},
- Simon J. Pierce⁸⁹,
- Francois Poisson²⁰,
- Lina Maria Quintero²³,
- Andrew J. Richardson⁹⁰,
- Paul J. Rogers⁵⁹,
- Christoph A. Rohner⁸⁹,
- David R. L. Rowat⁹¹,
- Melita Samoilys⁹²,
- Jayson M. Semmens⁸⁷,
- Marcus Sheaves⁸,
- George Shillinger^{19,24,93},
- Mahmood Shivji³²,
- Sarika Singh¹⁵,
- Gregory B. Skomal³⁶,
- Malcolm J. Smale⁹⁴,
- Laurenne B. Snyders¹⁵,
- German Soler^{19,23,87},
- Marc Soria²⁰,
- Kilian M. Stehfest⁸⁷,
- Simon R. Thorrold²⁸,
- Mariana T. Tolotti²⁰,
- Alison Towner^{58,77},
- Paulo Travassos¹⁰,

- [John P. Tyminski⁷²](#),
- [Frederic Vandeperre^{12,13,14}](#),
- [Jeremy J. Vaudo³²](#),
- [Yuuki Y. Watanabe^{95,96}](#),
- [Sam B. Weber⁹⁷](#),
- [Bradley M. Wetherbee^{32,98}](#),
- [Timothy D. White²⁴](#),
- [Sean Williams²⁹](#),
- [Patricia M. Zárate^{19,99}](#),
- [Robert Harcourt¹⁰⁰](#),
- [Graeme C. Hays¹⁰¹](#),
- [Mark G. Meekan⁵⁰](#),
- [Michele Thums⁵⁰](#),
- [Xabier Irigoien^{102,103}](#),
- [Victor M. Eguiluz¹⁰⁴](#),
- [Carlos M. Duarte²²](#),
- [Lara L. Sousa^{2,105}](#),
- [Samantha J. Simpson^{2,106}](#),
- [Emily J. Southall²](#) &
- [David W. Sims](#) ORCID: [orcid.org/0000-0002-0916-7363^{2,106,107}](https://orcid.org/0000-0002-0916-7363)

Nature volume **595**, pages E20–E28 (2021) [Cite this article](#)

- 38 Altmetric
- [Metrics details](#)

Subjects

- [Conservation biology](#)
- [Marine biology](#)

The [Original Article](#) was published on 07 July 2021

replying to A. V. Harry & J. M. Braccini *Nature*
<https://doi.org/10.1038/s41586-021-03463-w> (2021)

Access options

Subscribe to Journal

Get full journal access for 1 year

\$199.00

only \$3.90 per issue

[Subscribe](#)

All prices are NET prices.

VAT will be added later in the checkout.

Tax calculation will be finalised during checkout.

Rent or Buy article

Get time limited or full article access on ReadCube.

from \$8.99

[Rent or Buy](#)

All prices are NET prices.

Additional access options:

- [Log in](#)
- [Access through your institution](#)
- [Learn about institutional subscriptions](#)

Fig. 1: Comparing AIS longline fishing datasets.

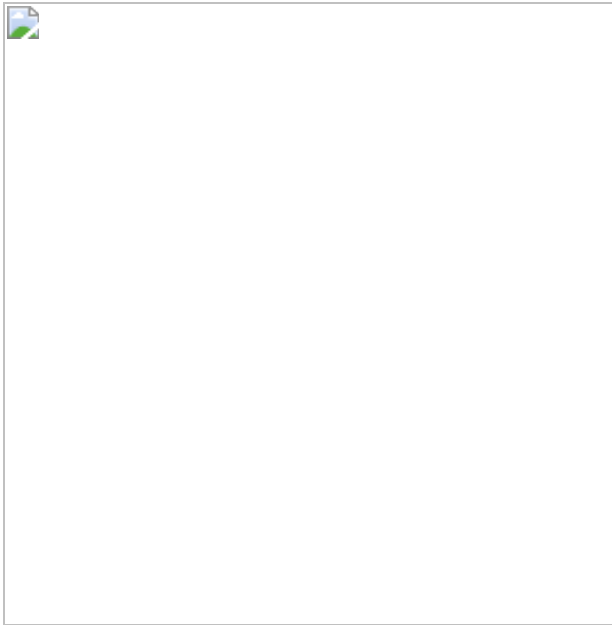
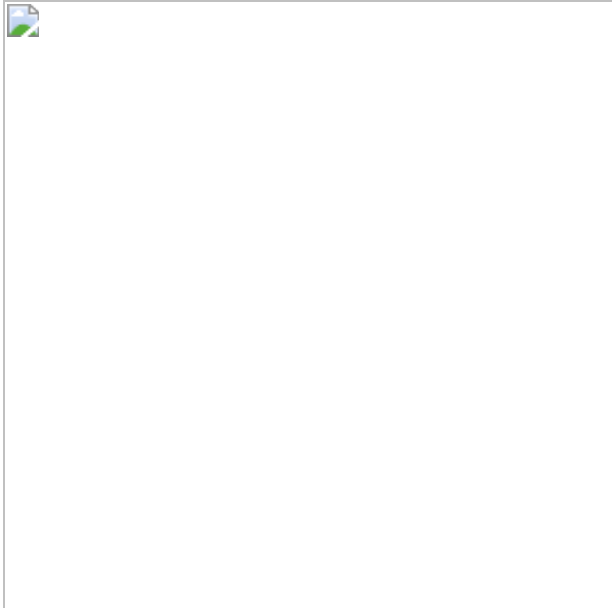


Fig. 2: Example effects of random deletions of fishing effort data on exposure risk patterns.



Data availability

Data used to prepare the maps (shark relative spatial density, longline-fishing effort and shark–longline-fishing overlap and FEI) are available on GitHub (<https://github.com/GlobalSharkMovement/GlobalSpatialRisk>).

Code availability

Code used to prepare the maps (shark relative spatial density, longline-fishing effort and shark–longline-fishing overlap and FEI) is available on GitHub (<https://github.com/GlobalSharkMovement/GlobalSpatialRisk>).

References

1. 1.

Queiroz, N. et al. Global spatial risk assessment of sharks under the footprint of fisheries. *Nature* **572**, 461–466 (2019).

[ADS](#) [CAS](#) [Article](#) [Google Scholar](#)

2. 2.

Harry, A., Braccini, M. Caution over the use of ecological big data for conservation. *Nature* <https://doi.org/10.1038/s41586-021-03463-w> (2021).

3. 3.

Kroodsma, D. A. et al. Tracking the global footprint of fisheries. *Science* **359**, 904–908 (2018).

[ADS](#) [CAS](#) [Article](#) [Google Scholar](#)

4. 4.

European Commission. European Union Fleet Register. version 1.0.8.8 https://webgate.ec.europa.eu/fleet-europa/index_en (accessed 10 April 2020).

5. 5.

Stevens, J. D. Management of shark fisheries in Northern Australia. *FAO Fisheries Technical Paper No. 378/2* <http://www.fao.org/3/x2097e/X2097E20.htm#ch16> (FAO, 1999).

6. 6.

Griffiths, S., Edgar, S., Wang, Y.-G. & Salini, J. Calculating recent foreign fishing vessel numbers using established estimators based on Coastwatch surveillance and apprehension data. *Project Number 2007/836* (Australian Fisheries Management Authority 2008).

7. 7.

Field, I. C., Meekan, M. G., Buckworth, R. C. & Bradshaw, C. J. A. Protein mining the world's oceans: Australasia as an example of illegal expansion-and-displacement fishing. *Fish Fish.* **10**, 323–328 (2009).

[Article](#) [Google Scholar](#)

8. 8.

Australian Fisheries Management Authority. Indonesian illegal fisher apprehended off Darwin convicted. <https://www.afma.gov.au/news-media/media-releases/indonesian-illegal-fisher-apprehended-darwin-convicted> (Australian Border Force and Australian Fisheries Management Authority, 1 November 2019).

9. 9.

Marshall, L. *The Fin Blue Line: quantifying Fishing Mortality using Shark Fin Morphology*. PhD Thesis, Univ. of Tasmania (2011).

10. 10.

Braccini, M., Molony, B. & Blay, N. Patterns in abundance and size of sharks in northwestern Australia: cause for optimism. *ICES J. Mar. Sci.* **77**, 72–82 (2020).

[Article](#) [Google Scholar](#)

11. 11.

Roff, G., Brown, C. J., Priest, M. A. & Mumby, P. J. Decline of coastal apex shark populations over the past half century. *Commun. Biol.* **1**, 223 (2018).

[Article](#) [Google Scholar](#)

12. 12.

Ferreira, L. C. & Simpfendorfer, C. *Galeocerdo cuvier*. e.T39378A2913541 (The IUCN Red List of Threatened Species, 2019).

13. 13.

Pirog, A. et al. Genetic population structure and demography of an apex predator, the tiger shark *Galeocerdo cuvier*. *Ecol. Evol.* **9**, 5551–5571 (2019).

[Article](#) [Google Scholar](#)

14. 14.

Hays, G. C. et al. Translating marine animal tracking data into conservation policy and management. *Trends Ecol. Evol.* **34**, 459–473 (2019).

[Article](#) [Google Scholar](#)

[Download references](#)

Acknowledgements

Funding support was provided by the Natural Environment Research Council (NERC) (NE/R00997/X/1), European Research Council (ERC-AdG-2019 883583 OCEAN DEOXYFISH) (D.W.S.), Australian Research Council (ARC DP210103091) (A.M.M.S. and D.W.S.), Fundação para a Ciência e a Tecnologia CEECIND/02857/2018 (N.Q.), PTDC/BIA-COM/28855/2017 (M.V.) and a 2020 Pew Fellowship in Marine Conservation (A.M.M.S.). This research is part of the Global Shark Movement Project (<http://globalsharkmovement.org/>).

Author information

Author notes

1. Taylor K. Chapple

Present address: Hatfield Marine Science Center, Oregon State University, Newport, OR, USA

2. Bonnie J. Holmes

Present address: The University of the Sunshine Coast, Sippy Downs, Queensland, Australia

Affiliations

1. Centro de Investigação em Biodiversidade e Recursos Genéticos/Research Network in Biodiversity and Evolutionary Biology, Campus Agrário de Vairão, Universidade do Porto, Vairão, Portugal

Nuno Queiroz, Ana Couto, Marisa Vedor, Ivo da Costa, Gonzalo Mucientes & António M. Santos

2. Marine Biological Association of the United Kingdom, Plymouth, UK

Nuno Queiroz, Nicolas E. Humphries, Lara L. Sousa, Samantha J. Simpson, Emily J. Southall & David W. Sims

3. Departamento de Biologia, Faculdade de Ciências da Universidade do Porto, Porto, Portugal

Marisa Vedor & António M. Santos

4. UWA Oceans Institute, Indian Ocean Marine Research Centre, University of Western Australia, Crawley, Western Australia, Australia

Ana M. M. Sequeira

5. School of Biological Sciences, University of Western Australia,
Crawley, Western Australia, Australia

Ana M. M. Sequeira

6. Spanish Institute of Oceanography, Santa Cruz de Tenerife, Spain

Francisco J. Abascal

7. Abercrombie and Fish, Port Jefferson Station, NY, USA

Debra L. Abercrombie

8. Marine Biology and Aquaculture Unit, College of Science and
Engineering, James Cook University, Cairns, Queensland, Australia

Katya Abrantes, Adam Barnett, Richard Fitzpatrick & Marcus Sheaves

9. Institute of Natural and Mathematical Sciences, Massey University,
Palmerston North, New Zealand

David Acuña-Marrero

10. Universidade Federal Rural de Pernambuco (UFRPE), Departamento
de Pesca e Aquicultura, Recife, Brazil

André S. Afonso, Natalia P. A. Bezerra, Fábio H. V. Hazin, Fernanda
O. Lana, Bruno C. L. Macena & Paulo Travassos

11. MARE, Marine and Environmental Sciences Centre, Instituto
Politécnico de Leiria, Peniche, Portugal

André S. Afonso

12. MARE, Laboratório Marítimo da Guia, Faculdade de Ciências da
Universidade de Lisboa, Cascais, Portugal

Pedro Afonso, Jorge Fontes & Frederic Vandeperre

13. Institute of Marine Research (IMAR), Departamento de Oceanografia e Pescas, Universidade dos Açores, Horta, Portugal

Pedro Afonso, Jorge Fontes, Bruno C. L. Macena & Frederic Vandeperre

14. Okeanos - Departamento de Oceanografia e Pescas, Universidade dos Açores, Horta, Portugal

Pedro Afonso, Jorge Fontes & Frederic Vandeperre

15. Department of Environmental Affairs, Oceans and Coasts Research, Cape Town, South Africa

Darrell Anders, Michael A. Meÿer, Sarika Singh & Laurenne B. Snyders

16. Large Marine Vertebrates Research Institute Philippines, Jagna, Philippines

Gonzalo Araujo

17. Fins Attached Marine Research and Conservation, Colorado Springs, CO, USA

Randall Arauz

18. Programa Restauración de Tortugas Marinas PRETOMA, San José, Costa Rica

Randall Arauz

19. MigraMar, Olema, CA, USA

Randall Arauz, Sandra Bessudo Lion, Eduardo Espinoza, Alex R. Hearn, Mauricio Hoyos, James T. Ketchum, A. Peter Klimley, Cesar Peñaherrera-Palma, George Shillinger, German Soler & Patricia M. Zárate

20. Institut de Recherche pour le Développement, UMR MARBEC (IRD, Ifremer, Univ. Montpellier, CNRS), Sète, France

Pascal Bach, Antonin V. Blaison, Laurent Dagorn, John D. Filmalter, Fabien Forget, Francois Poisson, Marc Soria & Mariana T. Tolotti

21. Biology Department, University of Massachusetts Dartmouth, Dartmouth, MA, USA

Diego Bernal & Heather Marshall

22. Red Sea Research Center, Division of Biological and Environmental Science and Engineering, King Abdullah University of Science and Technology, Thuwal, Saudi Arabia

Michael L. Berumen, Jesse E. M. Cochran & Carlos M. Duarte

23. Fundación Malpelo y Otros Ecosistemas Marinos, Bogota, Colombia

Sandra Bessudo Lion, Felipe Ladino, Lina Maria Quintero & German Soler

24. Hopkins Marine Station of Stanford University, Pacific Grove, CA, USA

Barbara A. Block, Taylor K. Chapple, George Shillinger & Timothy D. White

25. Department of Biological Sciences, Florida International University, North Miami, FL, USA

Mark E. Bond, Demian D. Chapman & Yannis P. Papastamatiou

26. Instituto de Ciências do Mar, Universidade Federal do Ceará, Fortaleza, Brazil

Ramon Bonfil

27. School of Fishery and Aquatic Sciences, University of Washington,
Seattle, WA, USA

Camrin D. Braun

28. Biology Department, Woods Hole Oceanographic Institution, Woods
Hole, MA, USA

Camrin D. Braun & Simon R. Thorrold

29. Shark Research and Conservation Program, Cape Eleuthera Institute,
Eleuthera, Bahamas

Edward J. Brooks, Annabelle Brooks & Sean Williams

30. University of Exeter, Exeter, UK

Annabelle Brooks

31. South Atlantic Environmental Research Institute, Stanley, Falkland
Islands

Judith Brown

32. Department of Biological Sciences, The Guy Harvey Research
Institute, Nova Southeastern University, Dania Beach, FL, USA

Michael E. Byrne, Mahmood Shivji, Jeremy J. Vaudo & Bradley M.
Wetherbee

33. School of Natural Resources, University of Missouri, Columbia, MO,
USA

Michael E. Byrne

34. Life and Environmental Sciences, University of Iceland, Reykjavik,
Iceland

Steven E. Campana

35. School of Marine Science and Policy, University of Delaware, Lewes, DE, USA

Aaron B. Carlisle

36. Massachusetts Division of Marine Fisheries, New Bedford, MA, USA

John Chisholm & Gregory B. Skomal

37. Marine Research Facility, Jeddah, Saudi Arabia

Christopher R. Clarke & James S. E. Lea

38. PSL, Labex CORAIL, CRIODE USR3278 EPHE-CNRS-UPVD, Papetoai, French Polynesia

Eric G. Clua

39. Agence de Recherche pour la Biodiversité à la Réunion (ARBRE), Réunion, Marseille, France

Estelle C. Crochelet

40. Institut de Recherche pour le Développement, UMR 228 ESPACE-DEV, Réunion, Marseille, France

Estelle C. Crochelet

41. Save Our Seas Foundation–D’Arros Research Centre (SOSF-DRC), Geneva, Switzerland

Ryan Daly & Clare A. Keating Daly

42. South African Institute for Aquatic Biodiversity (SAIAB), Grahamstown, South Africa

Ryan Daly, John D. Filmalter, Enrico Gennari & Alison A. Kock

43. Department of Fisheries Evaluation, Fisheries Research Division,
Instituto de Fomento Pesquero (IFOP), Valparaíso, Chile

Daniel Devia Cortés

44. School of Biological, Earth and Environmental Sciences, University
College Cork, Cork, Ireland

Thomas K. Doyle & Luke Harman

45. MaREI Centre, Environmental Research Institute, University College
Cork, Cork, Ireland

Thomas K. Doyle

46. College of Science and Engineering, Flinders University, Adelaide,
South Australia, Australia

Michael Drew, Matthew Heard & Charlie Huveneers

47. Department of Conservation, Auckland, New Zealand

Clinton A. J. Duffy

48. South African Institute for Aquatic Biodiversity, Geological Sciences,
UKZN, Durban, South Africa

Thor Erikson

49. Dirección Parque Nacional Galápagos, Puerto Ayora, Galápagos,
Ecuador

Eduardo Espinoza

50. Australian Institute of Marine Science, Indian Ocean Marine Research
Centre (UWA), Crawley Western Australia, Crawley, Australia

Luciana C. Ferreira, Mark G. Meekan & Michele Thums

51. Department of Fish and Wildlife Conservation, Virginia Tech,
Blacksburg, VA, USA

Francesco Ferretti

52. OCEARCH, Park City, Utah, USA

G. Chris Fischer

53. Bedford Institute of Oceanography, Dartmouth, Nova Scotia, Canada

Mark Fowler, Warren Joyce & Anna MacDonnell

54. National Institute of Water and Atmospheric Research, Wellington,
New Zealand

Malcolm P. Francis & Warrick S. Lyon

55. Beneath the Waves, Herndon, VA, USA

Austin J. Gallagher

56. Rosenstiel School of Marine and Atmospheric Science, University of
Miami, Miami, FL, USA

Austin J. Gallagher, Neil Hammerschlag & Emily R. Nelson

57. Oceans Research Institute, Mossel Bay, South Africa

Enrico Gennari

58. Department of Ichthyology and Fisheries Science, Rhodes University,
Grahamstown, South Africa

Enrico Gennari & Alison Towner

59. SARDI Aquatic Sciences, Adelaide, South Australia, Australia

Simon D. Goldsworthy & Paul J. Rogers

60. Zoological Society of London, London, UK

Matthew J. Gollock & Fiona Llewellyn

61. Galapagos Whale Shark Project, Puerto Ayora, Galapagos, Ecuador

Jonathan R. Green

62. Griffith Centre for Coastal Management, Griffith University School of Engineering, Griffith University, Gold Coast, Queensland, Australia

Johan A. Gustafson

63. Saving the Blue, Cooper City, FL, USA

Tristan L. Guttridge

64. Smithsonian Tropical Research Institute, Panama City, Panama

Hector M. Guzman

65. Leonard and Jayne Abess Center for Ecosystem Science and Policy, University of Miami, Coral Gables, FL, USA

Neil Hammerschlag

66. Galapagos Science Center, San Cristobal, Galapagos, Ecuador

Alex R. Hearn

67. Universidad San Francisco de Quito, Quito, Ecuador

Alex R. Hearn

68. Blue Water Marine Research, Tutukaka, New Zealand

John C. Holdsworth

69. University of QueenslandBrisbane, Queensland, Australia

Bonnie J. Holmes

70. Microwave Telemetry, Columbia, MD, USA

Lucy A. Howey & Lance K. B. Jordan

71. Pelagios-Kakunja, La Paz, Mexico

Mauricio Hoyos & James T. Ketchum

72. Mote Marine Laboratory, Center for Shark Research, Sarasota, FL,
USA

Robert E. Hueter, John J. Morris & John P. Tyminski

73. Biological Sciences, University of Windsor, Windsor, Ontario, Canada

Nigel E. Hussey

74. Cape Research and Diver Development, Simon's Town, South Africa

Dylan T. Irion

75. Institute of Zoology, Zoological Society of London, London, UK

David M. P. Jacoby

76. Centre for Sustainable Aquatic Ecosystems, Harry Butler Institute,
Murdoch University, Perth, Western Australia, Australia

Oliver J. D. Jewell

77. Dyer Island Conservation Trust, Western Cape, South Africa

Oliver J. D. Jewell & Alison Towner

78. Blue Wilderness Research Unit, Scottburgh, South Africa

Ryan Johnson

79. University of California Davis, Davis, CA, USA

A. Peter Klimley

80. Cape Research Centre, South African National Parks, Steenberg, South Africa

Alison A. Kock

81. Shark Spotters, Fish Hoek, South Africa

Alison A. Kock

82. Institute for Communities and Wildlife in Africa, Department of Biological Sciences, University of Cape Town, Rondebosch, South Africa

Alison A. Kock

83. Western Cape Department of Agriculture, Veterinary Services, Elsenburg, South Africa

Pieter Koen

84. Departamento de Biologia Marinha, Universidade Federal Fluminense (UFF), Niterói, Brazil

Fernanda O. Lana

85. Department of Zoology, University of Cambridge, Cambridge, UK

James S. E. Lea

86. Atlantic White Shark Conservancy, Chatham, MA, USA

Heather Marshall

87. Fisheries and Aquaculture Centre, Institute for Marine and Antarctic Studies, University of Tasmania, Hobart, Tasmania, Australia

Jaime D. McAllister, Jayson M. Semmens, German Soler & Kilian M. Stehfest

88. Pontificia Universidad Católica del Ecuador Sede Manabi, Portoviejo, Ecuador

Cesar Peñaherrera-Palma

89. Marine Megafauna Foundation, Truckee, CA, USA

Simon J. Pierce & Christoph A. Rohner

90. Conservation and Fisheries Department, Ascension Island Government, Georgetown, Ascension Island, UK

Andrew J. Richardson

91. Marine Conservation Society Seychelles, Victoria, Seychelles

David R. L. Rowat

92. CORDIO, East Africa, Mombasa, Kenya

Melita Samoilys

93. Upwell, Monterey, CA, USA

George Shillinger

94. Department of Zoology and Institute for Coastal and Marine Research, Nelson Mandela University, Port Elizabeth, South Africa

Malcolm J. Smale

95. National Institute of Polar Research, Tachikawa, Tokyo, Japan

Yuuki Y. Watanabe

96. SOKENDAI (The Graduate University for Advanced Studies),
Tachikawa, Tokyo, Japan

Yuuki Y. Watanabe

97. Centre for Ecology and Conservation, University of Exeter, Penryn,
UK

Sam B. Weber

98. Department of Biological Sciences, University of Rhode Island,
Kingston, RI, USA

Bradley M. Wetherbee

99. Department of Oceanography and Environment, Fisheries Research
Division, Instituto de Fomento Pesquero (IFOP), Valparaíso, Chile

Patricia M. Zárate

100. Department of Biological Sciences, Macquarie University, Sydney,
New South Wales, Australia

Robert Harcourt

101. School of Life and Environmental Sciences, Deakin University,
Geelong, Victoria, Australia

Graeme C. Hays

102. AZTI - BRTA, Pasaia, Spain

Xabier Irigoien

103. IKERBASQUE, Basque Foundation for Science, Bilbao, Spain

Xabier Irigoien

104. Instituto de Fisica Interdisciplinar y Sistemas Complejos, Consejo Superior de Investigaciones Cientificas, University of the Balearic Islands, Palma de Mallorca, Spain

Victor M. Eguiluz

105. Wildlife Conservation Research Unit, Department of Zoology, University of Oxford, Tubney, UK

Lara L. Sousa

106. Ocean and Earth Science, National Oceanography Centre Southampton, University of Southampton, Southampton, UK

Samantha J. Simpson & David W. Sims

107. Centre for Biological Sciences, University of Southampton, Southampton, UK

David W. Sims

Authors

1. Nuno Queiroz

[View author publications](#)

You can also search for this author in [PubMed](#) [Google Scholar](#)

2. Nicolas E. Humphries

[View author publications](#)

You can also search for this author in [PubMed](#) [Google Scholar](#)

3. Ana Couto

[View author publications](#)

You can also search for this author in [PubMed](#) [Google Scholar](#)

4. Marisa Vedor

[View author publications](#)

You can also search for this author in [PubMed](#) [Google Scholar](#)

5. Ivo da Costa

[View author publications](#)

You can also search for this author in [PubMed](#) [Google Scholar](#)

6. Ana M. M. Sequeira

[View author publications](#)

You can also search for this author in [PubMed](#) [Google Scholar](#)

7. Gonzalo Mucientes

[View author publications](#)

You can also search for this author in [PubMed](#) [Google Scholar](#)

8. António M. Santos

[View author publications](#)

You can also search for this author in [PubMed](#) [Google Scholar](#)

9. Francisco J. Abascal

[View author publications](#)

You can also search for this author in [PubMed](#) [Google Scholar](#)

10. Debra L. Abercrombie

[View author publications](#)

You can also search for this author in [PubMed](#) [Google Scholar](#)

11. Katya Abrantes

[View author publications](#)

You can also search for this author in [PubMed](#) [Google Scholar](#)

12. David Acuña-Marrero

[View author publications](#)

You can also search for this author in [PubMed](#) [Google Scholar](#)

13. André S. Afonso

[View author publications](#)

You can also search for this author in [PubMed](#) [Google Scholar](#)

14. Pedro Afonso

[View author publications](#)

You can also search for this author in [PubMed](#) [Google Scholar](#)

15. Darrell Anders

[View author publications](#)

You can also search for this author in [PubMed](#) [Google Scholar](#)

16. Gonzalo Araujo

[View author publications](#)

You can also search for this author in [PubMed](#) [Google Scholar](#)

17. Randall Arauz

[View author publications](#)

You can also search for this author in [PubMed](#) [Google Scholar](#)

18. Pascal Bach

[View author publications](#)

You can also search for this author in [PubMed](#) [Google Scholar](#)

19. Adam Barnett

[View author publications](#)

You can also search for this author in [PubMed](#) [Google Scholar](#)

20. Diego Bernal

[View author publications](#)

You can also search for this author in [PubMed](#) [Google Scholar](#)

21. Michael L. Berumen

[View author publications](#)

You can also search for this author in [PubMed](#) [Google Scholar](#)

22. Sandra Bessudo Lion

[View author publications](#)

You can also search for this author in [PubMed](#) [Google Scholar](#)

23. Natalia P. A. Bezerra

[View author publications](#)

You can also search for this author in [PubMed](#) [Google Scholar](#)

24. Antonin V. Blaison

[View author publications](#)

You can also search for this author in [PubMed](#) [Google Scholar](#)

25. Barbara A. Block

[View author publications](#)

You can also search for this author in [PubMed](#) [Google Scholar](#)

26. Mark E. Bond

[View author publications](#)

You can also search for this author in [PubMed](#) [Google Scholar](#)

27. Ramon Bonfil

[View author publications](#)

You can also search for this author in [PubMed](#) [Google Scholar](#)

28. Camrin D. Braun

[View author publications](#)

You can also search for this author in [PubMed](#) [Google Scholar](#)

29. Edward J. Brooks

[View author publications](#)

You can also search for this author in [PubMed](#) [Google Scholar](#)

30. Annabelle Brooks

[View author publications](#)

You can also search for this author in [PubMed](#) [Google Scholar](#)

31. Judith Brown

[View author publications](#)

You can also search for this author in [PubMed](#) [Google Scholar](#)

32. Michael E. Byrne

[View author publications](#)

You can also search for this author in [PubMed](#) [Google Scholar](#)

33. Steven E. Campana

[View author publications](#)

You can also search for this author in [PubMed](#) [Google Scholar](#)

34. Aaron B. Carlisle

[View author publications](#)

You can also search for this author in [PubMed](#) [Google Scholar](#)

35. Demian D. Chapman

[View author publications](#)

You can also search for this author in [PubMed](#) [Google Scholar](#)

36. Taylor K. Chapple

[View author publications](#)

You can also search for this author in [PubMed](#) [Google Scholar](#)

37. John Chisholm

[View author publications](#)

You can also search for this author in [PubMed](#) [Google Scholar](#)

38. Christopher R. Clarke

[View author publications](#)

You can also search for this author in [PubMed](#) [Google Scholar](#)

39. Eric G. Clua

[View author publications](#)

You can also search for this author in [PubMed](#) [Google Scholar](#)

40. Jesse E. M. Cochran

[View author publications](#)

You can also search for this author in [PubMed](#) [Google Scholar](#)

41. Estelle C. Crochelet

[View author publications](#)

You can also search for this author in [PubMed](#) [Google Scholar](#)

42. Laurent Dagorn

[View author publications](#)

You can also search for this author in [PubMed](#) [Google Scholar](#)

43. Ryan Daly

[View author publications](#)

You can also search for this author in [PubMed](#) [Google Scholar](#)

44. Daniel Devia Cortés

[View author publications](#)

You can also search for this author in [PubMed](#) [Google Scholar](#)

45. Thomas K. Doyle

[View author publications](#)

You can also search for this author in [PubMed](#) [Google Scholar](#)

46. Michael Drew

[View author publications](#)

You can also search for this author in [PubMed](#) [Google Scholar](#)

47. Clinton A. J. Duffy

[View author publications](#)

You can also search for this author in [PubMed](#) [Google Scholar](#)

48. Thor Erikson

[View author publications](#)

You can also search for this author in [PubMed](#) [Google Scholar](#)

49. Eduardo Espinoza

[View author publications](#)

You can also search for this author in [PubMed](#) [Google Scholar](#)

50. Luciana C. Ferreira

[View author publications](#)

You can also search for this author in [PubMed](#) [Google Scholar](#)

51. Francesco Ferretti

[View author publications](#)

You can also search for this author in [PubMed](#) [Google Scholar](#)

52. John D. Filmalter

[View author publications](#)

You can also search for this author in [PubMed](#) [Google Scholar](#)

53. G. Chris Fischer

[View author publications](#)

You can also search for this author in [PubMed](#) [Google Scholar](#)

54. Richard Fitzpatrick

[View author publications](#)

You can also search for this author in [PubMed](#) [Google Scholar](#)

55. Jorge Fontes

[View author publications](#)

You can also search for this author in [PubMed](#) [Google Scholar](#)

56. Fabien Forget

[View author publications](#)

You can also search for this author in [PubMed](#) [Google Scholar](#)

57. Mark Fowler

[View author publications](#)

You can also search for this author in [PubMed](#) [Google Scholar](#)

58. Malcolm P. Francis

[View author publications](#)

You can also search for this author in [PubMed](#) [Google Scholar](#)

59. Austin J. Gallagher

[View author publications](#)

You can also search for this author in [PubMed](#) [Google Scholar](#)

60. Enrico Gennari

[View author publications](#)

You can also search for this author in [PubMed](#) [Google Scholar](#)

61. Simon D. Goldsworthy

[View author publications](#)

You can also search for this author in [PubMed](#) [Google Scholar](#)

62. Matthew J. Gollock

[View author publications](#)

You can also search for this author in [PubMed](#) [Google Scholar](#)

63. Jonathan R. Green

[View author publications](#)

You can also search for this author in [PubMed](#) [Google Scholar](#)

64. Johan A. Gustafson

[View author publications](#)

You can also search for this author in [PubMed](#) [Google Scholar](#)

65. Tristan L. Guttridge

[View author publications](#)

You can also search for this author in [PubMed](#) [Google Scholar](#)

66. Hector M. Guzman

[View author publications](#)

You can also search for this author in [PubMed](#) [Google Scholar](#)

67. Neil Hammerschlag

[View author publications](#)

You can also search for this author in [PubMed](#) [Google Scholar](#)

68. Luke Harman

[View author publications](#)

You can also search for this author in [PubMed](#) [Google Scholar](#)

69. Fábio H. V. Hazin

[View author publications](#)

You can also search for this author in [PubMed](#) [Google Scholar](#)

70. Matthew Heard

[View author publications](#)

You can also search for this author in [PubMed](#) [Google Scholar](#)

71. Alex R. Hearn

[View author publications](#)

You can also search for this author in [PubMed](#) [Google Scholar](#)

72. John C. Holdsworth

[View author publications](#)

You can also search for this author in [PubMed](#) [Google Scholar](#)

73. Bonnie J. Holmes

[View author publications](#)

You can also search for this author in [PubMed](#) [Google Scholar](#)

74. Lucy A. Howey

[View author publications](#)

You can also search for this author in [PubMed](#) [Google Scholar](#)

75. Mauricio Hoyos

[View author publications](#)

You can also search for this author in [PubMed](#) [Google Scholar](#)

76. Robert E. Hueter

[View author publications](#)

You can also search for this author in [PubMed](#) [Google Scholar](#)

77. Nigel E. Hussey

[View author publications](#)

You can also search for this author in [PubMed](#) [Google Scholar](#)

78. Charlie Huvveneers

[View author publications](#)

You can also search for this author in [PubMed](#) [Google Scholar](#)

79. Dylan T. Irion

[View author publications](#)

You can also search for this author in [PubMed](#) [Google Scholar](#)

80. David M. P. Jacoby

[View author publications](#)

You can also search for this author in [PubMed](#) [Google Scholar](#)

81. Oliver J. D. Jewell

[View author publications](#)

You can also search for this author in [PubMed](#) [Google Scholar](#)

82. Ryan Johnson

[View author publications](#)

You can also search for this author in [PubMed](#) [Google Scholar](#)

83. Lance K. B. Jordan

[View author publications](#)

You can also search for this author in [PubMed](#) [Google Scholar](#)

84. Warren Joyce

[View author publications](#)

You can also search for this author in [PubMed](#) [Google Scholar](#)

85. Clare A. Keating Daly

[View author publications](#)

You can also search for this author in [PubMed](#) [Google Scholar](#)

86. James T. Ketchum

[View author publications](#)

You can also search for this author in [PubMed](#) [Google Scholar](#)

87. A. Peter Klimley

[View author publications](#)

You can also search for this author in [PubMed](#) [Google Scholar](#)

88. Alison A. Kock

[View author publications](#)

You can also search for this author in [PubMed](#) [Google Scholar](#)

89. Pieter Koen

[View author publications](#)

You can also search for this author in [PubMed](#) [Google Scholar](#)

90. Felipe Ladino

[View author publications](#)

You can also search for this author in [PubMed](#) [Google Scholar](#)

91. Fernanda O. Lana

[View author publications](#)

You can also search for this author in [PubMed](#) [Google Scholar](#)

92. James S. E. Lea

[View author publications](#)

You can also search for this author in [PubMed](#) [Google Scholar](#)

93. Fiona Llewellyn

[View author publications](#)

You can also search for this author in [PubMed](#) [Google Scholar](#)

94. Warrick S. Lyon

[View author publications](#)

You can also search for this author in [PubMed](#) [Google Scholar](#)

95. Anna MacDonnell

[View author publications](#)

You can also search for this author in [PubMed](#) [Google Scholar](#)

96. Bruno C. L. Macena

[View author publications](#)

You can also search for this author in [PubMed](#) [Google Scholar](#)

97. Heather Marshall

[View author publications](#)

You can also search for this author in [PubMed](#) [Google Scholar](#)

98. Jaime D. McAllister

[View author publications](#)

You can also search for this author in [PubMed](#) [Google Scholar](#)

99. Michael A. Meÿer

[View author publications](#)

You can also search for this author in [PubMed](#) [Google Scholar](#)

100. John J. Morris

[View author publications](#)

You can also search for this author in [PubMed](#) [Google Scholar](#)

101. Emily R. Nelson

[View author publications](#)

You can also search for this author in [PubMed](#) [Google Scholar](#)

102. Yannis P. Papastamatiou

[View author publications](#)

You can also search for this author in [PubMed](#) [Google Scholar](#)

103. Cesar Peñaherrera-Palma

[View author publications](#)

You can also search for this author in [PubMed](#) [Google Scholar](#)

104. Simon J. Pierce

[View author publications](#)

You can also search for this author in [PubMed](#) [Google Scholar](#)

105. Francois Poisson

[View author publications](#)

You can also search for this author in [PubMed](#) [Google Scholar](#)

106. Lina Maria Quintero

[View author publications](#)

You can also search for this author in [PubMed](#) [Google Scholar](#)

107. Andrew J. Richardson

[View author publications](#)

You can also search for this author in [PubMed](#) [Google Scholar](#)

108. Paul J. Rogers

[View author publications](#)

You can also search for this author in [PubMed](#) [Google Scholar](#)

109. Christoph A. Rohner

[View author publications](#)

You can also search for this author in [PubMed](#) [Google Scholar](#)

110. David R. L. Rowat

[View author publications](#)

You can also search for this author in [PubMed](#) [Google Scholar](#)

111. Melita Samoilys

[View author publications](#)

You can also search for this author in [PubMed](#) [Google Scholar](#)

112. Jayson M. Semmens

[View author publications](#)

You can also search for this author in [PubMed](#) [Google Scholar](#)

113. Marcus Sheaves

[View author publications](#)

You can also search for this author in [PubMed](#) [Google Scholar](#)

114. George Shillinger

[View author publications](#)

You can also search for this author in [PubMed](#) [Google Scholar](#)

115. Mahmood Shivji

[View author publications](#)

You can also search for this author in [PubMed](#) [Google Scholar](#)

116. Sarika Singh

[View author publications](#)

You can also search for this author in [PubMed](#) [Google Scholar](#)

117. Gregory B. Skomal

[View author publications](#)

You can also search for this author in [PubMed](#) [Google Scholar](#)

118. Malcolm J. Smale

[View author publications](#)

You can also search for this author in [PubMed](#) [Google Scholar](#)

119. Laurenne B. Snyders

[View author publications](#)

You can also search for this author in [PubMed](#) [Google Scholar](#)

120. German Soler

[View author publications](#)

You can also search for this author in [PubMed](#) [Google Scholar](#)

121. Marc Soria

[View author publications](#)

You can also search for this author in [PubMed](#) [Google Scholar](#)

122. Kilian M. Stehfest

[View author publications](#)

You can also search for this author in [PubMed](#) [Google Scholar](#)

123. Simon R. Thorrold

[View author publications](#)

You can also search for this author in [PubMed](#) [Google Scholar](#)

124. Mariana T. Tolotti

[View author publications](#)

You can also search for this author in [PubMed](#) [Google Scholar](#)

125. Alison Towner

[View author publications](#)

You can also search for this author in [PubMed](#) [Google Scholar](#)

126. Paulo Travassos

[View author publications](#)

You can also search for this author in [PubMed](#) [Google Scholar](#)

127. John P. Tyminski

[View author publications](#)

You can also search for this author in [PubMed](#) [Google Scholar](#)

128. Frederic Vandeperre

[View author publications](#)

You can also search for this author in [PubMed](#) [Google Scholar](#)

129. Jeremy J. Vaudo

[View author publications](#)

You can also search for this author in [PubMed](#) [Google Scholar](#)

130. Yuuki Y. Watanabe

[View author publications](#)

You can also search for this author in [PubMed](#) [Google Scholar](#)

131. Sam B. Weber

[View author publications](#)

You can also search for this author in [PubMed](#) [Google Scholar](#)

132. Bradley M. Wetherbee
[View author publications](#)

You can also search for this author in [PubMed](#) [Google Scholar](#)

133. Timothy D. White
[View author publications](#)

You can also search for this author in [PubMed](#) [Google Scholar](#)

134. Sean Williams
[View author publications](#)

You can also search for this author in [PubMed](#) [Google Scholar](#)

135. Patricia M. Zárate
[View author publications](#)

You can also search for this author in [PubMed](#) [Google Scholar](#)

136. Robert Harcourt
[View author publications](#)

You can also search for this author in [PubMed](#) [Google Scholar](#)

137. Graeme C. Hays
[View author publications](#)

You can also search for this author in [PubMed](#) [Google Scholar](#)

138. Mark G. Meekan
[View author publications](#)

You can also search for this author in [PubMed](#) [Google Scholar](#)

139. Michele Thums
[View author publications](#)

You can also search for this author in [PubMed](#) [Google Scholar](#)

140. Xabier Irigoien

[View author publications](#)

You can also search for this author in [PubMed](#) [Google Scholar](#)

141. Victor M. Eguiluz

[View author publications](#)

You can also search for this author in [PubMed](#) [Google Scholar](#)

142. Carlos M. Duarte

[View author publications](#)

You can also search for this author in [PubMed](#) [Google Scholar](#)

143. Lara L. Sousa

[View author publications](#)

You can also search for this author in [PubMed](#) [Google Scholar](#)

144. Samantha J. Simpson

[View author publications](#)

You can also search for this author in [PubMed](#) [Google Scholar](#)

145. Emily J. Southall

[View author publications](#)

You can also search for this author in [PubMed](#) [Google Scholar](#)

146. David W. Sims

[View author publications](#)

You can also search for this author in [PubMed](#) [Google Scholar](#)

Contributions

N.Q. and D.W.S. planned the data analysis. N.Q. led the data analysis with contributions from M.V. and D.W.S. N.E.H. contributed analysis tools.

D.W.S. led the manuscript writing with contributions from N.Q., N.E.H. and all authors. Seven of the original authors were not included in the Reply authorship; two authors retired from science and the remaining five, although supportive of our Reply, declined to join the authorship due to potential conflicts of interest with the authors of the Comment and/or their institutions.

Corresponding author

Correspondence to [David W. Sims](#).

Ethics declarations

Competing interests

The authors declare no competing interests.

Additional information

Publisher's note Springer Nature remains neutral with regard to jurisdictional claims in published maps and institutional affiliations.

Extended data figures and tables

[Extended Data Fig. 1 Comparing shark exposure risk between AIS longline fishing effort datasets.](#)

a–d, Estimated exposure risk of sharks to capture by GFW AIS longline fishing effort across ocean regions for Queiroz et al.¹ (**a**) compared with three improved data releases since the paper was published (**b–d**). The plots show minor effects of any changes on estimates of shark exposure risk from AIS longline fishing effort and confirm the global results and conclusions of our paper. **a**, Data from Queiroz et al.¹. **b**, Data from GWF 2012–2016. **c**, Data from GWF 2012–2018. **d**, Data from GWF 2018.

Extended Data Table 1 Mean monthly spatial overlap estimates (%) of pelagic shark space use and AIS longline fishing effort for different AIS datasets

[Full size table](#)

Extended Data Table 2 Effect of 1% random deletion of fishing effort grid cells within each region on risk exposure estimates

[Full size table](#)

Extended Data Table 3 Effect of 5% random deletion of fishing effort grid cells within each region on risk exposure estimates

[Full size table](#)

Supplementary information

Supplementary Information

This file contains Supplementary Methods, Supplementary Figures 1 and 2, and Supplementary Tables 1-7.

Reporting Summary

Rights and permissions

Reprints and Permissions

About this article



Check for
updates

Cite this article

Queiroz, N., Humphries, N.E., Couto, A. *et al.* Reply to: Caution over the use of ecological big data for conservation. *Nature* **595**, E20–E28 (2021). <https://doi.org/10.1038/s41586-021-03464-9>

Download citation

- Published: 07 July 2021
- Issue Date: 08 July 2021
- DOI: <https://doi.org/10.1038/s41586-021-03464-9>

Comments

By submitting a comment you agree to abide by our [Terms](#) and [Community Guidelines](#). If you find something abusive or that does not comply with our

terms or guidelines please flag it as inappropriate.

[Access through your institution](#)

[Change institution](#)

[Buy or subscribe](#)

Associated Content

[Global spatial risk assessment of sharks under the footprint of fisheries](#)

- Nuno Queiroz
- Nicolas E. Humphries
- David W. Sims

Advertisement

This article was downloaded by **calibre** from <https://www.nature.com/articles/s41586-021-03464-9>

| [Section menu](#) | [Main menu](#) |

- Matters Arising
- [Published: 07 July 2021](#)

Treatment of missing data determined conclusions regarding moralizing gods

- [Bret Beheim](#) ORCID: [orcid.org/0000-0003-4653-3155¹](https://orcid.org/0000-0003-4653-3155),
- [Quentin D. Atkinson](#) ORCID: [orcid.org/0000-0002-8499-7535²](https://orcid.org/0000-0002-8499-7535),
- [Joseph Bulbulia³](#),
- [Will Gervais⁴](#),
- [Russell D. Gray](#) ORCID: [orcid.org/0000-0002-9858-0191^{5,6}](https://orcid.org/0000-0002-9858-0191),
- [Joseph Henrich](#) ORCID: [orcid.org/0000-0002-5012-0065⁷](https://orcid.org/0000-0002-5012-0065),
- [Martin Lang⁸](#),
- [M. Willis Monroe](#) ORCID: [orcid.org/0000-0002-9126-2991⁹](https://orcid.org/0000-0002-9126-2991),
- [Michael Muthukrishna](#) ORCID: [orcid.org/0000-0002-7079-5166¹⁰](https://orcid.org/0000-0002-7079-5166),
- [Ara Norenzayan¹¹](#),
- [Benjamin Grant Purzycki](#) ORCID: [orcid.org/0000-0002-9595-7360¹²](https://orcid.org/0000-0002-9595-7360),
- [Azim Shariff](#) ORCID: [orcid.org/0000-0003-4444-460X¹¹](https://orcid.org/0000-0003-4444-460X),
- [Edward Slingerland⁹](#),
- [Rachel Spicer](#) ORCID: [orcid.org/0000-0002-2807-8796¹⁰](https://orcid.org/0000-0002-2807-8796) &
- [Aiyana K. Willard⁴](#)

[Nature](#) volume 595, pages E29–E34 (2021) [Cite this article](#)

- 1 Citations
- 94 Altmetric
- [Metrics details](#)

Subjects

- [History](#)
- [Religion](#)

The [Original Article](#) was published on 20 March 2019

arising from H. Whitehouse et al. *Nature* <https://doi.org/10.1038/s41586-019-1043-4> (2019)

Access options

Subscribe to Journal

Get full journal access for 1 year

\$199.00

only \$3.90 per issue

[Subscribe](#)

All prices are NET prices.

VAT will be added later in the checkout.

Tax calculation will be finalised during checkout.

Rent or Buy article

Get time limited or full article access on ReadCube.

from \$8.99

[Rent or Buy](#)

All prices are NET prices.

Additional access options:

- [Log in](#)
- [Access through your institution](#)
- [Learn about institutional subscriptions](#)

Fig. 1: Moralizing gods across 12 key regions.

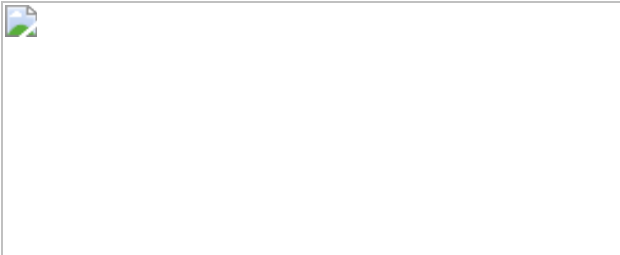


Fig. 2: Comparison of the original logistic regression model and a reanalysis removing unknown outcomes.



Data availability

Supplementary data are available at <https://github.com/babeheim/moralizing-gods-reanalysis>. All software is freely available under Creative Commons License CC BY-NC-SA 4.0. Source materials are available at <http://seshatdatabank.info>.

Code availability

Re-analysis code is available at <https://github.com/babeheim/moralizing-gods-reanalysis>. All software is freely available under Creative Commons License CC BY-NC-SA 4.0.

References

1. 1.

Whitehouse, H., et al. Complex societies precede moralizing gods throughout world history. *Nature* **568**, 226–229 (2019).

[ADS](#) [CAS](#) [Article](#) [Google Scholar](#)

2. 2.

Seshat: The Global History Databank (Evolution Institute & Seshat Project, 2015); <http://seshatdatabank.info/>

3. 3.

Watts, J. et al. Broad supernatural punishment but not moralizing high gods precede the evolution of political complexity in Austronesia. *Proc. R. Soc. Lond. B* **282**, 20142556 (2015).

[Google Scholar](#)

4. 4.

Little, R. J. A. & Rubin, D. B. *Statistical Analysis with Missing Data* (John Wiley & Sons, 2014).

5. 5.

McElreath, R. *Statistical Rethinking: A Bayesian Course with Examples in R and Stan* (Chapman and Hall/CRC, 2020).

6. 6.

Gelman, A. & Hill, J. *Data Analysis Using Regression and Multilevel/hierarchical Models*. (Cambridge University Press, 2007).

7. 7.

Wheatley, P. *The Pivot of the Four Quarters: A Preliminary Enquiry into the Origins and Character of the Ancient Chinese City* (Edinburgh

University Press, 1971)

[Download references](#)

Acknowledgements

We thank H. Whitehouse and co-authors for responding to our request for clarification and to our early notification of our intent to submit this report, and for making their code, source material, and data public. We thank three anonymous reviewers as well as the Department of Human Behavior, Ecology and Culture at the Max Planck Institute for Evolutionary Anthropology, H. Colleran, J. C. Jackson, R. McElreath, E. Ready and J. Watts for feedback, and A. Ashtari, A. Barnett and T. Hwang for research and administrative support.

Author information

Affiliations

1. Department of Human Behavior, Ecology and Culture, Max Planck Institute for Evolutionary Anthropology, Leipzig, Germany

Bret Beheim

2. School of Psychology, University of Auckland, Auckland, New Zealand

Quentin D. Atkinson

3. School of Psychology, Victoria University of Wellington, Wellington, New Zealand

Joseph Bulbulia

4. Centre for Culture and Evolution, Brunel University London, Uxbridge, UK

Will Gervais & Aiyana K. Willard

5. Department of Linguistic and Cultural Evolution, Max Planck Institute for Evolutionary Anthropology, Leipzig, Germany

Russell D. Gray

6. School of Psychology, University of Auckland, Auckland, New Zealand

Russell D. Gray

7. Department of Human Evolutionary Biology, Harvard University, Boston, MA, USA

Joseph Henrich

8. LEVYNA: Laboratory for the Experimental Research of Religion, Masaryk University, Brno, Czech Republic

Martin Lang

9. Department of Asian Studies, University of British Columbia, Vancouver, British Columbia, Canada

M. Willis Monroe & Edward Slingerland

10. Department of Psychological and Behavioural Science, London School of Economics, London, UK

Michael Muthukrishna & Rachel Spicer

11. Department of Psychology, University of British Columbia, Vancouver, British Columbia, Canada

Ara Norenzayan & Azim Shariff

12. Department of the Study of Religion, Aarhus University, Aarhus, Denmark

Benjamin Grant Purzycki

Authors

1. Bret Beheim

[View author publications](#)

You can also search for this author in [PubMed](#) [Google Scholar](#)

2. Quentin D. Atkinson

[View author publications](#)

You can also search for this author in [PubMed](#) [Google Scholar](#)

3. Joseph Bulbulia

[View author publications](#)

You can also search for this author in [PubMed](#) [Google Scholar](#)

4. Will Gervais

[View author publications](#)

You can also search for this author in [PubMed](#) [Google Scholar](#)

5. Russell D. Gray

[View author publications](#)

You can also search for this author in [PubMed](#) [Google Scholar](#)

6. Joseph Henrich

[View author publications](#)

You can also search for this author in [PubMed](#) [Google Scholar](#)

7. Martin Lang

[View author publications](#)

You can also search for this author in [PubMed](#) [Google Scholar](#)

8. M. Willis Monroe

[View author publications](#)

You can also search for this author in [PubMed](#) [Google Scholar](#)

9. Michael Muthukrishna

[View author publications](#)

You can also search for this author in [PubMed](#) [Google Scholar](#)

10. Ara Norenzayan

[View author publications](#)

You can also search for this author in [PubMed](#) [Google Scholar](#)

11. Benjamin Grant Purzycki

[View author publications](#)

You can also search for this author in [PubMed](#) [Google Scholar](#)

12. Azim Shariff

[View author publications](#)

You can also search for this author in [PubMed](#) [Google Scholar](#)

13. Edward Slingerland

[View author publications](#)

You can also search for this author in [PubMed](#) [Google Scholar](#)

14. Rachel Spicer

[View author publications](#)

You can also search for this author in [PubMed](#) [Google Scholar](#)

15. Aiyana K. Willard

[View author publications](#)

You can also search for this author in [PubMed](#) [Google Scholar](#)

Contributions

R.S., B.G.P., M.M., M.L., J.H., R.D.G., B.B. and Q.D.A. designed the reanalysis. R.S., M.L., B.G.P. and B.B. performed the re-analyses. R.S., M.L. and B.G.P. reviewed code. E.S. and M.W.M. reviewed and vetted historical coding. All authors wrote the manuscript.

Corresponding author

Correspondence to [Bret Beheim](#).

Ethics declarations

Competing interests

R.D.G., J.H., M.M., M.W.M., E.S. and R.S. are involved in the Database of Religious History (DRH) project, another freely available online historical database.

Additional information

Publisher's note Springer Nature remains neutral with regard to jurisdictional claims in published maps and institutional affiliations.

Extended data figures and tables

[Extended Data Fig. 1 The first appearance of writing and moralizing gods across NGAs.](#)

The solid line indicates when writing and moralizing gods (MGs) are first recorded in the same century, and the dashed lines show when writing appeared 100 years before moralizing gods and when moralizing gods appeared 100 years before writing. NGAs are coloured by whether social complexity data are available both before and after the appearance of moralizing gods or not. Only natural geographic areas with social

complexity data available both before and after the appearance of moralizing gods were included in the analysis (and only these natural geographic areas are shown in Fig. 1). It must be noted that while writing first appears at 2500 bc in the Kachi Plain, it is absent for the subsequent two polities in the dataset, and does not reappear until 300 bc —the same time as the first appearance of moralizing gods.

Extended Data Fig. 2 Distribution of social complexity score by ‘moralizing gods’ outcome status.

Before statistical analyses were performed in Whitehouse, et al.¹, all ‘unknown’ or ‘suspected unknown’ (NA) cases were treated as moralizing gods ‘absent’ (0) without explicit description in the manuscript. In box plots centre line shows median, box limits indicate upper and lower quartiles and whiskers span 1.5× interquartile range). $N = 801$ observations.

Extended Data Fig. 3 Social complexity before and after the appearance of moralizing gods.

Dots represent mean social complexity as calculated by Whitehouse, et al.¹ (a combination of population and territory size, infrastructure, hierarchy, and other factors, standardized between 0 and 1) collapsed across natural geographical area. Data are mean \pm s.e.m. The shading of lines connecting the dots in **a** reflects the weight that the difference (d_1, \dots, d_7 ; on d_1 and d_2 are shown) between the social complexity at time point n and time point 0 in the *t*-test analysis performed by Whitehouse, et al.¹ (that is, differences in social complexity are highest around time 0, hence driving the forward bias). Note that the increase in social complexity from time point -100 to 0 is coded as pre-moralizing gods, while the complexity often arrives via conquest or mission together with moralizing gods. **a**, The ‘first appearance’ of moralizing gods (MGs) in the archaeo-historical records follows a sharp increase (39%) in social complexity in the 12 geographical areas. **b**, The sharp increase in social complexity just before the appearance of moralizing gods is partially caused by ascribing properties of conquerors to the conquered regions in the Deccan, Kachi Plain and Sogdiana regions. **c**, Similarly, regions receiving moralizing gods via mission (Kansai, Niger

Inland Delta and Orkhon Valley) experience a sharp increase in social complexity. **d**, The remaining six natural geographical areas where moralizing gods were not first recorded through conquest by a larger empire or through mission show a steady rise in social complexity.

Supplementary information

Supplementary Methods

This file provides additional ethnographic justification and statistical details for the re-analyses of Whitehouse, et al. (2019), including Supplemental Figures 1-5, Supplementary Tables 1-4 and Supplementary References.

Reporting Summary

Rights and permissions

Reprints and Permissions

About this article



Check for
updates

Cite this article

Beheim, B., Atkinson, Q.D., Bulbulia, J. *et al.* Treatment of missing data determined conclusions regarding moralizing gods. *Nature* **595**, E29–E34 (2021). <https://doi.org/10.1038/s41586-021-03655-4>

Download citation

- Received: 02 May 2019

- Accepted: 18 February 2021
- Published: 07 July 2021
- Issue Date: 08 July 2021
- DOI: <https://doi.org/10.1038/s41586-021-03655-4>

Further reading

- [**Retraction Note: Complex societies precede moralizing gods throughout world history**](#)
 - Harvey Whitehouse
 - , Pieter FranÃ§ois
 - , Patrick E. Savage
 - , Thomas E. Currie
 - , Kevin C. Feeney
 - , Enrico Cioni
 - , Rosalind Purcell
 - , Robert M. Ross
 - , Jennifer Larson
 - , John Baines
 - , Barend ter Haar
 - , Alan Covey
 - & Peter Turchin

Nature (2021)

Comments

By submitting a comment you agree to abide by our [Terms](#) and [Community Guidelines](#). If you find something abusive or that does not comply with our terms or guidelines please flag it as inappropriate.

[Access through your institution](#)

[Change institution](#)

[Buy or subscribe](#)

Advertisement

This article was downloaded by **calibre** from <https://www.nature.com/articles/s41586-021-03655-4>

| [Section menu](#) | [Main menu](#) |

Amendments & Corrections

- [**Author Correction: Assembly of synaptic active zones requires phase separation of scaffold molecules**](#) [18 June 2021]
Author Correction •
- [**Retraction Note: Complex societies precede moralizing gods throughout world history**](#) [07 July 2021]
Retraction •

Author Correction: Assembly of synaptic active zones requires phase separation of scaffold molecules

[Download PDF](#)

- Author Correction
- [Published: 18 June 2021](#)

Author Correction: Assembly of synaptic active zones requires phase separation of scaffold molecules

- [Nathan A. McDonald¹](#),
- [Richard D. Fetter²](#) &
- [Kang Shen](#) ORCID: [orcid.org/0000-0003-4059-8249^{1,2}](https://orcid.org/0000-0003-4059-8249)

Nature volume 595, page E35 (2021)[Cite this article](#)

- 448 Accesses
- 3 Altmetric
- [Metrics details](#)

Subjects

- [Cell biology](#)
- [Cellular neuroscience](#)

The [Original Article](#) was published on 18 November 2020

[Download PDF](#)

Correction to: *Nature* <https://doi.org/10.1038/s41586-020-2942-0> Published online 18 November 2020

In Extended Data Fig. 1b of this Article, the graph for ‘SYD-2/liprin- α ’ was incorrect. The corrected graph is shown as Fig. 1 of this Amendment, together with the incorrect published graph, for transparency to readers. The accompanying source data is correct. The original Article has been corrected online.

Fig. 1: This figure displays the corrected and the incorrect published panels in Extended Data Fig. 1b of the original Article.



[Full size image](#)

Author information

Affiliations

1. Department of Biology, Stanford University, Stanford, CA, USA

Nathan A. McDonald & Kang Shen

2. Howard Hughes Medical Institute, Department of Biology, Stanford University, Stanford, CA, USA

Richard D. Fetter & Kang Shen

Authors

1. Nathan A. McDonald

[View author publications](#)

You can also search for this author in [PubMed](#) [Google Scholar](#)

2. Richard D. Fetter

[View author publications](#)

You can also search for this author in [PubMed](#) [Google Scholar](#)

3. Kang Shen

[View author publications](#)

You can also search for this author in [PubMed](#) [Google Scholar](#)

Corresponding author

Correspondence to [Kang Shen](#).

Rights and permissions

[Reprints and Permissions](#)

About this article



Check for
updates

Cite this article

McDonald, N.A., Fetter, R.D. & Shen, K. Author Correction: Assembly of synaptic active zones requires phase separation of scaffold molecules. *Nature* **595**, E35 (2021). <https://doi.org/10.1038/s41586-021-03340-6>

[Download citation](#)

- Published: 18 June 2021
- Issue Date: 08 July 2021
- DOI: <https://doi.org/10.1038/s41586-021-03340-6>

Comments

By submitting a comment you agree to abide by our [Terms](#) and [Community Guidelines](#). If you find something abusive or that does not comply with our terms or guidelines please flag it as inappropriate.

[Download PDF](#)

Advertisement

This article was downloaded by **calibre** from <https://www.nature.com/articles/s41586-021-03340-6>

| [Section menu](#) | [Main menu](#) |

Retraction Note: Complex societies precede moralizing gods throughout world history

[Download PDF](#)

- Retraction Note
- [Published: 07 July 2021](#)

Retraction Note: Complex societies precede moralizing gods throughout world history

- [Harvey Whitehouse](#)^{1 na1},
- [Pieter François](#)^{1,2 na1},
- [Patrick E. Savage](#)^{1,3 na1},
- [Thomas E. Currie](#)⁴,
- [Kevin C. Feeney](#)⁵,
- [Enrico Cioni](#)⁶,
- [Rosalind Purcell](#)⁶,
- [Robert M. Ross](#)^{1,7,8},
- [Jennifer Larson](#)⁹,
- [John Baines](#)¹⁰,
- [Barend ter Haar](#)¹¹,
- [Alan Covey](#)¹² &
- [Peter Turchin](#) ORCID: orcid.org/0000-0001-6996-7496^{13,14}

[Nature](#) volume 595, page 320 (2021) [Cite this article](#)

- 153 Altmetric
- [Metrics details](#)

Subjects

- [Anthropology](#)
- [Cultural evolution](#)
- [History](#)
- [Religion](#)

The [Original Article](#) was published on 20 March 2019

[Download PDF](#)

Retraction to: *Nature* <https://doi.org/10.1038/s41586-019-1043-4> Published online 20 March 2019

Following the publication of this Letter, Beheim and colleagues submitted a Matters Arising in which they argued that our primary results were called into question by our treatment of missing data¹. In our research, we attempted to test the ‘big gods’ hypothesis even-handedly using the best available evidence, and we made our data and code available during the review process and after publication, in line with best practice in open science. Nevertheless, we accept that we should have labelled moralizing gods as ‘absent’ or ‘inferred absent’ rather than ‘unknown’ in portions of our dataset before the dates of the first appearance, rather than converting ‘NAs’ to zeros during the phase of analysis. Since this Letter was published, we have thoroughly refined our data and analyses, and have found that our original conclusions are still strongly supported^{2,3}. However, the differences between our revised analyses and the original Letter are substantial enough to warrant a Retraction of the original Letter. We have submitted the enhanced analyses for peer review and potential publication in another journal. We encourage the community to refer to these new papers in future instead of this now-retracted Letter. We apologize to the scientific community for the unintended confusion.

References

1. 1.

Beheim, B. et al. Treatment of missing data determined conclusions regarding moralizing gods. *Nature* <https://doi.org/10.1038/s41586-021-03655-4> (2021).

2. 2.

Whitehouse, H. et al. Big Gods did not drive the rise of big societies throughout world history. Preprint at <https://doi.org/10.31219/osf.io/mbnvg> (2021).

3. 3.

Turchin, P., et al. Explaining the rise of moralizing religions: A test of competing hypotheses using the Seshat Databank. Preprint at <https://doi.org/10.31235/osf.io/2v59j> (2019).

[Download references](#)

Author information

Author notes

1. These authors contributed equally: Harvey Whitehouse, Pieter François, Patrick E. Savage

Affiliations

1. Centre for the Study of Social Cohesion, University of Oxford, Oxford, UK

Harvey Whitehouse, Pieter François, Patrick E. Savage & Robert M. Ross

2. St Benet's Hall, Oxford, UK

Pieter François

3. Faculty of Environment and Information Studies, Keio University,
Fujisawa, Japan

Patrick E. Savage

4. Human Behaviour & Cultural Evolution Group, Department of
Biosciences, University of Exeter, Penryn, UK

Thomas E. Currie

5. School of Computer Science and Statistics, Trinity College Dublin,
Dublin, Ireland

Kevin C. Feeney

6. Seshat: Global History Databank, Evolution Institute, San Antonio,
FL, USA

Enrico Cioni & Rosalind Purcell

7. ARC Centre of Excellence in Cognition and its Disorders and
Department of Psychology, Royal Holloway, University of London,
Egham, UK

Robert M. Ross

8. Department of Anthropology and Archaeology, University of Bristol,
Bristol, UK

Robert M. Ross

9. Department of Modern & Classical Language Studies, Kent State
University, Kent, OH, USA

Jennifer Larson

10. Faculty of Oriental Studies, University of Oxford, Oxford, UK

John Baines

11. Department of Chinese Language and Culture, Asia-Africa-Institute,
University of Hamburg, Hamburg, Germany

Barend ter Haar

12. Department of Anthropology, University of Texas at Austin, Austin,
TX, USA

Alan Covey

13. Department of Ecology and Evolutionary Biology, University of
Connecticut, Storrs, CT, USA

Peter Turchin

14. Complexity Science Hub Vienna, Wien, Austria

Peter Turchin

Authors

1. Harvey Whitehouse

[View author publications](#)

You can also search for this author in [PubMed](#) [Google Scholar](#)

2. Pieter François

[View author publications](#)

You can also search for this author in [PubMed](#) [Google Scholar](#)

3. Patrick E. Savage

[View author publications](#)

You can also search for this author in [PubMed](#) [Google Scholar](#)

4. Thomas E. Currie

[View author publications](#)

You can also search for this author in [PubMed](#) [Google Scholar](#)

5. Kevin C. Feeney

[View author publications](#)

You can also search for this author in [PubMed](#) [Google Scholar](#)

6. Enrico Cioni

[View author publications](#)

You can also search for this author in [PubMed](#) [Google Scholar](#)

7. Rosalind Purcell

[View author publications](#)

You can also search for this author in [PubMed](#) [Google Scholar](#)

8. Robert M. Ross

[View author publications](#)

You can also search for this author in [PubMed](#) [Google Scholar](#)

9. Jennifer Larson

[View author publications](#)

You can also search for this author in [PubMed](#) [Google Scholar](#)

10. John Baines

[View author publications](#)

You can also search for this author in [PubMed](#) [Google Scholar](#)

11. Barend ter Haar

[View author publications](#)

You can also search for this author in [PubMed](#) [Google Scholar](#)

12. Alan Covey

[View author publications](#)

You can also search for this author in [PubMed](#) [Google Scholar](#)

13. Peter Turchin

[View author publications](#)

You can also search for this author in [PubMed](#) [Google Scholar](#)

Corresponding author

Correspondence to [Patrick E. Savage](#).

Rights and permissions

[Reprints and Permissions](#)

About this article



Check for
updates

Cite this article

Whitehouse, H., François, P., Savage, P.E. *et al.* Retraction Note: Complex societies precede moralizing gods throughout world history. *Nature* **595**, 320 (2021). <https://doi.org/10.1038/s41586-021-03656-3>

[Download citation](#)

- Published: 07 July 2021
- Issue Date: 08 July 2021
- DOI: <https://doi.org/10.1038/s41586-021-03656-3>

Comments

By submitting a comment you agree to abide by our [Terms](#) and [Community Guidelines](#). If you find something abusive or that does not comply with our terms or guidelines please flag it as inappropriate.

[Download PDF](#)

Advertisement

This article was downloaded by **calibre** from <https://www.nature.com/articles/s41586-021-03656-3>

| [Section menu](#) | [Main menu](#) |